

New methods for light-mediated carbon-heteroatom cross-couplings

Inaugural-Dissertation

to obtain the academic degree

Doctor rerum naturalium (Dr. rer. nat.)

Submitted to the Department of Biology, Chemistry,
Pharmacy of Freie Universität Berlin

by

Sebastian Gisbertz

September 2021

This work was performed between July 2018 and July 2021 under the direction of Prof. Dr. Peter H. Seeberger in the Department of Biomolecular Systems, at the Max Planck Institute of Colloids and Interfaces.

1st reviewer: Prof. Dr. Peter H. Seeberger

2nd reviewer: Prof. Dr. Beate Kokschi

Date of oral defense: 23.02.2022

Acknowledgements

At this point I would like to thank everyone who made the last few years during the PhD an unforgettable time. Many of you weren't just excellent work colleagues but became also very good friends.

First of all, I'm deeply grateful to my supervisor Dr. Bartholomäus Pieber for the interesting topic of my PhD thesis and the opportunity to work according to my own ideas and thoughts. The permanent trust in my independent way of working and the inspiring scientific discussions were decisive for success this thesis.

I would like to thank Prof. Dr. Peter Seeberger for the great chance to perform my research in the Biomolecular Systems Department at the Max Planck Institute of Colloids and Interfaces and to supervise my PhD. I thank Prof. Dr. Beate Koksich for kindly agreeing to review this thesis.

I thank the International Max-Planck School on multi-scale biosystems to support my thesis with a scholarship.

Further I thank all collaborators for the fruitful and successful collaboration in several projects.

Since it would not be possible to work so smoothly without the permanent employees, I thank you warmly to all employees of the Biomolecular Systems department who take care of any matters to keep the business going. My special thanks go to Eva Settels as “good fairy” of analytics, Olaf Niemeyer for guarantee of functioning NMR and Dorothee Böhme for administrative help.

My gratitude goes to all members of the catalysis group for the great working environment: Amiera Madani, Cristian Cavedon, Lucia Anghileri, Susanne Reischauer and Noah Richter. I especially thank Cristian and Susanne for the pastime outside the laboratory and becoming good friends.

Lockdown time was not a piece of cake, game and BBQ nights with Susanne and Michael Traxler made it way more delightful, I really appreciate that.

I want thank my colleagues Agata Baryzewska, Antonella Rella, Ankita Malik, Eric Sletten, Giulio Fittolani, Jakob Wolf, Júlia Chaumel, Mara Guidi, Nieves Lopez Salas, Pietro Dallabernardina, Theodore Tyrikos-Ergas and all I may forgot to list for scientific advice and in particular for your friendship outside the institute. I am happy to have spent the PhD time

with all of you. A special shoutout to the core unit of the bouldering squad Cristian, Eric and Pietro.

To the former OSC Waldniel elite running crew, Kai Weyers, Martin Rohbeck, Niklas Podszus and René Giesen, for being excellent friends and the opportunity to always have a running wingman at home.

Last but not least, my biggest thanks go to my family and my girlfriend Nicole Bertges for the continued support during my studies and PhD. Both in calm and in turbulent times, I could always rely on you. You always have an open ear for me and always given me a place to retreat. Thank you that you exist!

List of Publications

Gisbertz, S.; Pieber, B. Heterogeneous photocatalysis in organic synthesis. *ChemPhotoChem* **2020**, 3, 611-620.

<https://doi.org/10.1002/cptc.202000014>

Pieber, B.; Malik, J. A.; Cavedon, C.; **Gisbertz, S.**; Savateev, A.; Cruz, D.; Heil, T.; Zhang, G.; Seeberger, P. H. Semi-Heterogeneous Dual Nickel/Photocatalysis using Carbon Nitrides: Esterification of Carboxylic Acids with Aryl Halides. *Angew. Chem. Int. Ed.* **2019**, 58, 9575-9580.

<https://doi.org/10.1002/anie.201902785>

Gisbertz, S.; Reischauer, S.; Pieber, B. Overcoming Limitations in Dual Photoredox/Nickel catalyzed C–N Cross-Couplings due to Catalyst Deactivation. *Nat. Catal.* **2020**, 4, 456-475.

<https://doi.org/10.1038/s41929-020-0473-6>

Rosso, C.; **Gisbertz, S.**; Williams, J. D.; Gemoets, H. P. L.; Debrouwer, W.; Pieber, B.; Kappe, C. O. An oscillatory plug flow photoreactor facilitates semi-heterogeneous dual nickel/carbon nitride photocatalytic C–N couplings. *React. Chem. Eng.* **2020**, 5, 597-604.

<https://doi.org/10.1039/D0RE00036A>

Cavedon, C.*; **Gisbertz, S.***; Vogl, S.; Richter, N.; Schrottke, S.; Teutloff, C.; Seeberger, P. H.; Thomas, A.; Pieber, B. Photocatalyst-Free, Visible-Light-Mediated Nickel Catalysis for Carbon–Heteroatom Cross-Couplings. *ChemRxiv. Preprint.* August 4, **2021**.

<https://doi.org/10.26434/chemrxiv-2021-kt2wr>

**These authors contributed equally.*

Table of Contents

Summary	1
Zusammenfassung	3
1 Introduction	5
1.1 C-N cross-couplings	5
1.2 Metallaphotocatalysis	12
1.3 Chromoselective catalysis	23
1.4 Flow chemistry for photochemical reactions	26
1.5 Aim of this Thesis	31
1.6 References	33
2 Heterogeneous photocatalysis in organic synthesis	45
2.1 Introduction	46
2.2 Metal oxides: TiO ₂	47
2.3 Bismuth oxide	59
2.4 CdSe, CdS	60
2.5 Lead halide perovskites	65
2.6 Carbon nitrides	67
2.7 Conjugated Microporous Polymers (CMPs)	75
2.8 Covalent Organic Frameworks (COFs)	83
2.9 Metal organic frameworks (MOFs)	87
2.10 Conclusions	93
2.11 References	94
3 Semi-heterogeneous dual nickel/photocatalysis using carbon nitrides: esterification of carboxylic acids with aryl halides	107
3.1 Introduction	109
3.2 Results and discussion	110
3.3 Conclusion	118
3.4 Supporting information	119
3.5 References	171

4	Overcoming Limitations in Dual Photoredox/Nickel catalyzed C–N Cross-Couplings due to Catalyst Deactivation	175
4.1	Introduction	177
4.2	Results and discussion	179
4.3	Conclusion	190
4.4	Supporting information	191
4.5	References	287
5	An oscillatory plug flow photoreactor facilitates semi-heterogeneous dual nickel/carbon nitride photocatalytic C–N couplings	295
5.1	Introduction	297
5.2	Results and discussion	299
5.3	Conclusions	309
5.4	Supporting information	310
5.5	References	338
6	Photocatalyst-free, visible-light-mediated nickel catalysis for carbon–heteroatom cross-couplings	345
6.1	Introduction	347
6.2	Ligand design and evaluation	349
6.3	Scope and limitations	353
6.4	Polymerization of czbpy for heterogeneous, visible-light-mediated nickel catalysis	355
6.5	Conclusion	358
6.6	Supporting information	359
6.7	References	433
7	Discussion & Outlook	441
7.1	Discussion of the individual works in a common context	441
7.2	Semi-heterogeneous dual nickel/photocatalytic carbon-heteroatom cross-couplings using graphitic carbon nitrides	444
7.3	Photocatalyst-free, visible-light-mediated nickel catalysis for carbon–heteroatom cross-couplings	448
7.4	Outlook	451
7.5	References	452

Statement of Authorship / Selbstständigkeitserklärung

I hereby certify that the herein presented dissertation was authored by myself and was completed using only the cited literature and sources. This thesis is submitted to the Department of Biology, Chemistry, Pharmacy of Freie Universität Berlin to obtain the academic degree Doctor rerum naturalium (Dr. rer. nat.) and has not been submitted for any other degree.

Hiermit versichere ich, dass ich die vorliegende Dissertation selbstständig und lediglich unter Benutzung der angegebenen Quellen und Hilfsmittel verfasst habe. Diese Arbeit wird beim Fachbereich Biologie, Chemie, Pharmazie der Freien Universität Berlin zur Erlangung des akademischen Grades Doctor rerum naturalium (Dr. rer. nat.) eingereicht und wurde für keinen anderen Abschluss eingereicht.

Potsdam, 14.09.2021

Sebastian Gisbertz

Summary

The selective formation of carbon-heteroatom bonds is important in synthetic organic chemistry due to the presence of heteroatoms in multiple natural products and active pharmaceutical ingredients. Over the last decade, photocatalysis has become a powerful tool for the formation and cleavage of bonds in synthetic chemistry. Carbon-carbon and carbon-heteroatom bond forming reactions that traditionally required rare and sophisticated palladium catalysts can be carried out using nickel catalysis in combination with visible-light photocatalysis under mild conditions. Key to the success of this strategy is the ability of the photocatalyst (PC) to engage in energy or electron transfer events that activate thermodynamically stable Ni^{II} intermediates and induce reductive elimination of the desired products. Still, the need of a dedicated photocatalyst based on noble metals, such as iridium- or ruthenium-polypyridyl complexes, represents a major drawback that results in high costs, tedious purification procedures, and renders the sustainability of these reactions low.

Heterogeneous semiconductors that absorb visible light are emerging as promising and sustainable alternatives to homogeneous noble metal-based photocatalysts (Chapter 2). In particular, graphitic carbon nitrides, a class of metal-free, polymeric semiconductors, are promising candidates for replacing homogeneous photocatalysts. These materials can be prepared from inexpensive and abundant bulk chemicals and absorb visible light up to 700 nm. Light irradiation generates an electron-hole pair, consisting of an excited electron in the conduction band and an electron hole in the valence band of the semiconductor, which can induce a single electron transfer event. A combination of the carbon nitride material CN-OA-m, a Ni^{II} salt and a bipyridyl ligand can catalyze the cross-coupling of aryl iodides and carboxylic acids using white light irradiation (Chapter 3). The carbon nitride material was prepared by polymerization of urea and oxamide and is insoluble in all common organic solvents. Simple centrifugation of the reaction mixture allowed recovering and reusing the photocatalyst up to five times without loss in reactivity.

The applicability of the heterogeneous photocatalyst was expanded to related C-N cross couplings. The deactivation of the nickel catalyst by the photocatalyst is responsible for limitations and reproducibility issues. (Chapter 4). Suitable methods that allow controlling the rate of oxidative addition and reductive elimination, or by stabilizing a key intermediate, expanded significantly the scope of this reaction.

A specially adapted continuous flow method was applied to run the improved C–N coupling method on large scales (Chapter 5). By combining an oscillatory pump with a microstructured plug flow photoreactor, a stable suspension of the heterogeneous photocatalyst can be maintained, circumventing clogging of the reactor channels. Short residence times (20 min) were achieved using optimized conditions and the recyclability of the photocatalyst was demonstrated over 10 cycles with no loss of activity. Moreover, the method was applied for the gram scale synthesis of an intermediate of the active pharmaceutical ingredient tetracaine.

In metallaphotocatalysis, an exogenous photocatalyst is normally responsible for utilizing the energy of photons to activate a nickel catalyst for carbon–heteroatom cross-couplings. A new ligand, 5,5'-dicarbazolyl-2,2'-bipyridyl (czbpy), was developed that forms a nickel complex, which absorbs light up to 450 nm. This homogeneous complex promotes the cross-couplings of aryl halides with various nucleophiles to form C–S, C–O and C–N bonds using visible light in the absence of an exogenous photocatalyst. The ligand can be polymerized to form porous organic polymer. This heterogeneous ligand framework can immobilize nickel and catalyze visible-light-mediated cross-couplings with similar activity to the homogeneous analogue. The heterogeneous catalytic material can be recovered after the reaction and reused several times without addition of the nickel salt at each cycle (Chapter 6).

Zusammenfassung

Die Knüpfung von Kohlenstoff-Heteroatom-Bindungen ist aufgrund des häufigen Vorkommens von Heteroatomen in zahlreichen Naturstoffen und pharmazeutischen Wirkstoffen ein wichtiges Forschungsgebiet in der synthetischen organischen Chemie. In den letzten zehn Jahren hat sich die Photokatalyse zu einem leistungsstarken Werkzeug für die Bildung und Spaltung von Bindungen in der Synthesechemie entwickelt. Kohlenstoff-Kohlenstoff- und Kohlenstoff-Heteroatom-Bindungsbildungsreaktionen, die traditionell seltene und hochentwickelte Palladiumkatalysatoren erforderten, können durch Nickelkatalyse in Kombination mit Photokatalyse mit sichtbarem Licht unter milden Bedingungen vollzogen werden. Der Schlüssel zum Erfolg dieser Strategie ist die Fähigkeit des Photokatalysators (PC), an Energie- oder Elektronentransferereignissen teilzunehmen, die thermodynamisch stabile Ni^{II} -Zwischenstufen aktivieren und somit eine reduktive Eliminierung der gewünschten Produkte induzieren. Die Notwendigkeit eines speziell angepassten Photokatalysators auf Basis von seltenen Edelmetallen wie Iridium- oder Ruthenium-Polypyridyl-Komplexen ist nachteilig, da die hohen Kosten und langwierigen Reinigungsverfahren die Nachhaltigkeit dieser Reaktionen negativ beeinflussen.

Als vielversprechende und nachhaltige Alternativen zum homogenen PC entwickeln sich heterogene Halbleiter, die sichtbares Licht absorbieren (Kapitel 2). Insbesondere graphitische Kohlenstoffnitride, eine Klasse metallfreier, polymerer Halbleiter, sind Hoffnungsträger für einen geeigneten Ersatz der seltenen, homogenen Photokatalysatoren. Diese Materialien können aus günstigen und reichlich vorhandenen Massenchemikalien hergestellt werden und absorbieren sichtbares Licht bis zu 700 nm. Eine Bestrahlung mit Licht erzeugt ein Elektron-Loch-Paar, bestehend aus einem angeregten Elektron im Leitungsband und einem Elektron-Loch im Valenzband des Halbleiters, die einen Einzelelektronentransfer induzieren können. Eine Kombination aus dem Kohlenstoffnitridmaterial CN-OA-m, einem Ni^{II} -Salz und einem Bipyridyl-Liganden kann die Kreuzkupplung von Aryliodiden und Carbonsäuren unter Weißlichtbestrahlung katalysieren (Kapitel 3). Das Kohlenstoffnitridmaterial wurde durch Polymerisation von Harnstoff und Oxamid hergestellt und ist in allen gängigen organischen Lösungsmitteln unlöslich. Durch einfaches Zentrifugieren des Reaktionsgemisches konnte der Photokatalysator bis zu fünfmal ohne Aktivitätsverlust gewonnen und wiederverwendet werden.

Die Anwendbarkeit des heterogenen Photokatalysators wurde auf verwandte C–N-Kreuzkupplungen ausgeweitet. Die Deaktivierung des Nickelkatalysators durch den Photokatalysator ist für Limitierungen in der Anwendung und eine schlechte Reproduzierbarkeit verantwortlich (Kapitel 4). Geeignete Methoden, die es ermöglichen, die Geschwindigkeit der oxidativen Addition und reductiven Eliminierung zu kontrollieren oder ein Schlüsselintermediat zu stabilisieren, erweiterten den Anwendungsbereich dieser Reaktion erheblich.

Eine speziell angepasste kontinuierliche Durchflussmethode wurde angewendet, um die verbesserte C–N-Kopplungsmethode im großen Maßstab durchzuführen (Kapitel 5). Durch die Kombination einer Oszillationspumpe mit einem mikrostrukturierten Pfropfenströmungs-Photoreaktor kann eine stabile Suspension des heterogenen Photokatalysators aufrechterhalten werden, wodurch ein Verstopfen der Reaktorkanäle vermieden wird. Unter optimierten Bedingungen wurden kurze Verweilzeiten (20 min) erreicht und die Recyclingfähigkeit des Photokatalysators über 10 Zyklen ohne Aktivitätsverlust nachgewiesen. Darüber hinaus wurde das Verfahren zur Synthese eines Zwischenprodukts des Wirkstoffs Tetracain im Grammmaßstab eingesetzt.

In der Metallphotokatalyse ist normalerweise ein exogener Photokatalysator dafür verantwortlich, die Energie von Photonen zu nutzen, um einen Nickelkatalysator für Kohlenstoff-Heteroatom-Kreuzkupplungen zu aktivieren. Der synthetisierte Ligand 5,5'-Dicarbazolyl-2,2'-bipyridyl (czbpy) bildet mit Nickel einen Komplex, der Licht bis zu 450 nm absorbieren kann. Der gebildete, homogene Nickelkomplex ist in der Lage die Kreuzkupplungen von Arylhalogeniden mit verschiedenen Nucleophilen unter Bildung von C–S-, C–O- und C–N-Bindungen mit sichtbarem Licht und ohne zusätzlichen Photokatalysator zu ermöglichen. Der Ligand kann zu einem porösen organischen Polymer umgesetzt werden. Dieses heterogene Ligandengerüst kann Nickel immobilisieren und durch sichtbares Licht vermittelte Kreuzkupplungen mit ähnlicher Aktivität wie das homogene Analogon katalysieren. Das heterogene, katalytische Material kann nach der Reaktion zurückgewonnen und mehrmals, ohne Zugabe des Nickelsalzes bei jedem Zyklus, wiederverwendet werden (Kapitel 6).

Chapter 1

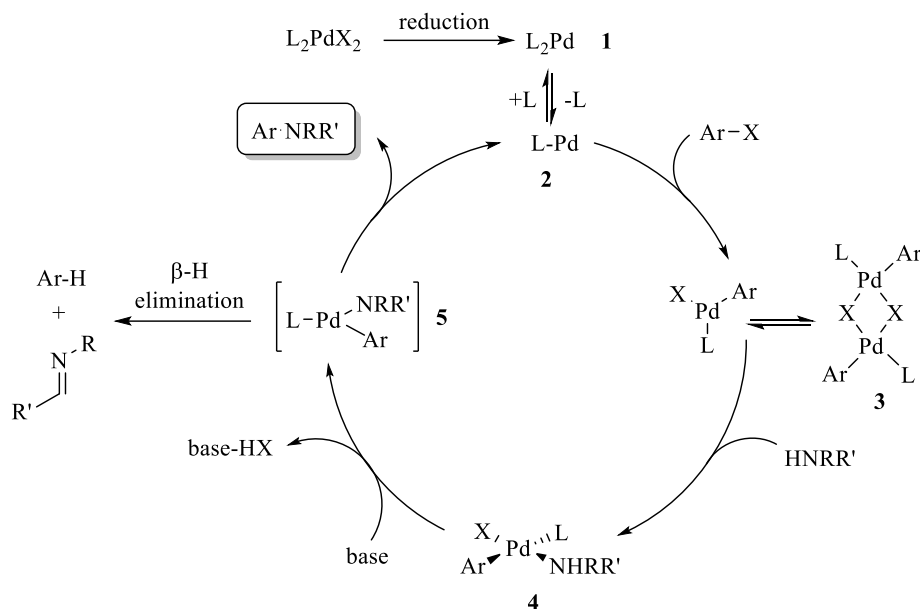
Introduction

This chapter provides a foundation for the scientific background and notions necessary to understand the concepts utilized within this thesis. Chapters 2 - 6 report the publications listed at page vii, reformatted but with unaltered content. For each publication, supporting information containing experimental details is included. A discussion of the individual projects and their interpretation within the overall dissertation is given in Chapter 7.

1.1 C–N cross-couplings

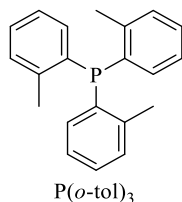
Aryl amines are common core motifs in many natural products, agrochemicals and pharmaceutically-relevant compounds.¹⁻² Transition metal catalyzed C–N cross-coupling reactions enable rapid construction of this scaffold from relatively simple starting materials.³ The Pd-catalyzed coupling of amines with aryl (pseudo)halides is the most applied method to form (hetero)aryl amines in academia and industry.^{2, 4} This reaction was independently developed by the groups of Buchwald⁵ and Hartwig⁶ and was inspired by earlier efforts of Migita and co-workers using amino stannane reagents⁷. In their initial studies, a range of secondary amines were coupled with functionalized bromoarenes to the corresponding arylamines using tri-*o*-tolylphosphine (P(*o*-tol)₃) as ligand for a Pd⁰ species, which is formed *in situ* from a Pd^{II} precatalyst. Mechanistic studies revealed that the catalytically Pd⁰ species **2**, containing one phosphine ligand, is formed after reduction of Pd^{II} precursor and through initial reversible dissociation of one phosphine ligand from inactive Pd⁰ species **1** (see Scheme 1.1, A).⁸ After that, oxidative addition of an aryl halide to **2** occurs and dimeric complex **3** is formed, which equilibrates with the corresponding monomer. It was examined that palladium in the presence of primary amines shows the tendency to form catalytically inactive palladium bis(amine) complexes by the reaction of **3** with an excess of the amine. This is admittedly responsible for the insufficient coupling of primary amines using the first generation of phosphine ligands.⁹ In the case of bromide bridged dimers, the cleavage of **3** readily proceeds in the presence of an amine to form **4**. In contrast, the process to cleave the iodide bridged analogue was found to be endergonic, which might be responsible for the lower efficiency observed in the amination of aryl iodides compared to aryl bromides.⁹ Due

to the enhanced acidity of the amine that results from the coordination to the palladium center in complex **4**, the *N*-nucleophile can be deprotonated by a strong metalorganic base, such as $\text{M}Ot\text{Bu}$ ($\text{M} = \text{Li}, \text{Na}$) or $\text{LiN}(\text{SiMe}_3)_2$. The resulting three-coordinate Pd^{II} alkylamido complex **5** can subsequently undergo reductive elimination to form the desired C–N bond. A β -hydride elimination from a palladium imine complex, which can be formed from **5** and leads to the formation of the reduced arene, competes with the reductive elimination of the desired product.



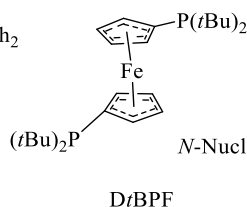
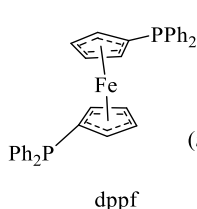
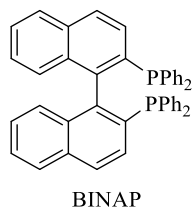
Scheme 1.1. Catalytic cycle proposed for the Pd-catalyzed amination of aryl halides using monophosphine ligands.

In comparison to other strategies for the formation of $\text{C}(\text{sp}^2)\text{-N}$ bonds, such as nucleophilic aromatic substitutions ($\text{S}_{\text{N}}\text{Ar}$),¹⁰ or copper-mediated Ullmann-Goldberg¹¹⁻¹³ and Chan-Lam couplings,¹⁴⁻¹⁵ the Pd-catalyzed Buchwald-Hartwig amination has a significantly broader substrate, and often works under milder conditions. Though some drawbacks of the Ullmann-Goldberg coupling, for example, have been overcome through the combination of copper-based catalyst with chelating ligands^{11-12, 16} The success of the Buchwald-Hartwig coupling results from the strategic development of phosphine-, and NHC-ligands by rational design (Figure 1.1). More specifically, different generations of ligands were developed over the last 25 years to fine-tune the performance and broaden the scope of this transformation based on mechanistic insights.⁴

1st generation of phosphine ligands: Monophosphine ligands

Base: MO*t*BU, LiN(SiMe₃)₂
 Temperature: 55-100°C
 Typical catalyst-loading: 1-5 mol%

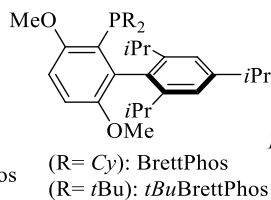
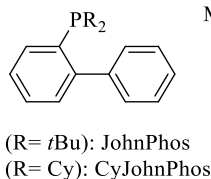
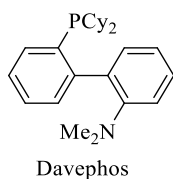
ArX: Aryl bromides *N*-Nucleophiles: Secondary amines

2nd generation of phosphine ligands: Aromatic bisphosphine ligands

Base: MO*t*BU
 Temperature: r.t.-110°C
 Typical catalyst-loading: 1-5 mol%

N-Nucleophiles: Primary & secondary amines, imines, lactams, azoles, sulfoximines

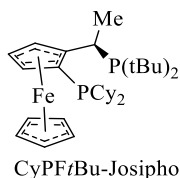
ArX: Aryl bromides, chlorides iodides, triflates, tosylates

3rd generation of phosphine ligands: Sterically hindered monophosphine ligands

Base: MO*t*BU, aqueous MOH,
 soluble organic bases
 Temperature: r.t.-110°C
 Typical catalyst-loading: 0.01-5 mol%

N-Nucleophiles: Primary & secondary amines, α,α,α -trisubstituted primary amines, amides, ammonia, indoles, carbamates

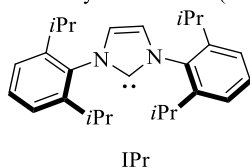
ArX: Aryl bromides, chlorides iodides, triflates, tosylates, mesylates

4th generation of phosphine ligands: Josiphos-based bidentate ligands

Base: MO*t*BU
 Temperature: r.t.-110°C
 Typical catalyst-loading: 0.001-1 mol%

ArX: Aryl bromides, chlorides iodides, triflates, tosylates, mesylates

N-Nucleophiles: Primary & secondary amines, hydrazones, lithium amides, ammonium salts, amides, ammonia

N-Heterocyclic Carbene (NHC) ligands:

Base: MO*t*BU
 Temperature: r.t.-80°C
 Typical catalyst-loading: 0.001- 1 mol%
 very short reaction times: 1min- 2h

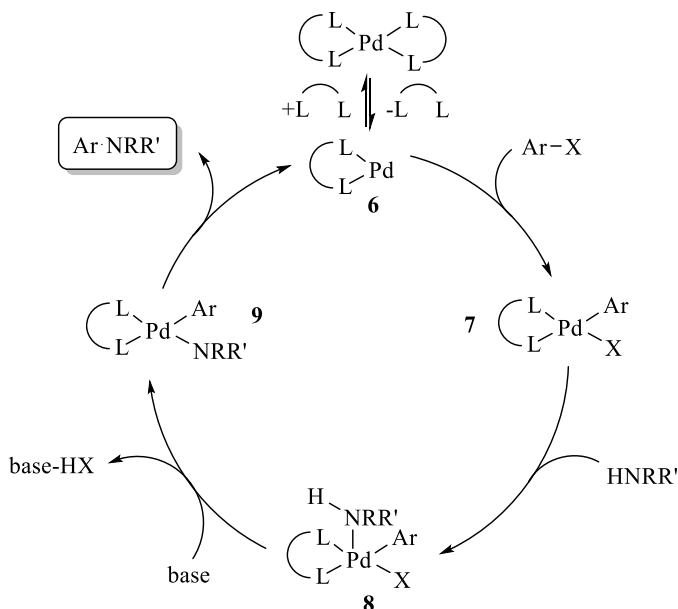
ArX: Aryl bromides, chlorides, tosylates

N-Nucleophiles: Secondary amines, anilines

Figure 1.1. Ligand evolution in palladium-catalyzed C–N cross-couplings.

The use of chelating aromatic bisphosphine ligands, like 2,2'-Bis(diphenylphosphino)-1,1'-binaphthyl (BINAP)¹⁷ or 1,1'-Bis(diphenylphosphino)ferrocene (dppf)¹⁸ as second generation of phosphine ligands facilitates reductive elimination of the desired product, thereby minimizing β -hydride elimination, which leads to undesired side-products in the

case of monophosphine ligands. This can be rationalized by the chelating effect that precludes the equilibration between four-coordinate Pd^{II} alkylamido complex **9** and an undesired palladium imine complexes that results from β -hydride elimination (see Scheme 1.2).



Scheme 1.2. Catalytic cycle proposed for the Pd-catalyzed amination of aryl halides using chelating bisphosphine as the ligand.

Thereby, successful arylation of primary amines was achieved.¹⁸⁻¹⁹ The complexes with these bidentate ligands enabled additionally the coupling of aryl iodides,²⁰ triflates,²¹ for the first time tosylates²² and the amination of aryl chlorides under mild conditions in certain cases.²² More sterically hindered bisphosphine variants enabled a broader scope of aryl halides and pseudohalides as well as *N*-nucleophiles.⁴

The oxidative addition of the aryl halide was identified as the rate-limiting step for bisphosphine ligands.⁴ High temperatures were required and the amination of aryl chlorides was still limited.²²⁻²³ Catalysts with higher activity that extend the substrate scope and allow for milder reaction conditions required synthesis of ligands that facilitate oxidative addition by increasing the electron density around the metal center. This was realized by sterically hindered dialkylbiaryl monophosphine ligands.²⁴ Strategic ligand design, which further included alkyl groups at the phosphine center of the ligand to promote oxidative addition

and enhanced steric bulk to support reductive elimination led to increased performance of the formed Pd complexes (Figure 1.2).

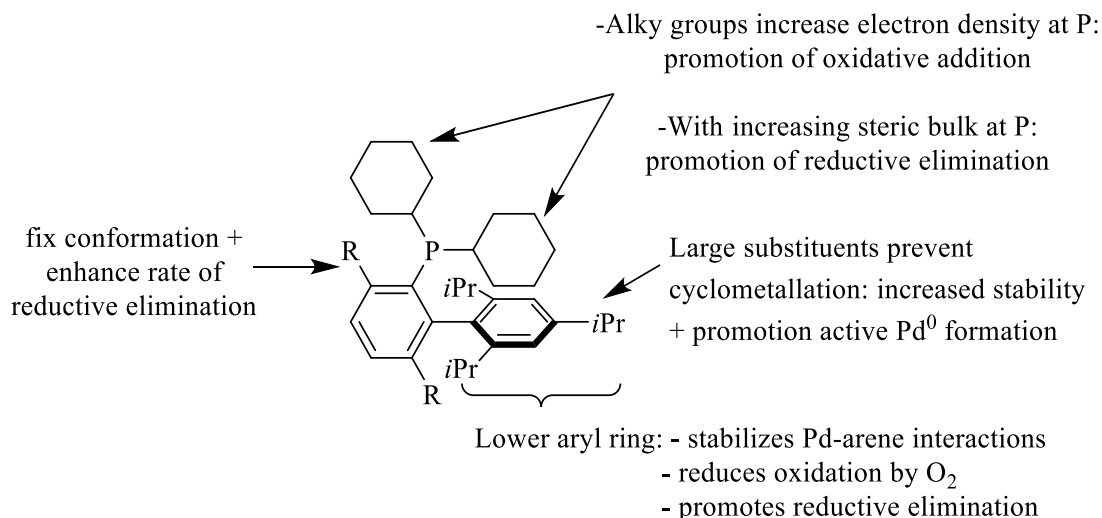


Figure 1.2. Influences of structural features of a dialkylbiaryl phosphine ligand onto the reaction performance in palladium-catalyzed C–N cross-couplings.²⁴⁻²⁵

The resulting, bulky monophosphine ligands, such as 2-Dicyclohexylphosphino-2'-(N,N-dimethylamino)biphenyl (DavePhos) and 2-(Dicyclohexylphosphino)3,6-dimethoxy-2',4',6'-triisopropyl-1,1'-biphenyl (BrettPhos) (see Figure 1.1), enabled the coupling of aryl bromides with primary and secondary amines at lower temperatures²³ and the challenging monoarylation of primary amines with aryl chlorides was achieved in certain cases.²⁶ Additionally, the scope could be extended to aryl mesylates²⁶ and the coupling of aryl chlorides with amides.²⁷ More recently it was even shown that the coupling of encumbered α,α,α -trisubstituted primary amines, which was challenging for a long time, is feasible with tailor-made dialkylbiaryl monophosphine ligands.²⁸

Although, remarkable achievements were obtained with biarylmonophosphine ligands, these protocols were still limited in terms of low selectivity for the monoarylation of primary amines and high catalyst loading was normally required for the amination of heteroaromatic halides. This challenge was tackled using Josiphos-based bidentate ligands ((2*R*)-1-[(1*R*)-1-(Dicyclohexylphosphino)ethyl]-2-(diphenylphosphino)ferrocene) (see Figure 1.1) that have customized steric and electronic properties to overcome these limitations.²⁹ The bulky groups surrounding the coordinating sites prevent a second arylation in the case of primary

Chapter 1

amine substrates, thereby increasing the selectivity towards monoarylated products. Due to high catalyst stability and resulting high turnover numbers it was feasible to use low catalyst loadings for the successful coupling of heteroaryl chlorides with primary nitrogen nucleophiles including amines, amides, imines, and hydrazones³⁰ as well as the amination of aryl bromides and iodides³¹ and (hetero)aryl tosylates.³² Even the challenging, selective monoarylation of ammonia was achieved using (R)-1-[(SP)-2-(Dicyclohexylphosphino)ferrocenyl]ethyl-di-tert-butylphosphine (CyPF-*t*-Bu) as ligand.³³

N-Heterocyclic carbenes (NHC) are a class of ligands for palladium-catalyzed C–N cross-couplings that proved to be a valuable alternative to phosphine ligands, because of their robustness and high degree of tunability.³⁴ Such catalysts show high productivity, work at room temperature³⁵ and reaction times of only a few minutes using low catalyst loadings,³⁶ (ppm amounts) were achieved. The coupling of (hetero)aryl bromides and chlorides proceeded effectively with secondary amines and anilines,³⁶ and also enabled aminations of aryl tosylates and triflates.³⁷ However, the coupling of base-sensitive substrates, and primary aliphatic amines remains challenging. To date, the scope of the developed protocols for this ligand class is limited compared to phosphine ligands, but the low catalyst loadings and high reactivity as well as their robustness and high degree of tunability of the well-defined Pd^{II} complexes of NHC ligands are benefits of this ligand class.^{34, 38-39}

The choice of ideal ligand strongly depends on the substrate combination. Numerous studies resulted in dedicated protocols that are able to access specific amines and aryl (pseudo)halides with high efficiency and improvements are constantly made in this field. It is worth noting, that other reaction parameters also have a significant impact on the C–N coupling. The efficient formation of the active, monoligated Pd⁰ catalyst species depends on the palladium source and is in this way a key factor in the selection of reaction conditions for Pd-catalyzed amination reactions.⁴⁰ Another important factor is the choice of the base and the reaction temperature. The deprotonation of the Pd^{II}-amine intermediate, which is formed in the catalytic cycle, can be rate-limiting when weak bases are used in Buchwald-Hartwig aminations.⁴¹ Therefore, mainly strong bases, such as NaOtBu, LHMDS, and high temperatures are needed to guarantee excellent reaction rates of the cross-coupling, but can interfere with the functional group tolerance and are often responsible for side product formation.²⁴

Even though it was shown that these methods are powerful tools, several drawbacks remain. With the exception of a tailored electron-deficient palladium complex bearing a modified dialkyl triarylmonophosphine ligand,⁴² strong inorganic bases are needed. For certain substrates high temperatures are required for efficient couplings, but this can lead to undesired formation of side products. Due to the low abundance of palladium in the Earth's crust⁴³ and the related high price,⁴⁴ sustainable and cost-effective alternatives are required. The most obvious alternative to Pd, which was already considered in the beginning of the development of the Buchwald-Hartwig amination, is nickel.⁴⁵ Although nickel-catalyzed aminations have been reported, these catalysts require elevated temperatures and/or strong bases,⁴⁶⁻⁴⁷ as well as sophisticated ligands.⁴⁸⁻⁵¹ The requirement of harsh conditions can be explained by the large energy barrier that has to be overcome to induce reductive elimination from Ni^{II}-aryl-amine intermediates, as shown in the seminal works by Hillhouse and coworkers.⁵²⁻⁵⁵ Besides tailoring ligands, two other concepts can be applied to address this issue. These are either manipulation of available oxidation states^{52, 56} or electronic excitation⁵⁷⁻⁶⁰ of nickel complexes. In recent years great attention has been paid to two powerful methodologies to displace stoichiometric reagents, which go along with stoichiometric waste and functional group intolerances,⁶¹ for single electron as well as energy transfer processes: electrochemistry⁶² and photocatalysis.⁶³

1.2 Metallaphotocatalysis

Basic principles in photocatalysis

Due to the changing trend in society towards sustainability, visible-light mediated photocatalysis became one of the fastest growing fields in organic chemistry over the last decade.⁶⁴ Major driving forces were the technical progress towards light sources with narrow emission windows, such as light emitting diodes (LEDs), and the development of molecules with long excited lifetimes, originally as components of e.g. dye-sensitized solar cells⁶⁵ and organic light-emitting diodes.⁶⁶

To identify and develop a photocatalyst for a desired transformation, the elementary, theoretical principles must be understood. Upon irradiation of a molecule with photons, which have the appropriate energy, transitions between the different energy levels of the light absorbing molecule are occurring. These transitions can be represented in a simplified manner with aid of a Jablonski diagram (Figure 1.3).

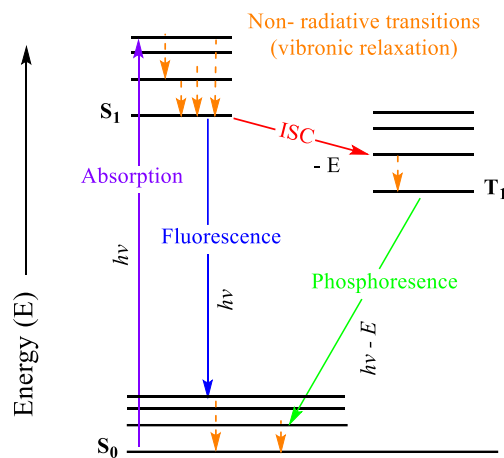


Figure 1.3. Jablonski diagram for the illustration of a molecule's electronic states and the transition between the states.

The starting point is the conversion of a molecule from its ground state S₀ to a singlet excited state S₁ upon the absorption of a photon with matching energy. At the electron level an electron is promoted from the highest occupied molecular orbital (HOMO) to the lowest unoccupied molecular orbital (LUMO) during this transition. Besides non-radiative transition *via* vibronic relaxation, two different processes can happen after excitation of the molecule to S₁. Either the relaxation of the molecule back to ground state S₀ with

simultaneous emission of energy as radiation (fluorescence) or the generation of a triplet excited state T_1 through intersystem crossing (ISC), which is associated with a loss of energy, occurs. In the second case the consecutive, radiative relaxation back from T_1 to S_0 (phosphorescence) is spin-forbidden. Consequently, triplet excited states are long-lived with lifetimes ranging from 100 ns to few μ s. In this way these T_1 states are suitable to take part in bimolecular processes and overcome limitation to be too short-lived for diffusion.

In a photochemical reaction, one of the reagents absorbs light, reaches an excited state and the desired reaction can take place. As the reagent would be otherwise inert, the excitation with light is needed. The major advantage of visible-light photocatalysis is that the desired reaction sequence is initiated by the excited state of a dedicated chromophore (photocatalyst, PC) upon absorption of photons with appropriate energy, whereas all other ingredients in the reaction mixture do not interact with this energy source as (organic) molecules typically only absorb UV light. By avoiding high energetic UV light, little potential exists for deleterious side reactions that might arise from photoexcitation of the substrate itself.⁶⁷ Further, off-cycle reactions of the photocatalyst lead to a lower quantum yield (Φ),⁶⁸ but scarcely to a diminished yield of the desired product.

The excited state of the photocatalyst (PC^*) can initiate reactions *via* different mechanisms. The two most important modes of action are photoredox catalysis (PRC) and energy transfer catalysis (EnT). In photoredox catalysis single electron transfer (SET) events between the photocatalyst and reagents are responsible for quenching of PC^* and formation of reactive radical intermediates (Figure 1.4). After excitation of the photocatalyst by light to S_1 and ISC to T_1 , the triplet excited state can be quenched in two different ways. This depends on several factors, such as redox potential of the triplet species and the type of quencher. In one case, a reductive quenching cycle is the mode of action. In course of this the excited PC is first quenched by an electron donor in a single electron oxidation step and after that the reduced form of the PC ($PC^{\cdot-}$) reduces an electron acceptor, which brings the PC back to its ground state S_0 . In the opposite case, in the so-called oxidative quenching cycle, PC^* first interacts with an electron acceptor and undergoes a single electron oxidation, which is responsible for the quenching. This is followed by a reduction of the oxidized form of the PC ($PC^{\cdot+}$) by single electron oxidation of an electron donor to turn over the catalyst.

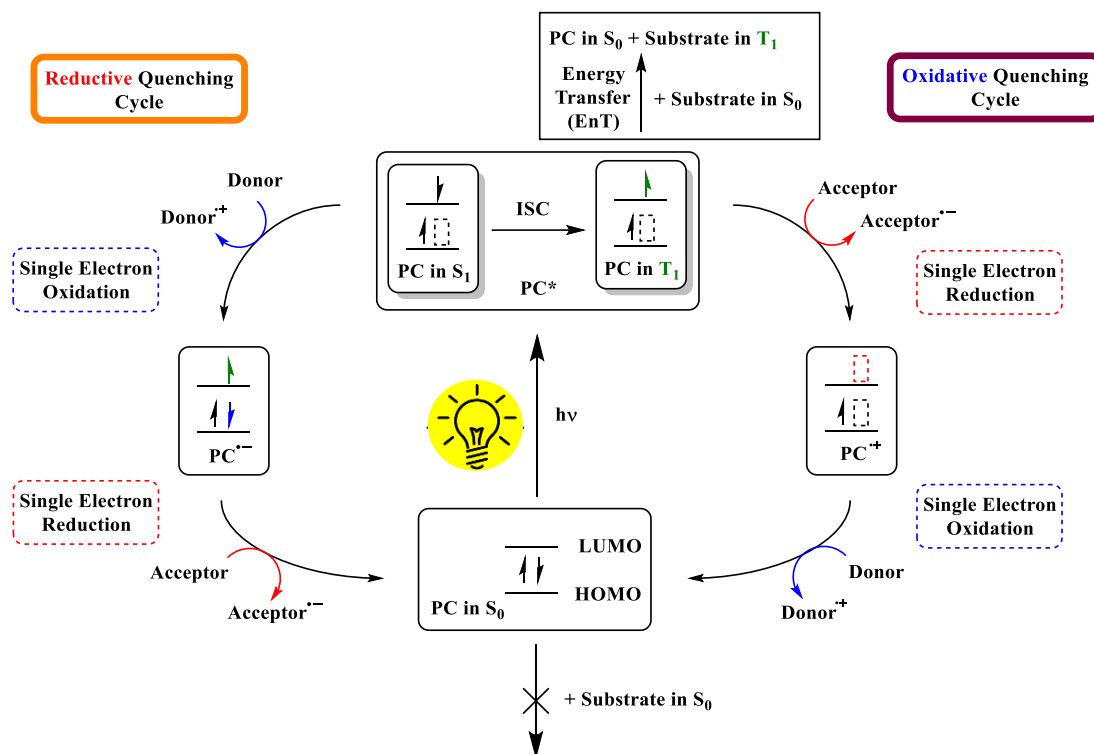


Figure 1.4. Possible pathways of photo(redox) catalysis after light illumination and quenching *via* electron transfer or energy transfer.

An excited state of a photocatalyst (PC*) can alternatively also transfer its excited state energy to a substrate, reagent or intermediate catalytic species, which acts as the acceptor (A). Two possible mechanisms are possible: Dexter-type or Förster-type energy transfer (Figure 1.5).⁶⁹

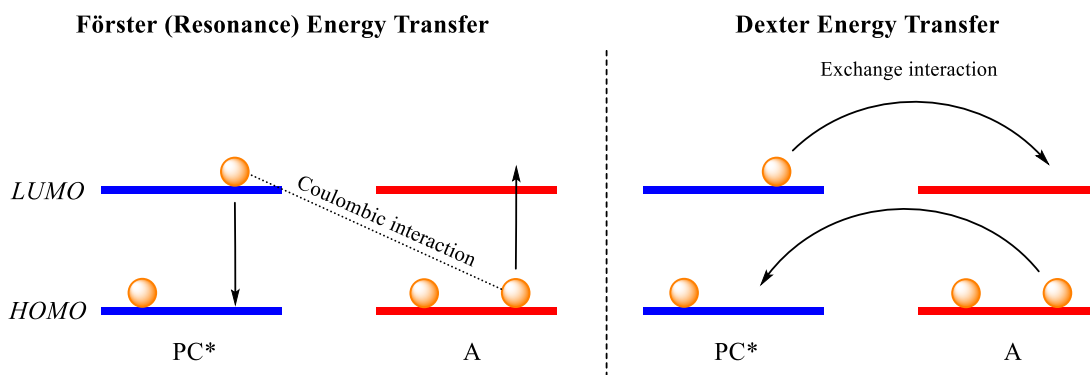


Figure 1.5. Förster vs. Dexter EnT process.

In the Förster theory, it is assumed that an electronic oscillation of D* induces *via* dipole-dipole (coulombic) interactions an electronic oscillation in the ground state of A, which

excites the electron from acceptor's HOMO to LUMO. The model of Dexter-type EnT describes the simultaneous intermolecular exchange of ground state and excited state electrons from the acceptor to PC*, respectively from PC* to acceptor (Figure 1.5). The electron in the LUMO of PC* is transferred into the LUMO of the acceptor and simultaneously one electron in the acceptor's HOMO into the HOMO of PC*. On this account, a direct physical contact, in terms of orbital overlap of PC* and A is demanded. This also means that the rate of Dexter EnT decays exponentially with increasing donor-acceptor separation. In case of a fast electron transfer the diffusion of PC* and A is the limiting factor. Thus, properties of the solvent can become significant parameters for the reaction. For the Förster theory a returned conversion of the photocatalyst triplet state to its singlet ground state is needed. The resulting dipole oscillation would induce a concurrent excitation of the substrate from its singlet ground state to an excited triplet state. However, two spatially separated spin reversal processes are prohibited⁶⁹ and therefore the Förster theory is unsuitable to describe the EnT process from a photocatalyst's excited triplet state to a substrate in solution. Based on this restrictions, Dexter-type EnT mechanism must be in action in EnT processes using photocatalysis for organic synthesis.

In order to use light as an abundant, non-hazardous, and sustainable reagent⁷⁰ in an efficient manner, a photocatalyst needs to fulfill different criteria. To avoid deleterious side reactions using UV light, the photocatalyst should absorb in the visible light region (400-700 nm). As the PC takes part in bimolecular processes, the excited states must survive the time range of diffusion of the PC to the substrates. Therefore, long-lived excited lifetimes are a key feature of an adequate PC. Additionally, the excited state of the PC should have the fitting energy or redox potentials for a respective transformation. The better the properties of the excited photocatalyst match the optimal excited state energy or redox potential of the tackled reaction, the better the selectivity and reaction rate will be.

Main classes of photocatalysts

There are different molecules and materials, which can meet these criteria. The most common photocatalyst can be assigned to three different classes: organometallic complexes, organic dyes and heterogeneous semiconductors.

Organometallic complexes like ruthenium and iridium-polyridyl complexes (Figure 1.6) are popular photocatalysts, because they undergo a metal-to-ligand charge transfer (MLCT) upon irradiation with visible light.⁶⁷

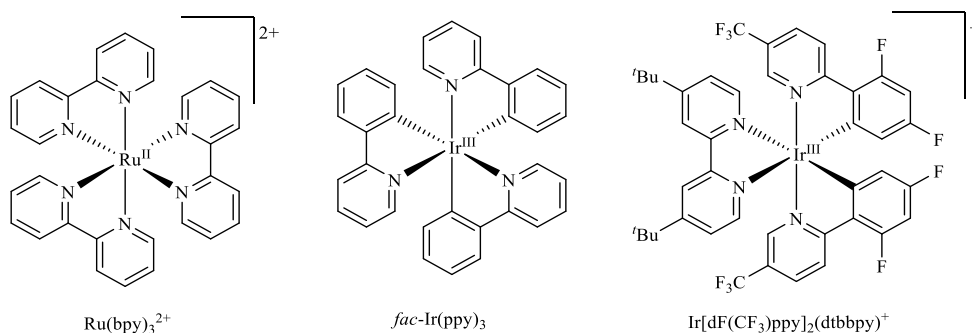


Figure 1.6. Selected noble metal-based organometallic photoredox catalyst.

The ligand-centered π^* orbital of these complexes is lower in energy than the metal-centered e_g -orbital, which implies that after visible light illumination an electron is transferred from the t_{2g} -orbital (metal) to the π^* orbital (ligand). This allows the ability to readily tune the redox potentials for a given reaction by altering the metal or changing the ligands. The resulting excited singlet states (S_1) can then go through a rapid intersystem-crossing (ISC) to form triplet states (T_1), which have long-lived triplet excited states (~ 1000 ns). These excited states can readily donate a high-energy electron from the ligand π^* orbital (function as a reductant) or accept an electron into the low-energy metal-centered hole (function as an oxidant). Alternatively, the energy of the excited states can also engage other molecules *via* EnT processes. This class of photocatalyst is very powerful due to their unique properties and ability to be designed for a specific reaction by the modification of the ligand and metal. However, their high cost and low sustainability based on the low abundance of these rare metals in the earth crust is a drawback. Copper complexes have been studied as alternatives, but didn't reach the efficiency of the rare metal complexes and found limited applications yet.⁷¹

Intensively studied, metal-free alternatives are organic dyes such as benzophenones, boron dipyrromethenes (BODIPY), phenoxazines and derivatives, xanthene dyes, cyanoarenes and acridinium salts, among others (Figure 1.7).⁷²

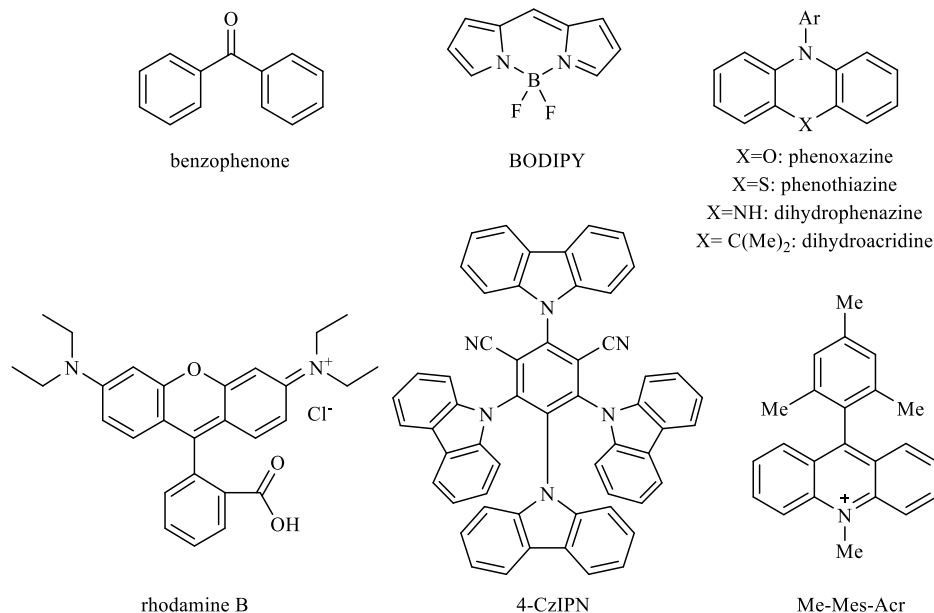


Figure 1.7. Selected organic dyes for photocatalysis.

The benefits of this photocatalyst's class are the low costs and the ability to tune the optical and electronical properties by chemical modification. A barrier for broad application is that only few organic dyes have long enough excited state lifetimes to participate in bimolecular energy or electron transfers. Dyes like 4-CzIPN and phenoxazine (Figure 1.7) meet the criteria of long excited state lifetimes as their excited single states can experience intersystem crossing to generate triplet states with lifetimes of several μs . Dyes like Rhodamine B or benzophenone derivatives do often not undergo ISC under synthetically relevant conditions and the excited-state lifetimes of their singlet excited states ranges in area of few ns, which is in most cases not suitable for bimolecular processes.

Sustainable, heterogeneous alternatives are medium bandgap semiconductors as the energy difference between valence (VB) and conduction band (CB) corresponds to energy of photons in the visible light region. Upon irradiation with visible light with photonic energy higher than the semiconductor's bandgap an electron is excited from VB to CB and thereby an electron-hole-pair is formed. The electron hole in the VB can undergo single electron

oxidation with electron donors and the excited electron in the CB can participate in single electron reductions of electron acceptors (Figure 1.8).

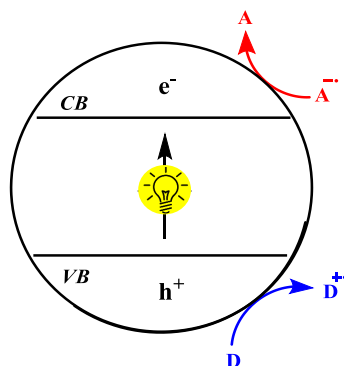


Figure 1.8. Charge separation in semiconductors upon light absorption and interaction with electron donor and acceptor.

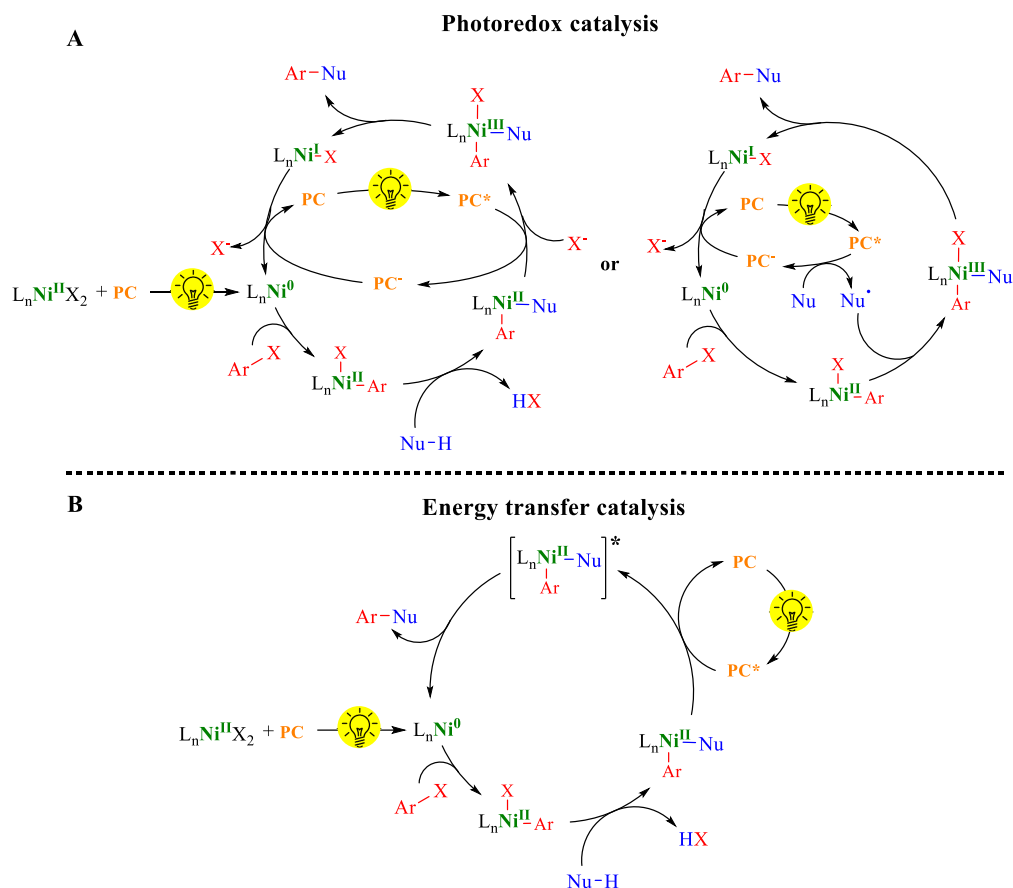
Inorganic semiconductors, which can harvest visible light for single electron transfer processes, are cadmium sulfide, cadmium selenide, lead perovskites and bismuth oxides. Carbon nitrides instead are organic, polymeric semiconductors that readily absorb visible light and were efficiently applied in heterogeneous photocatalysis.⁷³⁻⁷⁴ A detailed discussion of heterogeneous photocatalysts in organic synthesis can be found Chapter 2.

1.2.1 Dual nickel/ photocatalysis for carbon–heteroatom cross-couplings

As described in Chapter 1.1, the Ni^{II} intermediates in carbon-heteroatom cross-coupling reactions which are formed before reductive elimination, are thermodynamically stable. Therefore large energy barriers must be overcome to induce reductive elimination from, for example, Ni^{II}-aryl-amine or Ni^{II}-aryl-alkoxy intermediates.⁵²⁻⁵⁴ Harsh conditions and sophisticated tailor-made ligands were applied to destabilize these Ni^{II} intermediates and thereby enable reductive elimination.^{46, 50, 75} The enhanced reactivity of metal catalysts on account of oxidation state modulation or excitation represents a complementary opportunity to the powerful, but laborious approaches using tailor-made ligand design for transition metal complexes. The oxidation of a metal complex vastly increases the thermodynamic driving force to undergo reductive elimination. Thereby, the formation of e.g. C–N and C–O bonds using nickel becomes possible.^{52-54, 76} The modulation of the oxidation states can be achieved using stoichiometric oxidants or reductants,⁵⁶ but this can go along with stoichiometric side products⁵² and can suffer from intolerance of certain functional groups, such as ketones and aldehydes.⁶¹ A more elegant approach is the merger of transition metal catalysis and photocatalysis, which is termed metallaphotocatalysis.⁷⁷ There are several combinations of photocatalysis with different transition catalysts, such as copper⁷¹ or palladium complexes,⁷⁸ but dual nickel/ photocatalysis has by far the biggest impact, especially for carbon-heteroatom bond formation.⁷⁹ These methods benefit additionally from mild conditions, in terms of low temperatures and soluble, weak organic bases.

Depending on the substrates, different mechanisms were proposed. In case of the coupling of aryl halides with amines and alcohols, it was assumed that a photocatalytic reduction of a Ni^{II} precatalyst generates an active Ni⁰ catalytic species that induces a Ni⁰/Ni^{II}/Ni^{III}/Ni^I-cycle (Scheme 1.3, A, left).⁸⁰⁻⁸¹ After formation of the catalytically active Ni⁰ species oxidative addition of the aryl halide occurs and a ligand exchange of an halide ligand with the nucleophile takes place. The excited photocatalyst causes a single electron oxidation from the formed thermodynamically stable Ni^{II} intermediate to Ni^{III} species. Reductive elimination becomes facile, the product is released and a Ni^I intermediate formed. Both catalysts are returned to their original oxidation states by the interaction of reduced photocatalytic species with the Ni^I species. This effectuates a single electron reduction from Ni^I to Ni⁰ and oxidizes the reduced photocatalysts. Alternatively, for the coupling of aryl

halides with thiols and anilines, it was suggested that the nucleophile is oxidized by the excited photocatalyst and in the presence of base a radical species is formed (Scheme 1.3, A, right).⁸²⁻⁸⁴ This radical species is intercepted by the Ni^{II}-aryl halide species, which is generated by oxidative addition of the aryl halide to Ni⁰ species. The formed Ni^{III} complex undergoes facile reductive elimination. After reduction of the formed Ni^I intermediate by the reduced PC a new catalytic cycle is started.

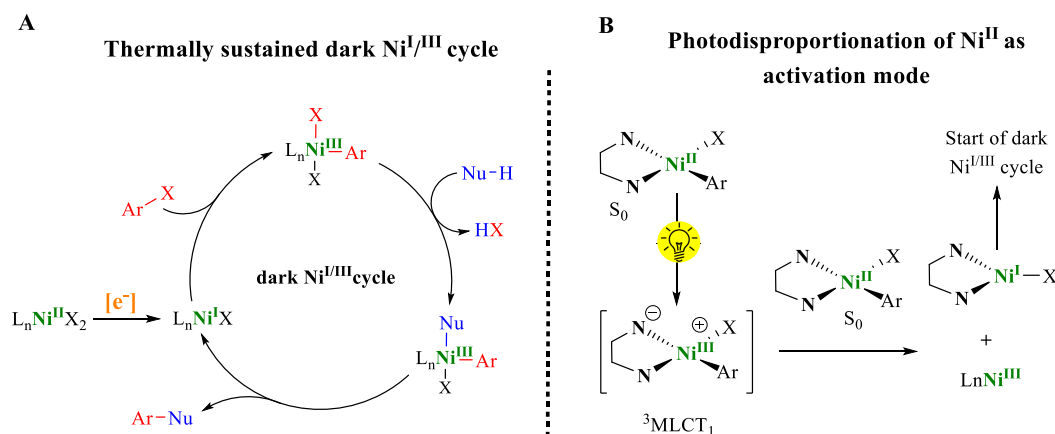


Scheme 1.3. (A) Photoredox catalyzed oxidation state modulations *via* SET for dual nickel/photoredox cross-coupling. (B) Activation of thermodynamic stable Ni^{II} intermediate with energy transfer catalysis.

Energy transfer catalysis was also proposed to be responsible for the destabilization of the stable Ni^{II} species to trigger reductive elimination in certain cases (Scheme 1.3, B).⁵⁹ After oxidative addition of an aryl halide to active Ni⁰, the Ni^{II} aryl halide intermediate undergoes rapid ligand exchange with a nucleophile to afford aryl-Ni^{II} nucleophile complex. Starting from this Ni^{II} species, a triplet excited-state Ni^{II} complex is generated *via* energy-transfer to facilitate the formation of carbon-heteroatom bonds. This mechanism was assumed for the

coupling of aryl halides with amines⁵⁹, sulfonamides⁸⁵ or carboxylic acids⁵⁷ based on different mechanistic investigations. Instead of normally required photoredox catalysts with long excited lifetimes and fitting redox potentials, for the dual nickel/photoredox catalyzed couplings involving sulfonamides and carboxylic acids initial control experiments showed that also organic photosensitizers can trigger the reactions. In case of C–O bond formation the reaction proceed even with moderate efficiency *via* direct excitation with a high-intensity light source in the absence of a photocatalyst after a longer reaction time. For the coupling of aryl halides with carboxylic and sulfonamides, Ir-based photocatalysts with higher triplet-state energies gave higher yield, while the higher the oxidation potential of the photocatalyst was, the lower the yield observed. Based on the positive correlation with triplet-state energies and negative correlation with oxidation potentials it was finally assumed that the transformations are facilitated by an energy-transfer process rather than SET. In a mechanistic study for dual nickel/photoredox catalyzed C–N bond formation the comparison between the calculated EnT rate constants by quantitative Förster theory and measured values by different nanosecond transient absorption (TA) and cyclic voltammetry (CV) quenching experiments prompted a Förster-type energy transfer from the excited-state photocatalyst to the Ni^{II} amine complex.⁵⁹

More recent mechanistic studies suggested another possible mechanism. After a photocatalytic single electron reduction of the Ni^{II} precatalyst, a Ni^I species might induces a self-sustained thermal Ni^I/Ni^{III} mechanism that does not require further photons (Scheme 1.4, A).⁸⁶⁻⁸⁸



Scheme 1.4. (A) Thermally-sustained dark Ni^I-Ni^{III} cycle induced by reduction with reductive species. (B) Photoinduced disproportionation of Ni^{II} complexes, which afterwards enters dark self-sustained Ni^I-Ni^{III} cycle.

Chapter 1

Catalyst deactivation can result from comproportionation of a Ni^{I} and Ni^{III} species or by reacting with radical cation of the base. The photocatalyst likely re-activates these deactivated species to form the catalytic active Ni^{I} species.⁸⁶ These findings are supported by the fact that a photocatalyst-free C–O and C–N couplings of aryl halides using substoichiometric amounts of zinc for the initial reduction of the inactive Ni^{II} complex to start the self-sustaining $\text{Ni}^{\text{I}}/\text{Ni}^{\text{III}}$ cycle were reported.⁸⁹

Photophysical studies of nickel-bipyridyl aryl complexes showed that these Ni^{II} complexes can absorb low-energetic UV-light and this cause metal-to-ligand charge transfer transitions.⁹⁰⁻⁹¹ In this way excited Ni^{II} complexes ($^3\text{MLCT}$) can react with a Ni^{II} ground state species (S_0) forming a Ni^{I} and Ni^{III} species (Figure 1.4, B). These are active in the before mentioned dark self-sustained catalysis for productive carbon-heteroatom bond formation. This was supported by the efficient formation of aryl ethers⁹² and aryl amines⁹³ using 390 nm irradiation and a nickel-polypyridyl aryl complex as precatalyst. In this case no additional photocatalyst for excitation of these nickel catalysts is needed, but the requirement of UV light irradiation is associated with side reactions and can hamper the reaction selectivity.⁶⁴

Regardless of the mechanisms, precious metal complexes as photocatalysts are predominantly used to harvest visible-light as energy source. Their limited amount within the Earth's crust contradicts the sustainability goal of replacing rare metals such as palladium with more abundant nickel in cross-couplings. A possible option to exchange noble metal-polypyridyl complexes⁶⁷ with synthetic organic dyes^{72, 94} can achieve comparable efficiencies, but photobleaching is problematic.⁹⁴⁻⁹⁵ All homogeneous catalysts are difficult to recycle, if possible at all. Promising, stable and recyclable alternative photocatalysts are semiconducting materials.^{73, 96-98} Different classes of semiconductors and other heterogeneous photocatalysts for synthetic applications are discussed in detail in Chapter 2.

1.3 Chromoselective photocatalysis

The vast majority of homogeneous iridium or ruthenium polypyridyl complexes and many organic dyes that have suitable redox potentials or triplet energies for photocatalysis suffer from their limitation to blue light. Photocatalytic strategies that use the entire visible light spectrum to enable efficient solar harvesting would be beneficial. A broader absorbance range of the photocatalyst can be used to alter the photocatalytic activity to, for example, influence the selectivities of a reaction by changing the irradiation wavelength.⁹⁹

I made use of the phenomena that the energy of photons can be utilized to control the activity of photochemical processes to overcome substrate scope limitations and reproducibility issues in metallaphotocatalytic C–N cross-couplings of cyclic secondary amines with electron poor aryl halides (all details can be found in chapter 4).¹⁰⁰ The observed limitations are caused by catalyst deactivation *via* the formation of nickel black. This arises from the accumulation of low valent Ni⁰ species due to the relatively slow oxidative addition in case of electron rich aryl halides. To countermeasure this undesired effect, the relative rate of oxidative addition (OA) must be equal or higher than the rate of reductive elimination (RE) (Figure 1.9).

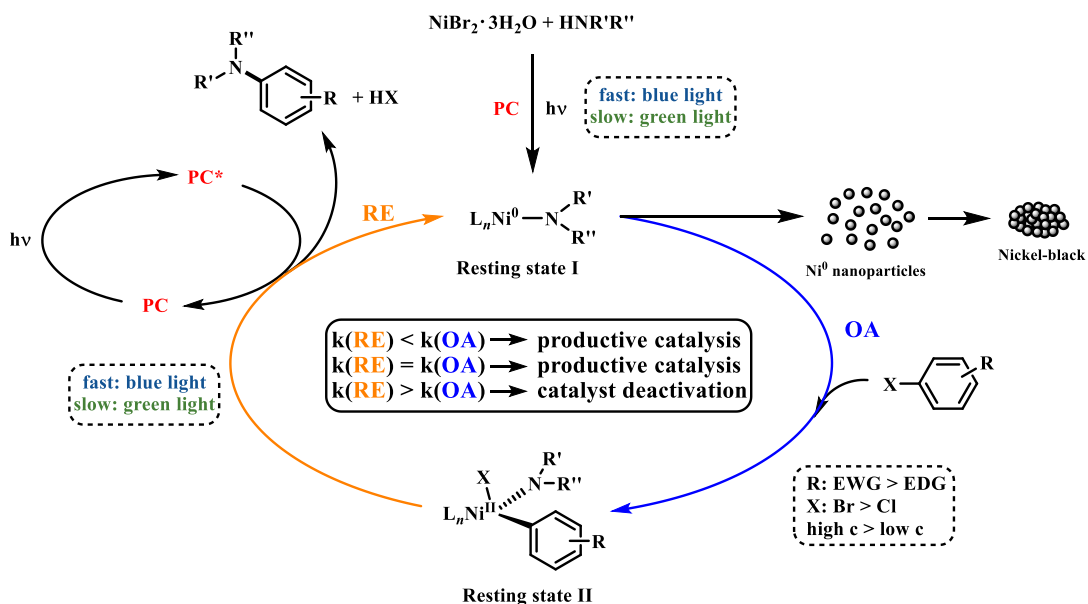


Figure 1.9. Overcoming limitations in metallaphotocatalysis using carbon nitride photocatalysis by changing the wavelength.

Overcoming this limitation was feasible by using a specific carbon nitride material (CN-OA-m) that is prepared through polymerization of urea and oxamide in molten salt, as photocatalyst. This material absorbs strong below 450 nm and only weakly at higher wavelengths, which enables to reduce the rate of reductive elimination at low photon energies. Thereby, the relative rate of oxidative addition became equal to or higher than the rate of reductive elimination, which was sufficient to avoid catalyst deactivation in certain cases. By using a high substrate concentration, the rate of oxidative addition could be increased and, in this way, even blue light irradiation could be used for the efficient and reproducible coupling of electron-rich aryl bromides and electron-poor aryl chlorides with amines.

It is worth noting that the same carbon nitride material has different oxidation potentials depending on the irradiation wavelength. This effect was used for photo-chemo-enzymatic cascades to switch between the formation of either the (*S*)- or (*R*)-enantiomer of 1-phenylethanol starting from ethylbenzene.¹⁰¹ Upon irradiation with blue light, π - π^* transitions generate strongly oxidizing electron holes (Figure 1.10). These enable the oxidation of ethylbenzene to acetophenone, which can be subsequently reduced with an enantioselective alcohol dehydrogenase from *Rhodococcus ruber* to yield (*S*)-1-phenylethanol in 93% ee. In the case of green light illumination, n - π^* transitions were induced (Figure 1.10). The resulting electron holes are comparably weak single electron oxidants and no conversion to acetophenone is observed. This enables the selective formation of H_2O_2 in an aqueous medium, which fuels the enantioselective biocatalytic hydroxylation of ethylbenzene to (*R*)-1-phenylethanol (99% ee) by an unspecific peroxygenase from *Agrocybe aegerita*.

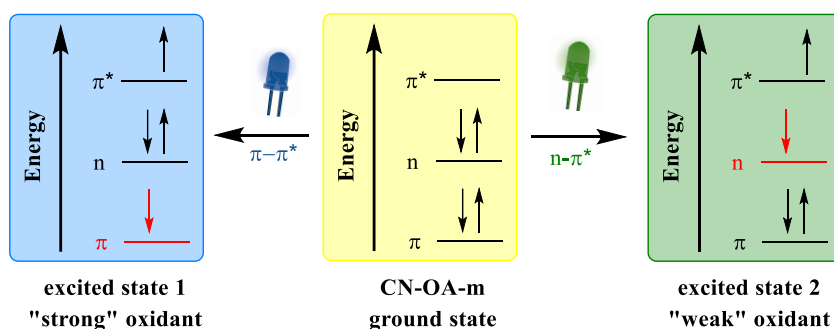


Figure 1.10. Different oxidation potential of CN-OA-m due to wavelength-dependent π - π^* or n - π^* transitions.¹⁰¹

A change in selectivity was also reported by varying between blue light and green light irradiation for the one or twofold C–H arylation of *N*-methylpyrrole with 1,3,5-tribromobenzene using Rhodamine 6G (Rh-6G) as PC.¹⁰² When the PC is irradiated with green light in the presence of a sacrificial electron donor (SED), in this case *N,N*-diisopropylethylamine (DIPEA), the radical anion Rh-6G^{•-}, which has a relatively low reduction potential of 1.0 V versus SCE (standard calomel electrode), is formed. This is sufficient for a selective monofunctionalization as only aryl bromides with low reduction potentials can be activated. Upon more energetic blue light illumination the radical anion Rh-6G^{•-} can be again excited to form the more reducing Rh-6G^{•-*} species with a reduction potential of 2.4 versus SCE. The underlying mechanism is that the quenching of the excited state of the PC with a sacrificial electron donor (SED) generates a relatively stable intermediate that is able to absorb another photon (consecutive photoinduced electron transfer, ConPET). Thereby, aryl bromides with higher reduction potentials can be activated and disubstitution of 1,3,5-tribromobenzene becomes feasible (Figure 1.11).

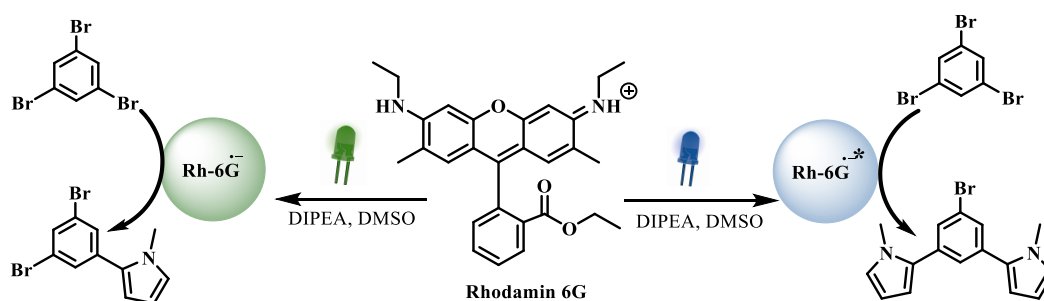


Figure 1.11. Switching between one (green light irradiation) or twofold (blue light irradiation) C–H arylation of *N*-methylpyrrole with 1,3,5-tribromobenzene using Rhodamin 6G as photocatalyst.

These examples show that the irradiation wavelength is a valuable parameter to tune the activity of a photocatalyst that can be used to control the selectivity in photocatalytic transformations.

1.4 Flow chemistry for photochemical reactions

An efficient photochemical reaction requires a homogenous and intense irradiation of the reaction mixture. All compounds in solution, like starting materials, products, additives and photocatalysts, act however as filters at the point of incident light. Thereby, the light intensity available for the rest of the reaction mixture is reduced and the photochemical reactions mainly occur efficiently in a limited area (millimeter magnitude) on the outside of the reactor, as the attenuation effect of photon transport - or absorption (A) - is exponentially decreasing with increasing penetration depth (d). This correlation is described by the Beer-Lambert-Bouguer law (Figure 1.12).¹⁰³

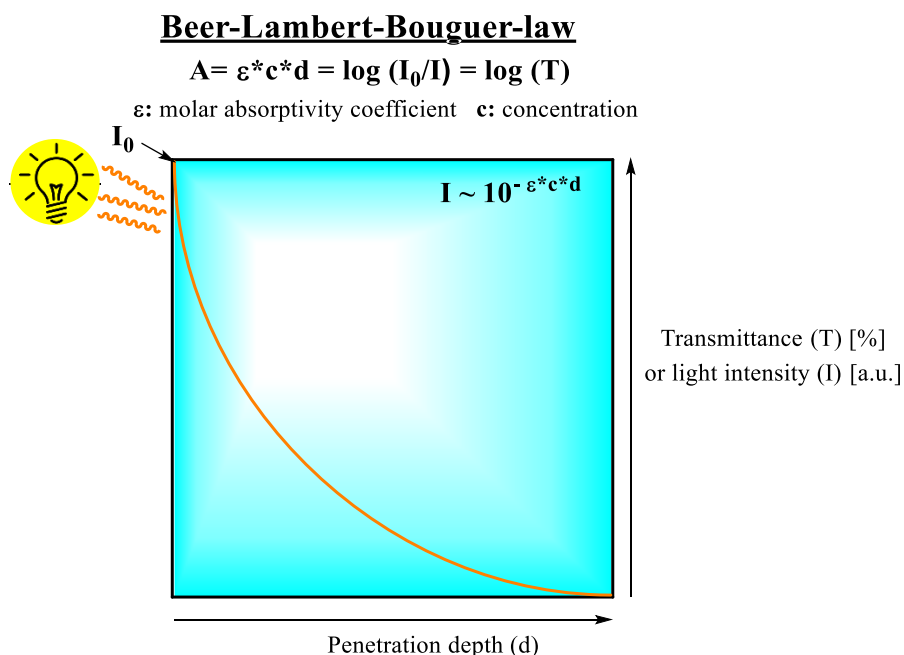


Figure 1.12. Equation of the Beer-Lambert-Bouguer law and attenuation of light intensity through a reaction media.²¹

Consequently, efficient irradiation becomes problematic in batch reactors, such as round-bottomed flasks, especially on higher scales. This results in long reaction times, increase the probability of side reactions and reproducibility issues. Photon equivalents are an important scaling parameter for photochemical reactions and can help to control a reaction, which was shown in a multi-kilogram-scale for a metallaphotocatalyzed C–N cross-coupling protocol.¹⁰⁴⁻¹⁰⁵ Due to the changing surface-area-to-volume ratios while scaling-up with batch reactors, either longer reactions times or increased light density with the aid of stronger lamps are required to provide the same photon equivalent as in small scales. This trend can

be also explained by the decreasing photon efficiency (ξ) (Equation 1) in large-scale batch reactors, which is defined as:

$$\xi = \frac{\text{reaction rate}}{\text{photon flux}} \quad (\text{Equation 1})$$

By changing from conventional batch reactors to flow approaches, unchanged surface-area-to-volume ratios can be ensured during upscaling and the photon efficiency can be more than 100 times higher than in typical batch reactors.¹⁰⁶ The narrow channel diameters of typically less than 1 mm allow for more efficient and uniform irradiation of the reaction mixture while upscaling in comparison to a dimension-enlarging strategy for scale-up using batch processes. As consequence, reduced reaction times are reached and it provides a straightforward opportunity to scale such transformations to synthetically useful quantities.^{104, 107} High reproducibility can be ensured through the precise control of the reaction time and temperature.¹⁰⁸ The reaction time corresponds to the residence time and can be precisely controlled by the flow velocity. Higher safety of operation can be guaranteed through an enhanced heat and mass transfer.

Since flow chemistry is a modular technique, each of the seven basic zones can be tuned to obtain the optimal setup for a specific reaction (Figure 1.13). These basic zones, in which a flow setup can be divided, are: fluid & reagent delivery, mixing, reactor, pressure regulation, collection, analysis, and purification.

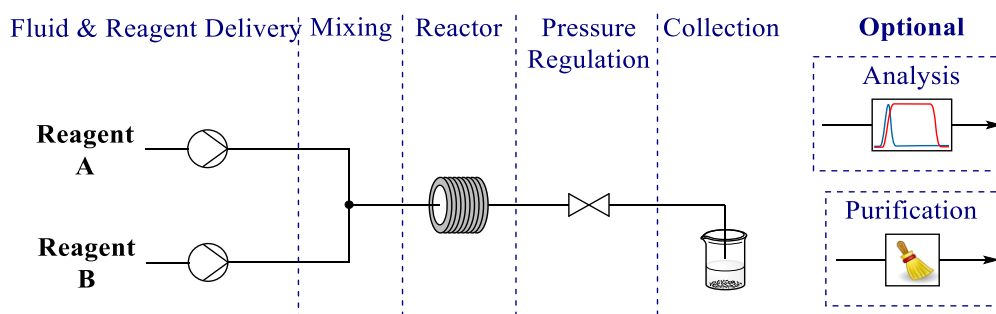


Figure 1.13. Seven basic segments of a standard two-feed continuous flow setup.

The first part of the setup, the fluid and reagent delivery system, is responsible for the accurate feed of the substances into the flow system. Different dedicated pumps or a gas supply equipped with a mass flow controller can set everything in motion. In case of different reagent and fluid streams a suitable mixing device combines the feeds before entering the core part of the setup, which is the reaction unit where the actual chemical reaction occurs.

Three main reactor types can be selected: chip, coil and pack-bed reactor. The ideal reactor type and material depends on the nature of a respective transformation. For photochemical reactions, a light transparent reactor unit and a dedicated light source, such as light emitting diode arrays (LEDs) are demanded. Due to their high surface-to-volume ratios, chip-based reactors provide the best heat and mass transfer ability among the before mentioned reactors types (Figure 1.14, left).¹⁰⁹ As a transparent reactor surface is required for photochemical transformations the interacting area is constructed from a light permeable material such as glass. Nevertheless, due to lower prices, coil reactors are preferred in synthetic flow chemistry (Figure 1.14, right). The tubing of coil reactors for photochemical applications are usually made of simple, commercially available inert, transparent fluoropolymers such as fluorinated ethylene propylene (FEP), or perfluoroalkoxy (PFA).¹¹⁰ The common outer diameters of these tubings are 1/8" or 1/16". For the inner diameters various sizes are available (0.01", 0.02", 0.03", 0.04", 1/16", etc.).

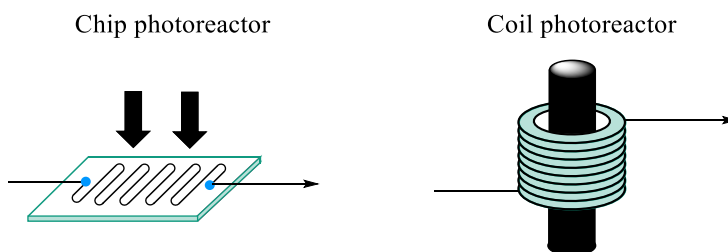


Figure 1.14. Reactor types for photochemical transformations in flow.

However, flow chemistry is not straightforward for every (photo)chemical protocol, especially when heterogeneous materials, such as insoluble photocatalysts or additives, are involved. In these cases a critical analysis of potential obstacles and overarching goals is needed to show if flow approaches outperform their batch counterparts.¹⁰⁸ Therefore, the development of more efficient photoreactors is still required. One of the existing main limitations of flow chemistry are chemical reactions involving solids, as these will settle leading to a heterogeneous distribution, irreproducible results, and/or clogging. This hampers the scale-up of photochemical reactions using heterogeneous PCs, which can have advantages in terms of recyclability and stability compared to the homogeneous PCs.⁹⁶ Heterogeneous materials are predominantly inserted in packed bed reactors to avoid clogging and settling,¹¹¹ but these reactor types are generally unsuitable for photocatalytic reactions, since photons will be solely adsorbed at the outer surface of the packed bed while the large part of the internal particles is shielded. In certain cases small diameter packed bed

reactors are suitable to overcome the sluggish irradiation¹¹², but this possibility is not a general solution due to the tedious packing and the foreseeable large pressure drops. Hence, there is the requirement of tailor-made reactor types for photocatalytic reactions that embody solids, such as additives or heterogeneous PC.

One possible solution on a laboratory scale is a system that generates serial micro-batch reactors (SMBRs).¹¹³ For the understanding of this technique the different behavior of biphasic gas-liquid systems depending on flow rates, viscosities, and channel properties in flow set-ups need to be defined. For gas-liquid flow reactions, bubble, slug, and annular flow regimes are commonly distinguished in flow reactors (Figure 1.15).

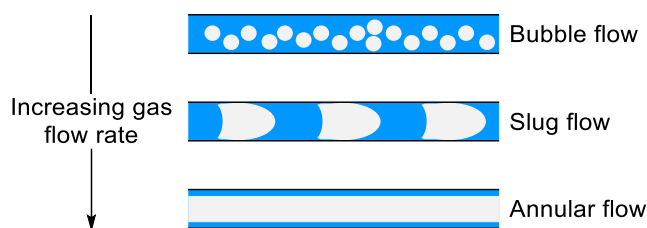


Figure 1.15. Common patterns for gas-liquid reactions in continuous flow.

In case of slug flow behavior small liquid compartments are separated by gaseous compartments. This can be controlled by the gas speed with mass-flow controllers and flow reactors enable further a precise control of the reaction time (= residence time) and reaction temperature. With the right feeding system, it is possible to dose a solid suspension into a segmented gas-liquid stream. Inside the formed small liquid units, which can be interpreted as small micro-batch reactors, the internal mixing phenomena caused by interior vortices inherent to the SMBRs result in a homogeneous and uniformly irradiated suspension. This internal and increased mass transfer is called Taylor flow (Figure 1.16).

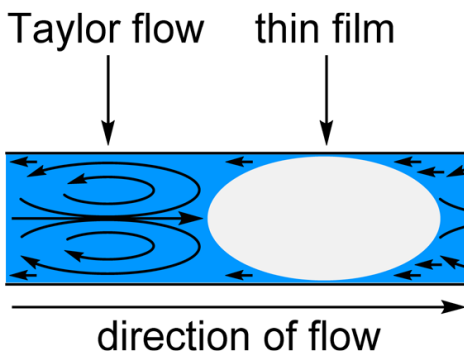


Figure 1.16. Taylor flow within the liquid phase of a gas-liquid mixture in a microfluidic channel.¹⁰⁸

Chapter 1

The natural Taylor flow in these small solid-liquid compartments mixes the slug to continuously re-suspend the used heterogeneous material, ensuring efficient irradiation and reproducible processing.

Another possibility to overcome the issues associated with the handling of solid particles in microreactors is the combination with oscillatory pumping.¹¹⁴ This avoids clogging and settling of the heterogeneous material in the reactor channels, and secures efficient mixing. In a collaborative work, we showed that my developed nickel/carbon nitride-catalyzed C–N cross-coupling protocol (Chapter 4) can greatly benefit from the intensified conditions using a combination of an oscillatory pump and a microstructured plug flow photoreactor (Chapter 5).¹¹⁵ The successful application of this set-up, for handling solids in flow, was more recently shown in further photocatalytic reactions.¹¹⁶⁻¹¹⁷

1.5 Aim of the Thesis

The focus of my doctoral research was the development and application of sustainable photocatalytic methods for synthetic organic chemistry. I aimed to substitute rare and expensive iridium and ruthenium polypyridyl complexes with heterogeneous photocatalysts in dual photo/nickel catalyzed carbon-heteroatom bond formations.

To achieve this goal, I initially investigated the use of graphitic carbon nitrides, a class of metal-free polymers that can be easily prepared from bulk chemicals. Using this semiconducting material, I participated in the development of a semi-heterogeneous protocol for the cross-coupling of aryl halides with carboxylic acids. Subsequently, I focused my research on developing a method to overcome the limitations of dual photoredox/nickel catalyzed C–N cross-couplings for electron-rich aryl halides using the same heterogeneous catalyst. I identified the underlying reason and was able to develop solutions for reproducible and selective C–N cross-couplings of electron-rich aryl bromides and electron-poor aryl chlorides using, for example chromoselective photocatalysis. In both coupling protocols, the carbon nitride photocatalyst could be successfully recycled multiple times using different strategies.

To scale the industrially important C–N coupling to synthetically useful quantities, I aimed to overcome the irradiation problems in batch using a dedicated continuous flow approach. The difficulties due to the problems associated with handling solids in flow were overcome by combining an oscillatory pump with a microstructured plug flow photoreactor. Here, a stable suspension of the photocatalyst can be maintained, circumventing clogging of the reactor channels. Intensified conditions allowed for a multi-gram scale-out reaction and the optimized conditions were applied in the synthesis of a key intermediate for an active pharmaceutical ingredient.

Finally, I aimed to avoid the requirement of a photocatalyst to harness the energy of visible-light for metallaphotocatalyzed carbon–heteroatom cross-couplings by using a bipyridine ligand that was decorated with two carbazole groups and forms a nickel complex that absorbs visible-light. This ligand showed high catalytic activity for the coupling of aryl iodides with sodium sulfinate, carboxylic acids and sulfonamides, and was also polymerized in a simple

Chapter 1

one-step procedure to afford a porous organic polymer. This resulted in a recyclable catalytic system with high catalytic activity and selectivity.

1.6 References

1. Roughley, S. D.; Jordan, A. M., The Medicinal Chemist's Toolbox: An Analysis of Reactions Used in the Pursuit of Drug Candidates. *J. Med. Chem.* **2011**, *54* (10), 3451-3479.
2. Ruiz-Castillo, P.; Buchwald, S. L., Applications of Palladium-Catalyzed C–N Cross-Coupling Reactions. *Chem. Rev.* **2016**, *116* (19), 12564-12649.
3. Bariwal, J.; Van der Eycken, E., C–N bond forming cross-coupling reactions: an overview. *Chem. Soc. Rev.* **2013**, *42* (24), 9283-9303.
4. Dorel, R.; Grugel, C. P.; Haydl, A. M., The Buchwald–Hartwig Amination After 25 Years. *Angew. Chem. Int. Ed.* **2019**, *58* (48), 17118-17129.
5. Guram, A. S.; Rennels, R. A.; Buchwald, S. L., A Simple Catalytic Method for the Conversion of Aryl Bromides to Arylamines. *Angew. Chem. Int. Ed. Engl.* **1995**, *34* (12), 1348-1350.
6. Louie, J.; Hartwig, J. F., Palladium-catalyzed synthesis of arylamines from aryl halides. Mechanistic studies lead to coupling in the absence of tin reagents. *Tetrahedron Lett.* **1995**, *36* (21), 3609-3612.
7. Masanori, K.; Masayuki, K.; Toshihiko, M., Palladium-Catalyzed Aromatic Amination of Aryl Bromides with N,N-di-ethylamino-tributyltin. *Chem. Lett.* **1983**, *12* (6), 927-928.
8. Paul, F.; Patt, J.; Hartwig, J. F., Palladium-catalyzed formation of carbon-nitrogen bonds. Reaction intermediates and catalyst improvements in the hetero cross-coupling of aryl halides and tin amides. *J. Am. Chem. Soc.* **1994**, *116* (13), 5969-5970.
9. Widenhofer, R. A.; Buchwald, S. L., Formation of Palladium Bis(amine) Complexes from Reaction of Amine with Palladium Tris(o-tolyl)phosphine Mono(amine) Complexes. *Organometallics* **1996**, *15* (16), 3534-3542.
10. Terrier, F., *Modern Nucleophilic Aromatic Substitution*. Wiley-VCH: Weinheim, 2013.
11. Evano, G.; Blanchard, N.; Toumi, M., Copper-Mediated Coupling Reactions and Their Applications in Natural Products and Designed Biomolecules Synthesis. *Chem. Rev.* **2008**, *108* (8), 3054-3131.
12. Sambigiato, C.; Marsden, S. P.; Blacker, A. J.; McGowan, P. C., Copper catalysed Ullmann type chemistry: from mechanistic aspects to modern development. *Chem. Soc. Rev.* **2014**, *43* (10), 3525-3550.

Chapter 1

13. Monnier, F.; Taillefer, M., Catalytic C-C, C-N, and C-O Ullmann-Type Coupling Reactions. *Angew. Chem. Int. Ed.* **2009**, *48* (38), 6954-6971.
14. West, M. J.; Fyfe, J. W. B.; Vantourout, J. C.; Watson, A. J. B., Mechanistic Development and Recent Applications of the Chan–Lam Amination. *Chem. Rev.* **2019**, *119* (24), 12491-12523.
15. Chen, J.-Q.; Li, J.-H.; Dong, Z.-B., A Review on the Latest Progress of Chan-Lam Coupling Reaction. *Advanced Synthesis & Catalysis* **2020**, *362* (16), 3311-3331.
16. Shafir, A.; Buchwald, S. L., Highly Selective Room-Temperature Copper-Catalyzed C–N Coupling Reactions. *J. Am. Chem. Soc.* **2006**, *128* (27), 8742-8743.
17. Wolfe, J. P.; Wagaw, S.; Buchwald, S. L., An Improved Catalyst System for Aromatic Carbon–Nitrogen Bond Formation: The Possible Involvement of Bis(Phosphine) Palladium Complexes as Key Intermediates. *J. Am. Chem. Soc.* **1996**, *118* (30), 7215-7216.
18. Driver, M. S.; Hartwig, J. F., A Second-Generation Catalyst for Aryl Halide Amination: Mixed Secondary Amines from Aryl Halides and Primary Amines Catalyzed by (DPPF)PdCl₂. *J. Am. Chem. Soc.* **1996**, *118* (30), 7217-7218.
19. Wolfe, J. P.; Buchwald, S. L., Scope and Limitations of the Pd/BINAP-Catalyzed Amination of Aryl Bromides. *J. Org. Chem.* **2000**, *65* (4), 1144-1157.
20. Louie, J.; Driver, M. S.; Hamann, B. C.; Hartwig, J. F., Palladium-Catalyzed Amination of Aryl Triflates and Importance of Triflate Addition Rate. *J. Org. Chem.* **1997**, *62* (5), 1268-1273.
21. Donnelly, K.; Baumann, M., Scalability of photochemical reactions in continuous flow mode. *Journal of Flow Chemistry* **2021**.
22. Hamann, B. C.; Hartwig, J. F., Sterically Hindered Chelating Alkyl Phosphines Provide Large Rate Accelerations in Palladium-Catalyzed Amination of Aryl Iodides, Bromides, and Chlorides, and the First Amination of Aryl Tosylates. *J. Am. Chem. Soc.* **1998**, *120* (29), 7369-7370.
23. Old, D. W.; Wolfe, J. P.; Buchwald, S. L., A Highly Active Catalyst for Palladium-Catalyzed Cross-Coupling Reactions: Room-Temperature Suzuki Couplings and Amination of Unactivated Aryl Chlorides. *J. Am. Chem. Soc.* **1998**, *120* (37), 9722-9723.
24. Surry, D. S.; Buchwald, S. L., Dialkylbiaryl phosphines in Pd-catalyzed amination: a user's guide. *Chem. Sci.* **2011**, *2* (1), 27-50.

25. Surry, D. S.; Buchwald, S. L., Biaryl Phosphane Ligands in Palladium-Catalyzed Amination. *Angew. Chem. Int. Ed.* **2008**, *47* (34), 6338-6361.
26. Fors, B. P.; Watson, D. A.; Biscoe, M. R.; Buchwald, S. L., A Highly Active Catalyst for Pd-Catalyzed Amination Reactions: Cross-Coupling Reactions Using Aryl Mesylates and the Highly Selective Monoarylation of Primary Amines Using Aryl Chlorides. *J. Am. Chem. Soc.* **2008**, *130* (41), 13552-13554.
27. Fors, B. P.; Dooleweerd, K.; Zeng, Q.; Buchwald, S. L., An efficient system for the Pd-catalyzed cross-coupling of amides and aryl chlorides. *Tetrahedron* **2009**, *65* (33), 6576-6583.
28. Ruiz-Castillo, P.; Blackmond, D. G.; Buchwald, S. L., Rational Ligand Design for the Arylation of Hindered Primary Amines Guided by Reaction Progress Kinetic Analysis. *J. Am. Chem. Soc.* **2015**, *137* (8), 3085-3092.
29. Hartwig, J. F., Evolution of a Fourth Generation Catalyst for the Amination and Thioetherification of Aryl Halides. *Acc. Chem. Res.* **2008**, *41* (11), 1534-1544.
30. Shen, Q.; Shekhar, S.; Stambuli, J. P.; Hartwig, J. F., Highly Reactive, General, and Long-Lived Catalysts for Coupling Heteroaryl and Aryl Chlorides with Primary Nitrogen Nucleophiles. *Angew. Chem. Int. Ed.* **2005**, *44* (9), 1371-1375.
31. Shen, Q.; Ogata, T.; Hartwig, J. F., Highly Reactive, General and Long-Lived Catalysts for Palladium-Catalyzed Amination of Heteroaryl and Aryl Chlorides, Bromides, and Iodides: Scope and Structure–Activity Relationships. *J. Am. Chem. Soc.* **2008**, *130* (20), 6586-6596.
32. Ogata, T.; Hartwig, J. F., Palladium-Catalyzed Amination of Aryl and Heteroaryl Tosylates at Room Temperature. *J. Am. Chem. Soc.* **2008**, *130* (42), 13848-13849.
33. Shen, Q.; Hartwig, J. F., Palladium-Catalyzed Coupling of Ammonia and Lithium Amide with Aryl Halides. *J. Am. Chem. Soc.* **2006**, *128* (31), 10028-10029.
34. Fortman, G. C.; Nolan, S. P., N-Heterocyclic carbene (NHC) ligands and palladium in homogeneous cross-coupling catalysis: a perfect union. *Chem. Soc. Rev.* **2011**, *40* (10), 5151-5169.
35. Navarro, O.; Marion, N.; Mei, J.; Nolan, S. P., Rapid Room Temperature Buchwald–Hartwig and Suzuki–Miyaura Couplings of Heteroaromatic Compounds Employing Low Catalyst Loadings. *Chemistry – A European Journal* **2006**, *12* (19), 5142-5148.

Chapter 1

36. Marion, N.; Navarro, O.; Mei, J.; Stevens, E. D.; Scott, N. M.; Nolan, S. P., Modified (NHC)Pd(allyl)Cl (NHC = N-Heterocyclic Carbene) Complexes for Room-Temperature Suzuki–Miyaura and Buchwald–Hartwig Reactions. *J. Am. Chem. Soc.* **2006**, *128* (12), 4101-4111.
37. Viciu, M. S.; Kelly, R. A.; Stevens, E. D.; Naud, F.; Studer, M.; Nolan, S. P., Synthesis, Characterization, and Catalytic Activity of N-Heterocyclic Carbene (NHC) Palladacycle Complexes. *Org. Lett.* **2003**, *5* (9), 1479-1482.
38. Marion, N.; Nolan, S. P., Well-Defined N-Heterocyclic Carbenes–Palladium(II) Precatalysts for Cross-Coupling Reactions. *Acc. Chem. Res.* **2008**, *41* (11), 1440-1449.
39. Froese, R. D. J.; Lombardi, C.; Pompeo, M.; Rucker, R. P.; Organ, M. G., Designing Pd–N-Heterocyclic Carbene Complexes for High Reactivity and Selectivity for Cross-Coupling Applications. *Acc. Chem. Res.* **2017**, *50* (9), 2244-2253.
40. Surry, D. S.; Buchwald, S. L., Dialkylbiaryl Phosphines in Pd-Catalyzed Amination: A User’s Guide. *Chemical science (Royal Society of Chemistry : 2010)* **2011**, *2* (1), 27-50.
41. Meyers, C.; Maes, B. U. W.; Loones, K. T. J.; Bal, G.; Lemièrre, G. L. F.; Dommissie, R. A., Study of a New Rate Increasing “Base Effect” in the Palladium-Catalyzed Amination of Aryl Iodides. *J. Org. Chem.* **2004**, *69* (18), 6010-6017.
42. Dennis, J. M.; White, N. A.; Liu, R. Y.; Buchwald, S. L., Breaking the Base Barrier: An Electron-Deficient Palladium Catalyst Enables the Use of a Common Soluble Base in C–N Coupling. *J. Am. Chem. Soc.* **2018**, *140* (13), 4721-4725.
43. Fleischer, M., The abundance and distribution of the chemical elements in the earth's crust. *J. Chem. Educ.* **1954**, *31* (9), 446.
44. Gandeepan, P.; Müller, T.; Zell, D.; Cera, G.; Warratz, S.; Ackermann, L., 3d Transition Metals for C–H Activation. *Chem. Rev.* **2019**, *119* (4), 2192-2452.
45. Ananikov, V. P., Nickel: The “Spirited Horse” of Transition Metal Catalysis. *ACS Catal.* **2015**, *5* (3), 1964-1971.
46. Wolfe, J. P.; Buchwald, S. L., Nickel-Catalyzed Amination of Aryl Chlorides. *J. Am. Chem. Soc.* **1997**, *119* (26), 6054-6058.
47. Kampmann, S. S.; Skelton, B. W.; Wild, D. A.; Koutsantonis, G. A.; Stewart, S. G., An Air-Stable Nickel(0) Phosphite Precatalyst for Primary Alkylamine C–N Cross-Coupling Reactions. *Eur. J. Org. Chem.* **2015**, *2015* (27), 5995-6004.

48. Lavoie, C. M.; Stradiotto, M., Bisphosphines: A Prominent Ancillary Ligand Class for Application in Nickel-Catalyzed C–N Cross-Coupling. *ACS Catal.* **2018**, *8* (8), 7228-7250.
49. Lavoie, C. M.; MacQueen, P. M.; Rotta-Loria, N. L.; Sawatzky, R. S.; Borzenko, A.; Chisholm, A. J.; Hargreaves, B. K. V.; McDonald, R.; Ferguson, M. J.; Stradiotto, M., Challenging nickel-catalysed amine arylations enabled by tailored ancillary ligand design. *Nat. Commun.* **2016**, *7*, 11073.
50. Tassone, J. P.; England, E. V.; MacQueen, P. M.; Ferguson, M. J.; Stradiotto, M., PhPAd-DalPhos: Ligand-Enabled, Nickel-Catalyzed Cross-Coupling of (Hetero)aryl Electrophiles with Bulky Primary Alkylamines. *Angew. Chem. Int. Ed.* **2019**, *58* (8), 2485-2489.
51. McGuire, R. T.; Paffile, J. F. J.; Zhou, Y.; Stradiotto, M., Nickel-Catalyzed C–N Cross-Coupling of Ammonia, (Hetero)anilines, and Indoles with Activated (Hetero)aryl Chlorides Enabled by Ligand Design. *ACS Catal.* **2019**, *9* (10), 9292-9297.
52. Koo, K.; Hillhouse, G. L., Carbon-Nitrogen Bond Formation by Reductive Elimination from Nickel(II) Amido Alkyl Complexes. *Organometallics* **1995**, *14* (9), 4421-4423.
53. Matsunaga, P. T.; Mavropoulos, J. C.; Hillhouse, G. L., Oxygen-atom transfer from nitrous oxide (N=N=O) to nickel alkyls. Syntheses and reactions of nickel(II) alkoxides. *Polyhedron* **1995**, *14* (1), 175-185.
54. Matsunaga, P. T.; Hillhouse, G. L.; Rheingold, A. L., Oxygen-atom transfer from nitrous oxide to a nickel metallacycle. Synthesis, structure, and reactions of [cyclic] (2,2'-bipyridine)Ni(OCH₂CH₂CH₂CH₂). *J. Am. Chem. Soc.* **1993**, *115* (5), 2075-2077.
55. Han, R.; Hillhouse, G. L., Carbon–Oxygen Reductive-Elimination from Nickel(II) Oxametallacycles and Factors That Control Formation of Ether, Aldehyde, Alcohol, or Ester Products. *J. Am. Chem. Soc.* **1997**, *119* (34), 8135-8136.
56. Tasker, S. Z.; Standley, E. A.; Jamison, T. F., Recent advances in homogeneous nickel catalysis. *Nature* **2014**, *509*, 299.
57. Welin, E. R.; Le, C.; Arias-Rotondo, D. M.; McCusker, J. K.; MacMillan, D. W. C., Photosensitized, energy transfer-mediated organometallic catalysis through electronically excited nickel(II). *Science* **2017**, *355* (6323), 380-385.

Chapter 1

58. Lim, C.-H.; Kudisch, M.; Liu, B.; Miyake, G. M., C–N Cross-Coupling via Photoexcitation of Nickel–Amine Complexes. *J. Am. Chem. Soc.* **2018**, *140* (24), 7667-7673.
59. Kudisch, M.; Lim, C.-H.; Thordarson, P.; Miyake, G. M., Energy Transfer to Ni–Amine Complexes in Dual Catalytic, Light-Driven C–N Cross-Coupling Reactions. *J. Am. Chem. Soc.* **2019**, *141* (49), 19479-19486.
60. Escobar, R. A.; Johannes, J. W., A Unified and Practical Method for Carbon–Heteroatom Cross-Coupling using Nickel/Photo Dual Catalysis. *Chemistry – A European Journal* **2020**, *26* (23), 5168-5173.
61. Mandal, T.; Jana, S.; Dash, J., Zinc-Mediated Efficient and Selective Reduction of Carbonyl Compounds. *Eur. J. Org. Chem.* **2017**, *2017* (33), 4972-4983.
62. Yan, M.; Kawamata, Y.; Baran, P. S., Synthetic Organic Electrochemical Methods Since 2000: On the Verge of a Renaissance. *Chem. Rev.* **2017**, *117* (21), 13230-13319.
63. Shaw, M. H.; Twilton, J.; MacMillan, D. W. C., Photoredox Catalysis in Organic Chemistry. *J. Org. Chem.* **2016**, *81* (16), 6898-6926.
64. Marzo, L.; Pagire, S. K.; Reiser, O.; König, B., Visible-Light Photocatalysis: Does It Make a Difference in Organic Synthesis? *Angew. Chem. Int. Ed.* **2018**, *57* (32), 10034-10072.
65. Kalyanasundaram, K.; Grätzel, M., Applications of functionalized transition metal complexes in photonic and optoelectronic devices. *Coord. Chem. Rev.* **1998**, *177* (1), 347-414.
66. Ulbricht, C.; Beyer, B.; Friebe, C.; Winter, A.; Schubert, U. S., Recent Developments in the Application of Phosphorescent Iridium(III) Complex Systems. *Adv. Mater.* **2009**, *21* (44), 4418-4441.
67. Prier, C. K.; Rankic, D. A.; MacMillan, D. W. C., Visible Light Photoredox Catalysis with Transition Metal Complexes: Applications in Organic Synthesis. *Chem. Rev.* **2013**, *113* (7), 5322-5363.
68. Miller, J. N., The determination of quantum yields. In *Standards in Fluorescence Spectrometry: Ultraviolet Spectrometry Group*, Miller, J. N., Ed. Springer Netherlands: Dordrecht, 1981; pp 68-78.
69. Strieth-Kalthoff, F.; James, M. J.; Teders, M.; Pitzer, L.; Glorius, F., Energy transfer catalysis mediated by visible light: principles, applications, directions. *Chem. Soc. Rev.* **2018**, *47* (19), 7190-7202.

70. Crisenza, G. E. M.; Melchiorre, P., Chemistry glows green with photoredox catalysis. *Nat. Commun.* **2020**, *11* (1), 803.
71. Hossain, A.; Bhattacharyya, A.; Reiser, O., Copper's rapid ascent in visible-light photoredox catalysis. *Science* **2019**, *364* (6439), eaav9713.
72. Romero, N. A.; Nicewicz, D. A., Organic Photoredox Catalysis. *Chem. Rev.* **2016**, *116* (17), 10075-10166.
73. Savateev, A.; Antonietti, M., Heterogeneous Organocatalysis for Photoredox Chemistry. *ACS Catal.* **2018**, *8* (10), 9790-9808.
74. Savateev, A.; Ghosh, I.; König, B.; Antonietti, M., Photoredox Catalytic Organic Transformations using Heterogeneous Carbon Nitrides. *Angew. Chem. Int. Ed.* **2018**, *57* (49), 15936-15947.
75. Ge, S.; Green, R. A.; Hartwig, J. F., Controlling First-Row Catalysts: Amination of Aryl and Heteroaryl Chlorides and Bromides with Primary Aliphatic Amines Catalyzed by a BINAP-Ligated Single-Component Ni(0) Complex. *J. Am. Chem. Soc.* **2014**, *136* (4), 1617-1627.
76. Camasso, N. M.; Sanford, M. S., Design, synthesis, and carbon-heteroatom coupling reactions of organometallic nickel(IV) complexes. *Science* **2015**, *347* (6227), 1218-1220.
77. Twilton, J.; Le, C.; Zhang, P.; Shaw, M. H.; Evans, R. W.; MacMillan, D. W. C., The merger of transition metal and photocatalysis. *Nat. Rev. Chem.* **2017**, *1*, 0052.
78. Shee, M.; Singh, N. D. P., Cooperative photoredox and palladium catalysis: recent advances in various functionalization reactions. *Catal. Sci. Technol.* **2021**, *11* (3), 742-767.
79. Zhu, C.; Yue, H.; Jia, J.; Rueping, M., Nickel-Catalyzed C-Heteroatom Cross-Coupling Reactions under Mild Conditions via Facilitated Reductive Elimination. *Angew. Chem. Int. Ed.* **2021**, *60*, 17810.
80. Corcoran, E. B.; Pirnot, M. T.; Lin, S.; Dreher, S. D.; DiRocco, D. A.; Davies, I. W.; Buchwald, S. L.; MacMillan, D. W. C., Aryl amination using ligand-free Ni(II) salts and photoredox catalysis. *Science* **2016**, *353* (6296), 279-283.
81. Terrett, J. A.; Cuthbertson, J. D.; Shurtleff, V. W.; MacMillan, D. W. C., Switching on elusive organometallic mechanisms with photoredox catalysis. *Nature* **2015**, *524*, 330.
82. Oderinde, M. S.; Jones, N. H.; Juneau, A.; Frenette, M.; Aquila, B.; Tentarelli, S.; Robbins, D. W.; Johannes, J. W., Highly Chemoselective Iridium Photoredox and Nickel

Chapter 1

Catalysis for the Cross-Coupling of Primary Aryl Amines with Aryl Halides. *Angew. Chem. Int. Ed.* **2016**, *55* (42), 13219-13223.

83. Oderinde, M. S.; Frenette, M.; Robbins, D. W.; Aquila, B.; Johannes, J. W., Photoredox Mediated Nickel Catalyzed Cross-Coupling of Thiols With Aryl and Heteroaryl Iodides via Thiyl Radicals. *J. Am. Chem. Soc.* **2016**, *138* (6), 1760-1763.

84. Key, R. J.; Vannucci, A. K., Nickel Dual Photoredox Catalysis for the Synthesis of Aryl Amines. *Organometallics* **2018**, *37* (9), 1468-1472.

85. Kim, T.; McCarver, S. J.; Lee, C.; MacMillan, D. W. C., Sulfonamidation of Aryl and Heteroaryl Halides through Photosensitized Nickel Catalysis. *Angew. Chem. Int. Ed.* **2018**, *57* (13), 3488-3492.

86. Till, N. A.; Tian, L.; Dong, Z.; Scholes, G. D.; MacMillan, D. W. C., Mechanistic Analysis of Metallaphotoredox C–N Coupling: Photocatalysis Initiates and Perpetuates Ni(I)/Ni(III) Coupling Activity. *J. Am. Chem. Soc.* **2020**, *142* (37), 15830-15841.

87. Qin, Y.; Sun, R.; Gianoulis, N. P.; Nocera, D. G., Photoredox Nickel-Catalyzed C–S Cross-Coupling: Mechanism, Kinetics, and Generalization. *J. Am. Chem. Soc.* **2021**, *143* (4), 2005-2015.

88. Sun, R.; Qin, Y.; Ruccolo, S.; Schnedermann, C.; Costentin, C.; Nocera, D. G., Elucidation of a Redox-Mediated Reaction Cycle for Nickel-Catalyzed Cross Coupling. *J. Am. Chem. Soc.* **2019**, *141* (1), 89-93.

89. Sun, R.; Qin, Y.; Nocera, D. G., General Paradigm in Photoredox Nickel-Catalyzed Cross-Coupling Allows for Light-Free Access to Reactivity. *Angew. Chem. Int. Ed.* **2020**, *59* (24), 9527-9533.

90. Shields, B. J.; Kudisch, B.; Scholes, G. D.; Doyle, A. G., Long-Lived Charge-Transfer States of Nickel(II) Aryl Halide Complexes Facilitate Bimolecular Photoinduced Electron Transfer. *J. Am. Chem. Soc.* **2018**, *140* (8), 3035-3039.

91. Ting, S. I.; Garakyaraghi, S.; Taliaferro, C. M.; Shields, B. J.; Scholes, G. D.; Castellano, F. N.; Doyle, A. G., 3d-d Excited States of Ni(II) Complexes Relevant to Photoredox Catalysis: Spectroscopic Identification and Mechanistic Implications. *J. Am. Chem. Soc.* **2020**, *142* (12), 5800-5810.

92. Yang, L.; Lu, H.-H.; Lai, C.-H.; Li, G.; Zhang, W.; Cao, R.; Liu, F.; Wang, C.; Xiao, J.; Xue, D., Light-Promoted Nickel Catalysis: Etherification of Aryl Electrophiles with

- Alcohols Catalyzed by a NiII-Aryl Complex. *Angew. Chem. Int. Ed.* **2020**, *59* (31), 12714-12719.
93. Li, G.; Yang, L.; Liu, J.-J.; Zhang, W.; Cao, R.; Wang, C.; Zhang, Z.; Xiao, J.; Xue, D., Light-Promoted C–N Coupling of Aryl Halides with Nitroarenes. *Angew. Chem. Int. Ed.* **2021**, *60* (10), 5230-5234.
94. Vega-Peñaloza, A.; Mateos, J.; Companyó, X.; Escudero-Casao, M.; Dell'Amico, L., A Rational Approach to Organo-Photocatalysis: Novel Designs and Structure-Property Relationships. *Angew. Chem. Int. Ed.* **2021**, *60* (3), 1082-1097.
95. Jo, M.; Choi, S.; Jo, J. H.; Kim, S.-Y.; Kim, P. S.; Kim, C. H.; Son, H.-J.; Pac, C.; Kang, S. O., Utility of Squaraine Dyes for Dye-Sensitized Photocatalysis on Water or Carbon Dioxide Reduction. *ACS Omega* **2019**, *4* (10), 14272-14283.
96. Gisbertz, S.; Pieber, B., Heterogeneous Photocatalysis in Organic Synthesis. *ChemPhotoChem* **2020**, *4* (7), 456-475.
97. Riente, P.; Noël, T., Application of metal oxide semiconductors in light-driven organic transformations. *Catal. Sci. Technol.* **2019**, *9* (19), 5186-5232.
98. Markushyna, Y.; Smith, C. A.; Savateev, A., Organic Photocatalysis: Carbon Nitride Semiconductors vs. Molecular Catalysts. *Eur. J. Org. Chem.* **2020**, *2020* (10), 1294-1309.
99. Protti, S.; Ravelli, D.; Fagnoni, M., Wavelength dependence and wavelength selectivity in photochemical reactions. *Photochemical & Photobiological Sciences* **2019**, *18* (9), 2094-2101.
100. Gisbertz, S.; Reischauer, S.; Pieber, B., Overcoming limitations in dual photoredox/nickel-catalysed C–N cross-couplings due to catalyst deactivation. *Nat. Catal.* **2020**, *3* (8), 611-620.
101. Schmermund, L.; Reischauer, S.; Bierbaumer, S.; Winkler, C. K.; Diaz-Rodriguez, A.; Edwards, L. J.; Kara, S.; Mielke, T.; Cartwright, J.; Grogan, G.; Pieber, B.; Kroutil, W., Chromoselective Photocatalysis Enables Stereocomplementary Biocatalytic Pathways**. *Angew. Chem. Int. Ed.* **2021**, *60* (13), 6965-6969.
102. Ghosh, I.; König, B., Chromoselective Photocatalysis: Controlled Bond Activation through Light-Color Regulation of Redox Potentials. *Angew. Chem. Int. Ed.* **2016**, *55* (27), 7676-7679.
103. Verschueren, R. H.; De Borggraeve, W. M., Electrochemistry and Photoredox Catalysis: A Comparative Evaluation in Organic Synthesis. *Molecules* **2019**, *24* (11), 2122.

Chapter 1

104. Corcoran, E. B.; McMullen, J. P.; Lévesque, F.; Wismer, M. K.; Naber, J. R., Photon Equivalents as a Parameter for Scaling Photoredox Reactions in Flow: Translation of Photocatalytic C–N Cross-Coupling from Lab Scale to Multikilogram Scale. *Angew. Chem. Int. Ed.* **2020**, *59* (29), 11964-11968.
105. Lévesque, F.; Di Maso, M. J.; Narsimhan, K.; Wismer, M. K.; Naber, J. R., Design of a Kilogram Scale, Plug Flow Photoreactor Enabled by High Power LEDs. *Organic Process Research & Development* **2020**, *24* (12), 2935-2940.
106. Cambié, D.; Bottecchia, C.; Straathof, N. J. W.; Hessel, V.; Noël, T., Applications of Continuous-Flow Photochemistry in Organic Synthesis, Material Science, and Water Treatment. *Chem. Rev.* **2016**, *116* (17), 10276-10341.
107. Harper, K. C.; Moschetta, E. G.; Bordawekar, S. V.; Wittenberger, S. J., A Laser Driven Flow Chemistry Platform for Scaling Photochemical Reactions with Visible Light. *ACS Central Science* **2019**, *5* (1), 109-115.
108. Plutschack, M. B.; Pieber, B.; Gilmore, K.; Seeberger, P. H., The Hitchhiker's Guide to Flow Chemistry. *Chem. Rev.* **2017**, *117* (18), 11796-11893.
109. Jensen, K. F.; Reizman, B. J.; Newman, S. G., Tools for chemical synthesis in microsystems. *Lab Chip* **2014**, *14* (17), 3206-3212.
110. Hook, B. D. A.; Dohle, W.; Hirst, P. R.; Pickworth, M.; Berry, M. B.; Booker-Milburn, K. I., A Practical Flow Reactor for Continuous Organic Photochemistry. *J. Org. Chem.* **2005**, *70* (19), 7558-7564.
111. Frost, C. G.; Mutton, L., Heterogeneous catalytic synthesis using microreactor technology. *Green Chemistry* **2010**, *12* (10), 1687-1703.
112. Woźnica, M.; Chaoui, N.; Taabache, S.; Blechert, S., THF: An Efficient Electron Donor in Continuous Flow Radical Cyclization Photocatalyzed by Graphitic Carbon Nitride. *Chemistry – A European Journal* **2014**, *20* (45), 14624-14628.
113. Pieber, B.; Shalom, M.; Antonietti, M.; Seeberger, P. H.; Gilmore, K., Continuous Heterogeneous Photocatalysis in Serial Micro-Batch Reactors. *Angew. Chem. Int. Ed.* **2018**, *57* (31), 9976-9979.
114. Bianchi, P.; Williams, J. D.; Kappe, C. O., Oscillatory flow reactors for synthetic chemistry applications. *Journal of Flow Chemistry* **2020**, *10* (3), 475-490.
115. Rosso, C.; Gisbertz, S.; Williams, J. D.; Gemoets, H. P. L.; Debrouwer, W.; Pieber, B.; Kappe, C. O., An oscillatory plug flow photoreactor facilitates semi-heterogeneous dual

nickel/carbon nitride photocatalytic C–N couplings. *Reaction Chemistry & Engineering* **2020**, *5* (3), 597-604.

116. Debrouwer, W.; Kimpe, W.; Dangreau, R.; Huvaere, K.; Gemoets, H. P. L.; Mottaghi, M.; Kuhn, S.; Van Aken, K., Ir/Ni Photoredox Dual Catalysis with Heterogeneous Base Enabled by an Oscillatory Plug Flow Photoreactor. *Organic Process Research & Development* **2020**, *24* (10), 2319-2325.

117. Bianchi, P.; Williams, J. D.; Kappe, C. O., Continuous flow processing of bismuth-photocatalyzed atom transfer radical addition reactions using an oscillatory flow reactor. *Green Chemistry* **2021**, *23* (7), 2685-2693.

Chapter 1

Chapter 2

Heterogeneous photocatalysis in organic synthesis

Gisbertz, S.; Pieber, B.

ChemPhotoChem 2020, 3, 611-620.

DOI: <https://doi.org/10.1002/cptc.202000014>

Abstract

Visible light photocatalysis relies mainly on expensive noble metal complexes and organic dyes that are not recyclable. Heterogeneous semiconductors, which are mainly applied for artificial photosynthesis and wastewater treatment, are a promising sustainable alternative and gain increasing attention. Inorganic and organic semiconductors with suitable bandgaps are among the most widely studied heterogeneous photocatalysts due to their high stability and recyclability. More recently, microporous materials, such as conjugated organic polymers, covalent organic frameworks, and metal organic frameworks that can be tuned and designed on a molecular level showed promising results. This review provides an overview of the most common heterogeneous photocatalysts with a focus on their applicability in organic synthesis.

Specific contribution

I collected and organized the literature existing on the topic at the time (December 2019). I outlined a structure for the work, prepared figures, tables and schemes and wrote the manuscript. Dr. B. Pieber revised and corrected the manuscript.

2.1 Introduction

Catalysis is a fundamental pillar of organic synthesis and is key to the production of commodity chemicals, complex pharmaceuticals, and agrochemicals. Catalysts are classified as either homogenous or heterogeneous. Homogeneous catalysis is, compared to heterogeneous catalysis, often characterized by a higher activity and selectivity.¹ Heterogeneous catalysts, on the contrary, can easily be separated and recycled. Combining the advantages of homogeneous and heterogeneous catalysis by anchoring soluble catalysts on insoluble supports is an appealing strategy,¹ but adds complexity to the catalytic system and often reduces the catalysts' activity and selectivity, or even result in complete deactivation. Heterogenized catalysts have often failed to outperform their soluble analogs and to achieve the potential of merging heterogeneous and homogeneous catalysis.²

In contrast to “conventional” catalysis (transition metal catalysis, organocatalysis, or Lewis acid catalysis), visible-light photocatalysis proceeds *via* electron or energy transfer to generate reactive intermediates of substrates or reagents rather than lowering the transition state energy.³⁻⁶ Irradiation of a PC, typically a homogeneous ruthenium or iridium polypyridyl complex, results in an excited species that can accept or donate a single electron, enabling photoredox catalysis (PRC) *via* oxidative or reductive quenching cycles (Figure 2.1, A). An excited photocatalyst can alternatively also transfer its excited state energy (EnT) to a substrate or reagent to induce chemical reactions.⁷⁻⁸ Heterogeneous photocatalysts, such as semiconductors, are operating by the same electron and energy transfer processes as homogeneous photocatalysts (Figure 2.1, B).⁹⁻¹⁰ This is in stark contrast to conventional catalysis, where homogeneous catalysts cannot be simply substituted by a heterogeneous material. When a semiconductor absorbs photons with sufficiently high energy, electrons are excited from the valence band (VB) to the conduction band (CB), generating simultaneously an oxidizing and a reducing species on a single particle. The generated electron holes (h^+) can oxidize electron donors whereas the electrons in the VB are able to reduce electron acceptors *via* single-electron transfer.

This review provides an overview of the most common, purely heterogeneous photocatalysts, that were successfully applied in organic synthesis focusing on catalysts and strategies that enable the use of visible light (> 400 nm). Our discussion includes “traditional” semiconductors (such as TiO_2), conjugated microporous polymers (CMPs),

covalent organic frameworks (COFs), and metal organic frameworks (MOFs). Examples of homogeneous photocatalysts that are immobilized on supports are not discussed.¹¹⁻¹⁴ Mechanistic discussions of the individual reactions and the photoelectronic properties of semiconducting materials are out of the scope of this review and can be found elsewhere.^{3-6, 9-10, 15-20}

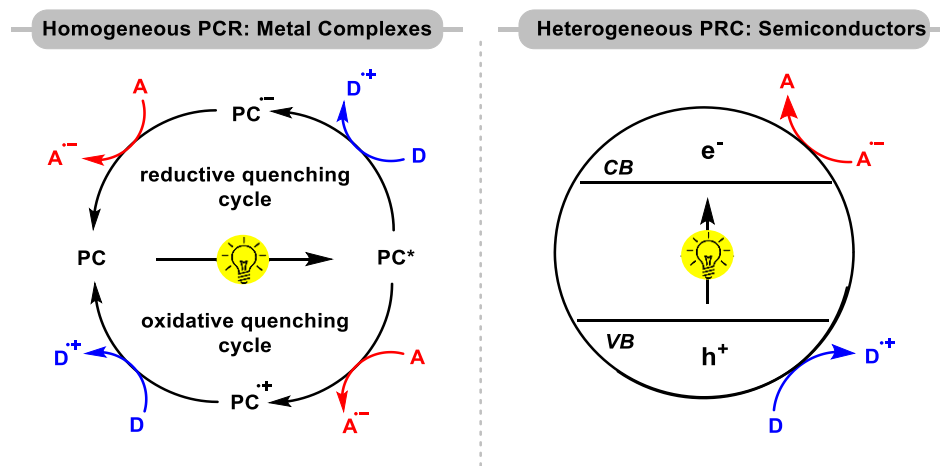
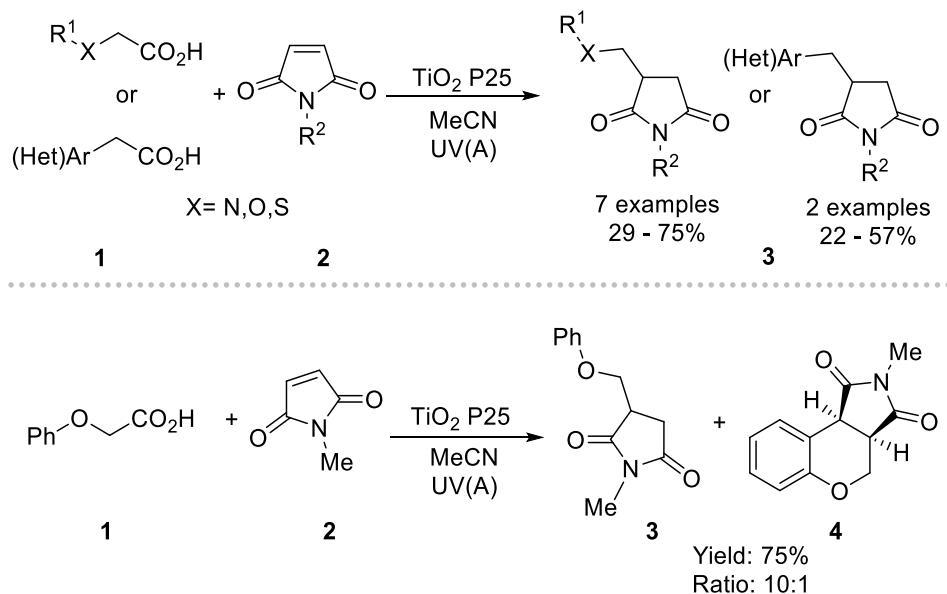


Figure 2.1. Homogeneous and heterogeneous photoredox catalysis.

2.2 Metal oxides: TiO₂

Titanium dioxide is a naturally occurring mineral that has various applications ranging from the use as white pigment in dyes or cosmetics to its employment as photocatalyst for water purification or energy conversion.²⁰ Although the large band gap semiconductor requires ultraviolet (UV) light irradiation to form electron-hole pairs, it is among the most frequently applied heterogeneous photocatalysts in organic synthesis.¹⁵ As the use of TiO₂ and other metal oxide semiconductors as PCs in organic synthesis was recently surveyed in an excellent review articles,^{15, 21-22} we limit our discussion to a representative set of examples. The radical decarboxylation of carboxylic acids, results in carbon-centered radicals, and can be initiated using UV(A) irradiation (>365 nm) in the presence of TiO₂ P25. This is the most commonly applied form of TiO₂ in photocatalysis and consists of the polymorphs anatase and rutile a ratio of 8:2. Under anhydrous, anaerobic conditions, the resulting stabilized carbon-centered radicals were coupled with *N*-substituted maleimides in moderate yields (Scheme 2.1).²³ In case of aryloxyacetic acids (**1**), mixtures of the desired radical addition product (**3**) and chromene derivatives (**4**), which are generated in a photocatalytic addition-cyclization cascade, were observed.



Scheme 2.1. Decarboxylative addition of carboxylic acids to *N*-substituted maleimides using TiO_2 and UV-light irradiation.

Irradiation with UV-light is, however, often associated with severe drawbacks as high-energy photons can cause selectivity issues by, for example, activating substrates or reagents directly. To overcome such issues, strategies that enable the utilization of visible light are intensively investigated.

2.2.1 Surface complexation of substrates/reagents and TiO_2

A straightforward, but limited strategy that is able to extend the absorption of TiO_2 to visible light is the formation of a surface complex between TiO_2 and a heteroatom-containing substrate that creates a new electron donor level above the VB of the metal oxide (Figure 2.2).¹⁰

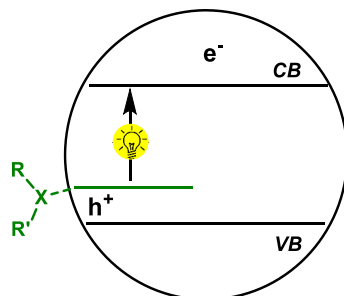
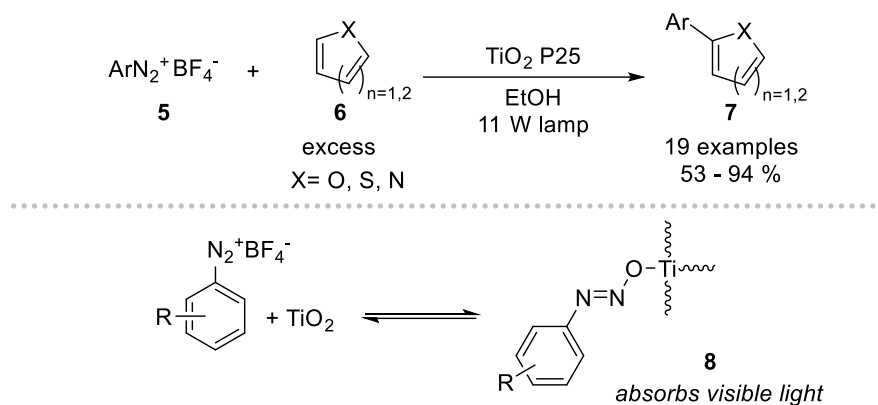


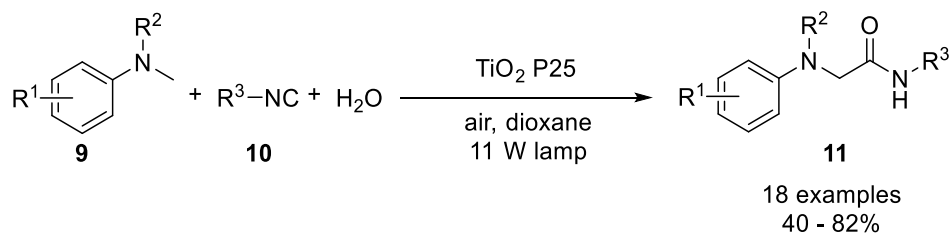
Figure 2.2. The formation of surface complexes between substrates and TiO_2 enables visible light harvesting.

Rueping and coworkers used this approach for the Meerwein-arylation of heteroaromatic compounds (**6**) with aryldiazonium salts (**5**) catalyzed by TiO₂ P25 (Scheme 2.2).²⁴ Mechanistic investigations indicated that a TiO₂-diazoether species (**8**), which absorbs visible light, is initially formed. The catalytic method enabled the arylation of furan, thiophene and pyridine in good to excellent yields.



Scheme 2.2. Meerwein arylation of heterocycles catalyzed by TiO₂ using visible light *via* the formation of a TiO₂-diazoether complex.

The same group reported on a TiO₂ P25 catalyzed multi-component Ugi-type reaction of *N,N*-dimethylanilines (**9**) with isocyanides (**10**) and water that results in the formation of α -amino amides (**11**, Scheme 2.3).²⁵ The formation of a surface complex between the aniline derivative (**9**) and TiO₂ was proposed to be responsible for visible light absorption. The metal oxide semiconductor was recycled five times without any loss in catalytic activity.

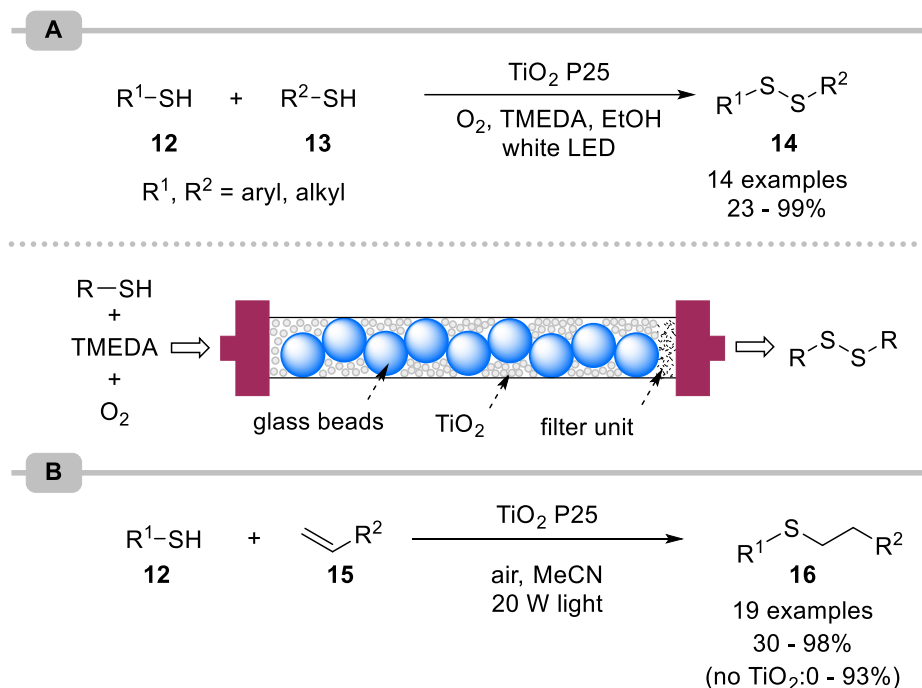


Scheme 2.3. Photocatalytic Ugi-type reaction using TiO₂ and visible light.

Surface interactions between *N,N,N',N'*-tetramethylethylenediamine (TMEDA) and TiO₂ enabled the synthesis of symmetrical and unsymmetrical disulfides (**14**) from thiols (**12**, **13**) using visible light (Scheme 2.4, A).²⁶ The reaction rate was significantly increased in a

continuous flow²⁷⁻²⁸ approach using a packed bed reactor. To avoid high-pressure drops due to aggregation of TiO₂ nanoparticles in the presence of TMEDA, glass beads were added as inert packing material.

Visible-light mediated thiol-ene reactions were shown to benefit from the presence of TiO₂ P25 (Scheme 2.4, B).²⁹ Binding of the thiol starting materials is likely responsible for the ability to use visible light as energy source. Although product formation was also observed in the absence of a catalyst in some cases, the efficiency and scope of this transformation was significantly increased when catalytic amounts of the heterogeneous semiconductor were added.



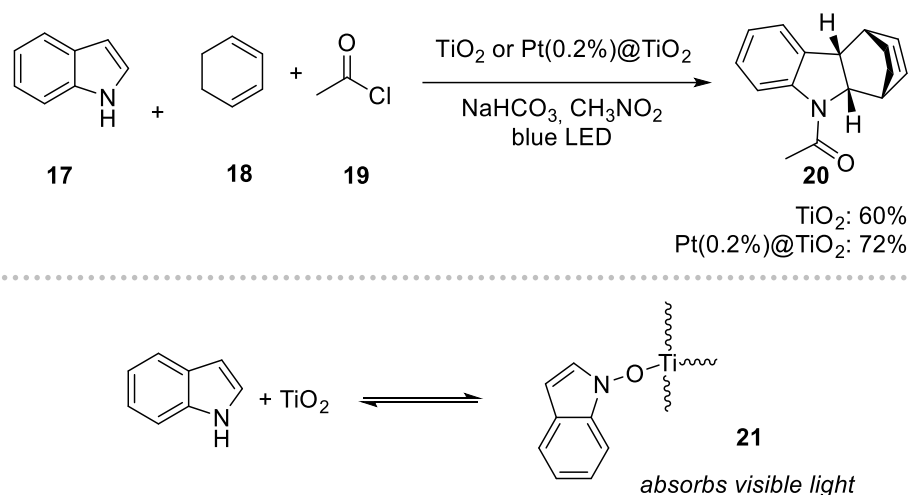
Scheme 2.4. (A) Disulfide formation and (B) thiol-ene reaction *via* SET oxidation of thiols by TiO₂ using visible light.

The groups of Scaiano and Yoon showed that a TiO₂-indole surface complex (**21**) can be excited with a 460 nm light source to promote the radical Diels-Alder reaction between indoles (**17**) and 1,3-cyclohexadienes (**18**) (Scheme 2.5).³⁰ To prevent fragmentation of the cycloaddition products, the reaction was carried out in presence of acetyl chloride (**19**) resulting in the desired acetylated tetrahydrocarbazoles (**20**). Platinum-doped titanium dioxide (Pt(0.2%)-TiO₂) was shown to double the photon efficiency in comparison to

undoped TiO_2 , and a range of protected tetrahydrocarbazoles (**20**) was synthesized in moderate to good yield.³¹ During a recycling study, a decrease in the activity of $\text{Pt}(0.2\%)\text{@TiO}_2$ was observed. The authors hypothesized that surface poisoning from organic compounds, most likely derived from indole, is responsible for catalyst deactivation.

2.2.2 Dye sensitized TiO_2

While surface complexation results only in a small redshift of the absorption of TiO_2 , decoration of the metal oxide semiconductor with sensitizers (dyes) extends the absorption to a broader range of the visible light spectrum. This strategy is applied in dye-sensitized solar cells (DSSCs),³² and dye-sensitized photocatalysts (DSPs) for light driven H_2 production.³³



Scheme 2.5. Radical Diels-Alder reaction catalyzed by TiO_2 using visible light.

Various functional groups are well established for the immobilization of dyes on TiO_2 in DSSCs including carboxylic acids, phosphonic acids, or sulfonic acids and various binding modes can be responsible for immobilization.³⁴ In most cases, an electron of the dye/sensitizer (sens) is excited from the HOMO to the LUMO, followed by injection into the CB of the semiconductor (type I sensitization, Figure 2.3). A “direct” electron-injection from the HOMO of the sensitizer into the semiconductor’s CB upon photoexcitation is the basis of type II sensitization.³⁵ This mechanism is analogous to metal-to-ligand charge-transfer (MLCT) in ruthenium and iridium polypyridyl complexes, and a new absorption band is formed upon binding. In both cases, the valence band position is irrelevant for light

harvesting, as photons are absorbed by the sensitizer. This avoids side reactions caused by highly reactive holes that would result from direct semiconductor excitation with UV light.

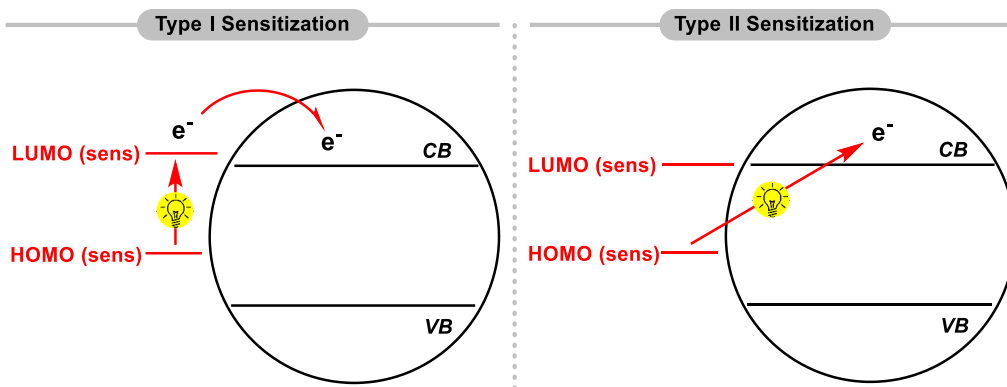
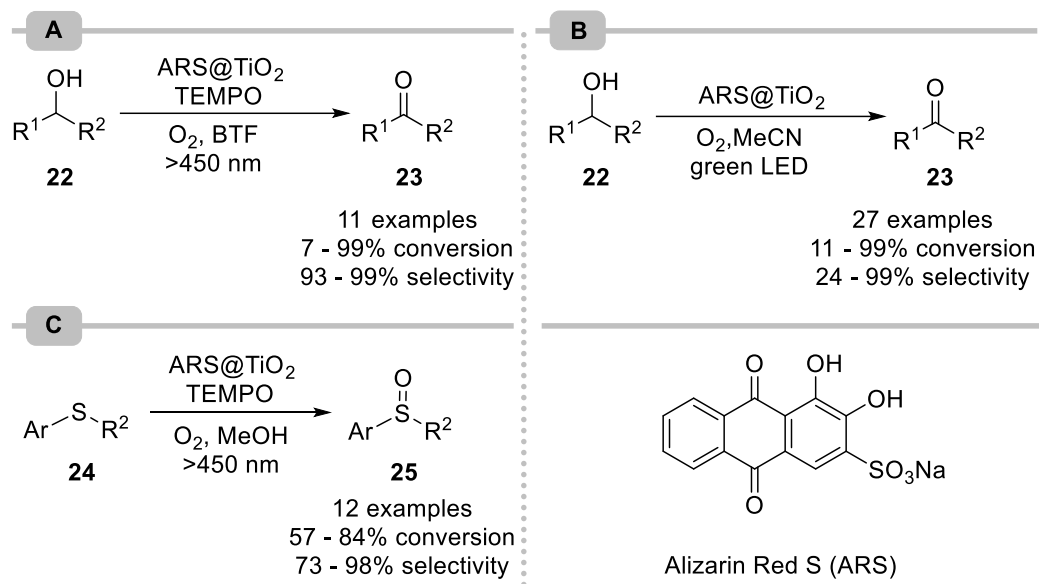


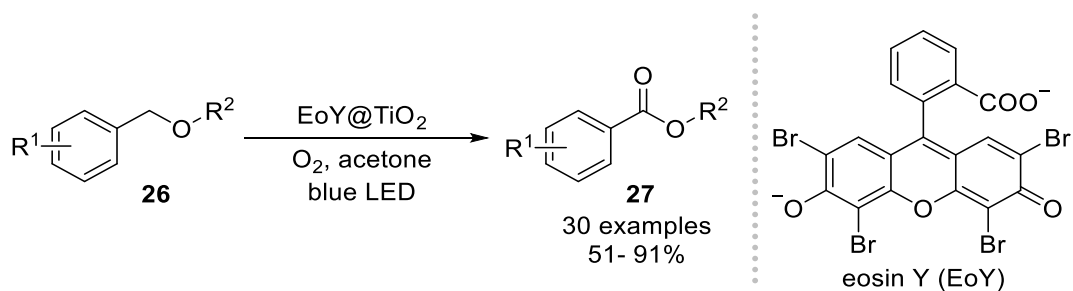
Figure 2.3. Sensitization of TiO₂.

Zhao and coworkers sensitized TiO₂ with alizarin red (ARS@TiO₂) for the aerobic, photocatalytic oxidation of alcohols (**22**) in presence of catalytic amounts of 2,2,6,6-tetramethylpiperidine-1-oxyl (TEMPO, Scheme 2.6, A).³⁶ The sensitized semiconductor is proposed to remove an electron from TEMPO, generating TEMPO⁺ that subsequently oxidizes the alcohols (**22**) to the corresponding aldehydes (**23**). Regeneration of the resulting TEMPO-H by the dye or O₂ closes the catalytic cycle. A similar system was presented using eosin Y as sensitizer.³⁷ More recently, Lang and coworkers showed that the reaction works also efficiently in the absence of TEMPO (Scheme 2.6, B).³⁸ The combination of ARS@TiO₂ and TEMPO was also applied for the photocatalytic oxidation of sulfides (**24**) to sulfoxides (**25**) in the presence of oxygen (Scheme 2.6, C).³⁹ TEMPO was shown to be crucial for the stability of the photocatalyst as its addition avoids photodegradation of ARS.



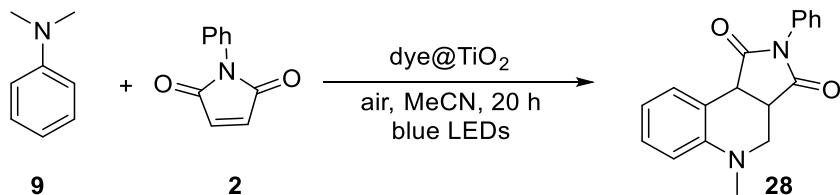
Scheme 2.6. Aerobic oxidation of alcohols (A, B) and sulfides (C) using ARS@TiO₂ as photocatalyst.

Eosin Y sensitized TiO₂ (EoY@TiO₂) enabled the aerobic oxidation of benzyl ethers (**26**) to the corresponding benzoate esters (**27**) in moderate to excellent yield (Scheme 2.7).⁴⁰ The method tolerates various functional groups and is applicable to benzyl protected amino acids and carbohydrates.



Scheme 2.7. Aerobic oxidation of benzyl ethers catalyzed by eosin Y sensitized TiO₂.

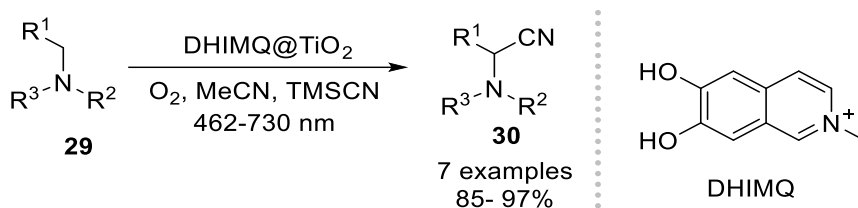
A comparison of various sensitizers immobilized on TiO₂ showed that ARS is well suited for a photocatalytic cascade radical C–C bond formation/cyclization of *N,N*-dimethylaniline (**28**) with *N*-phenylmaleimides (**2**) that results in **30** (Scheme 2.8).⁴¹ A decreased catalytic activity was observed during recycling experiments and could be correlated to a decrease of the amount of the dye due to leaching.



Alizarin red S -TiO ₂	Rhodamine B -TiO ₂	Rose Bengal -TiO ₂	Fluorescein -TiO ₂	Indigo carmine -TiO ₂	Bromocresol green-TiO ₂
91%	trace	12%	trace	51%	not detected

Scheme 2.8. TiO₂ sensitized with different dyes for the aerobic oxidative cyclization of *N,N*-dimethylaniline with *N*-phenyl maleimide. Reproduced with permission from Ref. [25]

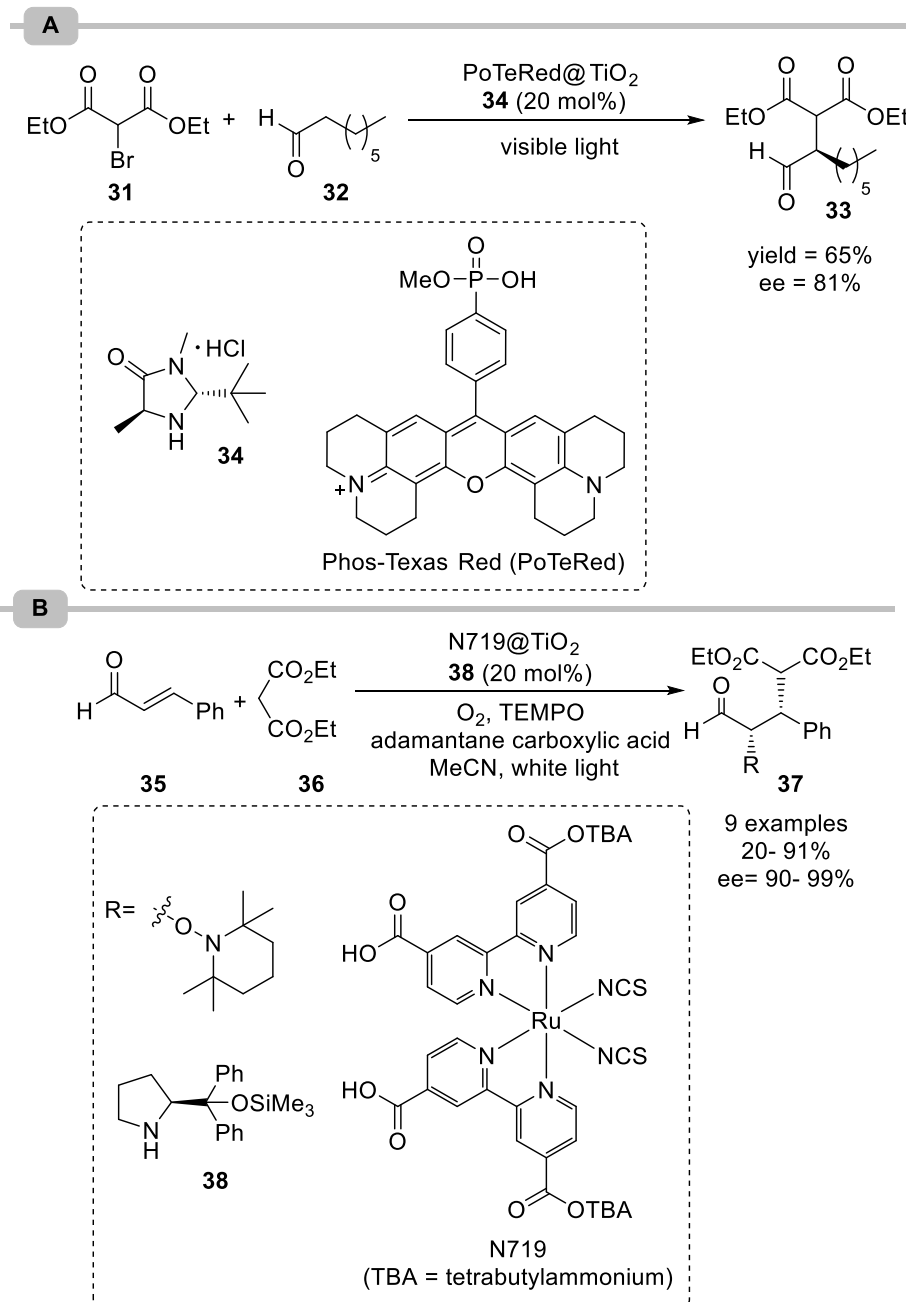
Opatz and colleagues designed a type II sensitizer by merging a chromophore with a redox-active catechol surface anchoring group.⁴² The resulting 6,7-dihydroxy-2-methylisoquinolinium (DHMIQ) was anchored on TiO₂ nanoparticles (DHMIQ@TiO₂) and showed a high activity as photocatalyst for the oxidative cyanation of tertiary amines (**28**) using trimethylsilyl cyanide (TMSCN, Scheme 2.9). The sensitized semiconductor was shown to harvest near-infrared (NIR) light, enabling the reaction even using a 730 nm light source.



Scheme 2.9. Photocyanation of amines using TiO₂ decorated with a type II sensitizer.

Photocatalysis can be combined with other catalytic strategies, such as organocatalysis (dual catalysis).⁴³⁻⁴⁴ König and coworkers showed that TiO₂ sensitized with Phos-Texas Red

(PoTeRed@TiO₂) can be used as PC in combination with catalytic amounts of an imidazolidinone organocatalyst (**34**) for the visible-light-promoted α -alkylation of octanal (**32**) with diethyl bromomalonate (**31**) resulting in enantioenriched **33** (ee = 81%) in 65% (Scheme 2.10, A).⁴⁵



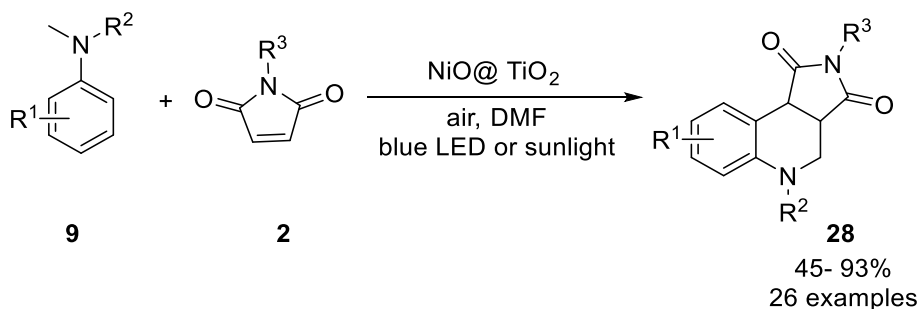
Scheme 2.10. Combination of sensitized TiO₂ and organocatalysis. (A) Visible-light-promoted α -alkylation of octanal with diethyl bromomalonate. (B) Tandem Michael addition/oxyaminations of α,β -unsaturated aldehydes.

More recently, the group of Jang combined TiO₂ sensitized with a ruthenium dye (N719@TiO₂) with asymmetric iminium catalysis using visible light irradiation (Scheme 2.10, B).⁴⁶ The authors were able to perform highly enantio- and diastereoselective tandem Michael addition/oxyaminations of α,β -unsaturated aldehydes (**35**) with **36**.

2.2.3 Metal doped TiO₂

Another possibility to extend the absorption of metal oxide semiconductors is metal doping *via* chemical or physical methods.²⁰ Modifying TiO₂ with metal nanoparticles can narrow the band gap, and increase the photocatalytic activity due to an improved charge separation, as well as the reduction of electron-hole recombination rates.

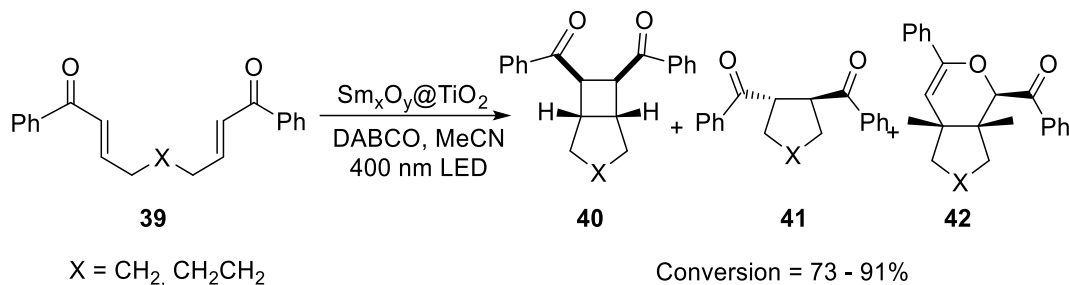
Shen and co-workers showed that the surface modification of TiO₂ with nickel(II) oxide results in a material that absorbs visible light and is able to induce the photocatalytic cascade radical C–C bond formation/cyclization of *N,N*-dimethylanilines (**9**) with *N*-phenylmaleimides (**2**, Scheme 2.11).⁴⁷ The red shift upon surface modification is attributed to a rise of the valence band potential resulting from metal doping. Importantly, the photocatalyst did not show any reduction in its activity over nine cycles during a recyclability study.



Scheme 2.11. Photocatalytic cyclization of tertiary anilines with maleimides using NiO doped TiO₂.

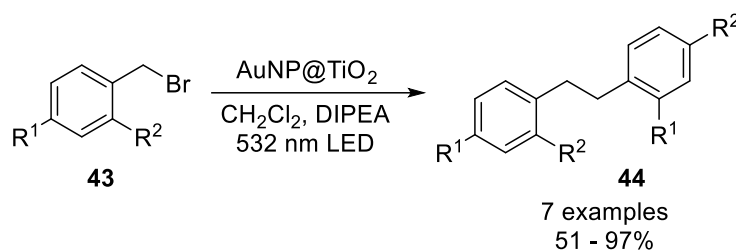
By decorating TiO₂ with samarium oxide nanoparticles, Scaiano and co-workers developed a single material (Sm_xO_y@TiO₂) that can be used for dual photo/Lewis acid catalyzed intramolecular [2+2] cycloadditions of symmetrical aryl (bis)enones (**39**, Scheme 2.12).⁴⁸ The desired cycloadducts (**40-42**) were formed in moderate to good yield (47- 72%) using 400 nm LEDs. The same system was also used for the photoreductive cyclization of

chalcones. Reusability studies showed no loss of efficiency over five cycles for the photoreductive coupling of chalcones.



Scheme 2.12. Dual Photo/Lewis acid catalysis with a single bifunctional nanomaterial.

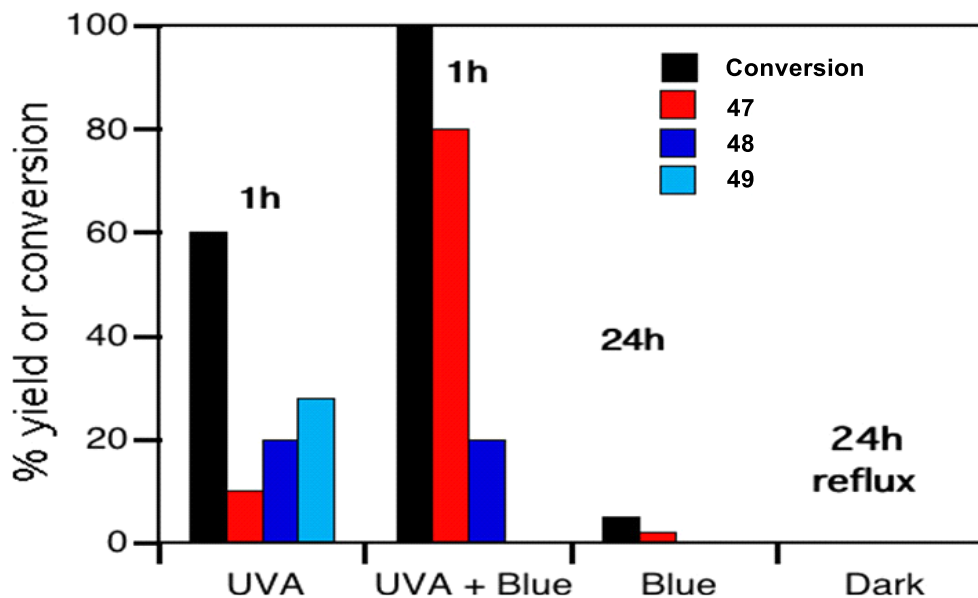
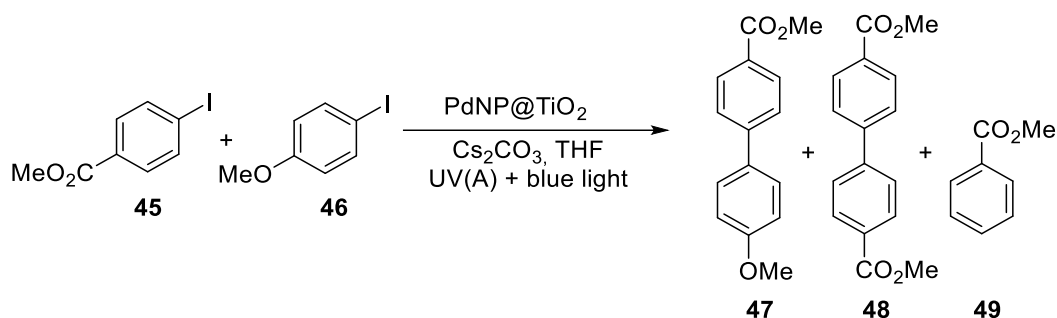
Gold nanoparticles (Au NPs) absorb visible light due to the surface plasmon resonance effect. Upon deposition on TiO₂, the CB of the metal oxide semiconductor can transfer excited electrons to an acceptor.¹⁰ This strategy was used for the dimerization of benzyl bromides (**43**) using green light (Scheme 2.13).⁴⁹ Studies with the radical trap TEMPO suggest that the mechanism proceeds *via* a benzyl radical intermediate. A decrease in the catalytic activity during a recyclability study was related to a growth of the Au particles from 2.5 to 4.1 nm.



Scheme 2.13. Reductive dimerization of benzyl bromides using AuNP@TiO₂ and green LED irradiation.

TiO₂ decorated palladium nanoparticles (NPs) with was used for the photocatalytic Ullmann cross-coupling of an electron-rich (**45**) and electron-poor (**46**) aryl iodides (Scheme 2.14).⁵⁰ Interestingly, only the combination of UVA (368 nm) and blue (465 nm) light resulted in a relatively selective formation of the desired cross-coupling product (**47**). If only blue light was used, almost no conversion was observed whereas UVA light alone suffered from low selectivity. The authors concluded that the Pd NPs capture the electrons from the conduction

band after excitation with UVA light, thereby increasing the lifetime of the electron-hole pair. Blue light is proposed to be exclusively absorbed by Pd NPs, initiating a final photoreductive elimination. Recyclability studies showed that the conversion stays constant over four cycles, whereas the selectivity decreases (50).



Scheme 2.14. Selectivity control in the photocatalytic Ullmann C–C coupling with Palladium doped TiO₂ using combined UVA and blue light. *Reproduced with permission from Ref. 33.*

The same group used Pd NPs on TiO₂ for light-mediated Sonogashira couplings.⁵¹ In this case, the photocatalyst lost its catalytic activity completely after two cycles. Since ICP-OES analysis showed no Pd leaching, catalyst poisoning by alkyne hydrogenation products on the surface was proposed as a plausible reason.

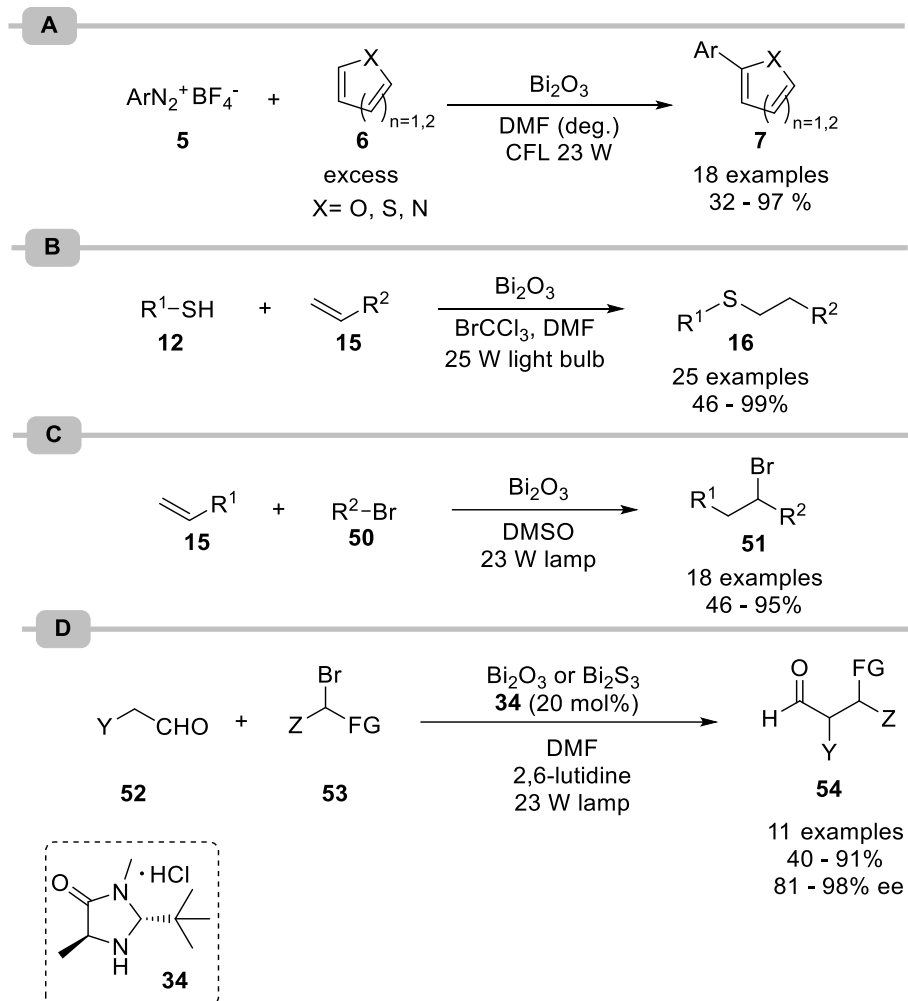
2.3 Bismuth oxide

Bismuth(III) oxide has a smaller band gap (2.1-2.8 eV) than TiO₂ and absorbs visible light without the need for any modifications. Pericàs and coworkers showed that catalytic amounts of Bi₂O₃ catalyze the Meerwein-type coupling of aryl diazonium salts (**5**), which were generated in-situ from anilines, with heteroaromatic compounds (**6**) using visible light irradiation (Scheme 2.15, A).⁵²

Fadeyi and colleagues used Bi₂O₃ for late-stage diversifications of complex biomolecules and active pharmaceutical ingredients via photocatalytic thiol-ene reaction using BrCCl₃ as radical source.⁵³

The visible light-induced atom-transfer radical addition (ATRA) of alkyl radicals to olefins was also reported using this versatile metal oxide photocatalyst (**15**, Scheme 2.15, C).⁵⁴ Here, the photoexcited state of Bi₂O₃ is capable to promote the cleavage of the C–Br bonds (of the ATRA donors) to form the alkyl radicals.

Similarly, alkyl radicals generated via Bi₂O₃ photocatalyzed C–Br bond cleavage were used for the enantioselective α -alkylation of aldehydes (**52**) in presence of a second-generation imidazolidinone catalyst (**34**, Scheme 2.15, D).⁵⁵



Scheme 2.15. (A) Meerwein arylation of heterocycles using Bi_2O_3 as photocatalyst. (B) Thiol-ene reaction *via* SET oxidation of thiols by Bi_2O_3 using visible light. (C) Atom-Transfer radical addition of bromo ATRA donors to olefins using Bi_2O_3 as visible light photocatalyst. (D) Visible-light-promoted α -alkylation of aldehydes with α -bromocarbonyl compounds combining organocatalysis and Bi_2O_3 as visible light photocatalyst.

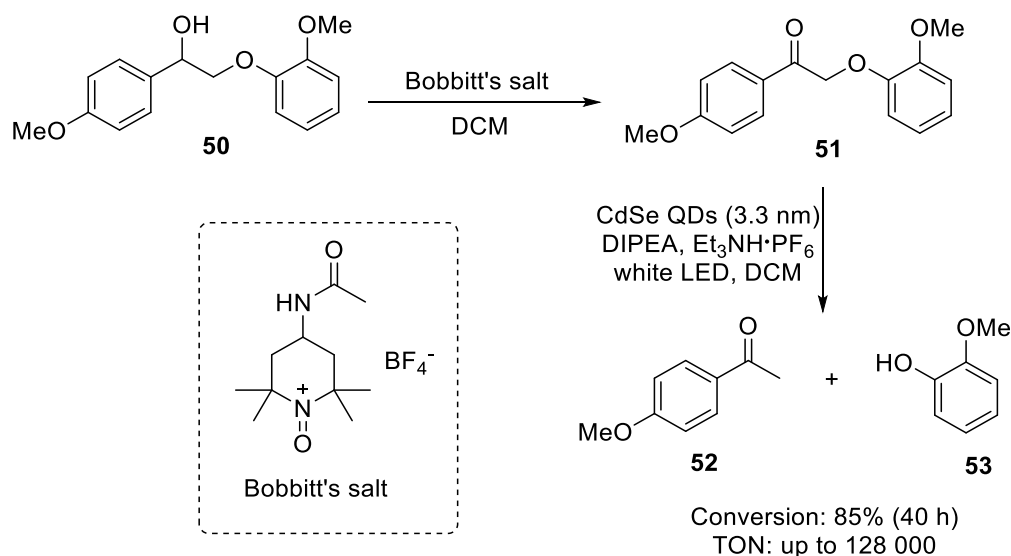
Other Bismuth based semiconductors, such as Bi_2WO_6 , BiVO_4 , and BiOCl can be also used as visible light photocatalyst for, for example the oxidation of alcohols⁵⁶⁻⁵⁷, toluene⁵⁸ or amines⁵⁹⁻⁶⁰.

2.4 CdSe, CdS

Cadmium sulfide and cadmium selenide are small band gap semiconductors that absorb visible light up to 540 nm. One of the main advantages of these materials is the straightforward preparation of colloidal nanocrystals (quantum dots, QDs). The optical

properties, including the CB and VB position, can be tuned by modifying the nanoparticle size.⁶¹

CdSe QDs were used for the photocatalytic C–O bond cleavage of a model substrate (**50**) that emulates the depolymerisation of β -O-4-linkages that are found in lignin (Scheme 15).⁶² An initial, thermal oxidation of **50** with Bobbitt's salt followed by the photocatalytic C–O bond cleavage yields 4-acetanisole (**52**) and guaiacol (**53**). The CdSe QDs (3.3 nm), that were stabilized by oleic acid and trioctylphosphine oxide, gave turnover numbers (TON) up to 128 000. A comparison with a molecular, homogeneous iridium photocatalyst ($[\text{Ir}(\text{ppy})_2(\text{dtbbpy})]\text{PF}_6$) showed that the QDs have a 15 times greater turnover frequency.

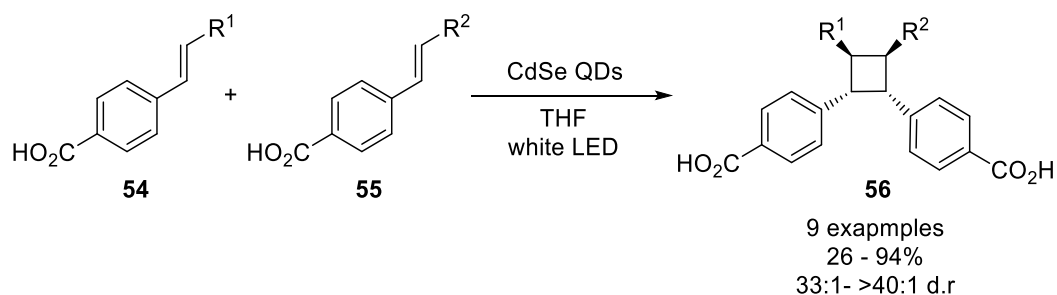


Scheme 2.16. Photocatalytic C–O cleavage of a lignin model structure using CdSe QDs.

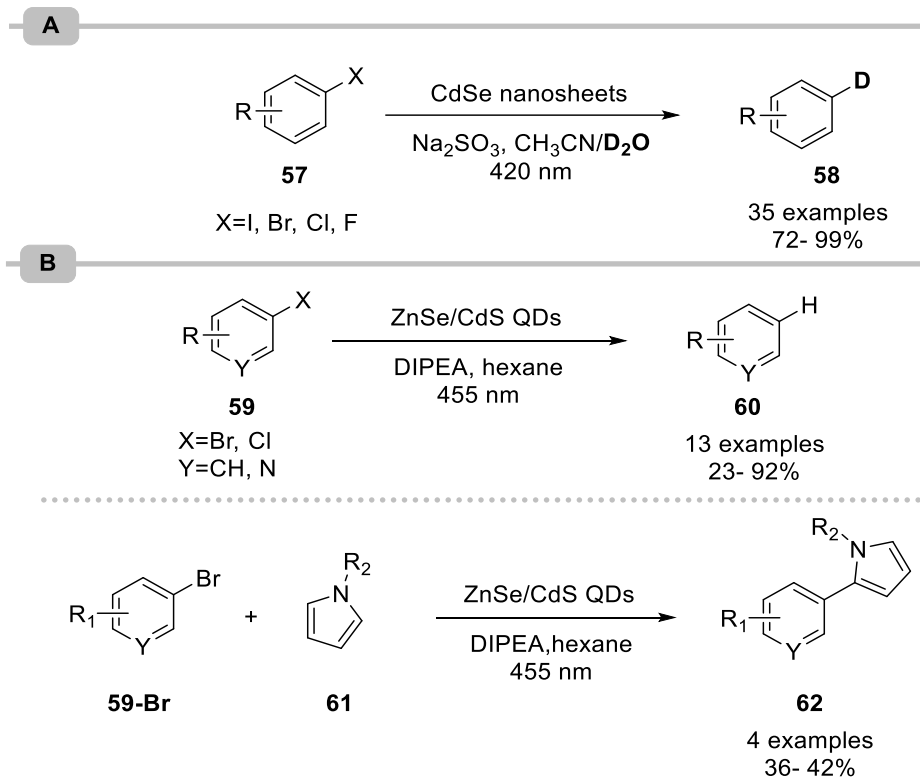
Weiss and colleagues reported on a stereoselective [2+2] cycloaddition of 4-vinylbenzoic acid derivatives (**54**, **55**) with tuneable regioselectivity using CdSe QDs that yields tetra-substituted *syn*-cyclobutanes (**56**, Scheme 2.17).⁶³ Transient absorption spectroscopy experiments indicated that the reaction proceeds *via* an energy transfer mechanism. The selectivity towards head-to-head products results from a reversible binding of the substrates/products *via* their carboxylic acid functionalities on the surface of the QDs. The authors proposed that the surface binding results in non-covalent π - π interactions between the rigid olefins that are responsible for the selective production of the kinetically

disfavoured *syn*-products. Depending on the position of the acid functionality in the substrate, different regioisomers can be formed selectively. The ability to precisely control the triplet energy levels of the QDs by tuning the particle size further enabled challenging intermolecular hetero-cycloadditions.

Porous CdSe nanosheets with a thickness of 1.7 nm were used for the photocatalytic deuteration of aryl halides (**57**) *via* photocatalytic D₂O splitting in presence of Na₂SO₃ as sacrificial electron donor (Scheme 2.18, A).⁶⁴ Similarly, ZnSe/CdS-core/shell quantum dots, enabled the reductive dehalogenation of electron deficient (hetero)aryl halides (**59**) using visible light in presence of DIPEA (Scheme 2.18, B).⁶⁵ The radical intermediates can be also trapped with *N*-substituted pyrrole (**61**) to generate the respective C–C coupling products.



Scheme 2.17. Regio- and stereoselective [2+2] cycloaddition of 4-vinylbenzoic acid using CdSe QDs under visible light irradiation.

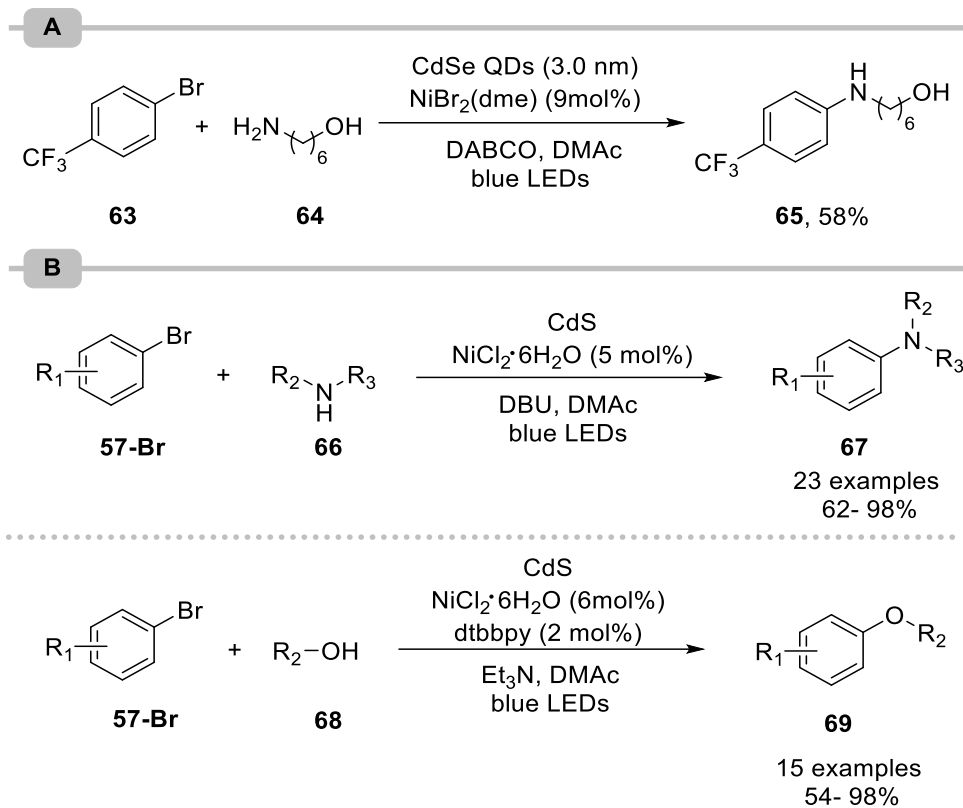


Scheme 2.18. (A) Deuteration of aryl halides by photocatalytic D_2O water splitting with porous CdSe sheets as photocatalyst. (B) Reductive dehalogenation of aryl halides and C-H arylation with pyrroles using ZnSe/CdS core/shell quantum dots as photocatalyst.

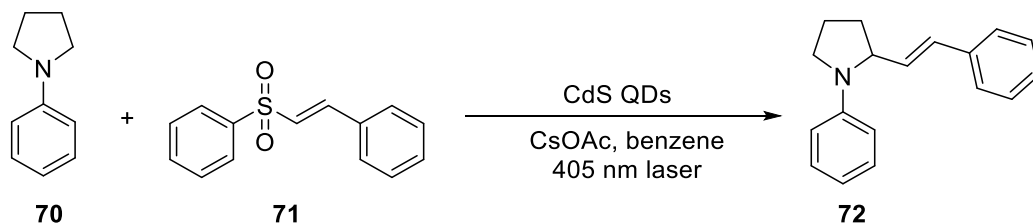
The versatility of CdSe QDs for photocatalytic organic synthesis was reported by Weix and coworkers.⁶⁶ The authors showed that single-sized CdSe QDs (3.0 ± 0.2 nm), stabilized by trioctylphosphine oxide and oleic acid, are efficient catalysts for a range of photoredox reactions including the β -alkylation of aldehydes, the β -aminoalkylation of ketones and the dehalogenation of aryl iodides. The authors further showed that the heterogeneous semiconductor is able to act as photocatalyst for the amination of aryl halides in combination with nickel catalysis (Scheme 2.19, A). Similarly, Xiao and coworkers used CdS in combination with nickel catalysis for C–N and C–O cross-couplings (Scheme 2.19, B).⁶⁷ Moderate to excellent yields were obtained for the coupling of various amines (**67**) and alcohols (**68**) with electron-poor aryl bromides (**57-Br**). The heterogeneous photocatalyst could be recycled ten times without significant loss in activity.

Weiss and colleagues demonstrated that tuning the ligand shell of CdS QDs can increase the reaction rate for the photocatalytic C–C coupling of 1-phenylpyrrolidine (**70**) and phenyl *trans*-styryl sulfone (**71**, Scheme 2.20).⁶⁸ Replacing a portion of the oleate ligand by octyl

phosphonate creates a mixed monolayer that increased the initial rate by a factor of 2.3 compared to CdS QDs with an oleate ligand shell. This phenomenon is attributed to a better permeability of the ligand shell that facilitates the rate-limiting charge transfer between 1-phenylpyrrolidine (**70**) and the QD core.



Scheme 2.19. Dual photo/nickel catalysis using semiconductors. (A) C–N cross-coupling using CdSe QDs. (B) C–N and C–O cross-couplings using CdS.

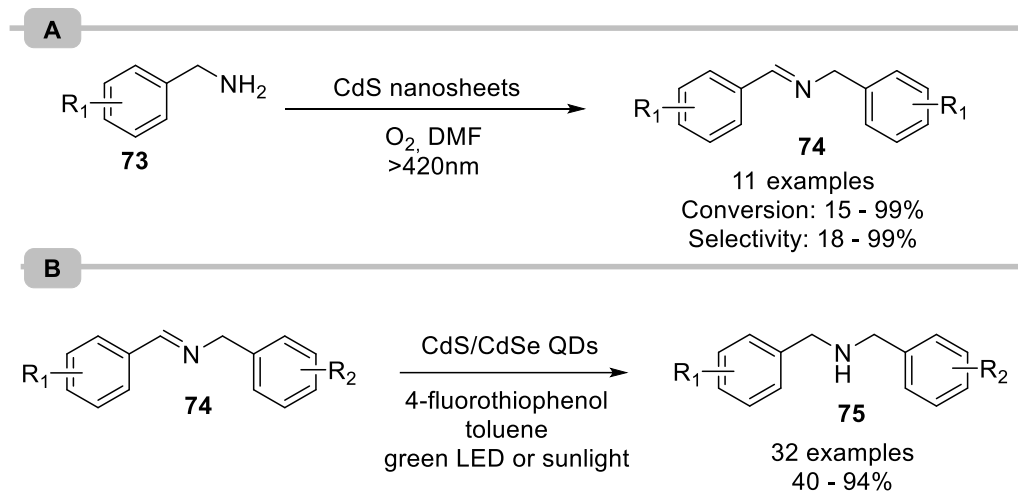


Scheme 2.20. Photocatalytic C–C coupling of 1-phenylpyrrolidine and phenyl trans-styryl sulfone using CdS QDs.

The oxidative coupling of amines (**73**) to imines (**74**) was achieved using visible light irradiation using CdS nanosheets in the presence of oxygen (Scheme 2.21, A).⁶⁹ The high

specific surface area (56.3 m²/g) of the porous CdS nanosheets contributed to an better performance compared to CdS nanoparticles.

The transfer hydrogenation of *N*-benzylidenebenzylamine derivatives (**74**) that gives the respective dibenzylamines (**75**) was realized using 4-fluorothiophenol as hole acceptor and hydrogen atom donor using green LEDs or sunlight and CdSe/CdS core/shell quantum dots as photocatalysts (Scheme 2.21, B).⁷⁰

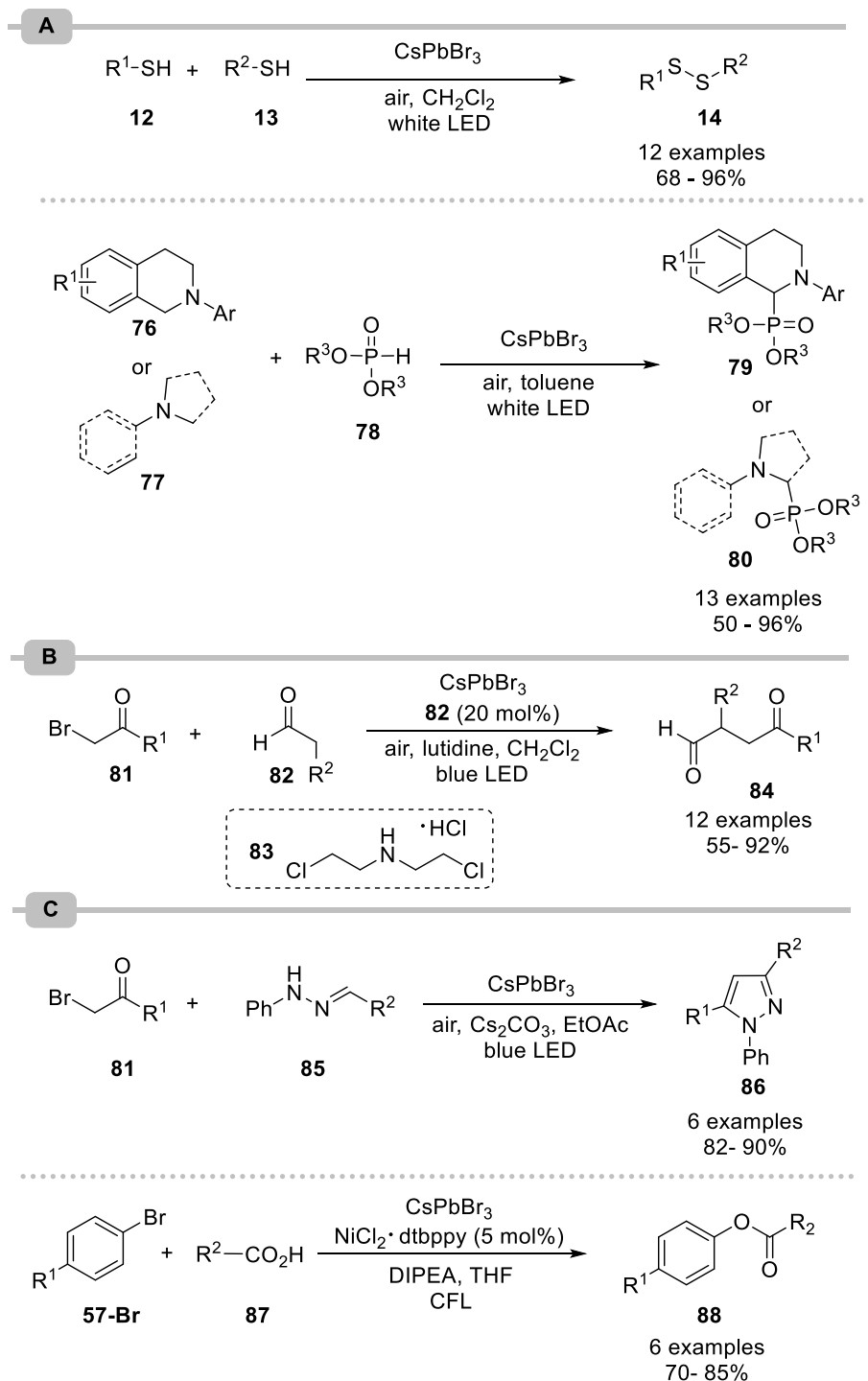


Scheme 2.21. (A) Photocatalytic oxidative coupling of benzyl amines to imines using CdS nanosheets. (B) Light-mediated transfer hydrogenation of *N*-benzylidenebenzylamine using core/shell CdS/CdSe QDs.

2.5 Lead halide perovskites

Lead-halide perovskite (APbX_n) are promising materials for photochemical applications with tunable optical band gaps depending on, for example, the halide composition.⁷¹ One of the few examples for the application of lead halide perovskites in organic synthesis is the photocatalytic formation of symmetrical and unsymmetrical disulfides (**14**) from thiols (**12**, **13**) using CsPbBr₃ under aerobic conditions (Scheme 2.22, A).⁷² The same catalytic system was also suitable for the light-mediated cross-dehydrogenative phosphorylation of *N*-aryl tetrahydroisoquinoline derivatives (**76**) or tertiary amines (**77**). Both reactions showed high efficiency and moderate to excellent yields (50-96%) were obtained. Changing bromine to iodine in the CsPbX₃ structure reduces the bandgap, but the lower oxidation potential led to lower photocatalytic activity towards the disulfide formation. CsPbCl₃, on the contrary, has

a higher oxidative potential, but the large bandgap makes it unsuitable for visible light photocatalysis.



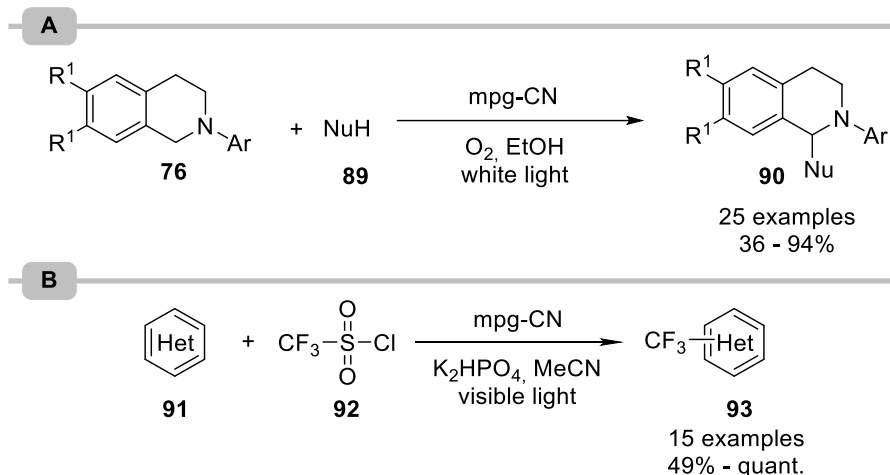
Scheme 2.22. (A) Disulfide formation and cross-dehydrogenative coupling between tertiary amines and phosphite esters using CsPbBr₃ as photocatalyst. (B) α -Alkylation of aldehydes using CsPbBr₃ as photocatalyst (C) Photocatalytic pyrazole synthesis and dual nickel/photo catalyzed esterification using CsPbBr₃ as photocatalyst.

CsPbBr₃ was also used in combination with an amine organocatalyst for the α -alkylation of aldehydes (Scheme 2.22, B).⁷³ The catalytic system showed TONs over 52,000 for the α -alkylation of aldehydes (**82**), which is three orders of magnitude higher than for molecular Ir or Ru photocatalysts. The application of CsPbBr₃ was further expanded to a range of other photocatalytic transformations that include the formation of pyrazoles (**86**), and the dual photo/nickel catalyzed cross-coupling of aryl bromides (**57-Br**) and carboxylic acids (**87**, Scheme 2.22, C).⁷⁴

2.6 Carbon nitrides

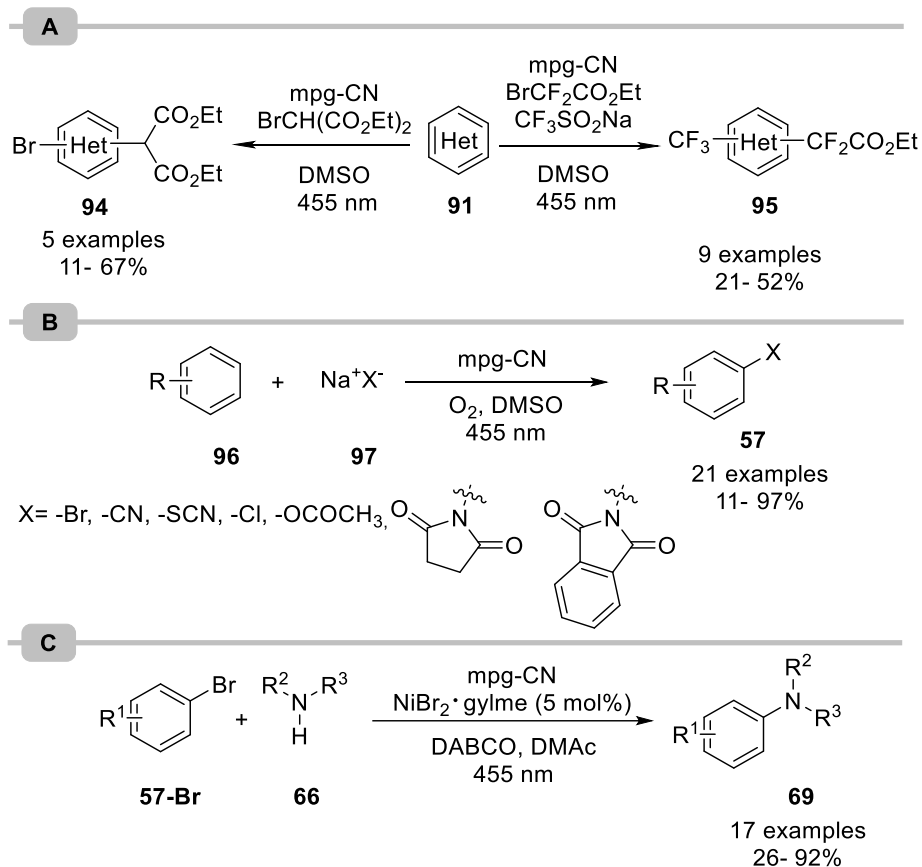
Graphitic carbon nitrides (g-CN), a class of metal-free polymers, are among the most studied materials for heterogeneous photocatalysis.⁷⁵ The organic semiconductors absorb light in the visible area (bandgap ~2.7 eV). In general, g-CN polymers are easy to synthesize from readily available and cheap precursors, such as urea, cyanamide, or melamine. The band gap and position of the valence and conduction band depend on several factors such as the C/N ratio, the polymerization degree or the crystallinity that can be tailored *via* the synthetic approach. We limit our discussion about their use as photocatalysts to a selected set of examples, as the field was recently summarized in several reviews.¹⁶⁻¹⁸

In a collaborative effort, the groups of Blechert, Wang and Antonietti pioneered the application of carbon nitride materials for synthetic purposes, showcasing the photocatalytic properties of these organic semiconductors for the oxidation of alcohols,⁷⁶ and amines.⁷⁷ The same groups further realized the photocatalytic aerobic dehydrogenative C–C coupling of *N*-aryl tetrahydroisoquinolines (**76**) with various nucleophiles (**89**), including nitroalkanes, dimethyl malonate and ketones using mesoporous graphitic carbon nitride (mpg-CN, Scheme 2.23, A). This material is prepared using silica nanoparticles as templates to obtain a high surface area (200 m²/g) that makes it ideally suited for catalytic applications. It was also used for the fluoroalkylation of (hetero)arenes (**91**) *via* the generation of CF₃ radicals in the single electron reduction of trifluoromethanesulfonyl chloride (Scheme 2.23, B).⁷⁸



Scheme 2.23. (A) Cross-dehydrogenative couplings and (B) the fluoroalkylation of (hetero)arenes using mpg-CN as photocatalyst.

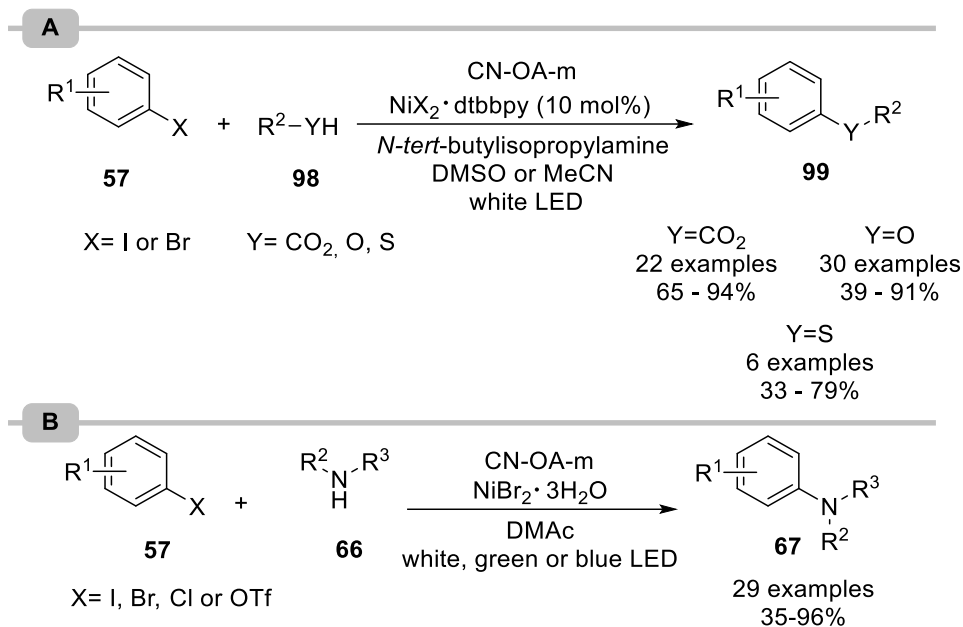
The versatility of mpg-CN as photocatalyst for organic synthesis was recently demonstrated for a range of reactions, including the twofold C-H functionalisation of heteroarenes (**89**, Scheme 2.24, A).⁷⁹ The authors further demonstrated the direct C-H functionalisation using metal salts that enabled, for example, brominations, cyanations and thiocyanations of arenes (Scheme 2.24, B). The heterogeneous, organic semiconductor was also used as photocatalyst in combination with a homogeneous nickel catalyst for the semi-heterogeneous dual photoredox nickel catalytic aryl amination of aryl bromides with secondary and primary amines (Scheme 2.24, C).



Scheme 2.24. (A) C-H bifunctionalisation of arenes using mpg-CN (B) C-H functionalisation using alkali metal salts as nucleophiles. (D) Ligand-free mpg-CN/nickel dual catalytic C–N cross-couplings of aryl bromides amines.

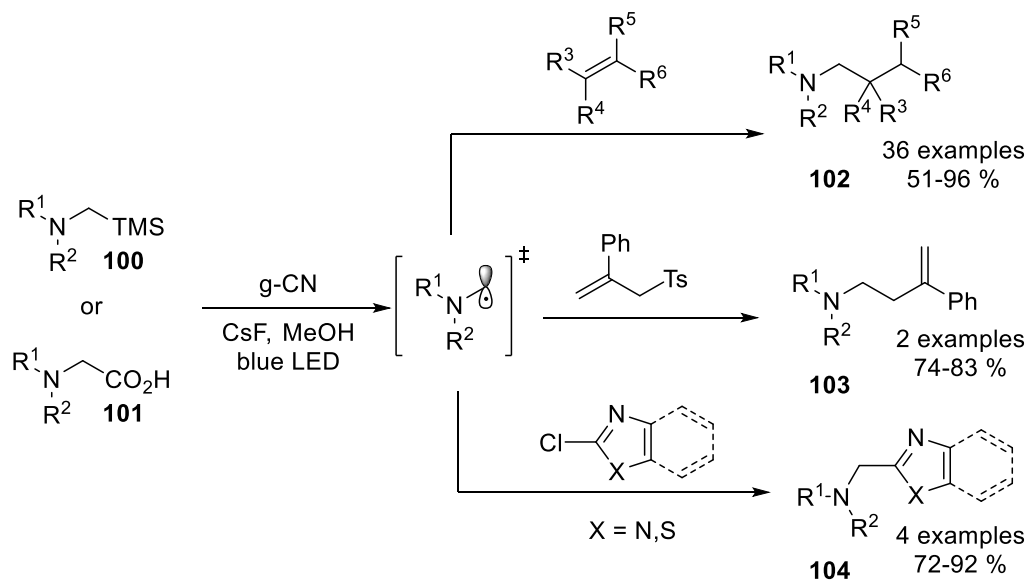
Similarly, a carbon nitride that is prepared through co-condensation of urea and oxamide followed by post-calcination in a molten salt (CN-OA-m) proved efficient for dual nickel/photocatalysis.⁸⁰⁻⁸² The semi-heterogeneous approach enabled the esterification and (thio)etherification of electron-poor aryl halides (**57**, Scheme 2.25, A). In these cases, the heterogeneous semiconductor could be reused several times without any loss in reactivity. Real-time monitoring of the esterification by *in situ* FTIR spectroscopy showed that the kinetic profile of the carbon nitride catalyzed protocol is similar to the reaction using homogeneous iridium photocatalysis.⁸⁰ Using a similar protocol the corresponding C–N cross-coupling did also enable the coupling with aryl halides that lack an electron withdrawing group, but suffered from severe reproducibility issues.⁸² The reactions frequently resulted in low yields and the heterogeneous, yellow PC became black. High amounts of deposited nickel were detected on the recovered carbon nitride by ICP-OES

analysis, indicating nickel-black formation. In addition, recycling of the heterogeneous PC was not successful: the yellow CN-OA-m turned dark green after three cycles due to nickel deposition and the amine formation decreased significantly. The authors demonstrated that these problems can be avoided by controlling the reactivity of the carbon nitride photocatalyst using higher wavelengths, or reducing catalyst-solvent interactions.



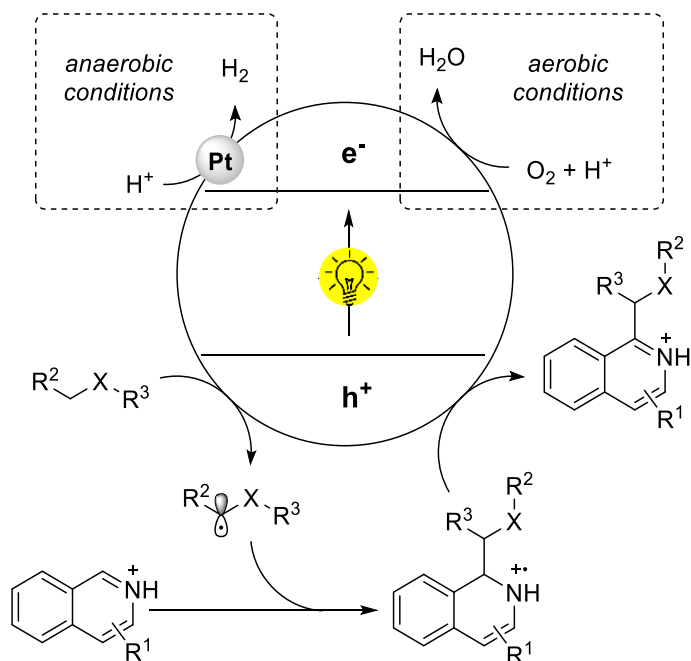
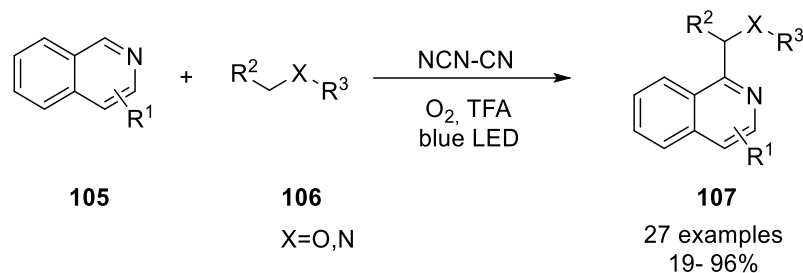
Scheme 2.25. Dual photo/nickel catalyzed carbon-heteroatom cross-couplings using CN-OA-m. (A) Esterification and thio(etherification) of aryl halides and (B) amination of aryl halides.

A graphitic carbon nitride that was prepared by pyrolysis of guanidine hydrochloride was used to generate α -aminoalkyl radicals *via* desilylative and decarboxylative photocatalytic single electron oxidations of α -silylamines (**100**) and α -amino acids (**101**, Scheme 2.26).⁸³ The resulting radicals were applied for the addition to alkenes, as well as allylations and heteroarylations. Other semiconductors (TiO₂, BiVO₄) did not show any activity towards the desired products under identical conditions. The authors further showed that the heterogeneous semiconductor does not lose its catalytic activity upon recycling.



Scheme 2.26. Desilylative and decarboxylative generation of α -aminoalkyl radicals using g-CN.

Reisner and coworkers showed that a cyanamide functionalized carbon nitride (NCN-CN) has a significantly higher activity than homogeneous Ir/ Ru photocatalysts in the photocatalytic Minisci-type reaction of electron-deficient *N*-heteroarenes (**105**) with alcohols, amides, and cyclic ethers (Scheme 2.27).⁸⁴ While no reaction was observed in the absence of O₂, the addition of Pt nanoparticles enabled the coupling under anaerobic conditions. The evolution of hydrogen indicated that the Pt NPs consume the generated electrons *via* proton reduction. The same functionalized carbon nitride material was used for the sulfonylation of alkenes where it also outperformed other photocatalysts, including eosin Y and other CN derivatives.⁸⁵

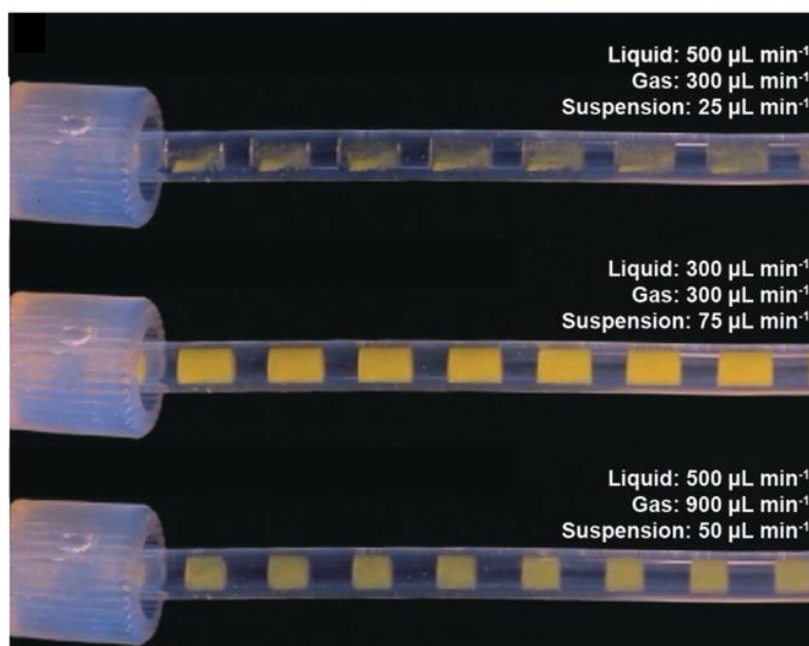
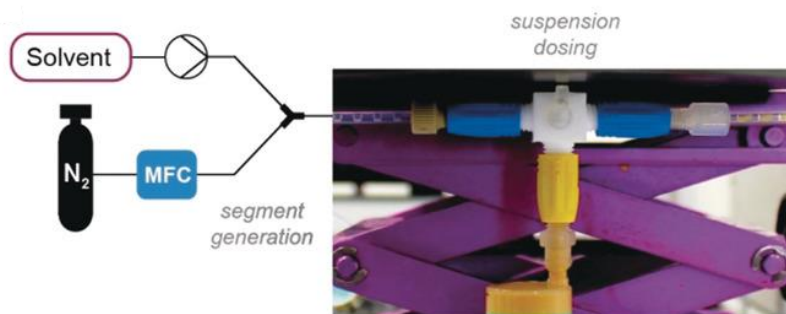
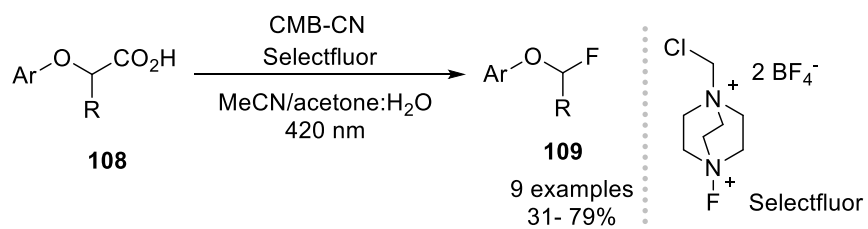


Scheme 2.27. Minisci-type coupling using carbon nitride catalysis.

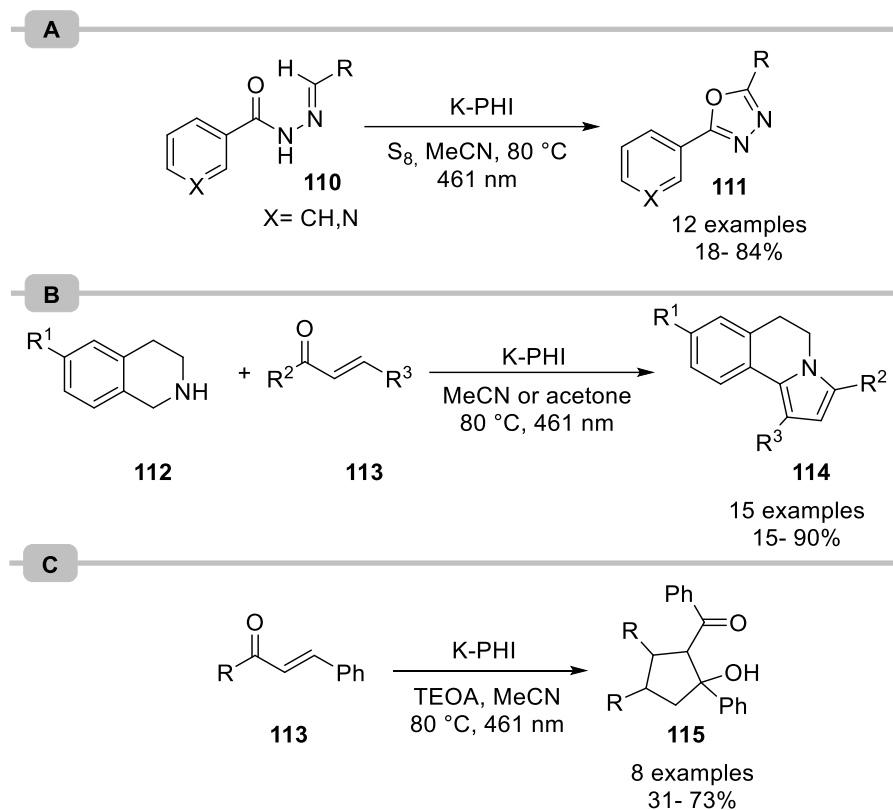
A carbon nitride material that was synthesized from cyanuric acid, melamine and barbituric acid (CMB-CN) was used for the decarboxylative fluorination of phenoxyacetic acids (**108**) and phenylacetic acid derivatives using Selectfluor in a continuous flow approach (Scheme 2.28).⁸⁶ A packed-bed reactor was not suitable as carbon nitride semiconductors are opaque. Handling of solid materials in other flow reactor types is challenging and leads to clogging. To overcome this general limitation, the authors developed a dedicated reactor system. The key innovation was the introduction of a catalyst suspension into a gas-liquid slug stream. The resulting serial micro batch reactors (SMBRs) can be fed into an irradiated coil reactor that is submerged in a thermostatic bath. The natural Taylor flow mixes the slug to continuously re-suspend the material, ensuring efficient irradiation and reproducible processing. In this system, the reaction time can be adapted by changing the gas and/or liquid

flow rate or the reactor volume while the catalyst stoichiometry can be varied by changing the rate of suspension dosing.

Potassium poly(heptazine imide), an ionic carbon nitride derivative with a high valence band potential of +2.54 eV *vs* RHE (g-CN: 1.82 eV *vs*. RHE), is perfectly suited for reactions that benefit from strong single electron oxidants. 1,3,4-oxadiazoles (**111**) can be effectively synthesized starting from *N*-acylhydrazones (**110**) using K-PHI as photocatalyst and S₈ as electron donor at 80°C in nonpolar solvents (Scheme 28, A).⁸⁷ When the reaction was carried out at lower temperatures (50°C), the rate decreased significantly and 43% instead of 80% yield were reached. Heating to 80°C was also crucial for high reaction rates during the light-mediated, K-PHI catalyzed synthesis of 1,3-disubstituted-5,6-dihydropyrrolo[2,1-*a*]isoquinolines (DHIPQs, **114**) from tetrahydroisoquinolines (**112**) and chalcones (**113**) using blue light (Scheme 2.29, B).⁸⁸ Chalcones (**113**) can also be (cyclo)dimerized with K-PHI photocatalysis in the presence of TEOA (triethanolamine) as electron donor, resulting in cyclopentanoles (**115**, Scheme 2.29, C).⁸⁹ Performing these reactions at 80 °C increased not only the reaction rate, but also resulted in higher selectivities compared to lower temperatures, likely due to thermodynamic control in the formation of the five-membered ring.



Scheme 2.28. Decarboxylative fluorination of phenoxy acid derivatives in continuous flow. *Reproduced with permission from Ref. [58]*



Scheme 2.29. (A) Photooxidation of *N*-acylhydrazones to 1,3,4-oxadiazoles with S_8 as oxidant and K-PHI as photocatalyst. (B) Oxidative condensation between tetrahydroisoquinolines and chalcone catalyzed by K-PHI. (C) Reductive cyclodimerization of chalcones using K-PHI as photocatalyst.

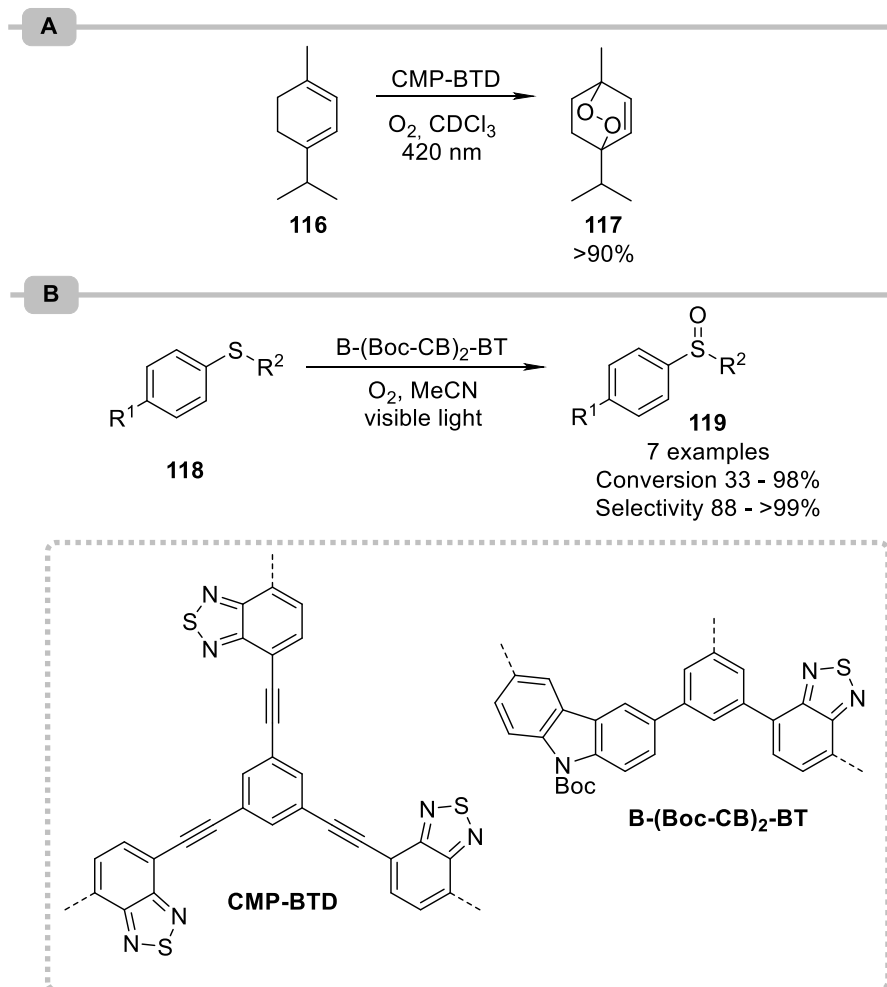
2.7 Conjugated Microporous Polymers (CMPs)

Conjugated microporous polymers (CMPs) have a well-defined, conjugated backbone that can be rationally designed, allowing to tune their electrical and optical properties.¹⁹ These amorphous polymers have a highly porous structure that stems from the covalent connection of rigid, contorted molecules.

Poly(benzothiadiazoles) are among the most common CMPs applied in organic synthesis and were recently reviewed.⁹⁰ The versatile PCs are commonly synthesized *via* metal-catalyzed cross-couplings of benzothiadiazole (acceptor) and other aromatic (donor) monomer units. A poly(benzothiadiazole) CMP was, for example, used for the formation of singlet oxygen (1O_2) and its utilization in the synthesis of ascaridole (**117**) from α -terpinene (**116**, Scheme 2.30, A).⁹¹ The CMP (CMP-BTD) was synthesized by the polymerization of 4,7-dibromobenzo[*c*][1,2,5]thiadiazole with 1,3,5-triethynylbenzene *via* Sonogashira cross-couplings. SiO_2 nanoparticles were used as templates to increase the porosity of the

polymeric materials. The BET surface was raised from 270 m²/g for a CMP (no SiO₂ template) to 660 m²/g, when 60 mg/mL SiO₂ nanoparticles were used. The high porosity and specific surface area were beneficial for an enhanced accessibility of the excited solid polymer for solubilized oxygen, leading to increased reaction rates. Using a continuous-flow system, a ¹O₂ production of up to 1 mmol/min was measured with a maximum quantum yield of 0.06. More recently, a similar CMP was shown to be also applicable for the stereoselective [2+2] cycloaddition of styrene derivatives.⁹²

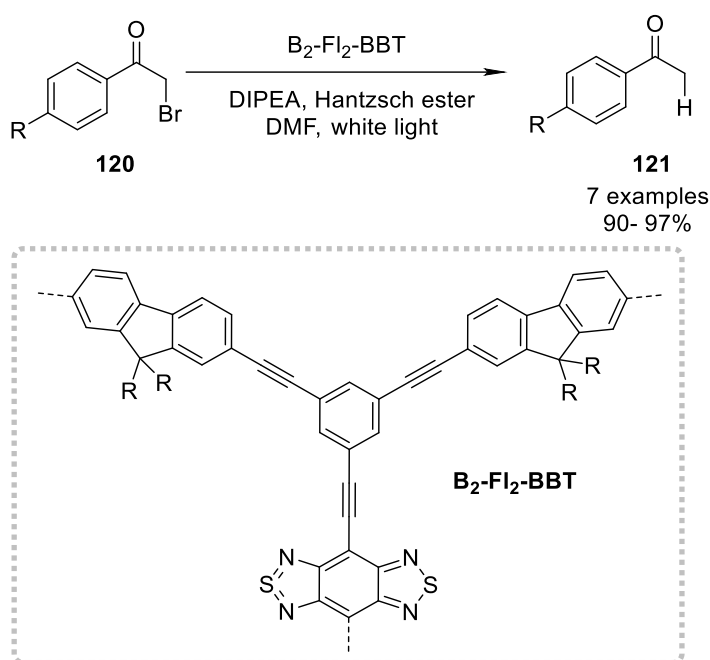
Zhang and coworkers synthesized a CMP *via* Suzuki-Miyaura-couplings of a benzothiadiazole monomer and a Boc-protected carbazole co-monomer using a high internal phase emulsion polymerization approach.⁹³ The resulting B-(Boc-CB)₂-BT was shown to be applicable as photocatalyst for the aerobic oxidation



Scheme 2.30. (A) Oxidation of α -terpinene to ascaridole with poly(benzothiadiazole) conjugated porous polymer (CMP-BTD) as photocatalyst for the photocatalytic production of ¹O₂. (B) Photocatalytic aerobic oxidation of aryl alkyl sulfides B-(Boc-CB)₂-BT.

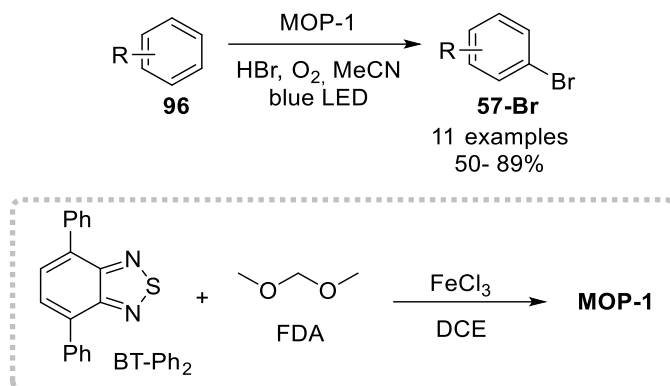
of aryl alkyl sulfides (**118**) to the corresponding sulfoxides (Scheme 2.30, B). The same reaction was also realized using a ferrocene-based CMP.⁹⁴

A benzobisthiadiazole CMP (B2-FI2-BBT) was prepared *via* Sonogashira couplings in high internal phase emulsion polymerization of a benzobisthiadiazole unit, a fluorene derivative, and 1,3,5-triethylenebenzene.⁹⁵ The resulting material showed a broad absorption range from visible to near-IR light and was applied as catalyst for the light-mediated debromination of α -bromoacetophenone derivatives (**120**) using Hantzsch ester as hydrogen donor and DIPEA as electron donor (**120**, Scheme 2.31).



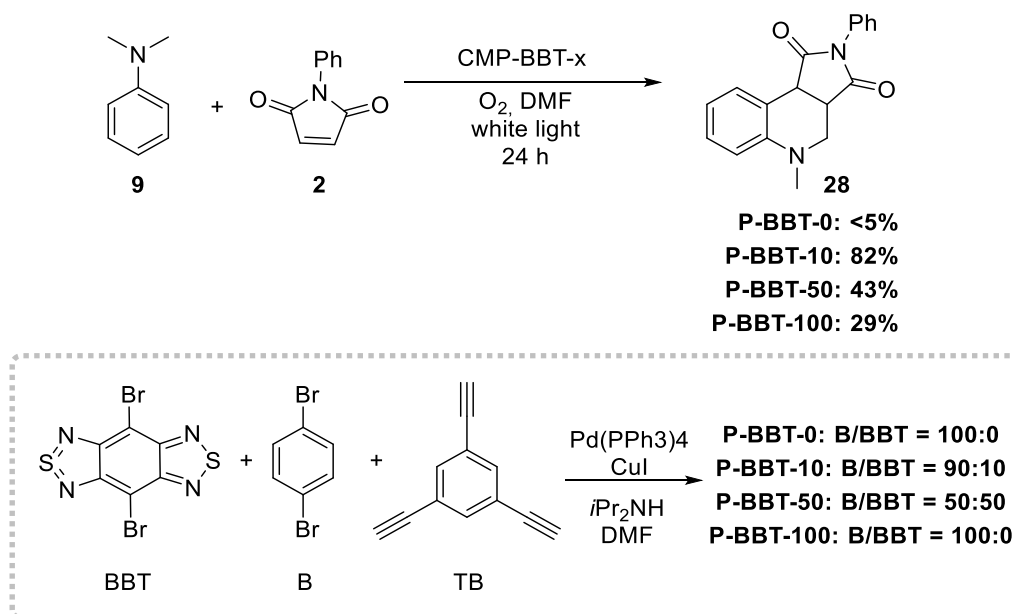
Scheme 2.31. Dehalogenation of haloketones using a poly-benzobisthiadiazole CMP as heterogeneous photocatalyst using visible light.

A Friedel-Crafts alkylation was used to prepare a poly(benzothiadiazole) CMP (MOP-1) using formaldehyde dimethyl acetal (FDA) as bridging agent and 4,7-diphenylbenzo[*c*][1,2,5]-thiadiazole (BT-Ph₂) as photoactive unit (Scheme 2.32).⁹⁶ The photocatalytically active polymer with a BET surface of 586 m²/g gave moderate to good yields for the bromination of electron rich aromatic compounds (**96**) using HBr in the presence of O₂.



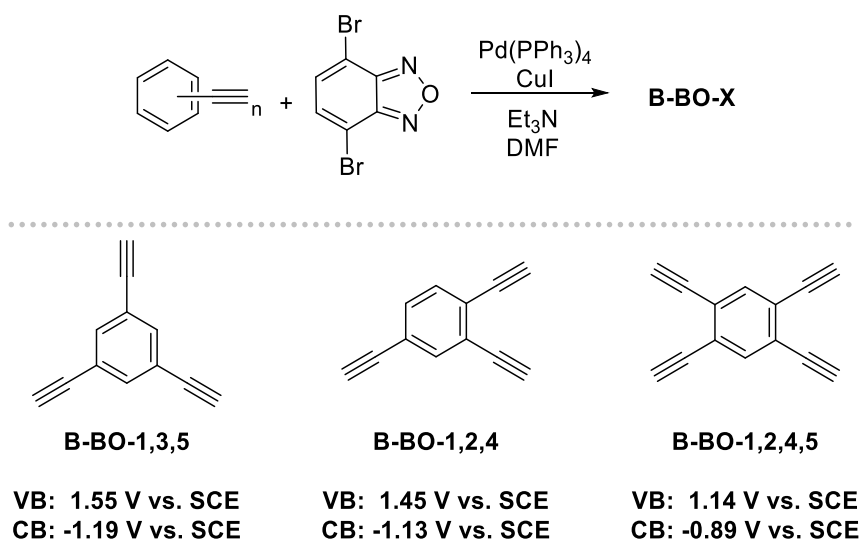
Scheme 2.32. Selective bromination of electron-rich aromatic compounds using microporous cross-linked organic polymers and HBr under blue light irradiation.

Fine-tuning of the VB and CB band levels can be carried out by varying the amount of the benzothiadiazole monomers during the CMP preparation. This enables the facile synthesis of a library of CMP materials with different bandgaps. Zhang and coworkers used this approach to study the activity of different polybenzobisthiadiazoles based CMPs for the photocatalytic synthesis of a 1,2,3,4-tetrahydroquinoline derivatives (**28**) by a cascade radical C–C bond formation/cyclization of *N,N*-dimethylaniline (**9**) with *N*-phenylmaleimide (**2**, Scheme 2.33).⁹⁷



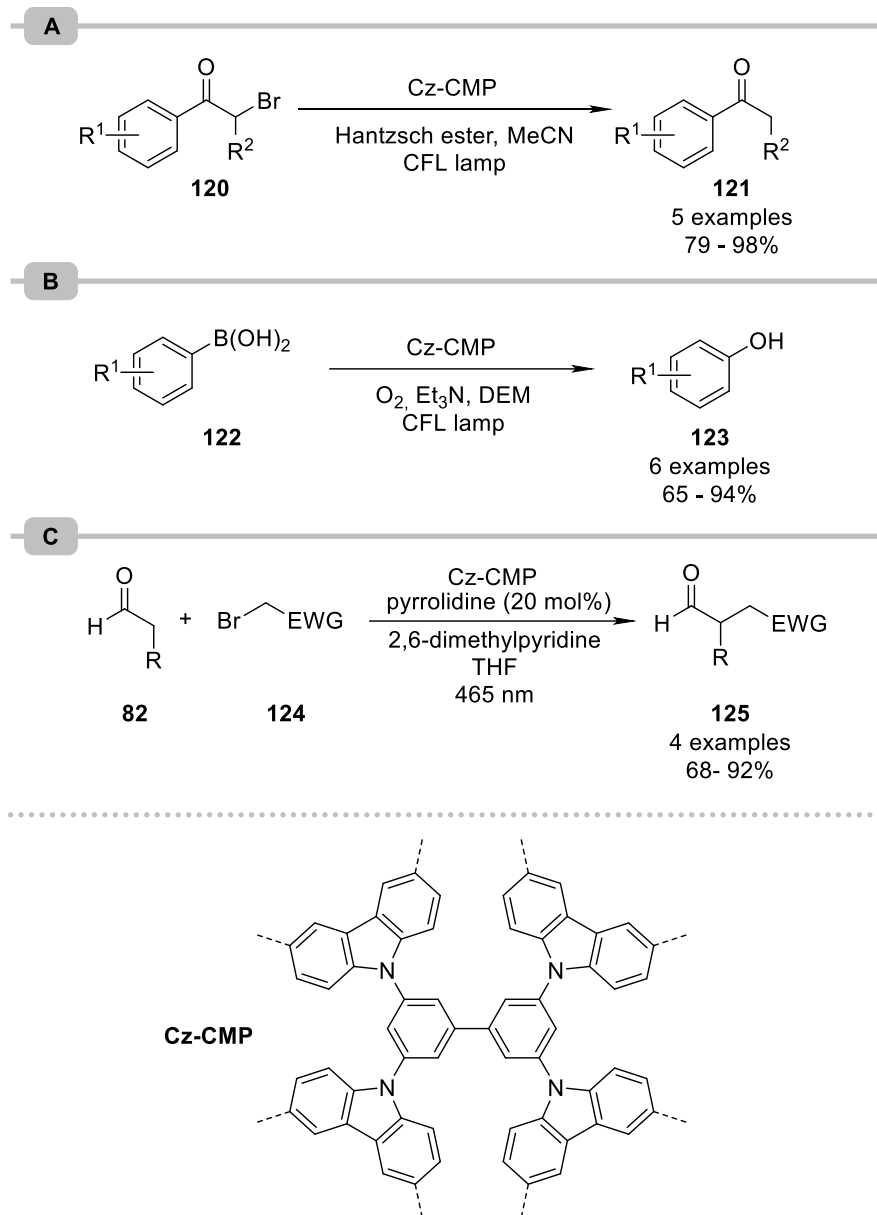
Scheme 2.33. Activity of different polybenzothiadiazoles based CMPs in the photocatalytic synthesis of 1,2,3,4-tetrahydroquinolines.

Benzooxadiazoles can be also used to prepare photocatalytically active CMP materials. Similarly to the above examples using benzothiadiazole monomers, bandgap engineering *via* the synthetic approach is feasible. This was showcased for the preparation of CMPs with different substitution patterns using Sonogashira-type couplings of different alkynes with 4,7-dibromobenzo[c][1,2,5]oxadiazole (Scheme 2.34).⁹⁸ While the material resulting from a benzene co-monomer that contains four alkyne functionalities (B-BO-1,2,4,5) showed an excellent light harvesting behaviour with an absorption range up to near IR light, a CMP made using B-BO-1,3,5 had the highest catalytic activity for the aerobic oxidation of amines due to its higher conduction band potential. This same CMP was further decorated with Pd nanoparticles to enable light-mediated Suzuki cross-couplings.⁹⁹



Scheme 2.34. Bandgap engineering by co-monomer variation during the synthesis of Poly(benzooxadiazole) CMPs.

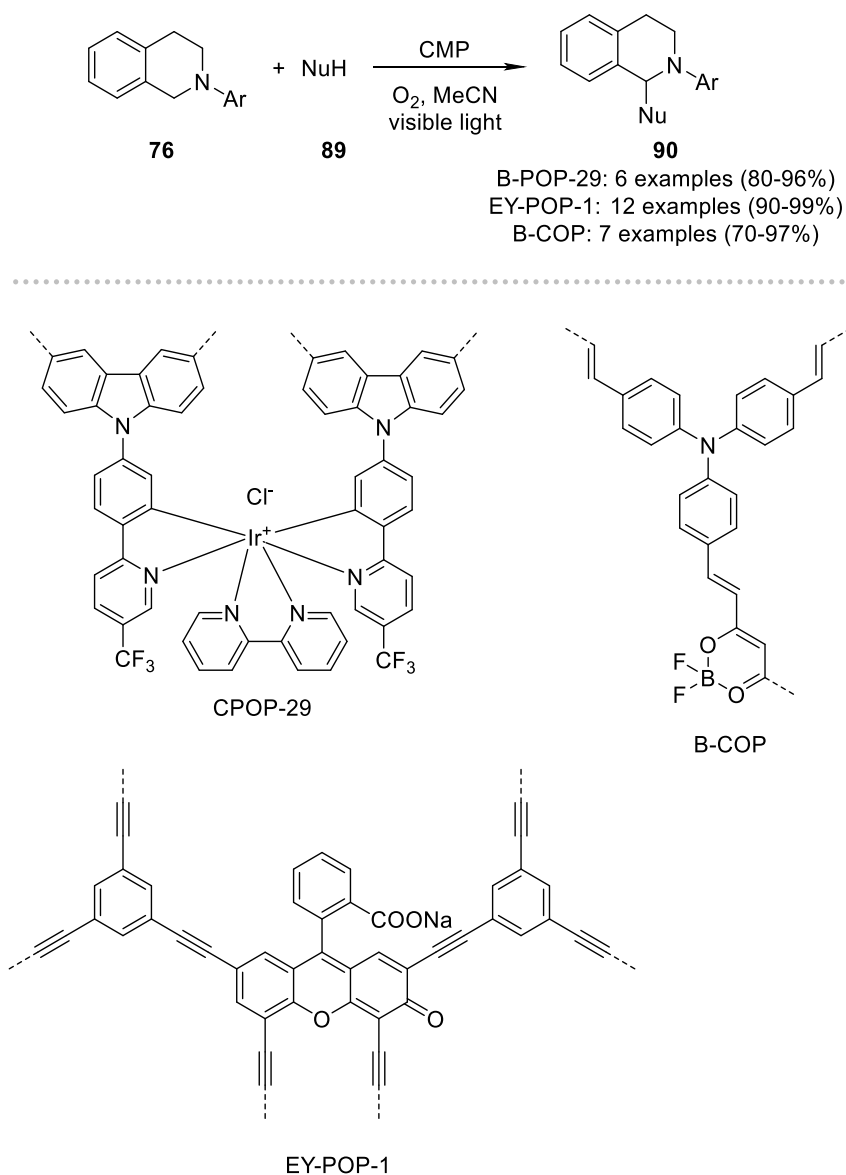
The oxidation of amines was used to showcase that truxene-based conjugated microporous polymer are photocatalytically active using visible light irradiation ($\lambda > 420$ nm) or natural sunlight.¹⁰⁰ Carbazolylic CMPs (Cz-CMPs), that were synthesized *via* Friedel-Crafts alkylations were applied as photocatalysts for the aerobic oxidation of amines and sulfides,¹⁰¹ the dehalogenation of phenacyl bromides (**120**), the oxidative hydroxylation of aryl boronic acids (**122**), and the redox neutral α -functionalisation of aldehydes in presence of an additional organocatalyst (**125**, Scheme 2.35).¹⁰² It was further shown that the heterogeneous photocatalytic material could be reused without losing its catalytic activity.



Scheme 2.35. A carbazaoic conjugated microporous polymer as photocatalyst for (A) the debromination of phenacyl bromides, (B) the hydroxylation of aryl boronic acid and (C) the alkylation of aldehydes.

A cationic, porous polycarbazole with incorporated, heteroleptic iridium polypyridyl units (CPOP-29) showed also good activity in the hydroxylation of aryl boronic acids and was further used for cross-dehydrogenative coupling of *N*-aryl tetrahydroisoquinoline derivatives (**76**) and several nucleophiles, such as phosphite esters and nitroalkanes (Scheme 2.36).¹⁰³ An enhanced activity was achieved by introducing CF₃ groups into the polymeric network, which led to superior light-absorption ability and a longer fluorescence lifetime.

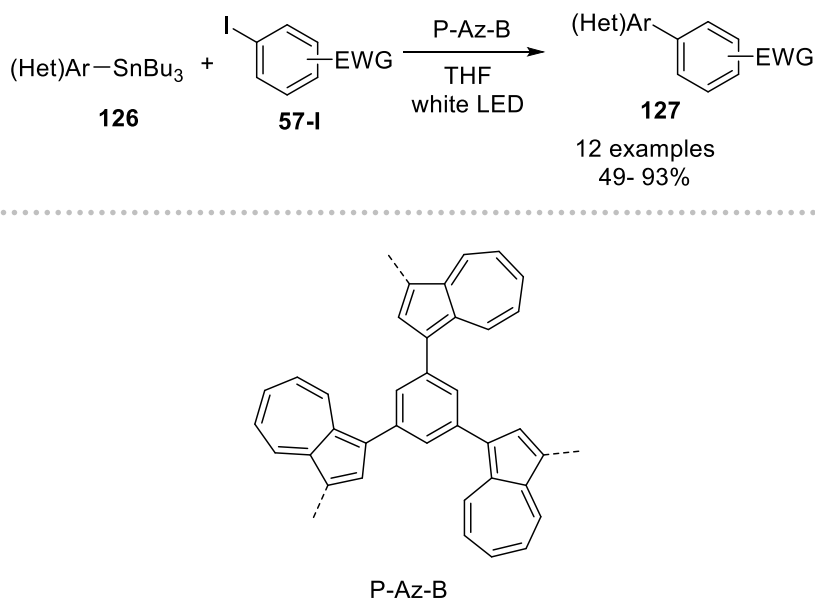
An Eosin Y dye-based porous organic polymer (EY-POP-1) can also be used for aza-Henry reactions.¹⁰⁴ Eosin Y was polymerized with 1,3,5-triethynylbenzene to obtain an extended π -conjugation structure. Importantly, the CMP was recycled 12 times without loss in efficiency. Additionally, a difluoroborate-based conjugated microporous polymer (B-COP) was tested for the same reaction.¹⁰⁵ The polymeric material with a broad absorption band in the visible light region (400-700 nm) was synthesized by a base-catalyzed condensation polymerization between difluoroboron β -diketonate and tris(4-formylphenyl) amine.



Scheme 2.36. Dehydrogenative C-H functionalisation of *N*-aryl substituted tetrahydroisoquinoline derivatives using different conjugated porous polymers and visible light irradiation.

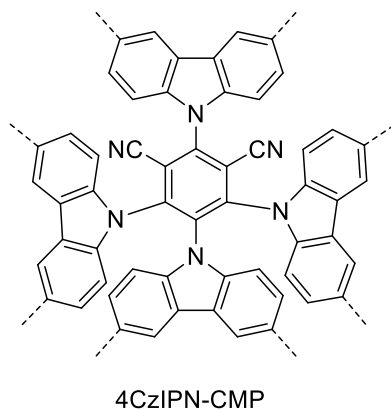
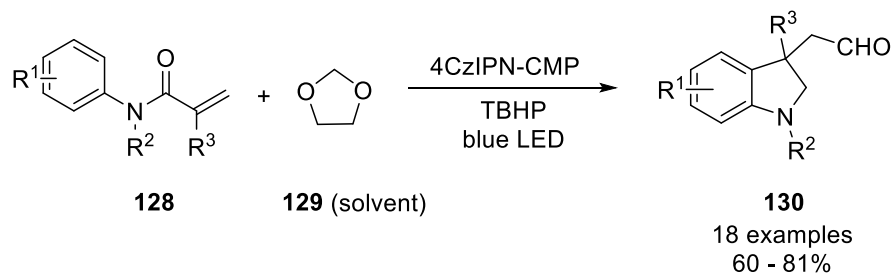
Chapter 2

A azulene-CMP (P-Az-B) enabled the visible-light mediated palladium-free Stille-type coupling of aromatic butyl stannanes (**126**) and aryl iodides (**57-I**) using white light (Scheme 2.37).¹⁰⁶ The method, however, works only for aryl halides that have strong electron-withdrawing substituents, which was rationalized by the stabilization of the formed aryl radical anion.



Scheme 2.37. Palladium-free Stille-type coupling using a conjugated microporous polymer and visible light irradiation.

Su and coworkers prepared a CMP *via* FeCl₃ catalyzed Friedel Crafts reactions of 4-CzIPN (1,2,3,5-Tetrakis(carbazol-9-yl)-4,6-dicyanobenzene), that is also a potent photocatalyst alone.¹⁰⁷ The recyclable catalyst absorbed up to 800 nm and had high thermal stability. Its photocatalytic activity was demonstrated for the generation of an alkoxyalkyl radical from 1,3-dioxolane that induces the 1,2-formylarylation of *N*-acrylamides (**128**), forming the corresponding 3-formyloxindole products (**130**, Scheme 2.38). The products were used for the construction of oxo- and aza-ring fused indolines and spirocyclic indole derivatives in thermal transformations.

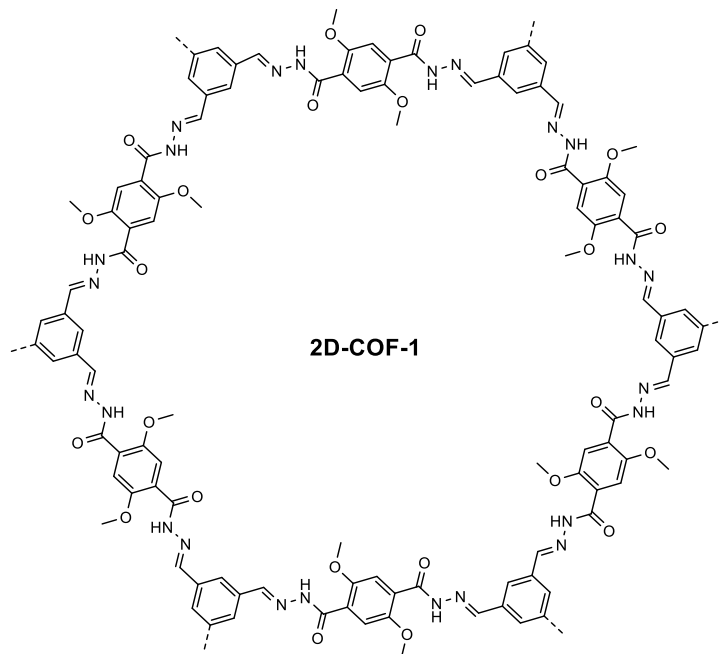
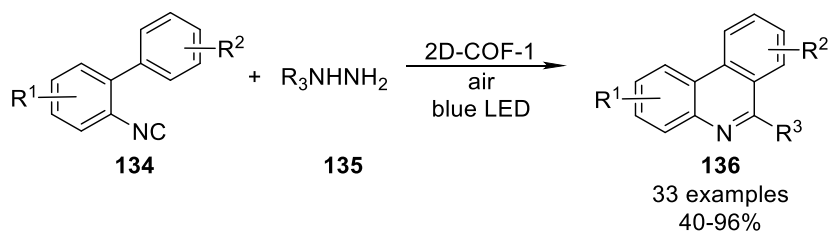


Scheme 2.38. Photocatalytic cascade radical cyclization of *N*-arylacrylamides *via* H-atom abstraction of 1,3-dioxalane using 4CzIPN-CMP as photocatalyst.

2.8 Covalent Organic Frameworks (COFs)

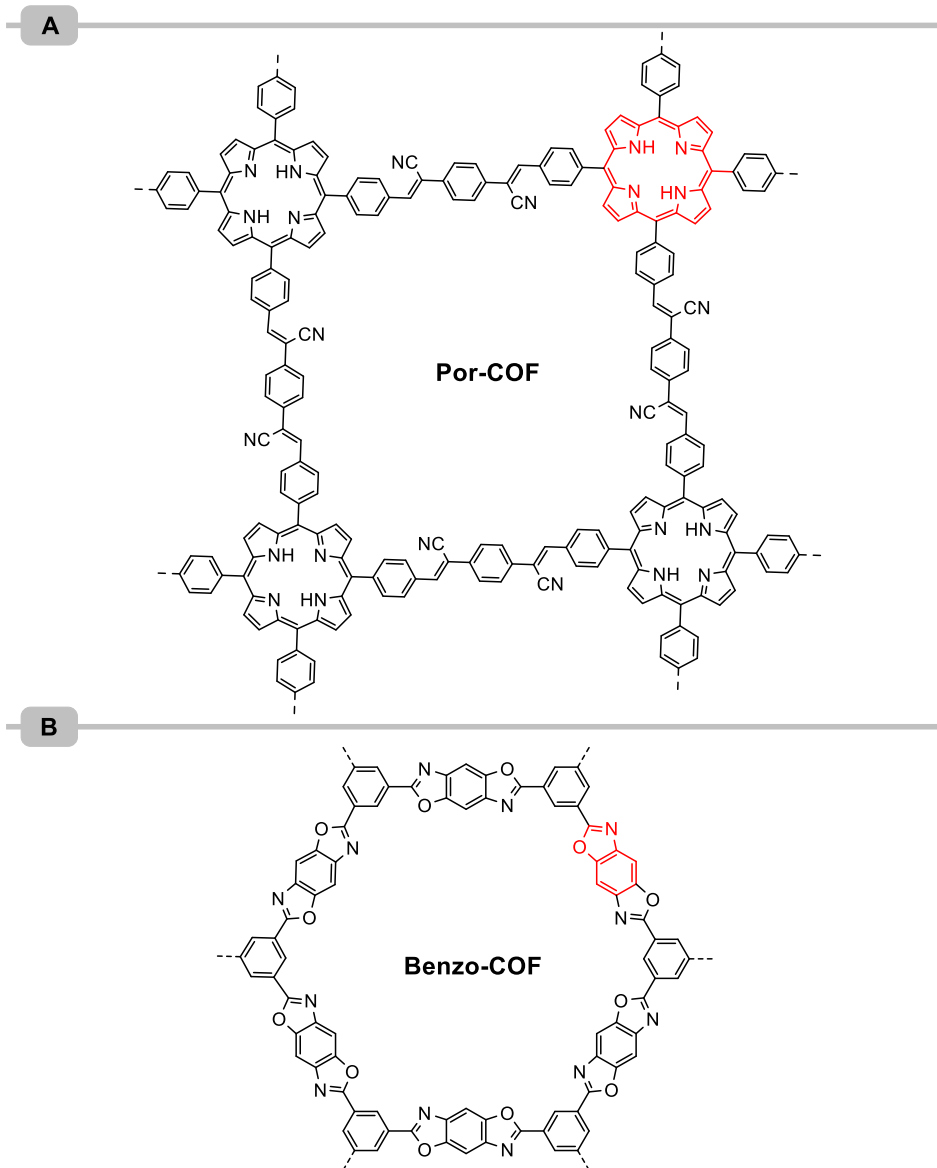
Covalent organic frameworks (COFs) are two- or three-dimensional, highly ordered structures that are constructed by covalently linked building blocks.¹⁰⁸ In contrast to amorphous CMPs, COFs are crystalline, porous materials. The potential applications of COFs include gas storage and separation, drug delivery, energy storage, and the use as photocatalysts.

Covalent triazine networks (CTF), a subclass of COFs, were used for the aerobic oxidation of benzyl alcohols,¹⁰⁹ and the cross-dehydrogenative coupling of *N*-aryl substituted tetrahydroisoquinoline with nucleophiles.¹¹⁰ More recently, an asymmetric CTF (asy-CTF), made *via* a TfOH-catalyzed trimerization of 5-(4-cyanophenyl)thiophene-2-carbonitrile, was used for the photocatalytic synthesis of benzophosphole oxides (**133**, Scheme 2.39).¹¹¹ The asymmetric donor-acceptor structure resulted in a higher activity than symmetrical analogues, which was rationalized by an enhanced charge separation and intramolecular electron transfer.



Scheme 2.40. Tandem radical-addition cyclization of 2-arylphenyl isocyanides with alkyl and aryl hydrazines using a hydrazine-based COF.

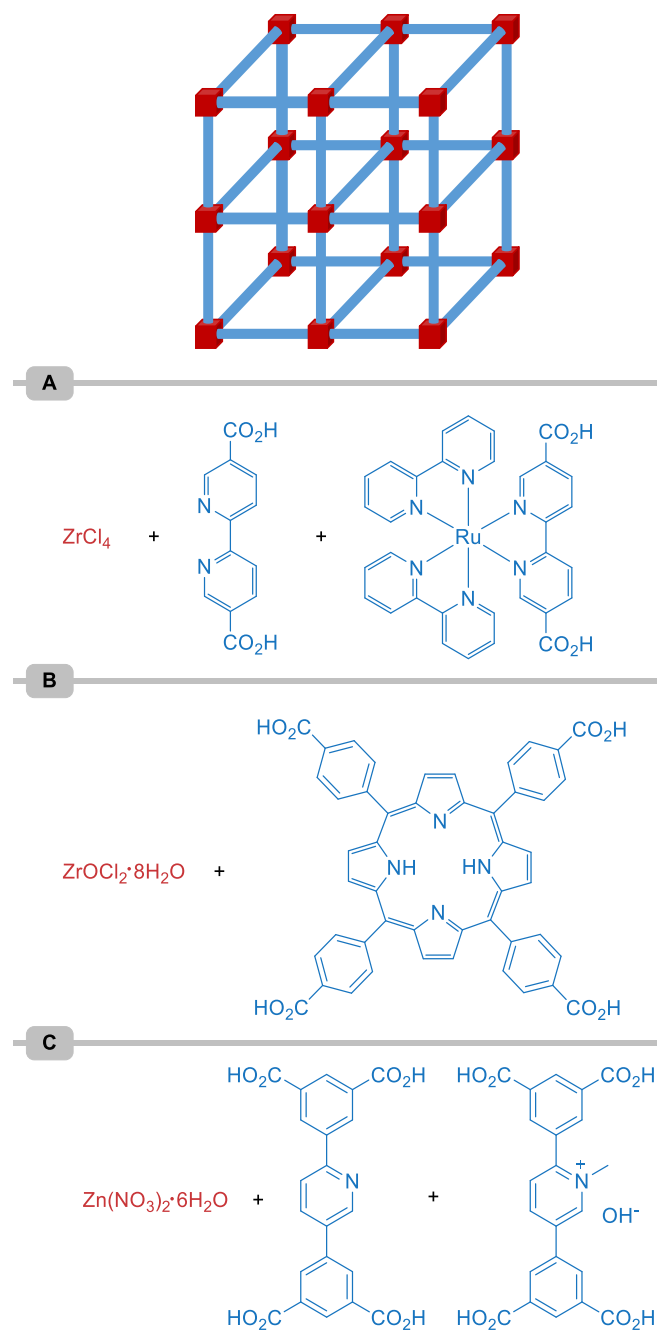
Other examples of COFs that were successfully applied in photocatalysis are two-dimensional, porphyrin- (Por-COF),¹¹⁴ and benzoxazole-based frameworks¹¹⁵ (Benzo-COF; Scheme 40). The fully organic, heterogeneous PCs were used to activate O₂ for the aerobic photocatalytic hydroxylation of aryl boronic acids (Benzo-COF), and the oxidation of amines (Por-COF).



Scheme 2.41. Photocatalytically active covalent organic frameworks with incorporated porphyrin (A) and benzoxazole (B) units.

2.9 Metal organic frameworks (MOFs)

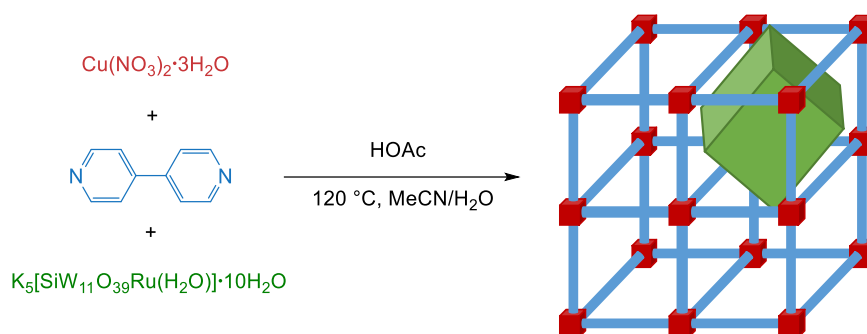
Metal organic frameworks (MOFs) are porous, highly ordered crystalline solids that consist of metal ions/cluster and organic linkers. In case of photocatalytically active MOFs, the metallic cluster (semiconductor), or a photocatalyst that is encapsulated in the pores of a photocatalytically inactive MOF can be responsible for their catalytic activity.¹¹⁶ The vast majority of MOF photocatalysts, however, gain their photocatalytic activity from the incorporation of a molecular dye into the organic linker structure (Scheme 2.42). This can be, for example, accomplished, by using the ligand of Ru polypyridyl complexes as linker in combination with $ZrCl_4$ in presence of acetic acid (A).¹¹⁷ Similarly an iridium polypyridyl complex serves as (metal)organic linker in a Zr-MOF.¹¹⁸ Jiang and coworkers showed that porphyrin dyes can be combined with $ZrOCl_2 \cdot 8H_2O$ to obtain a photocatalytically active MOF (B).¹¹⁹ Similarly, a porphyrin-based MOF can be obtained using indium metal clusters.¹²⁰ Zn-based MOFs were synthesized using a combination of bis(3,5-dicarboxyphenyl)pyridine and bis(3,5-dicarboxyphenyl)methylpyridinium (C).¹²¹ All of these heterogeneous materials showed promising photocatalytic activity in reactions involving the generation of reactive oxygen species that were discussed in the previous chapters, including the oxidation of amines, the hydroxylation of arylboronic acids, and the dehydrogenative C–C coupling of *N*-aryl tetrahydroisoquinolines with various nucleophiles.



Scheme 2.42. Precursors for metal organic frameworks that contain a photocatalytically active linker unit. (A) Zr-MOF with Ru polypyridyl complex. (B) Zr-MOF with porphyrin linker. (C) Zn-MOF using a combination of two ligands.

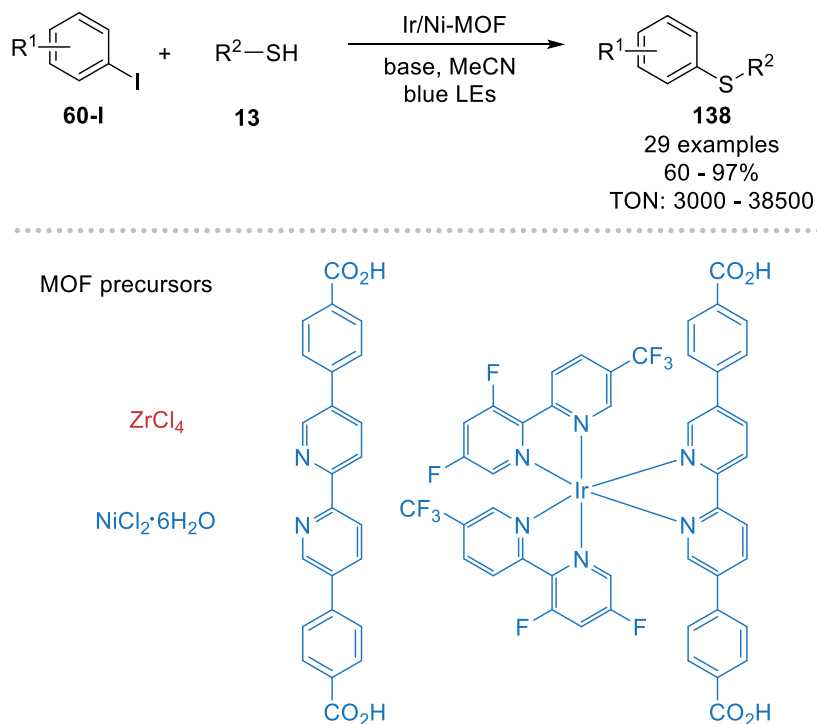
Duan and colleagues demonstrated that the incorporation of a photoactive polyoxometalate ($[\text{SiW}_{11}\text{O}_{29}\text{Ru}(\text{H}_2\text{O})]^{5-}$) in a copper(II)-bipyridine MOF (Scheme 2.43) is also able to catalyze the light-mediated photocatalytic aza-Henry reaction of *N*-aryl

tetrahydroisoquinolines with nitromethane in the presence of oxygen.¹²² Based on control experiments using $\text{K}_5[\text{SiW}_{11}\text{O}_{39}\text{Ru}(\text{H}_2\text{O})]\cdot 10\text{H}_2\text{O}$ as PC with and without $\text{Cu}(\text{NO}_3)_2\cdot 3\text{H}_2\text{O}$ as co-catalyst, the authors claimed that Cu activates the nucleophile and this effect is significantly enhanced when it is directly connected to the PC through the MOF structure due to close spatial proximity.



Scheme 2.43. Incorporation of a polyoxometalate photocatalyst in the pores of a photocatalytically inactive MOF.

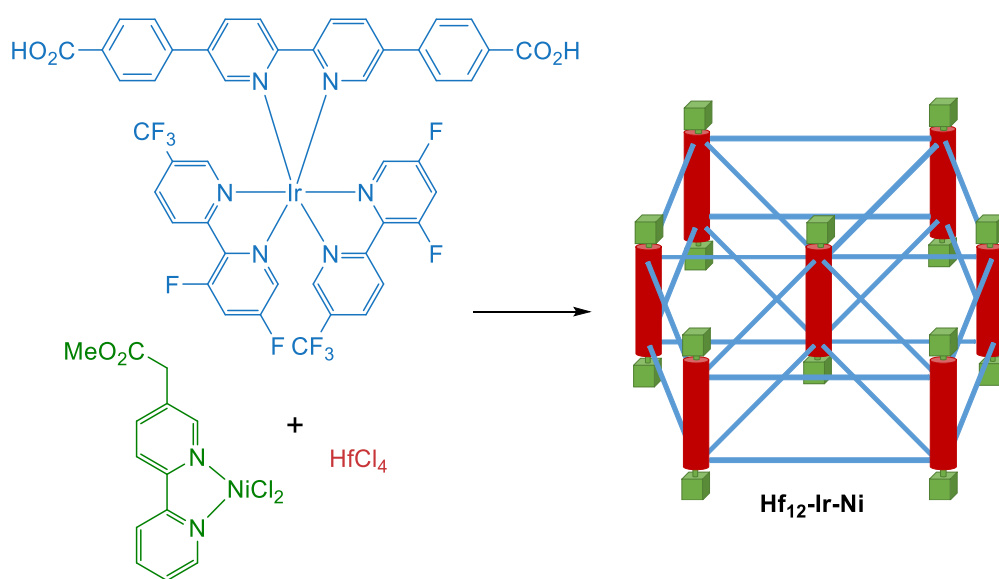
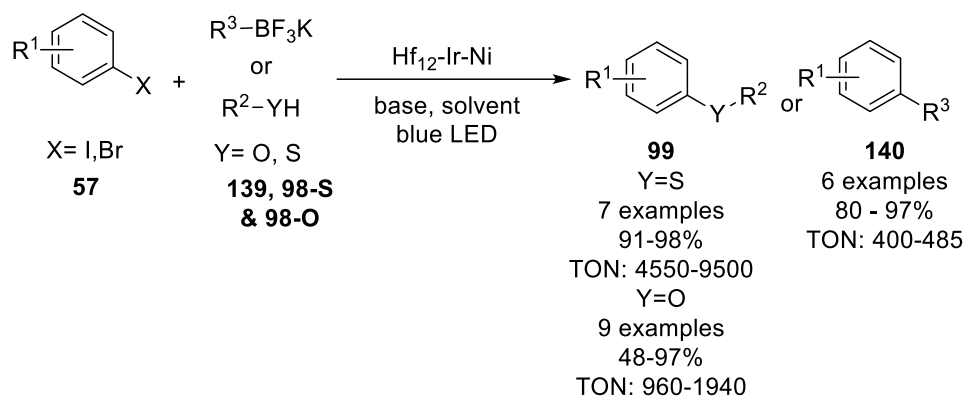
The same group developed a MOF (Zn-PYI) that contains a stereoselective organocatalyst (L- or D-pyrrolidin-2-ylimidazole) and a photocatalytically active triphenylamine moiety in the organic unit.¹²³ The asymmetric, photocatalytically active MOF enabled the α -alkylation of aliphatic aldehydes (**86**) with diethyl 2-bromomalonate (**31**) using visible light with high enantioselectivity (Scheme 43). More recently, the same reaction was catalysed by a MOF where a red shift of the ligand, that contains a chromophore and an asymmetric ligand, was observed after the MOF assembly.¹²⁴ This was attributed to a metal-to-ligand charge transfer between the metal (Zn, Zr or Ti) and the ligand.



Scheme 2.45. Fully heterogeneous dual nickel/ photocatalytic thioetherification using a Zr-MOF that contains a photocatalytically active Ir complex and a Ni complex in the organic unit.

More recently, a two-dimensional metal organic layer was constructed using Hafnium clusters that are bridged by photocatalytically active iridium complexes (Scheme 2.46).¹²⁶ The metal-organic layers were functionalized with a nickel complex, resulting in a single material that is capable of catalysing the cross-coupling reactions of aryl halides (**57**) with thiols (**98-S**), alcohols (**98-O**), or potassium trifluoroborates (**139**). The fully heterogeneous dual catalyst was recycled five times without losing its catalytic activity and only low amounts of leached Hf (<0.3%), Ir (<0.6%) and Ni (<0.1%) were determined by ICP-OES.

Chapter 2



Scheme 2.46. Fully heterogeneous dual nickel/ photocatalytic C–O, C–S and C–C cross-couplings using a Hf-MOF that contains a photocatalytically active Ir complex and a Ni complex in the organic unit.

2.10 Conclusions

A variety of heterogeneous materials has been employed as recyclable photocatalysts for organic synthesis. Inorganic semiconductors, especially TiO_2 , are most commonly used to replace homogeneous photocatalysts. Surface complexation, dye sensitization and doping are common methods to enable the wide-band gap semiconductor to harvest visible light up to near IR, which is rarely reached by homogeneous photocatalysts. The combination of photocatalysts with heterogeneous nanoparticles that are capable of photon upconversion is an alternative strategy for accessing near IR light and might be a promising concept for, for example, the application of photocatalysis in *in vivo* experiments.¹²⁷

However, apart from other inorganic semiconductors, purely organic semiconductors of the carbon nitride family have rapidly emerged to a useful alternative that harvest visible light without the need for doping. The straightforward preparation of these classical semiconductors from cheap starting materials is one of the main advantages. It was also shown that semiconductor photocatalysis could be used in synergy with other catalytic reactions in dual catalytic processes.

More recently, polymeric porous materials that include conjugated microporous polymers, covalent organic frameworks and metal organic frameworks are slowly implemented in photocatalytic organic transformations. The main advantage of these materials is their rational design. Their precise preparation using, for example, cross couplings enables straightforward tuning of their electrical and optical properties. Moreover, the incorporation of a photocatalytic unit and a second catalyst accesses a single, recyclable material that enables dual catalytic processes.

As each heterogeneous photocatalyst has advantages and disadvantages, the decision for the best material to be made case-by-case considering, the respective reaction, the reaction scale and the available light source. A problem that all heterogeneous photocatalysts have in common is their limited applicability for large-scale reactions. This problem is easy to address for homogeneous photocatalysis using flow technologies, but challenging for semiconductors and only a few approaches exist. It is therefore important to note that research in heterogeneous photocatalysis should not only focus on new transformations and improved catalysts, but also needs dedicated technologies for their applications.

2.11 References

1. Cole-Hamilton, D. J., Homogeneous Catalysis--New Approaches to Catalyst Separation, Recovery, and Recycling. *Science* **2003**, 299 (5613), 1702-1706.
2. Hübner, S.; de Vries, J. G.; Farina, V., Why Does Industry Not Use Immobilized Transition Metal Complexes as Catalysts? *Adv. Synth. Catal.* **2016**, 358 (1), 3-25.
3. Schultz, D. M.; Yoon, T. P., Solar Synthesis: Prospects in Visible Light Photocatalysis. *Science* **2014**, 343 (6174), 1239176.
4. Marzo, L.; Pagire, S. K.; Reiser, O.; König, B., Visible-Light Photocatalysis: Does It Make a Difference in Organic Synthesis? *Angew. Chem. Int. Ed.* **2018**, 57 (32), 10034-10072.
5. McAtee, R. C.; McClain, E. J.; Stephenson, C. R. J., Illuminating Photoredox Catalysis. *Trends Chem.* **2019**, 1 (1), 111-125.
6. Cavedon, C.; Seeberger, P. H.; Pieber, B., Photochemical Strategies for Carbon-Heteroatom Bond Formation. *Eur. J. Org. Chem.*, DOI: 10.1002/ejoc.201901173.
7. Strieth-Kalthoff, F.; James, M. J.; Teders, M.; Pitzer, L.; Glorius, F., Energy transfer catalysis mediated by visible light: principles, applications, directions. *Chem. Soc. Rev.* **2018**, 47 (19), 7190-7202.
8. Zhou, Q.-Q.; Zou, Y.-Q.; Lu, L.-Q.; Xiao, W.-J., Visible-Light-Induced Organic Photochemical Reactions through Energy-Transfer Pathways. *Angew. Chem. Int. Ed.* **2019**, 58 (6), 1586-1604.
9. Friedmann, D.; Hakki, A.; Kim, H.; Choi, W.; Bahnemann, D., Heterogeneous photocatalytic organic synthesis: state-of-the-art and future perspectives. *Green Chem.* **2016**, 18 (20), 5391-5411.
10. Lang, X.; Chen, X.; Zhao, J., Heterogeneous visible light photocatalysis for selective organic transformations. *Chem. Soc. Rev.* **2014**, 43 (1), 473-486.
11. Guerra, J.; Cantillo, D.; Kappe, C. O., Visible-light photoredox catalysis using a macromolecular ruthenium complex: reactivity and recovery by size-exclusion nanofiltration in continuous flow. *Catal. Sci. Technol.* **2016**, 6 (13), 4695-4699.
12. Yoo, W.-J.; Kobayashi, S., Efficient visible light-mediated cross-dehydrogenative coupling reactions of tertiary amines catalyzed by a polymer-immobilized iridium-based photocatalyst. *Green Chem.* **2014**, 16 (5), 2438-2442.

13. Ma, J.; Strieth-Kalthoff, F.; Dalton, T.; Freitag, M.; Schwarz, J. L.; Bergander, K.; Daniliuc, C.; Glorius, F., Direct Dearomatization of Pyridines via an Energy-Transfer-Catalyzed Intramolecular [4+2] Cycloaddition. *Chem* **2019**, *5* (11), 2854-2864.
14. Amara, Z.; Bellamy, J. F. B.; Horvath, R.; Miller, S. J.; Beeby, A.; Burgard, A.; Rossen, K.; Poliakoff, M.; George, M. W., Applying green chemistry to the photochemical route to artemisinin. *Nat. Chem.* **2015**, *7* (6), 489-495.
15. Riente, P.; Noël, T., Application of metal oxide semiconductors in light-driven organic transformations. *Catal. Sci. Technol.* **2019**, *9* (19), 5186-5232.
16. Savateev, A.; Ghosh, I.; König, B.; Antonietti, M., Photoredox Catalytic Organic Transformations using Heterogeneous Carbon Nitrides. *Angew. Chem. Int. Ed.* **2018**, *57* (49), 15936-15947.
17. Savateev, A.; Antonietti, M., Heterogeneous Organocatalysis for Photoredox Chemistry. *ACS Catal.* **2018**, *8* (10), 9790-9808.
18. Markushyna, Y.; Smith, C. A.; Savateev, A., Organic Photocatalysis: Carbon Nitride Semiconductors vs. Molecular Catalysts. *Eur. J. Org. Chem.*, DOI: 10.1002/ejoc.201901112.
19. Chaoui, N.; Trunk, M.; Dawson, R.; Schmidt, J.; Thomas, A., Trends and challenges for microporous polymers. *Chem. Soc. Rev.* **2017**, *46* (11), 3302-3321.
20. Schneider, J.; Matsuoka, M.; Takeuchi, M.; Zhang, J.; Horiuchi, Y.; Anpo, M.; Bahnemann, D. W., Understanding TiO₂ Photocatalysis: Mechanisms and Materials. *Chem. Rev.* **2014**, *114* (19), 9919-9986.
21. Hoffmann, N., Photocatalysis with TiO₂ Applied to Organic Synthesis. *Aust. J. Chem.* **2015**, *68* (11), 1621-1639.
22. Cheng, H.; Xu, W., Recent advances in modified TiO₂ for photo-induced organic synthesis. *Org. Biomol. Chem.* **2019**, *17* (47), 9977-9989.
23. Manley, D. W.; McBurney, R. T.; Miller, P.; Walton, J. C.; Mills, A.; O'Rourke, C., Titania-Promoted Carboxylic Acid Alkylations of Alkenes and Cascade Addition-Cyclizations. *J. Org. Chem.* **2014**, *79* (3), 1386-1398.
24. Zoller, J.; Fabry, D. C.; Rueping, M., Unexpected Dual Role of Titanium Dioxide in the Visible Light Heterogeneous Catalyzed C-H Arylation of Heteroarenes. *ACS Catal.* **2015**, *5* (6), 3900-3904.

Chapter 2

25. Vila, C.; Rueping, M., Visible-light mediated heterogeneous C–H functionalization: oxidative multi-component reactions using a recyclable titanium dioxide (TiO₂) catalyst. *Green Chem.* **2013**, *15* (8), 2056-2059.
26. Bottecchia, C.; Erdmann, N.; Tijssen, P. M. A.; Milroy, L.-G.; Brunsveld, L.; Hessel, V.; Noël, T., Batch and Flow Synthesis of Disulfides by Visible-Light-Induced TiO₂ Photocatalysis. *ChemSusChem* **2016**, *9* (14), 1781-1785.
27. Plutschack, M. B.; Pieber, B.; Gilmore, K.; Seeberger, P. H., The Hitchhiker's Guide to Flow Chemistry. *Chem. Rev.* **2017**, *117* (18), 11796-11893.
28. Cambié, D.; Bottecchia, C.; Straathof, N. J. W.; Hessel, V.; Noël, T., Applications of Continuous-Flow Photochemistry in Organic Synthesis, Material Science, and Water Treatment. *Chem. Rev.* **2016**, *116* (17), 10276-10341.
29. Bhat, V. T.; Duspara, P. A.; Seo, S.; Abu Bakar, N. S. B.; Greaney, M. F., Visible light promoted thiol-ene reactions using titanium dioxide. *Chem. Commun.* **2015**, *51* (21), 4383-4385.
30. Pitre, S. P.; Yoon, T. P.; Scaiano, J. C., Titanium dioxide visible light photocatalysis: surface association enables photocatalysis with visible light irradiation. *Chem. Commun.* **2017**, *53* (31), 4335-4338.
31. Pitre, S. P.; Scaiano, J. C.; Yoon, T. P., Photocatalytic Indole Diels–Alder Cycloadditions Mediated by Heterogeneous Platinum-Modified Titanium Dioxide. *ACS Catal.* **2017**, *7* (10), 6440-6444.
32. Hagfeldt, A.; Boschloo, G.; Sun, L.; Kloo, L.; Pettersson, H., Dye-Sensitized Solar Cells. *Chem. Rev.* **2010**, *110* (11), 6595-6663.
33. Willkomm, J.; Orchard, K. L.; Reynal, A.; Pastor, E.; Durrant, J. R.; Reisner, E., Dye-sensitized semiconductors modified with molecular catalysts for light-driven H₂ production. *Chem. Soc. Rev.* **2016**, *45* (1), 9-23.
34. Zhang, L.; Cole, J. M., Anchoring Groups for Dye-Sensitized Solar Cells. *ACS Appl. Mater. Interfaces* **2015**, *7* (6), 3427-3455.
35. Ooyama, Y.; Harima, Y., Photophysical and Electrochemical Properties, and Molecular Structures of Organic Dyes for Dye-Sensitized Solar Cells. *ChemPhysChem* **2012**, *13* (18), 4032-4080.

36. Zhang, M.; Chen, C.; Ma, W.; Zhao, J., Visible-Light-Induced Aerobic Oxidation of Alcohols in a Coupled Photocatalytic System of Dye-Sensitized TiO₂ and TEMPO. *Angew. Chem. Int. Ed.* **2008**, *47* (50), 9730-9733.
37. Zhang, Y.; Wang, Z.; Lang, X., Merging visible light photocatalysis of dye-sensitized TiO₂ with TEMPO: the selective aerobic oxidation of alcohols. *Catal. Sci. Technol.* **2017**, *7* (21), 4955-4963.
38. Li, X.; Shi, J.-L.; Hao, H.; Lang, X., Visible light-induced selective oxidation of alcohols with air by dye-sensitized TiO₂ photocatalysis. *Appl. Catal. B* **2018**, *232*, 260-267.
39. Lang, X.; Zhao, J.; Chen, X., Visible-Light-Induced Photoredox Catalysis of Dye-Sensitized Titanium Dioxide: Selective Aerobic Oxidation of Organic Sulfides. *Angew. Chem. Int. Ed.* **2016**, *55* (15), 4697-4700.
40. Ren, L.; Yang, M.-M.; Tung, C.-H.; Wu, L.-Z.; Cong, H., Visible-Light Photocatalysis Employing Dye-Sensitized Semiconductor: Selective Aerobic Oxidation of Benzyl Ethers. *ACS Catal.* **2017**, *7* (12), 8134-8138.
41. Hosseini-Sarvari, M.; Koohgard, M.; Firoozi, S.; Mohajeri, A.; Tavakolian, H., Alizarin red S–TiO₂-catalyzed cascade C(sp³)–H to C(sp²)–H bond formation/cyclization reactions toward tetrahydroquinoline derivatives under visible light irradiation. *New J. Chem.* **2018**, *42* (9), 6880-6888.
42. Nauth, A. M.; Schechtel, E.; Doren, R.; Tremel, W.; Opatz, T., TiO₂ Nanoparticles Functionalized with Non-innocent Ligands Allow Oxidative Photocyanation of Amines with Visible/Near-Infrared Photons. *J. Am. Chem. Soc.* **2018**, *140* (43), 14169-14177.
43. Hopkinson, M. N.; Sahoo, B.; Li, J.-L.; Glorius, F., Dual Catalysis Sees the Light: Combining Photoredox with Organo-, Acid, and Transition-Metal Catalysis. *Chem. Eur. J.* **2014**, *20* (14), 3874-3886.
44. Skubi, K. L.; Blum, T. R.; Yoon, T. P., Dual Catalysis Strategies in Photochemical Synthesis. *Chem. Rev.* **2016**, *116* (17), 10035-10074.
45. Cherevatskaya, M.; Neumann, M.; Földner, S.; Harlander, C.; Kümmel, S.; Dankesreiter, S.; Pfitzner, A.; Zeitler, K.; König, B., Visible-Light-Promoted Stereoselective Alkylation by Combining Heterogeneous Photocatalysis with Organocatalysis. *Angew. Chem. Int. Ed.* **2012**, *51* (17), 4062-4066.

Chapter 2

46. Yoon, H.-S.; Ho, X.-H.; Jang, J.; Lee, H.-J.; Kim, S.-J.; Jang, H.-Y., N719 Dye-Sensitized Organophotocatalysis: Enantioselective Tandem Michael Addition/Oxyamination of Aldehydes. *Org. Lett.* **2012**, *14* (13), 3272-3275.
47. Tang, J.; Grampp, G.; Liu, Y.; Wang, B.-X.; Tao, F.-F.; Wang, L.-J.; Liang, X.-Z.; Xiao, H.-Q.; Shen, Y.-M., Visible Light Mediated Cyclization of Tertiary Anilines with Maleimides Using Nickel(II) Oxide Surface-Modified Titanium Dioxide Catalyst. *J. Org. Chem.* **2015**, *80* (5), 2724-2732.
48. Hodgson, G. K.; Scaiano, J. C., Heterogeneous Dual Photoredox-Lewis Acid Catalysis Using a Single Bifunctional Nanomaterial. *ACS Catal.* **2018**, *8* (4), 2914-2922.
49. Lanterna, A. E.; Elhage, A.; Scaiano, J. C., Heterogeneous photocatalytic C–C coupling: mechanism of plasmon-mediated reductive dimerization of benzyl bromides by supported gold nanoparticles. *Catal. Sci. Technol.* **2015**, *5* (9), 4336-4340.
50. Marina, N.; Lanterna, A. E.; Scaiano, J. C., Expanding the Color Space in the Two-Color Heterogeneous Photocatalysis of Ullmann C–C Coupling Reactions. *ACS Catal.* **2018**, *8* (8), 7593-7597.
51. Elhage, A.; Lanterna, A. E.; Scaiano, J. C., Light-Induced Sonogashira C–C Coupling under Mild Conditions Using Supported Palladium Nanoparticles. *ACS Sus. Chem. Eng.* **2018**, *6* (2), 1717-1722.
52. Buglioni, L.; Riente, P.; Palomares, E.; Pericàs, M. A., Visible-Light-Promoted Arylation Reactions Photocatalyzed by Bismuth(III) Oxide. *Eur. J. Org. Chem.* **2017**, *2017* (46), 6986-6990.
53. Fadeyi, O. O.; Mousseau, J. J.; Feng, Y.; Allais, C.; Nuhant, P.; Chen, M. Z.; Pierce, B.; Robinson, R., Visible-Light-Driven Photocatalytic Initiation of Radical Thiol–Ene Reactions Using Bismuth Oxide. *Org. Lett.* **2015**, *17* (23), 5756-5759.
54. Riente, P.; Pericàs, M. A., Visible Light-Driven Atom Transfer Radical Addition to Olefins using Bi₂O₃ as Photocatalyst. *ChemSusChem* **2015**, *8* (11), 1841-1844.
55. Riente, P.; Matas Adams, A.; Albero, J.; Palomares, E.; Pericàs, M. A., Light-Driven Organocatalysis Using Inexpensive, Nontoxic Bi₂O₃ as the Photocatalyst. *Angew. Chem. Int. Ed.* **2014**, *53* (36), 9613-9616.
56. Zhang, Y.; Xu, Y.-J., Bi₂WO₆: A highly chemoselective visible light photocatalyst toward aerobic oxidation of benzylic alcohols in water. *RSC Adv.* **2014**, *4* (6), 2904-2910.

57. Zhang, Y.; Zhang, N.; Tang, Z.-R.; Xu, Y.-J., Identification of Bi₂WO₆ as a highly selective visible-light photocatalyst toward oxidation of glycerol to dihydroxyacetone in water. *Chem. Sci.* **2013**, *4* (4), 1820-1824.
58. Cao, X.; Chen, Z.; Lin, R.; Cheong, W.-C.; Liu, S.; Zhang, J.; Peng, Q.; Chen, C.; Han, T.; Tong, X.; Wang, Y.; Shen, R.; Zhu, W.; Wang, D.; Li, Y., A photochromic composite with enhanced carrier separation for the photocatalytic activation of benzylic C–H bonds in toluene. *Nat. Catal.* **2018**, *1* (9), 704-710.
59. Wu, Y.; Yuan, B.; Li, M.; Zhang, W.-H.; Liu, Y.; Li, C., Well-defined BiOCl colloidal ultrathin nanosheets: synthesis, characterization, and application in photocatalytic aerobic oxidation of secondary amines. *Chem. Sci.* **2015**, *6* (3), 1873-1878.
60. Yuan, B.; Chong, R.; Zhang, B.; Li, J.; Liu, Y.; Li, C., Photocatalytic aerobic oxidation of amines to imines on BiVO₄ under visible light irradiation. *Chem. Comm.* **2014**, *50* (98), 15593-15596.
61. Yoffe, A. D., Semiconductor quantum dots and related systems: Electronic, optical, luminescence and related properties of low dimensional systems. *Adv. Phys.* **2001**, *50* (1), 1-208.
62. Enright, M. J.; Gilbert-Bass, K.; Sarsito, H.; Cossairt, B. M., Photolytic C–O Bond Cleavage with Quantum Dots. *Chem. Mater.* **2019**, *31* (7), 2677-2682.
63. Jiang, Y.; Wang, C.; Rogers, C. R.; Kodaimati, M. S.; Weiss, E. A., Regio- and diastereoselective intermolecular [2+2] cycloadditions photocatalysed by quantum dots. *Nat. Chem.* **2019**, *11* (11), 1034-1040.
64. Liu, C.; Chen, Z.; Su, C.; Zhao, X.; Gao, Q.; Ning, G.-H.; Zhu, H.; Tang, W.; Leng, K.; Fu, W.; Tian, B.; Peng, X.; Li, J.; Xu, Q.-H.; Zhou, W.; Loh, K. P., Controllable deuteration of halogenated compounds by photocatalytic D₂O splitting. *Nat. Commun.* **2018**, *9* (1), 80.
65. Pal, A.; Ghosh, I.; Sapra, S.; König, B., Quantum Dots in Visible-Light Photoredox Catalysis: Reductive Dehalogenations and C–H Arylation Reactions Using Aryl Bromides. *Chem. Mater.* **2017**, *29* (12), 5225-5231.
66. Caputo, J. A.; Frenette, L. C.; Zhao, N.; Sowers, K. L.; Krauss, T. D.; Weix, D. J., General and Efficient C–C Bond Forming Photoredox Catalysis with Semiconductor Quantum Dots. *J. Am. Chem. Soc.* **2017**, *139* (12), 4250-4253.

67. Liu, Y.-Y.; Liang, D.; Lu, L.-Q.; Xiao, W.-J., Practical heterogeneous photoredox/nickel dual catalysis for C–N and C–O coupling reactions. *Chem. Commun.* **2019**, 55 (33), 4853-4856.
68. Zhang, Z.; Edme, K.; Lian, S.; Weiss, E. A., Enhancing the Rate of Quantum-Dot-Photocatalyzed Carbon-Carbon Coupling by Tuning the Composition of the Dot's Ligand Shell. *J. Am. Chem. Soc.* **2017**, 139 (12), 4246-4249.
69. Zhao, W.; Liu, C.; Cao, L.; Yin, X.; Xu, H.; Zhang, B., Porous single-crystalline CdS nanosheets as efficient visible light catalysts for aerobic oxidative coupling of amines to imines. *RSC Adv.* **2013**, 3 (45), 22944-22948.
70. Xi, Z.-W.; Yang, L.; Wang, D.-Y.; Pu, C.-D.; Shen, Y.-M.; Wu, C.-D.; Peng, X.-G., Visible-Light Photocatalytic Synthesis of Amines from Imines via Transfer Hydrogenation Using Quantum Dots as Catalysts. *J. Org. Chem.* **2018**, 83 (19), 11886-11895.
71. Saparov, B.; Mitzi, D. B., Organic–Inorganic Perovskites: Structural Versatility for Functional Materials Design. *Chem. Rev.* **2016**, 116 (7), 4558-4596.
72. Wu, W.-B.; Wong, Y.-C.; Tan, Z.-K.; Wu, J., Photo-induced thiol coupling and C–H activation using nanocrystalline lead-halide perovskite catalysts. *Catal. Sci. Technol.* **2018**, 8 (16), 4257-4263.
73. Zhu, X.; Lin, Y.; Sun, Y.; Beard, M. C.; Yan, Y., Lead-Halide Perovskites for Photocatalytic alpha-Alkylation of Aldehydes. *J. Am. Chem. Soc.* **2019**, 141 (2), 733-738.
74. Zhu, X.; Lin, Y.; San Martin, J.; Sun, Y.; Zhu, D.; Yan, Y., Lead halide perovskites for photocatalytic organic synthesis. *Nat. Commun.* **2019**, 10 (1), 2843.
75. Ong, W.-J.; Tan, L.-L.; Ng, Y. H.; Yong, S.-T.; Chai, S.-P., Graphitic Carbon Nitride (g-C₃N₄)-Based Photocatalysts for Artificial Photosynthesis and Environmental Remediation: Are We a Step Closer To Achieving Sustainability? *Chem. Rev.* **2016**, 116 (12), 7159-7329.
76. Su, F.; Mathew, S. C.; Lipner, G.; Fu, X.; Antonietti, M.; Blechert, S.; Wang, X., mpg-C(3)N(4)-Catalyzed selective oxidation of alcohols using O(2) and visible light. *J. Am. Chem. Soc.* **2010**, 132 (46), 16299-301.
77. Su, F.; Mathew, S. C.; Möhlmann, L.; Antonietti, M.; Wang, X.; Blechert, S., Aerobic Oxidative Coupling of Amines by Carbon Nitride Photocatalysis with Visible Light. *Angew. Chem. Int. Ed.* **2011**, 50 (3), 657-660.

78. Baar, M.; Blechert, S., Graphitic Carbon Nitride Polymer as a Recyclable Photoredox Catalyst for Fluoroalkylation of Arenes. *Chem. Eur. J.* **2015**, *21* (2), 526-530.
79. Ghosh, I.; Khamrai, J.; Savateev, A.; Shlapakov, N.; Antonietti, M.; König, B., Organic semiconductor photocatalyst can bifunctionalize arenes and heteroarenes. *Science* **2019**, *365* (6451), 360-366.
80. Pieber, B.; Malik, J. A.; Cavedon, C.; Gisbertz, S.; Savateev, A.; Cruz, D.; Heil, T.; Zhang, G.; Seeberger, P. H., Semi-heterogeneous Dual Nickel/Photocatalysis using Carbon Nitrides: Esterification of Carboxylic Acids with Aryl Halides. *Angew. Chem. Int. Ed.* **2019**, *58* (28), 9575-9580.
81. Cavedon, C.; Madani, A.; Seeberger, P. H.; Pieber, B., Semiheterogeneous Dual Nickel/Photocatalytic (Thio)etherification Using Carbon Nitrides. *Org. Lett.* **2019**, *21* (13), 5331-5334.
82. Gisbertz, S.; Reischauer, S.; Pieber, B., Overcoming Limitations in Dual Photoredox/Nickel catalyzed C–N Cross-Couplings due to Catalyst Deactivation. . *ChemRxiv*, preprint, DOI 10.26434/chemrxiv.10298735.v1.
83. Cai, Y.; Tang, Y.; Fan, L.; Lefebvre, Q.; Hou, H.; Rueping, M., Heterogeneous Visible-Light Photoredox Catalysis with Graphitic Carbon Nitride for α -Aminoalkyl Radical Additions, Allylations, and Heteroarylations. *ACS Catal.* **2018**, *8* (10), 9471-9476.
84. Vijeta, A.; Reisner, E., Carbon nitride as a heterogeneous visible-light photocatalyst for the Minisci reaction and coupling to H₂ production. *Chem. Comm.* **2019**, *55* (93), 14007-14010.
85. Meyer, A. U.; Lau, V. W. H.; König, B.; Lotsch, B. V., Photocatalytic Oxidation of Sulfinates to Vinyl Sulfones with Cyanamide-Functionalised Carbon Nitride. *Eur. J. Org. Chem.* **2017**, (15), 2179-2185.
86. Pieber, B.; Shalom, M.; Antonietti, M.; Seeberger, P. H.; Gilmore, K., Continuous Heterogeneous Photocatalysis in Serial Micro-Batch Reactors. *Angew. Chem. Int. Ed.* **2018**, *57* (31), 9976-9979.
87. Kurpil, B.; Otte, K.; Antonietti, M.; Savateev, A., Photooxidation of N-acylhydrazones to 1,3,4-oxadiazoles catalyzed by heterogeneous visible-light-active carbon nitride semiconductor. *Appl. Catal. B* **2018**, *228*, 97-102.

Chapter 2

88. Kurpil, B.; Otte, K.; Mishchenko, A.; Lamagni, P.; Lipiński, W.; Lock, N.; Antonietti, M.; Savateev, A., Carbon nitride photocatalyzes regioselective aminium radical addition to the carbonyl bond and yields N-fused pyrroles. *Nat. Commun.* **2019**, *10* (1), 945.
89. Kurpil, B.; Markushyna, Y.; Savateev, A., Visible-Light-Driven Reductive (Cyclo)Dimerization of Chalcones over Heterogeneous Carbon Nitride Photocatalyst. *ACS Catal.* **2019**, *9* (2), 1531-1538.
90. Li, R.; Byun, J.; Huang, W.; Ayed, C.; Wang, L.; Zhang, K. A. I., Poly(benzothiadiazoles) and Their Derivatives as Heterogeneous Photocatalysts for Visible-Light-Driven Chemical Transformations. *ACS Catal.* **2018**, *8* (6), 4735-4750.
91. Zhang, K.; Kopetzki, D.; Seeberger, P. H.; Antonietti, M.; Vilela, F., Surface Area Control and Photocatalytic Activity of Conjugated Microporous Poly(benzothiadiazole) Networks. *Angew. Chem. Int. Ed.* **2013**, *52* (5), 1432-1436.
92. Welin, E. R.; Le, C.; Arias-Rotondo, D. M.; McCusker, J. K.; MacMillan, D. W. C., Photosensitized, energy transfer-mediated organometallic catalysis through electronically excited nickel(II). *Science* **2017**, *355* (6323), 380-385.
93. Wang, Z. J.; Ghasimi, S.; Landfester, K.; Zhang, K. A. I., Highly porous conjugated polymers for selective oxidation of organic sulfides under visible light. *Chem. Commun.* **2014**, *50* (60), 8177-8180.
94. Ma, L.; Liu, Y.; Liu, Y.; Jiang, S.; Li, P.; Hao, Y.; Shao, P.; Yin, A.; Feng, X.; Wang, B., Ferrocene-Linkage-Facilitated Charge Separation in Conjugated Microporous Polymers. *Angew. Chem. Int. Ed.* **2019**, *58* (13), 4221-4226.
95. Wang, Z. J.; Ghasimi, S.; Landfester, K.; Zhang, K. A. I., A conjugated porous poly-benzobisthiadiazole network for a visible light-driven photoredox reaction. *J. Mater. Chem. A* **2014**, *2* (44), 18720-18724.
96. Li, R.; Wang, Z. J.; Wang, L.; Ma, B. C.; Ghasimi, S.; Lu, H.; Landfester, K.; Zhang, K. A. I., Photocatalytic Selective Bromination of Electron-Rich Aromatic Compounds Using Microporous Organic Polymers with Visible Light. *ACS Catal.* **2016**, *6* (2), 1113-1121.
97. Wang, Z. J.; Ghasimi, S.; Landfester, K.; Zhang, K. A. I., Bandgap Engineering of Conjugated Nanoporous Poly-benzobisthiadiazoles via Copolymerization for Enhanced Photocatalytic 1,2,3,4-Tetrahydroquinoline Synthesis under Visible Light. *Adv. Synth. Catal.* **2016**, *358* (16), 2576-2582.

98. Wang, Z. J.; Ghasimi, S.; Landfester, K.; Zhang, K. A. I., Molecular Structural Design of Conjugated Microporous Poly(Benzooxadiazole) Networks for Enhanced Photocatalytic Activity with Visible Light. *Adv. Mater.* **2015**, *27* (40), 6265-6270.
99. Wang, Z. J.; Ghasimi, S.; Landfester, K.; Zhang, K. A. I., Photocatalytic Suzuki Coupling Reaction Using Conjugated Microporous Polymer with Immobilized Palladium Nanoparticles under Visible Light. *Chem. Mater.* **2015**, *27* (6), 1921-1924.
100. Battula, V. R.; Singh, H.; Kumar, S.; Bala, I.; Pal, S. K.; Kailasam, K., Natural Sunlight Driven Oxidative Homocoupling of Amines by a Truxene-Based Conjugated Microporous Polymer. *ACS Catal.* **2018**, *8* (8), 6751-6759.
101. Su, C.; Tandiana, R.; Tian, B.; Sengupta, A.; Tang, W.; Su, J.; Loh, K. P., Visible-Light Photocatalysis of Aerobic Oxidation Reactions Using Carbazolic Conjugated Microporous Polymers. *ACS Catal.* **2016**, *6* (6), 3594-3599.
102. Luo, J.; Zhang, X.; Zhang, J., Carbazolic Porous Organic Framework as an Efficient, Metal-Free Visible-Light Photocatalyst for Organic Synthesis. *ACS Catal.* **2015**, *5* (4), 2250-2254.
103. Liang, H.-P.; Chen, Q.; Han, B.-H., Cationic Polycarbazole Networks as Visible-Light Heterogeneous Photocatalysts for Oxidative Organic Transformations. *ACS Catal.* **2018**, *8* (6), 5313-5322.
104. Wang, C.-A.; Li, Y.-W.; Cheng, X.-L.; Zhang, J.-P.; Han, Y.-F., Eosin Y dye-based porous organic polymers for highly efficient heterogeneous photocatalytic dehydrogenative coupling reaction. *RSC Adv.* **2017**, *7* (1), 408-414.
105. Liu, W. T.; Wu, S. J.; Su, Q.; Guo, B. X.; Ju, P. Y.; Li, G. H.; Wu, Q. L., Difluoroborate-based conjugated organic polymer: a high-performance heterogeneous photocatalyst for oxidative coupling reactions. *J. Mater. Sci.* **2019**, *54* (2), 1205-1212.
106. Ghasimi, S.; Bretschneider, S. A.; Huang, W.; Landfester, K.; Zhang, K. A. I., A Conjugated Microporous Polymer for Palladium-Free, Visible Light-Promoted Photocatalytic Stille-Type Coupling Reactions. *Adv. Sci.* **2017**, *4* (8), 1700101.
107. Ou, W.; Zhang, G.; Wu, J.; Su, C., Photocatalytic Cascade Radical Cyclization Approach to Bioactive Indoline-Alkaloids over Donor–Acceptor Type Conjugated Microporous Polymer. *ACS Catal.* **2019**, *9* (6), 5178-5183.
108. Diercks, C. S.; Yaghi, O. M., The atom, the molecule, and the covalent organic framework. *Science* **2017**, *355* (6328), eaal1585.

109. Huang, W.; Ma, B. C.; Lu, H.; Li, R.; Wang, L.; Landfester, K.; Zhang, K. A. I., Visible-Light-Promoted Selective Oxidation of Alcohols Using a Covalent Triazine Framework. *ACS Catal.* **2017**, *7* (8), 5438-5442.
110. Zhi, Y.; Li, Z.; Feng, X.; Xia, H.; Zhang, Y.; Shi, Z.; Mu, Y.; Liu, X., Covalent organic frameworks as metal-free heterogeneous photocatalysts for organic transformations. *J. Mater. Chem. A* **2017**, *5* (44), 22933-22938.
111. Huang, W.; Byun, J.; Rörich, I.; Ramanan, C.; Blom, P. W. M.; Lu, H.; Wang, D.; Caire da Silva, L.; Li, R.; Wang, L.; Landfester, K.; Zhang, K. A. I., Asymmetric Covalent Triazine Framework for Enhanced Visible-Light Photoredox Catalysis via Energy Transfer Cascade. *Angew. Chem. Int. Ed.* **2018**, *57* (27), 8316-8320.
112. Liu, S.; Pan, W.; Wu, S.; Bu, X.; Xin, S.; Yu, J.; Xu, H.; Yang, X., Visible-light-induced tandem radical addition–cyclization of 2-aryl phenyl isocyanides catalysed by recyclable covalent organic frameworks. *Green Chem.* **2019**, *21* (11), 2905-2910.
113. Liu, W.; Su, Q.; Ju, P.; Guo, B.; Zhou, H.; Li, G.; Wu, Q., A Hydrazone-Based Covalent Organic Framework as an Efficient and Reusable Photocatalyst for the Cross-Dehydrogenative Coupling Reaction of N-Aryltetrahydroisoquinolines. *ChemSusChem* **2017**, *10* (4), 664-669.
114. Chen, R.; Shi, J.-L.; Ma, Y.; Lin, G.; Lang, X.; Wang, C., Designed Synthesis of a 2D Porphyrin-Based sp² Carbon-Conjugated Covalent Organic Framework for Heterogeneous Photocatalysis. *Angew. Chem. Int. Ed.* **2019**, *58* (19), 6430-6434.
115. Wei, P.-F.; Qi, M.-Z.; Wang, Z.-P.; Ding, S.-Y.; Yu, W.; Liu, Q.; Wang, L.-K.; Wang, H.-Z.; An, W.-K.; Wang, W., Benzoxazole-Linked Ultrastable Covalent Organic Frameworks for Photocatalysis. *J. Am. Chem. Soc.* **2018**, *140* (13), 4623-4631.
116. Zeng, L.; Guo, X.; He, C.; Duan, C., Metal–Organic Frameworks: Versatile Materials for Heterogeneous Photocatalysis. *ACS Catal.* **2016**, *6* (11), 7935-7947.
117. Wang, C.; Xie, Z.; deKrafft, K. E.; Lin, W., Doping Metal–Organic Frameworks for Water Oxidation, Carbon Dioxide Reduction, and Organic Photocatalysis. *J. Am. Chem. Soc.* **2011**, *133* (34), 13445-13454.
118. Yu, X.; Cohen, S. M., Photocatalytic Metal–Organic Frameworks for Selective 2,2,2-Trifluoroethylation of Styrenes. *J. Am. Chem. Soc.* **2016**, *138* (38), 12320-12323.

119. Xu, C.; Liu, H.; Li, D.; Su, J.-H.; Jiang, H.-L., Direct evidence of charge separation in a metal–organic framework: efficient and selective photocatalytic oxidative coupling of amines via charge and energy transfer. *Chem. Sci.* **2018**, *9* (12), 3152-3158.
120. Johnson, J. A.; Luo, J.; Zhang, X.; Chen, Y.-S.; Morton, M. D.; Echeverría, E.; Torres, F. E.; Zhang, J., Porphyrin-Metalation-Mediated Tuning of Photoredox Catalytic Properties in Metal–Organic Frameworks. *ACS Catal.* **2015**, *5* (9), 5283-5291.
121. Li, H.; Yang, Y.; He, C.; Zeng, L.; Duan, C., Mixed-Ligand Metal–Organic Framework for Two-Photon Responsive Photocatalytic C–N and C–C Coupling Reactions. *ACS Catal.* **2019**, *9* (1), 422-430.
122. Shi, D.; He, C.; Qi, B.; Chen, C.; Niu, J.; Duan, C., Merging of the photocatalysis and copper catalysis in metal–organic frameworks for oxidative C–C bond formation. *Chem. Sci.* **2015**, *6* (2), 1035-1042.
123. Wu, P.; He, C.; Wang, J.; Peng, X.; Li, X.; An, Y.; Duan, C., Photoactive Chiral Metal–Organic Frameworks for Light-Driven Asymmetric α -Alkylation of Aldehydes. *J. Am. Chem. Soc.* **2012**, *134* (36), 14991-14999.
124. Zhang, Y.; Guo, J.; Shi, L.; Zhu, Y.; Hou, K.; Zheng, Y.; Tang, Z., Tunable chiral metal organic frameworks toward visible light–driven asymmetric catalysis. *Sci. Adv.* **2017**, *3* (8), e1701162.
125. Zhu, Y.-Y.; Lan, G.; Fan, Y.; Veroneau, S. S.; Song, Y.; Micheroni, D.; Lin, W., Merging Photoredox and Organometallic Catalysts in a Metal–Organic Framework Significantly Boosts Photocatalytic Activities. *Angew. Chem. Int. Ed.* **2018**, *57* (43), 14090-14094.
126. Lan, G.; Quan, Y.; Wang, M.; Nash, G. T.; You, E.; Song, Y.; Veroneau, S. S.; Jiang, X.; Lin, W., Metal–Organic Layers as Multifunctional Two-Dimensional Nanomaterials for Enhanced Photoredox Catalysis. *J. Am. Chem. Soc.* **2019**, *141* (40), 15767-15772.
127. Freitag, M.; Möller, N.; Rühling, A.; Strassert, C. A.; Ravoo, B. J.; Glorius, F., Photocatalysis in the Dark: Near-Infrared Light Driven Photoredox Catalysis by an Upconversion Nanoparticle/Photocatalyst System. *ChemPhotoChem* **2019**, *3* (1), 24-27.

Chapter 2

Chapter 3

Semi-heterogeneous dual nickel/photocatalysis using carbon nitrides: esterification of carboxylic acids with aryl halides

Pieber, B.; Malik, J. A.; Cavedon, C.; **Gisbertz, S.**; Savateev, A.; Cruz, D.; Heil, T.; Zhang, G.; Seeberger, P. H.

Angew. Chem. Int. Ed. **2019**, *58*, 9575-9580.

DOI: <https://doi.org/10.1002/anie.201902785>

Abstract

Cross-coupling reactions mediated by dual nickel/photocatalysis are synthetically attractive but rely mainly on expensive, non-recyclable noble metal complexes as photocatalysts. Heterogeneous semiconductors, which are commonly used for artificial photosynthesis and wastewater treatment, are a sustainable alternative. Graphitic carbon nitrides, a class of metal-free polymers that can be easily prepared from bulk chemicals, are heterogeneous semiconductors with high potential for photocatalytic organic transformations. Here, we demonstrate that graphitic carbon nitrides in combination with nickel catalysis can induce selective C–O cross-couplings of carboxylic acids with aryl halides, yielding the respective aryl esters in excellent yield and selectivity. The heterogeneous, organic photocatalyst exhibits a broad substrate scope, is able to harvest green light, and can be recycled multiple times. *In situ* FTIR was used to track the reaction progress to study this transformation at different irradiation wavelengths and reaction scales.

Specific contribution

Dr. B. Pieber conceived the project and optimized the reaction protocols.

Dr. J. Malik studied the reaction with the FT-IR setup.

C. Cavedon, Dr. G. Zhang and I prepared the carbon nitride materials used as photocatalyst.

C. Cavedon and I characterized them before and after the reactions.

Dr. B. Pieber, C. Cavedon and I investigated the scope and limitations of the protocol.

Dr. A. Savateev, Dr. D. Cruz and Dr. T. Heil performed material characterizations.

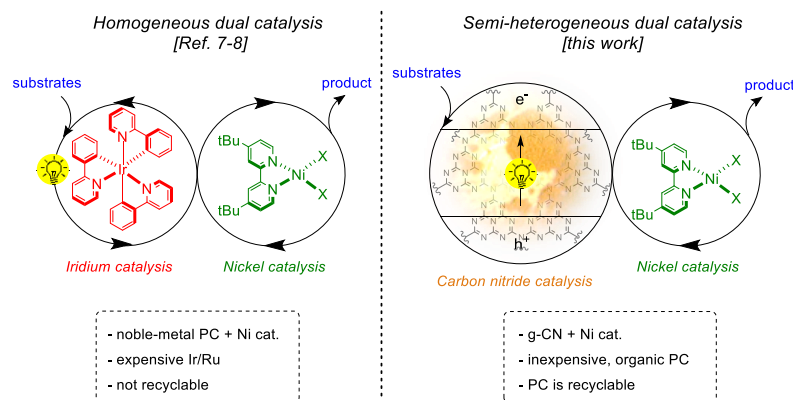
Dr. B. Pieber wrote the manuscript with contributions from all other authors.

3.1 Introduction

Transition-metal catalyzed cross-coupling reactions are key transformations in modern organic synthesis.¹ Numerous elegant and robust methods relying primarily on palladium catalysts to form carbon–carbon² and carbon–heteroatom³ bonds exist. The high economic and environmental cost of precious metal catalysts renders the catalytic systems unviable in the long-term. Nickel, an attractive alternative to rare metals, is capable of catalyzing many of the same transformations as palladium.⁴⁻⁶ The combination of nickel and photoredox catalysis has opened up new avenues for cross-coupling chemistry.⁷⁻⁸ However, ruthenium or iridium photocatalysts (PC) are still required to turn over the nickel species. Photoactive complexes with earth abundant metals⁹ or organic dyes¹⁰⁻¹³ are less efficient or prone to degradation.

Heterogeneous semiconductors are promising alternatives given their ease of preparation and straightforward recycling strategies by filtration or centrifugation.¹⁴⁻¹⁶ Graphitic carbon nitrides (g-CN), a class of metal-free polymers, are among the most potent materials for heterogeneous photocatalysis.¹⁷⁻¹⁸ Unlike the most widely studied semiconductor TiO₂ (band gap ~3.2 eV; onset of absorption: 380-390 nm), g-CN materials absorb light in the visible area (band gap <2.7 eV; onset of absorption: <450-460 nm). g-CN polymers are easy to synthesize from commodity chemicals, and exhibit a high thermal and chemical stability. The band gap and position of the valence and conduction band depend on several factors such as the C/N ratio, the polymerization degree, and the crystallinity, all of which can be tailored by the synthetic approach.¹⁷

Here, we describe the application of g-CN materials in dual nickel/photocatalysis in a semi-heterogeneous catalytic system (Scheme 3.1).

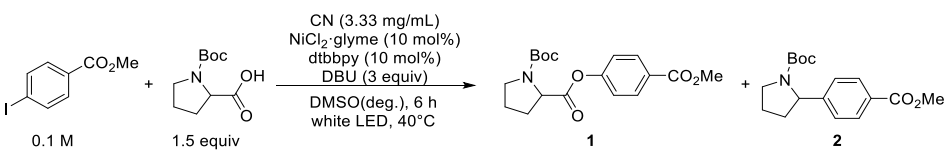


Scheme 3.1. Homogeneous versus semi-heterogeneous dual Ni/photocatalysis.

3.2 Results and discussion

Carbon nitride materials can catalyze esterification between *N*-(*tert*-Butoxycarbonyl)-proline (Boc-Pro-OH) and methyl 4-iodobenzoate using white LED (RGB) irradiation (Table 3.1). Mesoporous graphitic carbon nitride (mpg-CN),¹⁹ a modified carbon nitride derived from a cyanuric acid/melamide/barbituric acid complex (CMB_{0.05}-CN),²⁰ a sulfur-doped material (CNS₆₀₀),²¹ and the strongly oxidizing potassium poly(heptazine imide) (K-PHI),²² gave 12-15% of ester **1**. A carbon nitride derivative prepared through co-condensation of urea and oxamide followed by post-calcination in a molten salt (CN-OA-m)²³ showed the highest activity in the photocatalyst screening,²⁴ presumably due to its enhanced optical absorption in the visible region compared to most other known CN materials (Figure 3.4 in the Supporting Information). The absence of any detectable amounts of the corresponding decarboxylative C–C coupling product **2**²⁵ indicates a selective photosensitization rather than single-electron transfer.²⁶ This is in stark contrast to the usual reactivity of carbon nitride materials which are reported to follow single electron transfer (photoredox) pathways.¹⁸

Table 3.1. Screening of potential carbon nitride semiconductors.^[a]



Entry	CN catalyst	1 [%] ^[b]	2 [%] ^[b]
1	CN-OA-m	22	n.d.
2	CNS ₆₀₀	18	n.d.
3	mpg-CN	15	n.d.
4	K-PHI	14	n.d.
5	CMB _{0.05} -CN	12	n.d.

[a] Reaction conditions: methyl 4-iodobenzoate (0.3 mmol), Boc-Pro-OH (0.45 mmol), NiCl₂·glyme (10 mol%), dtbbpy (10 mol%), 1,8-diazabicyclo[5.4.0]undec-7-ene (DBU, 0.45 mmol), CN catalyst (10 mg), DMSO (anhydrous, 3 mL), white LEDs at 40 °C for 14 h. [b] Determined by ¹H-NMR using 1,3,5-trimethoxybenzene as internal standard. n.d. = not detected.

A systematic evaluation of all other reaction parameters indicated that a cocktail consisting of CN-OA-m (3.33 mg mL⁻¹), NiCl₂·glyme, 4,4'-di-*tert*-butyl-2,2'-dipyridyl (dtbbpy), and

N-tert-butylisopropylamine (BIPA) in dimethyl sulfoxide (DMSO) is particularly suitable, delivering the desired ester **1** in 96% after 14 h irradiation (Table 3.2, Entry 1).²⁴ The only side products were small amounts of the dehalogenated methylbenzoate **3** and the corresponding phenol **4**, which originates from either etherification with residual water²⁷⁻²⁸ or ester hydrolysis. The selectivity is identical to the homogeneous protocol using Ir(ppy)₃ (Entry 2, ppy = 2-phenylpyridine). Inexpensive Ni(OAc)₂·4H₂O shows similar catalytic activity (Entry 3), but an additional side product (methyl 4-acetoxybenzoate, 6%) resulted from the esterification of the aryl iodide with the acetate anion of Ni(OAc)₂·4H₂O. The method also selectively converts the corresponding bromide to the desired product **1**, albeit with lower efficiency (Entry 4). Control experiments showed that the reaction does not occur in the absence of carbon nitride, nickel catalyst, or light; and just small amounts of the desired product were observed in absence of ligand (10%) or base (3%).

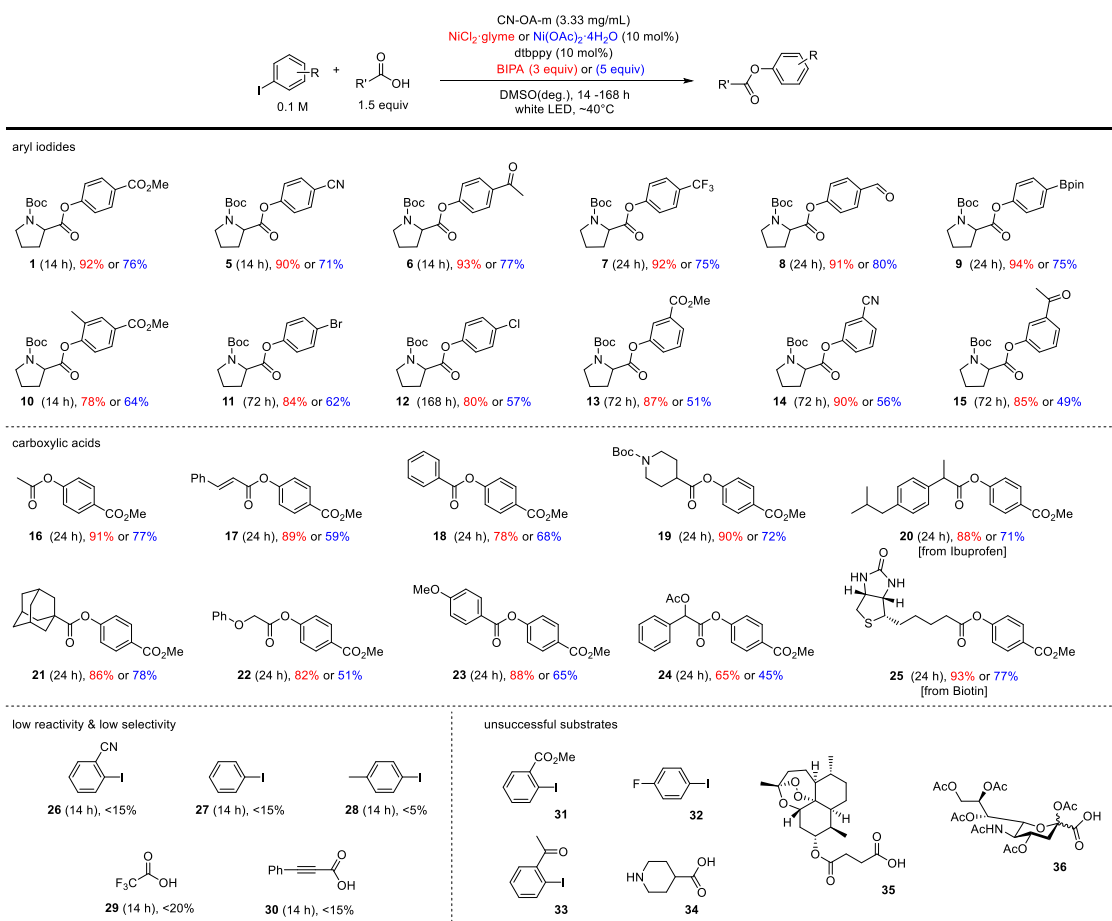
Table 3.2. Optimized conditions and control experiments^[a]

Entry	Conditions	1 [%] ^[b]	3 [%] ^[b]	4 [%] ^[b]
1	as shown	96	trace	2
2	Ir(ppy) ₃ (1mol%) instead of CN-OA-m	97	trace	1
3	Ni(OAc) ₂ ·4H ₂ O instead of NiCl ₂ ·glyme ^[c]	85	trace	4
4	4-Methyl bromobenzoate as substrate	68	5	2
5	No CN-OA-m	n.d.	n.d.	n.d.
6	No NiCl ₂ ·glyme	n.d.	2	1
7	No dtbbpy	10	3	2
8	No light	n.d.	n.d.	n.d.
9	No base	3	trace	n.d.

[a] Reaction conditions: methyl 4-iodobenzoate (0.3 mmol), Boc-Pro-OH (0.45 mmol), NiCl₂·glyme (10 mol%), dtbbpy (10 mol%), BIPA (0.9 mmol), CN-OA-m (10 mg), DMSO (anhydrous, 3 mL), white LEDs at 40 °C for 14 h. [b] Determined by ¹H-NMR using 1,3,5-trimethoxybenzene as internal standard. [c] 5 equiv BIPA were used. n.d. = not detected.

Chapter 3

The synthetic versatility of the catalytic system was evaluated using both nickel catalysts (Scheme 3.2).²⁴ The anhydrous $\text{NiCl}_2 \cdot \text{glyme}$ gave best results with 3 equiv of BIPA whereas inexpensive $\text{Ni}(\text{OAc})_2 \cdot 4\text{H}_2\text{O}$ necessitated a higher excess of the base (Table 3.9 and Figure 3.9 in the Supporting Information). Both systems work well with electron-deficient aryl iodides (**1**, **5-15**) whereas substrates lacking an electron-withdrawing group show low reactivity (**27**, **28**). A broad range of functional groups including esters (**1**, **10**, **13**), nitriles (**5**, **14**), ketones (**6**, **15**), aldehydes (**8**), and boronic acid pinacol esters (**9**) were tolerated under the conditions applied. *Para*-substituted aryl iodides (**1**, **5**, **6**) react significantly faster than their *meta* analogues (**13-15**). Although substituents in the *ortho*-position are tolerated (**10**), low reactivity for 2-iodobenzonitrile (**26**) was observed. Carbonyl groups in the 2-position (**31**, **33**) do not give the corresponding ester product.



Scheme 3.2. Scope of the semi-heterogeneous esterification of carboxylic acids with aryl iodides.

We assume that, after the initial oxidative addition of the aryl halide, coordination of the carbonyl oxygen to the metal center²⁹ hinders association of the carboxylate nucleophile. 1-Bromo-4-iodobenzene gave the desired product **11** without any detectable amount of the 1,4-diester, since the iodo- group reacts significantly faster and the resulting esterification product deactivates the aryl bromide towards a second esterification. With respect to the carboxylic acid coupling partner, a wide array of substrates can be efficiently coupled, including aliphatic (**16**, **19**, **21**, **22**), olefinic (**17**), and benzylic (**20**, **24**) carboxylic acids, as well as benzoic acid derivatives (**18**, **23**). The esterification of Biotin (**25**) shows the potential of the presented methodology for conjugation purposes. Artesunate (**35**), acetylated sialic acid (**36**) as well as the unprotected amine **34** did not give the desired ester under these reaction conditions. In all cases, Ni(OAc)₂·4H₂O resulted in a significantly lower selectivity than NiCl₂·glyme partly due to coupling of the acetate anion with the aryl iodide (up to 22%) and partly due to the formation of higher quantities of the dehalogenated and phenol side products (Table 3.16, 3.17).

A major advantage of carbon nitride catalysis is the potential to reuse the heterogeneous material.³⁰ With dual nickel/carbon nitride catalysis, however, deposition of Ni on the semiconducting material is possible and may alter its photocatalytic properties.¹⁷ As such, we sought to determine whether the CN-OA-m material is recyclable in our catalytic system (Figure 3.1). CN-OA-m was recovered after each reaction by centrifugation, washed, and used in the next reaction by adding fresh NiCl₂·glyme and dtbbpy.

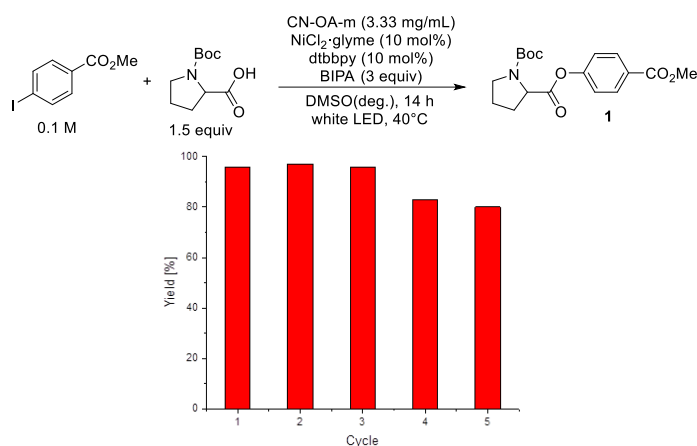


Figure 3.1. Reusability of CN-OA-m in the dual nickel/photocatalytic esterification of methyl 4-iodobenzoate with Boc-Pro-OH.

The material proved to be reusable without any loss of the catalytic activity over three cycles. Thereafter, a reduction in the yield of **1** from 96 to around 80% was noticed. This may result

from reduced availability of active catalytic sites for the photocatalytic step due to deposited Ni species,²⁴ but could be also rationalized by the loss of small amounts of the photocatalyst during the series of experiments. Analysis of the heterogeneous catalyst before and after a reaction using X-ray powder diffraction (XRD) showed the same characteristic peaks at 8° and 28° for CN-OA-m without any obvious Ni species in case of the recovered semiconductor (Figure 3.2, A). Similarly, identical FTIR (Figure 3.2, B) and UV/Vis spectra (Figure 3.2, C) were observed for the recovered and fresh CN-OA-m catalyst, thus demonstrating that the photocatalytic properties are not changed. The morphology of CN-OA-m shows a porous texture that was not altered during the catalytic transformation (Figure 3.2, E & F). Since highly dispersed Ni species are potentially undetectable by XRD,³¹ X-ray photoelectron spectroscopy (XPS) was used to detect Ni in the recovered material (Figure 3.2, D). The high resolution XPS Ni2 $p_{3/2}$ spectrum of the recovered CN-OA-m material shows two main deconvoluted peaks located at $853.7(\pm 0.02)$ eV and $852.5(\pm 0.02)$ eV that can be assigned to the binding energy of Ni^{2+} and Ni^0 species, respectively (Figure 3.15). Nickel deposition was further confirmed by ICP-OES analysis, which showed a Ni concentration of 1.4 % w/w, thus suggesting that 5-8% of the homogeneous nickel catalyst was deposited on the organic semiconductor.²⁴ Scanning transmission electron microscopy (STEM) was used to visualize nickel particles on the surface of the recovered CN-OA-m (Figure 3.2, G).

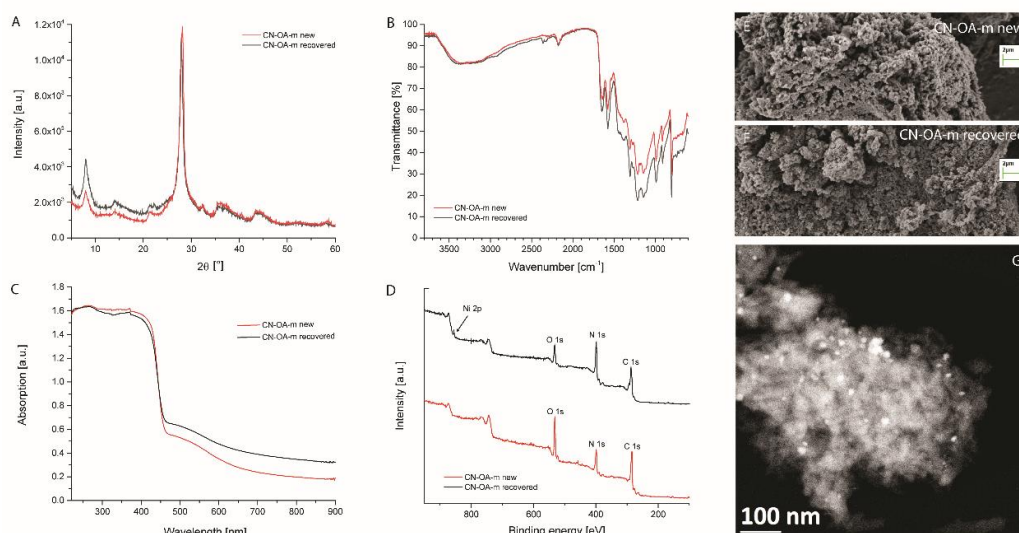


Figure 3.2. Analysis of new and recovered CN-OA-m by powder XRD (A), FTIR (B), UV/Vis (C) and XPS (D) spectroscopy as well as SEM analysis (E & F). HAADF-STEM image (G) of nickel particles (bright spots) attached to the recovered CN-OA-m.

To determine whether the immobilized nickel is catalytically active in the model reaction, the esterification was carried out with the recovered CN-OA-m material from one and five reaction cycles in the absence of additional NiCl₂·glyme. Both experiments resulted in no more than around 6% ester **1**, thus clearly indicating that the adsorbed, low-valent Ni species do not serve as effective catalytic species.²⁴

To study the scalability of the photocatalytic system and to determine whether it can harvest energy from varying light sources, a real-time monitoring strategy was developed.²⁴ Although NMR is often an ideal choice for kinetic analysis and has been used to track photocatalytic transformations,³² the presence of a heterogeneous component that broadens peaks, and the potential involvement of paramagnetic nickel species precluded its use. *In situ* FTIR analysis eliminates any interference from the heterogeneous photocatalyst,³³⁻³⁴ and provides high-fidelity reaction tracking under normal reaction conditions. When observing the reaction under optimized reaction conditions, an incipient peak at ~1764 cm⁻¹ (Figure 3.3, A), separable from the other two carbonyl stretches in the reaction mixture, was observed. This C=O stretch from the product's internal ester is heavily blue-shifted from the corresponding acid starting material. This peak served as a convenient measure of reaction progress (Figure 3.11). After a brief induction period, the catalysis reaches its maximum rate quickly and proceeds until completion (Figure 3.3B, black). A highly similar kinetic profile was observed using Ir(ppy)₃ (Figure 3.3B, grey), thus demonstrating that the heterogeneous catalyst has not only the same selectivity (Table 3.2) but also comparable efficiency to the state-of-the-art homogeneous noble-metal photocatalysts. Although slower than the aryl iodide, the bromide (Figure 3.3B, purple) furnished the product in 88% yield within 48 h (Supporting Information, Figure 3.12). Scale-up of the esterification from 0.3 mmol to 3.0 mmol (Figure 3.3B, orange) is facile, affording the desired ester **1** in 96% isolated yield on gram scale in roughly six instead of three hours when using this setup. Given that this scaled-up reaction has the same concentration of all components, the longer reaction time is mostly due to Beer–Lambert limitations inherent in using a larger reaction vessel (Supporting Information, Figure 3.10). The *in situ* method was also employed to assess the reaction's progress with different light settings from the same LED strips (Figure 3.3, C). Blue light (ca. 400 – 500 nm) catalyzes the reaction to completion, albeit more slowly because the energy from light above 500 nm is not available (Figure 3.6). Red light (600 – 650 nm), and a control experiment in the dark, afforded no meaningful amount of product. Encouragingly,

Chapter 3

green light (460 – 600 nm) produces partial completion in an overnight reaction, thus confirming that the heterogeneous photocatalyst is able to use a wide spectrum of visible light (Figure 3.4). After eight days, the reaction gave 72% **1** (Figure 3.14).

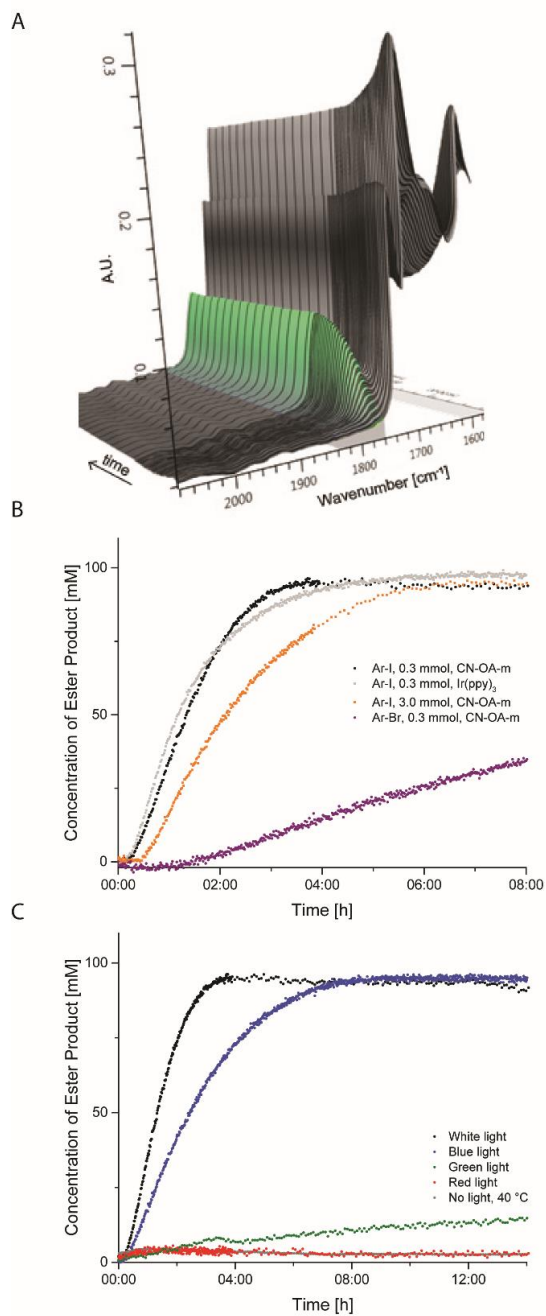
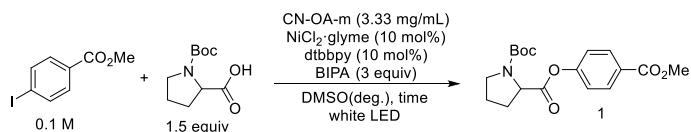


Figure 3.3. In situ reaction tracking of dual catalytic esterification. A, The internal ester peak at ~ 1764 cm^{-1} serves as a measure of reaction progress. B, Small-scale (0.3 mmol substrate) with the aryl iodide (black) and bromide (purple) as well as a gram-scale reaction (3.0 mmol methyl 4-iodobenzoate, orange) were easily tracked in situ. A comparison with Ir(ppy)₃ as PC shows a similar kinetic profile (grey). C, White light (black) and blue light (blue) catalyze the reactions quickly, while green light (green) also shows activity.

3.3 Conclusion

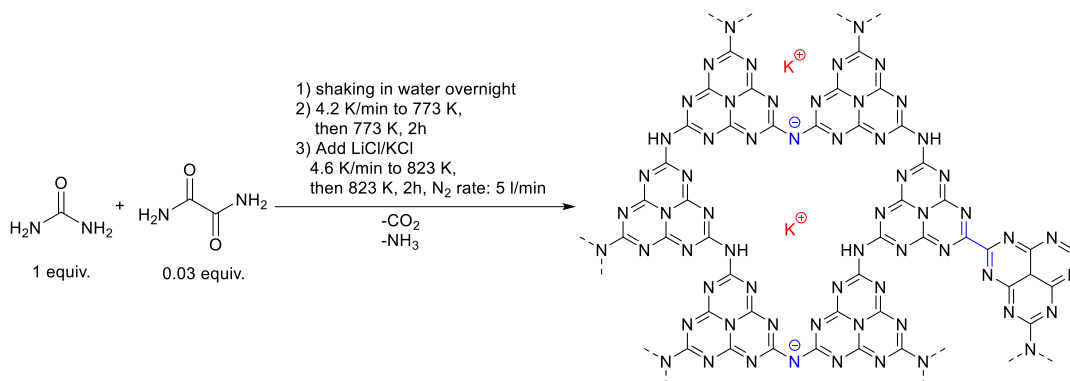
In conclusion, we have shown that a homogeneous nickel catalyst can be combined with a heterogeneous, metal-free carbon nitride semiconductor for dual catalysis. The insoluble photocatalyst can be recycled multiple times. Two nickel catalysts were studied in detail for a broad range of substrates, with $\text{NiCl}_2 \cdot \text{glyme}$ showing a significantly higher selectivity than $\text{Ni}(\text{OAc})_2 \cdot 4\text{H}_2\text{O}$, which nonetheless resulted in moderate to good yields of the desired esters. The organic semiconductor is able to harvest a broad range of the visible light spectrum (up to ca. 600 nm) as shown by *in situ* FTIR analysis. An FTIR reaction monitoring strategy was used for the first time, to the best of our knowledge, to study photocatalytic transformations. The inexpensive heterogeneous materials reported herein are an efficient and sustainable alternative to noble-metal complexes in photocatalysis.

3.4 Supporting information

3.4.1 General remarks

Substrates, reagents, and solvents were purchased from commercial suppliers and used without further purification. Methyl 4-(((trifluoromethyl)sulfonyl)oxy)benzoate,³⁵ methyl 4-(tosyloxy)benzoate³⁶ and methyl 4-((methylsulfonyl)oxy)benzoate³⁷ were prepared according to literature procedures. ¹H-, ¹³C- and ¹⁹F-NMR spectra were obtained using a Varian 400 spectrometer (400 MHz, Agilent), an Ascend™ 400 spectrometer (400 MHz, cryoprobe, Bruker) and a Varian 600 spectrometer (600 MHz, Agilent) at 298 K, and are reported in ppm relative to the residual solvent peaks. Peaks are reported as: s = singlet, d = doublet, t = triplet, q = quartet, m = multiplet or unresolved, with coupling constants in Hz. Analytical thin layer chromatography (TLC) was performed on pre-coated TLC-sheets, ALUGRAM Xtra SIL G/UV254 sheets (Macherey-Nagel) and visualized with 254 nm light or staining solutions followed by heating. Purification of final compounds was carried out by flash chromatography on the Reveleris X2 Flash Chromatography System from GRACE using prepacked columns with 40 μm silica gel. Silica 60 M (0.04-0.063 mm) silica gel (Sigma Aldrich) was used for dry loading of the crude compounds on the flash chromatography system. Centrifugation was carried out using an Eppendorf 5430 centrifuge. High-resolution mass spectral data were obtained using a Waters XEVO G2-XS 4K spectrometer with the XEVO G2-XS QTOF capability kit. *In situ* FTIR analysis was performed with a ReactIR™ 15 (Mettler-Toledo) console, with a DST 9.5mm SiComp™ probe attached. Emission spectra of LED lamps were recorded using 10 in. (24.5 cm) integrating sphere (Labsphere, Inc. Model LMS 1050) equipped with a diode array detector (International Light, Model RPS900). The UV/Vis spectrum of Ir(ppy)₂(dtbbpy)PF₆ was recorded using a UVmini-1240 spectrometer (Shimadzu).

3.4.2 Preparation of CN-OA-m



Scheme 3.3. Synthesis of CN-OA-m

The synthesis for CN-OA-m was carried out using a slightly adapted version of the literature procedure (Scheme 3.3)²³: For each batch of the photocatalyst, urea (10 g, 166.5 mmol) and oxamide (0.5 g, 5.7 mmol) were mixed in 10 ml of DI water to generate a homogeneous mixture. After drying at 373 K, the resulting solids were grinded, transferred into a crucible with a cover and heated up in an air-oven with a heating rate of 4.3 K/min to 773 K. After keeping the mixture for 2h at 773 K, the sample was allowed to cool to room temperature. Subsequently, KCl (3.3 g, 44.3 mmol) and LiCl (2.7 g, 63.7 mmol) were added and the solids were grinded to obtain a homogeneous mixture which was heated in an inert atmosphere (N₂ flow: 5 mL/min) to 823 K with a heating rate of 4.6 K/min. After keeping the mixture for 2 h at 823 K, the sample was allowed to cool to room temperature and the resulting solids were collected on a filter paper and washed with H₂O (3 x 100 mL). The resulting yellow material was dried at 373 K (average yield per batch: ~400 mg). All analytical data (FTIR, UV/Vis, XRD, SEM, etc.; see Section 3.4.7) are in full agreement with those published in the literature.²³

Each batch was tested under the same set of conditions and we always obtained similar catalytic activities (+/-5% based on ¹H-NMR with internal standard).

The cost of CN-OA-m was calculated to be 4.2 € g⁻¹ based on the prices of urea, oxamide, LiCl and KCl from Sigma-Aldrich (Merck).³⁸ As a comparison, the price of Ir(ppy)₃ is 2124 € g⁻¹.³⁸

The UV/Vis spectrum of CN-OA-m shows a strong absorption up to ~460 nm and a comparably weaker absorption band up to ~700 nm (Figure 3.4, A) which are attributed to

the $\pi\text{-}\pi^*$ electron transition of the sp^2 hybridization of C and N in the heptazine framework and $\text{n-}\pi^*$ electron transition involving the lone pairs of the edge nitrogen atoms in the heptazine units, respectively.²³ The capability of harvesting low energy light is therefore superior compared to Ir and Ru photocatalysts (see Figure 3.4, B for the UV/Vis spectrum of $\text{Ir}(\text{ppy})_2(\text{dtbbpy})\text{PF}_6$ as a representative example) which have only a low absorption band between 400 and 500 nm in the visible region, which corresponds to the metal-to-ligand charge transfer transition.

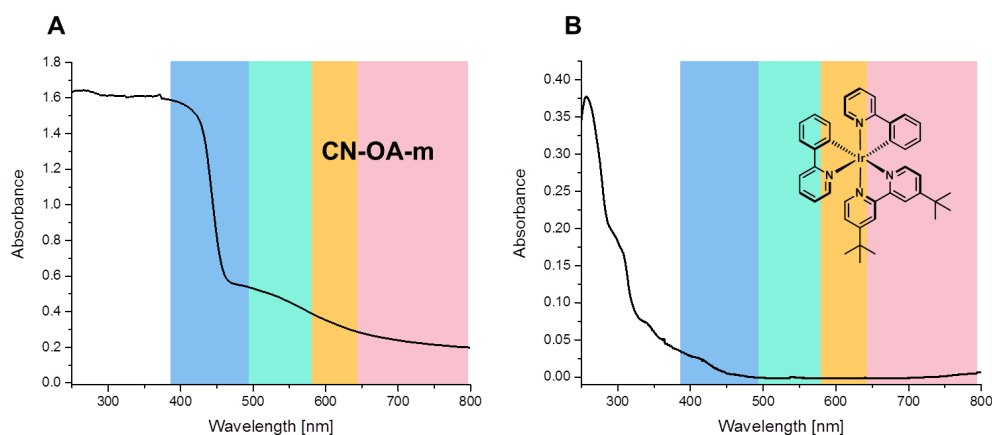
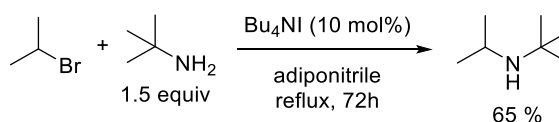


Figure 3.4. UV/Vis absorption spectra of CN-OA-m (A) and $\text{Ir}(\text{ppy})_2(\text{dtbbpy})\text{PF}_6$ (B).

3.4.3 Synthesis of *N-tert*-butylisopropylamine (BIPA)



Scheme 3.4. Synthesis of *N-tert*-butylisopropylamine (BIPA).³⁹

2-bromopropane (147.59 g, 1.2 mol), *tert*-butylamine (131.65 g, 1.8 mol, 1.5 eq) tetrabutylammonium iodide (44.33 g, 120 mmol, 0.10 eq) and adiponitrile (129.77 g, 1.20 mol, 1.0 eq) were weighed in a two-neck flask equipped with a reflux condenser. The resulting suspension was refluxed for 65 hours under vigorous stirring. Afterwards, a sodium hydroxide solution (5 M, 400 mL) was added and the mixture was extracted with pentane (5 x 100 ml). The combined pentane fractions were dried over magnesium sulfate. Distillation at atmospheric pressure afforded *N-tert*-butylisopropylamine (89.3 g, 0.78 mol, 65%) as a

colorless liquid. b.p. 98°C. $^1\text{H-NMR}$ (400 MHz, CDCl_3) δ 2.86 (hept, $J = 6.3$ Hz, 1H), 1.03 (s, 9H), 0.98 (d, $J = 6.3$ Hz, 6H). $^{13}\text{C-NMR}$ (101 MHz, CDCl_3) δ 50.81, 42.80, 29.91, 26.28. All analytical data are in full agreement with those published in the literature.³⁹

3.4.4 Setup for photochemical reactions

A flexible, red/green/blue LED strip⁴⁰ (RGB, 5m, 24 W/strip; Tween Light, BAHAG AG, Germany) was wrapped around a 115 mm borosilicate crystallization dish (Figure 3.5). Blue, green, red or white (illumination of all three LED colors - red/green/blue) light was used at full power for all experiments (For emission spectra of a single diode, see Figure 3.6). The evaporating dish was filled with ethylene glycol and the temperature was set to 40°C to maintain a constant temperature. The sealed reaction vessels were placed at the same distance from the LED strip during all experiments (Figure 3.5). All reactions were performed with a stirring speed of 1400 rpm.

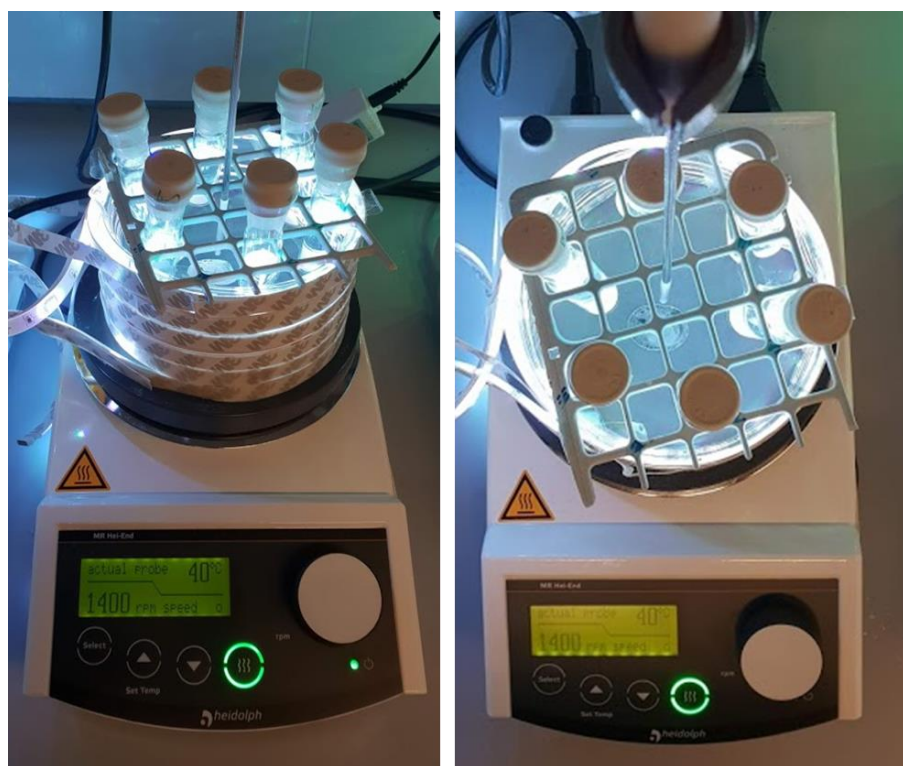


Figure 3.5. Experimental setup for photochemical reactions.

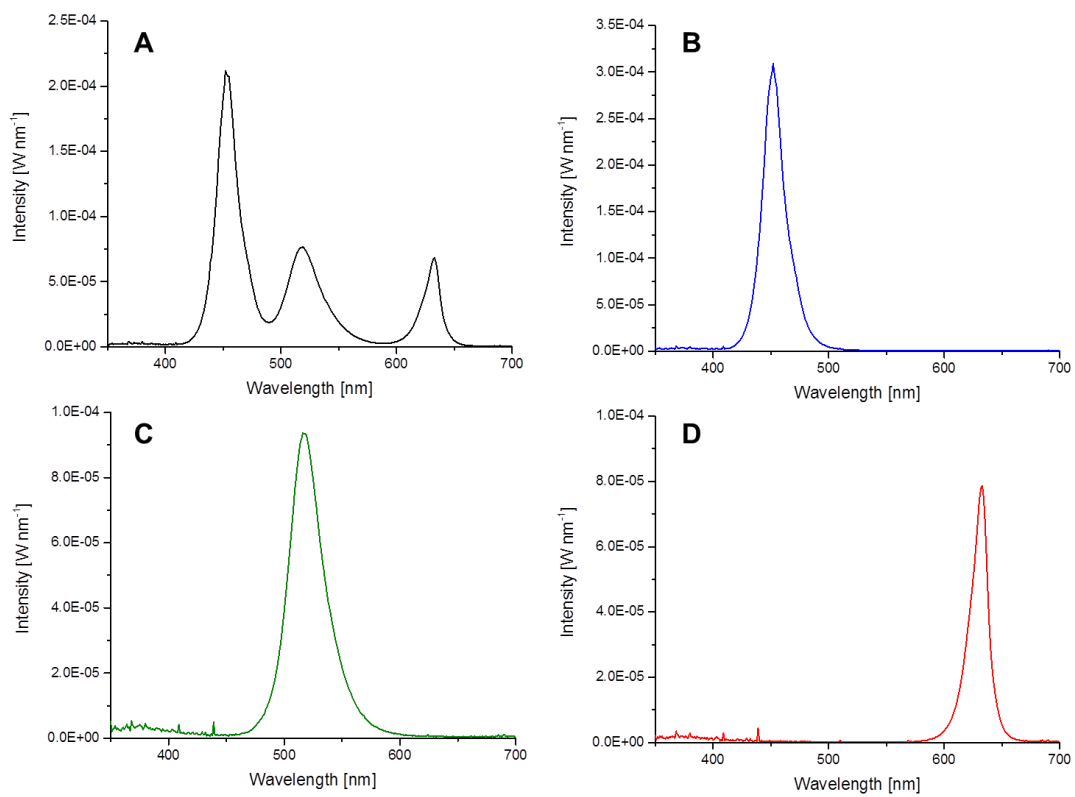


Figure 3.6. Emission spectra of the LED strips used for photochemical reactions. All experiments were carried out at maximum power. **A:** white light. **B:** blue light only. **C:** green light only. **D:** red light only.

3.4.5 Reaction optimization

General experimental procedure for screening experiments

An oven dried vial (19 x 100 mm) equipped with a stir bar was charged with the CN-material (10 mg), the carboxylic acid (0.45 mmol, 1.5 equiv.), the aryl halide (0.3 mmol, 1 equiv.), the Ni^{II} catalyst (30 μ mol, 10 mol%) and the ligand (30 μ mol, 10 mol%). Subsequently, the solvent (anhydrous, 3 mL) and the base (1-5 equiv.) were added and the vial was sealed with a septum and Parafilm. The reaction mixture was sonicated for 5-10 min followed by stirring for 5 min until a fine dispersion of the solids was achieved and the mixture was then degassed by bubbling Argon for 10 min. The mixture was irradiated in the photoreactor at 40 °C with rapid stirring (1400 rpm). After the respective reaction time, one equivalent of 1,3,5-trimethoxybenzene (0.3 mmol) was added. An aliquot of the reaction mixture (~200 μ L) was filtered, diluted with DMSO-d₆ and subjected to ¹H-NMR analysis. Alternatively, 1.5 mL CDCl₃ and 3 mL H₂O were added and the vial was sealed and vigorously shaken. After phase separation, the CDCl₃ layer was carefully removed using a syringe, filtered, and analyzed by ¹H-NMR. For representative NMR spectra, see Figure 3.7.

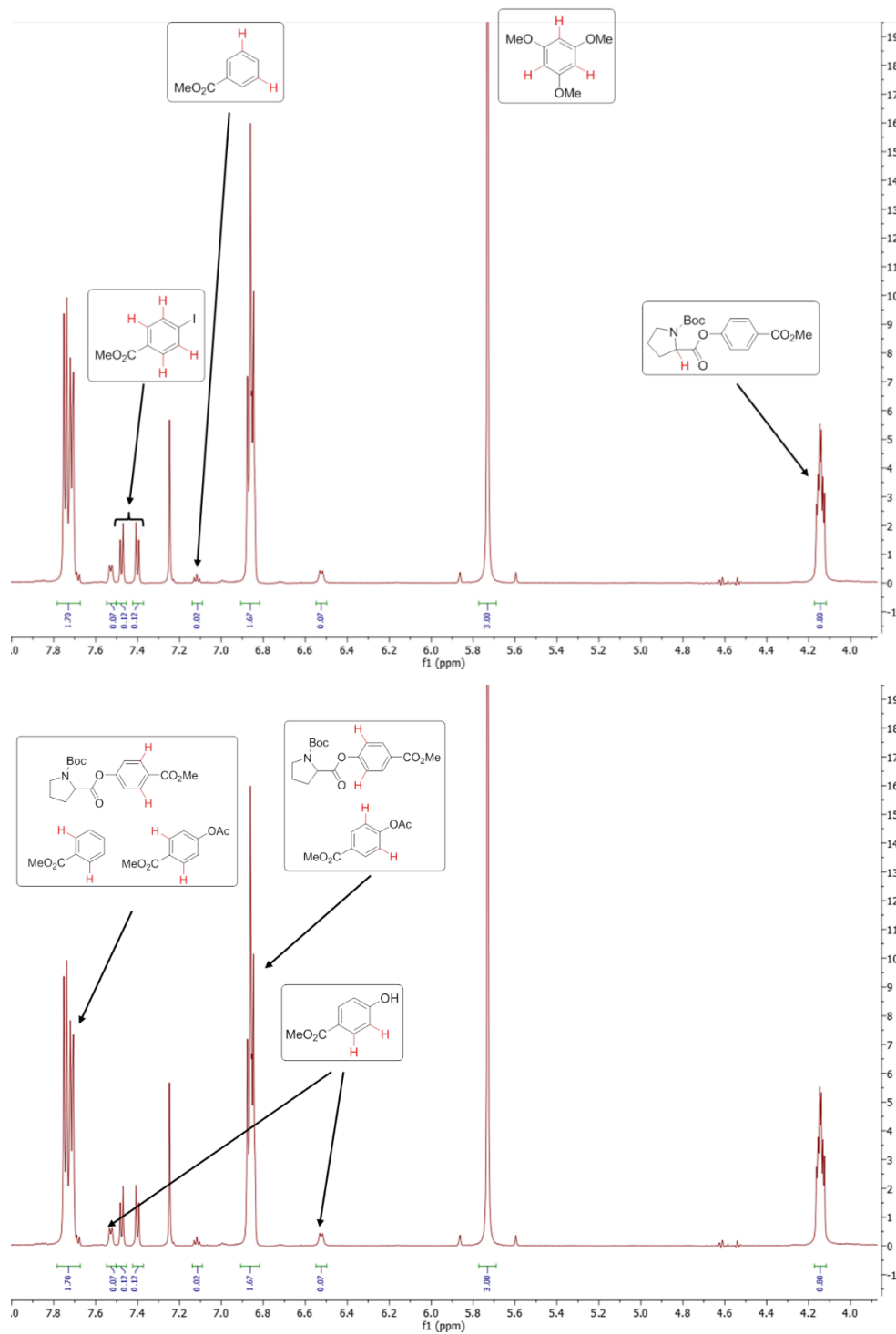
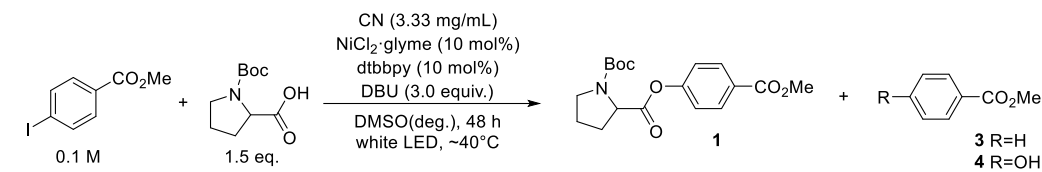


Figure 3.7. Example of a $^1\text{H-NMR}$ spectrum for determining NMR yields.

Screening of carbon nitride materials

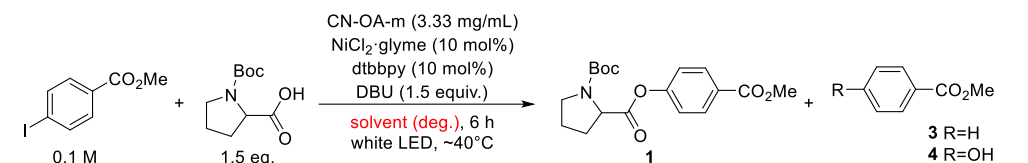
Table 3.3. Screening of carbon nitride materials.^a

Entry	CN catalyst	Conversion [%] ^b	1 [%] ^c	3 [%] ^c	4 [%] ^c
1	CN-OA-m	37	22	trace	7
2	CNS ₆₀₀	22	15	trace	trace
3	mpg-CN	29	15	trace	7
4	PHIK	29	14	trace	7
5	CMB _{0.05} -CN	26	12	trace	7

^aReaction conditions: methyl 4-iodobenzoate (0.3 mmol), *N*-Boc proline (0.45 mmol), NiCl₂·glyme (10 mol%), dtbbpy (10 mol%), DBU (0.45 mmol), carbon nitride (10 mg), DMSO (anhydrous, 3 mL), white LEDs at 40 °C for 6h. ^bConversion of methyl 4-iodobenzoate determined by ¹H-NMR using 1,3,5-trimethoxybenzene as internal standard. ^cNMR yields determined by ¹H-NMR using 1,3,5-trimethoxybenzene as internal standard.

Several carbon nitride materials were tested: Mesoporous graphitic carbon nitride (mpg-CN),¹⁹ a modified carbon nitride derived from a cyanuric acid/melamide/barbituric acid complex (CMB_{0.05}-CN),²⁰ a sulfur-doped material (CNS₆₀₀),²¹ a strongly oxidizing potassium poly(heptazine imide) (K-PHI),²² and a carbon nitride derivative prepared *via* co-condensation of urea and oxamide followed by post-calcination in a molten salt (CN-OA-m),²³ all using white LED (RGB) irradiation at a constant temperature of 40 °C.

Solvent screening

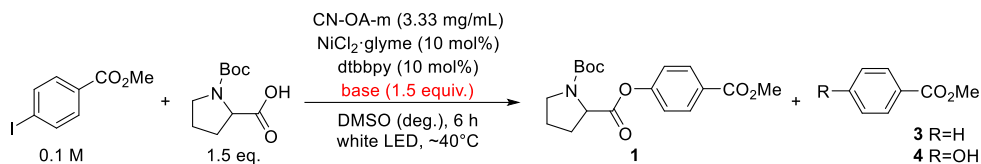
Table 3.4. Solvent screening.^a


Entry	Solvent	Conversion [%] ^b	1 [%] ^c	3 [%] ^c	4 [%] ^c
1	DMSO	37	22	trace	7
2	DMF	37	20	trace	trace
3	DMAc	24	15	trace	3
4	THF	10	7	trace	trace
5	dioxane	9	5	trace	trace
6	MeCN	14	trace	trace	trace
7	acetone	11	trace	trace	trace
8	DCM	11	trace	trace	trace
9	diglyme	14	trace	trace	trace
10	morpholine	11	trace	trace	trace
11	MeOH	15	trace	2	7

^aReaction conditions: methyl 4-iodobenzoate (0.3 mmol), *N*-Boc proline (0.45 mmol), NiCl₂·glyme (10 mol%), dtbbpy (10 mol%), DBU (0.45 mmol), CN-OA-m (10 mg), solvent (anhydrous, 3 mL), white LEDs at 40 °C for 6h. ^bConversion of methyl 4-iodobenzoate determined by ¹H-NMR using 1,3,5-trimethoxybenzene as internal standard. ^cNMR yields determined by ¹H-NMR using 1,3,5-trimethoxybenzene as internal standard.

Although DMSO and DMF gave similar results, DMSO was selected for further studies as DMF often contains readily oxidizable amine impurities that could interfere with the photocatalytic cycle.

Base screening

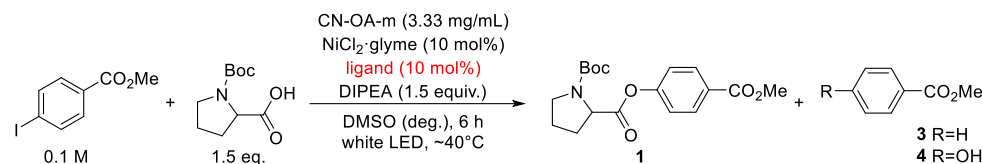
Table 3.5. Base screening.^a

Entry	Solvent	Conversion [%] ^b	1 [%] ^c	3 [%] ^c	4 [%] ^c
1	BIPA ^d	76	64	trace	trace
2	DIPEA	63	53	7	trace
3	CsF	44	38	trace	trace
4	dimethylaniline	73	34	n.d.o. ^e	20
5	DBU	37	22	trace	7
6	Et ₃ N	25	15	trace	trace
7	DABCO	16	8	trace	trace
8	DMAP	12	3	trace	trace
9	2,6-lutidine	12	n.d.	n.d. ^f	n.d.
10	Cs ₂ CO ₃	1	n.d.	n.d.	n.d.
11	TBD ^g	16	n.d.	n.d.	n.d.

^aReaction conditions: methyl 4-iodobenzoate (0.3 mmol), *N*-Boc proline (0.45 mmol), NiCl₂·glyme (10 mol%), dtbbpy (10 mol%), base (0.45 mmol), CN-OA-m (10 mg), DMSO (anhydrous, 3 mL), white LEDs at 40 °C for 6h. ^bConversion of methyl 4-iodobenzoate determined by ¹H-NMR using 1,3,5-trimethoxybenzene as internal standard. ^cNMR yields determined by ¹H-NMR using 1,3,5-trimethoxybenzene as internal standard. ^d*N*-tert-butylisopropylamine. ^enot determined due to overlapping peaks. ^fnot detected. ^g1,5,7-triazabicyclodec-5-ene.

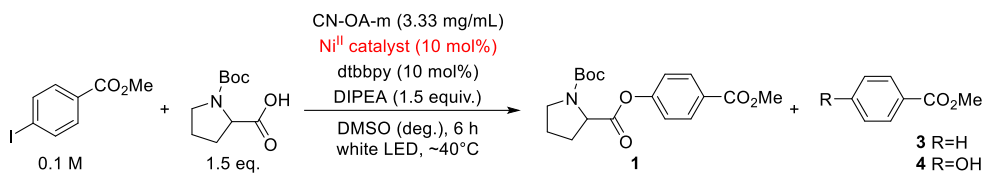
The base screening revealed that *N*-tert-butylisopropylamine (BIPA) performs best followed by Hünig's base (DIPEA) and CsF. The bulky secondary amine BIPA gave just trace amounts of the corresponding side products, whereas DIPEA showed significant amounts of the dehalogenated compound **3**. Nevertheless, the less selective tertiary amine base, was selected for further optimization as it is readily available in large quantities.

Ligand screening

Table 3.6. Ligand screening.^a

Entry	Ligand	Conversion [%] ^b	1 [%] ^c	3 [%] ^c	4 [%] ^c
1		63	53	7	trace
2		48	35	5	n.d. ^d
3		45	29	4	n.d.
4		35	24	3	n.d.
5		34	22	n.d.o. ^e	n.d.
6		28	21	3	n.d.
7		28	18	3	trace
8 ^f		12	8	n.d.o.	n.d.
9 ^f		31	n.d.	11	n.d.
10		15	n.d.	10	n.d.

^aReaction conditions: methyl 4-iodobenzoate (0.3 mmol), *N*-Boc proline (0.45 mmol), NiCl₂·glyme (10 mol%), ligand (10 mol%), DIPEA (0.45 mmol), CN-OA-m (10 mg), DMSO (anhydrous, 3 mL), white LEDs at 40 °C for 6 h. ^bConversion of methyl 4-iodobenzoate determined by ¹H-NMR using 1,3,5-trimethoxybenzene as internal standard. ^cNMR yields determined by ¹H-NMR using 1,3,5-trimethoxybenzene as internal standard. ^dnot detected. ^enot determined due to overlapping peaks. ^fcommercially available Ni^{II} phosphine complexes were used (no NiCl₂·glyme)

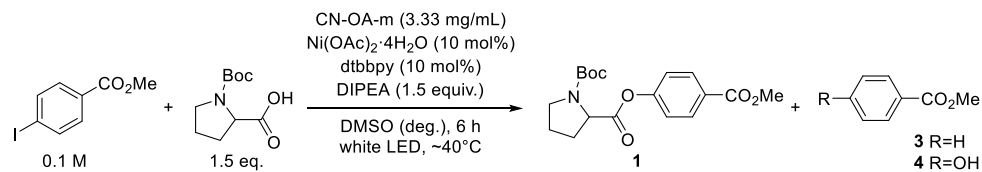
Screening of Ni^{II} sourcesTable 3.7. Screening of Ni^{II} sources.^a

Entry	Ni ^{II} catalyst	Conversion [%] ^b	1 [%] ^c	3 [%] ^c	4 [%] ^c	Price [€ mol ⁻¹] ^d
1	NiCl ₂ ·glyme	63	53	7	trace	4161
2 ^e	Ni(OAc) ₂ ·4H ₂ O	57	46	4	n.d. ^f	28
3	NiBr ₂	55	44	5	n.d.	411
4	NiCl ₂ ·6H ₂ O	51	40	n.d. ^g	n.d.	71
5	NiCl ₂	44	33	n.d.o.	n.d.	110
6	NiBr ₂ ·glyme	40	31	3	n.d.	10431
7	NiI ₂	35	27	n.d.o.	n.d.	2063
8	NiBr ₂ ·3H ₂ O	34	25	3	n.d.	116
9	Ni(ClO ₄) ₂ ·6H ₂ O	28	25	2	trace	171
10	Ni(NO ₃) ₂ ·6H ₂ O	26	24	2	trace	49
11	Ni(BF ₄) ₂ ·6H ₂ O	24	22	2	trace	223
12	Ni(SO ₄) ₂ ·6H ₂ O	32	22	n.d.o.	n.d.	41
13	Ni(acac) ₂	12	3	n.d.o.	n.d.	620
14	Ni(OTf) ₂	12	3	3	n.d.	12917

^aReaction conditions: methyl 4-iodobenzoate (0.3 mmol), *N*-Boc proline (0.45 mmol), Ni^{II} catalyst (10 mol%), dtbbpy (10 mol%), DIPEA (0.45 mmol), CN-OA-m (10 mg), DMSO (anhydrous, 3 mL), white LEDs at 40 °C for 6 h. ^bConversion of methyl 4-iodobenzoate determined by ¹H-NMR using 1,3,5-trimethoxybenzene as internal standard. ^cNMR yields determined by ¹H-NMR using 1,3,5-trimethoxybenzene as internal standard. ^dPrices according to Sigma Aldrich (Merck)³⁸. ^eTrace amounts of methyl 4-acetoxybenzoate were observed as additional side-product. ^fnot detected. ^gnot determined due to overlapping peaks.

$\text{NiCl}_2 \cdot \text{glyme}$ is the optimal catalyst with $\text{Ni}(\text{OAc})_2 \cdot 4\text{H}_2\text{O}$ showing similar catalytic activity. In the latter case, trace amounts of methyl 4-acetoxybenzoate were observed, resulting from the esterification of the aryl iodide with the acetate anion of $\text{Ni}(\text{OAc})_2 \cdot 4\text{H}_2\text{O}$. Combining the heterogeneous photocatalyst with the inexpensive $\text{Ni}(\text{OAc})_2 \cdot 4\text{H}_2\text{O}$ catalyst seemed most appealing.

Screening of reaction conditions

Table 3.8. Screening of reaction conditions.^a

Entry	Deviation from standard conditions	Conversion [%] ^b	1 [%] ^c	3 [%] ^c	4 [%] ^c
1	None	57	46	4	n.d. ^d
2	DMSO with 10% H ₂ O	16	7	2	trace
3	Stronger LED ^e	45	34	7	n.d.
4	70 °C	71	60	4	trace
5	6.66 mg/mL CN-OA-m	54	42	5	n.d.
6	20 mol% Ni ^{II} cat & ligand	52	45	4	n.d.
7	0.05 M	49	38	3	n.d.
8	0.2 M	58	48	4	n.d.
9	1 equiv. <i>N</i> -Boc-Pro-OH	49	37	5	n.d.
10	2.5 equiv. <i>N</i> -Boc-Pro-OH	59	49	4	n.d.
11	<i>N</i> -Boc-Pro-OH limiting with 2.5 eq. Ar-I	n.d.o. ^f	21	n.d.o.	n.d.

^aReaction conditions: methyl 4-iodobenzoate (0.3 mmol), *N*-Boc proline (0.45 mmol), Ni(OAc)₂·4H₂O (10 mol%), dtbbpy (10 mol%), DIPEA (0.45 mmol), CN-OA-m (10 mg), DMSO (anhydrous, 3 mL), white LEDs at 40 °C for 6h. Trace amounts of methyl 4-acetoxybenzoate were observed as additional side-product. ^bConversion of methyl 4-iodobenzoate determined by ¹H-NMR using 1,3,5-trimethoxybenzene as internal standard. ^cNMR yields determined by ¹H-NMR using 1,3,5-trimethoxybenzene as internal standard. ^dnot detected. ^eA 420 nm LED module (OLM-018 UV420, OSA Opto Light⁴¹) was used. ^fnot determined due to overlapping peaks.

The reaction time, stoichiometry of the nickel source as well as the ligand, the amount of photocatalyst, the stoichiometry of substrates, the reaction temperature, the LED power/lamp and overall concentration, were varied in order to push the reaction to

completion using a catalytic cocktail of CN-OA-m, Ni(OAc)₂·4H₂O, dtbbpy and DIPEA in DMSO. Full conversion of starting material was never achieved during these attempts.

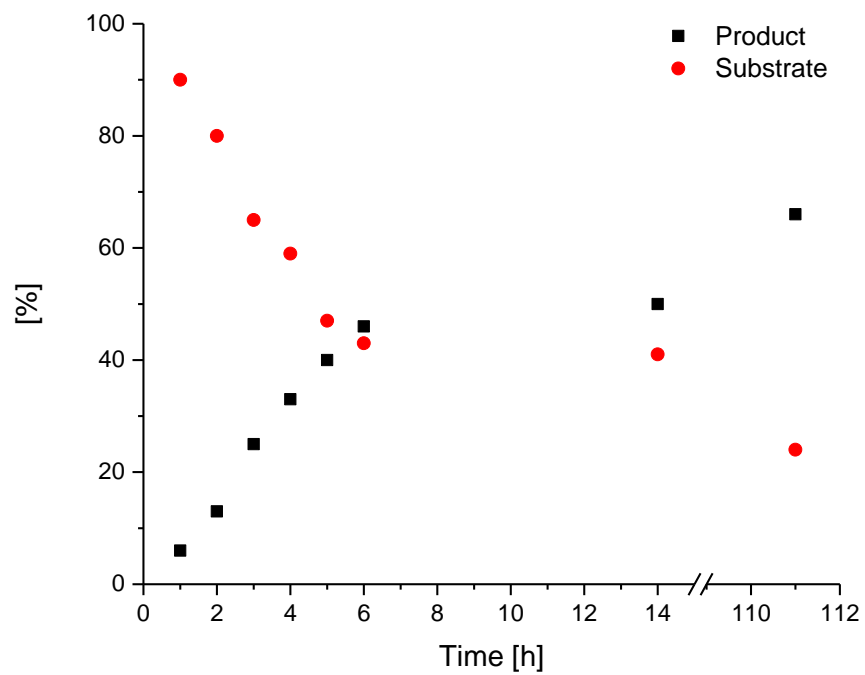
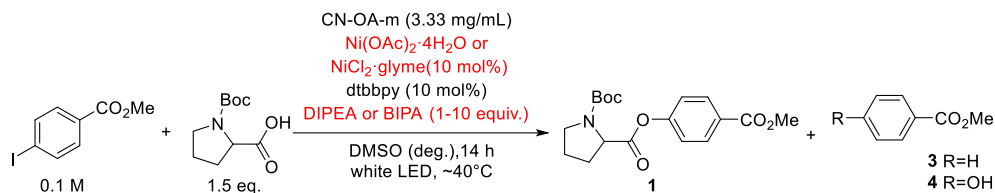


Figure 3.8. Time study using conditions from Table 3.8, Entry 1.

Correlation between the amount of base and reaction conversion using different combinations of nickel catalyst and base

Table 3.9. Correlation between the amount of base and reaction conversion using different combinations of nickel catalyst and base.^a



Entry	N ^{II} catalyst	Base (equiv.)	Conversion [%] ^b	1 [%] ^c	3 [%] ^c	4 [%] ^c
1	Ni(OAc) ₂ ·4H ₂ O	DIPEA (1.5)	59	50	5	n.d. ^d
2	Ni(OAc) ₂ ·4H ₂ O	DIPEA (2)	77	63	6	n.d.
3	Ni(OAc) ₂ ·4H ₂ O	DIPEA (2.5)	76	63	8	n.d.
4	Ni(OAc) ₂ ·4H ₂ O	DIPEA (3)	80	64	7	trace
5	Ni(OAc) ₂ ·4H ₂ O	DIPEA (3.5)	81	65	7	trace
6	Ni(OAc) ₂ ·4H ₂ O	DIPEA (4)	83	65	8	trace
7	Ni(OAc) ₂ ·4H ₂ O	DIPEA (4.5)	82	67	8	trace
8	Ni(OAc) ₂ ·4H ₂ O	DIPEA (5)	96	76	9	trace
9	Ni(OAc) ₂ ·4H ₂ O	DIPEA (6)	94	75	10	trace
10	Ni(OAc) ₂ ·4H ₂ O	DIPEA (10)	98	77	10	trace
11	Ni(OAc) ₂ ·4H ₂ O	BIPA (1.5)	71	60	trace	trace
12	Ni(OAc) ₂ ·4H ₂ O	BIPA (3)	78	73	trace	2
13	Ni(OAc) ₂ ·4H ₂ O	BIPA (3.5)	86	82	trace	3
14	Ni(OAc) ₂ ·4H ₂ O	BIPA (4)	85	80	trace	4
15	Ni(OAc) ₂ ·4H ₂ O	BIPA (4.5)	92	85	trace	4
16	Ni(OAc) ₂ ·4H ₂ O	BIPA (5)	96	85	trace	4
17 ^e	Ni(OAc) ₂ ·4H ₂ O	BIPA (5)	60	52	trace	trace
18	NiCl ₂ ·glyme	BIPA (1)	59	58	trace	trace

Entry	Ni ^{II} catalyst	Base (equiv.)	Conversion [%] ^b	1 [%] ^c	3 [%] ^c	4 [%] ^c
19	NiCl ₂ ·glyme	BIPA (1.5)	83	80	trace	trace
20	NiCl ₂ ·glyme	BIPA (2)	94	88	trace	trace
21	NiCl ₂ ·glyme	BIPA (3)	>99	96	trace	2
22	NiCl ₂ ·glyme	BIPA (4)	>99	94	trace	4
23	NiCl ₂ ·glyme	BIPA (5)	>99	94	trace	5

^aReaction conditions: methyl 4-iodobenzoate (0.3 mmol), *N*-Boc proline (0.45 mmol), Ni(OAc)₂·4H₂O or NiCl₂·glyme (10 mol%), dtbbpy (10 mol%), DIPEA or BIPA (1-10 equiv.), CN-OA-m (10 mg), DMSO (anhydrous, 3 mL), white LEDs at 40 °C for 14h. ^bConversion of methyl 4-iodobenzoate determined by ¹H-NMR using 1,3,5-trimethoxybenzene as internal standard. ^cNMR yields determined by ¹H-NMR using 1,3,5-trimethoxybenzene as internal standard. ^dnot detected. ^eReaction was carried out for 6h.

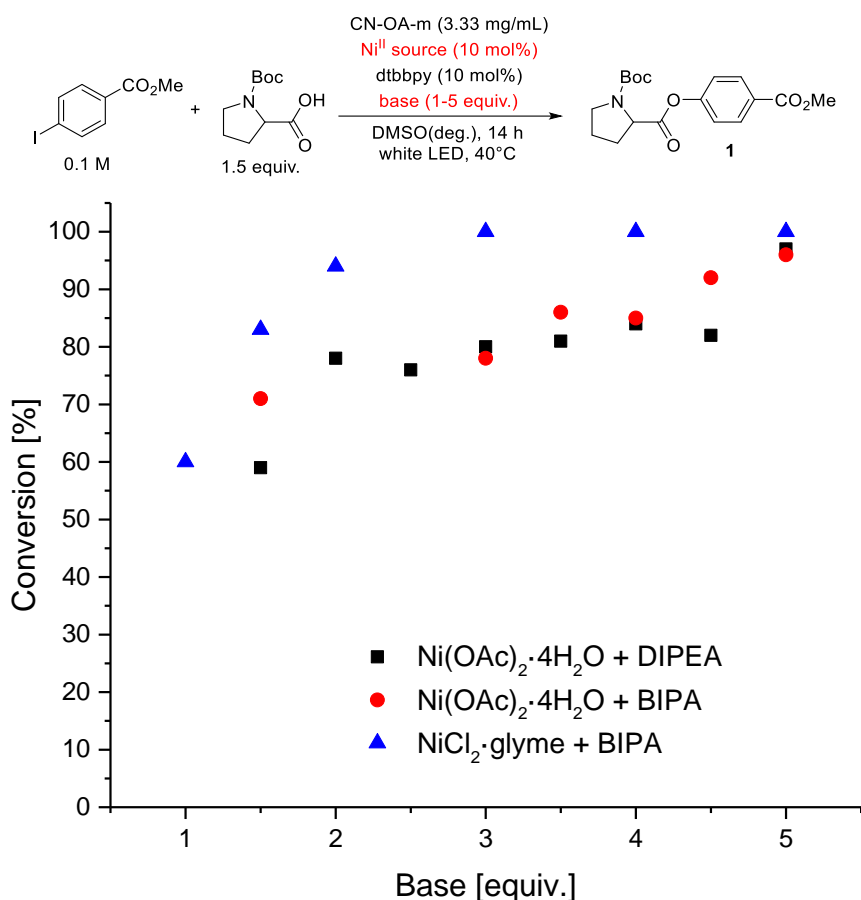
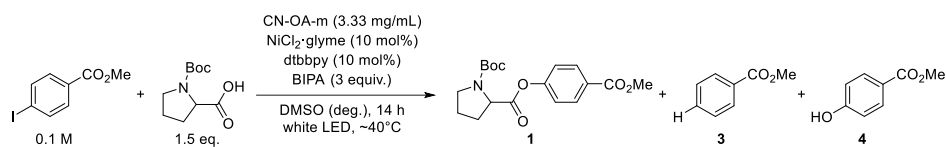


Figure 3.9. Correlation between the amount of base and reaction conversion using different combinations of nickel catalyst and base. Conversion of 4-methoxybenzoate determined by ¹H-NMR using 1,3,5-trimethoxybenzene as internal standard.

Chapter 3

After increasing the stoichiometry of DIPEA from 1.5 to 2 equivalents at a reaction time of 14 h the conversion improved from 50 to 63% (Figure 3.9, black). The use of up to 4.5 equivalents of DIPEA did not further improve the conversion, but at five equivalents almost full consumption of the starting material (94% conversion) and a 76% NMR yield of the desired ester **1** was observed. As a consequence of this behavior the use of BIPA was studied to see if this base-conversion relationship can be generalized (Figure 3.9, red). Here, an almost linear correlation was observed and again five equivalents of the bulky secondary amine were necessary for a nearly quantitative reaction within 14 h (93% conversion; 79% NMR yield of **1**). A combination of the most potent nickel catalyst ($\text{NiCl}_2 \cdot \text{glyme}$) and base (BIPA) gave full conversion and a significantly higher selectivity in favor for the desired product **1** (96% NMR yield) using only three equivalents of base within 14 h (Figure 3.9, blue). The distribution of side products differs significantly depending on the catalytic system. In case of $\text{Ni}(\text{OAc})_2 \cdot 4\text{H}_2\text{O}$ and five equiv. DIPEA, significant amounts of the dehalogenated methylbenzoate (**3**, 10%) were observed together with just trace amounts of the corresponding phenol **4**. In addition, 6% of the methyl 4-acetoxybenzoate is formed by esterification with the catalyst's acetate anion. When the base is replaced by BIPA, **4** becomes the main byproduct (4%) whereas just trace amounts of **3** were detected using both Ni^{II} catalysts (in addition, 6% of the acetate was observed when $\text{Ni}(\text{OAc})_2 \cdot 4\text{H}_2\text{O}$ was used).

Control studies

Table 3.10. Control studies.^a

Entry	Deviation from standard conditions	Conversion [%] ^b	1 [%] ^c	3 [%] ^c	4 [%] ^c
1	None	>99	96	trace	2
2	Ir(ppy) ₃ (1mol%) instead of CN-OA-m	>99	97	trace	1
3	No CN-OA-m	<1	n.d. ^d	n.d.	n.d.
4	No NiCl ₂ ·glyme	5	n.d.	2	1
5	No dtbbpy	12	10	3	2
6	No light	<1	n.d.	n.d.	n.d.
7	No degassing	<1	n.d.	n.d.	n.d.
8	No base	7	3	trace	n.d.

^aReaction conditions: methyl 4-iodobenzoate (0.3 mmol), *N*-Boc proline (0.45 mmol), NiCl₂·glyme (10 mol%), dtbbpy (10 mol%), BIPA (0.9 mmol), CN-OA-m (10 mg), DMSO (anhydrous, 3 mL), white LEDs at 40 °C for 14h. ^bConversion of methyl 4-iodobenzoate determined by ¹H-NMR using 1,3,5-trimethoxybenzene as internal standard. ^cNMR yields determined by ¹H-NMR using 1,3,5-trimethoxybenzene as internal standard. ^dnot detected.

Screening of aryl (pseudo)halides

Table 3.11. Base screening for the semi-heterogeneous esterification (selection)^a

Entry	X	1 [%] ^b	3 [%] ^b	4 [%] ^b
1	I	96	trace	4
2	Br	68	5	2
3	Cl	trace	n.d.c	n.d.
4	OTf	5	3	27
5	OTs	n.d.	n.d.	n.d.
6	OMs	n.d.	n.d.	trace

^aReaction conditions: methyl 4-iodobenzoate (0.3 mmol), *N*-Boc proline (0.45 mmol), NiCl₂·glyme (10 mol%), dtbbpy (10 mol%), BIPA (0.9 mmol), CN-OA-m (10 mg), DMSO (anhydrous, 3 mL), white LEDs at 40 °C for 14h. ^bNMR yields determined by ¹H-NMR using 1,3,5-trimethoxybenzene as internal standard. ^cn.d. not detected.

The most selective method using NiCl₂·glyme and three equivalents of BIPA was applied to different aryl (pseudo)halides (Table 3.11). Apart from aryl iodides, the method selectively converts the corresponding bromide to the desired product **1**, albeit with lower efficiency (Entry 2). Chloride (Entry 3) and triflate (Entry 4) produced small amounts of the ester. The triflate starting material further results in significant amounts of phenol **4**, most likely due to hydrolysis. Neither the mesylate nor the tosylate reacted under these conditions.

3.4.6 Reaction monitoring using *in situ* FTIR spectroscopy.

General procedure for ReactIR experiments.

Roughly two hours prior to each kinetic experiment, the ReactIR console was purged and filled with liquid nitrogen. A background spectrum was recorded shortly before attaching the reaction vessel to the ReactIR probe. To maintain a constant operating temperature during the course of longer experiments, the ReactIR console was replenished with new liquid nitrogen every 12 hours.

General conditions for the reaction setup were nearly identical to that of the above described screening and optimization experiments (see Section 3.4.5) A custom-made vial with a sidearm attached (19 x 100 mm, see below) was equipped with a stir bar and charged with CN-OA-m (10 mg), *N*-Boc Proline (0.45 mmol, 1.5 equiv.), methyl 4-iodobenzoate (0.3 mmol, 1 equiv.), NiCl₂·glyme (30 μmol, 10 mol%), and dtbbpy (30 μmol, 10 mol%). Subsequently, DMSO (anhydrous, 3 mL) and BIPA (0.9 mmol, 3.0 equiv.) were added and both necks of the vial were sealed with septa and Parafilm. The reaction mixture was sonicated for 5-10 min followed by stirring for 5 min until fine dispersion of the solids was achieved. The flask was then transported to the ReactIR where the larger septum was removed and the vessel immediately attached to the probe. To ensure an airtight seal, a PTFE adapter was affixed to the probe, to which the vessel was snugly attached. The vessel was continually degassed with Ar for 15 minutes through the sidearm. The mixture was stirred for 7-10 minutes again to re-ensure mixing of the components while data collection started on the ReactIR. After this period the LED lights were turned on with the desired color, and this initiation time was marked with the ReactIR proprietary software.

To the raw ReactIR absorbance data a negative second derivative function was applied to aid in separation of peaks. After subtraction of reference spectra, the product peak arrives at ~1764 cm⁻¹ while disappearance of the starting material can be observed at a peak around ~761 cm⁻¹. Raw data from iCiR was ported to Excel (Microsoft) or OriginPro 2015 (OriginLab) for processing and plotting.

Initial concentrations of all starting materials were determined from reaction stoichiometry. Final concentration of the product was determined from ¹H-NMR analysis or isolated yield. This method was validated as described below.

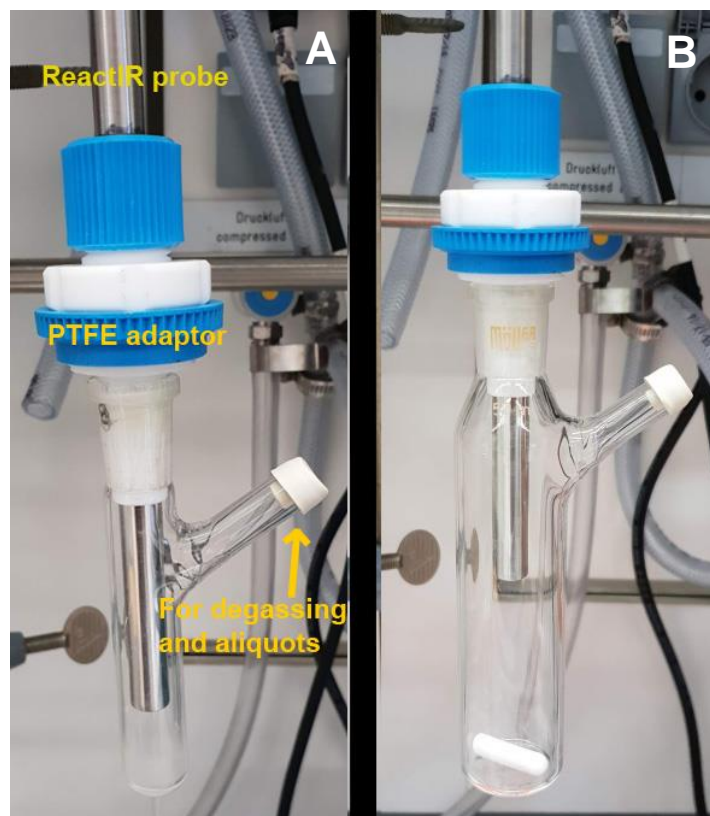


Figure 3.10. Vessels used for kinetics experiments with sidearm attached to enable degassing after attachment to the ReactIR probe. Left (**A**) setup used for all experiments on 0.3 mmol scale. Right (**B**) setup used for scale-up (3.0 mmol).

NMR validation of ReactIR experiments

A reaction with typical conditions was assembled on the ReactIR, from which periodic aliquots were removed *via* the sidearm. The timepoints of these aliquots were noted, and each aliquot was analyzed with ^1H -NMR, integrating for yield by integrating product peaks against total area of starting materials, products, and side products.

ReactIR yield was calculated from raw absorbance data that was normalized and scaled, tethered to isolated yield. Blue light was chosen for the NMR correlation experiment as it was shown to be slightly slower than white and therefore amenable to more data points. The overlay below between two completely independent methods indicates that ReactIR is a competent measure of reaction progress.

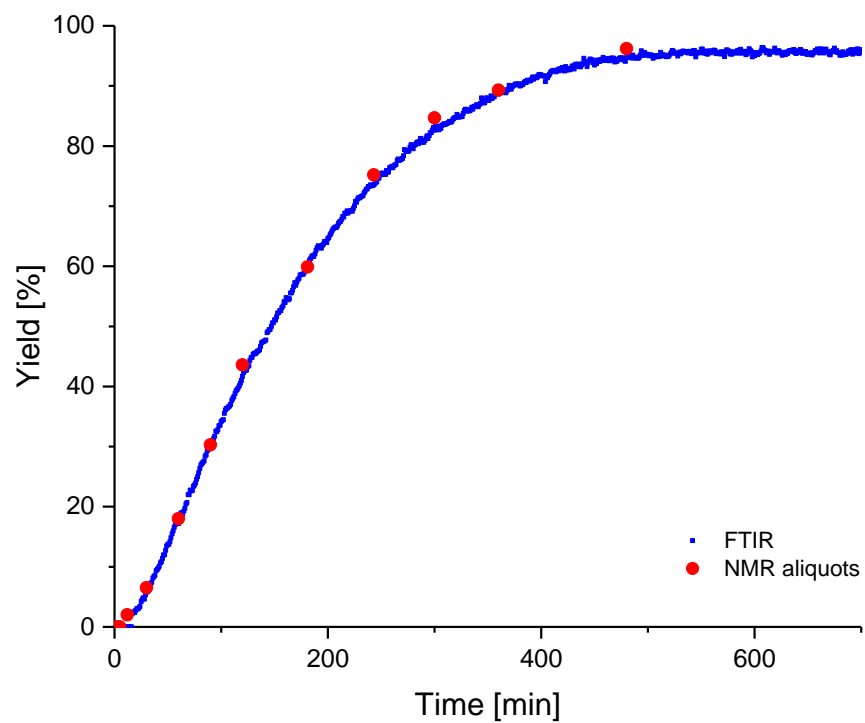
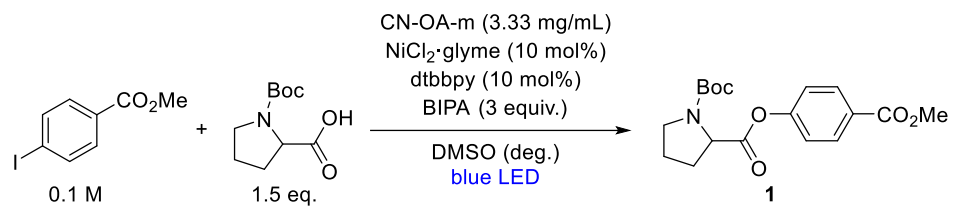


Figure 3.11. Correlation of NMR conversion to IR yield that validates *in situ* FTIR as a method to observe kinetics of the photocatalytic transformation.

Scale-up of esterification

A custom-made vial with a sidearm attached (Fig. 3.10, B) equipped with a stir bar was charged with CN-OA-m (100 mg), *N*-Boc Proline (968.6 mg, 4.5 mmol, 1.5 equiv.), methyl 4-iodobenzoate (786.2 mg, 3.0 mmol, 1.0 equiv.), NiCl₂·glyme (65.9 mg, 0.3 mmol, 0.1 equiv.), and dtbbpy (80.5 mg, 0.3 mmol, 0.1 equiv.). Subsequently, DMSO (anhydrous, 30 mL) and BIPA (1.43 mL, 9.0 mmol, 3.0 equiv.) were added and both necks of the vial were sealed with septa and Parafilm. The reaction mixture was repeatedly cycled through sonication and stirring until fine dispersion of the materials was achieved. The flask was then transported to the ReactIR where the larger septum was removed and the vessel immediately attached to the probe. To ensure an airtight seal, a PTFE adapter was affixed to the probe, to which the vessel was snugly attached. The vessel was continually degassed with Ar for 45 minutes through the sidearm, upon which the needles were removed from the sidearm. The mixture was stirred for 7-10 minutes at 850 rpm again to re-ensure mixing of the components while data collection started on the ReactIR. After this period the LED lights were turned on with white light, and this initiation time was marked with the ReactIR proprietary software. After the reaction arrived at completion as indicated by ReactIR, the catalyst was removed by centrifugation (3000 rpm, 20 min) and the liquid phase was diluted with H₂O (250 mL) and extracted with dichloromethane (3 x 250 mL). The combined organic phases were washed with brine (200 mL), dried over Na₂SO₄, and concentrated. The product was purified by flash column chromatography (SiO₂, Hexane/EtOAc) on a Grace™ Reveleris™ system using an 80g cartridge. We observed some mixed fractions containing small amounts of the phenol byproduct and the desired product. These mixed fractions were combined, washed with 0.5 M NaOH in DCM, dried over Na₂SO₄, filtered, evaporated, and combined with the pure fractions. The reaction gave 1.01 g (2.9 mmol, 96%) of the title compound as white powder. ¹H NMR (400 MHz, CDCl₃) rotameric mixture, δ 8.07 (m, 2H), 7.19 (m, 2H), 4.52 (dd, *J* = 8.6, 4.3 Hz, 0.4H), 4.46 (dd, *J* = 8.7, 4.3 Hz, 0.6H), 3.91 (m, 3H), 3.69 – 3.40 (m, 2H), 2.47 – 2.28 (m, 1H), 2.16 (m, 1H), 2.10 – 1.86 (m, 2H), 1.46 (m, 9H). ¹³C NMR (151 MHz, CDCl₃) rotameric mixture, resonances for minor rotamer are enclosed in parenthesis δ (171.10) 171.05, (166.30) 166.16, (154.42) 154.16, 153.60, 131.20 (131.07), 127.81 (127.65), (121.46) 121.09, 80.31 (80.09), 59.18 (59.07), 52.19 (52.13), (46.61) 46.42, 31.00 (29.94), 28.38, (24.52) 23.70. HRMS (ESI) *m/z* calcd for C₁₈H₂₃NNaO₆ [(M+Na)⁺] 372.1417, found 372.1443.

Aryl bromide experiment

The general procedure outlined at the beginning of this section was followed with white light, with the exception that 0.3 mmol methyl 4-bromobenzoate (64.5 mg) was used instead methyl 4-iodobenzoate (Figure 3.12). After 48 hours, the final reaction mixture gave 88% product by NMR integration against an internal standard, per Figure 3.7.

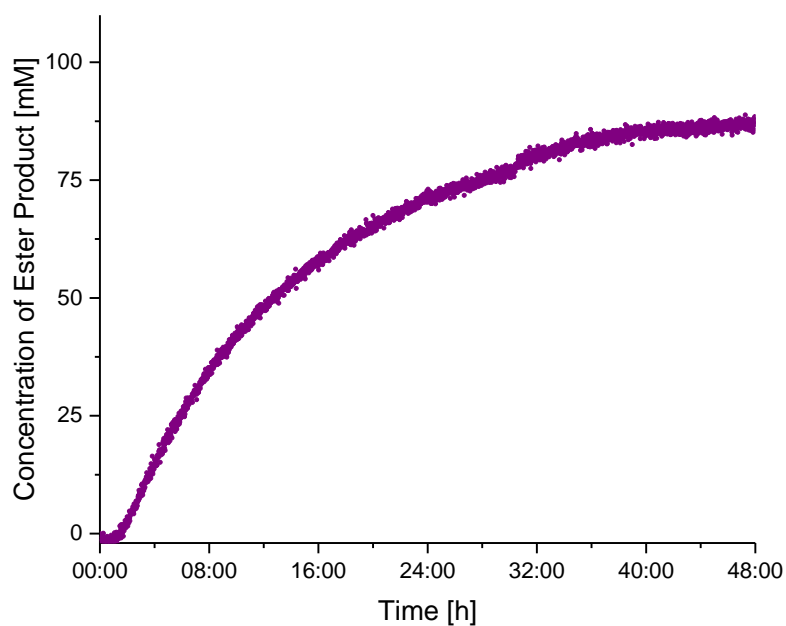
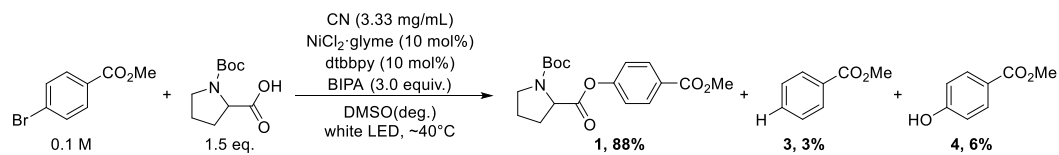


Figure 3.12. *In situ* FTIR reaction monitoring of the dual catalytic esterification of methyl 4-bromobenzoate.

Ir(ppy)₃ as photocatalyst instead of CN-OA-m

The general procedure outlined at the beginning of this section was followed with white light, with the exception that 1 mol% (2.0 mg, 0.003 mmol) Ir(ppy)₃ was added as a photocatalyst instead of CN-OA-m. As the solution contained no heterogeneous component, the sonication and stirring times prior to degassing were reduced to roughly two minutes each. The reaction gave 96% product by NMR integration against an internal standard, per Figure 3.7.

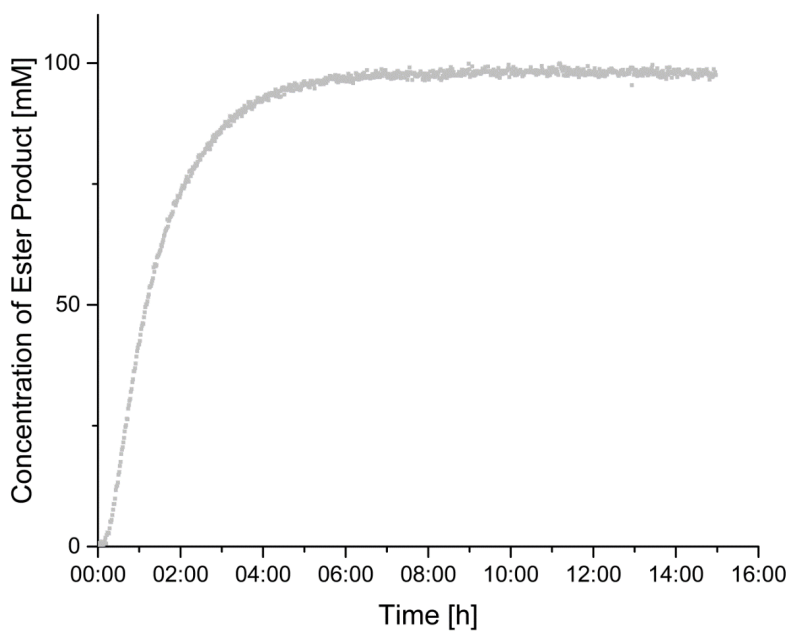
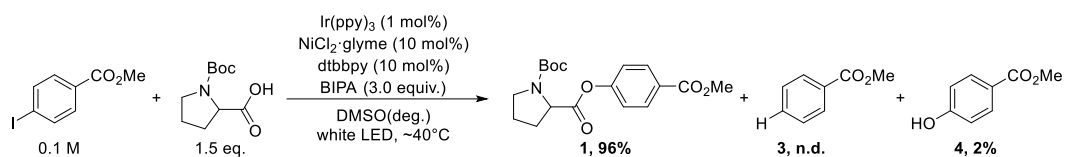


Figure 3.13. *In situ* FTIR reaction monitoring of the homogeneous dual catalytic esterification.

Green light experiment

The general procedure outlined at the beginning of this section, with the standard 0.3 mmol of methyl 4-iodobenzoate, was followed with green light (Figure 3.14). After over 8 days, the final reaction mixture gave 72% product by NMR integration against an internal standard, per Figure 3.7.

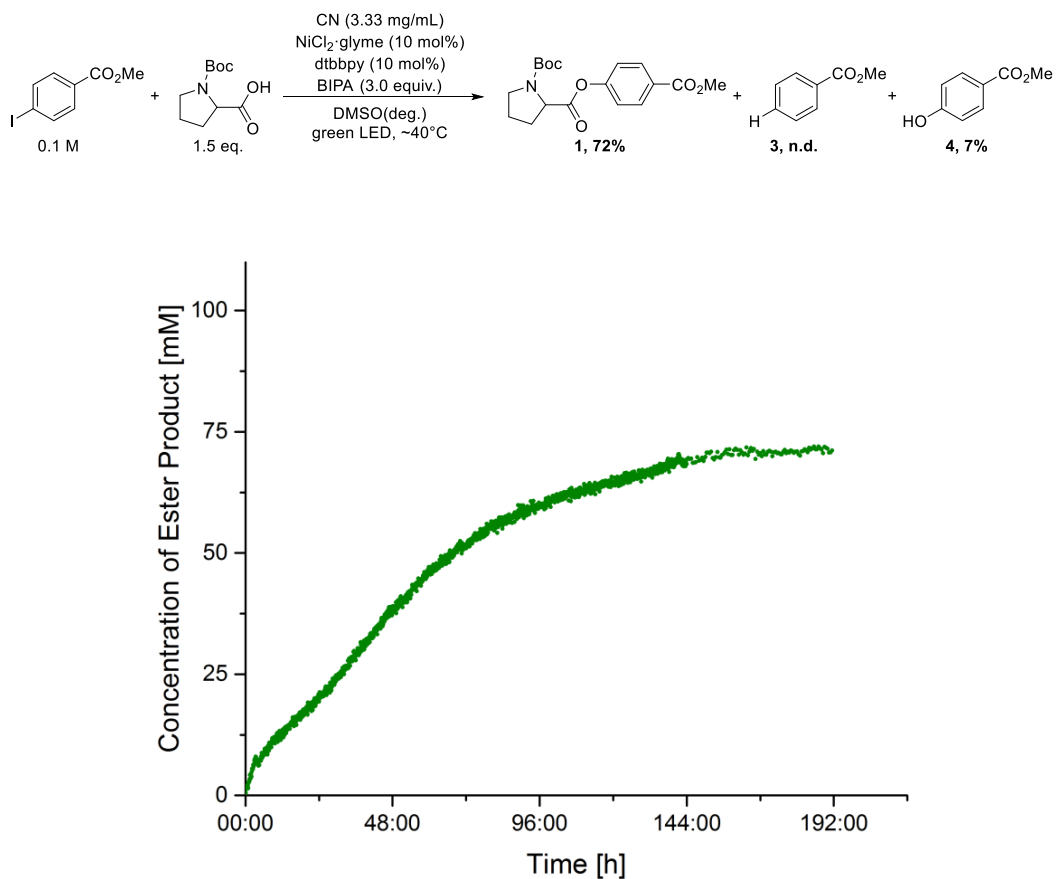


Figure 3.14. *In situ* FTIR reaction monitoring of the dual catalytic esterification using green LED irradiation.

3.4.7 Catalyst Recycling

Comparison of new and recovered CN-OA-m.

The catalyst from the large scale experiment (See section 3.4.6) was washed twice with DMSO (30 mL, followed by centrifugation at 3000 rpm for 20 min and separation of the liquid phase) and acetone (30 mL, followed by centrifugation at 3000 rpm for 20 min and separation of the liquid phase), dried overnight at 120°C and subjected to XRD, FTIR, UV-Vis, XPS as well as SEM and TEM analysis. For comparison, an unused sample of CN-OA-m from the same batch was also analyzed.

FTIR spectra were recorded on a Thermo Scientific Nicolet iD5 spectrometer. Diffuse reflectance UV/Vis spectra of powders were recorded on a Shimadzu UV-2600 spectrometer equipped with an integrating sphere. For XRD measurements, a Bruker D8 Advanced X-ray diffractometer with Cu K α radiation was used. Scanning electron microscopy (SEM) images were obtained on a LEO 1550-Gemini microscope. Energy-dispersive X-ray (EDX) investigations were conducted on a Link ISIS-300 system (Oxford Microanalysis Group) equipped with a Si(Li) detector and an energy resolution of 133 eV. Inductively coupled plasma - optical emission spectrometry (ICP-OES) was carried out using a Horiba Ultra 2 instrument equipped with photomultiplier tube detection. X-ray photoelectron spectroscopic (XPS) measurements were carried out with a *CISSY set-up*, equipped with a *SPECS XR 50* X-ray gun with Mg K α excitation radiation (1254.6 eV) and combined with a lens analyzer module (*CLAM*) under ultra-high vacuum (UHV, 1.5×10^{-8} Pa). The calibration was performed using the Au 4f $_{7/2}$ (84.0 eV) binding energy scale as reference. Quantitative analysis and deconvolution were achieved using “*peakfit*” and “*Igor*” software with *Lorentzian-Gaussian* functions and Shirley background deletion in photoemission spectra. The STEM images were acquired using a double-corrected Jeol ARM200F, equipped with a cold field emission gun. For the investigation, the acceleration voltage was set to 200kV, the emission was put to 5 μ A and a condenser aperture with a diameter of 20 μ m was used. With these settings, the microscope reaches a lattice resolution below 1Å. The STEM specimens were prepared by dissolving a powder sample of the material in ethanol, sonicating the solution for 15 minutes and finally dropping a few drops onto a copper TEM grid coated with holey carbon film. Once the solution had dried off, the specimens were investigated.

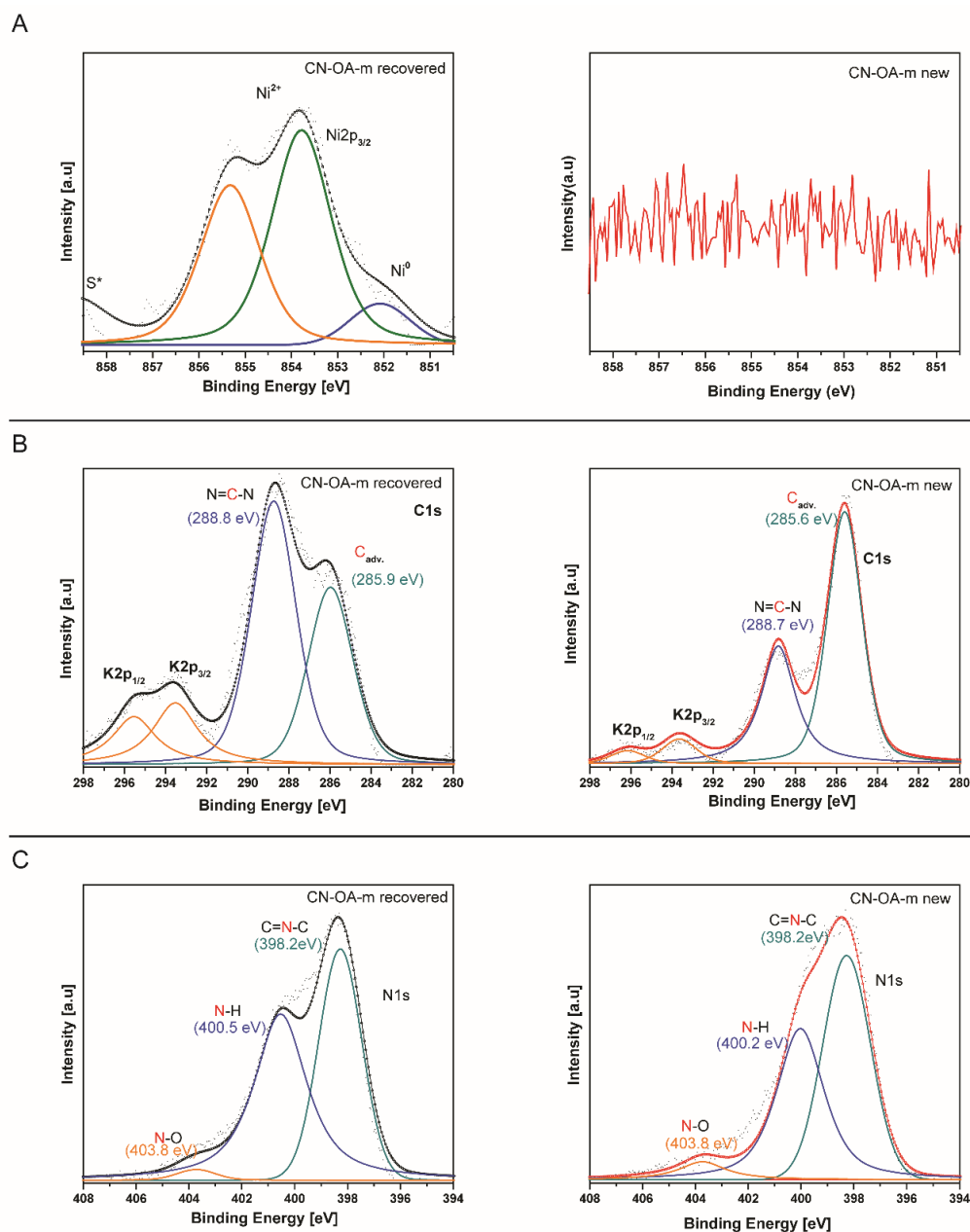


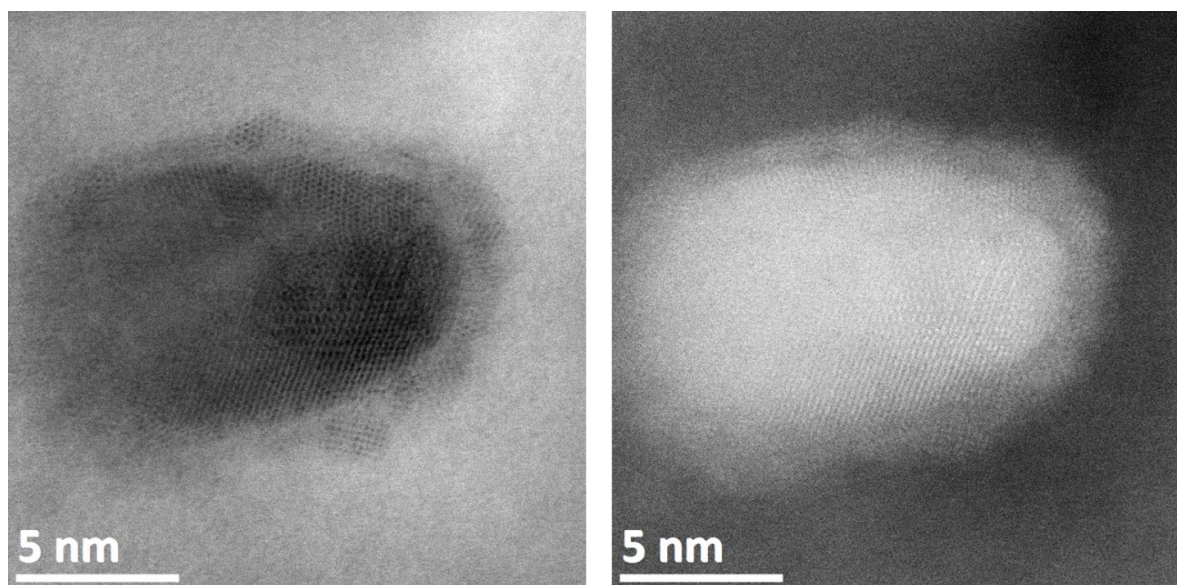
Figure 3.15: High-resolution XPS analysis spectra for core levels of: Ni 2p_{3/2} (A), C 1s (B) and N 1s (C), for recovered and new CN-OA-m. Each spectrum has been deconvoluted using Lorentzian-Gaussian peak fitting functions with Shirley background deletion. A, The high resolution XPS Ni 2p_{3/2} spectrum of the recovered CN-OA-m material shows two main deconvoluted peaks located at 853.7(±0.02) eV and 852.5(±0.02) eV, which can be assigned to the binding energy of Ni²⁺ and Ni⁰ species, respectively. B, The high resolution XPS C 1s spectrum of the used and recovered material shows typical CC and NC=N bonding with XPS shifts to higher binding energy, ascribed to Ni deposition in case of the recovered material. C, The N 1s spectra reveals three peaks assigned to sp²-hybridized N in the triazine system (C=N=C), amino groups (C-NH), and a weak N-O peak. A shift to high binding energy is present in the recovered material in case of the C-NH peak, presumably due to the presence of Ni.

Table 3.12. EDX elemental composition acquired from new and recovered CN-OA-m.

Sample	% w/w N	% w/w C	% w/w O	% w/w K	% w/w Ni
CN-OA-m new	45.91	38.47	5.64	9.51	0.03
CN-OA-m recovered	52.85	30.03	4.52	9.23	3.01

Table 3.13. XPS elemental composition acquired from new and recovered CN-OA-m.

Sample	% at N	% at C	% at K	% at Ni
CN-OA-m new	51.57	42.51	0.92	0
CN-OA-m recovered	59.49	37.73	2.45	0.56

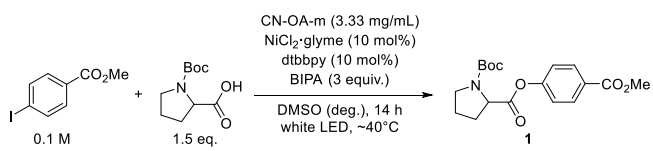
**Figure 3.16.** HAADF brightfield/darkfield image with higher resolution, showing the polycrystallinity/the shell-core structure of the particles.

High-angle annular dark-field (HAADF) images show round- to oval-shaped particles with sizes ranging from 5-15 nm. Especially the larger particles are usually polycrystalline and most particles feature a crystalline shell structure of lower density with about 1 nm thickness.

Recycling studies

An oven dried vial (19 x 100 mm) equipped with a stir bar was charged with the CN-material (10 mg), the carboxylic acid (0.45 mmol, 1.5 equiv.), the aryl halide (0.3 mmol, 1 equiv.), the Ni^{II} catalyst (30 μmol, 10 mol%), and the ligand (30 μmol, 10 mol%). Subsequently, the solvent (anhydrous, 3 mL) and the base (1-5 equiv) were added and the vial was sealed with a septum and Parafilm. The reaction mixture was sonicated for 5-10 min followed by stirring for 5 min until fine dispersion of the solids was achieved and the mixture was then degassed by bubbling Argon for 10 min. The mixture was irradiated in the photoreactor (white light) at 40 °C with rapid stirring (1400 rpm). After the respective reaction time, one equivalent of 1,3,5-trimethoxybenzene (0.3 mmol) was added and the mixture was stirred for 5 min. The reaction mixture was centrifuged at 3000 rpm for 20 min and the liquid phase was carefully separated and analyzed by ¹H-NMR. The solid was washed with DMSO (anhydrous, 6 mL, followed by centrifugation at 3000 rpm for 20 min and separation of the liquid phase), lyophilized (overnight) and reused in the next reaction.

Table 3.14. Reusability of CN-OA-m.^a



Cycle	1 [%] ^b
1	96
2	97
3	96
4	83
5	80
6 ^c	6

^aReaction conditions: methyl 4-iodobenzoate (0.3 mmol), *N*-Boc proline (0.45 mmol), NiCl₂·glyme (10 mol%), dtbbpy (10 mol%), BIPA (0.9 mmol), CN-OA-m (10 mg - reused), DMSO (anhydrous, 3 mL), white LEDs at 40 °C for 14h. ^bNMR yields determined by ¹H-NMR using 1,3,5-trimethoxybenzene as internal standard. ^cNo NiCl₂·glyme added.

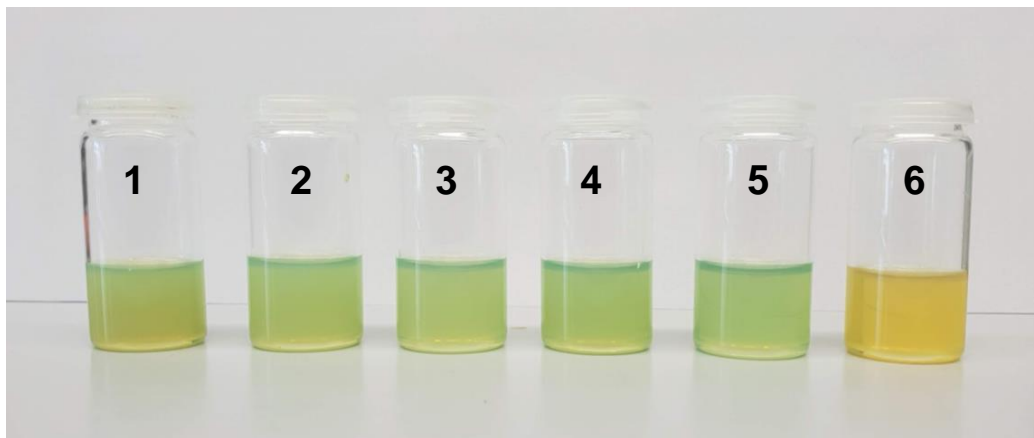


Figure 3.17. Reaction mixtures (see Table 3.14) after catalyst separation by centrifugation.

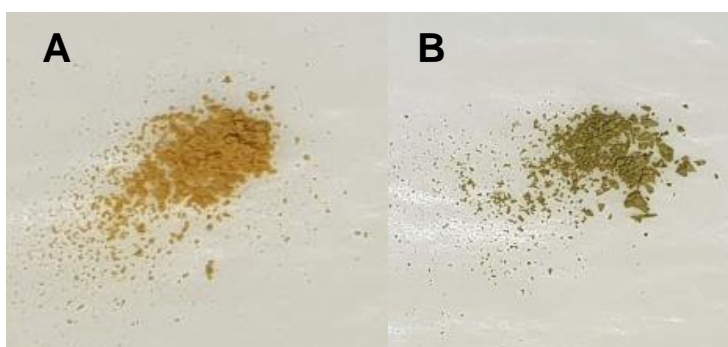
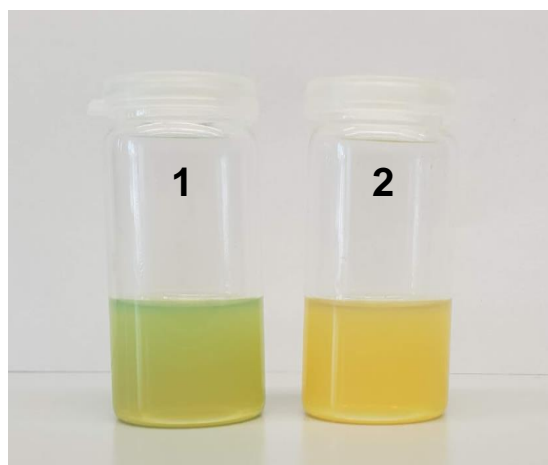


Figure 3.18. Fresh CN-OA-m (A) and CN-OA-m after five recycling experiments (B).

Table 3.15. Reusability of CN-OA-m without additional NiCl₂·glyme.^a

Cycle	1 [%] ^b
1	96
2 ^c	6

^aReaction conditions: methyl 4-iodobenzoate (0.3 mmol), *N*-Boc proline (0.45 mmol), NiCl₂·glyme (10 mol%), dtbbpy (10 mol%), BIPA (0.9 mmol), CN-OA-m (10 mg - reused), DMSO (anhydrous, 3 mL), white LEDs at 40 °C for 14h. ^bNMR yields determined by ¹H-NMR using 1,3,5-trimethoxybenzene as internal standard. ^cNo NiCl₂·glyme added.

**Figure 3.19.** Reaction mixtures (see Table 3.15) after catalyst separation by centrifugation.

3.4.8 Scope and Limitations

General procedure for the nickel/carbon nitride catalyzed esterification of aryl iodides.

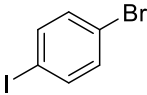
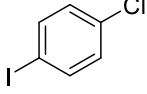
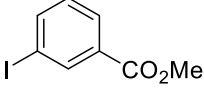
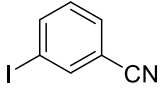
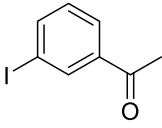
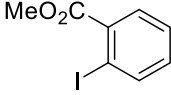
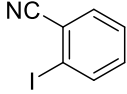
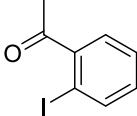
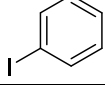
An oven dried vial (19 x 100 mm) equipped with a stir bar was charged with CN-OA-m (20 mg), the carboxylic acid (0.9 mmol, 1.5 equiv.), the aryl halide (0.6 mmol, 1 equiv.), NiCl₂·glyme (Method A, 13.2 mg, 60 μmol, 10 mol%) or Ni(OAc)₂·4 H₂O (Method B & C 14.9 mg, 60 μmol, 10 mol%), and 4,4'-di-tert-butyl-2,2'-dipyridyl (16.1 mg, 60 μmol, 10 mol%). Subsequently, DMSO (anhydrous, 6 mL) and *N*-tert-butylisopropylamine (BIPA, Method A: 285 μL, 1.8 mmol, 3 equiv.; Method B: 476 μL, 3 mmol, 5 equiv.) or *N,N*-diisopropylethylamine (DIPEA, Method C: 523 μL, 3 mmol, 5 equiv.) were added and the vial was sealed with a septum and Parafilm. The reaction mixture was sonicated for 5-10 min followed by stirring for 5 min until fine dispersion of the solids was achieved and the mixture was then degassed by bubbling Argon for 10 min. The mixture was irradiated in the photoreactor (white light) at 40 °C with rapid stirring (1400 rpm). After the respective reaction time, one equivalent of maleic acid (internal standard 69.6 mg, 0.6 mmol) was added and the mixture was stirred for 5 min. An aliquot of the reaction mixture (~200 μL) was filtered, diluted with DMSO-d₆ and subjected to ¹H-NMR analysis (See table S13 & S14). Thereafter, the NMR sample was combined with the reaction mixture, diluted with H₂O (40 mL) and extracted with dichloromethane (3 x 30 mL). The combined organic phases were washed with brine (50 mL), dried over Na₂SO₄ and concentrated. The product was purified by flash column chromatography (SiO₂, Hexane/EtOAc or dichloromethane/MeOH) on a Grace™ Reveleris™ system using a 12 g cartridge. In some cases we observed some mixed fractions containing small amounts of the phenol byproduct and the desired product. These could be easily purified by a basic extraction (DCM and 0.5 M NaOH) followed by drying over Na₂SO₄ and solvent evaporation to maximize the reaction yield. Alternatively, we also tried the basic extraction (using saturated K₂CO₃ or 0.5 M NaOH) before column chromatography but in most cases this resulted in poorly separated phases (emulsion) and was also less efficient in terms of phenol removal.

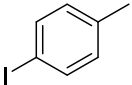
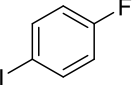
Table 3.16. Screening of reaction conditions for the aryl iodide substrate scope.^a

Method A: NiCl₂·glyme + 3 equiv. BIPA
 Method B: Ni(OAc)₂·4H₂O + 5 equiv. BIPA
 Method C: Ni(OAc)₂·4H₂O + 5 equiv. DIPEA

Aryl iodide	Method	Time [h]	Product [%] ^b	Substrate [%] ^b	Phenol [%] ^b	Dehalo [%] ^b	Acetate [%] ^b	Isolated [%]
	C	14	73	6	trace	10	6	72
	B	14	79	7	4	1	6	76
	A	14	96	--	4	trace	-- ^c	92
	C	14	70	13	4	12	8	n.d. ^d
	B	14	75	trace	8	1	15	71
	A	14	95	trace	4	1	--	90
	C	14	74	11	1	6	9	n.d.
	B	14	80	9	3	2	8	77
	A	14	97	--	2	trace	--	93
	C	14	55	30	trace	8	6	n.d.
	B	14	69	14	3	1	13	n.d.
	B	24	77	3	6	2	13	75
	A	24	96	--	2	trace	--	92
	C	14	25	53	1	14	13	n.d.
	B	14	64	18	2	2	12	n.d.
	B	24	83	--	3	2	12	80
	A	24	96	trace	2	2	--	91
	C	14	49	41	--	5	5	n.d.
	B	14	70	20	trace	trace	6	n.d.
	B	24	81	2	2	2	10	75
	A	24	97	--	trace	2	--	94
	C	14	C	58	23	--	8	n.d.
	B	14	B	71	12	2	1	64
	A	14	A	83	2	1	1	78

Chapter 3

Aryl iodide	Method	Time [h]	Product [%] ^b	Substrate [%] ^b	Phenol [%] ^b	Dehalo [%] ^b	Acetate [%] ^b	Isolated [%]
	C	14	11	83	trace	--	--	n.d.
	B	14	26	64	trace	--	4	n.d.
	B	72	66	12	3	--	9	62
	A	72	89	--	1	--	--	84
	C	14	12	80	--	3	1	n.d.
	B	14	25	72	trace	trace	5	n.d.
	B	72	49	41	1	4	9	n.d.
	B	168	64	--	6	5	15	57
	A	168	86	5	3	--	--	80
	A ^e	168	9	91	--	--	--	n.d.
	C	14	<10	73	--	--	--	n.d.
	B	14	33	58	--	4	--	n.d.
	B	72	64	12	trace	10	17	51
	A	72	92	--	trace	7	--	87
	C	14	10	70	--	29	trace	n.d.
	B	14	32	54	trace	4	6	n.d.
	B	72	61	15	4	10	11	56
	A	72	94	trace	--	--	--	90
	C	14	6	89	--	3	--	n.d.
	B	14	24	64	trace	3	--	n.d.
	B	72	56	19	1	6	--	49
	A	72	90	--	--	10	--	85
	B	14	trace	82	--	--	--	n.d.
	A	14	trace	87	--	--	--	n.d.
	B	14	13	70	--	--	--	n.d.
	B	72	17	35	--	--	--	n.d.
	A	14	29	65	--	--	--	n.d.
	B	14	--	83	--	--	--	n.d.
	A	14	--	82	--	--	--	n.d.
	B	14	15	58	--	--	--	n.d.
	A	14	13	87	--	--	--	n.d.

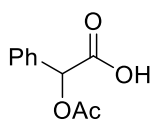
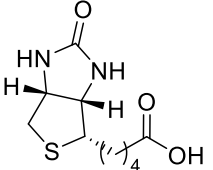
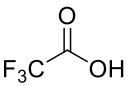
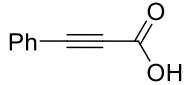
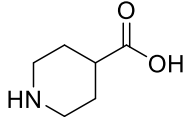
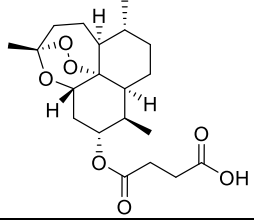
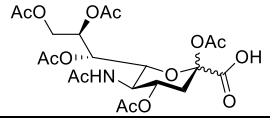
Aryl iodide	Method	Time [h]	Product [%] ^b	Substrate [%] ^b	Phenol [%] ^b	Dehalo [%] ^b	Acetate [%] ^b	Isolated [%]
	B	14	<5	90	--	--	--	n.d.
	A	14	5	89	--	--	--	n.d.
	B	14	trace	91	--	--	--	n.d.
	A	14	trace	93	--	--	--	n.d.

^aConditions: Reaction conditions as described in the general procedure (Section 3.4.8) ^bNMR yields determined by ¹H-NMR using 1,3,5-trimethoxybenzene as internal standard. ^cThe substance could be either not detected or not clearly assigned in the ¹H-NMR spectrum ^dNot determined. ^eNo CN-OA-m added.

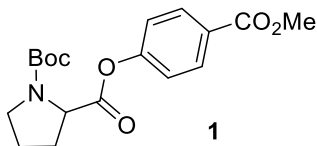
Table 3.17. Screening of reaction conditions for the carboxylic acid substrate scope.^a

Method A: NiCl₂·glyme + 3 equiv. BIPA
 Method B: Ni(OAc)₂·4H₂O + 5 equiv. BIPA

Carboxylic acid	Method	Time [h]	Product [%] ^b	Substrate [%] ^b	Phenol [%] ^b	Dehalo [%] ^b	Acetate [%] ^b	Isolated [%]
	B	14	59	23	7	trace	product	n.d. ^c
	B	24	88	5	5	trace	product	77
	A	24	95	--	4	trace	-- ^d	91
	B	14	47	31	--	--	--	n.d.
	B	24	64	15	--	--	--	59
	A	24	92	--	--	--	--	89
	B	14	62	--	6	trace	12	n.d.
	B	24	71	--	8	trace	14	68
	A	24	84	--	9	--	--	78
	B	14	--	17	6	trace	--	n.d.
	B	24	--	4	8	trace	--	72
	A	24	93	--	5	trace	0	90
	B	14	--	16	9	trace	--	n.d.
	B	24	--	--	10	trace	--	71
	A	24	93	--	6	trace	0	88
	B	14	42	41	3	2	3	n.d.
	B	24	61	24	4	3	5	n.d.
	B	24	86	--	5	3	6	78
	A	72	92	--	3	5	0	86
	B	14	48	14	20	trace	17	n.d.
	B	24	53	--	24	--	22	51
	A	24	87	--	12	trace	0	82
	B	14	60	28	--	trace	11	n.d.
	B	24	73	3	--	2	16	65
	A	24	94	--	1	--	0	88

Carboxylic acid	Method	Time [h]	Product [%] ^b	Substrate [%] ^b	Phenol [%] ^b	Dehalo [%] ^b	Acetate [%] ^b	Isolated [%]
	B	14	46	14	23	--	7	n.d.
	B	24	61	--	32	--	4	45
	A	24	71	--	21	--	--	65
	B	14	--	33	4	trace	--	n.d.
	B	24	--	12	6	trace	--	77
	A	24	96	trace	3	--	--	93
	B	14	17	50	21	--	--	n.d.
	B	14	14	59	10	--	--	n.d.
	B	14	--	85	13	--	--	n.d.
	B	14	--	76	19	--	--	n.d.
	B	14	--	100	--	--	--	n.d.

^aConditions: Reaction conditions as described in the general procedure (Section 3.4.8) ^bNMR yields determined by ¹H-NMR using 1,3,5-trimethoxybenzene as internal standard. ^cNot determined. ^dThe substance could be either not detected or not clearly assigned in the ¹H-NMR spectrum

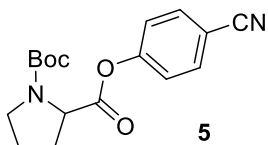


1-(*tert*-Butyl) 2-(4-(methoxycarbonyl)phenyl) pyrrolidine-1,2-dicarboxylate. From (*tert*-butoxycarbonyl)proline (193.7 mg, 0.9 mmol, 1.5 equiv) and methyl 4-iodobenzoate (157.2 mg, 0.6 mmol 1 equiv.). The title compound was isolated as a yellowish solid using an elution gradient of 0-10% of ethyl acetate in hexane.

Reaction time: 14 h

Method A: 192.6 mg, 92% Method B: 159.9 mg, 76% Method C: 150.7 mg, 72%

^1H NMR (400 MHz, CDCl_3) rotameric mixture, δ 8.07 (m, 2H), 7.19 (m, 2H), 4.52 (dd, $J = 8.6, 4.3$ Hz, 0.4H), 4.46 (dd, $J = 8.7, 4.3$ Hz, 0.6H), 3.91 (m, 3H), 3.69 – 3.40 (m, 2H), 2.47 – 2.28 (m, 1H), 2.16 (m, 1H), 2.10 – 1.86 (m, 2H), 1.46 (m, 9H). ^{13}C NMR (151 MHz, CDCl_3) rotameric mixture, resonances for minor rotamer are enclosed in parenthesis δ (171.10) 171.05, (166.30) 166.16, (154.42) 154.16, 153.60, 131.20 (131.07), 127.81 (127.65), (121.46) 121.09, 80.31 (80.09), 59.18 (59.07), 52.19 (52.13), (46.61) 46.42, 31.00 (29.94), 28.38, (24.52) 23.70. HRMS (ESI) m/z calcd for $\text{C}_{18}\text{H}_{23}\text{NNaO}_6$ $[(\text{M}+\text{Na})^+]$ 372.1417, found 372.1443.



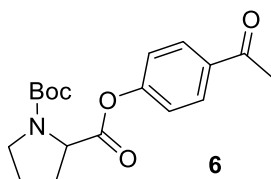
1-(*tert*-Butyl) 2-(4-cyanophenyl) pyrrolidine-1,2-dicarboxylate. From (*tert*-butoxycarbonyl)proline (193.7 mg, 0.9 mmol, 1.5 equiv) and 4-iodobenzonitrile (137.4 mg, 0.6 mmol 1 equiv.). The title compound was isolated as white solid using an elution gradient of 0-10% of ethyl acetate in hexane.

Reaction time: 14 h

Method A: 171.1 mg, 90% Method B: 135.5 mg, 71%

^1H NMR (600 MHz, CDCl_3) rotameric mixture, δ 7.67 (m, 2H), 7.27 – 7.21 (m, 2H, contains residual solvent signal of CDCl_3), 4.49 (dd, $J = 8.6, 4.6$ Hz, 0.5H), 4.44 (dd, $J = 8.7, 4.4$ Hz, 0.5H), 3.65 – 3.38 (m, 2H), 2.44 – 2.26 (m, 1H), 2.20 – 1.88 (m, 3H), 1.44 (m, 9H). ^{13}C NMR (151 MHz, CDCl_3) rotameric mixture, resonances for minor rotamer are enclosed in parenthesis δ (170.93) 170.78, (154.45) 154.08, 153.79 (153.48) 133.73 (133.59), (122.63)

122.23, (118.24) 118.06, (109.91) 109.71, 80.39 (80.24), 59.12 (59.04), (46.61) 46.43, (30.99) 29.92, 28.37, (24.58) 23.71. HRMS (ESI) m/z calcd for $C_{17}H_{22}N_2NaO_5$ [(M+Na)⁺] 339.1315, found 339.1301.

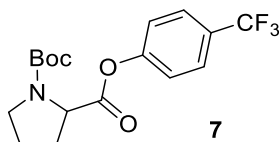


2-(4-Acetylphenyl) 1-(tert-butyl) pyrrolidine-1,2-dicarboxylate. From (*tert*-butoxycarbonyl)proline (193.7 mg, 0.9 mmol, 1.5 equiv) and 4'-iodoacetophenone (147.6 mg, 0.6 mmol 1 equiv.). The title compound was isolated as white solid using an elution gradient of 0-10% of ethyl acetate in hexane.

Reaction time: 14 h

Method A: 186.7 mg, 93% Method B: 154.3 mg, 77%

¹H NMR (600 MHz, CDCl₃) rotameric mixture δ 7.98 (m, 2H), 7.20 (m, 2H), 4.52 (dd, J = 8.6, 4.4 Hz, 0.4H), 4.45 (dd, J = 8.7, 4.4 Hz, 0.6H), 3.64 – 3.42 (m, 2H), 2.58 (m, 3H), 2.37 (m, 1H), 2.20 – 2.11 (m, 1H), 2.07 – 1.90 (m, 2H), 1.46 (m, 9H). ¹³C NMR (151 MHz, CDCl₃) rotameric mixture, resonances for minor rotamer are enclosed in parenthesis δ (196.86) 196.68, (171.13) 171.07, 154.51 (154.44), 154.22 (153.59), 134.81 (134.70), 129.98 (129.86), (121.64) 121.27, 80.33 (80.12), 59.18 (59.07), (46.61) 46.43, 31.01 (29.95), 28.39, 26.56, (24.53) 23.71. HRMS (ESI) m/z calcd for $C_{18}H_{23}NNaO_5$ [(M+Na)⁺] 356.1468, found 356.1458. These data are in full agreement with those previously published in the literature.²⁶



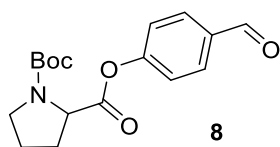
1-(tert-Butyl) 2-(4-(trifluoromethyl)phenyl) pyrrolidine-1,2-dicarboxylate. From (*tert*-butoxycarbonyl)proline (193.7 mg, 0.9 mmol, 1.5 equiv) and 1-iodo-4-(trifluoromethyl)benzene (163.2 mg, 0.6 mmol 1 equiv.). The title compound was isolated as yellowish oil using an elution gradient of 0-5% of ethyl acetate in hexane.

Reaction time: 24 h

Method A: 199.2 mg, 92% Method B: 161.2 mg, 75%

Chapter 3

^1H NMR (400 MHz, CDCl_3) rotameric mixture δ 7.63 (m, 2H), 7.26 – 7.18 (m, 2H, contains residual solvent signal of CDCl_3), 4.50 (dd, $J = 8.5, 4.4$ Hz, 0.4H), 4.44 (dd, $J = 8.7, 4.4$ Hz, 0.6H), 3.67 – 3.40 (m, 2H), 2.44 – 2.27 (m, 1H), 2.20 – 2.08 (m, 1H), 2.07 – 1.88 (m, 2H), 1.44 (m, 9H). ^{13}C NMR (101 MHz, CDCl_3) rotameric mixture, resonances for minor rotamer are enclosed in parenthesis δ (171.23) 171.12, (154.45) 153.58, (153.24) 152.98, 128.18 (d, $J = 32.6$ Hz) (128.02 (d, $J = 32.8$ Hz)), 126.86 (q, $J = 3.7$ Hz) (126.70 (q, $J = 3.8$ Hz)), (123.83 (d, $J = 271.9$ Hz)) 123.74 (d, $J = 272.1$ Hz), (121.98) 121.61, 80.34 (80.16), 59.11 (59.02), (46.61) 46.43, 31.00 (29.95), 28.37, (24.54) 23.71. ^{19}F NMR (564 MHz, CDCl_3) rotameric mixture δ -62.29, -62.34. HRMS (ESI) m/z calcd for $\text{C}_{17}\text{H}_{20}\text{F}_3\text{NNaO}_4$ [(M+Na) $^+$] 382.1236, found 382.1251.

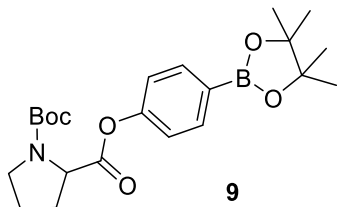


1-(*tert*-Butyl) 2-(4-formylphenyl) pyrrolidine-1,2-dicarboxylate. From (*tert*-butoxycarbonyl)proline (193.7 mg, 0.9 mmol, 1.5 equiv) and 4-iodobenzaldehyde (139.2 mg, 0.6 mmol 1 equiv.). The title compound was isolated as yellowish oil using an elution gradient of 0-10% of ethyl acetate in hexane.

Reaction time: 24 h

Method A: 173.4 mg, 91% Method B: 153.2 mg, 80%

^1H NMR (400 MHz, CDCl_3) rotameric mixture δ 9.97 (m, 1H), 7.90 (m, 2H), 7.41 – 7.20 (m, 2H, contains residual solvent signal of CDCl_3), 4.51 (dd, $J = 8.5, 4.4$ Hz, 0.4H), 4.45 (dd, $J = 8.7, 4.4$ Hz, 0.6H), 3.66 – 3.39 (m, 2H), 2.45 – 2.27 (m, 1H), 2.15 (m, 1H), 2.09 – 1.90 (m, 2H), 1.45 (m, 9H). ^{13}C NMR (101 MHz, CDCl_3) rotameric mixture, resonances for minor rotamer are enclosed in parenthesis δ (190.98) 190.80, (171.07) 170.98, (155.49) 155.18, (154.46) 153.57, 134.03 (133.95), 131.28 (131.17), (122.27) 121.89, 80.38 (80.19), 59.16 (59.06), (46.62) 46.44, 31.01 (29.95), 28.38, (24.56) 23.73. HRMS (ESI) m/z calcd for $\text{C}_{18}\text{H}_{21}\text{NNaO}_5$ [(M+Na) $^+$] 342.1312, found 342.1294.

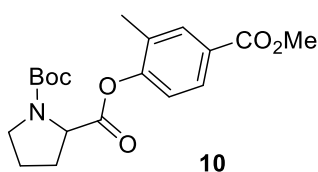


1-(*tert*-Butyl) 2-(4-(4,4,5,5-tetramethyl-1,3,2-dioxaborolan-2-yl)phenyl) pyrrolidine-1,2-dicarboxylate. From (*tert*-butoxycarbonyl)proline (193.7 mg, 0.9 mmol, 1.5 equiv) and 4-iodophenylboronic acid pinacol ester (198.0 mg, 0.6 mmol 1 equiv.). The title compound was isolated as white solid using an elution gradient of 0-5% of ethyl acetate in hexane. In order to avoid hydrolysis of the boronic acid no washing with a NaOH solution can be carried out and mixed fractions have to be discarded or further purified by a second column chromatography step.

Reaction time: 24 h

Method A: 234.9 mg, 94 % Method B: 188.3 mg, 75%

^1H NMR (600 MHz, CDCl_3) rotameric mixture δ 7.81 (m, 2H), 7.09 (m, 2H), 4.51 (dd, $J = 8.6, 4.2$ Hz, 0.4H), 4.43 (dd, $J = 8.7, 4.3$ Hz, 0.6H), 3.66 – 3.37 (m, 2H), 2.42 – 2.26 (m, 1H), 2.20 – 2.12 (m, 1H), 2.03 (m, 1H), 1.93 (m, 1H), 1.45 (m, 9H), 1.32 (m, 12H). ^{13}C NMR (151 MHz, CDCl_3) rotameric mixture, resonances for minor rotamer are enclosed in parenthesis δ 171.29, (154.42) 153.71, (153.29) 153.06, 136.19 (136.08), 126.61 (brs), (120.80) 120.44, 83.89 (83.82), 80.22 (79.95), 59.20 (59.07), (46.60) 46.42, 30.99 (29.97), (28.39) 28.36, 24.83, (24.46) 23.69. HRMS (ESI) m/z calcd for $\text{C}_{22}\text{H}_{32}\text{BNNaO}_6$ [(M+Na) $^+$] 440.2215, found 440.224.



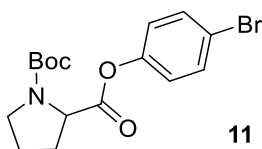
1-(*tert*-Butyl) 2-(4-(methoxycarbonyl)-2-methylphenyl) pyrrolidine-1,2-dicarboxylate. From (*tert*-butoxycarbonyl)proline (193.7 mg, 0.9 mmol, 1.5 equiv) and methyl 4-iodo-3-methylbenzoate (165.6 mg, 0.6 mmol 1 equiv.). The title compound was isolated as colorless oil using an elution gradient of 0-10% of ethyl acetate in hexane.

Reaction time: 14 h

Method A: 170.2 mg, 78% Method B: 138.5 mg, 64%

Chapter 3

^1H NMR (600 MHz, CDCl_3) rotameric mixture δ 7.97 – 7.84 (m, 2H), 7.09 (m, 1H), 4.56 (dd, $J = 8.6, 4.1$ Hz, 0.5H), 4.52 (dd, $J = 8.8, 3.8$ Hz, 0.5H), 3.89 (m, 3H), 3.65 – 3.42 (m, 2H), 2.45 – 2.30 (m, 1H), 2.26 – 2.14 (m, 4H), 2.11 – 1.92 (m, 2H), 1.46 (m, 9H). ^{13}C NMR (151 MHz, CDCl_3) rotameric mixture, resonances for minor rotamer are enclosed in parenthesis δ (170.90) 170.66, (166.50) 166.36, (154.38) 153.67, 152.98 (152.74), 132.73 (132.60), (130.64) 130.18, 128.60 (128.50), 127.88 (127.78), (121.95) 121.51, 80.36 (80.04), 59.05 (58.98), 52.14 (52.08), (46.58) 46.40, 31.13 (30.08), 28.40, (24.53) 23.59, 16.21 (16.14). HRMS (ESI) m/z calcd for $\text{C}_{19}\text{H}_{25}\text{NNaO}_6$ $[(\text{M}+\text{Na})^+]$ 386.1574, found 386.1565.

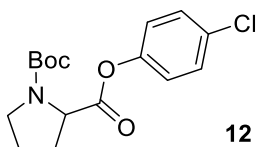


2-(4-Bromophenyl) 1-(*tert*-butyl) pyrrolidine-1,2-dicarboxylate. From (*tert*-butoxycarbonyl)proline (193.7 mg, 0.9 mmol, 1.5 equiv) and 1-bromo-4-iodobenzene (169.7 mg, 0.6 mmol 1 equiv.). The title compound was isolated as yellowish oil using an elution gradient of 0-5% of ethyl acetate in hexane.

Reaction time: 72 h

Method A: 185.8 mg, 84% Method B: 137.3 mg, 62%

^1H NMR (600 MHz, CDCl_3) rotameric mixture δ 7.51 – 7.44 (m, 2H), 6.99 (m, 2H), 4.49 (dd, $J = 8.6, 4.4$ Hz, 0.4H), 4.42 (dd, $J = 8.7, 4.3$ Hz, 0.6H), 3.64 – 3.38 (m, 2H), 2.34 (m, 1H), 2.18 – 1.89 (m, 3H), 1.45 (m, 9H). ^{13}C NMR (151 MHz, CDCl_3) rotameric mixture, resonances for minor rotamer are enclosed in parenthesis δ (171.34) 171.26, (154.42) 153.61, (149.80) 149.57, 132.51 (132.35), (123.26) 122.86, 118.95 (118.83), 80.26 (80.06), 59.12 (59.01), (46.60) 46.41, 31.00 (29.94), 28.39, (24.51) 23.69. HRMS (ESI) m/z calcd for $\text{C}_{16}\text{H}_{20}\text{BrNNaO}_4$ $[(\text{M}+\text{Na})^+]$ 392.0468, found 392.0452.



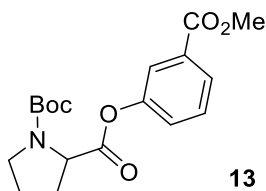
1-(*tert*-butyl) 2-(4-chlorophenyl) pyrrolidine-1,2-dicarboxylate. From (*tert*-butoxycarbonyl)proline (193.7 mg, 0.9 mmol, 1.5 equiv) and 1-chloro-4-iodobenzene (143.1

mg, 0.6 mmol 1 equiv.). The title compound was isolated as yellowish oil using an elution gradient of 0-5% of ethyl acetate in hexane.

Reaction time: 168 h

Method A: 156.0 mg, 80% Method B: 111.2 mg, 57%

^1H NMR (400 MHz CDCl_3) rotameric mixture δ 7.41 – 7.31 (m, 2H), 7.12 – 7.02 (m, 2H), 4.52 (dd, $J = 8.6, 4.3$ Hz, 0.4H), 4.46 (dd, $J = 8.7, 4.4$ Hz, 0.6H), 3.84 – 3.34 (m, 2H), 2.48 – 2.28 (m, 1H), 2.24 – 2.09 (m, 1H), 2.10 – 1.90 (m, 2H), 1.48 (m, 9H). ^{13}C NMR (101 MHz, CDCl_3) rotameric mixture, resonances for minor rotamer are enclosed in parenthesis δ (171.50) 171.42, (154.47) 153.67, (149.24) 149.02, 131.32 (131.15), 129.58 (129.42), (122.88) 122.50, 80.31 (80.12), 59.13 (59.03), (46.64) 46.45, 31.05 (30.00), 28.43, (24.56) 23.74. HRMS (ESI) m/z calcd for $\text{C}_{16}\text{H}_{20}\text{ClNNaO}_4$ [(M+Na) $^+$] 348.0973, found 348.0952.

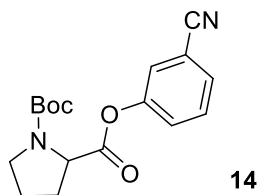


1-(*tert*-Butyl) 2-(3-(methoxycarbonyl)phenyl) pyrrolidine-1,2-dicarboxylate. From (*tert*-butoxycarbonyl)proline (193.7 mg, 0.9 mmol, 1.5 equiv) and methyl 3-iodobenzoate (157.2 mg, 0.6 mmol 1 equiv.). The title compound was isolated as yellowish oil using an elution gradient of 0-10% of ethyl acetate in hexane.

Reaction time: 72 h

Method A: 182.1 mg, 87% Method B: 107.1 mg, 51%

^1H NMR (600 MHz, CDCl_3) rotameric mixture δ 7.90 (m, 1H), 7.75 (m, 1H), 7.44 (m, 1H), 7.35 – 7.27 (m, 1H), 4.52 (dd, $J = 8.6, 4.3$ Hz, 0.4H), 4.45 (dd, $J = 8.7, 4.3$ Hz, 0.6H), 3.90 (m, 3H), 3.64 – 3.41 (m, 2H), 2.36 (m, 1H), 2.17 (m, 1H), 2.10 – 1.90 (m, 2H), 1.46 (m, 9H). ^{13}C NMR (151 MHz, CDCl_3) rotameric mixture, resonances for minor rotamer are enclosed in parenthesis δ 171.41 (171.40), (166.15) 166.00, (154.44) 153.66, (150.68) 150.50, 131.73 (131.55), 129.50 (129.35), 127.06 (126.99), (126.28) 125.74, (122.62) 122.43, 80.34 (80.06), 59.12 (59.02), 52.31 (52.23), (46.60) 46.44, 31.01 (29.96), 28.38, (24.50) 23.70. HRMS (ESI) m/z calcd for $\text{C}_{18}\text{H}_{23}\text{NNaO}_6$ [(M+Na) $^+$] 372.1417, found 372.1407.

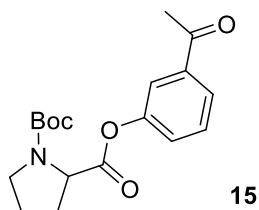


1-(*tert*-Butyl) 2-(3-cyanophenyl) pyrrolidine-1,2-dicarboxylate. From (*tert*-butoxycarbonyl)proline (193.7 mg, 0.9 mmol, 1.5 equiv) and 3-iodobenzonitrile (137.4 mg, 0.6 mmol 1 equiv.). The title compound was isolated as yellowish oil using an elution gradient of 0-10% of ethyl acetate in hexane.

Reaction time: 72 h

Method A: 169.8 mg, 90% Method B: 107.1 mg, 56%

^1H NMR (600 MHz, CDCl_3) rotameric mixture δ 7.57 – 7.30 (m, 4H), 4.49 (dd, $J = 8.6, 4.6$ Hz, 0.5H), 4.44 (dd, $J = 8.8, 4.4$ Hz, 0.5H), 3.64 – 3.40 (m, 2H), 2.37 (m, 1H), 2.18 – 1.89 (m, 3H), 1.45 (m, 9H). ^{13}C NMR (151 MHz, CDCl_3) rotameric mixture, resonances for minor rotamer are enclosed in parenthesis δ (171.15) 171.01, (154.46) 153.51, (150.89) 150.66, 130.47 (130.30), 129.65 (129.53), (126.54) 126.06, (125.24) 124.87, (117.80) 117.68, (113.59) 113.37, 80.41 (80.25), (59.05) 58.99, (46.62) 46.43, 31.00 (29.93), 28.40 (28.38), 24.58 (23.70). HRMS (ESI) m/z calcd for for $\text{C}_{17}\text{H}_{22}\text{N}_2\text{NaO}_5$ [(M+Na) $^+$] 339.1315, found 339.1300



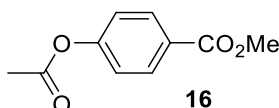
2-(3-Acetylphenyl) 1-(*tert*-butyl) pyrrolidine-1,2-dicarboxylate. From (*tert*-butoxycarbonyl)proline (193.7 mg, 0.9 mmol, 1.5 equiv) and 3-iodoacetophenone (147.6 mg, 0.6 mmol 1 equiv.). The title compound was isolated as yellowish oil using an elution gradient of 0-10% of ethyl acetate in hexane.

Reaction time: 72 h

Method A: 170.0 mg, 85% Method B: 98.5 mg, 49%

^1H NMR (400 MHz CDCl_3) rotameric mixture δ 7.84 – 7.76 (m, 1H), 7.68 – 7.63 (m, 1H), 7.46 (m, 1H), 7.36 – 7.26 (m, 1H), 4.51 (dd, $J = 8.6, 4.4$ Hz, 0.4H), 4.45 (dd, $J = 8.7, 4.3$ Hz, 0.6H), 3.65 – 3.39 (m, 2H), 2.58 (m, 3H), 2.46 – 2.28 (m, 1H), 2.23 – 1.88 (m, 3H), 1.46 (m,

9H). ^{13}C NMR (101 MHz, CDCl_3) rotameric mixture, resonances for minor rotamer are enclosed in parenthesis δ (197.09) 196.83, (171.52) 171.48, (154.46) 153.64, (150.94) 150.77, 138.53 (138.39), 129.75 (129.60), (126.45) 125.96, 125.95 (125.72), (121.30) 120.90, 80.33 (80.10), 59.10 (59.03), (46.62) 46.44, 31.02 (29.97), 28.39, (26.71) 26.69, (24.54) 23.72. HRMS (ESI) m/z calcd for $\text{C}_{18}\text{H}_{23}\text{NNaO}_5$ $[(\text{M}+\text{Na})^+]$ 356.1468, found 356.1458.

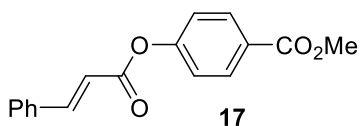


Methyl 4-acetoxybenzoate. From acetic acid (54.0 mg, 0.9 mmol, 1.5 equiv) and methyl 4-iodobenzoate (157.2 mg, 0.6 mmol 1 equiv.). The title compound was isolated as a white solid using an elution gradient of 0-5% of ethyl acetate in hexane.

Reaction time: 24 h

Method A: 105.7 mg, 91% Method B: 89.4 mg, 77%

^1H NMR (400 MHz, CDCl_3) δ 8.05 (d, $J = 8.8$ Hz, 2H), 7.15 (d, $J = 8.9$ Hz, 2H), 3.89 (s, 3H), 2.30 (s, 3H). ^{13}C NMR (101 MHz, CDCl_3) δ 168.83, 166.26, 154.23, 131.13, 127.67, 121.56, 52.18, 21.14. HRMS (ESI) m/z calcd for $\text{C}_{10}\text{H}_{11}\text{O}_4$ $[(\text{M}+\text{H})^+]$ 195.0652, found 195.0632. These data are in full agreement with those previously published in the literature.²⁶

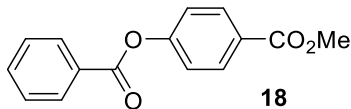


Methyl 4-(cinnamoyloxy)benzoate. From *trans*-cinnamic acid (133.3 mg, 0.9 mmol, 1.5 equiv) and methyl 4-iodobenzoate (157.2 mg, 0.6 mmol 1 equiv.). The title compound was isolated as a white solid using an elution gradient of 0-5% of ethyl acetate in hexane.

Reaction time: 24 h

Method A: 151.0 mg, 89% Method B: 100.3 mg, 59%

^1H NMR (400 MHz, CDCl_3) δ 8.14 – 8.04 (m, 2H), 7.87 (d, $J = 16.0$ Hz, 1H), 7.63 – 7.55 (m, 2H), 7.46 – 7.39 (m, 3H), 7.27 – 7.21 (m, 2H, contains residual solvent signal of CDCl_3), 6.61 (d, $J = 16.0$ Hz, 1H), 3.91 (s, 3H). ^{13}C NMR (101 MHz, CDCl_3) δ 166.33, 164.78, 154.43, 147.22, 133.95, 131.15, 130.89, 129.02, 128.35, 127.59, 121.62, 116.75, 52.19. HRMS (ESI) m/z calcd for $\text{C}_{17}\text{H}_{15}\text{O}_4$ $[(\text{M}+\text{H})^+]$ 283.0951, found 283.0965.

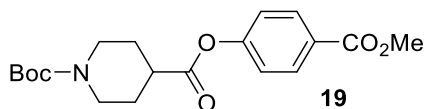


Methyl 4-(benzoyloxy)benzoate. From benzoic acid (109.9 mg, 0.9 mmol, 1.5 equiv) and methyl 4-iodobenzoate (157.2 mg, 0.6 mmol 1 equiv.). The title compound was isolated as a white solid using an elution gradient of 0-5% of ethyl acetate in hexane.

Reaction time: 24 h

Method A: 119.7 mg, 78 % Method B: 104.1 mg, 68%

^1H NMR (400 MHz, CDCl_3) δ 8.22 – 8.16 (m, 2H), 8.13 – 8.10 (m, 2H), 7.67 – 7.60 (m, 1H), 7.55 – 7.47 (m, 2H), 7.29 (d, $J = 9.0$ Hz, 2H), 3.92 (s, 3H). ^{13}C NMR (101 MHz, CDCl_3) δ 166.31, 164.61, 154.57, 133.86, 131.20, 130.21, 129.05, 128.64, 127.74, 121.74, 52.21. HRMS (ESI) m/z calcd for $\text{C}_{15}\text{H}_{13}\text{O}_4$ $[(\text{M}+\text{H})^+]$ 257.0809, found 257.0797. These data are in full agreement with those previously published in the literature.²⁶

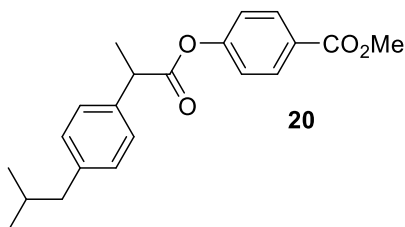


1-(tert-Butyl) 4-(4-(methoxycarbonyl)phenyl) piperidine-1,4-dicarboxylate. From 1-Boc-piperidine-4-carboxylic acid (206.4 mg, 0.9 mmol, 1.5 equiv) and methyl 4-iodobenzoate (157.2 mg, 0.6 mmol 1 equiv.). The title compound was isolated as a white solid using an elution gradient of 0-20% of ethyl acetate in hexane.

Reaction time: 24 h

Method A: 197.0 mg, 90% Method B: 156.5 mg, 72%

^1H NMR (600 MHz, CDCl_3) δ 8.05 (d, $J = 8.7$ Hz, 2H), 7.13 (d, $J = 8.7$ Hz, 2H), 4.08 (brs, 2H), 3.90 (s, 3H), 2.91 (m, 2H), 2.71 (tt, $J = 11.0, 3.9$ Hz, 1H), 2.02 (m, 2H), 1.76 (dtd, $J = 13.4, 11.2, 4.0$ Hz, 2H), 1.46 (s, 9H). ^{13}C NMR (151 MHz, CDCl_3) δ 172.48, 166.21, 154.62, 154.23, 131.15, 127.75, 121.42, 79.73, 52.17, 42.88 (brs), 41.24, 28.40, 27.86. HRMS (ESI) m/z calcd for $\text{C}_{19}\text{H}_{25}\text{NNaO}_6$ $[(\text{M}+\text{Na})^+]$ 386.1574, found 386.1590.

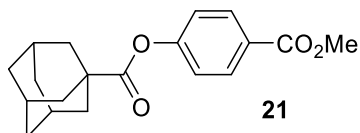


Methyl 4-((2-(4-isobutylphenyl)propanoyl)oxy)benzoate. From ibuprofen (185.7 mg, 0.9 mmol, 1.5 equiv) and methyl 4-iodobenzoate (157.2 mg, 0.6 mmol 1 equiv.). The title compound was isolated as yellowish solid using an elution gradient of 0-5% of ethyl acetate in hexane.

Reaction time: 24 h

Method A: 180.3 mg, 88% Method B: 144.4 mg, 71%

^1H NMR (600 MHz, CDCl_3) δ 8.02 (d, $J = 8.7$ Hz, 2H), 7.28 (d, $J = 8.1$ Hz, 2H), 7.14 (d, $J = 7.9$ Hz, 2H), 7.07 (d, $J = 8.7$ Hz, 2H), 3.94 (q, $J = 7.2$ Hz, 1H), 3.89 (s, 3H), 2.47 (d, $J = 7.2$ Hz, 2H), 1.86 (dp, $J = 13.6, 6.8$ Hz, 1H), 1.60 (d, $J = 7.1$ Hz, 3H), 0.90 (d, $J = 6.6$ Hz, 6H). ^{13}C NMR (151 MHz, CDCl_3) δ 172.64, 166.27, 154.50, 140.96, 136.86, 131.02, 129.55, 127.58, 127.16, 121.42, 52.13, 45.28, 45.02, 30.16, 22.36, 18.42. HRMS (ESI) m/z calcd for $\text{C}_{21}\text{H}_{25}\text{O}_4$ [(M+H) $^+$] 341.1748, found 341.1735.

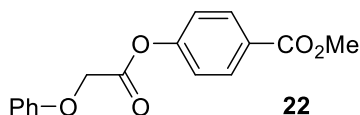


4-(Methoxycarbonyl)phenyl (1S,3s)-adamantane-1-carboxylate. From 1-adamantanecarboxylic acid (162.2 mg, 0.9 mmol, 1.5 equiv) and methyl 4-iodobenzoate (157.2 mg, 0.6 mmol 1 equiv.). The title compound was isolated as a white solid using an elution gradient of 0-5% of ethyl acetate in hexane.

Reaction time: 72 h

Method A: 162.0 mg, 86% Method B: 147.0 mg, 78%

^1H NMR (600 MHz, CDCl_3) δ 8.04 (d, $J = 8.7$ Hz, 2H), 7.11 (d, $J = 8.7$ Hz, 2H), 3.90 (s, 3H), 2.08 (s, 3H), 2.04 (m, 6H), 1.80 – 1.73 (m, 6H). ^{13}C NMR (151 MHz, CDCl_3) δ 175.58, 166.35, 154.85, 131.04, 127.38, 121.58, 52.12, 41.12, 38.67, 36.38, 27.83. HRMS (ESI) m/z calcd for $\text{C}_{19}\text{H}_{23}\text{O}_4$ [(M+H) $^+$] 315.1584, found 315.1584. These data are in full agreement with those previously published in the literature.²⁶

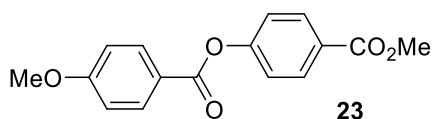


Methyl 4-(2-phenoxyacetoxy)benzoate. From 2-phenoxyacetic acid (136.9 mg, 0.9 mmol, 1.5 equiv) and methyl 4-iodobenzoate (157.2 mg, 0.6 mmol 1 equiv.). The title compound was isolated as a white solid using an elution gradient of 0-5% of ethyl acetate in hexane (Method A) or isocratic DCM (Method B) as the product precipitated and clogged the column at higher yields.

Reaction time: 24 h

Method A: 140.6 mg, 82% Method B: 88.1 mg, 51%

^1H NMR (400 MHz, CDCl_3) δ 8.08 (d, $J = 8.8$ Hz, 2H), 7.34 (dd, $J = 8.8, 7.4$ Hz, 2H), 7.20 (d, $J = 8.8$ Hz, 2H), 7.04 (t, $J = 7.4$ Hz, 1H), 6.99 (dd, $J = 8.8, 1.0$ Hz, 2H), 4.90 (s, 2H), 3.92 (s, 3H). ^{13}C NMR (101 MHz, CDCl_3) δ 167.03, 166.13, 157.57, 153.59, 131.26, 129.70, 128.12, 122.14, 121.31, 114.72, 65.36, 52.26. HRMS (ESI) m/z calcd for $\text{C}_{16}\text{H}_{15}\text{O}_5$ $[(\text{M}+\text{H})^+]$ 287.0914, found 287.0920.

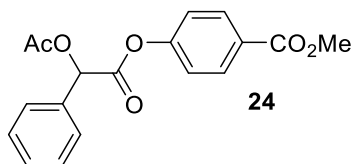


4-(Methoxycarbonyl)phenyl 4-methoxybenzoate. From 4-methoxybenzoic acid (136.9 mg, 0.9 mmol, 1.5 equiv) and methyl 4-iodobenzoate (157.2 mg, 0.6 mmol 1 equiv.). For determining NMR yields, 3mL of DCM were added to the reaction mixture to dissolve precipitated product. In addition to the general workup procedure a basic washing step (0.5 M NaOH) was carried out before washing with brine in order to remove excess 4-methoxybenzoic acid. The title compound was isolated as a white solid using an elution gradient of 0-5% of ethyl acetate in hexane.

Reaction time: 24 h

Method A: 150.8 mg, 88% Method B: 112.4 mg, 65%

^1H NMR (600 MHz, CDCl_3) δ 8.14 (d, $J = 8.9$ Hz, 2H), 8.10 (d, $J = 8.7$ Hz, 2H), 7.28 (d, $J = 8.7$ Hz, 2H), 6.98 (d, $J = 8.8$ Hz, 2H), 3.92 (s, 3H), 3.89 (s, 3H). ^{13}C NMR (151 MHz, CDCl_3) δ 166.36, 164.30, 164.09, 154.74, 132.36, 131.14, 127.55, 121.79, 121.33, 113.91, 55.52, 52.16. HRMS (ESI) m/z calcd for $\text{C}_{16}\text{H}_{15}\text{O}_5$ $[(\text{M}+\text{H})^+]$ 287.0914, found 287.0916.

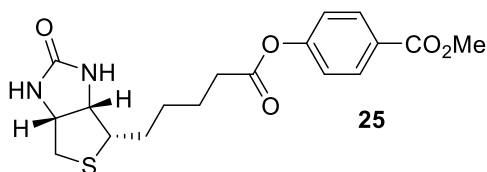


Methyl 4-(2-acetoxy-2-phenylacetoxy)benzoate. From 2-acetoxy-2-phenylacetic acid (174.8 mg, 0.9 mmol, 1.5 equiv) and methyl 4-iodobenzoate (157.2 mg, 0.6 mmol 1 equiv.). The title compound was isolated as a white solid using an elution gradient of 0-5% of ethyl acetate in hexane.

Reaction time: 24 h

Method A: 128.1 mg, 65% Method B: 87.6 mg, 45%

^1H NMR (600 MHz, CDCl_3) δ 8.02 (d, $J = 8.7$ Hz, 2H), 7.57 (dd, $J = 7.5, 2.2$ Hz, 2H), 7.47 – 7.41 (m, 3H), 7.08 (d, $J = 8.7$ Hz, 2H), 6.09 (s, 1H), 3.89 (s, 3H), 2.23 (s, 3H). ^{13}C NMR (151 MHz, CDCl_3) δ 170.45, 166.99, 166.13, 153.76, 132.87, 131.13, 129.65, 129.02, 128.08, 127.72, 121.24, 74.55, 52.19, 20.62. HRMS (ESI) m/z calcd for $\text{C}_{18}\text{H}_{16}\text{NaO}_6$ [(M+Na) $^+$] 351.0839, found 351.0843.



Methyl 4-((5-(2-oxohexahydro-1H-thieno[3,4-d]imidazol-4-yl)pentanoyl)oxy)benzoate. From biotin (219.9 mg, 0.9 mmol, 1.5 equiv) and methyl 4-iodobenzoate (157.2 mg, 0.6 mmol 1 equiv.). The title compound was isolated as a yellowish solid using an elution gradient of 0-10% of methanol in dichloromethane.

Reaction time: 24 h

Method A: 210.8 mg, 93% Method B: 174.1 mg, 77%

^1H NMR (600 MHz, Chloroform- d) δ 8.05 (d, $J = 8.7$ Hz, 2H), 7.15 (d, $J = 8.7$ Hz, 2H), 5.93 (brs, 1H, disappears upon addition of D_2O), 5.32 (brs, 0.7H, disappears upon addition of D_2O), 4.49 (dd, $J = 7.7, 4.9$ Hz, 1H), 4.31 (dd, $J = 7.7, 4.6$ Hz, 1H), 3.89 (s, 3H), 3.17 (m, 1H), 2.90 (m, 1H), 2.72 (m, 1H), 2.59 (m, 2H), 1.86 – 1.64 (m, 4H), 1.52 (m, 2H). ^{13}C NMR (151 MHz, CDCl_3) δ 171.56, 166.26, 163.85 (brs), 154.27, 131.12, 127.65, 121.58, 61.99, 60.12, 55.49, 52.19, 40.56, 33.97, 28.34, 28.27, 24.66. HRMS (ESI) m/z calcd for $\text{C}_{18}\text{H}_{23}\text{N}_2\text{O}_5\text{S}$ [(M+H) $^+$] 379.1322, found 379.1314.

Copies of NMR spectra of isolated compounds

Copies of NMR spectra of isolated compounds are available in the Supporting Information through the website of the Publisher. DOI: <https://doi.org/10.1002/anie.201902785>

3.5 References

- (1) Crabtree, R. H. *The organometallic chemistry of the transition metals*, 5th ed.; Wiley: Hoboken, 2009.
- (2) Johansson Seechurn, C. C. C.; Kitching, M. O.; Colacot, T. J.; Snieckus, V. Palladium-Catalyzed Cross-Coupling: A Historical Contextual Perspective to the 2010 Nobel Prize. *Angew. Chem. Int. Ed.* **2012**, *51*, 5062-5085.
- (3) Hartwig, J. F. Carbon–heteroatom bond formation catalysed by organometallic complexes. *Nature* **2008**, *455*, 314-322.
- (4) Tasker, S. Z.; Standley, E. A.; Jamison, T. F. Recent advances in homogeneous nickel catalysis. *Nature* **2014**, *509*, 299-309.
- (5) Rosen, B. M.; Quasdorf, K. W.; Wilson, D. A.; Zhang, N.; Resmerita, A.-M.; Garg, N. K.; Percec, V. Nickel-Catalyzed Cross-Couplings Involving Carbon–Oxygen Bonds. *Chem. Rev.* **2011**, *111*, 1346-1416.
- (6) Ananikov, V. P. Nickel: The “Spirited Horse” of Transition Metal Catalysis. *ACS Catal.* **2015**, *5*, 1964-1971.
- (7) Twilton, J.; Le, C.; Zhang, P.; Shaw, M. H.; Evans, R. W.; MacMillan, D. W. C. The merger of transition metal and photocatalysis. *Nat. Rev. Chem.* **2017**, *1*, 0052.
- (8) Milligan, J. A.; Phelan, J. P.; Badir, S. O.; Molander, G. A. Alkyl Carbon–Carbon Bond Formation by Nickel/Photoredox Cross-Coupling. *Angew. Chem. Int. Ed.* **2019**, *58*, 6152-6163.
- (9) Wenger, O. S. Photoactive Complexes with Earth-Abundant Metals. *J. Am. Chem. Soc.* **2018**, *140*, 13522-13533.
- (10) Romero, N. A.; Nicewicz, D. A. Organic Photoredox Catalysis. *Chem. Rev.* **2016**, *116*, 10075-10166.
- (11) Lévêque, C.; Cheneberg, L.; Corcé, V.; Ollivier, C.; Fensterbank, L. Organic photoredox catalysis for the oxidation of silicates: applications in radical synthesis and dual catalysis. *Chem. Commun.* **2016**, *52*, 9877-9880.
- (12) Du, Y.; Pearson, R. M.; Lim, C.-H.; Sartor, S. M.; Ryan, M. D.; Yang, H.; Damrauer, N. H.; Miyake, G. M. Strongly Reducing, Visible-Light Organic Photoredox Catalysts as Sustainable Alternatives to Precious Metals. *Chem. Eur. J.* **2017**, *23*, 10962-10968.
- (13) Fischer, C.; Sparr, C. Direct Transformation of Esters into Heterocyclic Fluorophores. *Angew. Chem. Int. Ed.* **2018**, *57*, 2436-2440.

Chapter 3

- (14) Friedmann, D.; Hakki, A.; Kim, H.; Choi, W.; Bahnemann, D. Heterogeneous photocatalytic organic synthesis: state-of-the-art and future perspectives. *Green Chem.* **2016**, *18*, 5391-5411.
- (15) Lang, X.; Chen, X.; Zhao, J. Heterogeneous visible light photocatalysis for selective organic transformations. *Chem. Soc. Rev.* **2014**, *43*, 473-486.
- (16) Chen, J.; Cen, J.; Xu, X.; Li, X. The application of heterogeneous visible light photocatalysts in organic synthesis. *Catal. Sci. Technol.* **2016**, *6*, 349-362.
- (17) Ong, W.-J.; Tan, L.-L.; Ng, Y. H.; Yong, S.-T.; Chai, S.-P. Graphitic Carbon Nitride (g-C₃N₄)-Based Photocatalysts for Artificial Photosynthesis and Environmental Remediation: Are We a Step Closer To Achieving Sustainability? *Chem. Rev.* **2016**, *116*, 7159-7329.
- (18) Savateev, A.; Ghosh, I.; König, B.; Antonietti, M. Photoredox Catalytic Organic Transformations using Heterogeneous Carbon Nitrides. *Angew. Chem. Int. Ed.* **2018**, *57*, 15936-15947.
- (19) Goettmann, F.; Fischer, A.; Antonietti, M.; Thomas, A. Chemical Synthesis of Mesoporous Carbon Nitrides Using Hard Templates and Their Use as a Metal-Free Catalyst for Friedel–Crafts Reaction of Benzene. *Angew. Chem. Int. Ed.* **2006**, *45*, 4467-4471.
- (20) Shalom, M.; Guttentag, M.; Fettkenhauer, C.; Inal, S.; Neher, D.; Llobet, A.; Antonietti, M. In Situ Formation of Heterojunctions in Modified Graphitic Carbon Nitride: Synthesis and Noble Metal Free Photocatalysis. *Chem. Mater.* **2014**, *26*, 5812-5818.
- (21) Zhang, J.; Sun, J.; Maeda, K.; Domen, K.; Liu, P.; Antonietti, M.; Fu, X.; Wang, X. Sulfur-mediated synthesis of carbon nitride: Band-gap engineering and improved functions for photocatalysis. *Energy Environ. Sci.* **2011**, *4*, 675-678.
- (22) Savateev, A.; Pronkin, S.; Epping, J. D.; Willinger, M. G.; Wolff, C.; Neher, D.; Antonietti, M.; Dontsova, D. Potassium Poly(heptazine imides) from Aminotetrazoles: Shifting Band Gaps of Carbon Nitride-like Materials for More Efficient Solar Hydrogen and Oxygen Evolution. *ChemCatChem* **2017**, *9*, 167-174.
- (23) Zhang, G.; Li, G.; Lan, Z.-A.; Lin, L.; Savateev, A.; Heil, T.; Zafeiratos, S.; Wang, X.; Antonietti, M. Optimizing Optical Absorption, Exciton Dissociation, and Charge Transfer of a Polymeric Carbon Nitride with Ultrahigh Solar Hydrogen Production Activity. *Angew. Chem. Int. Ed.* **2017**, *56*, 13445-13449.
- (24) See the Supporting Information (section 3.4) for details.

- (25) Zuo, Z.; Ahneman, D. T.; Chu, L.; Terrett, J. A.; Doyle, A. G.; MacMillan, D. W. C. Merging photoredox with nickel catalysis: Coupling of α -carboxyl sp^3 -carbons with aryl halides. *Science* **2014**, *345*, 437-440.
- (26) Welin, E. R.; Le, C.; Arias-Rotondo, D. M.; McCusker, J. K.; MacMillan, D. W. C. Photosensitized, energy transfer-mediated organometallic catalysis through electronically excited nickel(II). *Science* **2017**, *355*, 380-385.
- (27) Terrett, J. A.; Cuthbertson, J. D.; Shurtleff, V. W.; MacMillan, D. W. C. Switching on elusive organometallic mechanisms with photoredox catalysis. *Nature* **2015**, *524*, 330-334.
- (28) Yang, L.; Huang, Z.; Li, G.; Zhang, W.; Cao, R.; Wang, C.; Xiao, J.; Xue, D. Synthesis of Phenols: Organophotoredox/Nickel Dual Catalytic Hydroxylation of Aryl Halides with Water. *Angew. Chem. Int. Ed.* **2018**, *57*, 1968-1972.
- (29) Cámpora, J.; Matas, I.; Maya, C. M.; Palma, P.; Álvarez, E. Self-Addition of Metallacyclic Nickel Enolate Complexes Stabilized by Monodentate Phosphine Ligands. *Organometallics* **2006**, *25*, 3124-3129.
- (30) Pieber, B.; Shalom, M.; Antonietti, M.; Seeberger, P. H.; Gilmore, K. Continuous Heterogeneous Photocatalysis in Serial Micro-Batch Reactors. *Angew. Chem. Int. Ed.* **2018**, *57*, 9976-9979.
- (31) Yang, H. B.; Hung, S.-F.; Liu, S.; Yuan, K.; Miao, S.; Zhang, L.; Huang, X.; Wang, H.-Y.; Cai, W.; Chen, R.; Gao, J.; Yang, X.; Chen, W.; Huang, Y.; Chen, H. M.; Li, C. M.; Zhang, T.; Liu, B. Atomically dispersed Ni(i) as the active site for electrochemical CO₂ reduction. *Nat. Energy* **2018**, *3*, 140-147.
- (32) Feldmeier, C.; Bartling, H.; Riedle, E.; Gschwind, R. M. LED based NMR illumination device for mechanistic studies on photochemical reactions – Versatile and simple, yet surprisingly powerful. *J. Magn. Res.* **2013**, *232*, 39-44.
- (33) Malig, T. C.; Koenig, J. D. B.; Situ, H.; Chehal, N. K.; Hultin, P. G.; Hein, J. E. Real-time HPLC-MS reaction progress monitoring using an automated analytical platform. *React. Chem. Eng.* **2017**, *2*, 309-314.
- (34) Sheng, F.; Chow, P. S.; Yu, Z. Q.; Tan, R. B. H. Online Classification of Mixed Co-Crystal and Solute Suspensions using Raman Spectroscopy. *Org. Process Res. Dev.* **2016**, *20*, 1068-1074.

Chapter 3

(35) Yu, P.; Morandi, B. Nickel-Catalyzed Cyanation of Aryl Chlorides and Triflates Using Butyronitrile: Merging Retro-hydrocyanation with Cross-Coupling. *Angew. Chem. Int. Ed.* **2017**, *56*, 15693-15697.

(36) Wang, J.; Zhao, J.; Gong, H. Nickel-catalyzed methylation of aryl halides/tosylates with methyl tosylate. *Chem. Commun.* **2017**, *53*, 10180-10183.

(37) Mori, A.; Mizusaki, T.; Ikawa, T.; Maegawa, T.; Monguchi, Y.; Sajiki, H. Mechanistic Study of a Pd/C-Catalyzed Reduction of Aryl Sulfonates Using the Mg–MeOH–NH₄OAc System. *Chem. Eur. J.* **2007**, *13*, 1432-1441.

(38) <https://www.sigmaaldrich.com> (Germany, January 2019).

(39) Brown, H. C.; Kanth, J. V. B.; Dalvi, P. V.; Zaidlewicz, M. Molecular Addition Compounds. 15. Synthesis, Hydroboration, and Reduction Studies of New, Highly Reactive tert-Butyldialkylamine–Borane Adducts. *J. Org. Chem.* **1999**, *64*, 6263-6274.

(40) https://www.bauhaus.info/led-baender/tween-light-led-band/p/22517610?gclid=EAIAIQobChMIoLWto9zl3wIVTZSyCh3YDweqEAQYASABEgJmRfD_BwE&s_kwid=AL!5677!3!190027496787!!!g!462716337331!&pla_prpaid=462716337331&ef_id=EAIAIQobChMIoLWto9zl3wIVTZSyCh3YDweqEAQYASABEgJmRfD_BwE:G:s&pla_adgrid=41635814775&pla_campid=225980581&pla_prch=online&pla_prid=22517610&cid=PSEGoo225980581_41635814775&pla_adt=pla (Germany, January 2019).

(41) https://www.osa-opto.com/module_prodcuts.html (Germany, January 2019).

Chapter 4

Overcoming Limitations in Dual Photoredox/Nickel catalyzed C–N Cross-Couplings due to Catalyst Deactivation

Gisbertz, S.; Reischauer, S.; Pieber, B.

Nat. Catal. **2020**, 4, 456-475.

DOI: <https://doi.org/10.1038/s41929-020-0473-6>

Abstract

Dual photoredox/nickel catalyzed C–N cross-couplings suffer from low yields for electron-rich aryl halides. The formation of catalytically inactive nickel-black is responsible for this limitation and causes severe reproducibility issues. We demonstrate that catalyst deactivation can be avoided by using a carbon nitride photocatalyst. The broad absorption of the heterogeneous photocatalyst enables a wavelength dependent control of the rate of reductive elimination to prevent nickel-black formation during the coupling of cyclic, secondary amines and aryl halides. A second approach, that is applicable to a broader set of electron-rich aryl halides, is to run the reactions at high concentrations to increase the rate of oxidative addition. Less nucleophilic, primary amines can be coupled with electron-rich aryl halides by stabilizing low-valent nickel intermediates with a suitable additive. The developed protocols enable reproducible, selective C–N cross-couplings of electron-rich aryl bromides and can be also applied for electron-poor aryl chlorides.

Specific contribution

Dr. B. Pieber and I conceived the research study.

Dr. B. Pieber and I designed all experiments.

I performed all synthetic experiment.

S. Reischauer and I carried out characterizations of materials and studies on the Ni-black formation.

I organized the data and wrote the manuscript with contributions from S. Reischauer.

Dr. B. Pieber revised and corrected the manuscript and directed the research study.

4.1 Introduction

The palladium-catalyzed formation of carbon–nitrogen bonds (Buchwald-Hartwig) ranks among the most widely applied reactions in synthetic chemistry.¹ Nickel is an attractive alternative to palladium due to its higher abundance, but the requirement of air-sensitive Ni⁰ complexes, sophisticated ligands, as well as strong reductants, and bases for C–N bond formations have hampered its use.²⁻⁴ Air-stable nickel pre-catalysts have been developed, but still strong alkoxide bases and complex ligands are needed (Figure 4.1, a).⁵⁻⁹ In combination with electrochemistry, ligated Ni^{II} salts catalyze the C–N cross-coupling under mild conditions (Figure 4.1, b).¹⁰⁻¹¹ Ligand-free Ni^{II} salts were used together with UV light (365 nm),¹² or visible light photocatalysis *via* photoredox (PRC),¹³⁻¹⁷ or energy transfer (EnT)¹⁸⁻¹⁹ processes (Figure 4.1, c). Although synthetically attractive, electro- and photochemically mediated, nickel-catalyzed C–N couplings are limited to electron-poor aryl halides. Aryl halides that do not contain electron withdrawing groups are usually either unreactive,¹⁵ or give low yields,^{11-12, 16-17, 19} and only a few examples with a good isolated yield are reported (for a detailed analysis, see the Supplementary Information).¹³

Electro- and photochemically mediated methods rely on the initial reduction of the Ni^{II} catalyst to a low valent (Ni⁰ or Ni^I) species, followed by oxidative addition that is slow for electron-rich aryl halides.^{11, 20} This bottleneck potentially leads to the accumulation of nickel(0) species that aggregate, resulting in catalyst deactivation. In the electrochemically driven, nickel-catalyzed aryl amination, nickel-black deposition was observed on the cathode and could be avoided by using Ni(bpy)₃Br₂ (bpy = 2,2' bipyridine) instead of a 1:1 mixture of NiBr₂·glyme and dtbbpy (4,4'-di-tert-butyl-2,2'-bipyridine), thereby expanding the scope to a few electron-rich heteroaryl halides.¹¹ Stabilizing bipyridine ligands are unsuitable for light-mediated, nickel-catalyzed C–N cross-couplings,¹²⁻¹⁷ but catalyst deactivation or nickel-black formation was not reported. It is, however, well known that Ni^{II} salts – in presence of amines as sacrificial electron donors (SED) – can be used intentionally for the photochemical preparation of Ni⁰ nanoparticles (Figure 4.1, d).²¹⁻²³

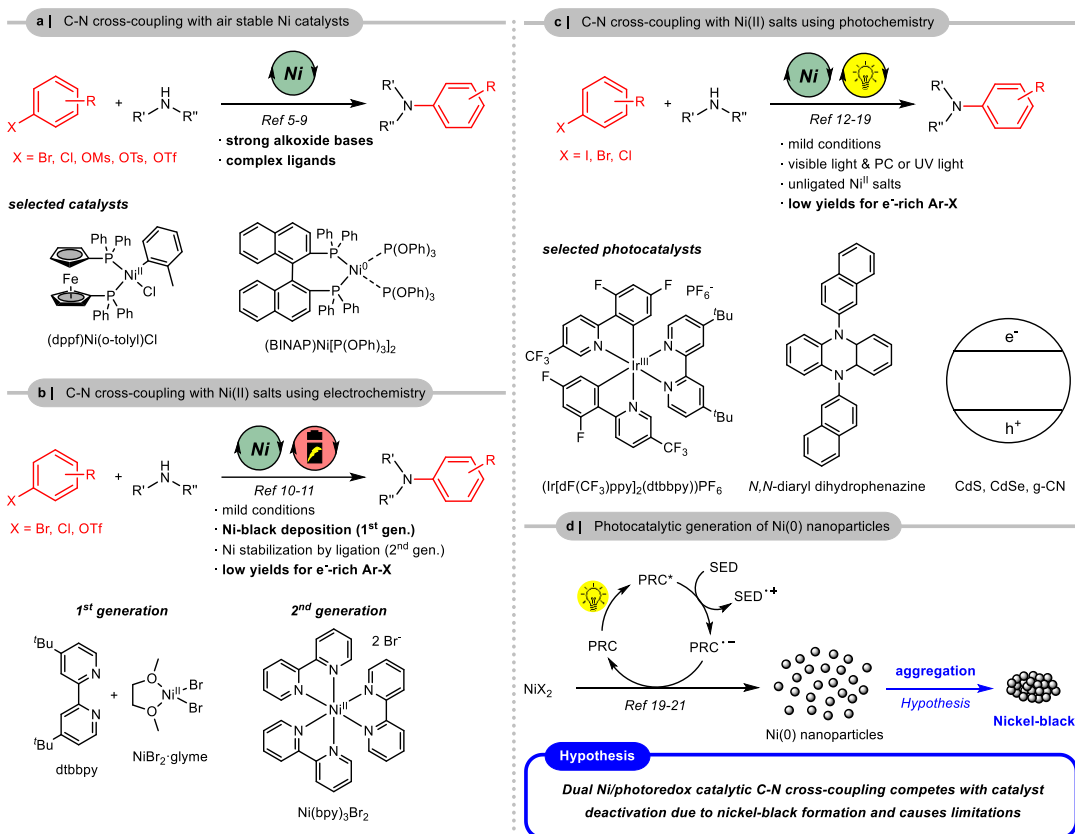
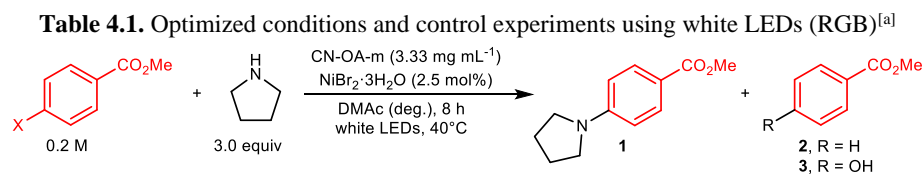


Figure 4.1. Nickel catalyzed C–N cross-coupling reactions. **a**, air stable Ni precatalysts require strong bases and sophisticated ligands. **b**, electrochemically enabled, Ni-catalyzed aminations and; **c**, photochemically driven, Ni-catalyzed aminations are limited to electron-poor aryl halides. **d**, photocatalytic reduction of Ni^{II} salts is used for nanoparticle formation potentially leads to nickel-black formation in catalysis.

Here, we show that catalyst deactivation *via* nickel-black formation is responsible for the low yields when electron-rich aryl bromides are used in dual photoredox/nickel catalyzed C–N cross-couplings. Deposition of the catalytically inactive, low-valent nickel species further deactivates a heterogeneous photocatalyst, hampering its recyclability. We demonstrate that nickel-black formation can be avoided by i) decelerating the light-mediated reductive elimination, ii) enhancing the oxidative addition or, iii) stabilizing low-valent nickel intermediates. The resulting protocols enable selective and reproducible couplings of amines with electron-poor, -neutral, and -rich aryl halides, and allow for recycling of the heterogeneous photocatalyst.

4.2 Results and discussion

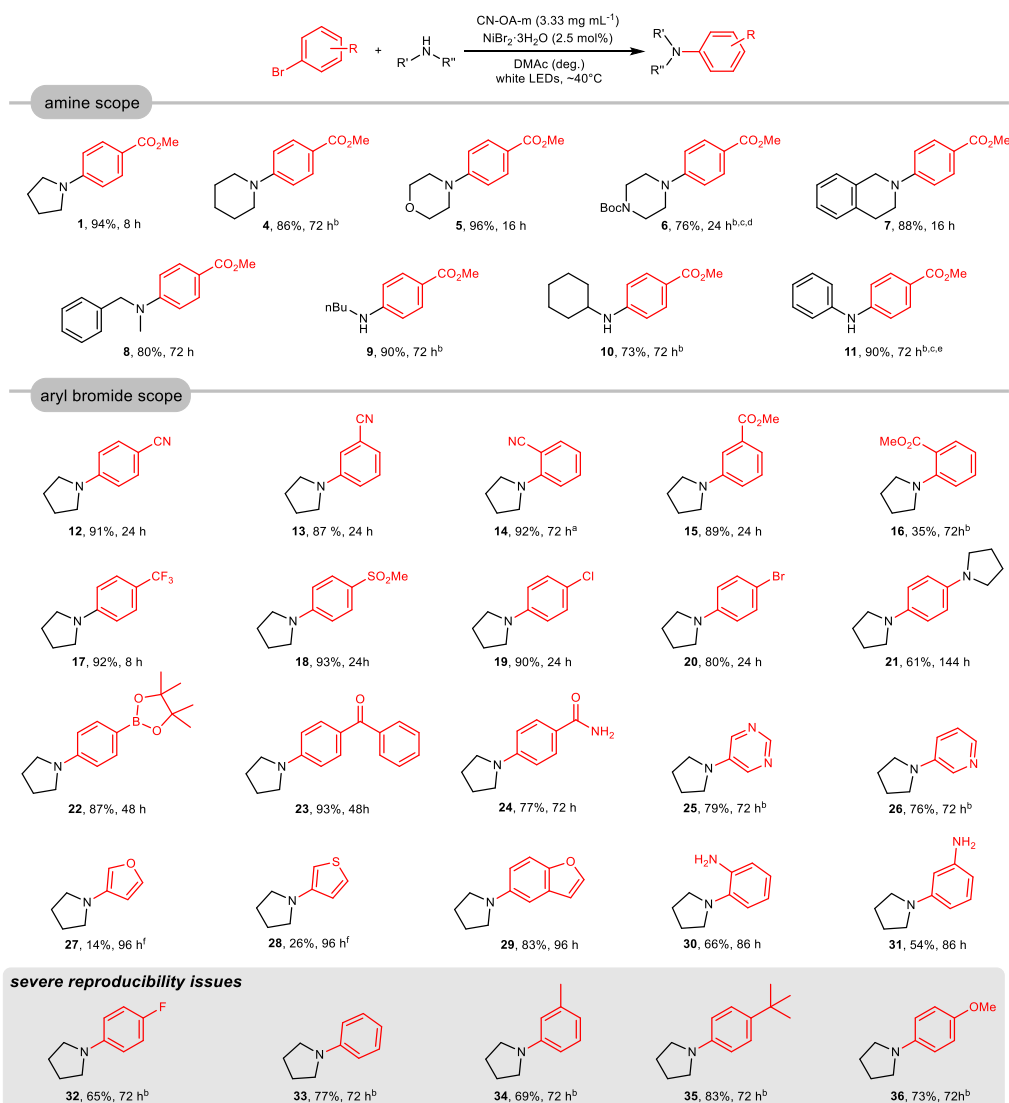
Our investigations started by optimizing the dual nickel/photoredox catalyzed amination of methyl 4-bromobenzoate with pyrrolidine using the carbon nitride CN-OA-m as photocatalyst (Table 4.1). This heterogeneous material has a broader optical absorption in the visible region compared to most other known CN materials and can be easily prepared on gram scale *via* co-condensation of urea and oxamide followed by post-calcination in a molten salt (see Supplementary Information).²⁴⁻²⁶ Nearly quantitative formation of the desired alkyl aryl amine (**1**) was obtained within 8 h when CN-OA-m (3.33 mg mL⁻¹), NiBr₂·3H₂O (2.5 mol%) and three equivalents of the amine were used without any additional base in dimethylacetamide (DMAc) as solvent (Table 4.1, Entry 1-2).²⁷ The reaction was easily scaled up by increasing the reaction time, affording **1** on a gram scale within 14 hours (see Supplementary Information).²⁸



Entry	X	Conditions	Conversion [%] ^b	1 [%] ^c	2 [%] ^c	3 [%] ^c
1	Br	as shown	quant.	98	2	n.d.
2	Br	1.66 mg mL ⁻¹ CN-OA-m	quant.	96	2	1
3	I	as shown	quant.	99	1	n.d.
4	Cl	168 h	76	72	4	n.d.
5	OTf	72 h	75	67	5	2
6	Br	no CN-OA-m	5	n.d.	2	1
7	Br	no NiBr ₂ ·3H ₂ O	5	n.d.	n.d.	n.d.
8	Br	no light	<1	n.d.	n.d.	n.d.
9	Br	no degassing	10	10	n.d.	n.d.

^aReaction conditions: methyl 4-bromobenzoate (1.2 mmol), pyrrolidine (3.6 mmol), NiBr₂·3H₂O (2.5 mol%), CN-OA-m (20 mg), DMAc (anhydrous, 6 mL), white LEDs (RGB) at 40 °C for 8 h. ^bConversion aryl halide determined by ¹H-NMR using 1,3,5-trimethoxybenzene as internal standard. ^cNMR yields were determined by ¹H-NMR using 1,3,5-trimethoxybenzene as internal standard. n.d. = not detected. dtbbpy = 4,4'-di-*tert*-butyl-2,2'-bipyridine.

Aside from aryl bromides, aryl iodides coupled with similar efficiency and selectivity (Entry 3). The optimized protocol further enabled C–N couplings using aryl chlorides and aryl triflates, but these reactions did not go to completion (Entry 4-5). Control studies in the absence of CN-OA-m, NiBr₂·3H₂O and light did not result in the formation of the desired product, and the presence of oxygen significantly decreased the reaction rate (Entry 6-9). With the optimized conditions in hand, the versatility of the semi-heterogeneous catalytic system was evaluated (Table 4.2). The reaction of methyl 4-bromobenzoate with cyclic secondary amines generally gave high yields for the corresponding aryl amines (**1**, **4-7**). A secondary amine with low steric hindrance also resulted in the desired aryl amine (**8**), but the majority of acyclic secondary amines did not react under these conditions (see Supplementary Information). Aliphatic and aromatic primary amines reacted efficiently (**9-11**). Aryl halides containing electron-withdrawing groups coupled with high selectivity; nitriles (**12-14**), carbonyl groups (**1**, **15**, **23-24**), trifluoromethyl- (**15**) as well as methylsulfonyl-groups (**16**), halides (**17-18**), boronic acid pinacol esters (**22**), and electron-poor heteroaromatic bromides (**25**, **26**) were tolerated in the dual catalytic amination. 1,4-Dibromobenzene can undergo selective mono- (**20**) or di-amination (**21**) by varying the reaction time and stoichiometry of the amine coupling partner. Similar to related C–O bond formations,²⁴⁻²⁵ a carbonyl-group in the 2-position only gave moderate yield (**16**). Low reactivity was observed for electron-rich heterocycles (**27**, **28**). Notably, good isolated yields were obtained for the C–N coupling of pyrrolidine with a range of electron-rich aryl bromides (**29-36**).²⁹ However, in the case of 1-bromo-4-fluorobenzene (**32**),³⁰ bromobenzene (**33**), 3-bromotoluene (**34**), 1-bromo-4-*tert*-butylbenzene (**35**), and 4-bromoanisole (**36**) these values are not representative, as these substrates suffered from severe reproducibility issues. These reactions frequently resulted in low yields and the heterogeneous PRC became black, whereas almost no color change was observed in case of aryl halides that do not suffer from these reproducibility issues. High amounts of deposited nickel were detected on the recovered, black carbon nitride material by ICP-OES analysis, indicating nickel-black formation (see Supplementary Information).

Table 4.2. Scope of the semi-heterogeneous amination of amines and aryl bromides.^[a]

Deactivation of metal catalysts *via* deposition is a common problem in palladium catalysis (Pd-black formation) and can be addressed by avoiding high concentrations of Pd⁰ species that agglomerate.³¹ In light-mediated, nickel catalyzed C–N cross-couplings, a Ni⁰ complex was proposed to be the catalytically active species that is initially formed *via* a photoredox-catalyzed hydrogen atom transfer (HAT).²⁰ We assumed that, in the case of electron-rich aryl halides, slow oxidative addition results in the accumulation of unstabilized Ni⁰ that aggregate. Since the heterogeneous photocatalyst absorbs only weakly above 450 nm,²⁵ we assumed that the formation of nickel-black can be decelerated using higher wavelengths. As anticipated, when a mixture of pyrrolidine and CN-OA-m in DMAc was irradiated with green light (520 nm), nickel black formation was significantly slower than with blue light (450 nm, see Supplementary Information). To our delight, the coupling of pyrrolidine and 1-bromo-4-fluorobenzene was highly selective and reproducible using 520 nm LEDs (Method B), and the desired compound (**32**) was obtained in 85-91% in six parallel experiments (Figure 4.2, a). The same set of experiments using blue LEDs (~450 nm, Method A) exhibited large variations in yield. While five experiments gave 60-70% of **32**, only 5-6% of the desired amine were formed for two reactions where the reaction mixture turned black. Careful analysis of the heterogeneous material recovered from the low yielding reactions identified the nature and quantity of the deposited Ni species (see Supplementary Information). ICP-OES analysis showed a Ni concentration of 126 mg g⁻¹ for the reaction irradiated with blue light and only 36 mg g⁻¹ for the material after an experiment using green LEDs. Elemental analysis *via* energy-dispersive X-ray spectroscopy (EDX) is in agreement with these results. X-ray powder diffraction (XRD) confirmed the deposition of low valent nickel species, with a significantly higher concentration on the material irradiated with blue light. High resolution X-ray photoelectron spectroscopy (XPS) for core levels of Ni2p_{3/2} spectrum of the recovered CN-OA-m from experiments using 450 nm LEDs (Method A) showed two main deconvoluted peaks located at 853.7 (±0.02) eV and 852.5 (±0.02) eV that can be assigned to the binding energy of Ni^{II} and Ni⁰ species.

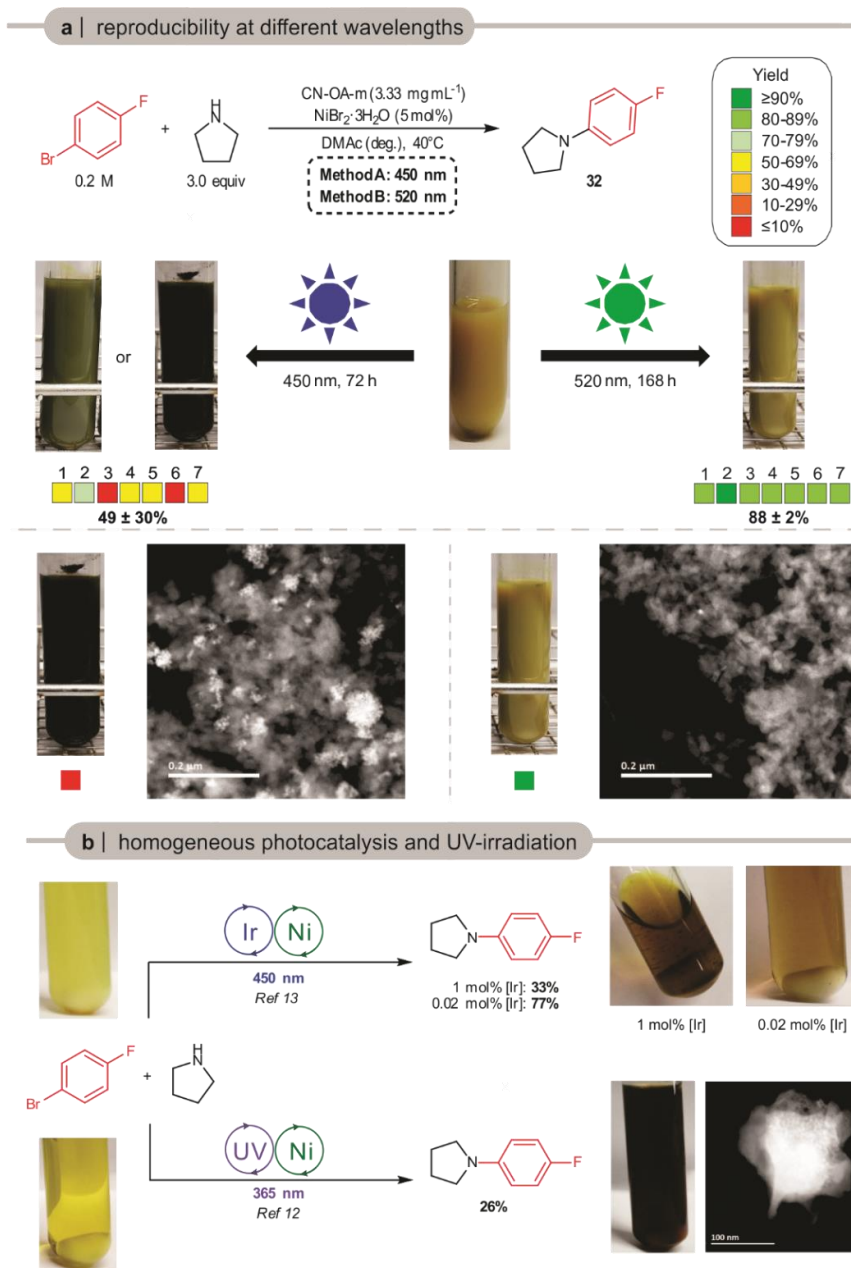


Figure 4.2. Catalyst deactivation during the reaction of 4-bromofluorobenzene with pyrrolidine. a, Reproducibility using blue (450 nm) and green (520 nm) LED irradiation. The reaction mixture turned dark green or black and suffered from severe reproducibility issues at 450 nm, whereas almost no color change and reproducible results were obtained at 520 nm. HAADF-STEM images show nickel particle agglomerates (bright spots) on CN-OA-m recovered the experiment using blue light and almost no agglomerates when 520 nm were used. **b,** Nickel-black formation was also observed using the homogeneous $(\text{Ir}[\text{dF}(\text{CF}_3)_2\text{ppy}]_2(\text{dtbbpy}))\text{PF}_6$ ($= [\text{Ir}]$) photocatalyst and in the PRC-free reaction using UV light. For experimental details, see the Supplementary Information.

Only Ni^{II} was detected on the material recovered from experiments using 520 nm LEDs (Method B) by XPS. Scanning transmission electron microscopy (STEM) was used to visualize nickel particles on the surface of the recovered CN-OA-m from both methods. High-angle annular dark-field (HAADF) images show a high amount of nickel particles that agglomerated (nickel-black) on the CN-OA-m recovered from experiments using 450 nm LEDs (Method A), whereas the material from experiments using 520 nm LEDs (Method B) contained almost no agglomerates (Figure 4.2, a).

Nickel-black formation was also shown to be responsible for low yields using other light-mediated protocols for the same model reaction (Figure 4.2, b). A reaction with 1 mol% of the homogeneous PRC (Ir[dF(CF₃)ppy]₂(dtbbpy))PF₆,¹⁷ resulted in low selectivity towards the desired coupling product (**32**, 33% yield), and small amounts of a black precipitate were formed during the reaction. Decreasing the amount of (Ir[dF(CF₃)ppy]₂(dtbbpy))PF₆ to 0.02 mol% increased the yield of **32** significantly (77%) and no particle formation was observed. Here, the amount of the PRC plays a crucial role to avoid nickel-black formation and the optimal catalyst loading needs to be determined for each substrate individually. The PRC-free, UV light-mediated protocol¹² resulted in no more than 26% of **32** and a black precipitate was formed in high amounts (Figure 4.2, c). STEM imaging and EDX spectroscopy confirmed that these solids consist of nickel and organic matter that is presumably resulting from substrate/product degradation by the high-energy light source (see Supplementary Information for details).

The dual carbon nitride/nickel catalyzed protocol using green light (520 nm, Method B) did also enable selective, reproducible C–N cross-couplings of bromobenzene (**33**), and 3-bromotoluene (**34**) with pyrrolidine, but did not eliminate catalyst deactivation issues in the cases of 1-bromo-4-*tert*-butylbenzene (**35**), and 4-bromoanisole (**36**) (Figure 4.3, a). Although almost quantitative product formation was observed in some cases, the reactions sometimes gave low yields and black reaction mixtures. In the case of 1-bromo-4-*tert*-butylbenzene, for example, six parallel reactions using 450 nm (Method A) gave 52-70% of the desired product (**35**), whereas up to 92% as well as only 28 % were obtained under identical conditions using 520 nm (Method B). Efforts to increase the reproducibility and to minimize the nickel-black formation by changing the light intensity, distance between the reaction mixture and light source, varying the amount of both catalysts, changing the solvent or nickel catalyst, and adding MTBD (7-Methyl-1,5,7-triazabicyclo(4.4.0)dec-5-ene)¹⁷ or

dtbbpy to stabilize intermediate nickel species were not successful. We hypothesized that the formation of Ni⁰ agglomerates can be addressed by increasing the concentration of the reaction mixture for two reasons. First, a higher concentration would increase the rate of oxidative addition, thus minimizing the accumulation of Ni⁰ species. Second, catalyst deactivation might not only be accelerated by higher photon energies, but also a competitive binding of the amine and the solvent (DMAc) with low-valent nickel intermediates. In palladium catalysis, for example, PdArylXL_n intermediates were reported to form complexes with various solvents, including DMAc, that undergo β-hydride elimination followed by the formation of Pd⁰ and Aryl-H.³² Although pyrrolidine was shown to be the primary ligand in light-mediated, nickel catalyzed aminations,²⁰ the high excess of DMAc potentially results in solvent-catalyst interactions that could contribute to Ni-black formation. Indeed, running the reaction at 1.2 M instead of 0.2 M resulted in reproducible reactions and the desired products (**32-36**) were obtained in high yields, even at 450 nm (Method C). These results could not be further improved using 520 nm irradiation, suggesting that the nickel-black formation can be outpaced at high concentrations independent of the photon energy in our semi-heterogeneous catalytic system (see Supplementary Information).³³

A reinvestigation of the coupling of methyl 4-chlorobenzoate with pyrrolidine was carried out using all protocols (see Supplementary Information). The standard protocol (Method A) afforded the desired coupling product (**1**) in 65% within seven days. Longer irradiation did not result in higher yields and only increased the amount of the dehalogenated side product, indicating complete catalyst deactivation.

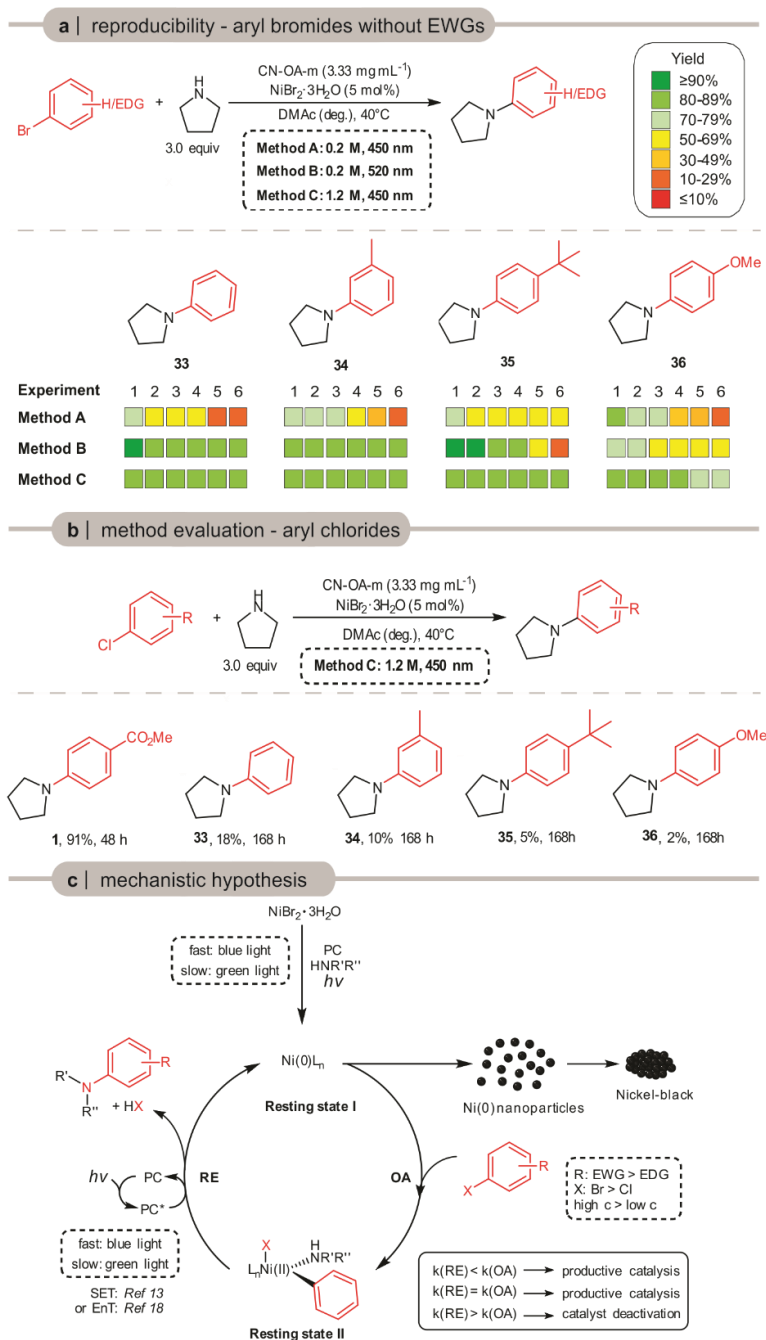


Figure 4.3. Evaluation of different protocols for coupling aryl bromides and aryl chlorides with pyrrolidine. **a**, Reproducibility study for aryl bromides without electron withdrawing groups using different C–N coupling protocols. NMR yields are reported **b**, Evaluation of Method C for the coupling of aryl halides and pyrrolidine. ^aIsolated yield. ^bNMR-yield **c**, Simplified mechanism of productive catalysis and catalyst deactivation. The reductive elimination (RE) likely follows either a three-step photoredox ($\text{Ni}^{\text{II}}\text{-Ni}^{\text{III}}\text{-Ni}^{\text{I}}\text{-Ni}^{\text{0}}$),¹⁷ or a two-step energy transfer ($\text{Ni}^{\text{II}}\text{-Ni}^{\text{II}*}\text{-Ni}^{\text{0}}$) process.¹⁸⁻¹⁹

With green light (Method B), 83% of **1** was obtained within 14 days. The optimized method using 450 nm LEDs and a lower amount of solvent (Method C) significantly enhanced the C–N coupling and resulted in 92% of **1** within two days (Figure 4.3, b). When the best conditions (Method C) were applied for electron-neutral, and -rich aryl chlorides, a clear trend was observed (Figure 3, b). Chlorobenzene gave 18% of **33** within 168 hours, and substrates with electron-donating substituents gave even lower yields. In all cases the formation of nickel black was observed.

Taking all experiments together, we propose that catalyst deactivation is avoided when the relative rate of oxidative addition (OA) is equal or higher than the relative rate of reductive elimination (RE), avoiding accumulation of Ni⁰ species (Resting state **I**, Figure 4.3, c). This is (under all conditions) the case for activated (electron-poor) aryl bromides. In case of 4-bromobenzene and 3-bromotoluene, the rate of RE (and the initial formation of Ni⁰) was sufficiently decelerated by using green light (slow OA, slow RE). At higher concentrations, the rate of OA is increased significantly, resulting in efficient productive catalysis for all tested, electron-rich aryl bromides (fast OA, fast RE). For non-activated, electron-rich aryl chlorides OA becomes too slow and Ni⁰ accumulation cannot be avoided under the conditions reported herein.

Next, we sought to study if the deposition of nickel-black also affects the recyclability of CN-OA-m by altering its photocatalytic activity. During the coupling of pyrrolidine with methyl 4-bromobenzoate using white (RGB) LEDs, the reaction mixture became greenish-brown (Figure 4.4, a). ICP-OES analysis of the heterogeneous material showed a nickel content of ~14 mg g⁻¹. The formation of product decreased significantly when the heterogeneous PRC was recycled (Figure 4.4, b).³⁴ Further, the yellow PRC turned dark green to black and the amount of deposited Ni rose to ~61 mg g⁻¹ over five recycling experiments. At higher wavelengths (520 nm, Method B), the model reaction required 48 h instead of 8 h for full conversion (Figure 4.4, a). Although the reaction mixture did not change its color, the amount of deposited Ni was similar to the white LED experiment (~14 mg g⁻¹). The photocatalyst did, however, not lose its catalytic activity during five recycling experiments and was recovered as a yellow solid that contained a lower amount of deposited nickel (~39 mg g⁻¹) compared to the white light experiment (Figure 4.4, b).

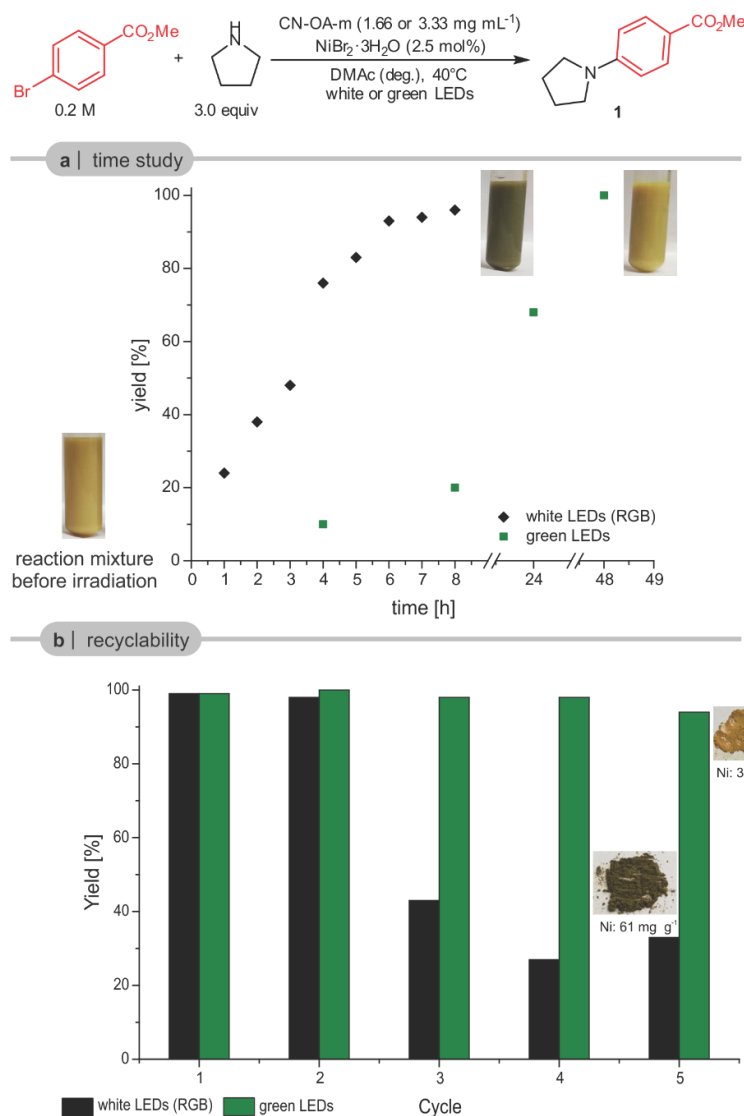


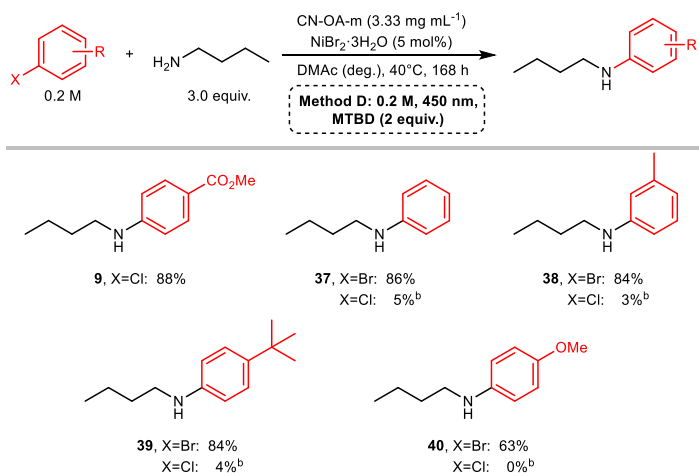
Figure 4.4. Reduction of catalyst deactivation using higher wavelengths. **a**, Time study for the coupling of methyl 4-bromobenzoate and pyrrolidine using white (RGB) and green (~520 nm) LED irradiation. The heterogeneous photocatalyst turned green using white light (RGB) irradiation whereas no color change was observed when green light (~520 nm) was used. **b**, The recyclability of CN-OA-m is excellent using green (~520 nm) LEDs. Deactivation of the PRC by nickel-black depositions was observed using white (RGB) LEDs. For experimental details, see the Supplementary Information.

Scanning transmission electron microscopy (STEM) of CN-OA-m from both recycling studies showed a significant amount of nickel agglomerates (nickel-black) for CN-OA-m from the experiments using white LEDs, whereas almost no agglomerates were detected on the semiconductor recovered from the recycling study using green LEDs (see Supplementary Information).

Finally, we sought to determine if deactivation of the nickel catalyst could also be avoided when less nucleophilic, primary amines are used. These substrates are usually less efficient

and give lower yields than cyclic, secondary amines, even with electron-deficient aryl bromides.^{12-13, 18-19, 28} By studying the cross-coupling of *n*-butylamine with 1-bromo-4-*tert*-butylbenzene, we observed only 8% of the desired product (**39**) during a 16 h experiment using blue light (Method A, see Supplementary Information). Notably, running the reaction at higher concentrations decreased the yield, indicating that low-valent Ni(*n*-butylamine)_n species are rather inefficient towards OA and a higher concentration in this case might even accelerate catalyst deactivation. Increasing the temperature from 40 to 60 °C resulted in up to 42% of the desired coupling product (**39**), but concomitant deactivation of the nickel catalyst was observed. Switching to green light or performing the reaction at 80 °C did not improve these result.

The above described strategies to accelerate OA or decelerate RE were not successful. It was previously reported that the addition of DBU and MTBD has a positive effect on the reaction outcome with primary amines, but the reason for that remains unclear.^{15, 17} We assumed that coordination of these additives to the active, low valent nickel species i) might activate the low-valent nickel complex towards OA, and ii) has a stabilizing effect that would increase the lifetime of resting state **I** by inhibiting nickel-black formation. We could ultimately prove this stabilizing affect during control experiments in the absence of aryl halides (see Supplementary Information). When NiBr₂·3H₂O was irradiated in the presence of pyrrolidine with blue light, Ni-black was rapidly formed. However, the formation of nickel black takes significantly longer in the presence of MTBD. Further, a comparison of the coupling of 1-bromo-4-*tert*-butylbenzene with *n*-butylamine with and without additives showed a higher catalytic activity when MTBD was added. After a short optimization, we obtained conditions that enabled the coupling of electron-poor aryl bromides with *n*-butylamine in good to excellent selectivity at 40°C (Table 4.3). This method was also applicable for an electron-poor aryl chloride, but, similar to the coupling with pyrrolidine, deactivated aryl chlorides remain a limitation.

Table 4.3. Semi-heterogeneous amination of primary amines and aryl halides.^[a]

^aReaction conditions: aryl halide (1.2 mmol), *n*-butylamine (3.6 mmol), CN-OA-m (20 mg), NiBr₂·3H₂O (60 μmol), 7-Methyl-1,5,7-triazabicyclo[4.4.0]dec-5-ene (MTBD) (2.4 mmol), DMAc (anhydrous, 6.0 mL), blue LEDs at 40 °C. Isolated yields are reported. ^bYield was determined by ¹H-NMR using 1,3,5-trimethoxybenzene as internal standard.

4.3 Conclusion

The formation of nickel-black limits the applicability of light-mediated, nickel catalyzed C–N cross-couplings. In particular, aryl bromides lacking electron-withdrawing groups suffer from reproducibility problems due to deactivation of the nickel catalyst. Deposition of nickel particles (nickel-black) not only deactivates the homogeneous nickel catalyst, but also the heterogeneous carbon nitride photocatalyst. Careful studies using dual carbon nitride/nickel catalysis showed that nickel-black formation likely results from a slow oxidative addition in case of electron-rich aryl bromides, leading to accumulation of low-valent nickel species that agglomerate. We showed that this issue can be overcome by i) decreasing the rate of the reductive elimination, ii) increasing the rate of oxidative addition, and iii) stabilizing low-valent nickel intermediates with a suitable additive. Our strategies enable reproducible, highly selective C–N cross-couplings of electron-rich, -neutral and -poor aryl bromides with primary and cyclic, secondary amines and can even be used for efficient reactions of electron-poor aryl chlorides.

4.4 Supporting information

4.4.1 General remarks

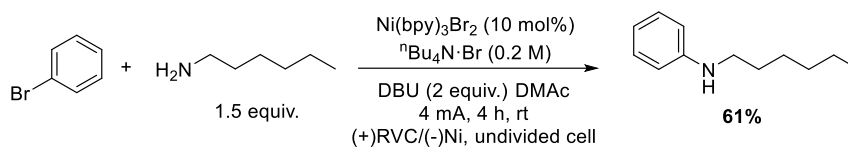
Substrates, reagents, and solvents were purchased from commercial suppliers and used without further purification. Methyl 4-(trifluoromethylsulfonyloxy)benzoate,³⁵ methyl 4-(tosyloxy)benzoate³⁶, methyl 4-((methylsulfonyl)oxy)benzoate³⁷ and *N*-tert-butylisopropylamine (BIPA)³⁸ were prepared according to literature procedures. ¹H-, ¹³C- and ¹⁹F-NMR spectra were obtained using a Varian 400 spectrometer (400 MHz, Agilent), an Ascend™ 400 spectrometer (400 MHz, cryoprobe, Bruker) and a Varian 600 spectrometer (600 MHz, Agilent) at 298 K, and are reported in ppm relative to the residual solvent peaks. Peaks are reported as: s = singlet, d = doublet, t = triplet, q = quartet, m = multiplet or unresolved, with coupling constants in Hz. Analytical thin layer chromatography (TLC) was performed on pre-coated TLC-sheets, ALUGRAM Xtra SIL G/UV₂₅₄ sheets (Macherey-Nagel) and visualized with 254 nm light or staining solutions followed by heating. Purification of final compounds was carried out by flash chromatography on the Reveleris X2 Flash Chromatography System from GRACE using prepacked columns with 40 μm silica gel. Silica 60 M (0.04-0.063 mm) silica gel (Sigma Aldrich) was used for dry loading of the crude compounds on the flash chromatography system. Centrifugation was carried out using an Eppendorf 5430 centrifuge. High-resolution mass spectral data were obtained using a HR-EI-MS (Waters Autospec Premier) and a Waters XEVO G2-XS 4K spectrometer with the XEVO G2-XS QTOF capability kit. Emission spectra of LED lamps were recorded using 10 in. (24.5 cm) integrating sphere (Labsphere, Inc. Model LMS 1050) equipped with a diode array detector (International Light, Model RPS900). The UV/Vis spectrum of Ir(ppy)₂(dtbbpy)PF₆ was recorded using a UVmini-1240 spectrometer (Shimadzu). Inductively coupled plasma - optical emission spectrometry (ICP-OES) was carried out using a Horiba Ultra 2 instrument equipped with photomultiplier tube detection. FTIR spectra were recorded on a Thermo Scientific Nicolet iD5 spectrometer. Diffuse reflectance UV/Vis spectra of powders were recorded on a Shimadzu UV-2600 spectrometer equipped with an integrating sphere. For XRD measurements, a Bruker D8 Advanced X-ray diffractometer with Cu Kα radiation was used. Scanning electron microscopy (SEM) images were obtained on a LEO 1550-Gemini microscope. Energy-dispersive X-ray (EDX) investigations were conducted on a Link ISIS-300 system (Oxford Microanalysis Group)

Chapter 4

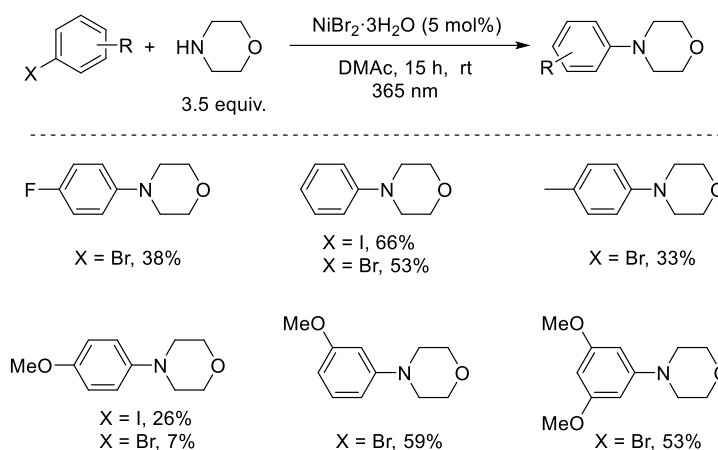
equipped with a Si(Li) detector and an energy resolution of 133 eV. X-ray photoelectron spectroscopic (XPS) measurements were carried out with a CISSY set-up, equipped with a SPECS XR 50 X-ray gun with Mg K α excitation radiation (1254.6 eV) and combined with a lens analyzer module (CLAM) under ultra-high vacuum (UHV, 1.5×10^{-8} Pa). The calibration was performed using the Au 4f $_{7/2}$ (84.0 eV) binding energy scale as reference. Quantitative analysis and deconvolution were achieved using “peakfit” and “Igor” software with Lorentzian-Gaussian functions and Shirley background deletion in photoemission spectra. The STEM images were acquired using a double-corrected Jeol ARM200F, equipped with a cold field emission gun. For the investigation, the acceleration voltage was set to 200 kV, the emission was put to 5 μ A and a condenser aperture with a diameter of 20 μ m was used. With these settings, the microscope reaches a lattice resolution below 1 Å. The STEM specimens were prepared by dissolving a powder sample of the material in ethanol, sonicating the solution for 15 minutes and finally dropping a few drops onto a copper TEM grid coated with holey carbon film. Once the solution had dried off, the specimens were investigated.

4.4.2 Literature analysis: aryl halides without electron withdrawing groups

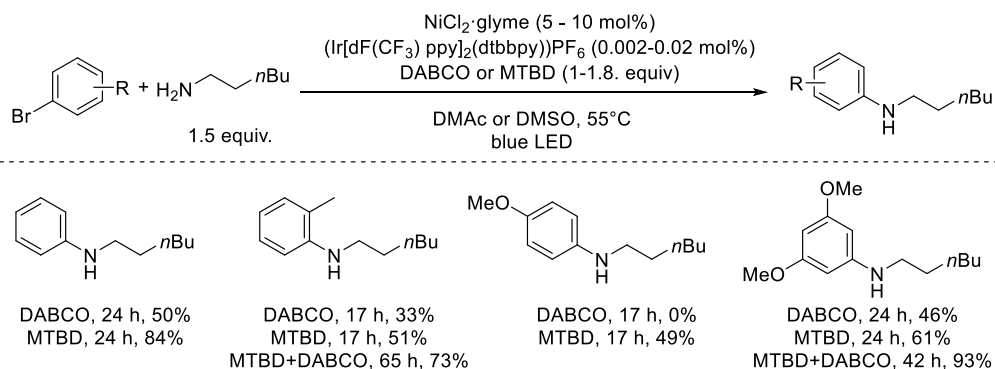
a) Electrochemically driven, Ni-catalyzed amination¹¹

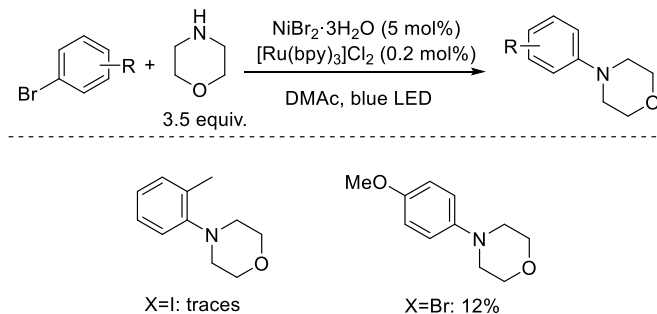
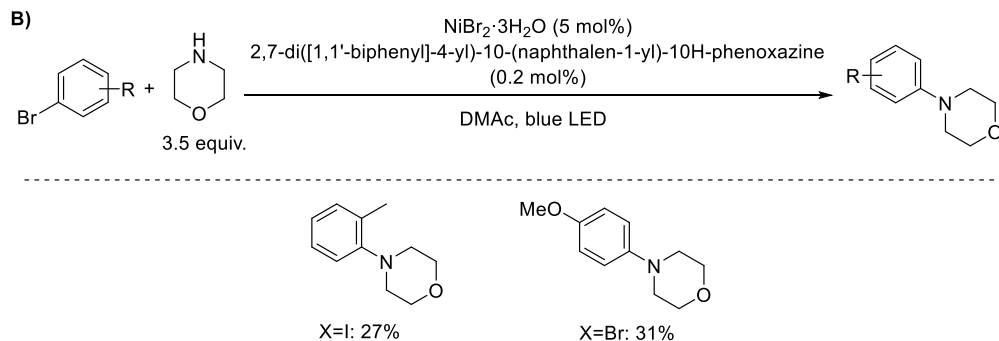
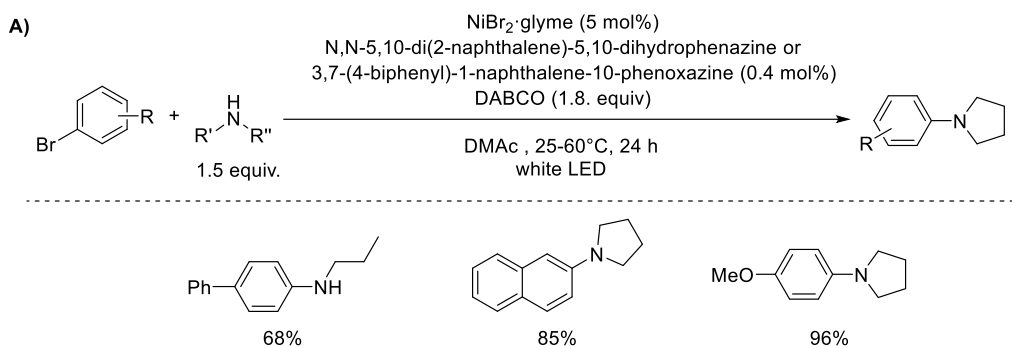


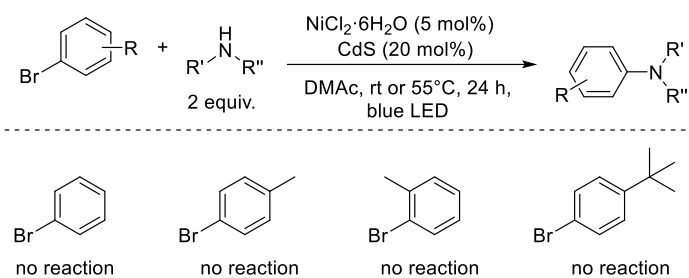
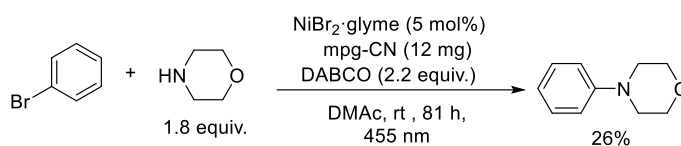
b) UV-light mediated, Ni-catalyzed amination¹²



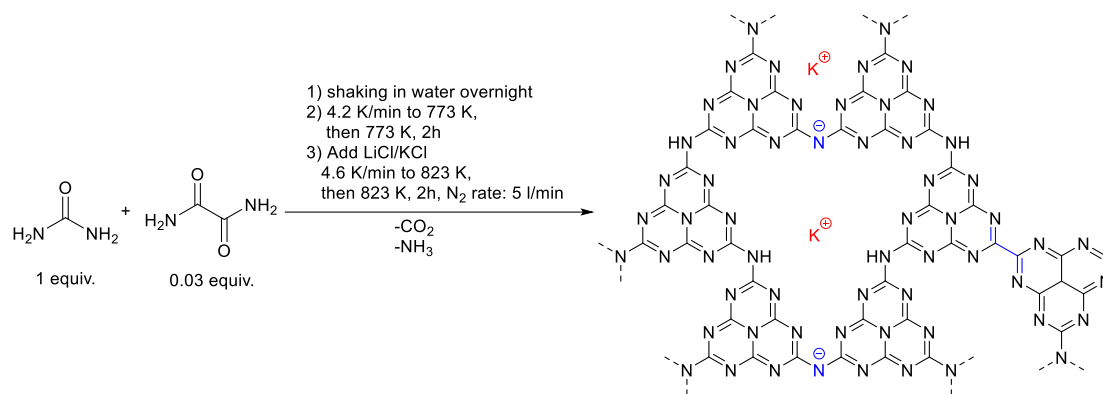
c) Dual nickel/photo catalyzed amination using $(\text{Ir}[\text{dF}(\text{CF}_3)\text{ppy}]_2(\text{dtbbpy}))\text{PF}_6$ ¹⁷



d) Dual nickel/photo catalyzed amination using $[\text{Ru}(\text{ppy})_3]\text{Cl}_2$ ³⁹e) Dual nickel/photoredox catalyzed amination using organic dyes^{13, 39}

f) Dual nickel/photoredox catalyzed amination using CdS¹⁵g) Dual nickel/photoredox catalyzed amination using mpg-CN¹⁶

4.4.3 Preparation of CN-OA-m



Scheme 4.1. Synthesis of CN-OA-m.

The synthesis for CN-OA-m was carried out using a slightly adapted version of the literature procedure (Scheme 4.1)²⁶: For each batch of the photocatalyst, urea (10 g, 166.5 mmol) and oxamide (0.5 g, 5.7 mmol) were mixed in 10 ml of DI water to generate a homogeneous mixture. After drying at 373 K, the resulting solids were grinded, transferred into a crucible with a cover and heated up in an air-oven with a heating rate of 4.3 K/min to 773 K. After keeping the mixture for 2h at 773 K, the sample was allowed to cool to room temperature. Subsequently, KCl (3.3 g, 44.3 mmol) and LiCl (2.7 g, 63.7 mmol) were added and the solids were grinded to obtain a homogeneous mixture which was heated in an inert atmosphere (N₂ flow: 5 mL/min) to 823 K with a heating rate of 4.6 K/min. After keeping the mixture for 2 h at 823 K, the sample was allowed to cool to room temperature and the resulting solids were collected on a filter paper and washed with H₂O (3 x 100 mL). The resulting yellow material was dried at 373 K (average yield per batch: ~425 mg). All analytical data (FTIR, UV/Vis, XRD, SEM, etc.; see Section 4.4.8) are in full agreement with those published in the literature.²⁶

The UV/Vis spectrum of CN-OA-m shows a strong absorption up to ~460 nm and a comparably weaker absorption band up to ~700 nm (Figure 4.5, A) which are attributed to the π - π^* electron transition of the sp² hybridization of C and N in the heptazine framework and n- π^* electron transition involving the lone pairs of the edge nitrogen atoms in the heptazine units, respectively.²⁶ The capability of harvesting low energy light is therefore superior compared to Ir and Ru photocatalysts (see Figure 4.5, B for the UV/Vis spectrum of Ir[dF(CF₃)ppy]₂(dtbbpy)PF₆ as a representative example) which have only a low absorption band between 400 and 500 nm in the visible region, which corresponds to the metal-to-ligand charge transfer transition.

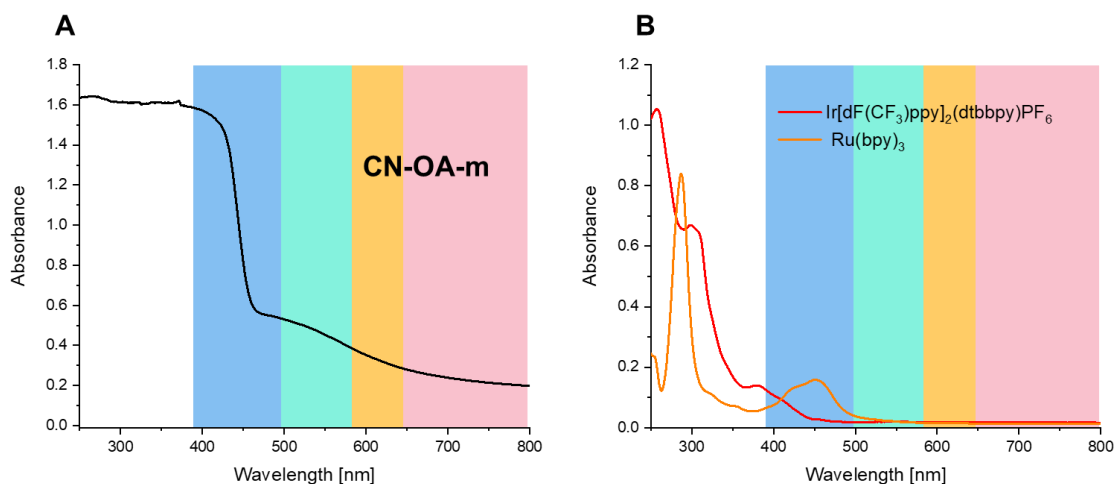


Figure 4.5. UV/VIS-absorption spectra of CN-OA-m (A) and Ir[dF(CF₃)ppy]₂(dtbbpy)PF₆ (B).

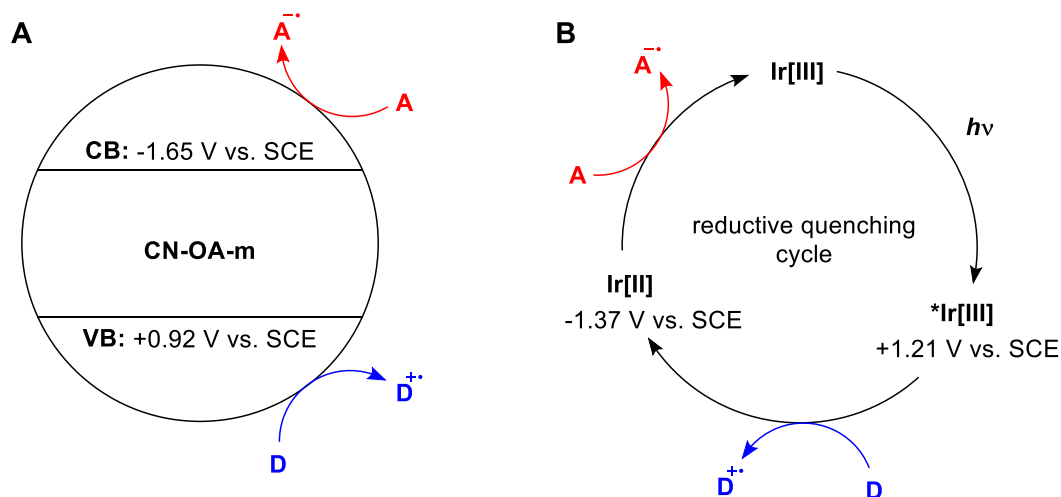


Figure 4.6. Comparison of the photoredox properties of CN-OA-m (A) and Ir[dF(CF₃)ppy]₂(dtbbpy)PF₆ (=Ir[III]) during an reductive quenching cycle (B). The photoredox properties of CN-OA-m were originally measured against Ag/AgCl²⁶ and were converted for better comparison. The half-reaction reduction potential for the oxidation of representative Ni^{II} to Ni^{III} complexes was, to the best of our knowledge not reported. For bpy(Ni^{II}(Mes)OMe), however, $E^{1/2}_{\text{red}}$ was determined to be +0.71 V vs Ag/AgCl (0.67 V vs. SCE),⁴⁰ which is thermodynamically feasible for both photocatalysts. It has to be noted that the reaction might also be triggered by energy transfer instead of than single transfer.

4.4.4 Setup for photochemical reactions

A flexible, red/green/blue LED strip⁴¹ (RGB, 5m, 24 W/strip; Tween Light, BAHAG AG, Germany) was wrapped around a 115 mm borosilicate crystallization dish (Figure 4.7, A). Blue, green, red or white (illumination of all three LED colors - red/green/blue) light was used at full power for all experiments (For emission spectra of a single diode, see Figure 4.8). The evaporating dish was filled with ethylene glycol and the temperature was set to 40°C to maintain a constant temperature. The sealed, cylindrical reaction vessels (16 x 100 mm) were placed at the same distance from the LED strip during all experiments (Figure 4.7, A). All reactions were performed with a stirring speed of 600 (1 mL) or 1400 rpm (3 or 6 mL). For large scale aminations a flexible, red/green/blue LED strip (RGB, 5m, 24 W/strip; Tween Light, BAHAG AG, Germany) was wrapped around a 115mm borosilicate beaker (Figure 4.7, B). The scale-up reaction was performed in a sealed, cylindrical reaction vessel (25 x 140 mm) with a stirring speed of 700 rpm and without additional heating (Figure 4.7, B).

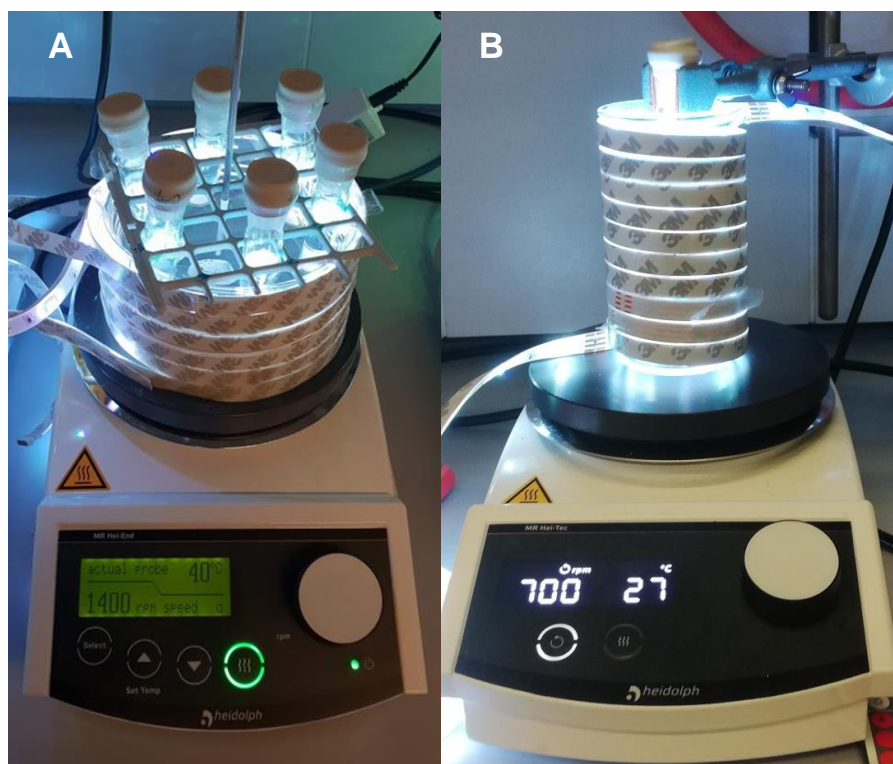


Figure 4.7. Experimental setup for general photochemical reactions (A) and for the scale-up reaction (B).

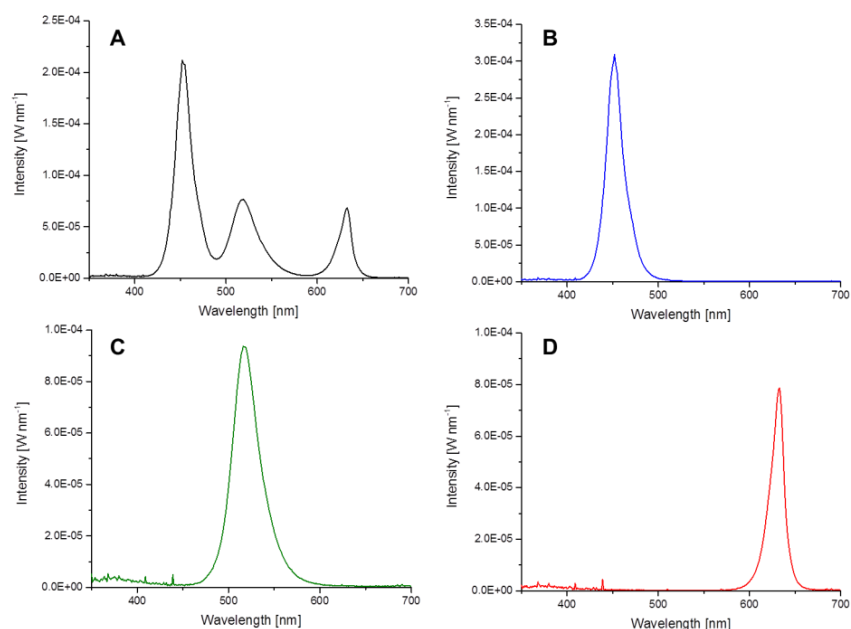


Figure 4.8. Emission spectra of the LED strips used for photochemical reactions. All experiments were carried out at maximum power. **A:** white light (RGB). **B:** blue light only. **C:** green light only. **D:** red light only.

A Kessil® PR 160-370nm lamp,⁴² a stir plate and a fan for cooling was used for UV-light experiments (Figure 4.9, A). All experiments were carried out with maximum lamp power. The sealed reaction vessels (16 x 100 mm) were placed at the same distance (4 cm) from the light source during all experiments. All reactions were performed with vigorous stirring.

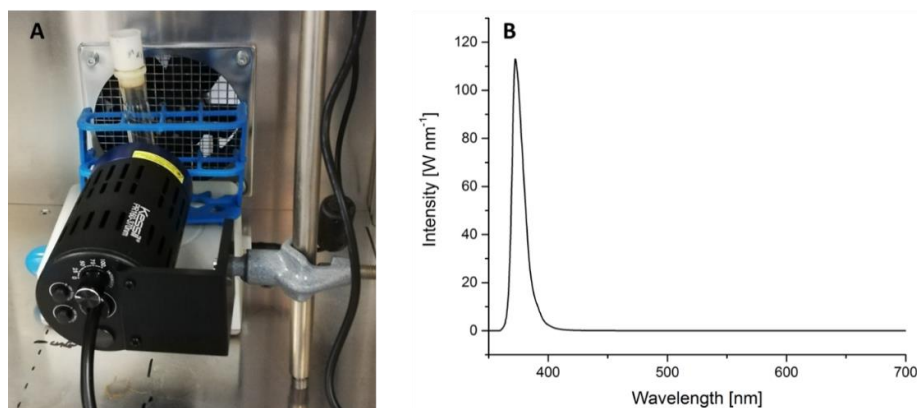


Figure 4.9. **A:** Picture of the Set-up for UV-light experiments **B:** Emission spectra of the Kessil® PR 160-370nm lamp used for photochemical reactions. All experiments were carried out at maximum power.

4.4.5 Reaction optimization

4.4.5.1 General experimental procedure for screening experiments

An oven dried vial (16 x 100 mm) equipped with a stir bar was charged with methyl 4-bromobenzoate (0.3 mmol, 64.5 mg, 1 equiv.), the base (0.9 mmol, 3.0 equiv.), the Ni^{II} catalyst (30 μ mol, 10 mol%) and the carbon nitride material (10 mg). Subsequently, pyrrolidine (0.45 mmol, 37.0 μ L, 1.5 equiv.) and the solvent (anhydrous, 3 mL) were added and the vial was sealed with a septum and Parafilm. The reaction mixture was sonicated for 5-10 min followed by stirring for 5 min until a fine dispersion of the solids was achieved and the mixture was then degassed by bubbling N₂ for 10 min. The mixture was irradiated in the photoreactor at 40 °C with rapid stirring (1400 rpm). After the respective reaction time, one equivalent of 1,3,5-trimethoxybenzene (0.3 mmol, 50.5 mg) was added. An aliquot of the reaction mixture (~300 μ L) was filtered, diluted with DMSO-d₆ and subjected to ¹H-NMR analysis. (Alternatively, 1.5 mL CDCl₃ and 3 mL H₂O were added and the vial was sealed and vigorously shaken. After phase separation, the CDCl₃ layer was carefully removed using a syringe, filtered, and analyzed by ¹H-NMR.) For representative NMR spectra, see Figure 4.10.

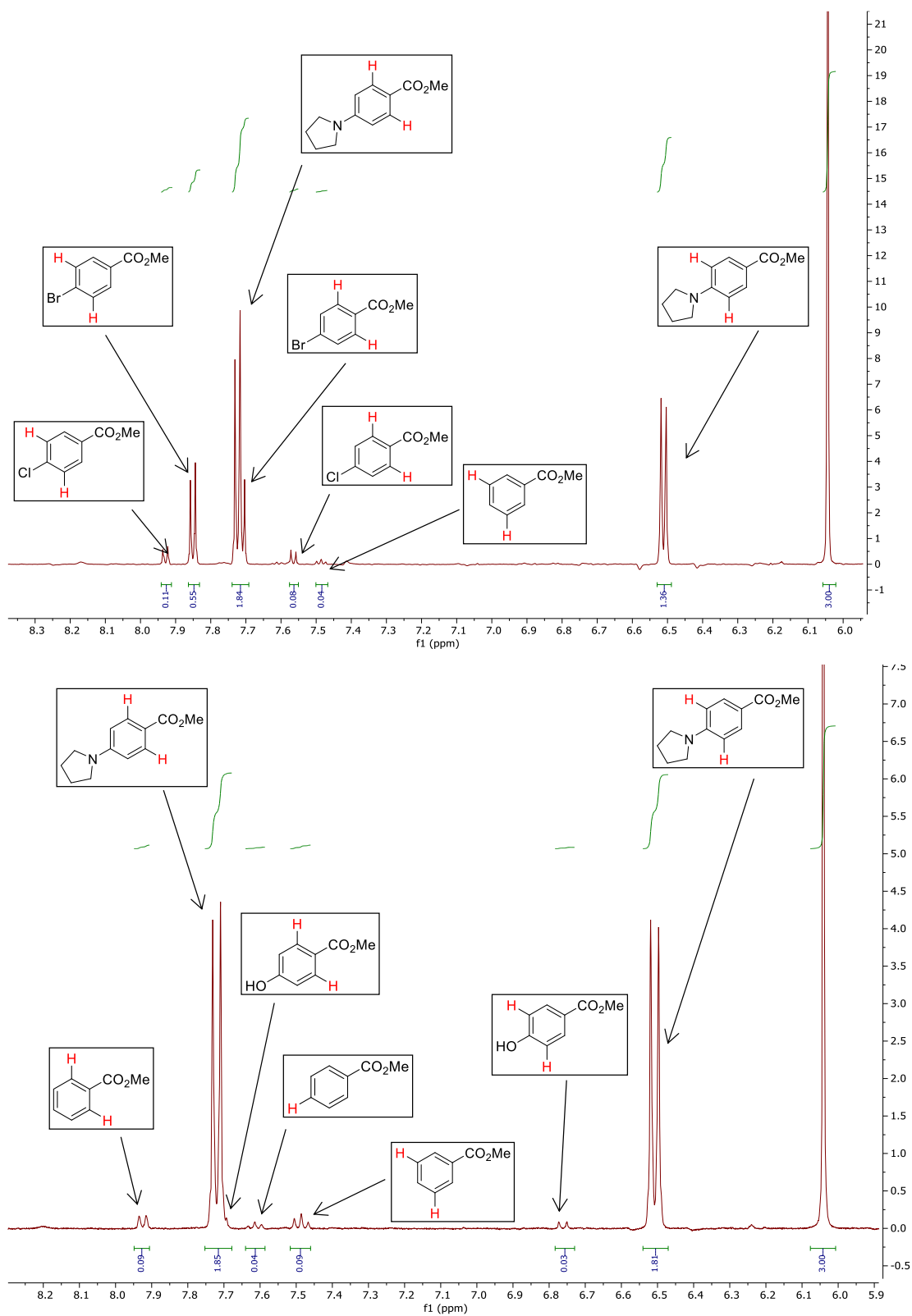


Figure 4.10. Examples of $^1\text{H-NMR}$ spectra for determining NMR yields.

4.4.5.2 Screening of carbon nitride material

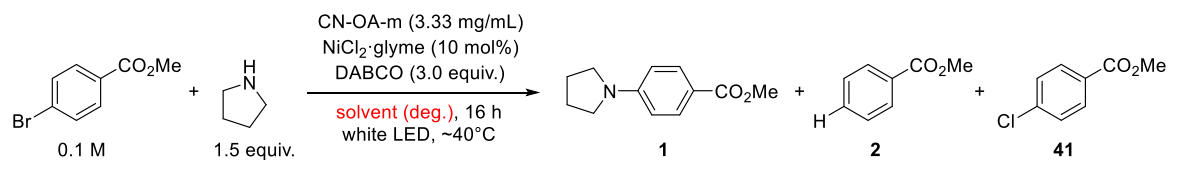
Table 4.4. Screening of carbon nitride materials.^a

Entry	CN catalyst	Conversion [%] ^b	1 [%] ^c	2 [%] ^c	41 [%] ^c
1	CN-OA-m	73	65	2	5
2	CMB _{0.05} -CN	25	21	2	trace
3	mpg-CN	23	19	trace	trace
4	PHIK	18	14	trace	trace
5	CNS ₆₀₀	9	6	trace	trace

^aReaction conditions: methyl 4-bromobenzoate (0.3 mmol), pyrrolidine (0.45 mmol), NiCl₂·glyme (10 mol%), DABCO (0.9 mmol), carbon nitride (10 mg), DMAc (anhydrous, 3 mL), white LEDs at 40 °C for 16h. ^bConversion of methyl 4-bromobenzoate determined by ¹H-NMR using 1,3,5-trimethoxybenzene as internal standard. ^cNMR yields determined by ¹H-NMR using 1,3,5-trimethoxybenzene as internal standard.

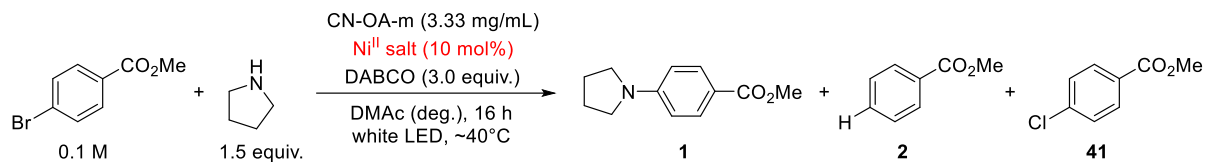
Several carbon nitride materials were tested: Mesoporous graphitic carbon nitride (mpg-CN),⁴³ a modified carbon nitride derived from a cyanuric acid/melamide/barbituric acid complex (CMB_{0.05}-CN),⁴⁴ a sulfur-doped material (CNS₆₀₀),⁴⁵ a strongly oxidizing potassium poly(heptazine imide) (K-PHI),⁴⁶ and a carbon nitride derivative prepared *via* co-condensation of urea and oxamide followed by post-calcination in a molten salt (CN-OA-m),²⁶ all using white LED (RGB) irradiation at a constant temperature of 40 °C.

4.4.5.3 Solvent screening

Table 4.5. Solvent screening.^a


Entry	Solvent	Conversion [%] ^b	1 [%] ^c	2 [%] ^c	41 [%] ^c
1	DMAc	74	66	2	4
2	DMSO	28	24	trace	trace
3	DMF	n.d.o ^d	18	trace	trace
4	MeCN	19	14	trace	trace
5	diglyme	15	11	trace	trace
6	toluene	6	6	trace	trace
7	DCM	11	trace	trace	trace

^aReaction conditions: methyl 4-bromobenzoate (0.3 mmol), pyrrolidine (0.45 mmol), NiCl₂·glyme (10 mol%), DABCO (0.9 mmol), CN-OA-m (10 mg), solvent (anhydrous, 3 mL), white LEDs at 40 °C for 16h. ^bConversion of methyl 4-bromobenzoate determined by ¹H-NMR using 1,3,5-trimethoxybenzene as internal standard. ^cNMR yields determined by ¹H-NMR using 1,3,5-trimethoxybenzene as internal standard. ^d not detected due to overlapping peaks.

4.4.5.4 Screening of Ni^{II} sourcesTable 4.6. Screening Ni^{II} sources.^a

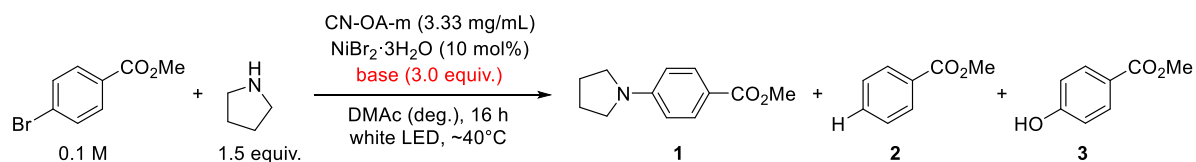
Entry	Ni ^{II} catalyst	Conversion [%] ^b	1 [%] ^c	2 [%] ^c	41 [%] ^c	Price [€ mol ⁻¹] ^d
1	NiI ₂	90	86	2	n.d.	2063
2	NiBr ₂ ·glyme	87	80	3	n.d.	10431
3	NiCl ₂	85	76	4	5	110
4	NiBr ₂	74	72	trace	n.d.	411
5	NiBr ₂ ·3H ₂ O	71	68	3	n.d.	116
6	NiCl ₂ ·glyme	74	66	trace	9	4161
7	Ni(ClO ₄) ₂ ·6H ₂ O	62	59	trace	n.d.	171
8	Ni(NO ₃) ₂ ·6H ₂ O	52	52	trace	n.d.	49
9	Ni(OTf) ₂	55	51	3	n.d.	12917
10	NiCl ₂ ·6H ₂ O	45	35	4	2	71
11	Ni(BF ₄) ₂ ·6H ₂ O	24	23	2	n.d.	223
12	Ni(TMHD) ₂	10	5	2	n.d.	35294
13	Ni(OAc) ₂ ·4H ₂ O	9	5	4	n.d.	28
14	Ni(SO ₄) ₂ ·6H ₂ O	9	4	2	n.d.	41
15	Ni(acac) ₂	3	n.d.	trace	n.d.	620

^aReaction conditions: methyl 4-bromobenzoate (0.3 mmol), pyrrolidine (0.45 mmol), Ni^{II} catalyst (10 mol%), DABCO (0.9 mmol), CN-OA-m (10 mg), DMAc (anhydrous, 3 mL), white LEDs at 40 °C for 16 h. ^bConversion of methyl 4-bromobenzoate determined by ¹H-NMR using 1,3,5-trimethoxybenzene as internal standard. ^cNMR yields determined by ¹H-NMR using 1,3,5-trimethoxybenzene as internal standard. ^dPrices according to Sigma Aldrich (Merck)^x.

NiBr₂·3H₂O gave the best combination of price, selectivity (chloride formation in case of NiCl₂), activity and handling (NiI₂ and NiBr₂ are highly hygroscopic).

4.4.5.5 Base screening

Table 4.7. Base screening.^a



Entry	Base	Conversion [%] ^b	1 [%] ^c	2 [%] ^c	3 [%] ^c
1	TMP ^d	quant.	91	3	2
2	BIPA ^e	90	89	trace	n.d. ^f
3	DABCO ^g	71	68	3	trace
4	K ₂ HPO ₄	68	63	4	trace
5	dimethylaniline	59	62	n.d.	n.d.
6	CaCO ₃	65	61	trace	trace
7	2,6-lutidine	62	60	3	n.d.
8	without base	65	58	4	trace
9	tetramethylguanidine	53	43	n.d.	n.d.
10	DIPEA ^h	49	42	6	n.d.
11	Et ₃ N	42	35	5	trace
12	DMAPI ⁱ	43	31	6	trace
13	K ₃ PO ₄	33	21	trace	trace
14	DBU ^j	27	19	trace	trace
15	Na ₂ CO ₃	17	14	trace	trace
16	NaHCO ₃	14	8	4	trace
17	NaOtBu	29	5	trace	trace

Entry	Base	Conversion [%] ^b	1 [%] ^c	2 [%] ^c	3 [%] ^c
19	NaOH	quant.	n.d.	n.d.	n.d.
20	K ₂ CO ₃	8	n.d.	trace	n.d.
21	NaH ₂ PO ₄	10	n.d.	n.d.	n.d.
18	KOH	quant.	4	n.d.	n.d.
22	LiOH	43	n.d.	n.d.	n.d.
23	Cs ₂ CO ₃	11	n.d.	5	trace
24	CsF	7	n.d.	trace	n.d.
25	CsOAc	2	n.d.	n.d.	n.d.
26	HMDS ^k	quant.	n.d.	n.d.	n.d.

^aReaction conditions: methyl 4-bromobenzoate (0.3 mmol), pyrrolidine (0.45 mmol), NiBr₂·3H₂O (10 mol%), base (0.9 mmol), CN-OA-m (10 mg), DMAc (anhydrous, 3 mL), white LEDs at 40 °C for 16h.

^bConversion of methyl 4-bromobenzoate determined by ¹H-NMR using 1,3,5-trimethoxybenzene as internal standard. ^cNMR yields determined by ¹H-NMR using 1,3,5-trimethoxybenzene as internal standard.

^d2,2,6,6-tetramethylpiperidin ^e*N-tert*-butylisopropylamine. ^fnot detected. ^g1,4-diazabicyclo[2.2.2]octane.

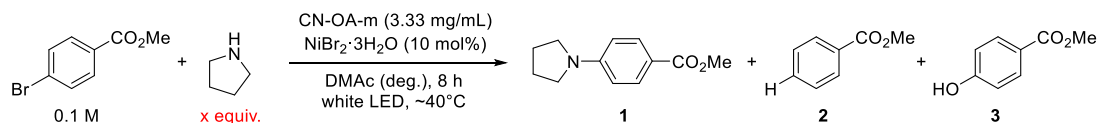
^h*N,N*-diisopropylethylamine. ⁱ4-(dimethylamino)pyridine. ^j1,8-diazabicyclo[5.4.0]undec-7-ene.

^kGexamethyldisilazane

N-tert-butylisopropylamine (BIPA) and 2,2,6,6-tetramethylpiperidine (TMP) gave best results. No C-N coupling between the aryl halide and these secondary, sterically hindered amines was observed. The absence of a base resulted in 58% yield indicating that the amine substrate can play several roles simultaneously (substrate, ligand, base). All other tested bases did not significantly increase the yield compared to the base-free method.

4.4.5.6 Screening of conditions

Table 4.8. Screening of amine equivalents for the base-free method.



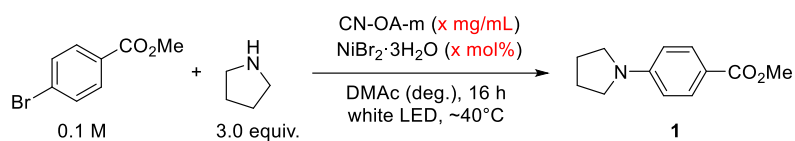
Entry	Pyrrolidine [equiv.]	Conversion	1	2	3
		[%] ^b	[%] ^c	[%] ^c	[%] ^c
1	1	33	24	4	1
2	1.5	53	43	6	1
3	2.0	67	59	7	1
4	2.5	91	83	6	2
5	3.0	quant.	94	5	2
6	3.5	quant.	92	6	3

^aReaction conditions: methyl 4-bromobenzoate (0.3 mmol), pyrrolidine (x equiv.), NiBr₂·3H₂O (10 mol%), CN-OA-m (10 mg), DMAc (anhydrous, 3 mL), white LEDs at 40 °C for 8 h. ^bConversion of methyl 4-bromobenzoate determined by ¹H-NMR using 1,3,5-trimethoxybenzene as internal standard. ^cNMR yields determined by ¹H-NMR using 1,3,5-trimethoxybenzene as internal standard.

Table 4.9. Screening of base (BIPA) equivalents for reactions with 1.5 equiv. pyrrolidine.^a

Entry	BIPA [equiv.]	Conversion	1	2	3
		[%] ^b	[%] ^c	[%] ^c	[%] ^c
1	-	65	58	5	n.d. ^d
2	0.5	68	58	5	3
3	1	87	81	4	2
4	1.5	91	82	5	n.d.
5	2.0	92	84	5	n.d.

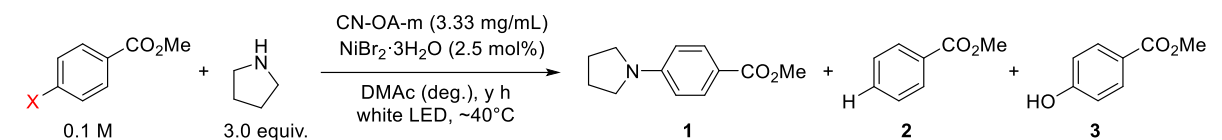
^aReaction conditions: methyl 4-bromobenzoate (0.3 mmol), pyrrolidine (0.45 mmol), NiBr₂·3H₂O (5 mol%), CN-OA-m (10 mg), BIPA (0-2 equiv.), DMAc (anhydrous, 3 mL), white LEDs at 40 °C for 16 h. ^bConversion of methyl 4-bromobenzoate determined by ¹H-NMR using 1,3,5-trimethoxybenzene as internal standard. ^cNMR yields determined by ¹H-NMR using 1,3,5-trimethoxybenzene as internal standard. ^dnot detected.

Table 4.10. Effect of the amount of NiBr₂·3H₂O and CN-OA-m on the yield of **1**.^a

Entry	NiBr ₂ ·3H ₂ O [mol%]	CN-OA-m [g/mL]	Conversion [%] ^b	1 [%] ^c
1	10	3.33	quant.	95
2	5	3.33	quant.	98
3	5	1.66	quant.	97
4	2.5	1.66	quant.	98
5	1	1.66	47	47
6	2.5	0.88	56	56

^aReaction conditions: methyl 4-bromobenzoate (0.3 mmol), pyrrolidine (0.9 mmol), NiBr₂·3H₂O (y mol%), base (0.9 mmol), CN-OA-m (x mg), DMAc (anhydrous, 3 mL), white LEDs at 40 °C for 16h. ^bConversion of methyl 4-bromobenzoate determined by ¹H-NMR using 1,3,5-trimethoxybenzene as internal standard. ^cNMR yields determined by ¹H-NMR using 1,3,5-trimethoxybenzene as internal standard.

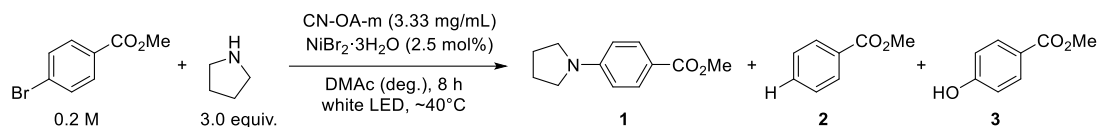
4.4.5.7 Screening of aryl (pseudo)halides

Table 4.11. Screening of aryl (pseudo)halides.^a

Entry	X	Time [h]	Conversion [%] ^b	1 [%] ^c	2 [%] ^c	3 [%] ^c
1	I	8	quant.	99	1	n.d.
2	Br	8	quant.	98	2	1
3	Cl	168	76	72	4	n.d.
4	OTf	72	75	67	5	2
5	OTs	16	2	n.d.	n.d.	n.d.
6	OMs	16	5	n.d.	n.d.	4

^aReaction conditions: aryl (pseudo)halide (0.3 mmol), pyrrolidine (0.9 mmol), NiBr₂·3H₂O (2.5 mol%), CN-OA-m (10 mg), DMAc (anhydrous, 3 mL), white LEDs at 40 °C for x h. ^bConversion of methyl 4-bromobenzoate determined by ¹H-NMR using 1,3,5-trimethoxybenzene as internal standard. ^cNMR yields determined by ¹H-NMR using 1,3,5-trimethoxybenzene as internal standard. ^dnot detected.

4.5.5.8 Control studies

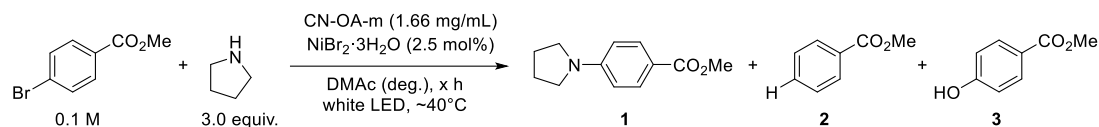
Table 4.12. Control studies.^a

Entry	Deviation from standard conditions	Conversion [%] ^b	1 [%] ^c	2 [%] ^c	3 [%] ^c
1	None	quant.	98	2	n.d. ^d
2	dtbbpy ^e (2.5 mol%) as ligand	48	45	2	n.d.
3	No CN-OA-m	5	n.d.	2	1
4	No NiBr ₂ ·3H ₂ O	5	n.d.	n.d.	n.d.
5	No light	<1	n.d.	n.d.	n.d.
6	No degassing	10	10	n.d.	n.d.

^aReaction conditions: methyl 4-bromobenzoate (1.2 mmol), pyrrolidine (3.6 mmol), NiBr₂·3H₂O (2.5 mol%), CN-OA-m (20 mg), DMAc (anhydrous, 6 mL), white LEDs at 40 °C for 8 h. ^bConversion of methyl 4-bromobenzoate determined by ¹H-NMR using 1,3,5-trimethoxybenzene as internal standard. ^cNMR yields determined by ¹H-NMR using 1,3,5-trimethoxybenzene as internal standard. ^dnot detected. ^e4,4'-Di-tert-butyl-2,2'-bipyridyl.

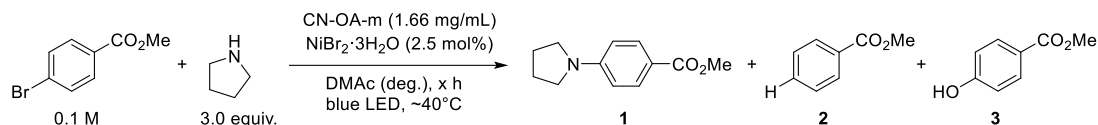
4.4.5.9 Time/Wavelength study

Table 4.13. Time study using white light.



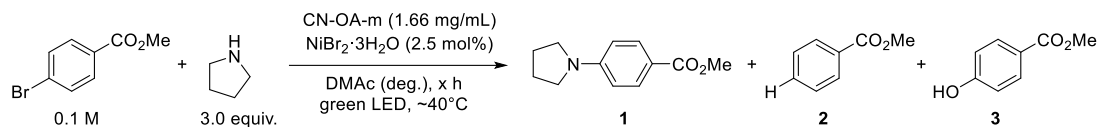
Entry	Time [h]	Conversion [%] ^b	1 [%] ^c	2 [%] ^c	3 [%] ^c
1	1	25	24	n.d. ^d	n.d.
2	2	39	38	n.d.	n.d.
3	3	48	48	trace	n.d.
4	4	77	76	1	n.d.
5	5	87	83	2	n.d.
6	6	91	91	2	n.d.
7	7	97	94	3	n.d.
8	8	quant.	96	2	1

^aReaction conditions: methyl 4-bromobenzoate (0.6 mmol), pyrrolidine (1.8 mmol), NiBr₂·3H₂O (2.5 mol%), CN-OA-m (10 mg), DMAc (anhydrous, 6 mL), white LEDs at 40 °C for x h. ^bConversion of methyl 4-bromobenzoate determined by ¹H-NMR using 1,3,5-trimethoxybenzene as internal standard. ^cNMR yields determined by ¹H-NMR using 1,3,5-trimethoxybenzene as internal standard. ^dnot detected.

Table 4.14. Time study using blue light.

Entry	Time [h]	Conversion [%] ^b	1 [%] ^c	2 [%] ^c	3 [%] ^c
1	2	51	51	n.d. ^d	n.d.
2	4	77	80	trace	n.d.
3	5.5	quant.	>99	trace	n.d.

^aReaction conditions: methyl 4-bromobenzoate (0.6 mmol), pyrrolidine (1.8 mmol), NiBr₂·3H₂O (2.5 mol%), CN-OA-m (10 mg), DMAc (anhydrous, 6 mL), blue LEDs at 40 °C for x h. ^bConversion of methyl 4-bromobenzoate determined by ¹H-NMR using 1,3,5-trimethoxybenzene as internal standard. ^cNMR yields determined by ¹H-NMR using 1,3,5-trimethoxybenzene as internal standard. ^dnot detected.

Table 4.15. Time study using green light.

Entry	Time [h]	Conversion [%] ^b	1 [%] ^c	2 [%] ^c	3 [%] ^c
1	4	10	10	n.d. ^d	n.d.
2	8	21	20	n.d.	n.d.
3	24	69	68	n.d.	n.d.
4	48	quant.	>99	n.d.	n.d.

^aReaction conditions: methyl 4-bromobenzoate (0.6 mmol), pyrrolidine (1.8 mmol), NiBr₂·3H₂O (2.5 mol%), CN-OA-m (10 mg), DMAc (anhydrous, 6 mL), green LEDs at 40 °C for x h. ^bConversion of methyl 4-bromobenzoate determined by ¹H-NMR using 1,3,5-trimethoxybenzene as internal standard. ^cNMR yields determined by ¹H-NMR using 1,3,5-trimethoxybenzene as internal standard. ^dnot detected.

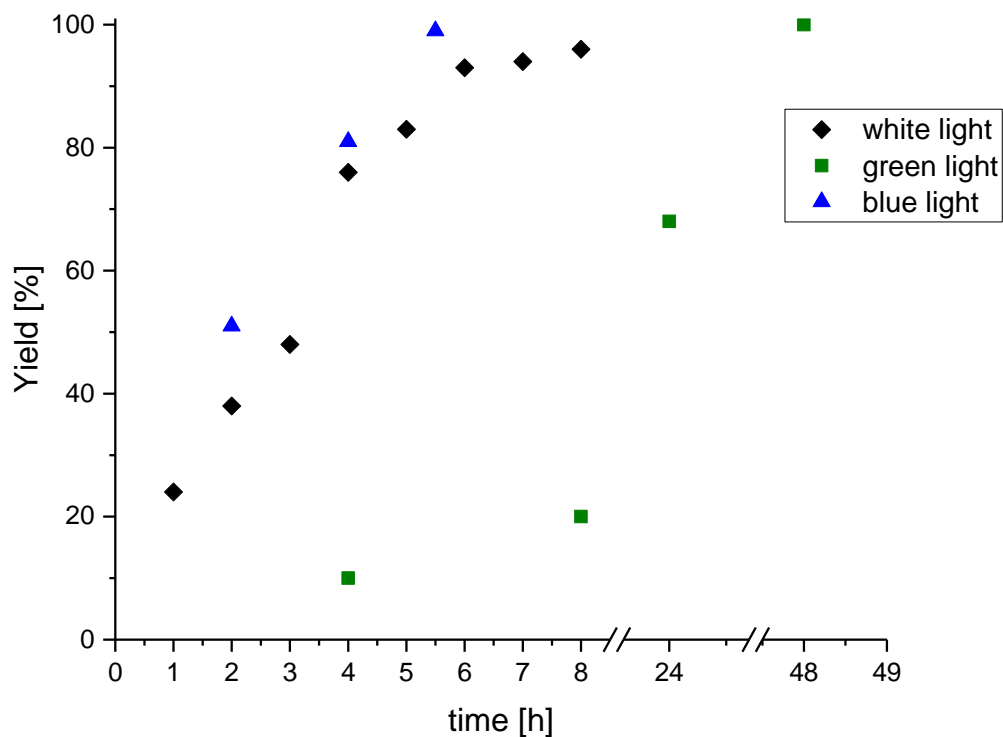


Figure 4.11. Time study using blue, green and white light for model reaction.

For ICP-OES experiments, the reaction mixture was centrifuged at 3000 rpm for 20 min and the liquid phase was carefully separated and analyzed by $^1\text{H-NMR}$. The carbon nitride was washed with DMAc (anhydrous, 6 mL, followed by centrifugation at 3000 rpm for 20 min and separation of the liquid phase), water (6 mL, followed by centrifugation at 3000 rpm for 20 min and separation of the liquid phase) and lyophilized (overnight) before analysis.

Table 4.16. ICP-OES measurements of the nickel content on the new and recovered CN-OA-m after 8 h white light and 48 h green light standard reaction.

Sample	Ni [mg/g CN]	% adsorbed Ni
CN-OA-m new	0.117	/
CN-OA-m white light standard reaction 1	14.2	16.1
CN-OA-m green light standard reaction	13.8	15.7

**Figure 4.12.** Fresh CN-OA-m (A), CN-OA-m after 8 h white light irradiation for standard reaction (B) and CN-OA-m after 48 h green light irradiation for standard reaction (C).

Note: Although 1.66 mg mL^{-1} of CN-OA-m is suitable for the C-N cross-coupling, a higher loading (3.33 mg mL^{-1}) was used for further experiments in order to obtain enough material for material characterization (ICP-OES, EDX, SEM, TEM, etc).

4.4.6 Recycling studies

An oven dried vial (13 x 80 mm) equipped with a stir bar was charged with CN-OA-m (20 mg), 4-bromomethylbenzoate (258.0 mg, 1.2 mmol, 1.0 equiv.) and NiBr₂·3H₂O (8.2 mg, 30 μmol, 2.5 mol%). Subsequently, pyrrolidine (256.0 mg, 295.6 μl, 3.6 mmol, 3.0 equiv.) and DMAc (anhydrous, 6 mL) were added and the vial was sealed with a septum and Parafilm. The reaction mixture was sonicated for 5-10 min followed by stirring for 5 min until fine dispersion of the solids was achieved and the mixture was then degassed by bubbling N₂ for 10 min. The mixture was irradiated in the photoreactor (white light or green light) at 40 °C with rapid stirring (1400 rpm). After the respective reaction time, one equivalent of 1,3,5-trimethoxybenzene (202.0 mg, 1.2 mmol) was added and the mixture was stirred for 5 min. The reaction mixture was centrifuged at 3000 rpm for 20 min and the liquid phase was carefully separated and analyzed by ¹H-NMR. The carbon nitride was washed with DMAc (anhydrous, 6 mL, followed by centrifugation at 3000 rpm for 20 min and separation of the liquid phase), lyophilized (overnight) and reused in the next reaction.

Table 4.17. Reusability of CN-OA-m using white light.^a

Cycle	1 [%] ^b
1	99
2	98
3	43
4	27
5	33

^aReaction conditions: methyl 4-bromobenzoate (1.2 mmol), pyrrolidine (3.6 mmol), NiBr₂·3H₂O (2.5 mol%), CN-OA-m (20 mg - reused), DMAc (anhydrous, 6 mL), white LEDs at 40 °C for 16h. ^bNMR yields determined by ¹H-NMR using 1,3,5-trimethoxybenzene as internal standard.

Table 4.18. Reusability of CN-OA-m without additional NiBr₂·3H₂O using white light.^a

Cycle	1 [%] ^b
1	99
2 ^c	1

^aReaction conditions: methyl 4-bromobenzoate (1.2 mmol), pyrrolidine (3.6 mmol), NiBr₂·3H₂O (2.5 mol%), CN-OA-m (20 mg - reused), DMAc (anhydrous, 6 mL), white LEDs at 40 °C for 16h. ^bNMR yields determined by ¹H-NMR using 1,3,5-trimethoxybenzene as internal standard. ^cNo NiBr₂·3H₂O added.

Table 4.19. Reusability of CN-OA-m using green light.^a

Cycle	1 [%] ^b
1	99
2	99
3	98
4	98
5	94

^aReaction conditions: methyl 4-bromobenzoate (1.2 mmol), pyrrolidine (3.6 mmol), NiBr₂·3H₂O (2.5 mol%), CN-OA-m (20 mg - reused), DMAc (anhydrous, 6 mL), green LEDs at 40 °C for 48h. ^bNMR yields determined by ¹H-NMR using 1,3,5-trimethoxybenzene as internal standard.

Table 4.20. ICP-OES measurements of the nickel content on recovered CN-OA-m after white light and green light recyclability tests.

Sample	Ni [mg/g CN]	% adsorbed Ni
CN-OA-m white light recyclability tests	60.5	13.7
CN-OA-m green light recyclability tests	38.8	8.8



Figure 4.13. Fresh CN-OA-m (A), CN-OA-m after recyclability tests with white light irradiation (B) and CN-OA-m after recyclability tests with green light irradiation (C).

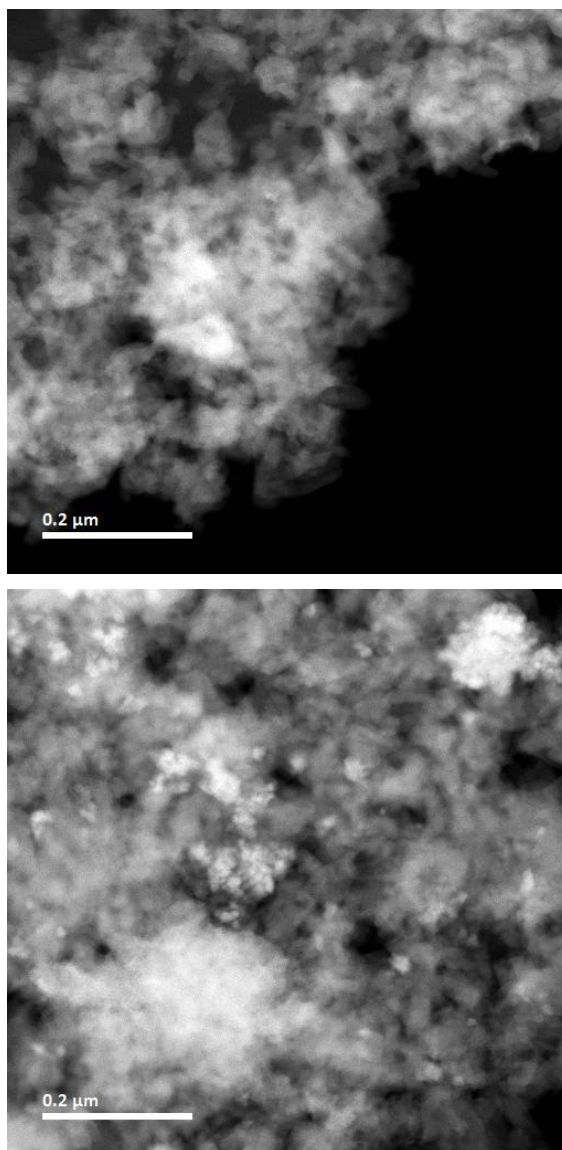


Figure 4.14. HAADF-STEM brightfield images show almost no nickel particle agglomerates (bright spots) on CN-OA-m after recyclability tests with green light irradiation (left) and a significant amount of agglomerates after recyclability tests with white light irradiation (right).

4.4.7. Scale-up of amination

An oven dried vial (25 x 140 mm) (Figure S11, A) equipped with a stir bar was charged with NiBr₂·3H₂O (54.5 mg, 0.2 mmol, 2.5 mol%), methyl 4-bromobenzoate (1.720 g, 8.0 mmol, 1 equiv.) and CN-OA-m (133.3 mg). Subsequently, pyrrolidine (1.706 g, 1.97 ml, 24.0 mmol, 3 equiv.) and DMAc (anhydrous, 6 mL) were added and the vial was sealed with a septum and parafilm. The reaction mixture was sonicated for 10 min and the mixture was then degassed by bubbling N₂ for 30 min and stirring the reaction mixture. The mixture was irradiated in a beaker wrapped with a LED-band (Figure S2, B) at ~40°C with rapid stirring (700 rpm). The completion of the reaction (14 h) was confirmed by taking an aliquot and measuring ¹H-NMR of the crude mixture in DMSO-d₆. The catalyst was removed by centrifugation (3000 rpm, 20 min) and the liquid phase was diluted with H₂O (200 mL) and extracted with ethyl acetate (3 x 200 mL). The combined organic phases were washed with H₂O (200 mL), a sat. NaHCO₃ solution (200 ml), and brine (200 mL), dried over Na₂SO₄ and concentrated. The crude product was purified by flash column chromatography (SiO₂, Hexane/EtOAc; gradient 0-5% ethyl acetate in hexane; 2. Isocratic 5% ethyl acetate in hexane)) on a Grace™ Reveleris™ system using a 24 g cartridge to afford (1-(4-methylbenzoate)pyrrolidine) (**1**) in 93 % (1.5338 g, 7.47 mmol) as a white solid (Figure S12).

¹H NMR (400 MHz, CDCl₃) δ 7.88 (d, *J* = 8.7 Hz, 2H), 6.46 (d, *J* = 8.7 Hz, 2H), 3.83 (s, 3H), 3.40 – 3.09 (m, 4H), 2.05 – 1.86 (m, 4H). ¹³C NMR (101 MHz, Chloroform-*d*) δ = 167.57, 150.79, 131.31, 116.16, 110.62, 51.37, 47.47, 25.41. HRMS (ESI-TOF) *m/z* calcd. for C₁₂H₁₆NO₂ [(M+H)⁺]: 206.1176; found: 206.116.

These data are in full agreement with those previously published in the literature.⁴⁷



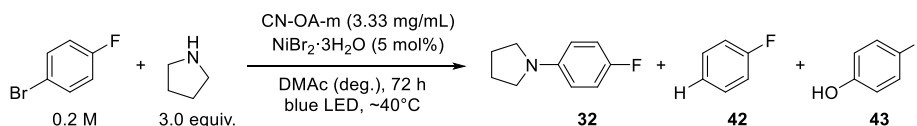
Figure 4.15. Vessel dimensions of vial for scale-up reaction (A) and vial for “standard scale” reactions (B).



Figure 4.16. Isolated product (1-(4-methylbenzoate)pyrrolidine) (**1**) from 8 mmol scale.

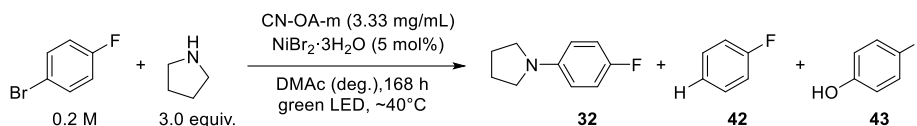
4.4.8 Studies on the reaction of 4-bromofluorobenzene with pyrrolidine.

Method A: Dual CN-OA-m/Ni catalysis with irradiation at 450 nm

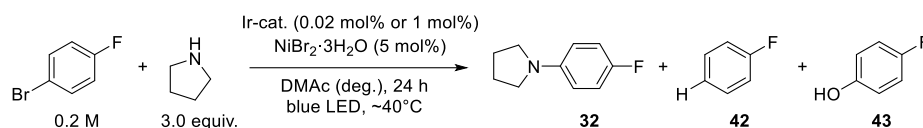


An oven dried vial (19 x 80 mm) equipped with a stir bar was charged with the CN-OA-m (20 mg), 4-bromofluorobenzene (210.0 mg, 131.8 μ l, 1.2 mmol, 1.0 equiv.) and NiBr₂·3H₂O (16.4 mg, 60 μ mol, 5.0 mol%). Subsequently, pyrrolidine (256.0 mg, 295.6 μ l, 3.6 mmol, 3.0 equiv.) and DMAc (anhydrous, 6 mL) were added and the vial was sealed with a septum and Parafilm. The reaction mixture was sonicated for 5-10 min followed by stirring for 5 min until fine dispersion of the solids was achieved and the mixture was then degassed by bubbling N₂ for 10 min. The mixture was irradiated in the photoreactor (blue light function of RGB LED strip) at 40 °C with rapid stirring (1400 rpm). After 72 h, one equivalent of 1,3,5-trimethoxybenzene (1.2 mmol) was added and the mixture was stirred for 5 min. An aliquot of the reaction mixture (~300 μ L) was filtered, diluted with DMSO-d₆ and subjected to ¹H-NMR analysis.

Method B: Dual CN-OA-m/Ni catalysis with irradiation at 520 nm



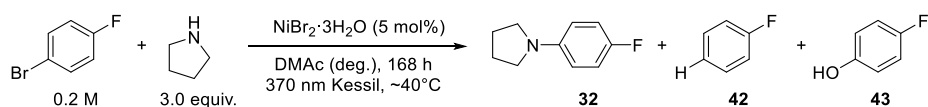
An oven dried vial (19 x 80 mm) equipped with a stir bar was charged with the CN-OA-m (20 mg), 4-bromofluorobenzene (210.0 mg, 131.8 μ l, 1.2 mmol, 1.0 equiv.) and (16.4 mg, 60 μ mol, 5.0 mol%). Subsequently, pyrrolidine (256.0 mg, 295.6 μ l, 3.6 mmol, 3.0 equiv.) and DMAc (anhydrous, 6 mL) were added and the vial was sealed with a septum and Parafilm. The reaction mixture was sonicated for 5-10 min followed by stirring for 5 min until fine dispersion of the solids was achieved and the mixture was then degassed by bubbling N₂ for 10 min. The mixture was irradiated in the photoreactor (green light function of RGB LED strip) at 40 °C with rapid stirring (1400 rpm). After 168 h, one equivalent of 1,3,5-trimethoxybenzene (1.2 mmol) was added and the mixture was stirred for 5 min. An aliquot of the reaction mixture (~300 μ L) was filtered, diluted with DMSO-d₆ and subjected to ¹H-NMR analysis.

Method “Ir”: Dual Ir/Ni catalysis with irradiation at 420 nm

Ir1: An oven dried vial (19 x 80 mm) equipped with a stir bar was charged with 4-bromofluorobenzene (210.0 mg, 131.8 μ l, 1.2 mmol, 1.0 equiv.) and NiBr₂·3H₂O (16.4 mg, 60 μ mol, 5.0 mol%) and a solution of Ir[dF(CF₃)ppy]₂(dtbbpy)PF₆ (0.27 mg, 0.02 mol%) in DMAc (48 μ l). Subsequently, pyrrolidine (256.0 mg, 295.6 μ l, 3.6 mmol, 3.0 equiv.) and DMAc (anhydrous, 6 mL) were added and the vial was sealed with a septum and Parafilm.

Ir2: An oven dried vial (19 x 80 mm) equipped with a stir bar was charged with 4-bromofluorobenzene (52.5 mg, 33.0 μ l, 0.3 mmol, 1.0 equiv.), NiBr₂·3H₂O (4.1 mg, 15 μ mol, 5.0 mol%) and a solution of Ir [dF(CF₃)ppy]₂(dtbbpy)PF₆ (3.37 mg, 1 mol%) in DMAc (600 μ l). Subsequently, pyrrolidine (64.0 mg, 73.9 μ l, 0.9 mmol, 3.0 equiv.) and DMAc (anhydrous, 2.4 mL) were added and the vial was sealed with a septum and Parafilm. The reaction mixture was sonicated for 5-10 min followed by stirring for 5 min and the mixture was then degassed by bubbling N₂ for 10 min. The mixture was irradiated in the photoreactor (blue light function of LED-band) at 40 °C with rapid stirring (1400 rpm). After 24 h, one equivalent of 1,3,5-trimethoxybenzene (Ir1: 202.0 mg, 1.2 mmol/ Ir2: 50.5 mg, 0.3 mmol) was added and the mixture was stirred for 5 min. An aliquot of the reaction mixture (~300 μ L) was filtered, diluted with DMSO-d₆ and subjected to ¹H-NMR analysis.

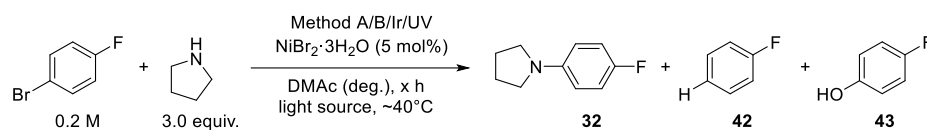
Note: In case if procedure C2, the formation of small amounts of black particles was observed after the reaction.

Method “UV”: Ni catalysis with irradiation at 370 nm

An oven dried vial (19 x 80 mm) equipped with a stir bar was charged 4-bromofluorobenzene (210.0 mg, 131.8 μ l, 1.2 mmol, 1.0 equiv.) and NiBr₂·3H₂O (16.4 mg, 60 μ mol, 5.0 mol%). Subsequently, pyrrolidine (256.0 mg, 295.6 μ l, 3.6 mmol, 3.0 equiv.) and DMAc (anhydrous, 6 mL) were added and the vial was sealed with a septum and Parafilm. The reaction mixture was sonicated for 5-10 min followed by stirring for 5 min and the mixture was then degassed by bubbling N₂ for 10 min. The mixture was irradiated with UV light using the Kessil[®] PR 160-370 nm lamp with rapid stirring (~800 rpm) and cooling by a fan. After 3 h (UV1), 15 h (UV2), 72 h (UV3) and 168 h (UV4) one equivalent of 1,3,5-trimethoxybenzene (202.0 mg, 1.2 mmol) was added and the mixture was stirred for 5 min. An aliquot of the reaction mixture (~300 μ L) was filtered, diluted with DMSO-d₆ and subjected to ¹H-NMR analysis.

Note: The color of the reaction solution changed from yellowish to black and a significant amount of black particles was formed.

The reaction mixtures of procedure A, B, and UV were centrifuged at 3000 rpm for 20 min. The carbon nitride from the blue (procedure A) and green light experiment (procedure B) and the black particles formed during the UV-light experiment (procedure UV) were washed with DMAc (anhydrous 6 mL, followed by centrifugation at 3000 rpm for 20 min and separation of the liquid phase) and acetone (6 mL, followed by centrifugation at 3000 rpm for 20 min and separation of the liquid phase), lyophilized (overnight) and subjected to FTIR, UV-Vis, XRD, , ICP-OES, EDX, XPS as well as SEM and TEM analysis. For comparison, an unused sample of CN-OA-m from the same batch was also analyzed.

Table 4.21. Coupling of 4-bromofluorobenzene and pyrrolidine using different light sources and catalysts.

Entry	Procedure	Conversion [%] ^a	32 [%] ^b	42 [%] ^b	43 [%] ^b
1	A	93	70	6	9
2	A	92	69	7	8
3	A	91	68	6	9
4	A	92	63	7	6
5	A	87	60	7	9
6	A	18	6	2	n.d. ^c
7	A	22	5	n.d.	3
<hr/>					
8	B	quant.	91	5	2
9	B	quant.	89	1	10
10	B	quant.	89	9	1
11	B	99	86	9	2
12	B	quant.	88	1	10
13	B	97	86	2	9
14	B	quant.	84	9	n.d.
<hr/>					
15	Ir1	quant.	77	7	4
16	Ir2	79	33	20	13
<hr/>					
17	UV1	18	7	3	n.d.
18	UV2	39	17	9	4
19	UV3	94	26	32	16
20	UV4	quant.	10	23	9

^aConversion of 4-bromofluorobenzene determined by ¹H-NMR using 1,3,5-trimethoxybenzene as internal standard. ^bNMR yields determined by ¹H-NMR using 1,3,5-trimethoxybenzene as internal standard. ^cnot detected.

4.4.8.1 Powder X-ray diffraction (XRD) and X-ray photoelectron spectroscopy (XPS)

The powder X-ray diffraction spectra (PXRD) of the black material generated during the UV-light experiment (Table 4.21, Entry 17) showed diffraction peaks at 44° , 51° and 76° that could be assigned to the (1 1 1), (2 0 0), (2 2 0) planes of nickel(0) (Figure S13). Spectra of the recovered CN-OA-m (Table 4.20, Entry 7 & 8) materials show a characteristic peak at 27.4° , which corresponds to the in-planar structural packing and inter-planar stacking peaks of the aromatic systems of CN-OA-m. Nickel(0) (diffraction peaks at 44° , 51° and 76°) was detected in the material recovered from experiment using blue LEDs (Method A), and, although in significantly lower quantity, in the material recovered from the experiment using green LEDs (Method B).

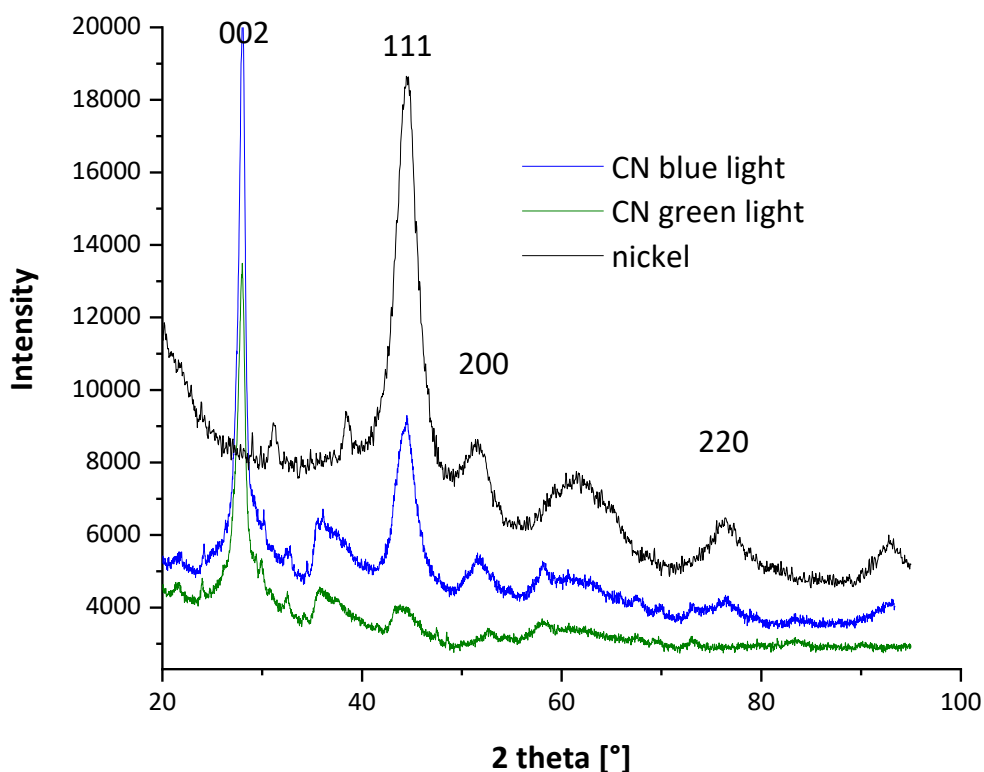


Figure 4.17. XRD measurements of the material generated by UV-light (black line), CN-OA-m after method A with blue light irradiation (blue line) and CN-OA-m after method B with green light irradiation (green line).

XPS scans of the solid material generated during UV light experiments and CN-OA-m recovered from the experiments using blue (Method A) and green LED (Method B) irradiation confirmed the presence of nickel in both samples (Figure 4.18). High-resolution XPS analysis spectra for core levels of Ni2p confirm the presence of Ni²⁺ and Ni⁰ at 854.6 (± 0.02) eV and 852.3 (± 0.02) eV, for CN-OA-m recovered from method A (blue light) and the material generated during UV light irradiation (Figure S14, A). Only Ni²⁺ (854.6 (± 0.02) eV) species were detected in the CN-OA-m sample recovered from the experiment using method B (green light). The high-resolution XPS spectra of the C 1s core level spectra shows typical C-C and N-C=N bonding signals for all CN-OA-m samples (Figure 4.18, B). The N 1s spectra contain two main peaks that are typical for carbon nitrides and can be assigned to i) sp² bonded nitrogen in tri-s-triazine groups (C-N=C), and ii) sp³ amino groups (C-NH) for all CN-OA-m samples. The calculated elemental composition indicates a two times higher concentration of nickel on CN-OA-m recovered from method A (blue light) compared to CN-OA-m recovered from method B (green light) (Table 4.22).

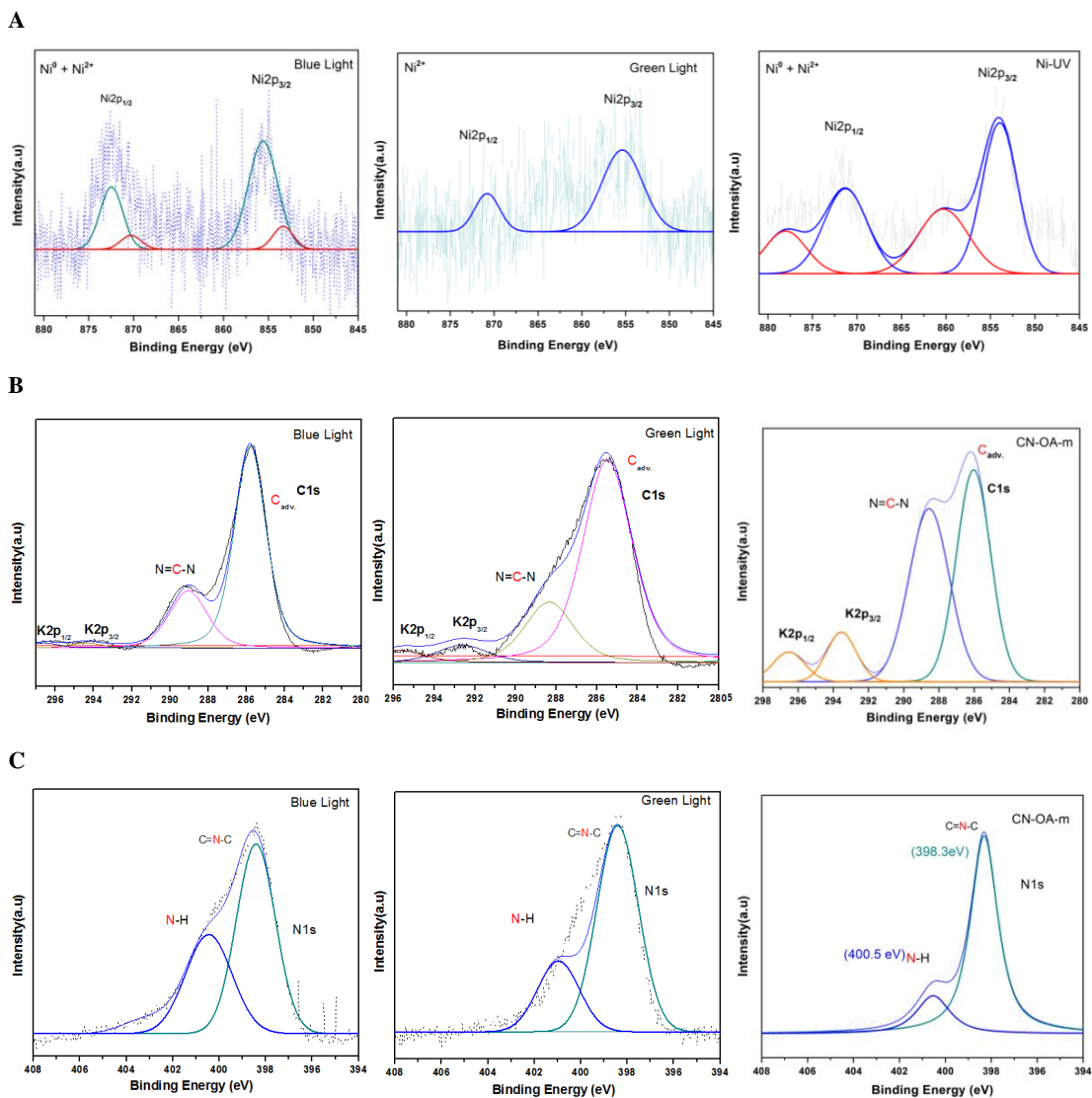


Figure 4.18. A) High-resolution XPS analysis spectra for core levels of Ni $2p_{3/2}$: CN-OA-m recovered from experiments using method A (blue light) and method B (green light), and the heterogeneous material generated during UV-light experiments (Ni-UV). B) High-resolution XPS analysis spectra for core levels of C $1s$: CN-OA-m recovered from experiments using method A (blue light) and method B (green light), and unused CN-OA-m. C) High-resolution XPS analysis spectra for core levels of N $1s$: CN-OA-m recovered from experiments using method A (blue light) and method B (green light), and unused CN-OA-m. has been deconvoluted using *Lorentzian-Gaussian* peak fitting functions with Shirley background deletion.

Table 4.22. XPS Elemental composition of CN-OA-m and CN-OA-m recovered from experiments using method A and B.

Sample	% w/w N	% w/w C	% w/w K	% w/w Ni
CN-OA-m	57.257	41.191	1.552	---
CN-OA-m blue light^a	61.094	37.718	0.365	0.822
CN-OA-m green light^b	59.021	39.983	0.709	0.377

^aSample recovered from experiment described in Table 4.21, Entry 7. ^bSample recovered from experiment described in Table 4.21, Entry 8.

4.4.8.2 Scanning transmission electron microscopy (STEM)

4.4.8.2.1 CN-OA-m recovered from method A (blue LEDs) and method B (green LEDs)

Scanning transmission electron microscopy (STEM) was used to visualize nickel particles on the surface of the recovered CN-OA-m. High-angle annular dark-field (HAADF) images show round- to oval-shaped particles with sizes ranging 10-20 nm. The polycrystalline particle consist of smaller ones (1-5 nm), which agglomerated on the surface (Figure 4.19 and 4.20). The images show the porous structure of CN-OA-m containing particles that show a diffraction pattern indicating Ni-species deposition. The exact lattice of a selected nickel particle is shown in higher resolution. The STEM images of CN-OA-m recovered from experiments using method B (green LED) (Figure 4.20) show a significantly lower amount of (agglomerated) nickel particles compared to using method A (blue LED, Figure 4.19). This confirms the results obtained using XRD (Figure 4.17), XPS (Figure 4.18), EDX (Table 4.23) and ICP-OES (Table 4.24) analysis.

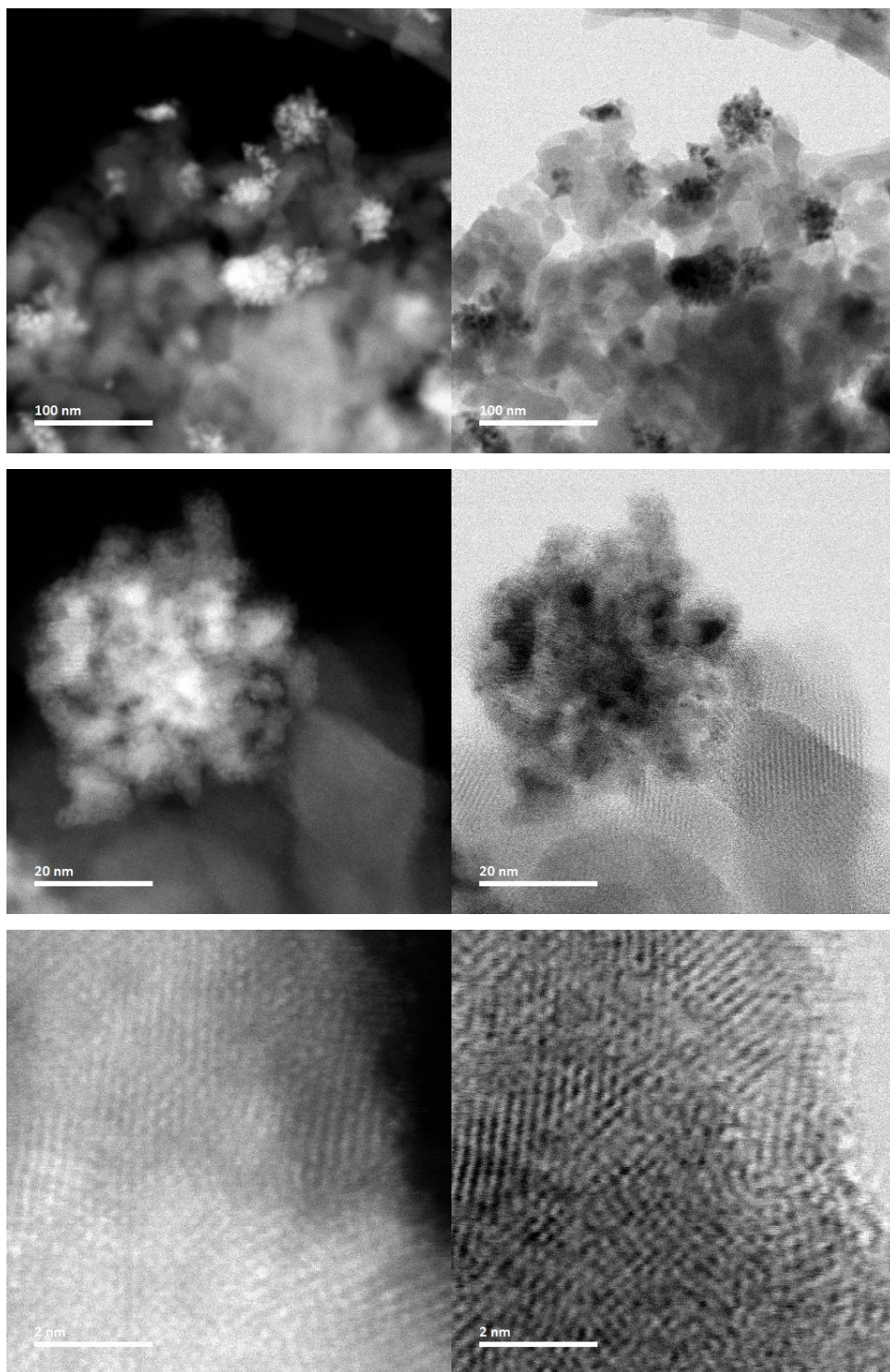


Figure 4.19. HAADF-STEM brightfield (left)/darkfield (right) images showing nickel particles (bright spots in brightfield and dark spots in darkfield) on CN-OA-m recovered from the experiment using method A (blue LED).

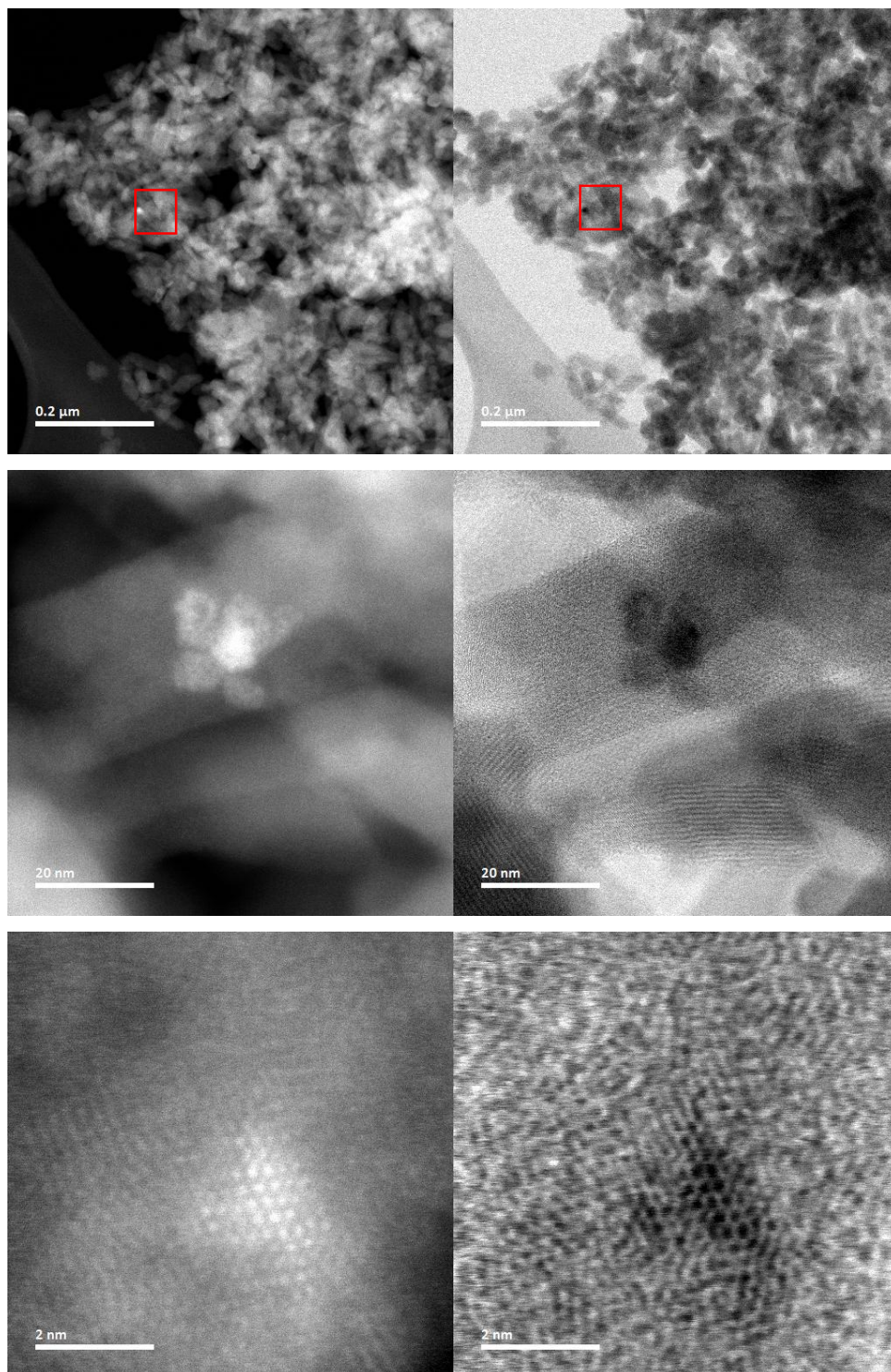


Figure 4.20. HAADF-STEM brightfield (left)/darkfield (right) showing a nickel particle (bright spot in brightfield and dark spot in darkfield) on CN-OA-m recovered from the experiment using method B (green LED).

4.4.8.2.2 Heterogeneous material generated during experiments using the UV method (photocatalyst-free and UV-light)

The STEM image shows the solid material formed using method C (UV-light). Although the particle mainly consists of nickel, lighter elements can be additionally identified. EDX analysis (Table 4.23) shows the presence of carbon, indicating that agglomerated nickel species incorporate organic materials. This is in agreement with the low mass-balance observed during these reactions (e.g. Table 4.21, Entry 20), suggesting substrate/product degradation presumably by the high energy light source.

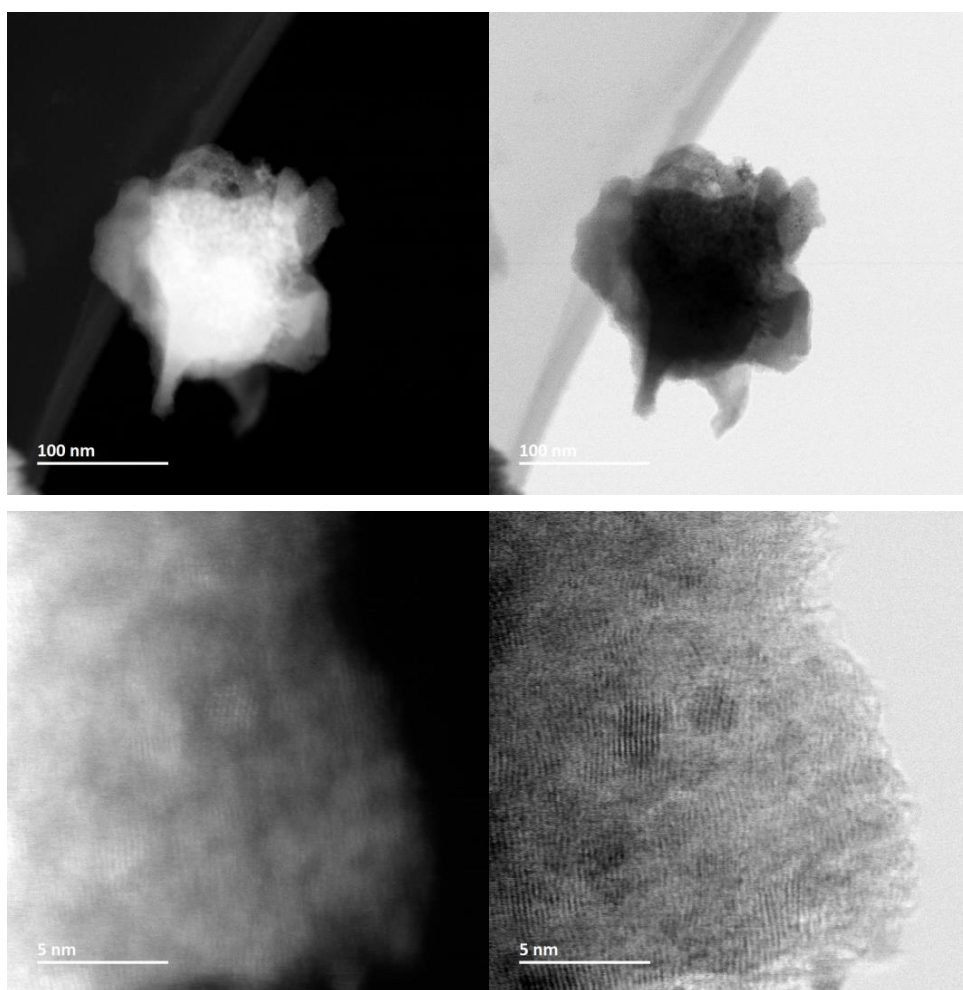


Figure 4.21. HAADF-STEM brightfield (left)/darkfield (right) images of nickel particles (bright spots in brightfield and dark spots in darkfield) after UV-light method (photocatalyst-free).

4.4.8.3 Scanning electron microscopy (SEM)

SEM images of the new and recovered CN-OA-m samples showed a porous texture that was not altered during the catalytic transformation (Figure 4.22).

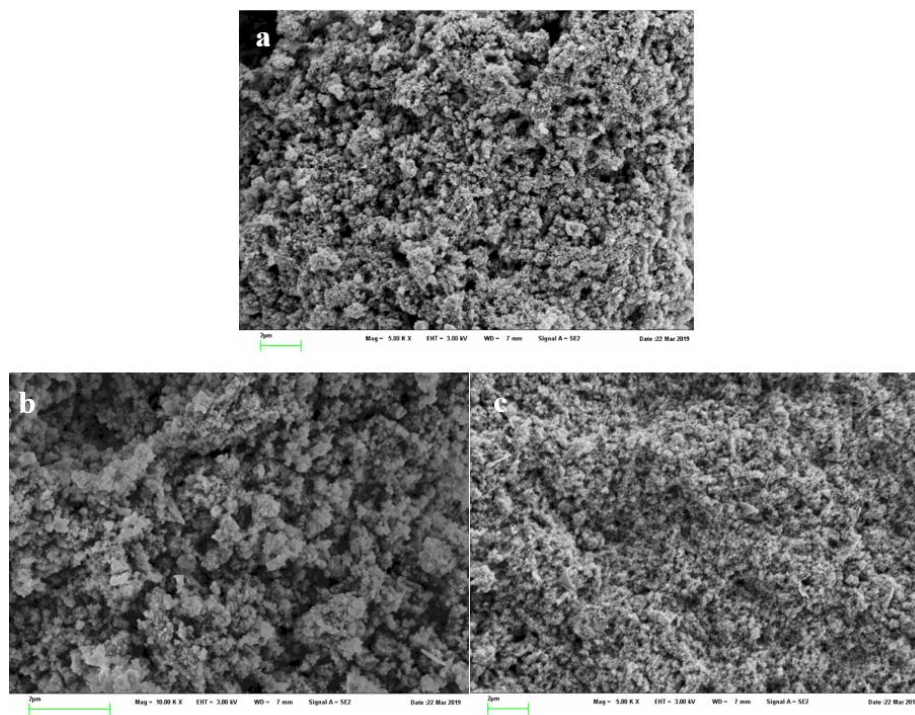


Figure 4.22. SEM images of CN-OA-m new (A), CN-OA-m recovered from the cross-coupling using blue light (Table 4.21, Entry 7) (B), and CN-OA-m recovered from the cross-coupling using green light (Table 4.21, Entry 8) (C).

4.4.8.4 Energy-dispersive X-ray spectroscopy (EDX) and inductively coupled plasma atomic emission spectroscopy (ICP-OES)

Elemental analysis via EDX (Table 4.23) and ICP-OES (Table 4.24) analysis of the recovered CN-OA-m samples shows a 3 times higher Ni concentration for the blue light experiment. The material from the blue light experiment contains ~12-14 w/w % Ni suggesting that ~70% of the homogeneous nickel catalyst were deposited on the CN-OA-m during the model reaction. The material from the green light experiment contains ~3-4 w/w % Ni suggesting that ~70% of the homogeneous nickel catalyst were deposited on the CN-OA-m during the model reaction.

Table 4.23. EDX elemental composition acquired from new and recovered CN-OA-m.

Sample	% w/w N	% w/w C	% w/w O	% w/w K	% w/w Ni
CN-OA-m	42.56	37.59	3.65	1.06	0.05
CN-OA-m from Method A (blue light) ^a	36.25	30.27	7.16	8.60	13.90
CN-OA-m from Method B (green light) ^b	47.19	29.46	7.79	8.86	3.38
Solid from UV- experiment ^c	22.8	21.00	18.92	-	26.71

^aSample recovered from experiment described in Table 4.21, Entry 7. ^bSample recovered from experiment described in Table 4.21, Entry 8. ^cSample recovered from experiment described in Table 4.21, Entry 17.

Table 4.24. ICP-OES measurements of the nickel content on the new and recovered CN-OA-m.

Sample	Ni [mg/g CN]	% absorbed Ni
CN-OA-m new	0.69	0.39
CN-OA-m from Method A (blue light) ^a	126	71.2
CN-OA-m from Method B (green light) ^b	35.5	20.1

^aSample recovered from experiment described in Table 4.21, Entry 7.

^bSample recovered from experiment described in Table 4.21, Entry 8.

4.4.8.5 Fourier-transform infrared spectroscopy (FTIR) and Ultraviolet-visible spectroscopy (UV-VIS)

FTIR spectra of the new and recovered CN-OA-m samples were identical (Figure 4.23).

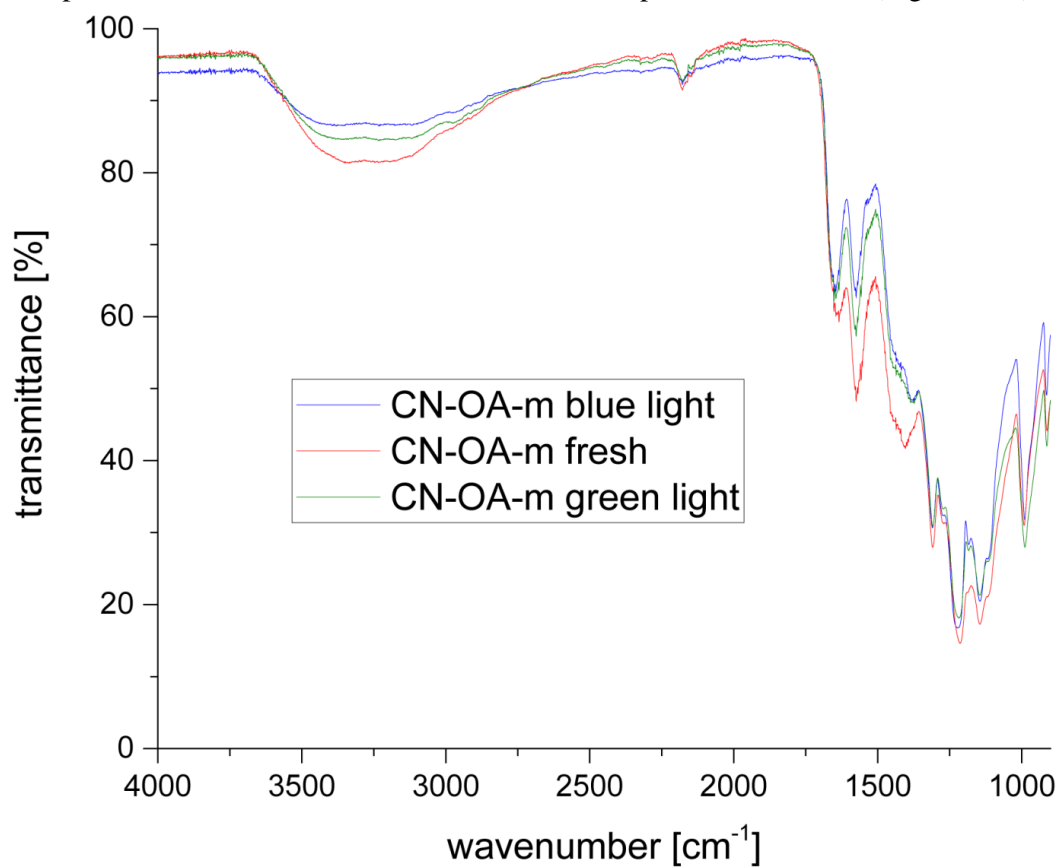


Figure 4.23. FTIR spectra of CN-OA-m new (red), CN-OA-m recovered from the cross-coupling using blue light (blue), and CN-OA-m recovered from the cross-coupling using green light (green).

The UV-Vis spectra of the CN-OA-m recovered from the cross-coupling using green light and CN-OA-m recovered from the cross-coupling using blue showed an increased absorption in the visible region (>460 nm) compared to a unused CN-OA-m sample.

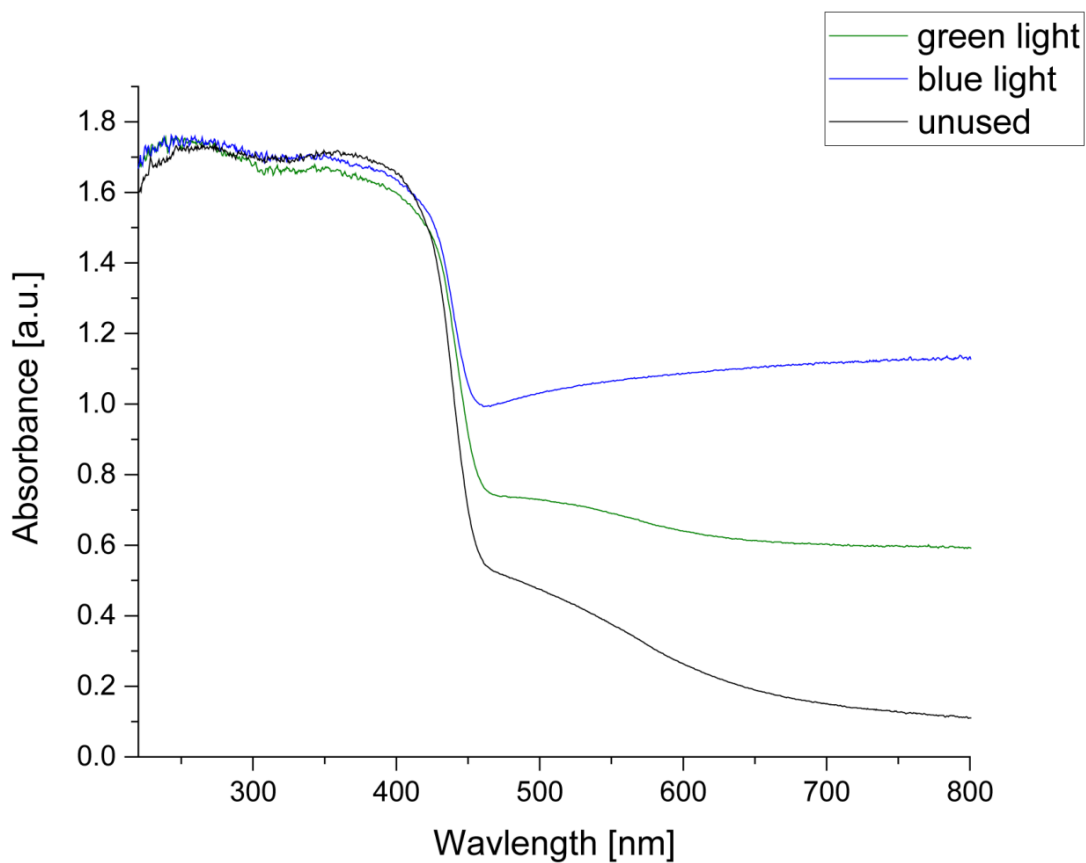
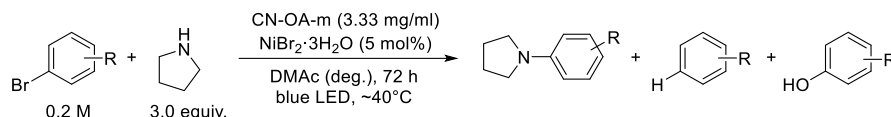


Figure 4.24. UV/Vis absorption spectra of CN-OA-m new (grey), CN-OA-m recovered from the cross-coupling using blue light (blue), and CN-OA-m recovered from the cross-coupling using green light (green).

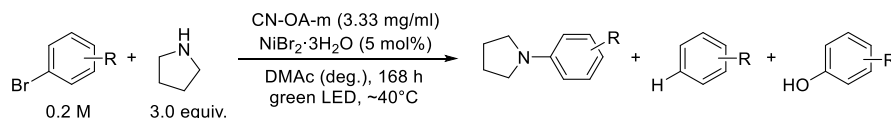
4.4.9 Studies on the reaction of bromobenzene, 3-bromotoluene, 1-bromo-4-*tert*-butylbenzene, and 4-bromoanisole with pyrrolidine.

Method A: Dual CN-OA-m/Ni catalysis with irradiation at 450 nm



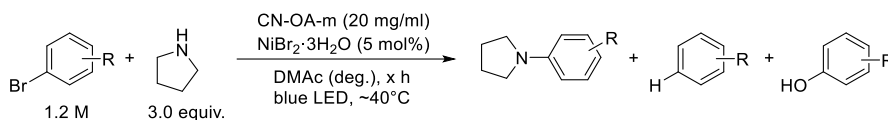
An oven dried vial (19 x 80 mm) equipped with a stir bar was charged with the CN-OA-m (20 mg), aryl bromide (1.2 mmol, 1.0 equiv.) and NiBr₂·3H₂O (16.4 mg, 60 μmol, 5.0 mol%). Subsequently, pyrrolidine (256.0 mg, 295.6 μl, 3.6 mmol, 3.0 equiv.) and DMAc (anhydrous, 6 mL) were added and the vial was sealed with a septum and Parafilm. The reaction mixture was sonicated for 5-10 min followed by stirring for 5 min until fine dispersion of the solids was achieved and the mixture was then degassed by bubbling N₂ for 10 min. The mixture was irradiated in the photoreactor (blue light function of RGB LED strip) at 40 °C with rapid stirring (1400 rpm). After 72 h, one equivalent of 1,3,5-trimethoxybenzene (1.2 mmol) was added and the mixture was stirred for 5 min. An aliquot of the reaction mixture (~300 μL) was filtered, diluted with DMSO-d₆ and subjected to ¹H-NMR analysis.

Method B: Dual CN-OA-m/Ni catalysis with irradiation at 520 nm

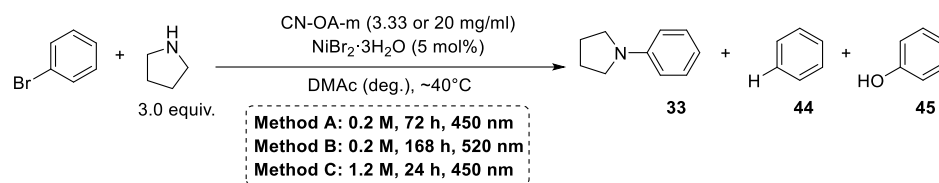


An oven dried vial (19 x 80 mm) equipped with a stir bar was charged with the CN-OA-m (20 mg), aryl bromide (1.2 mmol, 1.0 equiv.) and NiBr₂·3H₂O (16.4 mg, 60 μmol, 5.0 mol%). Subsequently, pyrrolidine (256.0 mg, 295.6 μl, 3.6 mmol, 3.0 equiv.) and DMAc (anhydrous, 6 mL) were added and the vial was sealed with a septum and Parafilm. The reaction mixture was sonicated for 5-10 min followed by stirring for 5 min until fine dispersion of the solids was achieved and the mixture was then degassed by bubbling N₂ for 10 min. The mixture was irradiated in the photoreactor (green light function of RGB LED strip) at 40 °C with rapid stirring (1400 rpm). After 168 h, one equivalent of 1,3,5-trimethoxybenzene (1.2 mmol) was added and the mixture was stirred for 5 min. An aliquot of the reaction mixture (~300 μL) was filtered, diluted with DMSO-d₆ and subjected to ¹H-NMR analysis.

Method C: Dual CN-OA-m/Ni catalysis with irradiation at 450 nm and higher concentration (1.2 M)



An oven dried vial (19 x 80 mm) equipped with a stir bar was charged with the CN-OA-m (20 mg), aryl bromide (1.2 mmol, 1.0 equiv.) and NiBr₂·3H₂O (16.4 mg, 60 μmol, 5.0 mol%). Subsequently, pyrrolidine (256.0 mg, 295.6 μl, 3.6 mmol, 3.0 equiv.) and DMAc (anhydrous, 1 mL) were added and the vial was sealed with a septum and Parafilm. The reaction mixture was sonicated for 5-10 min followed by stirring for 5 min until fine dispersion of the solids was achieved and the mixture was then degassed by bubbling N₂ for 10 min. The mixture was irradiated in the photoreactor (blue light function of RGB LED strip) at 40 °C with moderate stirring (600 rpm). After respective reaction time, one equivalent of 1,3,5-trimethoxybenzene (202.0 mg, 1.2 mmol) was added and the mixture was stirred for 5 min. An aliquot of the reaction mixture (~300 μL) was filtered, diluted with DMSO-d₆ and subjected to ¹H-NMR analysis.

Table 4.25. Coupling of bromobenzene and pyrrolidine using methods A-C.

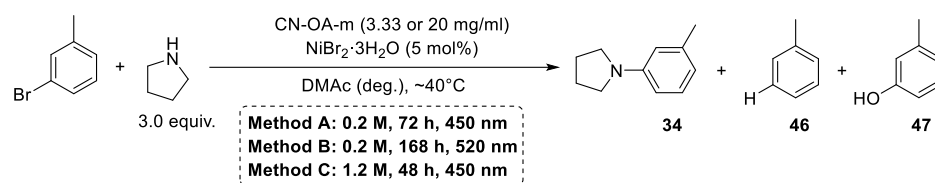
Entry	Procedure	Conversion [%] ^a	33 [%] ^b	44 [%] ^b	45 [%] ^b
1	A	quant.	74	8	11
2	A	quant.	68	11	10
3	A	quant.	67	11	12
4	A	quant.	66	10	11
5	A	67	44	7	6
6	A	56	32	5	4
<hr/>					
7	B	quant.	94	4	3
8	B	quant.	93	4	3
9	B	quant.	91	5	5
10	B	quant.	90	4	4
11	B	quant.	88	4	5
12	B	quant.	87	4	5
<hr/>					
13	C	quant.	86	8	4
14	C	quant.	85	7	3
15	C	99	85	8	3
16	C	quant.	85	9	3
17	C	quant.	84	8	3
18	C	quant.	84	9	3
19	C ^d	quant.	85	5	2
20	C ^d	quant.	82	5	1

Chapter 4

^aConversion of bromobenzene determined by ¹H-NMR using 1,3,5-trimethoxybenzene as internal standard.

^bNMR yields determined by ¹H-NMR using 1,3,5-trimethoxybenzene as internal standard. ^cnot detected.

^dCarried out using 520 nm LEDs and 168 h reaction time.

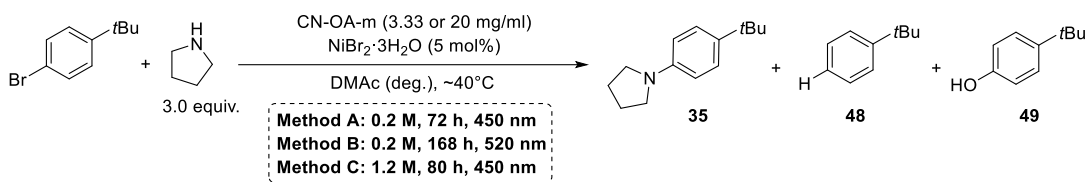
Table 4.26. Coupling of 3-bromotoluene and pyrrolidine using methods A-C.

Entry	Procedure	Conversion [%] ^a	34 [%] ^b	46 [%] ^b	47 [%] ^b
1	A	quant.	74	17	6
2	A	quant.	72	17	6
3	A	quant.	72	18	4
4	A	quant.	61	18	12
5	A	64	31	12	9
6	A	52	20	13	8
<hr/>					
7	B	quant.	93	5	4
8	B	quant.	86	10	4
9	B	quant.	85	10	5
10	B	quant.	84	10	5
11	B	quant.	84	10	7
12	B	quant.	83	10	6
<hr/>					
13	C	quant.	85	14	2
14	C	quant.	84	14	3
15	C	quant.	83	14	3
16	C	quant.	83	14	3
17	C	quant.	82	15	3
18	C	quant.	81	16	3
19	C ^d	quant.	80	6	0

^aConversion of 3-bromotoluene determined by ¹H-NMR using 1,3,5-trimethoxybenzene as internal standard.

^bNMR yields determined by ¹H-NMR using 1,3,5-trimethoxybenzene as internal standard. ^cnot detected.

^dCarried out using 520 nm LEDs and 168 h reaction time.

Table 4.27. Coupling of 1-bromo-4-*tert*-butylbenzene and pyrrolidine using methods A-C.

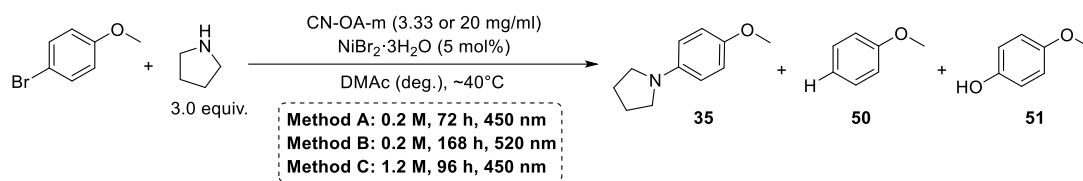
Entry	Procedure	Conversion [%] ^a	35 [%] ^b	48 [%] ^b	49 [%] ^b
1	A	98	70	13	9
2	A	99	69	17	7
3	A	quant.	67	14	8
4	A	88	57	16	9
5	A	82	53	15	9
6	A	90	52	13	7

7	B	quant.	92	5	3
8	B	96	90	4	2
9	B	94	87	3	3
10	B	91	85	3	2
11	B	57	50	4	2
12	B	30	28	1	2

13	C	quant.	82	9	2
14	C	quant.	80	9	1
15	C	quant.	80	9	2
16	C	quant.	80	9	2
17	C	quant.	80	9	3
18	C	quant.	80	10	3
19	C ^d	91	82	4	0

^aConversion of 1-bromo-4-*tert*-butylbenzene determined by ¹H-NMR using 1,3,5-trimethoxybenzene as internal standard. ^bNMR yields determined by ¹H-NMR using 1,3,5-trimethoxybenzene as internal standard.

^cnot detected. ^dCarried out using 520 nm LEDs and 72 h reaction time.

Table 4.28. Coupling of 4-bromoanisole and pyrrolidine using methods A-C.

Entry	Procedure	Conversion [%] ^a	35 [%] ^b	50 [%] ^b	51 [%] ^b
1	A	86	80	6	n.d. ^c
2	A	91	78	12	2
3	A	90	72	10	5
4	A	66	53	8	2
5	A	43	32	4	2
6	A	13	4	n.d.	2
7	B	82	77	7	0
8	B	83	77	6	0
9	B	76	68	6	0
10	B	68	60	4	4
11	B	68	60	4	3
12	B	58	52	4	2
13	C	quant.	81	8	5
14	C	quant.	80	11	5
15	C	quant.	80	11	5
16	C	quant.	80	8	4
17	C	quant.	79	11	4
18	C	quant.	77	9	6
19	C ^d	quant.	84	8	1
20	C ^d	quant.	83	8	0

Chapter 4

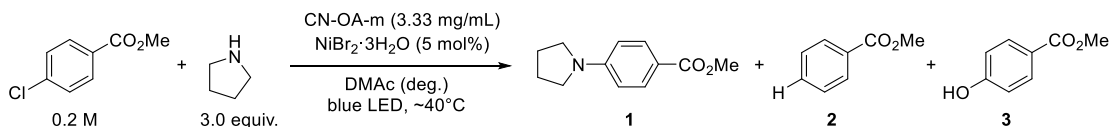
^aConversion of 4-bromoanisole determined by ¹H-NMR using 1,3,5-trimethoxybenzene as internal standard.

^bNMR yields determined by ¹H-NMR using 1,3,5-trimethoxybenzene as internal standard. ^cnot detected.

^dCarried out using 520 nm LEDs and 168 h reaction time.

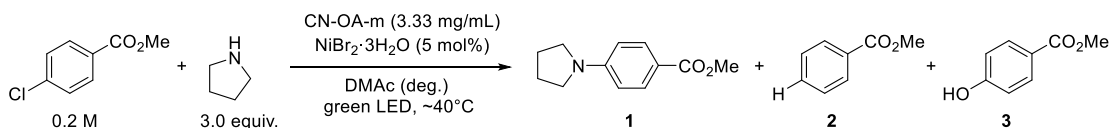
4.4.10 Studies on the reaction of pyrrolidine with aryl chlorides

Method A: Dual CN-OA-m/Ni catalysis with irradiation at 450 nm

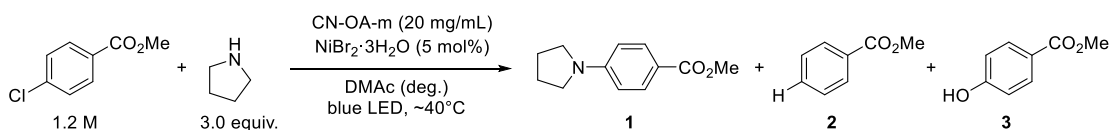


An oven dried vial (19 x 80 mm) equipped with a stir bar was charged with the CN-OA-m (20 mg), methyl 4-chloromethylbenzoate (204.7 mg, 1.2 mmol, 1.0 equiv.) and NiBr₂·3H₂O (16.4 mg, 60 μmol, 5.0 mol%). Subsequently, pyrrolidine (64.0 mg, 295.6 μl, 3.6 mmol, 3.0 equiv.) and DMAc (anhydrous, 6 mL) were added and the vial was sealed with a septum and Parafilm. The reaction mixture was sonicated for 5-10 min followed by stirring for 5 min until fine dispersion of the solids was achieved and the mixture was then degassed by bubbling N₂ for 10 min. The mixture was irradiated in the photoreactor (blue light of LED-band) at 40 °C with rapid stirring (1400 rpm). After respective reaction time, one equivalent of 1,3,5-trimethoxybenzene (202.0 mg, 1.2 mmol) was added and the mixture was stirred for 5 min. An aliquot of the reaction mixture (~300 μL) was filtered, diluted with DMSO-d₆ and subjected to ¹H-NMR analysis.

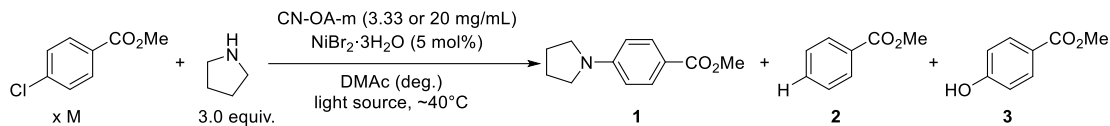
Method B: Dual CN-OA-m/Ni catalysis with irradiation at 520 nm



An oven dried vial (19 x 80 mm) equipped with a stir bar was charged with the CN-OA-m (20 mg), methyl 4-chloromethylbenzoate (204.7 mg, 1.2 mmol, 1.0 equiv.) and NiBr₂·3H₂O (16.4 mg, 60 μmol, 5.0 mol%). Subsequently, pyrrolidine (64.0 mg, 295.6 μl, 3.6 mmol, 3.0 equiv.) and DMAc (anhydrous, 6 mL) were added and the vial was sealed with a septum and Parafilm. The reaction mixture was sonicated for 5-10 min followed by stirring for 5 min until fine dispersion of the solids was achieved and the mixture was then degassed by bubbling N₂ for 10 min. The mixture was irradiated in the photoreactor (blue light of LED-band) at 40 °C with rapid stirring (1400 rpm). After respective reaction time, one equivalent of 1,3,5-trimethoxybenzene (202.0 mg, 1.2 mmol) was added and the mixture was stirred for 5 min. An aliquot of the reaction mixture (~300 μL) was filtered, diluted with DMSO-d₆ and subjected to ¹H-NMR analysis.

Method C: Dual CN-OA-m/Ni catalysis with irradiation at 450 nm and higher concentration (1.2 M)

An oven dried vial (19 x 80 mm) equipped with a stir bar was charged with the CN-OA-m (20 mg), methyl 4-chloromethylbenzoate (204.7 mg, 1.2 mmol, 1.0 equiv.) and NiBr₂·3H₂O (16.4 mg, 60 μmol, 5.0 mol%). Subsequently, pyrrolidine (64.0 mg, 295.6 μl, 3.6 mmol, 3.0 equiv.) and DMAc (anhydrous, 1 mL) were added and the vial was sealed with a septum and Parafilm. The reaction mixture was sonicated for 5-10 min followed by stirring for 5 min until fine dispersion of the solids was achieved and the mixture was then degassed by bubbling N₂ for 10 min. The mixture was irradiated in the photoreactor (blue light or green function of LED-band) at 40 °C with moderate stirring (600 rpm). After respective reaction time, one equivalent of 1,3,5-trimethoxybenzene (202.0 mg, 1.2 mmol) was added and the mixture was stirred for 5 min. An aliquot of the reaction mixture (~300 μL) was filtered, diluted with DMSO-d₆ and subjected to ¹H-NMR analysis.

Table 4.29. Coupling of methyl 4-chlorobenzoate and pyrrolidine using methods A-C.

Entry	Method	Time [days]	Conversion [%] ^a	1 [%] ^b	2 [%] ^b	3 [%] ^b
1	A	3	47	37	2	n.d. ^c
2	A	7	78	65	7	3
3	A	14	91	65	16	7
4	B	3	59	41	1	12
5	B	7	76	72	4	n.d.
6	B	14	89	83	n.d.	9
7	C	1	79	75	3	1
8	C	2	97	92	3	2
9	C	3	97	89	4	2
10	C	4	99	89	3	2

^aConversion of methyl 4-chlorobenzoate determined by ¹H-NMR using 1,3,5-trimethoxybenzene as internal standard. ^bNMR yields determined by ¹H-NMR using 1,3,5-trimethoxybenzene as internal standard. ^cnot detected

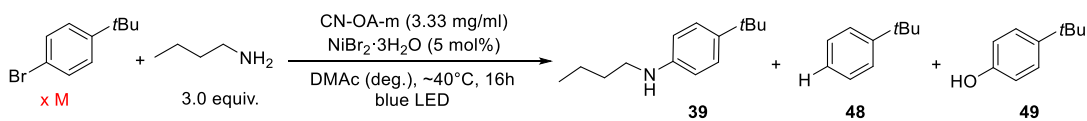
Table 4.30. NMR-Yields for the coupling of electroneutral and electron-rich aryl chlorides with pyrrolidine at 40 °C and blue LED irradiation using method C.

Aryl chloride				
Yield ^a	18%	10%	5%	2%

^aNMR yields determined by ¹H-NMR using 1,3,5-trimethoxybenzene as internal standard.

4.4.11 Studies on the coupling of *n*-butylamine with aryl halides

Table 4.31. Coupling of 1-bromo-4-*tert*-butylbenzene and *n*-butylamine using different concentrations at 40 °C and blue light.

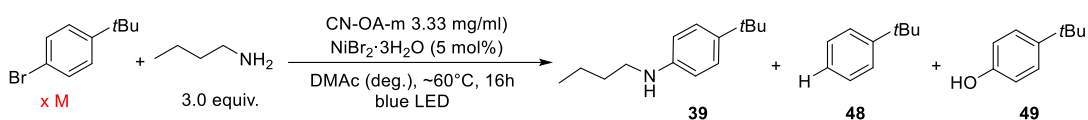


Entry	Concentration [mol/L]	Conversion [%] ^a	39 [%] ^b	48 [%] ^b	49 [%] ^b
1	0.2	8	8	n.d. ^c	n.d.
2	0.4	6	6	n.d.	n.d.
3	0.6	4	4	n.d.	n.d.
4	0.8	3	3	n.d.	n.d.
5	1.2	2	2	n.d.	n.d.

^aConversion of 1-bromo-4-*tert*-butylbenzene determined by ¹H-NMR using 1,3,5-trimethoxybenzene as internal standard. ^bNMR yields determined by ¹H-NMR using 1,3,5-trimethoxybenzene as internal standard.

^cnot detected.

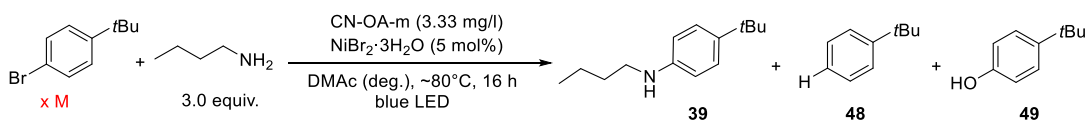
Table 4.32. Coupling of 1-bromo-4-*tert*-butylbenzene and *n*-butylamine using different concentrations at 60 °C and blue light.



Entry	Concentration [mol/L]	Conversion [%] ^a	39 [%] ^b	48 [%] ^b	49 [%] ^b
1	0.2	22	20	2	n.d. ^c
2	0.4	15	13	2	n.d.
3	0.6	11	10	1	n.d.
4	0.8	9	8	1	n.d.
5	1.2	7	6	1	n.d.

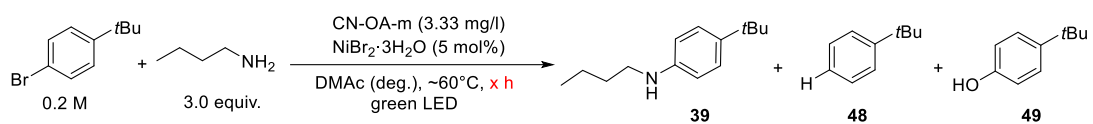
^aConversion of 1-bromo-4-*tert*-butylbenzene determined by ¹H-NMR using 1,3,5-trimethoxybenzene as internal standard. ^bNMR yields determined by ¹H-NMR using 1,3,5-trimethoxybenzene as internal standard. ^cnot detected.

Table 4.33. Coupling of 1-bromo-4-*tert*-butylbenzene and *n*-butylamine using different concentrations at 80 °C.



Entry	Concentration [mol/L]	Conversion [%] ^a	39 [%] ^b	48 [%] ^b	49 [%] ^b
1	0.2	26	26	n.d. ^c	n.d.
2	0.4	14	12	2	n.d.
3	0.6	10	10	n.d.	n.d.
4	0.8	15	15	n.d.	n.d.
5	1.2	6	4	2	n.d.

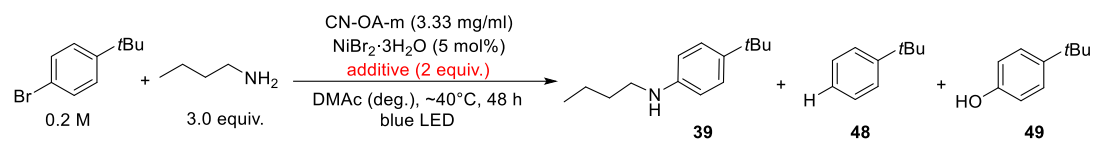
^aConversion of 1-bromo-4-*tert*-butylbenzene determined by ¹H-NMR using 1,3,5-trimethoxybenzene as internal standard. ^bNMR yields determined by ¹H-NMR using 1,3,5-trimethoxybenzene as internal standard. ^cnot detected.

Table 4.34. Coupling of 1-bromo-4-*tert*-butylbenzene and *n*-butylamine at 60 °C and green light irradiation.

Entry	Time [h]	Conversion [%] ^a	37 [%] ^b	45 [%] ^b	46 [%] ^b
1	72	20	20	n.d. ^c	n.d.
2	96	20	20	n.d.	n.d.

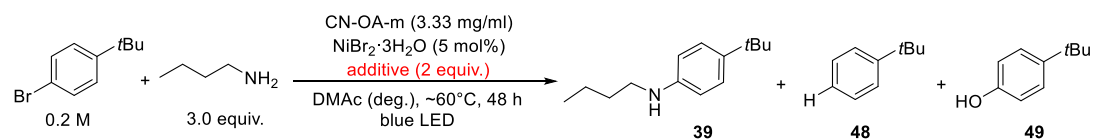
^aConversion of 1-bromo-4-*tert*-butylbenzene determined by ¹H-NMR using 1,3,5-trimethoxybenzene as internal standard. ^bNMR yields determined by ¹H-NMR using 1,3,5-trimethoxybenzene as internal standard.

^cnot detected.

Table 4.35. Additive screening for the coupling of 1-bromo-4-*tert*-butylbenzene and *n*-butylamine at 40 °C.

Entry	base	Conversion [%] ^a	39 [%] ^b	48 [%] ^b	49 [%] ^b
1	MTBD ^c	51	48	2	n.d. ^d
2	DABCO ^e	20	20	n.d.	n.d.
3	none	14	14	n.d.	n.d.
4	quinuclidine ^f	14	14	n.d.	n.d.
6	Pyrrolidine ^g	14	13	1	n.d.
7	DBU ^h	11	10	1	n.d.
5	BIPA ⁱ	10	9	1	n.d.

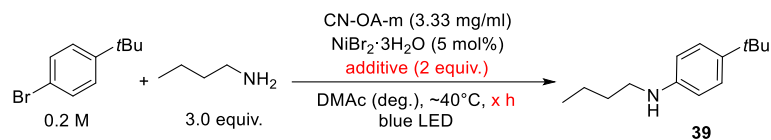
^aConversion of 1-bromo-4-*tert*-butylbenzene determined by ¹H-NMR using 1,3,5-trimethoxybenzene as internal standard. ^bNMR yields determined by ¹H-NMR using 1,3,5-trimethoxybenzene as internal standard. ^c7-Methyl-1,5,7-triazabicyclo[4.4.0]dec-5-ene. ^dnot detected. ^e1,4-diazabicyclo[2.2.2]octane. ^f1-Azabicyclo[2.2.2]octane. ^g10 mol%. ^h1,8-Diazabicyclo(5.4.0)undec-7-ene. ⁱ*N*-*tert*-butylisopropylamine.

Table 4.36. Additive screening for the coupling of 1-bromo-4-*tert*-butylbenzene and *n*-butylamine at 60 °C.

Entry	base	Conversion [%] ^a	39 [%] ^b	48 [%] ^b	49 [%] ^b
1	MTBD ^c	62	55	6	n.d. ^d
2	DABCO ^e	64	49	9	5
3	none	46	39	7	n.d.

^aConversion of 1-bromo-4-*tert*-butylbenzene determined by ¹H-NMR using 1,3,5-trimethoxybenzene as internal standard. ^bNMR yields determined by ¹H-NMR using 1,3,5-trimethoxybenzene as internal standard. ^c7-Methyl-1,5,7-triazabicyclo[4.4.0]dec-5-ene. ^dnot detected. ^e1,4-diazabicyclo[2.2.2]octane.

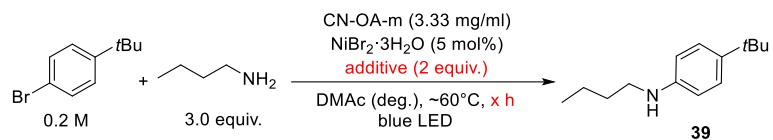
Table 4.37. Time study using no additive, DABCO, and MTBD for the coupling of 1-bromo-4-*tert*-butylbenzene and *n*-butylamine at 40 °C and blue LED irradiation. ^a












additive		48 h		96 h		168 h
none		Yield: 14%		Yield: 16%		Yield: 18%
DABCO ^b		Yield: 20%		Yield: 35%		Yield: 37%
MTBD ^c		Yield: 48%		Yield: 72%		Yield: 85%

^aNMR yields determined by ¹H-NMR using 1,3,5-trimethoxybenzene as internal standard. ^b1,4-diazabicyclo[2.2.2]octane. ^c7-Methyl-1,5,7-triazabicyclo[4.4.0]dec-5-ene.

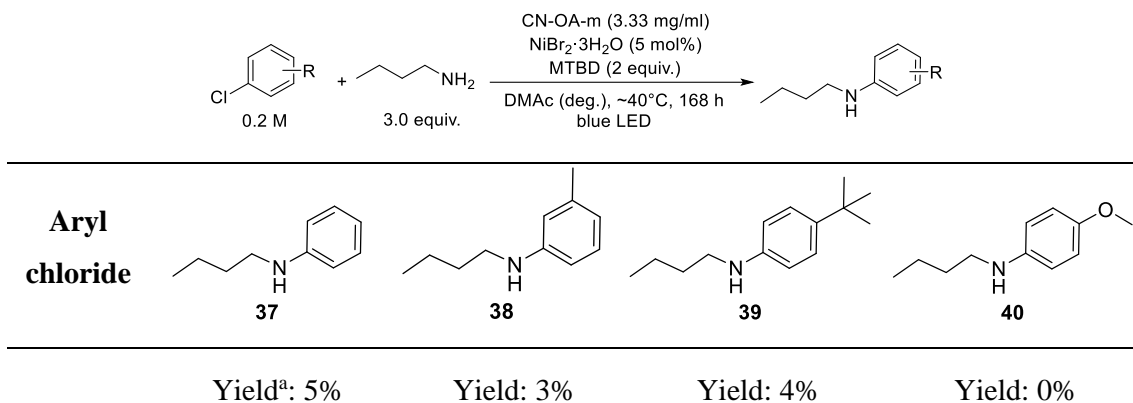
Table 4.38. Time study using no additive, DABCO and MTBD for the coupling of 1-bromo-4-*tert*-butylbenzene and *n*-butylamine at 60 °C and blue LED irradiation. ^a



additive		48 h		96 h		168 h
none		Yield: 39%		Yield: 30%		Yield: 42%
DABCO ^b		Yield: 49%		Yield: 42%		Yield: 35%
MTBD ^c		Yield: 55%		Yield: 50%		Yield: 38%

^aNMR yields determined by ¹H-NMR using 1,3,5-trimethoxybenzene as internal standard. ^b1,4-diazabicyclo[2.2.2]octane. ^c7-Methyl-1,5,7-triazabicyclo[4.4.0]dec-5-ene.

Table 4.39. NMR-Yields for the coupling of electro-neutral and electron-rich aryl chlorides with *n*-butylamine using MTBD at 40 °C and blue LED irradiation.



^aNMR yields determined by ¹H-NMR using 1,3,5-trimethoxybenzene as internal standard. ^bMTBD= 7-Methyl-1,5,7-triazabicyclo[4.4.0]dec-5-ene.

4.4.12 Nickel-black formation: Time studies in absence of aryl halides

General procedure. An oven dried vial (19 x 80 mm) equipped with a stir bar was charged with CN-OA-m (20 mg), and $\text{NiBr}_2 \cdot 3\text{H}_2\text{O}$ (0.06 mmol). Subsequently, the amine (3.6 mmol) (and - in case of additive experiments - 7-Methyl-1,5,7-triazabicyclo[4.4.0]dec-5-ene (MTBD, 2.4 mmol), or 1,4-diazabicyclo[2.2.2]octane (DABCO, 2.4 mmol)) and DMAc (anhydrous, Method A, B, and D: 6 mL, Method C: 1 mL) were added and the vial was sealed with a septum and Parafilm. The reaction mixture was sonicated for 5-10 min until fine dispersion of the solids was achieved and the mixture was then degassed by bubbling N_2 for 10 min. The mixture was irradiated in the photoreactor (blue (450 nm) or green (520 nm) light at 40 or 60°C. Pictures of the reaction mixtures were taken regularly to study the rate of Ni-black formation.

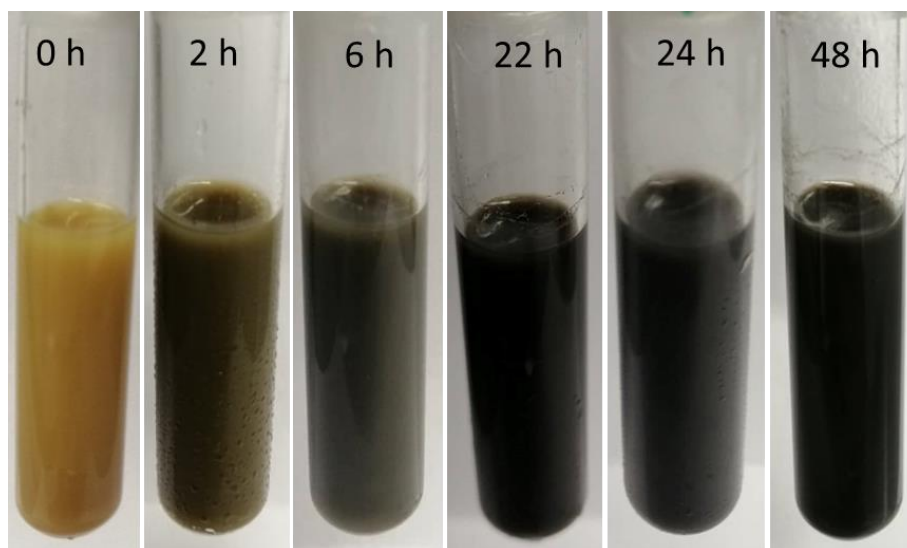
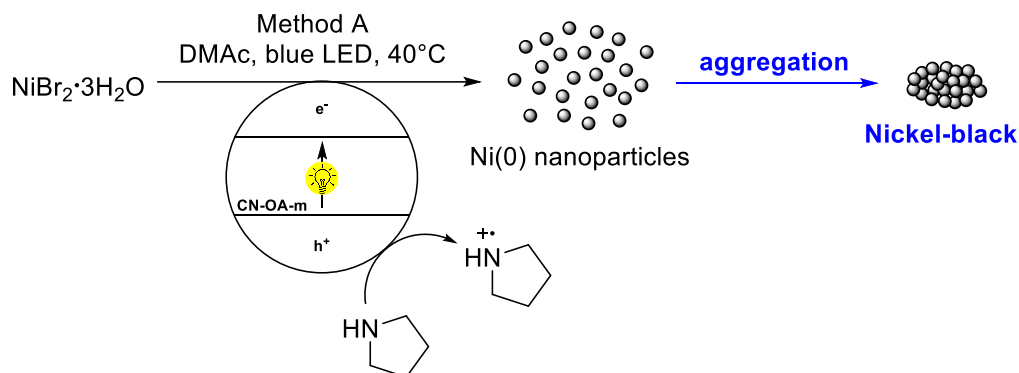


Figure 4.25. Time-dependent discoloration of the solution for method A due to nickel particle formation over time using $\text{NiBr}_2 \cdot 3\text{H}_2\text{O}$ as nickel source, CN-OA-m as photoredox catalyst (PRC) and pyrrolidine as single electron donor (SED) in DMAc (0.2M) under blue light irradiation at 40 °C.

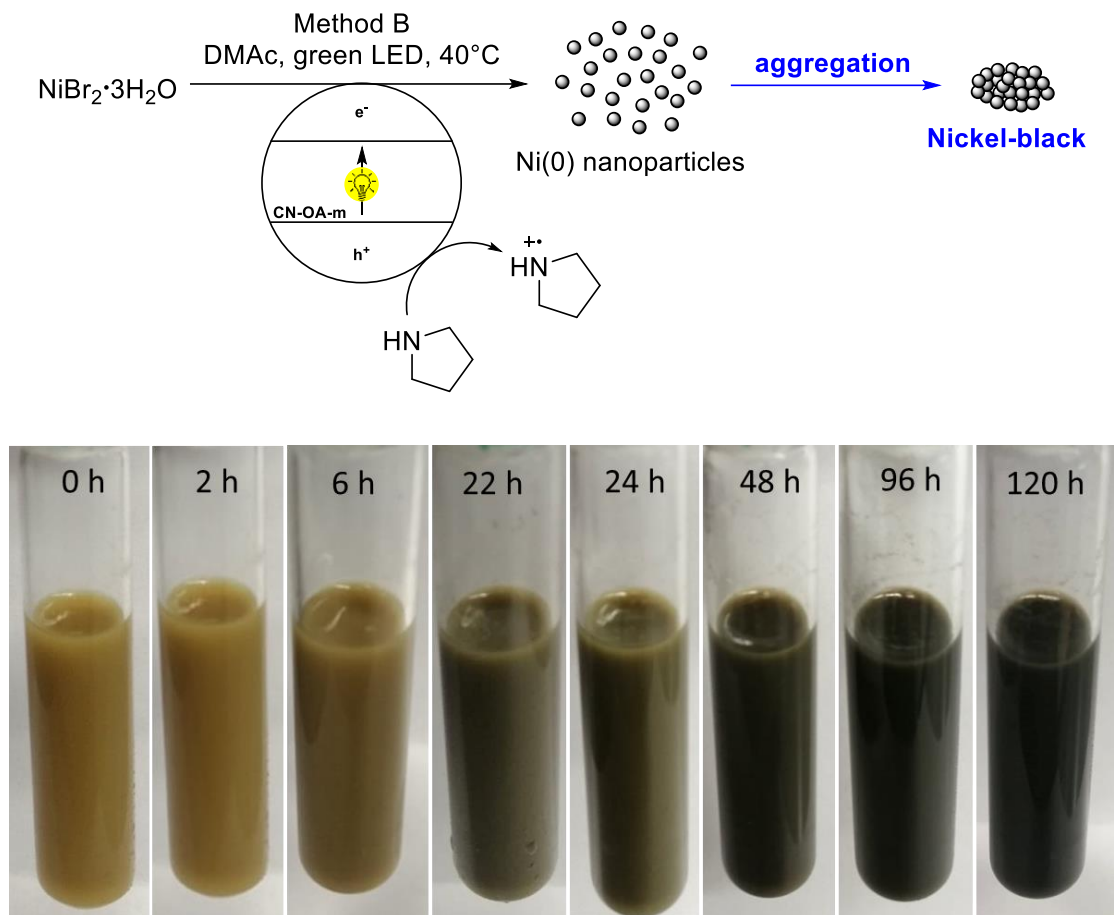


Figure 4.26. Time-dependent discoloration of the solution for method B due to nickel particle formation over time using $\text{NiBr}_2 \cdot 3\text{H}_2\text{O}$ as nickel source, CN-OA-m as photoredox catalyst (PRC) and pyrrolidine as single electron donor (SED) in DMAc (0.2M) under green light irradiation at 40°C .

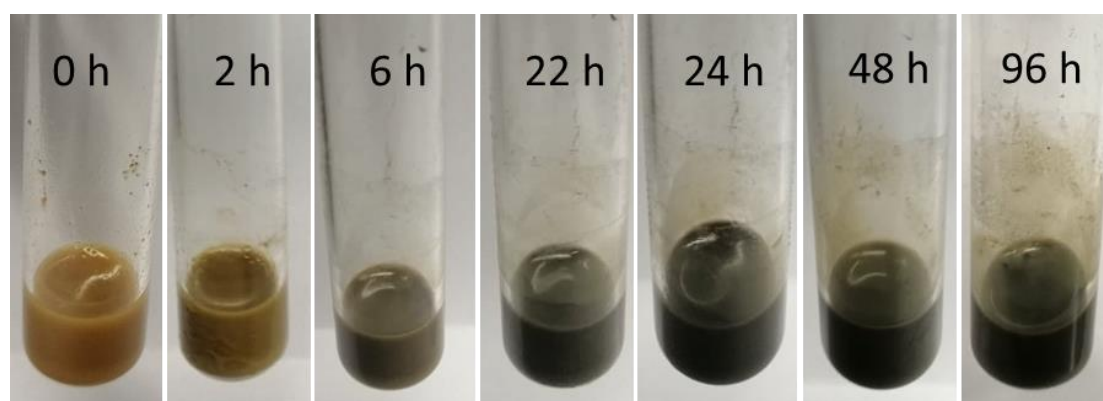
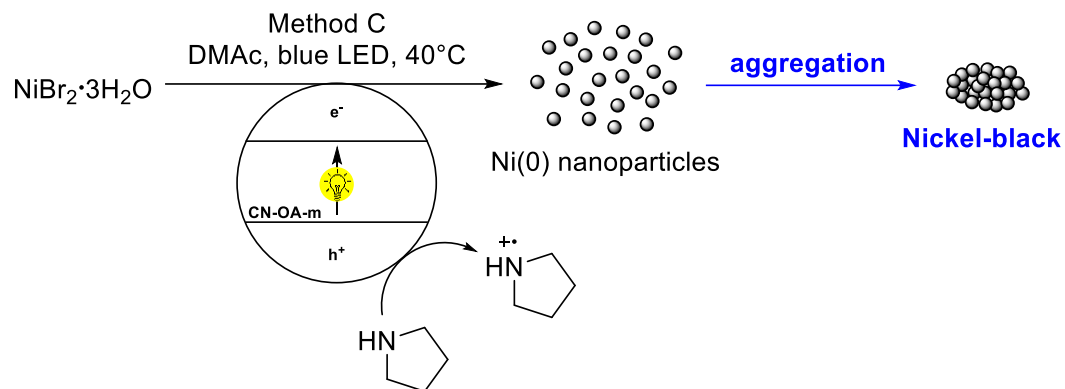


Figure 4.27. Time-dependent discoloration of the solution for method C due to nickel particle formation over time using $\text{NiBr}_2 \cdot 3\text{H}_2\text{O}$ as nickel source, CN-OA-m as photoredox catalyst (PRC) and pyrrolidine as single electron donor (SED) in DMAc (1.2 M) under blue light irradiation at 40 °C.

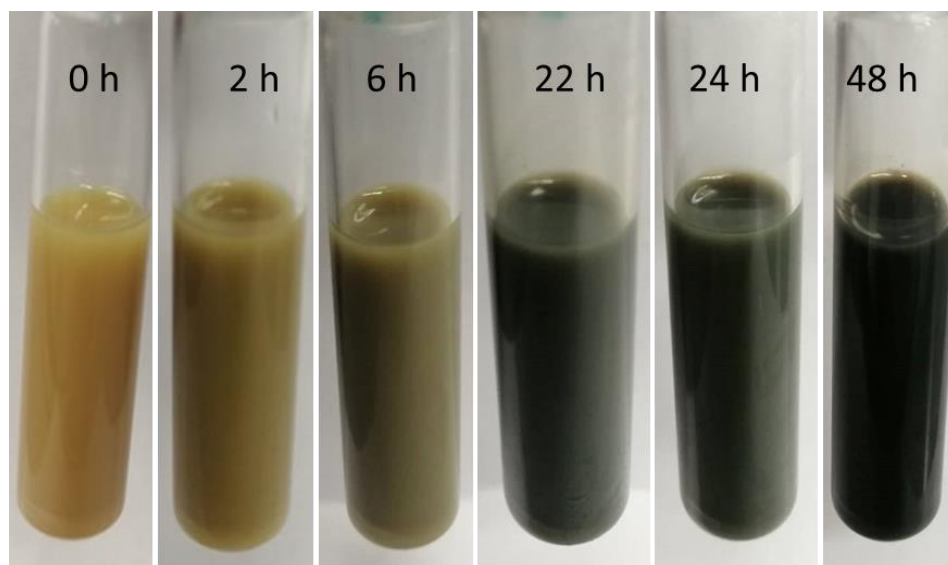
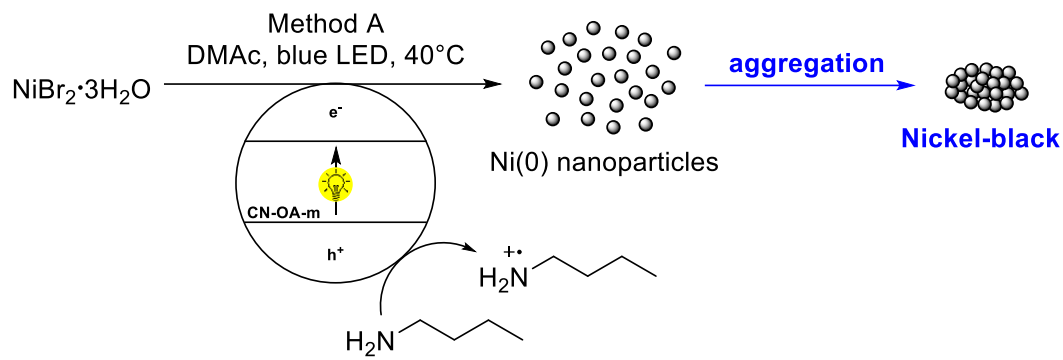


Figure 4.28. Time-dependent discoloration of the solution for method A due to nickel particle formation over time using $\text{NiBr}_2 \cdot 3\text{H}_2\text{O}$ as nickel source, CN-OA-m as photoredox catalyst (PRC) and n-butylamine as single electron donor (SED) in DMAc (0.2M) under blue light irradiation at 40 °C.

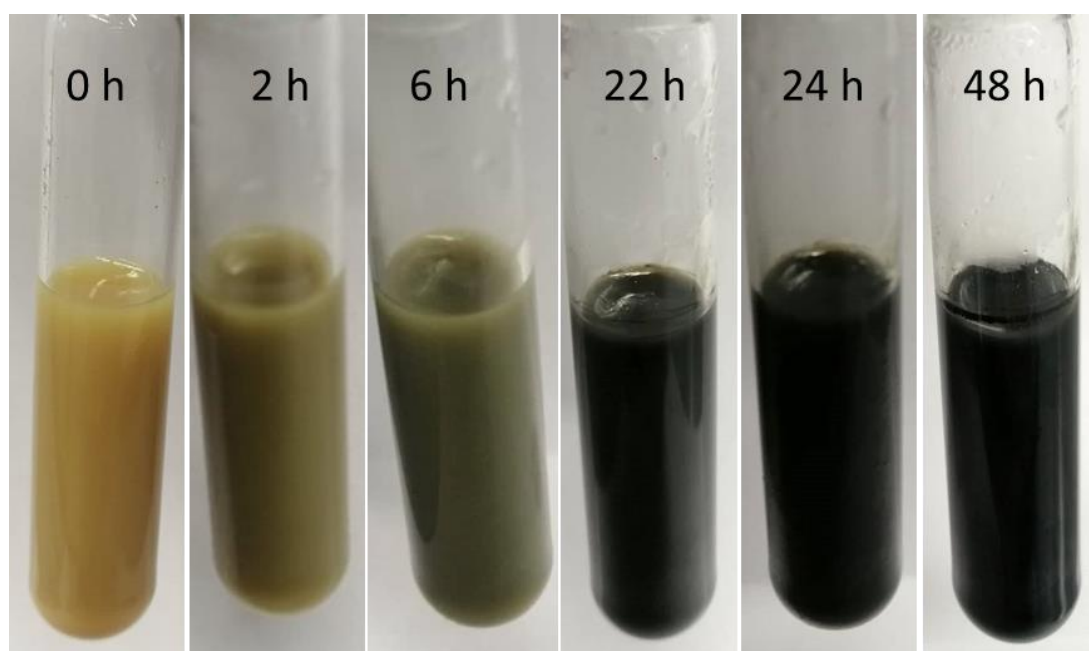
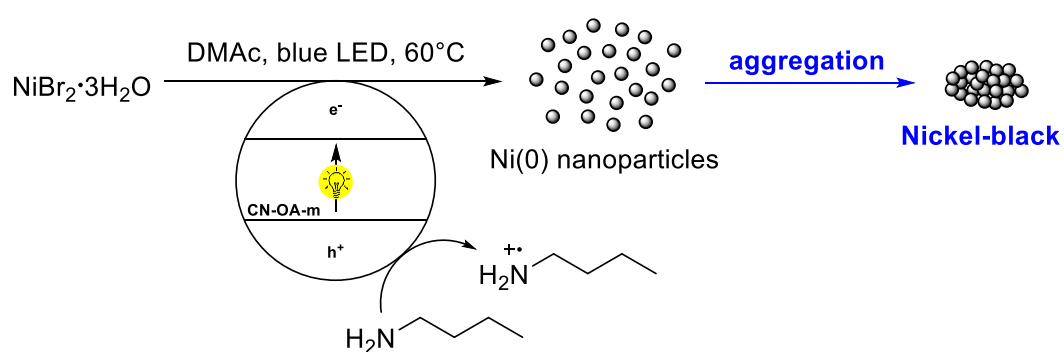


Figure 4.29. Time-dependent discoloration of the solution for method A due to nickel particle formation over time using $\text{NiBr}_2 \cdot 3\text{H}_2\text{O}$ as nickel source, CN-OA-m as photoredox catalyst (PRC) and n-butylamine as single electron donor (SED) in DMAc (0.2M) under blue light irradiation at 60 °C.

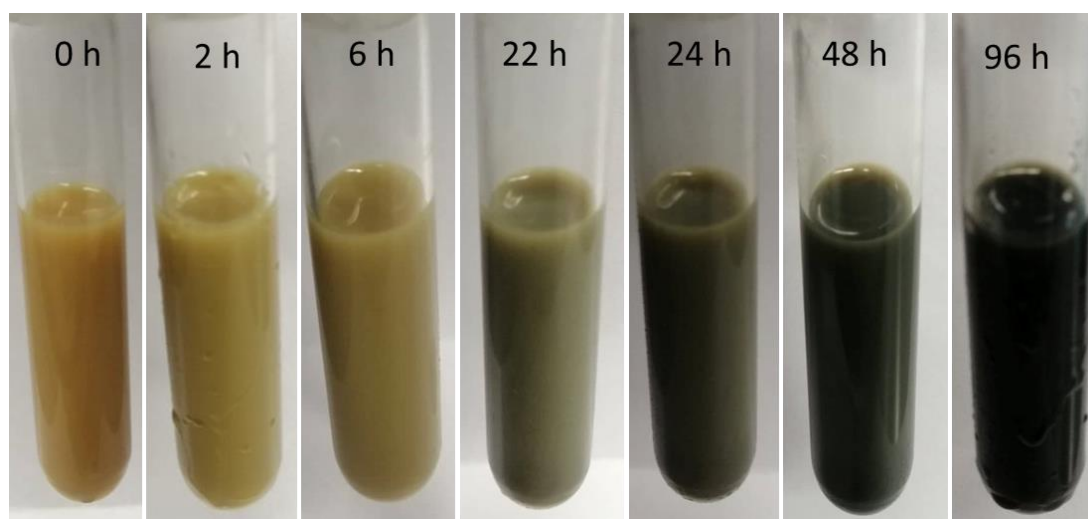
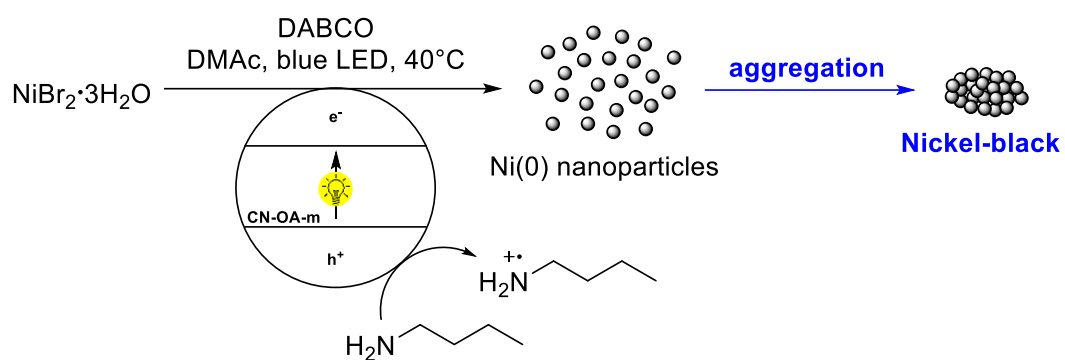


Figure 4.30. Time-dependent discoloration of the solution for method A due to nickel particle formation over time using $\text{NiBr}_2 \cdot 3\text{H}_2\text{O}$ as nickel source, CN-OA-m as photoredox catalyst (PRC) and n-butylamine and DABCO as single electron donor (SED) in DMAc (0.2M) under blue light irradiation at 40 °C.

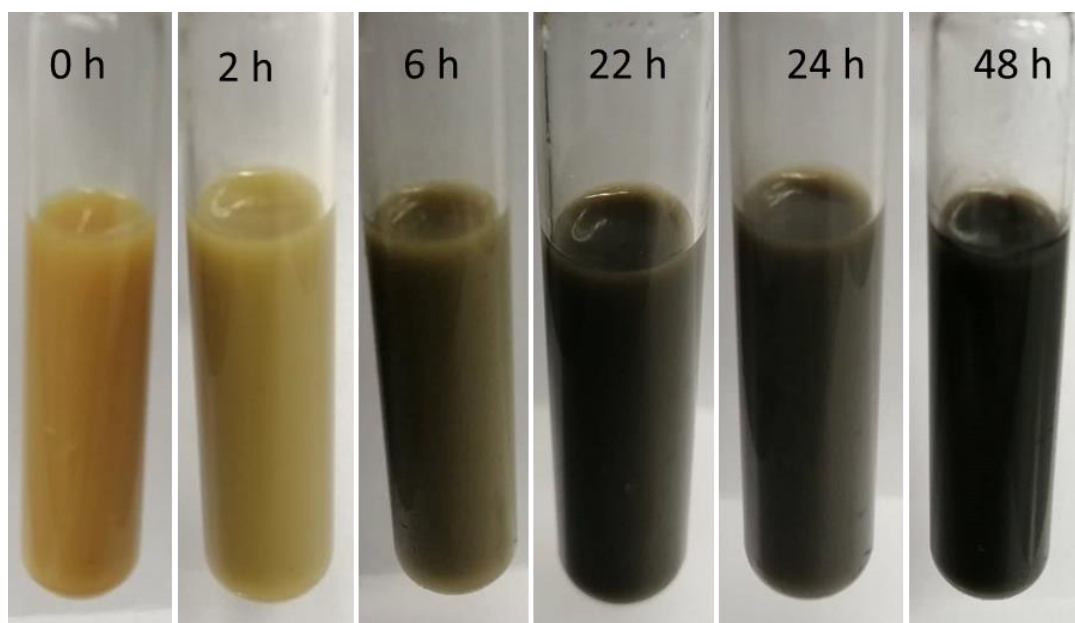
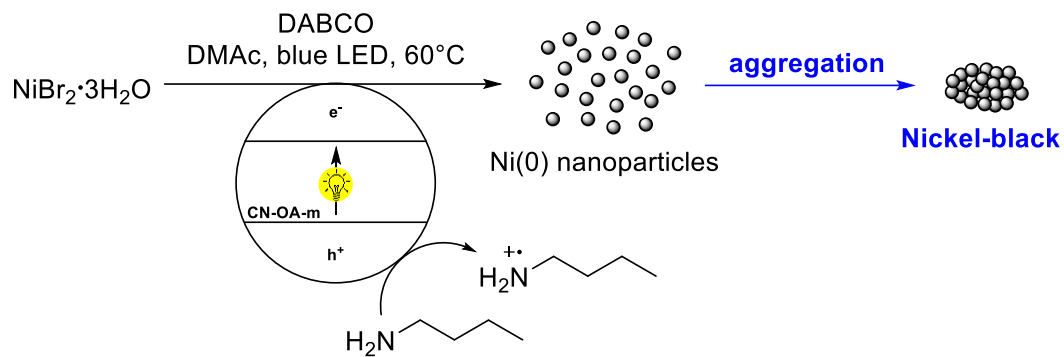


Figure 4.31. Time-dependent discoloration of the solution for method A due to nickel particle formation over time using $\text{NiBr}_2 \cdot 3\text{H}_2\text{O}$ as nickel source, CN-OA-m as photoredox catalyst (PRC) and n-butylamine and DABCO as single electron donor (SED) in DMAc (0.2M) under blue light irradiation at 60°C .

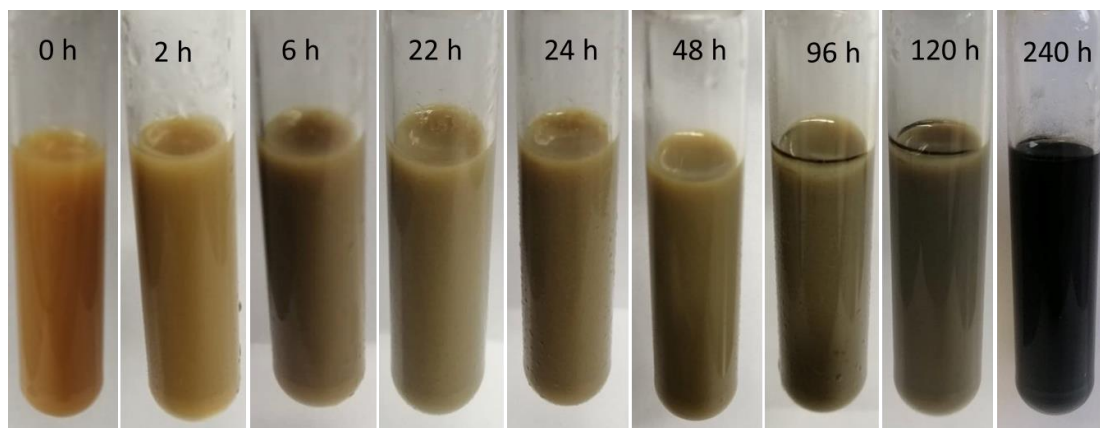
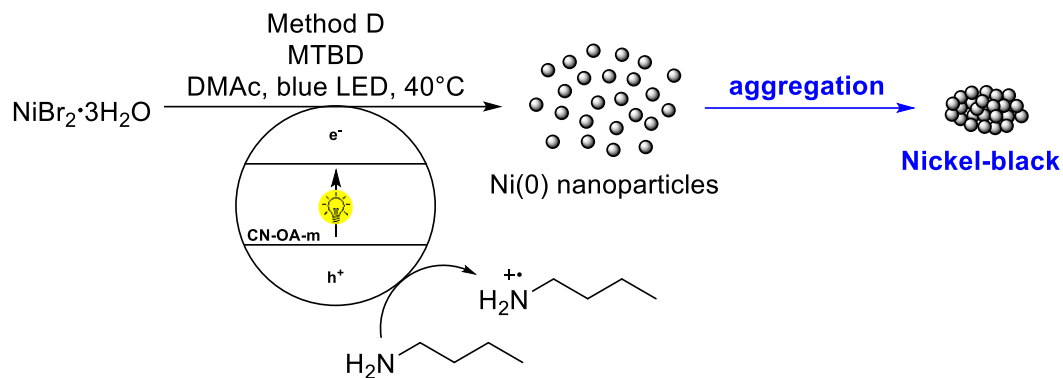


Figure 4.32. Time-dependent discoloration of the solution for method A due to nickel particle formation over time using $\text{NiBr}_2 \cdot 3\text{H}_2\text{O}$ as nickel source, CN-OA-m as photoredox catalyst (PRC) and n-butylamine and MTBD as single electron donor (SED) in DMAc (0.2M) under blue light irradiation at 40 °C.

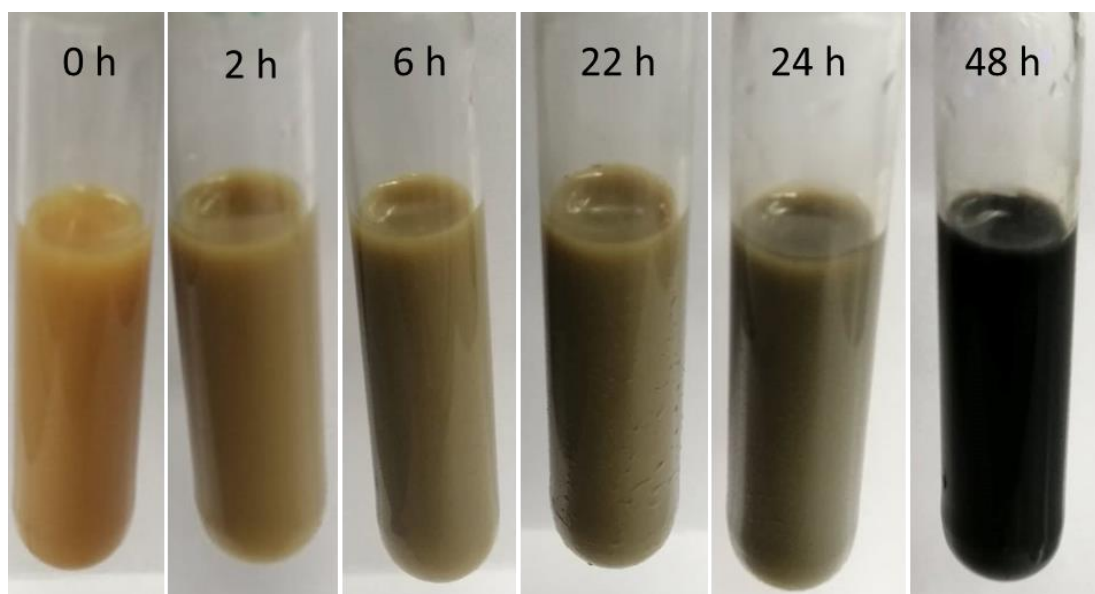
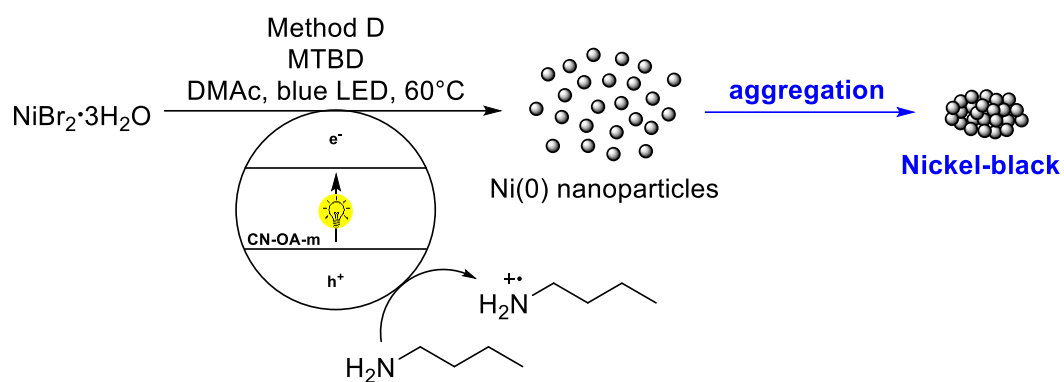
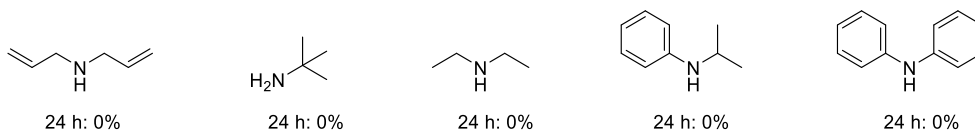


Figure 4.33. Time-dependent discoloration of the solution for method A due to nickel particle formation over time using $\text{NiBr}_2 \cdot 3\text{H}_2\text{O}$ as nickel source, CN-OA-m as photoredox catalyst (PRC) and n-butylamine and MTBD as single electron donor (SED) in DMAC (0.2M) under blue light irradiation at 60 °C.

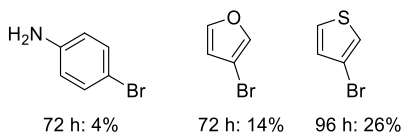
4.4.13 Scope and limitations

General experimental procedure (Table 4.2). An oven dried vial (13 x 95 mm) equipped with a stir bar was charged with $\text{NiBr}_2 \cdot 3\text{H}_2\text{O}$ (8.2 mg, 30 μmol , 2.5 mol%), aryl bromide (1.2 mmol, 1 equiv.) and CN-OA-m (20 mg). Subsequently, the amine (3.6 mmol, 3 equiv.) and DMAc (anhydrous, 6 mL) were added and the vial was sealed with a septum and parafilm. The reaction mixture was sonicated for 5-10 min and the mixture was then degassed by bubbling N_2 for 10 min. The mixture was irradiated in the batch reactor (described above) at 40°C with rapid stirring (1400 rpm). After the respective reaction time, one equivalent of 1,3,5-trimethoxybenzene (202.0 mg, 1.2 mmol, internal standard) was added. An aliquot (~300 μL) of the reaction mixture was diluted with DMSO-d_6 and subjected to $^1\text{H-NMR}$ analysis. The liquid phase was diluted with H_2O (40 mL) and extracted with ethyl acetate (3 x 30 mL). The combined organic phases were washed with H_2O (40 mL), NaHCO_3 solution (40 mL) and brine (40 mL), dried over Na_2SO_4 and concentrated. The crude product was purified by flash column chromatography (SiO_2 , Hexane/EtOAc, dichloromethane/EtOAc or dichloromethane/MeOH) on a Grace™ Reveleris™ system using a 12 g cartridge to afford the desired product. The final product was characterized by $^1\text{H-NMR}$, $^{13}\text{C-NMR}$, $^{19}\text{F-NMR}$ and HRMS (ESI-TOF).

Unsuccessful amines for the coupling with methyl 4-bromobenzoate (with NMR-yields)



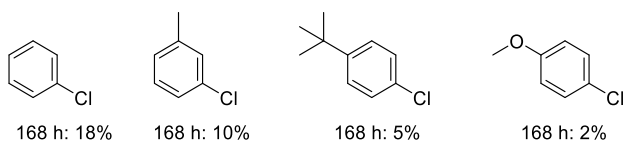
Unsuccessful aryl bromides for the coupling with pyrrolidine (with NMR-yields)



Method B: Coupling of pyrrolidine with electron-neutral aryl bromides and aryl bromides with weakly electron donating substituents (Figure 4.2 & 4.3). An oven dried vial (19 x 80 mm) equipped with a stir bar was charged with the CN-OA-m (20 mg), aryl bromide (1.2 mmol, 1.0 equiv.) and NiBr₂·3H₂O (16.4 mg, 60 μmol, 5.0 mol%). Subsequently, pyrrolidine (256.0 mg, 295.6 μl, 3.6 mmol, 3.0 equiv.) and DMAc (anhydrous, 6 mL) were added and the vial was sealed with a septum and Parafilm. The reaction mixture was sonicated for 5-10 min followed by stirring for 5 min until fine dispersion of the solids was achieved and the mixture was then degassed by bubbling N₂ for 10 min. The mixture was irradiated in the photoreactor (green light function of RGB LED strip) at 40 °C with rapid stirring (1400 rpm). After 168 h, one equivalent of 1,3,5-trimethoxybenzene (1.2 mmol) was added and the mixture was stirred for 5 min. An aliquot of the reaction mixture (~300 μL) was filtered, diluted with DMSO-d₆ and subjected to ¹H-NMR analysis. The combined organic phases were washed with H₂O (40 mL), NaHCO₃ solution (40 ml) and brine (40 mL), dried over Na₂SO₄ and concentrated. The crude product was purified by flash column chromatography (SiO₂, Hexane/EtOAc, dichloromethane/EtOAc or dichloromethane/MeOH) on a Grace™ Reveleris™ system using a 12 g cartridge to afford the desired product. The final product was characterized by ¹H-NMR, ¹³C-NMR, ¹⁹F-NMR and HRMS (ESI-TOF).

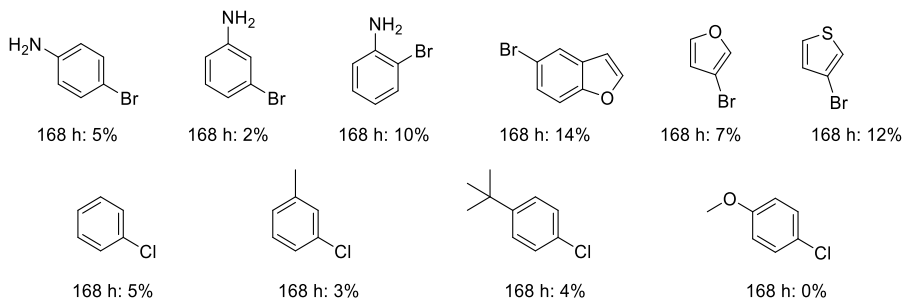
Method C: Coupling of pyrrolidine with electron-rich aryl bromides and electron-deficient aryl chlorides (Figure 4.3). An oven dried vial (19 x 80 mm) equipped with a stir bar was charged with the CN-OA-m (20 mg), aryl bromide (1.2 mmol, 1.0 equiv.) and NiBr₂·3H₂O (16.4 mg, 60 μmol, 5.0 mol%). Subsequently, pyrrolidine (256.0 mg, 295.6 μl, 3.6 mmol, 3.0 equiv.) and DMAc (anhydrous, 1 mL) were added and the vial was sealed with a septum and Parafilm. The reaction mixture was sonicated for 5-10 min followed by stirring for 5 min until fine dispersion of the solids was achieved and the mixture was then degassed by bubbling N₂ for 10 min. The mixture was irradiated in the photoreactor (blue light function of RGB LED strip) at 40 °C with moderate stirring (600 rpm). After respective reaction time, one equivalent of 1,3,5-trimethoxybenzene (202.0 mg, 1.2 mmol) was added and the mixture was stirred for 5 min. An aliquot of the reaction mixture (~300 μL) was filtered, diluted with DMSO-d₆ and subjected to ¹H-NMR analysis. The combined organic phases were washed with H₂O (40 mL), NaHCO₃ solution (40 ml) and brine (40 mL), dried over Na₂SO₄ and concentrated. The crude product was purified by flash column chromatography (SiO₂, Hexane/EtOAc, dichloromethane/EtOAc or dichloromethane/MeOH) on a Grace™ Reveleris™ system using a 12 g cartridge to afford the desired product. The final product was characterized by ¹H-NMR, ¹³C-NMR, ¹⁹F-NMR and HRMS (ESI-TOF).

Unsuccessful aryl halides for the coupling with pyrrolidine

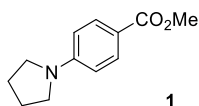


Method D: Coupling of *n*-butylamine with aryl bromides and aryl chlorides (Table 4.3).

An oven dried vial (19 x 80 mm) equipped with a stir bar was charged with the CN-OA-m (20 mg), aryl bromide (1.2 mmol, 1.0 equiv.) and NiBr₂·3H₂O (16.4 mg, 60 μmol, 5.0 mol%). Subsequently, pyrrolidine (256.0 mg, 295.6 μl, 3.6 mmol, 3.0 equiv.) and DMAc (anhydrous, 1 mL) were added and the vial was sealed with a septum and Parafilm. The reaction mixture was sonicated for 5-10 min followed by stirring for 5 min until fine dispersion of the solids was achieved and the mixture was then degassed by bubbling N₂ for 10 min. The mixture was irradiated in the photoreactor (blue light function of RGB LED strip) at 40 °C with moderate stirring (600 rpm). After respective reaction time, one equivalent of 1,3,5-trimethoxybenzene (202.0 mg, 1.2 mmol) was added and the mixture was stirred for 5 min. An aliquot of the reaction mixture (~300 μL) was filtered, diluted with DMSO-d₆ and subjected to ¹H-NMR analysis. The combined organic phases were washed with H₂O (40 mL), NaHCO₃ solution (40 ml) and brine (40 mL), dried over Na₂SO₄ and concentrated. The crude product was purified by flash column chromatography (SiO₂, Hexane/EtOAc, dichloromethane/EtOAc or dichloromethane/MeOH) on a GraceTM RevelerisTM system using a 12 g cartridge to afford the desired product. The final product was characterized by ¹H-NMR, ¹³C-NMR, ¹⁹F-NMR and HRMS (ESI-TOF).

Unsuccessful aryl halides for the coupling with *n*-butylamine (with NMR-yields).

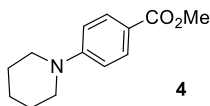
Chapter 4



1-(4-methylbenzoate)pyrrolidine. From pyrrolidine (256.0 mg, 295.6 μ l, 3.6 mmol, 3.0 equiv.) and 4-bromomethylbenzoate (258.0 mg, 1.2 mmol, 1.0 equiv.) or 4-chloromethylbenzoate (204.7 mg, 1.2 mmol, 1.0 equiv.) using 1 ml instead of 6 ml DMAc. Reaction time: 8 h (Br) and 48 h (Cl). Purification with flash chromatography (1. gradient 0-5% ethyl acetate in hexane; 2. Isocratic 5% ethyl acetate in hexane) afforded the title compound (231.1 mg, 1.13 mmol, 94%) for aryl bromide and (224.6 mg, 1.09 mmol, 91%) for aryl chloride as a white solid.

^1H NMR (400 MHz, Chloroform-*d*) δ 7.88 (d, J = 8.7 Hz, 2H), 6.46 (d, J = 8.7 Hz, 2H), 3.83 (s, 3H), 3.40 – 3.09 (m, 4H), 2.05 – 1.86 (m, 4H). ^{13}C NMR (101 MHz, Chloroform-*d*) δ = 167.58, 150.79, 131.32, 116.17, 110.62, 51.37, 47.47, 25.41. HRMS (ESI-TOF) m/z calcd. for $\text{C}_{12}\text{H}_{16}\text{NO}_2$ [(M+H) $^+$]: 206.1176; found: 206.1158.

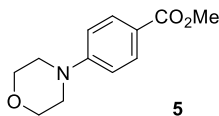
These data are in full agreement with those previously published in the literature.⁴⁷



Methyl 4-(piperidin-1-yl)benzoate. From piperidine (306.5 mg, 356.4 μ l, 3.6 mmol, 3.0 equiv.) and 4-bromomethylbenzoate (258.0 mg, 1.2 mmol, 1.0 equiv.). Reaction time: 72 h. Double amount of $\text{NiBr}_2 \cdot 3\text{H}_2\text{O}$ (16.4 mg, 60 μ mol, 5.0 mol%) was used. Purification with flash chromatography (1. gradient 0-5% ethyl acetate in hexane; 2. Isocratic 5% ethyl acetate in hexane) afforded the title compound (225.8 mg, 1.03 mmol, 86%) as a white solid.

^1H NMR (600 MHz, Chloroform-*d*) δ 7.87 (d, J = 9.1 Hz, 2H), 6.82 (d, J = 9.0 Hz, 2H), 3.83 (s, 3H), 3.28 (m, 4H), 1.67 – 1.56 (m, 6H). ^{13}C NMR (151 MHz, Chloroform-*d*) δ 167.18, 154.46, 131.19, 118.61, 113.52, 51.49, 48.73, 25.35, 24.32. HRMS (ESI-TOF) m/z calcd. for $\text{C}_{13}\text{H}_{18}\text{NO}_2$ [(M+H) $^+$]: 220.1332 ; found: 220.1340.

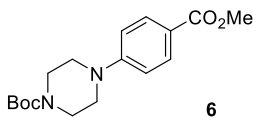
These data are in full agreement with those previously published in the literature.⁴⁸



Methyl 4-morpholinobenzoate. From morpholine (313.6 mg, 313.6 μ l, 3.6 mmol, 3.0 equiv.) and 4-bromomethylbenzoate (258.0 mg, 1.2 mmol, 1.0 equiv.). Reaction time: 16 h. Purification with flash chromatography (gradient 0-2% ethyl acetate in DCM; 2. Isocratic 2% ethyl acetate in DCM) afforded the title compound (255.5 mg, 1.15 mmol, 96%) as a white solid.

^1H NMR (400 MHz, Chloroform-*d*) δ 7.93 (d, J = 9.0 Hz, 2H), 6.86 (d, J = 9.0 Hz, 2H), 3.92 – 3.72 (m, 7H), 3.26 (d, J = 5.1 Hz, 4H). ^{13}C NMR (101 MHz, Chloroform-*d*) δ 167.04, 154.15, 131.21, 120.34 113.50, 66.59, 51.71, 47.72. HRMS (ESI-TOF) m/z calcd. for $\text{C}_{12}\text{H}_{16}\text{NO}_3$ [(M+H) $^+$]: 222.1125; found: 222.1139.

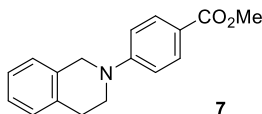
These data are in full agreement with those previously published in the literature.⁴⁹



tert-Butyl 4-(4-(methoxycarbonyl)phenyl)piperazine-1-carboxylate. From *tert*-butyl piperazine-1-carboxylate (335.3 mg, 1.8 mmol, 3.0 equiv.) and 4-bromomethylbenzoate (129.0 mg, 0.6 mmol, 1.0 equiv.) using 5 mol% $\text{NiBr}_2 \cdot 3\text{H}_2\text{O}$ (8.2 mg, 60 μ mol) and pyrrolidine (4.3 mg, 4.9 μ l, 0.06 mmol, 10 mol%) as additive. Reaction time: 24 h. Purification with flash chromatography (1. gradient 0-3% ethyl acetate in DCM; 2. Isocratic 3% ethyl acetate in DCM) afforded the title compound (146.2 mg, 0.45 mmol, 76%) as a white solid. The pyrrolidine-coupled side-product was formed in 10% yield, as determined by analysis of the crude mixture by ^1H NMR spectroscopy.

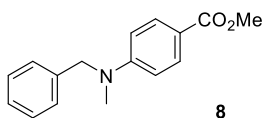
^1H NMR (400 MHz, Chloroform-*d*) δ 7.92 (d, J = 8.9 Hz, 2H), 6.85 (d, J = 8.9 Hz, 2H), 3.86 (s, 3H), 3.57 (m, 4H), 3.29 (m, 4H), 1.48 (s, 9H). ^{13}C NMR (101 MHz, Chloroform-*d*) δ 167.48, 155.09, 154.41, 131.69, 120.63, 114.42, 80.56, 52.15, 47.98, 43.46, 28.92, 28.78. HRMS (ESI-TOF) m/z calcd. for $\text{C}_{17}\text{H}_{25}\text{N}_2\text{O}_4$ [(M+H) $^+$]: 321.1809; found: 321.1818

These data are in full agreement with those previously published in the literature.⁴⁸



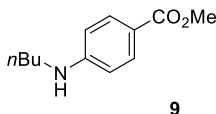
Methyl 4-(3,4-dihydroisoquinolin-2(1H)-yl)benzoate. From 1,2,3,4-tetrahydroisoquinoline (479.5 mg, 456.7 μ l, 3.6 mmol, 3.0 equiv.) and 4-bromomethylbenzoate (258.0 mg, 1.2 mmol, 1.0 equiv.). Reaction time: 16 h. Purification with flash chromatography (1. gradient 0-5% ethyl acetate in hexane; 2. Isocratic 5% ethyl acetate in hexane) afforded the title compound (281.6 mg, 1.06 mmol, 88%) as a white solid. ^1H NMR (600 MHz, Chloroform-*d*) δ 7.97 (d, $J = 9.0$ Hz, 2H), 7.23 – 7.13 (m, 4H), 6.86 (d, $J = 9.0$ Hz, 2H), 4.49 (s, 2H), 3.88 (s, 3H), 3.62 (t, $J = 5.9$ Hz, 2H), 2.97 (t, $J = 5.8$ Hz, 2H). ^{13}C NMR (151 MHz, Chloroform-*d*) δ 167.29, 153.00, 135.02, 133.80, 131.36, 128.22, 126.73, 126.51, 126.37, 118.29, 112.10, 51.56, 49.01, 44.78, 29.04. HRMS (ESI-TOF) m/z calcd. for $\text{C}_{17}\text{H}_{18}\text{NO}_2$ [(M+H) $^+$]: 268.1332; found: 268.1344

These data are in full agreement with those previously published in the literature.⁵⁰



Methyl 4-(benzyl(methyl)amino)benzoate. From *N*-methylbenzylamine (438.6 mg, 467.1 μ l, 3.6 mmol, 3.0 equiv.) and 4-bromomethylbenzoate (258.0 mg, 1.2 mmol, 1.0 equiv.). Reaction time: 72 h. Purification with flash chromatography (1.gradient 0-4% ethyl acetate in hexane; 2. Isocratic 4% ethyl acetate in hexane) afforded the title compound (245.4 mg, 0.96 mmol, 80%) as a white solid. ^1H NMR (400 MHz, Chloroform-*d*) δ 7.92 (d, $J = 9.1$ Hz, 2H), 7.34 (t, $J = 7.2$ Hz, 2H), 7.28 (d, $J = 7.2$ Hz, 1H), 7.20 (d, $J = 7.1$ Hz, 2H), 6.71 (d, $J = 9.1$ Hz, 2H), 4.62 (s, 2H), 3.86 (s, 3H), 3.12 (s, 3H). ^{13}C NMR (101 MHz, Chloroform-*d*) δ 167.39, 152.75, 137.79, 131.43, 128.78, 127.20, 126.46, 117.37, 110.88, 55.92, 51.52, 38.69. HRMS (ESI-TOF) m/z calcd. for $\text{C}_{16}\text{H}_{18}\text{NO}_2$ [(M+H) $^+$]: 256.1332; found: 256.1344

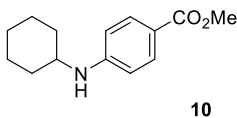
These data are in full agreement with those previously published in the literature.⁵¹



Methyl 4-(butylamino)benzoate. From *n*-butylamine (263.3 mg, 355.8 μ l, 3.6 mmol, 3.0 equiv.) and 4-bromomethylbenzoate (258.0 mg, 1.2 mmol, 1.0 equiv.) or 4-chloromethylbenzoate (204.7 mg, 1.2 mmol, 1.0 equiv.) and 7-Methyl-1,5,7-triazabicyclo[4.4.0]dec-5-ene (MTBD) (367.8 mg, 344.7 μ l, 2.4 mmol, 2.0 equiv.) using 5 mol% $\text{NiBr}_2 \cdot 3\text{H}_2\text{O}$ (16.4 mg, 60 μ mol.). Reaction time: 72 h (9-Br) and 168 h (9-Cl). Purification with flash chromatography (1. gradient 0-8% ethyl acetate in hexane; 2. Isocratic 8% ethyl acetate in hexane) afforded the title compounds (223.2 mg, 1.08 mmol, 90%) from aryl bromide and (219.6 mg, 1.06 mmol, 88%) from aryl chloride as a white solid.

^1H NMR (400 MHz, Chloroform-*d*) δ 7.85 (d, J = 8.6 Hz, 2H), 6.52 (d, J = 8.6 Hz, 2H), 4.21 (brs, 1H), 3.83 (s, 3H), 3.16 – 3.07 (m, 2H), 1.63 – 1.52 (m, 2H), 1.41 (h, J = 7.3, 6.9 Hz, 2H), 0.94 (td, J = 7.3, 1.0 Hz, 3H). ^{13}C NMR (101 MHz, Chloroform-*d*) δ 167.45, 152.17, 131.61, 118.05, 111.45, 51.57, 43.19, 31.42, 20.29, 13.92. HRMS (ESI-TOF) m/z calcd. for $\text{C}_{12}\text{H}_{18}\text{NO}_2$ [(M+H) $^+$]: 208.1332; found: 208.1342.

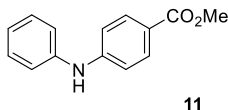
These data are in full agreement with those previously published in the literature.⁵²



Methyl 4-(cyclohexylamino)benzoate. From cyclohexylamine (357.0 mg, 415.4 μ l, 3.6 mmol, 3.0 equiv.) and 4-bromomethylbenzoate (258.0 mg, 1.2 mmol, 1.0 equiv.) using 5 mol% $\text{NiBr}_2 \cdot 3\text{H}_2\text{O}$ (16.4 mg, 60 μ mol.). Reaction time: 72 h. Purification with flash chromatography (1. gradient 0-5% ethyl acetate in hexane; 2. Isocratic 5% ethyl acetate in hexane) afforded the title compound (203.2 mg, 0.87 mmol, 73%) as a white solid.

^1H NMR (400 MHz, Chloroform-*d*) δ 7.82 (d, J = 8.8 Hz, 2H), 6.51 (d, J = 8.9 Hz, 2H), 4.01 (brs, 1H), 3.83 (s, 3H), 3.30 (m, 1H), 2.06 – 2.00 (m, 2H), 1.81 – 1.73 (m, 2H), 1.69 – 1.61 (m, 1H), 1.42 – 1.32 (m, 2H), 1.28 – 1.13 (m, 3H). ^{13}C NMR (101 MHz, Chloroform-*d*) δ 167.36, 151.10, 131.60, 117.56, 111.59, 51.47, 51.24, 33.10, 25.73, 24.87. HRMS (ESI-TOF) m/z calcd. for $\text{C}_{14}\text{H}_{20}\text{NO}_2$ [(M+H) $^+$]: 234.1489; found: 234.1500.

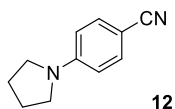
These data are in full agreement with those previously published in the literature.⁵³



Methyl 4-(butylamino)benzoate. From aniline (335.5 mg, 329.2 μ l, 3.6 mmol, 3.0 equiv.) and 4-bromomethylbenzoate (258.0 mg, 1.2 mmol, 1.0 equiv.) using 5 mol% $\text{NiBr}_2 \cdot 3\text{H}_2\text{O}$ (8.2 mg, 60 μ mol) and pyrrolidine (4.3 mg, 4.9 μ l, 0.06 mmol, 10 mol) as well as *N-tert*-butylisopropylamine (BIPA) (414.8 mg, 570.6 μ l, 3.6 mmol, 3.0 equiv.) as additives. Reaction time: 72 h. Purification with flash chromatography (1. gradient 0-10% ethyl acetate in hexane; 2. Isocratic 10% ethyl acetate in hexane) afforded the title compound (246.7 mg, 1.09 mmol, 90%) as a white solid. The pyrrolidine-coupled side-product was formed in 2% yield, as determined by analysis of the crude mixture by ^1H NMR spectroscopy.

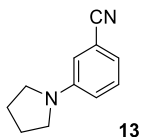
^1H NMR (400 MHz, Chloroform-*d*) δ 7.93 (d, $J = 8.1$ Hz, 2H), 7.34 (m, 2H), 7.18 (d, $J = 7.7$ Hz, 2H), 7.07 (t, $J = 7.4$ Hz, 1H), 6.99 (d, $J = 8.6$ Hz, 2H), 6.19 (brs, 1H), 3.88 (s, 3H). ^{13}C NMR (101 MHz, Chloroform-*d*) δ 167.08, 148.16, 140.88, 131.50, 129.51, 123.07, 120.94, 120.42, 114.56, 51.77. HRMS (ESI-TOF) m/z calcd. for $\text{C}_{14}\text{H}_{14}\text{NO}_2$ [(M+H) $^+$]: 228.1019; found: 228.1033.

These data are in full agreement with those previously published in the literature.⁵⁴



1-(4-benzonitrile)pyrrolidine. From pyrrolidine (256.0 mg, 295.6 μ l, 3.6 mmol, 3.0 equiv.) and 4-bromobenzonitrile (218.4 mg, 1.2 mmol, 1.0 equiv.). Reaction time: 24 h. Purification with flash chromatography (1. gradient 0-5% ethyl acetate in hexane; 2. Isocratic 5% ethyl acetate in hexane) afforded the title compound (189.6mg, 1.11 mmol, 92%) as a white solid. ^1H NMR (400 MHz, Chloroform-*d*) δ 7.42 (d, $J = 8.8$ Hz, 2H), 6.48 (d, $J = 8.9$ Hz, 2H), 3.32 – 3.28 (m, 4H), 2.09 – 1.94 (m, 4H). ^{13}C NMR (101 MHz, Chloroform-*d*) δ 150.00, 133.43, 121.11, 111.47, 96.38, 47.51, 25.44. HRMS (ESI-TOF) m/z calcd. for $\text{C}_{11}\text{H}_{13}\text{N}_2$ [(M+H) $^+$]: 173.1074; found: 173.1081.

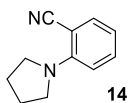
These data are in full agreement with those previously published in the literature.⁵⁵



1-(3-benzonitrile)pyrrolidine. From pyrrolidine (256.0 mg, 295.6 μ l, 3.6 mmol, 3.0 equiv.) and 3-bromobenzonitrile (218.4 mg, 1.2 mmol, 1.0 equiv.). Reaction time: 24 h. No internal standard (1,3,5-trimethoxybenzene was used) due to poor separation from the product during flash chromatography. Purification with flash chromatography (1. gradient 0-5% ethyl acetate in hexane; 2. Isocratic 5% ethyl acetate in hexane) afforded the title compound (180.4 mg, 1.05 mmol, 87%) as a white solid.

^1H NMR (400 MHz, Chloroform-*d*) δ 7.30 – 7.23 (m, 1H), 6.90 (m, 1H), 6.77 – 6.69 (m, 2H), 3.34 – 3.23 (m, 4H), 2.13 – 1.99 (m, 4H). ^{13}C NMR (101 MHz, Chloroform-*d*) δ 147.62, 129.73, 119.95, 118.50, 115.78, 114.24, 112.63, 47.55, 25.46. HRMS (ESI-TOF) m/z calcd. for $\text{C}_{11}\text{H}_{13}\text{N}_2$ [(M+H) $^+$]: 173.1074; found: 173.1080

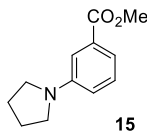
These data are in full agreement with those previously published in the literature.⁵⁶



1-(2-benzonitrile)pyrrolidine. From pyrrolidine (256.0 mg, 295.6 μ l, 3.6 mmol, 3.0 equiv.) and 2-bromobenzonitrile (218.4 mg, 1.2 mmol, 1.0 equiv.) using 5 mol% $\text{NiBr}_2 \cdot 3\text{H}_2\text{O}$ (8.2 mg, 60 μ mol). Reaction time: 72 h. No internal standard (1,3,5-trimethoxybenzene was used) due to poor separation from the product during flash chromatography. Purification with flash chromatography (eluents: 1. gradient 0-5% ethyl acetate in hexane; 2. Isocratic 5% ethyl acetate in hexane) afforded the title compound (190.5 mg, 1.11 mmol, 92%) as a colorless oil.

^1H NMR (400 MHz, Chloroform-*d*) δ 7.42 (m, 1H), 7.31 (m, 1H), 6.67 – 6.59 (m, 2H), 3.63 – 3.53 (m, 4H), 2.03 – 1.94 (m, 4H). ^{13}C NMR (101 MHz, Chloroform-*d*) δ 150.04, 135.72, 133.40, 121.51, 115.86, 114.24, 94.27, 49.81, 25.76. HRMS (ESI-TOF) m/z calcd. for $\text{C}_{11}\text{H}_{13}\text{N}_2$ [(M+H) $^+$]: 173.1074; found: 173.1081

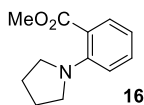
These data are in full agreement with those previously published in the literature.³⁵



1-(3-methylbenzoate)pyrrolidine. From pyrrolidine (256.0 mg, 295.6 μ l, 3.6 mmol, 3.0 equiv.) and 3-bromomethylbenzoate (258.0 mg, 1.2 mmol, 1.0 equiv.). Reaction time: 24 h. No internal standard (1,3,5-trimethoxybenzene was used) due to poor separation from the product during flash chromatography. Purification with flash chromatography (1. gradient 0-5% ethyl acetate in hexane; 2. Isocratic 5% ethyl acetate in hexane) afforded the title compound (218.4 mg, 1.06 mmol, 89%) as a colorless oil.

^1H NMR (400 MHz, Chloroform-*d*) δ 7.32 (d, J = 7.6 Hz, 1H), 7.25 (t, J = 7.8 Hz, 1H), 7.22 – 7.91 (s, 1H), 6.71 (m, 1H), 3.89 (s, 3H), 3.29 (t, J = 6.6 Hz, 4H), 2.00 (t, J = 6.6 Hz, 4H). ^{13}C NMR (101 MHz, Chloroform-*d*) δ 167.89, 147.78, 130.73, 129.02, 116.39, 115.93, 112.38, 52.00, 47.70, 25.48. HRMS (ESI-TOF) m/z calcd. for $\text{C}_{12}\text{H}_{16}\text{NO}_2$ [(M+H) $^+$]: 206.17556; found: 206.1185.

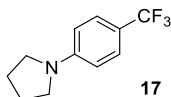
These data are in full agreement with those previously published in the literature.⁴⁹



1-(2-methylbenzoate)pyrrolidine. From pyrrolidine (256.0 mg, 295.6 μ l, 3.6 mmol, 3.0 equiv.) and 2-bromomethylbenzoate (258.0 mg, 1.2 mmol, 1.0 equiv.) using 5 mol% $\text{NiBr}_2 \cdot 3\text{H}_2\text{O}$ (8.2 mg, 60 μ mol). Reaction time: 72 h. No internal standard (1,3,5-trimethoxybenzene was used) due to poor separation from the product during flash chromatography. Purification with flash chromatography (1. gradient 0-5% ethyl acetate in hexane; 2. Isocratic 5% ethyl acetate in hexane) afforded the title compound (87.2 mg, 0.42 mmol, 35%) as a colourless oil.

^1H NMR (400 MHz, Chloroform-*d*) δ 7.57 (m, 1H), 7.31 (t, J = 8.7 Hz, 1H), 6.79 (m, 1H), 6.71 (t, J = 7.4 Hz, 1H), 3.88 (s, 3H), 3.28 – 3.19 (m, 4H), 1.99 – 1.88 (m, 4H). ^{13}C NMR (101 MHz, Chloroform-*d*) δ 169.57, 147.93, 131.79, 131.08, 117.09, 115.63, 113.95, 52.00, 50.87, 25.88. HRMS (ESI-TOF) m/z calcd. for $\text{C}_{12}\text{H}_{16}\text{NO}_2$ [(M+H) $^+$]: 206.17556; found: 206.1185.

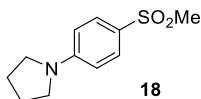
These data are in full agreement with those previously published in the literature.⁵⁷



1-(4-(trifluoromethyl)phenyl)pyrrolidine. From pyrrolidine (256.0 mg, 295.6 μ l, 3.6 mmol, 3.0 equiv.) and 4-bromobenzotrifluoride (270.0 mg, 168.0 μ l, 1.2 mmol, 1.0 equiv.). Reaction time: 8 h. Purification with flash chromatography (1. gradient 0-3% ethyl acetate in hexane; 2. Isocratic 3% ethyl acetate in hexane) afforded the title compound (238.2 mg, 1.11 mmol, 92%) as a white solid.

^1H NMR (400 MHz, Chloroform-*d*) δ 7.48 (d, J = 8.7 Hz, 2H), 6.58 (d, J = 8.7 Hz, 2H), 3.37 – 3.27 (m, 4H), 2.10 – 2.00 (m, 4H). ^{13}C NMR (101 MHz, Chloroform-*d*) δ 149.76, 126.38 (q, J = 3.7 Hz), 125.42 (q, J = 269.9 Hz), 116.56 (q, J = 32.5 Hz), 110.84, 47.53, 25.48. ^{19}F NMR (376 MHz, Chloroform-*d*) δ -60.58(s, 3F). HRMS (ESI-TOF) m/z calcd. for $\text{C}_{11}\text{H}_{13}\text{F}_3\text{N}$ [(M+H) $^+$]: 216.0922 ; found: 216.1008.

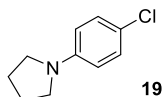
These data are in full agreement with those previously published in the literature.⁵⁸



1-(4-(methylsulfonyl)phenyl)pyrrolidine. From pyrrolidine (256.0 mg, 295.6 μ l, 3.6 mmol, 3.0 equiv.) and 4-bromophenyl methylsulfone (282.1 mg, 1.2 mmol, 1.0 equiv.). Reaction time: 24 h. Purification with flash chromatography (1. gradient 0-2% ethyl acetate in DCM; 2. Isocratic 2% ethyl acetate in DCM) afforded the title compound (251.0 mg, 1.11 mmol, 93%) as a white solid.

^1H NMR (600 MHz, Chloroform-*d*) δ 7.65 (d, J = 8.9 Hz, 2H), 6.51 (d, J = 9.0 Hz, 2H), 3.30 – 3.24 (m, 4H), 2.94 (s, 3H), 2.05 – 1.93 (m, 4H). ^{13}C NMR (151 MHz, Chloroform-*d*) δ 150.89, 129.02, 125.04, 110.98, 47.61, 45.13, 25.39. HRMS (ESI-TOF) m/z calcd. for $\text{C}_{11}\text{H}_{16}\text{NO}_2\text{S}$ [(M+H) $^+$]: 226.0897; found: 226.0907.

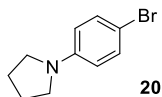
These data are in full agreement with those previously published in the literature.⁵⁹



1-(4-chlorophenyl)pyrrolidine. From pyrrolidine (256.0 mg, 295.6 μ l, 3.6 mmol, 3.0 equiv.) and 4-bromochlorobenzene (229.7 mg, 1.2 mmol, 1.0 equiv.). Reaction time: 24 h. Purification with flash chromatography (1. gradient 0-2% ethyl acetate in hexane; 2. Isocratic 2% ethyl acetate in hexane) afforded the title compound (196.8 mg, 1.08 mmol, 90%) as a white solid.

^1H NMR (600 MHz, Chloroform-*d*) δ 7.17 (d, J = 8.9 Hz, 2H), 6.48 (d, J = 8.9 Hz, 2H), 3.28 – 3.18 (m, 4H), 2.06 – 1.97 (m, 4H). ^{13}C NMR (151 MHz, Chloroform-*d*) δ 146.49, 128.81, 120.04, 112.61, 47.73, 25.48. HRMS (ESI-TOF) m/z calcd. for $\text{C}_{10}\text{H}_{13}\text{ClN}$ [(M+H) $^+$]: 182.0731; found: 182.0738.

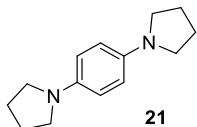
These data are in full agreement with those previously published in the literature.⁴⁷



1-(4-bromophenyl)pyrrolidine. From pyrrolidine (256.0 mg, 295.6 μ l, 3.6 mmol, 3.0 equiv.) and 1,4-dibromobenzene (283.1 mg, 1.2 mmol, 1.0 equiv.). Reaction time: 24 h. Purification with flash chromatography (1. gradient 0-2% ethyl acetate in hexane; 2. Isocratic 2% ethyl acetate in hexane) afforded the title compound (218.4 mg, 0.97 mmol, 80%) as a white solid.

^1H NMR (400 MHz, Chloroform-*d*) δ 7.28 (d, J = 8.9 Hz, 2H), 6.42 (d, J = 8.9 Hz, 2H), 3.29 – 3.16 (m, 4H), 2.05 – 1.96 (m, 4H). ^{13}C NMR (101 MHz, Chloroform-*d*) δ 146.82, 131.68, 113.19, 107.08, 47.68, 25.50. HRMS (ESI-TOF) m/z calcd. for $\text{C}_{10}\text{H}_{13}\text{BrN}$ [(M+H) $^+$]: 226.0226; found: 226.0231.

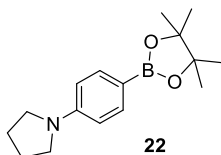
These data are in full agreement with those previously published in the literature.⁶⁰



1-di(4-pyrrolidin-1-yl)benzene. From pyrrolidine (853.3 mg, 985.3 μ l, 12.0 mmol, 10 equiv.) and 1,4-dibromobenzene (283.1 mg, 1.2 mmol, 1.0 equiv.). Reaction time: 144 h. Purification with flash chromatography (1. gradient 0-5% ethyl acetate in hexane; 2. Isocratic 5% ethyl acetate in hexane) afforded the title compound (157.3 mg, 0.73 mmol, 61%) as a white solid. For analysis via NMR spectroscopy, the final product was treated with deuterated trifluoro acetic acid in D_2O .

1H NMR (400 MHz, deuterium oxide) δ 7.17 (s, 4H), 3.20 (m, 8H), 1.68 (m, 8H). ^{13}C NMR (101 MHz, deuterium oxide) δ 143.24, 126.02, 61.01, 25.62. HRMS (ESI-TOF) m/z calcd. for $C_{14}H_{21}N_2$ [(M+H) $^+$]: 217.1700; found: 217.1709

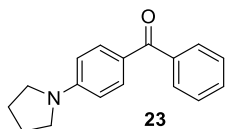
These data are in full agreement with those previously published in the literature.⁶¹



1-(4-(4,4,5,5-tetramethyl-1,3,2-dioxaborolan-2-yl)phenyl)pyrrolidine. From pyrrolidine (256.0 mg, 295.6 μ l, 3.6 mmol, 3.0 equiv.) and 4-bromomethyl-phenylboronic acid pinacol ester (339.6 mg, 1.2 mmol, 1.0 equiv.). Reaction time: 48 h. No internal standard (1,3,5-trimethoxybenzene was used) due to poor separation from the product during flash chromatography. Purification with flash chromatography (1. gradient 0-10% ethyl acetate in hexane; 2. Isocratic 2% ethyl acetate in hexane) afforded the title compound (284.3 mg, 1.04 mmol, 87%) as a white solid.

1H NMR (400 MHz, Chloroform-*d*) δ 7.70 (d, J = 8.6 Hz, 2H), 6.55 (d, J = 8.6 Hz, 2H), 3.39 – 3.17 (m, 4H), 2.13 – 1.92 (m, 4H), 1.35 (s, 12H). ^{13}C NMR (101 MHz, Chloroform-*d*) δ 150.00, 136.24, 113.94, 110.93, 83.06, 47.40, 25.46, 24.88. HRMS (ESI-TOF) m/z calcd. for $C_{16}H_{25}BNO_2$ [(M+H) $^+$]: 274.1973; found: 274.1987.

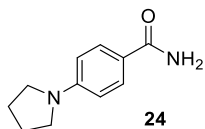
These data are in full agreement with those previously published in the literature.⁶²



phenyl(4-(pyrrolidin-1-yl)phenyl)methanone. From pyrrolidine (256.0 mg, 295.6 μ l, 3.6 mmol, 3.0 equiv.) and 4-bromobenzophenone (313.3 mg, 1.2 mmol, 1.0 equiv.). Reaction time: 48 h. Purification with flash chromatography (1. gradient 0-5% ethyl acetate in hexane; 2. Isocratic 5% ethyl acetate in hexane) afforded the title compound (281.9 mg, 1.12 mmol, 93%) as a white solid.

^1H NMR (600 MHz, Chloroform-*d*) δ 7.78 (d, J = 8.9 Hz, 2H), 7.72 – 7.66 (m, 2H), 7.49 (t, J = 7.4 Hz, 1H), 7.45 – 7.37 (m, 2H), 6.51 (d, J = 8.9 Hz, 2H), 3.38 – 3.27 (m, 4H), 2.02 – 1.95 (m, 4H). ^{13}C NMR (151 MHz, Chloroform-*d*) δ 195.01, 150.88, 139.51, 132.90, 130.95, 129.37, 127.97, 124.20, 110.63, 47.58, 25.42. HRMS (ESI-TOF) m/z calcd. for $\text{C}_{17}\text{H}_{17}\text{NO}$ [(M+H) $^+$]: 252.1383; found: 252.1394.

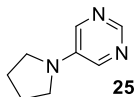
These data are in full agreement with those previously published in the literature.⁶³



1-(4-benzamide)pyrrolidine. From pyrrolidine (256.0 mg, 295.6 μ l, 3.6 mmol, 3.0 equiv.) and 4-bromobenzamide (240.0 mg, 1.2 mmol, 1.0 equiv.). Reaction time: 72 h. Purification with flash chromatography (1. gradient 0-5% methanol in DCM; 2. Isocratic 5% methanol in DCM) afforded the title compound (175.0 mg, 0.92 mmol, 77%) as a white solid.

^1H NMR (400 MHz, DMSO-*d*₆) δ 7.69 (d, J = 8.8 Hz, 2H), 7.58 – 7.52 (brs, 1H), 6.86 – 6.80 (brs, 1H), 6.47 (d, J = 8.8 Hz, 2H), 3.23 (s, 4H), 1.92 (s, 4H). ^{13}C NMR (101 MHz, DMSO-*d*₆) δ 168.05, 149.49, 129.08, 120.24, 110.47, 47.22, 25.01. HRMS (ESI-TOF) m/z calcd. for $\text{C}_{11}\text{H}_{15}\text{N}_2\text{O}$ [(M+H) $^+$]: 191.1179; found: 191.1188.

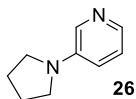
These data are in full agreement with those previously published in the literature.⁶⁴



5-(4-pyrrolidin-1-yl)pyrimidine. From pyrrolidine (256.0 mg, 295.6 μ l, 3.6 mmol, 3.0 equiv.) and 5-bromopyrimidine (190.8 mg, 1.2 mmol, 1.0 equiv.) using 5 mol% NiBr₂·3H₂O (16.4 mg, 60 μ mol). Reaction time: 72 h. Purification with flash chromatography (1. gradient 0-50% ethyl acetate in hexane with 1% Et₃N; 2. Isocratic 50% ethyl acetate in hexane with 1% Et₃N) afforded the title compound (141.3 mg, 0.95 mmol, 79%) as a colorless solid.

¹H NMR (400 MHz, Chloroform-*d*) δ 8.47 (s, 1H), 7.97 (s, 2H), 3.32 – 3.16 (m, 4H), 2.06 – 1.90 (m, 4H). ¹³C NMR (101 MHz, Chloroform-*d*) δ 146.60, 141.09, 139.35, 46.84, 25.27. HRMS (ESI-TOF) *m/z* calcd. for C₈H₁₂N₃ [(M+H)⁺]: 150.1026 ; found: 150.1033.

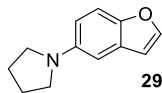
These data are in full agreement with those previously published in the literature.⁶⁵



3-(pyrrolidin-1-yl)pyridine. From pyrrolidine (256.0 mg, 295.6 μ l, 3.6 mmol, 3.0 equiv.) and 3-bromopyridine (189.6 mg, 115.6 μ l, 1.2 mmol, 1.0 equiv.) using 5 mol% NiBr₂·3H₂O (16.4 mg, 60 μ mol). Reaction time: 72 h. Purification with flash chromatography (1. gradient 0-40% ethyl acetate in hexane with 1% Et₃N; 2. Isocratic 40% ethyl acetate in hexane with 1% Et₃N) afforded the title compound (135.2 mg, 0.91 mmol, 76%) as a colorless oil.

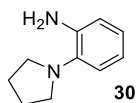
¹H NMR (400 MHz, Chloroform-*d*) δ 7.96 – 7.81 (m, 2H), 7.03 (m, 1H), 6.72 (m, 1H), 3.21 (m, 4H), 2.00 – 1.87 (m, 4H). ¹³C NMR (101 MHz, Chloroform-*d*) δ 143.68, 136.74, 134.23, 123.49, 117.60, 47.19, 25.32. HRMS (ESI-TOF) *m/z* calcd. for C₉H₁₃N₂ [(M+H)⁺]: 149.1074 ; found: 149.1081

These data are in full agreement with those previously published in the literature.⁶⁶



1-(benzofuran-5-yl)pyrrolidine. From pyrrolidine (256.0 mg, 295.6 μ l, 3.6 mmol, 3.0 equiv.) and 5-bromobenzofurane (236.4 mg, 150.3 μ l, 1.2 mmol, 1.0 equiv.) using 5 mol% NiBr₂·3H₂O (16.4 mg, 60 μ mol). Reaction time: 96 h. No internal standard (1,3,5-trimethoxybenzene was used) due to poor separation from the product during flash chromatography. Purification with flash chromatography (1. gradient 0-2% ethyl acetate in hexane; 2. Isocratic 2% ethyl acetate in hexane) afforded the title compound (188.5 mg, 1.01 mmol, 84%) as a colourless oil.

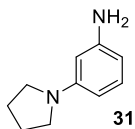
¹H NMR (600 MHz, Chloroform-*d*) δ 7.61 (d, *J* = 2.2 Hz, 1H), 7.47 (d, *J* = 8.9 Hz, 1H), 6.79 (d, *J* = 2.5 Hz, 1H), 6.74 (d, *J* = 2.2 Hz, 1H), 6.71 (dd, *J* = 8.9, 2.5 Hz, 1H), 3.37 (m, 4H), 2.18 – 2.02 (m, 4H). ¹³C NMR (151 MHz, Chloroform-*d*) δ 148.33, 145.31, 145.25, 128.51, 111.58, 110.69, 106.67, 102.17, 48.76, 25.66. HRMS (EI-TOF) *m/z* calcd. for C₁₂H₁₃NO [(M*)⁺]: 187.0997 ; found: 187.0982



2-(pyrrolidin-1-yl)aniline. From pyrrolidine (256.0 mg, 295.6 μ l, 3.6 mmol, 3.0 equiv.) and 2-bromoaniline (206.4 mg, 135.8 μ l, 1.2 mmol, 1.0 equiv.) using 5 mol% NiBr₂·3H₂O (16.4 mg, 60 μ mol). Reaction time: 86 h. Purification with flash chromatography (1. gradient 0-10% ethyl acetate in hexane with 1% Et₃N; 2. Isocratic 10% ethyl acetate in hexane with 1% Et₃N) afforded the title compound (128.6 mg, 0.79 mmol, 66%) as a colorless oil.

¹H NMR (600 MHz, Chloroform-*d*) δ 7.04 (dd, *J* = 7.9, 1.4 Hz, 1H), 6.93 (td, *J* = 7.5, 1.4 Hz, 1H), 6.78 (m, 2H), 3.88 (brs, 2H), 3.15 – 2.98 (m, 4H), 2.03 – 1.80 (m, 4H). ¹³C NMR (151 MHz, Chloroform-*d*) δ 141.59, 137.93, 123.65, 118.85, 118.78, 115.66, 51.09, 24.35. HRMS (EI-TOF) *m/z* calcd. for C₁₀H₁₄N₂ [(M*)⁺]: 162.1157; found: 162.1164

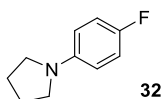
These data are in full agreement with those previously published in the literature.⁶⁷



3-(pyrrolidin-1-yl)aniline. From pyrrolidine (256.0 mg, 295.6 μ l, 3.6 mmol, 3.0 equiv.) and 3-bromoaniline (206.4 mg, 130.6 μ l, 1.2 mmol, 1.0 equiv.) using 5 mol% NiBr₂·3H₂O (16.4 mg, 60 μ mol). Reaction time: 86 h. Purification with flash chromatography (1. gradient 0-3% ethyl acetate in hexane; 2. Isocratic 3% ethyl acetate in hexane; 3. Gradient 3-10% ethyl acetate in hexane; 4. Isocratic 10% ethyl acetate in hexane) afforded the title compound (104.3 mg, 0.64 mmol, 54%) as a slidely brownish oil.

¹H NMR (600 MHz, Chloroform-*d*) δ 7.02 (t, *J* = 8.0 Hz, 1H), 6.05 (m, 2H), 5.92 (t, *J* = 2.3 Hz, 1H), 3.57 (brs, 2H), 3.32 – 3.22 (m, 4H), 2.03 – 1.92 (m, 4H). ¹³C NMR (151 MHz, Chloroform-*d*) δ 148.97, 147.28, 129.79, 103.09, 102.81, 98.39, 47.43, 25.31. HRMS (EI-TOF) *m/z* calcd. for C₁₀H₁₄N₂ [(M)⁺]: 162.1157; found: 162.1151

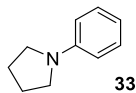
These data are in full agreement with those previously published in the literature.⁶⁸



1-(4-fluorophenyl)pyrrolidine. From pyrrolidine (256.0 mg, 295.6 μ l, 3.6 mmol, 3.0 equiv.) and 4-bromofluorobenzene (210.0 mg, 131.8 μ l, 1.2 mmol, 1.0 equiv.) using 5 mol% NiBr₂·3H₂O (16.4 mg, 60 μ mol). Reaction time: 72 h. Purification with flash chromatography (1. gradient 0-3% ethyl acetate in hexane; 2. Isocratic 3% ethyl acetate in hexane) afforded the title compound (128.8 mg, 0.78 mmol, 65 %) as a white solid.

¹H NMR (400 MHz, Chloroform-*d*) δ 6.99 – 6.89 (m, 2H), 6.52 – 6.44 (m, 2H), 3.30 – 3.19 (m, 4H), 2.05 – 1.96 (m, 4H). ¹³C NMR (101 MHz, Chloroform-*d*) δ 154.81 (d, *J* = 233.3 Hz), 144.78, 115.48 (d, *J* = 22.0 Hz), 112.05 (d, *J* = 7.1 Hz), 48.10, 25.50. ¹⁹F NMR (564 MHz, Chloroform-*d*) δ -131.00 (s, 1F). HRMS (ESI-TOF) *m/z* calcd. for C₁₀H₁₃FN [(M+H)⁺]: 166.1027 ; found: 166.1033.

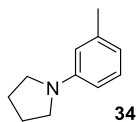
These data are in full agreement with those previously published in the literature.⁶⁰



1-phenylpyrrolidine. From pyrrolidine (256.0 mg, 295.6 μ l, 3.6 mmol, 3.0 equiv.) and bromobenzene (188.4 mg, 125.6 μ l, 1.2 mmol, 1.0 equiv.) using 5 mol% $\text{NiBr}_2 \cdot 3\text{H}_2\text{O}$ (16.4 mg, 60 μ mol). Reaction time: 72 h. Purification with flash chromatography (1. gradient 0-2% ethyl acetate in hexane; 2. Isocratic 2% ethyl acetate in hexane) afforded the title compound (136.9 mg, 0.93 mmol, 77%) as a colourless oil.

^1H NMR (400 MHz, Chloroform-*d*) δ 7.35 (m, 2H), 6.78 (t, $J = 7.3$ Hz, 1H), 6.69 (d, $J = 8.0$ Hz, 2H), 3.43 – 3.30 (m, 4H), 2.13 – 2.05 (m, 4H). ^{13}C NMR (101 MHz, Chloroform-*d*) δ 148.04, 129.25, 115.49, 111.77, 47.71, 25.61. HRMS (ESI-TOF) m/z calcd. for $\text{C}_{10}\text{H}_{14}\text{N}$ [(M+H) $^+$]: 148.1121; found: 148.1122.

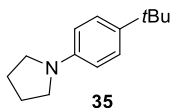
These data are in full agreement with those previously published in the literature.⁴⁷



1-(m-tolyl)pyrrolidine. From pyrrolidine (256.0 mg, 295.6 μ l, 3.6 mmol, 3.0 equiv.) and 3-bromotoluene (188.4 mg, 145.6 μ l, 1.2 mmol, 1.0 equiv.) using 5 mol% $\text{NiBr}_2 \cdot 3\text{H}_2\text{O}$ (16.4 mg, 60 μ mol). Reaction time: 72 h. Purification with flash chromatography (1. gradient 0-2% ethyl acetate in hexane; 2. Isocratic 2% ethyl acetate in hexane) afforded the title compound (134.0 mg, 0.93 mmol, 69%) as a colorless oil.

^1H NMR (400 MHz, Chloroform-*d*) δ 7.24-7.16 (t, $J = 8.8$ Hz, 1H), 6.58 (d, $J = 7.4$ Hz, 1H), 6.51 – 6.44 (m, 2H), 3.35 (m, 4H), 2.41 (s, 3H), 2.11 – 2.00 (m, 4H). ^{13}C NMR (101 MHz, Chloroform-*d*) δ 148.13, 138.86, 129.09, 116.44, 112.45, 108.99, 47.68, 25.56, 21.98. HRMS (ESI-TOF) m/z calcd. for $\text{C}_{11}\text{H}_{16}\text{N}$ [(M+H) $^+$]: 162.1278; found: 162.1282.

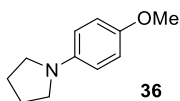
These data are in full agreement with those previously published in the literature.⁵⁸



1-(4-(tert-butyl)phenyl)pyrrolidine. From pyrrolidine (256.0 mg, 295.6 μ l, 3.6 mmol, 3.0 equiv.) and 4-bromotertbutylbenzene (255.7 mg, 208.8 μ l, 1.2 mmol, 1.0 equiv.) using 5 mol% $\text{NiBr}_2 \cdot 3\text{H}_2\text{O}$ (16.4 mg, 60 μ mol). Reaction time: 72 h. Purification with flash chromatography (1. gradient 0-3% ethyl acetate in hexane; 2. Isocratic 3% ethyl acetate in hexane) afforded the title compound (203.2 mg, 1.00 mmol, 83%) as a white solid.

^1H NMR (400 MHz, Chloroform-*d*) δ 7.37 (d, $J = 7.0$ Hz, 2H), 6.64 (d, $J = 7.0$ Hz, 2H), 3.42 – 3.30 (m, 4H), 2.11 – 2.02 (m, 4H), 1.40 (s, 9H). ^{13}C NMR (101 MHz, Chloroform-*d*) δ 145.94, 138.03, 125.99, 111.43, 47.79, 33.82, 31.70, 25.56. HRMS (ESI-TOF) m/z calcd. for $\text{C}_{14}\text{H}_{22}\text{N}$ [(M+H) $^+$]: 204.1747; found: 204.1759.

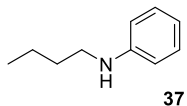
These data are in full agreement with those previously published in the literature.⁴⁷



1-(4-methoxyphenyl)pyrrolidine. From pyrrolidine (256.0 mg, 295.6 μ l, 3.6 mmol, 3.0 equiv.) and 4-bromoanisole (224.4 mg, 150.2 μ l, 1.2 mmol, 1.0 equiv.) using 5 mol% $\text{NiBr}_2 \cdot 3\text{H}_2\text{O}$ (16.4 mg, 60 μ mol). Reaction time: 72 h. No internal standard (1,3,5-trimethoxybenzene was used) due to poor separation from the product during flash chromatography. Purification with flash chromatography (1. gradient 0-5% ethyl acetate in hexane; 2. Isocratic 5% ethyl acetate in hexane) afforded the title compound (154.7 mg, 0.87 mmol, 73%) as a white solid.

^1H NMR (400 MHz, Chloroform-*d*) δ 6.88 (d, $J = 8.1$ Hz, 2H), 6.57 (d, $J = 8.1$ Hz, 2H), 3.78 (s, 3H), 3.32 – 3.18 (m, 4H), 2.07 – 1.94 (m, 4H). ^{13}C NMR (101 MHz, Chloroform-*d*) δ 150.75, 143.25, 115.01, 112.59, 56.01, 48.24, 25.41. HRMS (ESI-TOF) m/z calcd. for $\text{C}_{11}\text{H}_{16}\text{NO}$ [(M+H) $^+$]: 178.1227; found: 178.1236

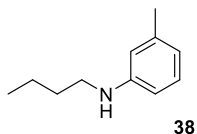
These data are in full agreement with those previously published in the literature.⁴⁷



N-butylaniline. From *n*-butylamine (263.3 mg, 355.8 μ l, 3.6 mmol, 3.0 equiv.), 7-Methyl-1,5,7-triazabicyclo[4.4.0]dec-5-ene (MTBD) (367.8 mg, 344.7 μ l, 2.4 mmol, 2.0 equiv.) and bromobenzene (188.4 mg, 125.6 μ l, 1.2 mmol, 1.0 equiv.) using 5 mol% NiBr₂·3H₂O (16.4 mg, 60 μ mol.). Reaction time: 168 h. Purification with flash chromatography (1. gradient 0-2% ethyl acetate in hexane; 2. Isocratic 2% ethyl acetate in hexane) afforded the title compound (154.6 mg, 1.04 mmol, 86%) as a colourless oil.

¹H NMR (400 MHz, Chloroform-*d*) δ 7.20 (dd, $J = 7.4, 7.6$ Hz, 2H), 6.72 (t, $J = 7.4$ Hz, 1H), 6.64 (d, $J = 7.6$ Hz, 2H), 3.65 (brs, 1H), 3.14 (t, $J = 7.1$ Hz, 1H), 1.71 – 1.56 (m, 1H), 1.47 (dq, $J = 9.4, 7.3$ Hz, 1H), 0.99 (t, $J = 7.3$ Hz, 2H). ¹³C NMR (101 MHz, Chloroform-*d*) δ 148.51, 129.33, 117.30, 112.90, 43.87, 31.74, 20.42, 14.04. HRMS (EI-TOF) m/z calcd. for C₁₀H₁₅N [(M*)⁺]: 149.1204; found: 149.1203

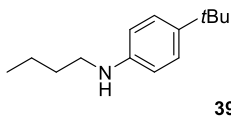
These data are in full agreement with those previously published in the literature.⁶⁹



N-butyl-3-methylaniline. From *n*-butylamine (263.3 mg, 355.8 μ l, 3.6 mmol, 3.0 equiv.), 7-Methyl-1,5,7-triazabicyclo[4.4.0]dec-5-ene (MTBD) (367.8 mg, 344.7 μ l, 2.4 mmol, 2.0 equiv.) and 3-bromotoluene (205.2 mg, 145.6 μ l, 1.2 mmol, 1.0 equiv.) using 5 mol% NiBr₂·3H₂O (16.4 mg, 60 μ mol.). Reaction time: 168 h. Purification with flash chromatography (1. gradient 0-2% ethyl acetate in hexane; 2. Isocratic 2% ethyl acetate in hexane) afforded the title compound (163.7 mg, 1.00 mmol, 84%) as a colourless oil.

¹H NMR (400 MHz, Chloroform-*d*) δ 7.18 – 7.05 (m, 1H), 6.58 (d, $J = 7.5$ Hz, 1H), 6.54 – 6.44 (m, 2H), 3.72 (brs, 1H), 3.15 (t, $J = 7.1$ Hz, 2H), 2.33 (s, 3H), 1.72 – 1.58 (m, 2H), 1.55 – 1.38 (m, 2H), 1.01 (t, $J = 7.3$ Hz, 3H). ¹³C NMR (101 MHz, Chloroform-*d*) δ 148.52, 139.05, 129.18, 118.26, 113.69, 110.09, 43.90, 31.75, 21.73, 20.41, 14.02. HRMS (EI-TOF) m/z calcd. for C₁₁H₁₈N [(M+H)⁺]: 163.1361; found: 163.1360

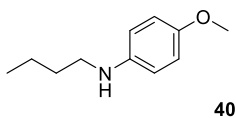
These data are in full agreement with those previously published in the literature.⁶⁹



4-(tert-butyl)-N-butylaniline. From *n*-butylamine (263.3 mg, 355.8 μ l, 3.6 mmol, 3.0 equiv.), 7-Methyl-1,5,7-triazabicyclo[4.4.0]dec-5-ene (MTBD) (367.8 mg, 344.7 μ l, 2.4 mmol, 2.0 equiv.) and 4-bromotertbutylbenzene (255.7 mg, 208.8 μ l, 1.2 mmol, 1.0 equiv.) using 5 mol% NiBr₂·3H₂O (16.4 mg, 60 μ mol.). Reaction time: 168 h. Purification with flash chromatography (1. gradient 0-2% ethyl acetate in hexane; 2. Isocratic 2% ethyl acetate in hexane) afforded the title compound (206.4 mg, 1.01 mmol, 84%) as a colourless oil.

¹H NMR (600 MHz, Chloroform-*d*) δ 7.35 (d, J = 8.8 Hz, 2H), 6.70 (d, J = 8.8 Hz, 2H), 3.61 (s, 1H), 3.24 (t, J = 7.2 Hz, 2H), 1.77 – 1.70 (m, 2H), 1.62 – 1.53 (m, 2H), 1.44 (s, 9H), 1.11 (t, J = 7.4 Hz, 3H). ¹³C NMR (151 MHz, Chloroform-*d*) δ 146.36, 139.92, 126.09, 112.51, 44.02, 33.94, 31.91, 31.69, 20.45, 14.06. HRMS (EI-TOF) m/z calcd. for C₁₄H₂₃N [(M*)⁺]: 205.1830; found: 205.1834

These data are in full agreement with those previously published in the literature.⁶⁹



N-butyl-4-methoxyaniline. From *n*-butylamine (263.3 mg, 355.8 μ l, 3.6 mmol, 3.0 equiv.), 7-Methyl-1,5,7-triazabicyclo[4.4.0]dec-5-ene (MTBD) (367.8 mg, 344.7 μ l, 2.4 mmol, 2.0 equiv.) and 4-bromoanisole (224.4 mg, 150.2 μ l, 1.2 mmol, 1.0 equiv.) using 5 mol% NiBr₂·3H₂O (16.4 mg, 60 μ mol.). Reaction time: 168 h. Purification with flash chromatography (1. gradient 0-4% ethyl acetate in hexane; 2. Isocratic 4% ethyl acetate in hexane) afforded the title compound (135.7 mg, 0.76 mmol, 63%) as a colourless oil.

¹H NMR (600 MHz, Chloroform-*d*) δ 6.79 (d, J = 8.9 Hz, 2H), 6.61 (d, J = 8.9 Hz, 2H), 3.75 (s, 3H), 3.57 (s, 1H), 3.07 (t, J = 7.1 Hz, 2H), 1.67 – 1.54 (m, 2H), 1.51 – 1.35 (m, 2H), 0.96 (t, J = 7.3 Hz, 3H). ¹³C NMR (151 MHz, Chloroform-*d*) δ 152.24, 142.66, 115.01, 114.37, 55.95, 45.01, 31.82, 20.45, 14.06. HRMS (EI-TOF) m/z calcd. for C₁₁H₁₇NO [(M*)⁺]: 179.1310; found: 179.1303

These data are in full agreement with those previously published in the literature.⁶⁹

Chapter 4

Copies of NMR spectra of isolated compounds

Copies of NMR spectra of isolated compounds are available in the Supporting Information through the website of the Publisher. DOI: <https://doi.org/10.1038/s41929-020-0473-6>

4.5 References

1. Roughley, S. D.; Jordan, A. M., The Medicinal Chemist's Toolbox: An Analysis of Reactions Used in the Pursuit of Drug Candidates. *J. Med. Chem.* **2011**, *54* (10), 3451-3479.
2. Wolfe, J. P.; Buchwald, S. L., Nickel-Catalyzed Amination of Aryl Chlorides. *J. Am. Chem. Soc.* **1997**, *119* (26), 6054-6058.
3. Ge, S.; Green, R. A.; Hartwig, J. F., Controlling First-Row Catalysts: Amination of Aryl and Heteroaryl Chlorides and Bromides with Primary Aliphatic Amines Catalyzed by a BINAP-Ligated Single-Component Ni(0) Complex. *J. Am. Chem. Soc.* **2014**, *136* (4), 1617-1627.
4. Tassone, J. P.; England, E. V.; MacQueen, P. M.; Ferguson, M. J.; Stradiotto, M., PhPAd-DalPhos: Ligand-Enabled, Nickel-Catalyzed Cross-Coupling of (Hetero)aryl Electrophiles with Bulky Primary Alkylamines. *Angew. Chem. Int. Ed.* **2019**, *58* (8), 2485-2489.
5. Kelly, R. A.; Scott, N. M.; Díez-González, S.; Stevens, E. D.; Nolan, S. P., Simple Synthesis of CpNi(NHC)Cl Complexes (Cp = Cyclopentadienyl; NHC = N-Heterocyclic Carbene). *Organometallics* **2005**, *24* (14), 3442-3447.
6. Park, N. H.; Teverovskiy, G.; Buchwald, S. L., Development of an Air-Stable Nickel Precatalyst for the Amination of Aryl Chlorides, Sulfamates, Mesylates, and Triflates. *Org. Lett.* **2014**, *16* (1), 220-223.
7. Kampmann, S. S.; Skelton, B. W.; Wild, D. A.; Koutsantonis, G. A.; Stewart, S. G., An Air-Stable Nickel(0) Phosphite Precatalyst for Primary Alkylamine C–N Cross-Coupling Reactions. *Eur. J. Org. Chem.* **2015**, *2015* (27), 5995-6004.
8. Shields, J. D.; Gray, E. E.; Doyle, A. G., A Modular, Air-Stable Nickel Precatalyst. *Org. Lett.* **2015**, *17* (9), 2166-2169.
9. McGuire, R. T.; Paffile, J. F. J.; Zhou, Y.; Stradiotto, M., Nickel-Catalyzed C–N Cross-Coupling of Ammonia, (Hetero)anilines, and Indoles with Activated (Hetero)aryl Chlorides Enabled by Ligand Design. *ACS Catal.* **2019**, *9* (10), 9292-9297.
10. Li, C.; Kawamata, Y.; Nakamura, H.; Vantourout, J. C.; Liu, Z.; Hou, Q.; Bao, D.; Starr, J. T.; Chen, J.; Yan, M.; Baran, P. S., Electrochemically Enabled, Nickel-Catalyzed Amination. *Angew. Chem. Int. Ed.* **2017**, *56* (42), 13088-13093.
11. Kawamata, Y.; Vantourout, J. C.; Hickey, D. P.; Bai, P.; Chen, L.; Hou, Q.; Qiao, W.; Barman, K.; Edwards, M. A.; Garrido-Castro, A. F.; deGruyter, J. N.; Nakamura, H.;

Knouse, K.; Qin, C.; Clay, K. J.; Bao, D.; Li, C.; Starr, J. T.; Garcia-Irizarry, C.; Sach, N.; White, H. S.; Neurock, M.; Minter, S. D.; Baran, P. S., Electrochemically Driven, Ni-Catalyzed Aryl Amination: Scope, Mechanism, and Applications. *J. Am. Chem. Soc.* **2019**, *141* (15), 6392-6402.

12. Lim, C.-H.; Kudisch, M.; Liu, B.; Miyake, G. M., C–N Cross-Coupling via Photoexcitation of Nickel–Amine Complexes. *J. Am. Chem. Soc.* **2018**, *140* (24), 7667-7673.

13. Du, Y.; Pearson, R. M.; Lim, C.-H.; Sartor, S. M.; Ryan, M. D.; Yang, H.; Damrauer, N. H.; Miyake, G. M., Strongly Reducing, Visible-Light Organic Photoredox Catalysts as Sustainable Alternatives to Precious Metals. *Chemistry – A European Journal* **2017**, *23* (46), 10962-10968.

14. Caputo, J. A.; Frenette, L. C.; Zhao, N.; Sowers, K. L.; Krauss, T. D.; Weix, D. J., General and Efficient C–C Bond Forming Photoredox Catalysis with Semiconductor Quantum Dots. *J. Am. Chem. Soc.* **2017**, *139* (12), 4250-4253.

15. Liu, Y.-Y.; Liang, D.; Lu, L.-Q.; Xiao, W.-J., Practical heterogeneous photoredox/nickel dual catalysis for C–N and C–O coupling reactions. *Chem. Commun.* **2019**, *55* (33), 4853-4856.

16. Ghosh, I.; Khamrai, J.; Savateev, A.; Shlapakov, N.; Antonietti, M.; König, B., Organic semiconductor photocatalyst can bifunctionalize arenes and heteroarenes. *Science* **2019**, *365* (6451), 360-366.

17. Corcoran, E. B.; Pirnot, M. T.; Lin, S.; Dreher, S. D.; DiRocco, D. A.; Davies, I. W.; Buchwald, S. L.; MacMillan, D. W. C., Aryl amination using ligand-free Ni(II) salts and photoredox catalysis. *Science* **2016**, *353* (6296), 279-283.

18. Escobar, R. A.; Johannes, J. W., A Unified and Practical Method for Carbon–Heteroatom Cross-Coupling using Nickel/Photo Dual Catalysis. *Chemistry – A European Journal* **2020**, *26* (23), 5168-5173.

19. Kudisch, M.; Lim, C.-H.; Thordarson, P.; Miyake, G. M., Energy Transfer to Ni–Amine Complexes in Dual Catalytic, Light-Driven C–N Cross-Coupling Reactions. *J. Am. Chem. Soc.* **2019**, *141* (49), 19479-19486.

20. Qi, Z.-H.; Ma, J., Dual Role of a Photocatalyst: Generation of Ni(0) Catalyst and Promotion of Catalytic C–N Bond Formation. *ACS Catal.* **2018**, *8* (2), 1456-1463.

21. Wang, C.; Cao, S.; Fu, W.-F., A stable dual-functional system of visible-light-driven Ni(ii) reduction to a nickel nanoparticle catalyst and robust in situ hydrogen production. *Chem. Commun.* **2013**, 49 (96), 11251-11253.
22. Rodríguez, J. L.; Valenzuela, M. A.; Pola, F.; Tiznado, H.; Poznyak, T., Photodeposition of Ni nanoparticles on TiO₂ and their application in the catalytic ozonation of 2,4-dichlorophenoxyacetic acid. *J. Mol. Catal. A: Chem.* **2012**, 353-354, 29-36.
23. Indra, A.; Menezes, P. W.; Kailasam, K.; Hollmann, D.; Schröder, M.; Thomas, A.; Brückner, A.; Driess, M., Nickel as a co-catalyst for photocatalytic hydrogen evolution on graphitic-carbon nitride (sg-CN): what is the nature of the active species? *Chem. Commun.* **2016**, 52 (1), 104-107.
24. Cavedon, C.; Madani, A.; Seeberger, P. H.; Pieber, B., Semiheterogeneous Dual Nickel/Photocatalytic (Thio)etherification Using Carbon Nitrides. *Org. Lett.* **2019**, 21 (13), 5331-5334.
25. Pieber, B.; Malik, J. A.; Cavedon, C.; Gisbertz, S.; Savateev, A.; Cruz, D.; Heil, T.; Zhang, G.; Seeberger, P. H., Semi-heterogeneous Dual Nickel/Photocatalysis using Carbon Nitrides: Esterification of Carboxylic Acids with Aryl Halides. *Angew. Chem. Int. Ed.* **2019**, 58 (28), 9575-9580.
26. Zhang, G.; Li, G.; Lan, Z.-A.; Lin, L.; Savateev, A.; Heil, T.; Zafeiratos, S.; Wang, X.; Antonietti, M., Optimizing Optical Absorption, Exciton Dissociation, and Charge Transfer of a Polymeric Carbon Nitride with Ultrahigh Solar Hydrogen Production Activity. *Angew. Chem. Int. Ed.* **2017**, 56 (43), 13445-13449.
27. Bulky, secondary amines such as N-tert-butylisopropylamine and 2,2,6,6-tetramethylpiperidine do not couple with aryl halides and can be used as a base if 1.5 equivalents of pyrrolidine are used (see Supplementary Information).
28. The reactions can be efficiently carried out on larger scales using continuous flow chemistry: Rosso, C. *et al.* An oscillatory plug flow photoreactor facilitates semi-heterogeneous dual nickel/carbon nitride photocatalytic C–N couplings: Rosso, C.; Gisbertz, S.; Williams, J. D.; Gemoets, H. P. L.; Debrouwer, W.; Pieber, B.; Kappe, C. O., An oscillatory plug flow photoreactor facilitates semi-heterogeneous dual nickel/carbon nitride photocatalytic C–N couplings. *React. Chem. Eng.* **2020**, 5 (3), 597-604.

Chapter 4

29. Interestingly, although 2- and 3-bromoaniline (30 & 31) gave good yields, only a very low amount of the desired product (<5%) was formed when 4-bromoaniline was used (see Supplementary Information).
30. The strong resonance donating effect of fluorine appears sufficient to counteract the inductive withdrawing effect in dual photoredox/nickel catalyzed cross-couplings resulting in low reactivity (see Refs. 22-23).
31. Crabtree, R. H., Deactivation in Homogeneous Transition Metal Catalysis: Causes, Avoidance, and Cure. *Chem. Rev.* **2015**, *115* (1), 127-150.
32. Molina de la Torre, J. A.; Espinet, P.; Albéniz, A. C., Solvent-Induced Reduction of Palladium-Aryls, a Potential Interference in Pd Catalysis. *Organometallics* **2013**, *32* (19), 5428-5434.
33. It has to be noted that a higher concentration does not increase the yield in case of $(\text{Ir}[\text{dF}(\text{CF}_3)\text{ppy}]_2(\text{dtbbpy}))\text{PF}_6$.
34. When no $\text{NiBr}_2 \cdot 3\text{H}_2\text{O}$ is added to the recovered CN-OA-m material containing deposited nickel, only trace amounts of the C-N coupling product were observed (see Supplementary Information).
35. Yu, P.; Morandi, B., Nickel-Catalyzed Cyanation of Aryl Chlorides and Triflates Using Butyronitrile: Merging Retro-hydrocyanation with Cross-Coupling. *Angew. Chem. Int. Ed.* **2017**, *56* (49), 15693-15697.
36. Wang, J.; Zhao, J.; Gong, H., Nickel-catalyzed methylation of aryl halides/tosylates with methyl tosylate. *Chem. Commun.* **2017**, *53* (73), 10180-10183.
37. Mori, A.; Mizusaki, T.; Ikawa, T.; Maegawa, T.; Monguchi, Y.; Sajiki, H., Mechanistic Study of a Pd/C-Catalyzed Reduction of Aryl Sulfonates Using the Mg–MeOH–NH₄OAc System. *Chem. Eur. J.* **2007**, *13* (5), 1432-1441.
38. Brown, H. C.; Kanth, J. V. B.; Dalvi, P. V.; Zaidlewicz, M., Molecular Addition Compounds. 15. Synthesis, Hydroboration, and Reduction Studies of New, Highly Reactive tert-Butyldialkylamine–Borane Adducts. *J. Org. Chem.* **1999**, *64* (17), 6263-6274.
39. Kudisch, M.; Lim, C.-H.; Thordarson, P.; Miyake, G. M., Energy Transfer to Ni-amine Complexes in Dual Catalytic, Light-driven C–N Cross-Coupling Reactions. *J. Am. Chem. Soc.* **2019**, *141* (49), 19479–19486.

40. Terrett, J. A.; Cuthbertson, J. D.; Shurtleff, V. W.; MacMillan, D. W. C., Switching on elusive organometallic mechanisms with photoredox catalysis. *Nature* **2015**, *524*, 330-334.
41. https://www.bauhaus.info/led-baender/tween-light-led-band/p/22517610?gclid=EAIaIQobChMIoLWto9zl3wIVTZSyCh3YDweqEAQYASABEgJmRfD_BwE&s_kwcid=AL!5677!3!190027496787!!!g!462716337331!&pla_prpaid=462716337331&ef_id=EAIaIQobChMIoLWto9zl3wIVTZSyCh3YDweqEAQYASABEgJmRfD_BwE:G:s&pla_adgrid=41635814775&pla_campid=225980581&pla_prch=online&pla_prd=22517610&cid=PSEGoo225980581_41635814775&pla_adt=pla (Germany; 2019 October 16).
42. <https://www.kessil.com/photoreaction/index.php> (Germany, March 2020)
43. Goettmann, F.; Fischer, A.; Antonietti, M.; Thomas, A., Chemical Synthesis of Mesoporous Carbon Nitrides Using Hard Templates and Their Use as a Metal-Free Catalyst for Friedel–Crafts Reaction of Benzene. *Angew. Chem. Int. Ed.* **2006**, *45* (27), 4467-4471.
44. Shalom, M.; Guttentag, M.; Fettkenhauer, C.; Inal, S.; Neher, D.; Llobet, A.; Antonietti, M., In Situ Formation of Heterojunctions in Modified Graphitic Carbon Nitride: Synthesis and Noble Metal Free Photocatalysis. *Chem. Mater.* **2014**, *26* (19), 5812-5818.
45. Zhang, J.; Sun, J.; Maeda, K.; Domen, K.; Liu, P.; Antonietti, M.; Fu, X.; Wang, X., Sulfur-mediated synthesis of carbon nitride: Band-gap engineering and improved functions for photocatalysis. *Energy Environ. Sci.* **2011**, *4* (3), 675-678.
46. Savateev, A.; Pronkin, S.; Epping, J. D.; Willinger, M. G.; Wolff, C.; Neher, D.; Antonietti, M.; Dontsova, D., Potassium Poly(heptazine imides) from Aminotetrazoles: Shifting Band Gaps of Carbon Nitride-like Materials for More Efficient Solar Hydrogen and Oxygen Evolution. *ChemCatChem* **2017**, *9* (1), 167-174.
47. Hamid, M. H.; Allen, C. L.; Lamb, G. W.; Maxwell, A. C.; Maytum, H. C.; Watson, A. J.; Williams, J. M., Ruthenium-catalyzed N-alkylation of amines and sulfonamides using borrowing hydrogen methodology. *J. Am. Chem. Soc.* **2009**, *131* (5), 1766-74.
48. Sandtorv, A. H.; Stuart, D. R., Metal-free Synthesis of Aryl Amines: Beyond Nucleophilic Aromatic Substitution. *Angew. Chem. Int. Ed.* **2016**, *55* (51), 15812-15815.
49. Urgaonkar, S.; Xu, J.-H.; Verkade, J. G., Application of a New Bicyclic Triaminophosphine Ligand in Pd-Catalyzed Buchwald–Hartwig Amination Reactions of Aryl Chlorides, Bromides, and Iodides. *J. Org. Chem.* **2003**, *68* (22), 8416-8423.

50. Lin, S.-X.; Sun, G.-J.; Kang, Q., A visible-light-activated rhodium complex in enantioselective conjugate addition of α -amino radicals with Michael acceptors. *Chem. Commun.* **2017**, 53 (54), 7665-7668.
51. Wolfe, J. P.; Buchwald, S. L., Scope and Limitations of the Pd/BINAP-Catalyzed Amination of Aryl Bromides. *J. Org. Chem.* **2000**, 65 (4), 1144-1157.
52. Xie, X.; Zhang, T. Y.; Zhang, Z., Synthesis of Bulky and Electron-Rich MOP-type Ligands and Their Applications in Palladium-Catalyzed C–N Bond Formation. *J. Org. Chem.* **2006**, 71 (17), 6522-6529.
53. Liu, K.-J.; Zeng, X.-L.; Zhang, Y.; Wang, Y.; Xiao, X.-S.; Yue, H.; Wang, M.; Tang, Z.; He, W.-M., Palladium-Catalyzed Reductive Coupling of Nitroarenes with Phenols-leading to N-Cyclohexylanilines. *Synthesis* **2018**, 50 (23), 4637-4644.
54. Suárez-Pantiga, S.; Hernández-Ruiz, R.; Virumbrales, C.; Pedrosa, M. R.; Sanz, R., Reductive Molybdenum-Catalyzed Direct Amination of Boronic Acids with Nitro Compounds. *Angew. Chem. Int. Ed.* **2019**, 58 (7), 2129-2133.
55. Desmarets, C.; Schneider, R.; Fort, Y., Nickel(0)/Dihydroimidazol-2-ylidene Complex Catalyzed Coupling of Aryl Chlorides and Amines. *J. Org. Chem.* **2002**, 67 (9), 3029-3036.
56. Wolfe, J. P.; Tomori, H.; Sadighi, J. P.; Yin, J.; Buchwald, S. L., Simple, Efficient Catalyst System for the Palladium-Catalyzed Amination of Aryl Chlorides, Bromides, and Triflates. *J. Org. Chem.* **2000**, 65 (4), 1158-1174.
57. Yoshida, H.; Morishita, T.; Ohshita, J., Direct Access to Anthranilic Acid Derivatives via CO₂ Incorporation Reaction Using Arynes. *Org. Lett.* **2008**, 10 (17), 3845-3847.
58. Brenner, E.; Schneider, R.; Fort, Y., Nickel-catalysed couplings of aryl chlorides with secondary amines and piperazines. *Tetrahedron* **1999**, 55 (44), 12829-12842.
59. Johnson, T. C.; Elbert, Bryony L.; Farley, A. J. M.; Gorman, T. W.; Genicot, C.; Lallemand, B.; Pasau, P.; Flasz, J.; Castro, J. L.; MacCoss, M.; Dixon, D. J.; Paton, R. S.; Schofield, C. J.; Smith, M. D.; Willis, M. C., Direct sulfonylation of anilines mediated by visible light. *Chem. Sci.* **2018**, 9 (3), 629-633.
60. Hollmann, D.; Bähn, S.; Tillack, A.; Parton, R.; Altink, R.; Beller, M., A novel salt-free ruthenium-catalyzed alkylation of aryl amines. *Tetrahedron Lett.* **2008**, 49 (40), 5742-5745.

61. Ju, Y.; Varma, R. S., An Efficient and Simple Aqueous N-Heterocyclization of Aniline Derivatives: Microwave-Assisted Synthesis of N-Aryl Azacycloalkanes. *Org. Lett.* **2005**, *7* (12), 2409-2411.
62. Lim, S.; Song, D.; Jeon, S.; Kim, Y.; Kim, H.; Lee, S.; Cho, H.; Lee, B. C.; Kim, S. E.; Kim, K.; Lee, E., Cobalt-Catalyzed C–F Bond Borylation of Aryl Fluorides. *Org. Lett.* **2018**, *20* (22), 7249-7252.
63. Wolfe, J. P.; Buchwald, S. L., Palladium-Catalyzed Amination of Aryl Triflates. *J. Org. Chem.* **1997**, *62* (5), 1264-1267.
64. Lakshminarayana, N.; Prasad, Y. R.; Gharat, L.; Thomas, A.; Narayanan, S.; Raghuram, A.; Srinivasan, C. V.; Gopalan, B., Synthesis and evaluation of some novel dibenzo[b,d]furan carboxylic acids as potential anti-diabetic agents. *Eur. J. Med. Chem.* **2010**, *45* (9), 3709-3718.
65. Charles, M. D.; Schultz, P.; Buchwald, S. L., Efficient Pd-Catalyzed Amination of Heteroaryl Halides. *Org. Lett.* **2005**, *7* (18), 3965-3968.
66. Maiti, D.; Fors, B. P.; Henderson, J. L.; Nakamura, Y.; Buchwald, S. L., Palladium-catalyzed coupling of functionalized primary and secondary amines with aryl and heteroaryl halides: two ligands suffice in most cases. *Chem. Sci.* **2011**, *2* (1), 57-68.
67. Perez Garcia, P. M.; Di Franco, T.; Epenoy, A.; Scopelliti, R.; Hu, X., From Dimethylamine to Pyrrolidine: The Development of an Improved Nickel Pincer Complex for Cross-Coupling of Nonactivated Secondary Alkyl Halides. *ACS Catal.* **2016**, *6* (1), 258-261.
68. Wang, Y.; Ling, J.; Zhang, Y.; Zhang, A.; Yao, Q., N-(1-Oxy-2-picolyl)oxalamic Acid as an Efficient Ligand for Copper-Catalyzed Amination of Aryl Iodides at Room Temperature. *Eur. J. Org. Chem.* **2015**, *2015* (19), 4153-4161.
69. Afanasenko, A.; Elangovan, S.; Stuart, M. C. A.; Bonura, G.; Frusteri, F.; Barta, K., Efficient nickel-catalysed N-alkylation of amines with alcohols. *Catal. Sci. Technol.* **2018**, *8* (21), 5498-5505.

Chapter 4

Chapter 5

An oscillatory plug flow photoreactor facilitates semi-heterogeneous dual nickel/carbon nitride photocatalytic C–N couplings

Rosso, C.; **Gisbertz, S.**; Williams, J. D.; Gemoets, H. P. L.; Debrouwer, W.; Pieber, B.; Kappe, C. O.

React. Chem. Eng. **2020**, *5*, 597-604.

DOI: <https://doi.org/10.1039/D0RE00036A>

Abstract

Carbon nitride materials have emerged as an efficient and sustainable class of heterogeneous photocatalysts, particularly when paired with nickel in dual catalytic cross-coupling reactions. Performing these transformations on larger scales using a continuous process is difficult due to the problems associated with handling solids in flow. By combining an oscillatory pump with a microstructured plug flow photoreactor, a stable suspension of the photocatalyst can be maintained, circumventing clogging of the reactor channels. Through careful tuning of the oscillator properties, the residence time distribution (RTD) was optimized, whilst maintaining a stable catalyst suspension. Short residence times (20 min) were achieved using optimized conditions and the recyclability of the photocatalyst was demonstrated over 10 cycles with no loss of activity. During a stable 4.5 hour scale-out demonstration, the model substrate could be isolated on 12 g scale (90% yield, 2.67 g/h). Moreover, the method was applied for the gram scale synthesis of an intermediate of the active pharmaceutical ingredient tetracaine.

Specific contribution

Dr. B. Pieber, Prof. C. O. Kappe and I conceived the idea behind the project.

Dr. B. Pieber, Dr. J. D. Williams, C. Rosso, and I designed all experiments.

I verified the feasibility of this approach by screening and optimizing the coupling protocol.

I synthesized and characterized the carbon nitride material.

C. Rosso carried out the experiment in flow.

Dr. H. P. Gemoets and Dr. W. Debrouwer developed the microstructured plug flow HANU-reactor.

C. Rosso wrote the manuscript with contributions from all authors.

Dr. B. Pieber and Prof. C. O. Kappe directed the research study and corrected and revised the manuscript.

5.1 Introduction

Due to the ubiquitous presence of aryl amines in natural products and pharmaceutically-relevant compounds, C–N cross-coupling reactions have become one of the most highly utilized transformations in organic synthesis.¹ Over the past two decades, the Buchwald-Hartwig coupling has been steadily improved to efficiently access this moiety using palladium catalysis.²⁻³ Nonetheless, interest has been renewed through the possibility to overcome the typical limitations of those procedures in terms of sustainability, cost (of both metal and ligand) and harsh conditions.⁴ Nickel is an appealing alternative to palladium due to its abundance,⁵ yet must be merged with electro- or photocatalysis,⁶⁻¹⁸ due to the inability of Ni^{II} to undergo reductive elimination, unless strong bases and complex ligands are used.¹⁹

As recently demonstrated, dual nickel/photo catalytic cross-coupling methods represent a promising alternative to palladium catalyzed methods. However, such metallaphotoredox catalysis methodologies usually require UV irradiation or precious metal-based photoredox catalysts to turn over the nickel catalyst,^{7-9, 20} while the use of organic photocatalysts is sometimes limited due to photobleaching.²¹ Heterogeneous semiconductors, on the contrary, are stable, noble-metal free, and easy to prepare.²²⁻²³ Among all heterogeneous photocatalysts, including cadmium-based semiconductors,^{12-13, 24} carbon nitride materials (CNs) hold tremendous promise.²⁵⁻²⁸

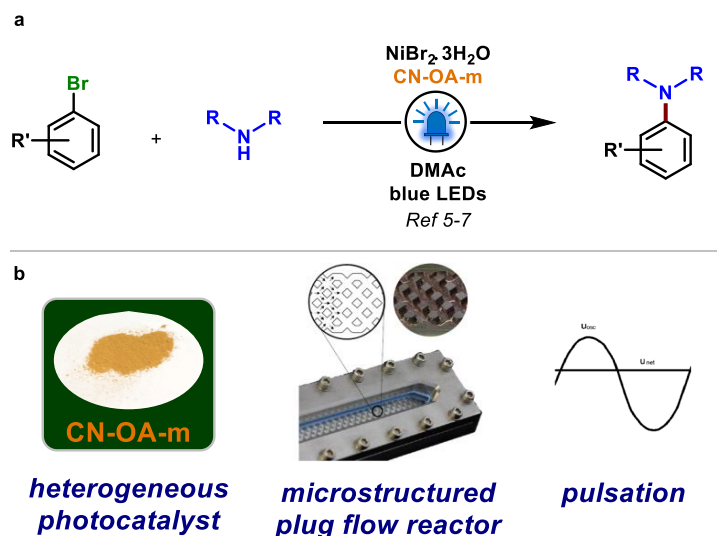


Figure 5.1. (a) General scheme for the metallaphotoredox aryl amination reaction catalyzed by nickel/CN-OA-m catalysis under visible light irradiation. (b) The visual aspect of CN-OA-m photocatalyst and concept representation of the reactor in combination with an external pulsation.

These organic semiconductors are stable, non-toxic, and capable of promoting, amongst other transformations, a series of cross-coupling reactions in the presence of nickel.²⁹⁻³² Recently, mesoporous graphitic carbon nitride (mpg-CN) was shown to efficiently catalyze C-N cross couplings when irradiated with blue light.²⁷ A similar protocol used a carbon nitride derivative, synthesized by co-condensation of urea and oxamide, followed by post-calcination in a molten salt (CN-OA-m).¹⁴ Interestingly, this catalytic system was able to convert both electron-rich and electron-poor aryl halides using blue or green light irradiation, avoiding catalyst deactivation via the formation of nickel-black. The CN-OA-m photocatalyst could be recycled multiple times without any loss of its catalytic activity. The straightforward recycling strategies (centrifugation or filtration) of the carbon nitrides make them attractive for cost-efficient and sustainable processes.²²⁻²³ Photochemical transformations are generally difficult to scale-up in batch reactors as light penetration is limited (as described by the Beer–Lambert law).³³ Continuous flow photochemistry can address these drawbacks by maintaining a short irradiated path length, which also significantly improves the efficiency of photochemical reactions, leading to shorter reaction times and higher productivity.³⁴⁻³⁸ The use of solid compounds, such as CN photocatalysts, in a flow setup remains one of the central challenges in continuous processing.³⁹⁻⁴⁰ Indeed, complex reactor designs (agitated cells or multijet oscillating disk) or continuous stirred-tank reactor (CSTR) cascades have been proposed as solutions, but maintain their intrinsic limitations of complex moving parts or poor residence time distributions.⁴¹⁻⁵⁰ Another alternative is the use of a pulsator that prevents settling of solid materials, without having issues surrounding the long term wear of moving reactor parts. This principle has been demonstrated in baffled and baffle-less tubular flow reactors for several applications (e.g. crystallizations, precipitations⁵¹⁻⁵⁶ and few examples of synthetic transformations).⁵⁷ However, to our knowledge, no successful efforts have been reported utilizing an oscillatory microstructured plug flow photoreactor to enable continuous heterogeneous catalysis. Herein we report a strategy for handling solids in flow for heterogeneous photocatalysis, by using a microstructured plug flow photoreactor in combination with pulsation delivered by a pulsator. The oscillation, combined with narrow channels formed by static mixing elements in the reactor, is designed to maintain a homogenized suspension of the carbon nitride particles, mitigating the risk of settling and reactor wall fouling, regardless of the net flow

rate. The feasibility of this technology was evaluated for a nickel/photo catalytic aryl amination using CN-OA-m under visible light irradiation (Figure 5.1).

5.2 Results and discussion

Reaction setup and preliminary experiments

A commercially available plug flow photoreactor (HANUTM reactor, Creaflow) was employed in this study.⁵⁸ It is comprised of a Hastelloy baseplate housing a flow channel with a series of cubic static mixing elements, topped with lid and glass or quartz window to allow visible/UV light irradiation (15 mL internal volume, 2 × 2 mm channel depth and width). A symmetrical pulse was delivered by an oscillatory diaphragm pulsator unit, positioned between the reactor and a metering pump (which generates the net flow through the system). The static mixing elements split and recombine the process stream under the imposed pulsation. The narrow channels increase pulsation velocity and improve turbulence inside the reactor, encouraging suspension of solids, even at low net flow rates. In addition, the excellent film refreshment promotes efficient photon utilization for photochemical transformations. The flow reactor is equipped with an integrated heat exchanger which enables temperature control (heating or cooling) to ensure isothermal conditions.

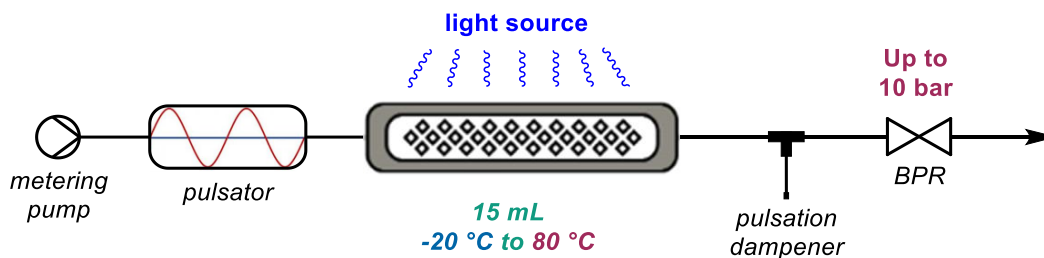


Figure 5.2. Schematic representation of the reaction setup including metering pump, pulsator, reaction plate, light source, pulsation dampener and BPR. For a photograph of the setup see the Figure 5.7. and Figure 5.16.

In a typical reaction, the heterogeneous reaction mixture was kept suspended in a stirred feed vessel and fed into the system through the peristaltic metering pump, under the appropriate pulsation regime. The arrangement was pressurized at 3 bar using a back pressure regulator (BPR) capable of handling solids (BPR-10, Zaiput) and a pulsation dampener (air-filled tube connected by a Y-piece) was placed between the reactor and the BPR, in order to prevent cavitation or suction of air from the end of the system during the backward pulsation (Figure 5.2).

The amination of ethyl 4-bromobenzoate (**1**) with pyrrolidine (**2a**, 3 equiv.) under blue light irradiation was selected as a model reaction. Initial reaction conditions were adapted from a previous publication: nickel(II) bromide trihydrate (2.5 mol%) and CN-OA-m (3.33 mg/mL) as metal and photocatalyst, respectively, in *N,N*-dimethylacetamide (DMAc, [1] = 0.2 M) (Figure 5.3 a).¹⁴ In a preliminary experiment, the pulsation amplitude was set to 70% (~0.32 mL per stroke) and the pulsation frequency to 3 Hz (100%) (see 5.4 for details). By using the specified pulsation, the solid/liquid suspension was observed to be stable along the whole system. Gratifyingly, the C–N coupling product **3a** was observed by HPLC in 66% and 77% assay yield at 40 and 50 °C respectively using a residence time of 15 min.

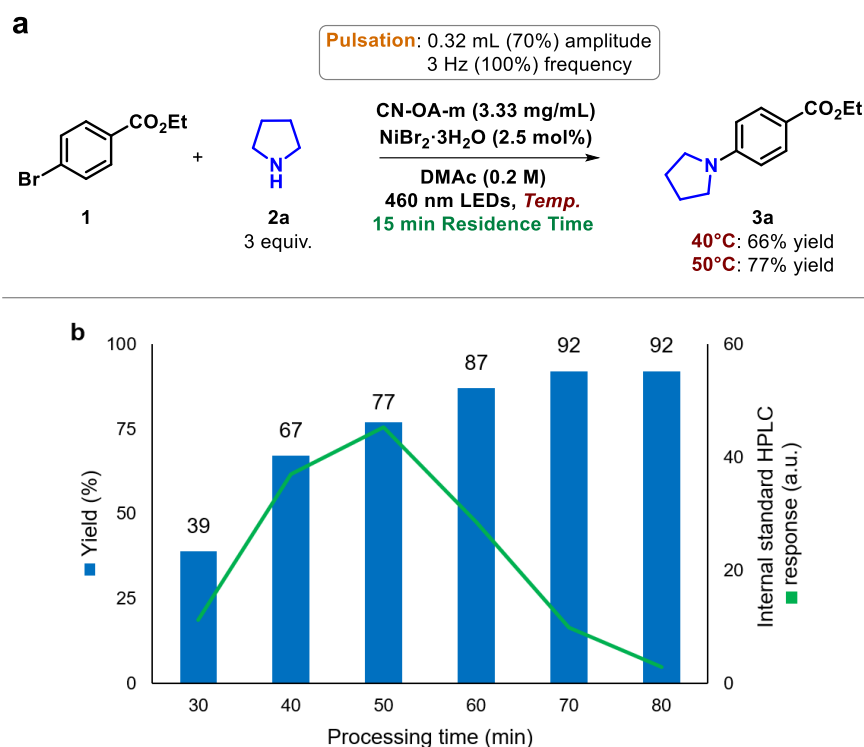


Figure 5.3. (a) Reaction scheme for preliminary photochemical aryl amination experiments. Yields were determined by HPLC assay at the maximum concentration (50 min) using 4-ethylbiphenyl as the internal standard. (b) HPLC response of internal standard, relative to concentration (green line) and yield (blue bars) profile over the collection time, determined by HPLC using 4-ethylbiphenyl as the internal standard.

The material exiting the reactor was monitored over time by HPLC, providing both its relative concentration at the analyzed time point (Figure 5.3 b, green line) and the assay yield of desired product **3a** (Figure 5.3 b, blue bars). Surprisingly, an unusual concentration/yield course was observed during these first trials. An ideal distribution of the two parameters over the time should follow a Gaussian-type profile, where the highest concentration corresponds to the highest yield.^{14, 34, 59} Conversely, the observed trend showed an increasing yield after

the maximum concentration was reached - a strong deviation from the expected trend. The very same concentration/yield profile was also observed in the absence of any insoluble component, suggesting that this effect is not due to the solid photocatalyst (see **5.4.3.1** for details). To ascertain that this is phenomenon is unrelated to issues in reaching steady state conditions, the reaction was carried out with a 50 mL stock solution (in place of 25 mL), in which case an identical trend in yield was observed. Furthermore, no difference was seen when the reactor was filled with the reaction mixture prior to turning on the lamps (ensuring a constant concentration of reaction mixture at the beginning of the reaction, see **5.4.3.1** for details). A similar observation (with opposite effect) has been made in a recent report on handling solids in a photo CSTR cascade, which was explained by a poor residence time distribution.⁴⁸

As further validation, an experiment without photocatalyst (background reaction only) was performed both in this reactor and in a smaller plate-based photoreactor (Lab Photo Reactor, Corning).⁶⁰⁻⁶¹ In the smaller volume reactor, the expected concentration/yield plots were observed (see **5.4**), implying that this deviation is due to the reactor itself. Accordingly, further efforts were devoted to the characterization of the reactor, in order to understand and minimize this effect.

Residence time distribution studies

In order to understand the reactor performance, a series of residence time distribution (RTD) experiments were designed and carried out. Specifically, these focused on the two novel process parameters in this reactor setup: pulsation amplitude (mL displaced per pump stroke) and frequency (number of strokes per second, Hz). First, the correlation between the programmed pulsation amplitude and displaced volume was quantified, proving its linearity, with a maximum displaced volume of ~0.44 mL per stroke (see 5.4.3.3 for details).

Subsequently, an array of RTD experiments were carried out, using a colored tracer pulse and a UV/vis cell, at different pulsation amplitudes and frequencies (see 5.4.3.4 for details). As benchmark, a curve was plotted in the absence of pulsation, which resulted in a fairly wide distribution profile (Figure 5.4 a yellow curve). The distribution profiles proved to be even broader at high pulsation amplitudes (>30% amplitude). These results could be quantified by low Bodenstein numbers (dimensionless number, Bo , which characterizes the extent of axial dispersion within the reactor), calculated from the mathematical deconvolution of the tracer experiments. The Bodenstein value should be maximized, and

values below 100 represent an appreciable level of axial dispersion (i.e. non-ideal plug flow behavior).⁶² For higher pulsation amplitudes, a decrease from 35 (at 0.12 mL amplitude) to 10 (at 0.32 mL amplitude) was observed. Gratifyingly, the lowest pulsation amplitude of 0.04 mL actually provided a significantly narrower residence time distribution curve compared to the benchmark case (without pulsation), implying a significant decrease in axial dispersion. The corresponding Bo values quantify this observation, providing a substantial increase from 48 (no pulsation) to 128 (at 0.04 mL amplitude).

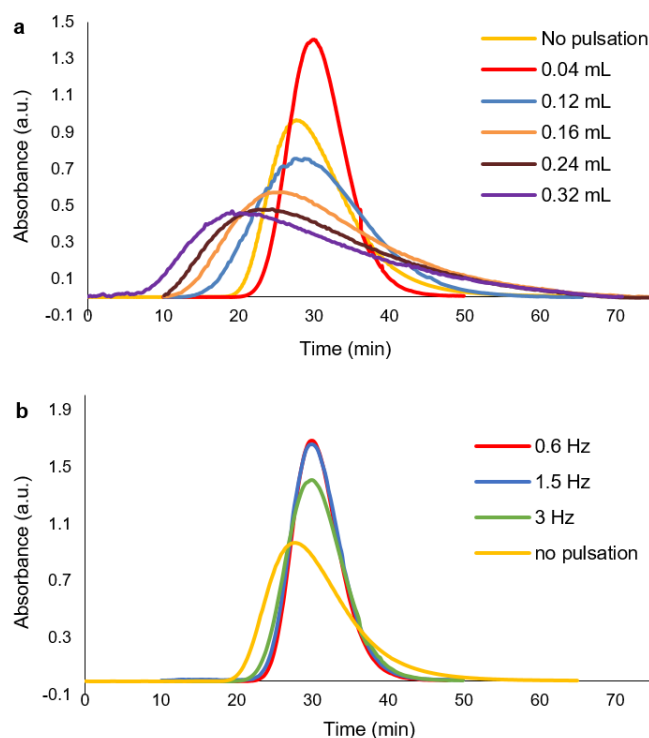


Figure 5.4. RTD profiles using pulses of rose bengal dye in DMAc. Conditions: flow rate = 0.75 mL/min, back pressure = 3 bar, injected tracer volume = 1 mL. (a) Experiments performed at 3 Hz (100%) pulsation frequency and different pulsation amplitudes. (b) Experiments performed at 0.04 mL (<5%) pulsation amplitude using different pulsation frequencies.

The effect of pulsation frequency showed a trend of increasing Bo with decreased pulsation amplitude from 3 to 0.6 Hz (Figure 5.4 b). A maximum Bo value of 184 could be achieved (0.04 mL, 0.6 Hz), demonstrating plug flow behavior for the microstructured flow photoreactor. These observations serve to reinforce the significant benefits of using an oscillatory flow regime in combination with flow reactors in order to enable the handling of solids in continuous flow.

The numerical interpretation of the initial RTD ($Bo = 10$) trials therefore confirm the presence of a non-ideal plug flow behaviour, (see 5.4.3.4 for details). This result is consistent with the observed chemical result (Figure 5.3 b), since the initial reactions were performed under conditions providing an extremely low Bo value (0.32 mL, 3 Hz, $Bo = 10$). Based on this correlation, setting suitable pulsation parameters is essential to ensure proper suspension of the solid photocatalyst, whilst maintaining plug flow behavior (minimizing backmixing).

Optimization of the light-mediated C–N coupling

In light of the preliminary results in the model aryl amination, further optimization experiments were performed minimizing the pulsation amplitude and frequency (Table 5.1). As anticipated, reducing the pulsation amplitude from 0.32 mL (70%) to 0.16 mL (30%) led to an increase in yield of product **3a** from 77% to 83% (entry 2, this reaction was performed in triplicate to illustrate reproducibility, see Figure 5.23). In addition, lowering the amplitude to 0.12 mL (20%, the minimum value capable of keeping CN-OA-m suspended) and extending the residence time to 20 min, provided compound **3a** in 94% yield (entry 4). Finally, decreasing the pulsation frequency to the minimum affordable value of 1.5 Hz (50%) resulted in a quantitative formation of **3a** (entry 5). Furthermore, the observed yield/concentration began to follow a more expected trend, demonstrating a quasi plug flow behavior for the reaction setup (see 5.4 for details). Remarkably, this demonstrates that finding the ideal compromise between sufficient solid suspension and reduced backmixing ensures excellent solid-handling and high yields of product **3a**. Compared with the previously reported procedure in batch, this flow procedure offers a significant improvement in terms of reaction time (20 minutes vs 8 hours).¹⁴

Table 5.1. Metallaphotoredox aryl amination optimization study.^a

Entry	Residence time (min)	Pulsation amplitude (mL / %)	Pulsation frequency (Hz / %)	Yield ^b (%)
1	15	0.32 / 70	3 / 100	77
2	15	0.16 / 30	3 / 100	83
3	15	0.12 / 20	3 / 100	86
4	20	0.12 / 20	3 / 100	94
5	20	0.12 / 20	1.5 / 50	99

^aReaction conditions: ethyl 4-bromobenzoate (**1**, 5 mmol scale), pyrrolidine (**2a**, 3 equiv.), NiBr₂·3H₂O (2.5 mol%) and CN-OA-m (3.33 mg/mL) in DMAc (0.2 M) under blue light irradiation (460 nm). Reactions were performed using a 25 mL stock solution. ^bYield was determined by HPLC assay at the time point where concentration was at a maximum, using 4-ethylbiphenyl as the internal standard.

Photocatalyst recyclability

Likely the most substantial benefits of using a heterogeneous photocatalyst are its ease of separation (i.e. filtration) and potential recyclability.^{31-32, 63} Therefore, we sought to determine whether the CN-OA-m catalyst is recyclable in this setup under the optimized reaction conditions. Previous studies have shown that the deposition of nickel-black agglomerates, formed over time, on the heterogeneous material can affect its catalytic properties.¹⁴ We envisage that, due to the far shorter irradiation time in flow, it may be possible to limit the nickel catalyst deactivation, allowing more effective recycling of the heterogeneous photocatalyst.

The CN-OA-m was recovered after each run by centrifugation, was washed, and used again in the next run by adding fresh nickel(II) bromide. Gratifyingly, no loss of activity was observed over six cycles (Fig. 5). Thereafter, a minor reduction in the yield of **3a** was observed (from 99% to 95% yield in the tenth cycle), but this can be rationalized by the loss of small amounts of CN-OA-m (~3 mg per experiment) during the manual recovery operations between experiments. Indeed, by using fresh CN-OA-m in the same quantity as the last cycle, a comparable result was obtained (94% yield) confirming our hypothesis. This outcome suggests that catalyst deactivation can be avoided by using intensified conditions to prevent deleterious off-cycle side reactions.

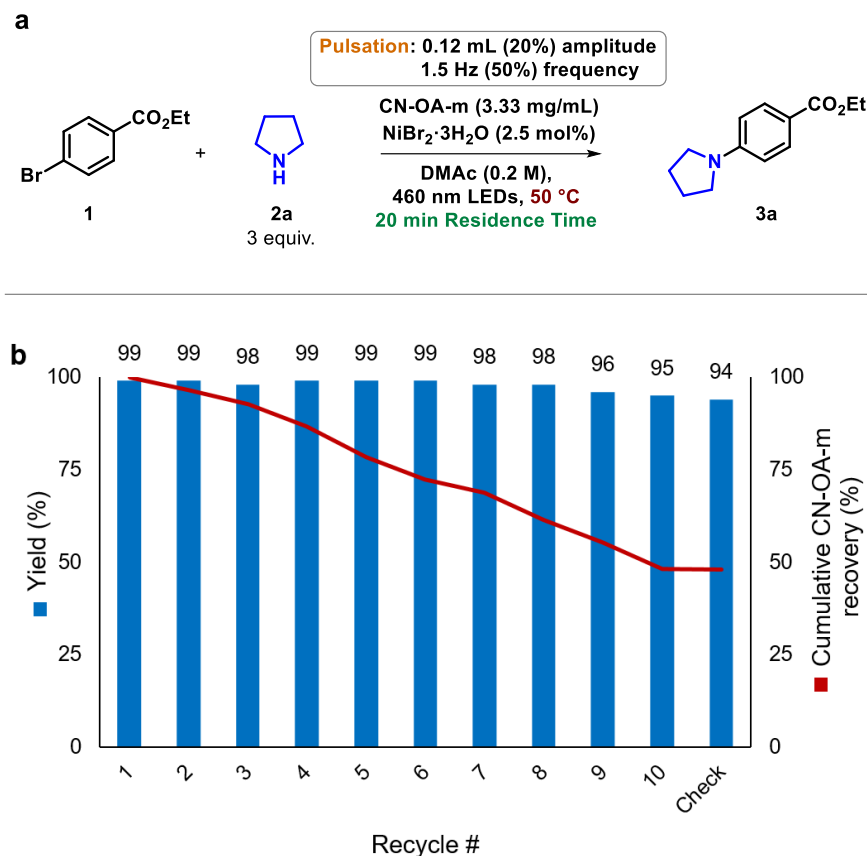


Figure 5.5. (a) Reaction scheme for the CN-OA-m recycling experiments under the optimized conditions. (b) Catalytic performance of recovered CN-OA-m over ten cycles. Yield of product **3** (green bars) were determined by HPLC assay using 4-ethylbiphenyl as the internal standard at the concentration maximum over the collection time. CN-OA-m recovery (red line) was determined by weighing the recovered material after centrifugation, washing and drying.

Scale-out synthesis

A scale-out experiment was performed in order to demonstrate the stability, robustness and scalability of our protocol. It should be noted that the preparation of the CN-OA-m photocatalyst by simple calcination,^{14, 31-32} results in particles that differ in size and aggregation tendency.⁶⁴ The material was observed to have two distinct median particle sizes (D50), of ~5 μm and ~20 μm . The larger type of these particles led to a further complication in handling for long periods, due to settling in the outlet tube of the reactor, even at adequately high pulsation (see 5.4.8 for details). Attempts to mill the particles to smaller sizes were unsuccessful.

In order to avoid this problem, the reaction setup was altered in a manner such that the reaction pathway was continually descending from the metering pump to the collection

vessel (see Figure 5.16). Moreover, a vibrating motor was installed on the pump inlet and every 15 minutes a small argon bubble was introduced into the system from the headspace of the starting mixture vessel. Using these modifications, the model reaction was carried out in a stable manner for over 5 hours, using the previously optimized conditions, but with a higher concentration (0.3 M instead of 0.2 M, without changing the CN-OA-m loading).

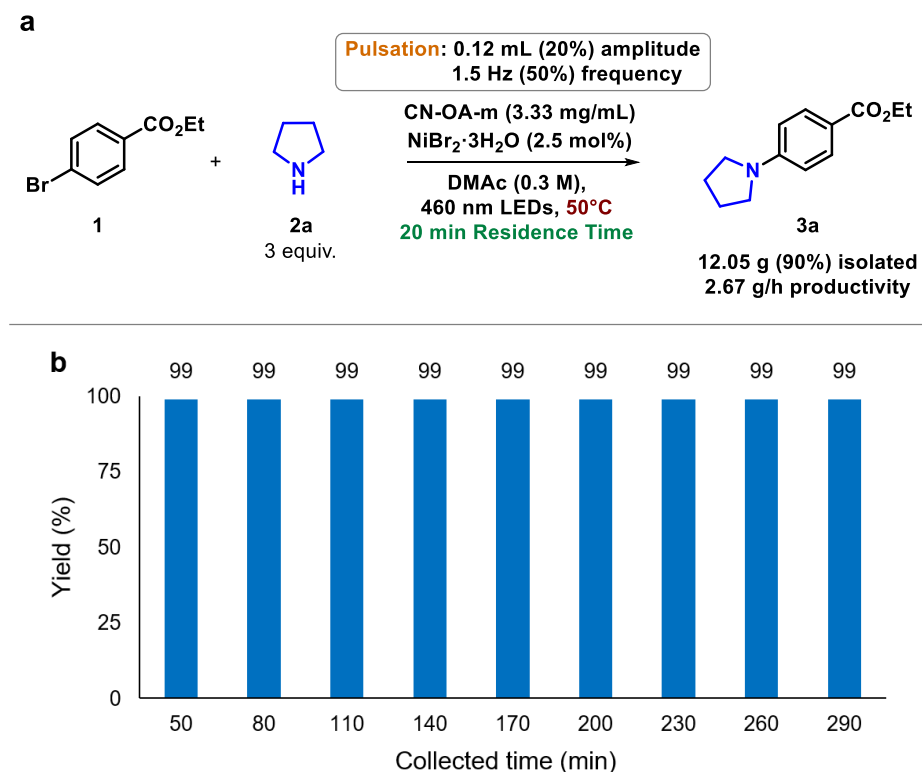


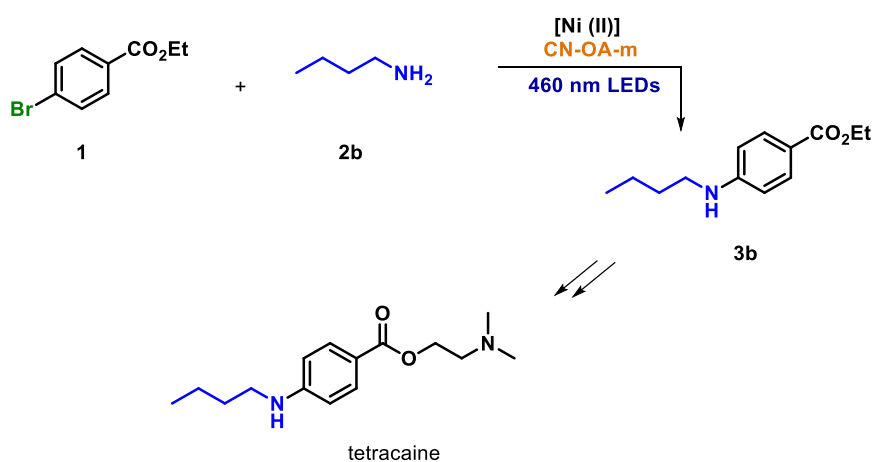
Figure 5.6. (a) Reaction scheme for the CN-OA-m long run experiment under the optimized conditions, with its yield and productivity. (b) Yield of product **3** at 30 minute time increments throughout the scale out synthesis. These were determined by HPLC assay using 4-ethylbiphenyl as the internal standard.

HPLC analysis revealed a stable assay yield of >99% for the duration of the experiment (Figure 5.6 b). The output material was collected for 4.5 hours of steady state operation, resulting in 12.05 g (90% isolated yield) of the desired coupling product **3a**, without column chromatography. This corresponds to an exceptionally high productivity of 2.67 g/h (15 mmol/h), a value to our knowledge only surpassed by some homogeneous Ir- or Ru-based photoredox catalyzed CN couplings.^{16, 65} It is noteworthy that the larger version of the HANUTM reactor (150 mL volume, 10 × scale up) maintains all of its process

characteristics (e.g. channel dimensions, mass-, heat-, and light transfer capacities, RTD), thus allows for straightforward scale-up of such procedures.⁵⁸

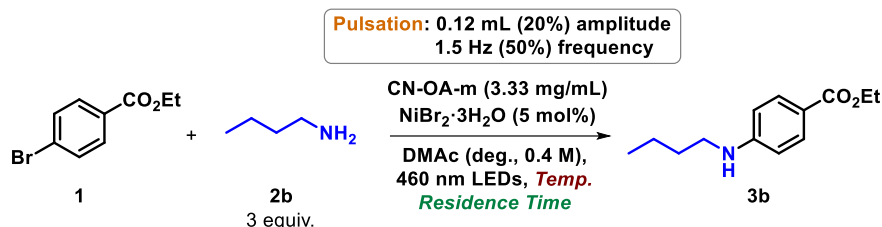
Tetracaine precursor synthesis

Finally, we envisaged that this protocol could be used for the preparation of an active pharmaceutical ingredient (API) precursor. In particular, tetracaine,⁶⁶ a local anaesthetic selected by the World Health Organization (WHO) as an essential medicine,⁶⁷ contains a butylamino aryl core, which can be accessed from precursor **3b** by a coupling reaction between **1** and butylamine **2b** (Scheme 5.1). The final API can then be obtained from **3b** by simple transesterification with N,N-dimethylamino ethanol.⁶⁸



Scheme 5.1. Reaction scheme for the preparation of tetracaine through a photochemical aryl amination.

Despite the use of reactive aryl bromide **1**, the coupling reaction with primary aliphatic amines is challenging and requires harsher conditions. In fact, this difference in reactivity is so substantial that recent studies have been published with the specific aim to improve their reactivity.^{8, 11} An optimization study was performed starting from the previous conditions with optimized oscillation settings (Table 5.2). Using the previously optimized conditions, but with a slightly elevated temperature of 60°C, product **3b** was observed in only 24% yield (entry 1). Then, increasing the concentration to 0.4 M and the nickel loading to 5 mol%, without varying the photocatalyst amount, led to a reasonable increment in yield of **3b** to 38% (entry 2). An extended residence time of 60 minutes subsequently resulted in 69% yield (entry 3). Finally, further increasing the temperature to 80°C led to the formation of **3b** in almost quantitative yield (94%, entry 4).

Table 5.2. Tetracaine precursor optimization study.^a

Entry	Residence time (min)	Temperature (°C)	Conc (M)	NiBr ₂ ·3H ₂ O (mol%)	Yield ^b (%)
1	20	60	0.2	2.5	24
2	20	60	0.4	5	38
3	60	60	0.4	5	69
4	60	80	0.4	5	94

^aReaction conditions: ethyl 4-bromobenzoate (**1**, 5 – 10 mmol scale), butylamine (**2b**, 3 equiv.), NiBr₂·3H₂O (2.5 – 5 mol%) and CN-OA-m (3.33 mg/mL) in DMAc (0.2 – 0.4 M) under blue light irradiation (460 nm). Reactions were performed using a 25 mL stock solution and 20 or 60 min residence time (0.75 or 0.25 mL/min). ^bYield was determined by HPLC using 4-ethylbiphenyl as the internal standard.

It is noteworthy that under these harsh reaction conditions, the formation of a small amount of nickel-black agglomerate was observed. Notwithstanding, the result obtained is of relevance for the preparation of the API precursor, since it can be produced in a significantly shorter reaction time, when compared with the state of the art.^{8,20} Consequently, in order to isolate product **3b**, the amination reaction was carried out over a runtime of more than four hours employing the optimized conditions. The coupled product **3b** was collected in the steady state for 80 minutes (92% average HPLC assay yield), leading to an isolated yield of 1.49 g (84%), which corresponds to a productivity of 1.12 g/h (see 5.4.7 for details).

5.3 Conclusions

We demonstrated the utility of an oscillatory plug flow photoreactor, capable of handling solids in continuous flow for an industrially relevant metallaphotoredox C–N coupling reaction. A thorough investigation of the system performance in terms of RTD led to finding the ideal match toward processability of solids and reactor performance. Following an optimization study, excellent yield was achieved in a model C–N coupling reaction on multi-gram scale, using a short residence time. A gram-scale operation of several hours runtime demonstrated the ability to successfully scale heterogeneous photocatalysis processes by the implementation of oscillatory flow reactor technology. The intensified conditions achieved using the flow photoreactor allowed for facile recycling of the carbon nitride photocatalyst over ten cycles. Finally, a pharmaceutically relevant intermediate was synthesized using slightly modified conditions, showing its applicability for preparative scale production of medicinally relevant compounds.

5.4 Supporting information

5.4.1 General experimental information

Commercial reagents and solvents were purchased (Sigma-Aldrich, Fluka, Alfa Aesar, Fluorochem or VWR) and used as received, without further purification, unless otherwise stated.

Ethyl 4-bromobenzoate (**1**), pyrrolidine (**2a**), butylamine (**2b**), nickel(II) bromide trihydrate, and 4-ethylbiphenyl were all commercially available. Carbon nitride photocatalyst, CN-OA-m, was synthesized according to the literature procedure.³²

Chromatographic purification of products was accomplished using a Biotage Isolera automated flash chromatography system with cartridges packed with KP-SIL, 60 Å (32–63 µm particle size).

For thin layer chromatography (TLC) analysis, Merck pre-coated TLC plates (silica gel 60 GF254, 0.25 mm) were employed, using UV light as the visualizing agent (254 nm), basic aqueous potassium permanganate (KMnO₄) stain solution or iodine and heat as developing agents.

Organic solutions were concentrated under reduced pressure on a Büchi rotatory evaporator.

NMR spectra were recorded on Bruker 300 MHz spectrometer (¹H: 300 MHz, ¹³C: 75 MHz, ¹⁹F: 282 MHz). The chemical shifts (δ) for ¹H, ¹³C and ¹⁹F are given in ppm relative to residual signals of the solvent (CDCl₃ at 7.26 ppm ¹H-NMR and 77.16 ppm ¹³C-NMR). Coupling constants are given in Hertz (Hz). The following abbreviations are used to indicate the multiplicity: s, singlet; d, doublet; t, triplet; q, quartet; dd, doublet of doublets; ddd, doublet of doublet of doublets; m, multiplet.

Analytical HPLC (Shimadzu LC20) analysis were carried out on a C18 reversed-phase (RP) analytical column (150 mm × 4.6 mm, particle size 5 µm) at 37 °C using mobile phases A (90:10 v/v water/acetonitrile + 0.1% TFA) and B (MeCN +0.1% TFA) at a flow rate of 1.5 mL/min. The following gradient was applied: linear increase from 30% to 100% B over 10 min.

UV-Vis spectra were recorded using a fiber-coupled Avantes Starline AvaSpec-2048 spectrometer, with an Avantes AvaLight-DHc lamp as the light source. These spectra were processed using Avasoft 8.7 software.

Centrifugation was performed using an Eppendorf Centrifuge 5804.

Laser diffraction (LD) analyses were carried out on a Sympatec Helos H2395 particle sizing instrument. Approximately 1 mg of solid was added to 50 mL of deionized water in a cuvette, followed by a small drop of tween 80 surfactant (to aid suspension). The sample in the cuvette was then sonicated for approximately 5 s, and was stirred at 1000 rpm during measurements. Two separate 30 s measurements were taken, to cover a combined particle size range of 0.45-875 μm .

5.4.2 Photoreactor setup

All photochemical reactions were conducted in a commercial continuous-flow reactor: Creaflow HANU™ Reactor (Figure 5.7).

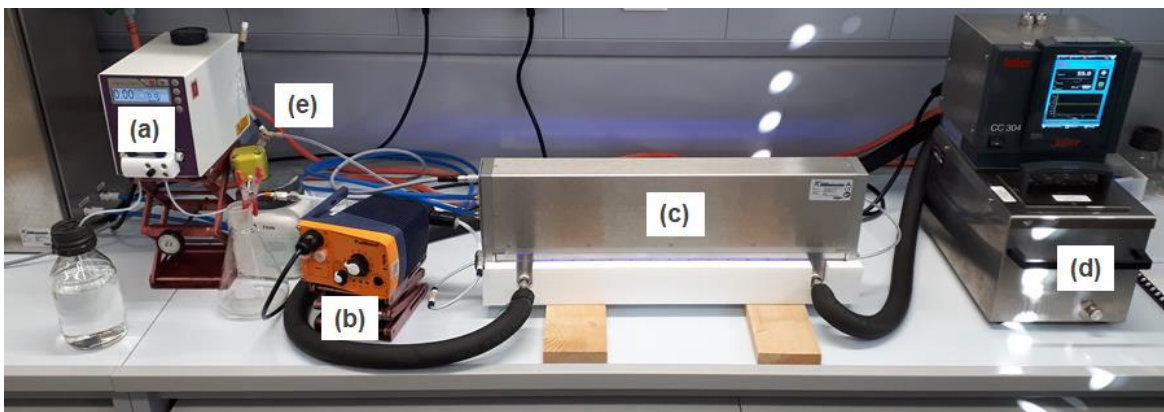


Figure 5.7. Photograph of commercial photoreactor setup: a) metering peristaltic pump (SF-10, Vapourtec); b) pulsator (Creaflow customized ProMinent (beta/4) pump with PTFE/carbon pump head); c) Reactor Module consisting of a HANU™ reactor and Peshl LED module; d) temperature control for reaction plate (Huber); e) backpressure regulator (BPR-10, Zaiput) with Creaflow pulsation dampener. Photograph of the LED control panel, containing the cooling system, has been omitted.

Reactor module (HANU™ HX 15-C276-CUB reactor, Creaflow): A Hastelloy-based microstructured plug flow reactor (540 × 60 × 60 mm size; channel dimensions: 480 × 20 × 2 mm, 15 mL internal volume) held in a PTFE housing.

Light source: LED module (“novaLIGHT FLED75” water cooled high-performance LED array, Peshl Ultraviolet) was mounted on the top of the reactor plate (35 mm from the center of the reaction channel). The LED panel (460 nm) was equipped with 36 LEDs (3 strips of 12 LEDs).

Table 5.3. Power and radiation flow of LEDs used in this study.

Wavelength (nm)	Maximum Current (mA)	Radiation Flow at Maximum Current (W)	Width at 50% intensity (nm)
460	700	33.75 ^[a]	17.5

^[a]Radiative flow extrapolated from data (at lower current) provided by the LED manufacturer.

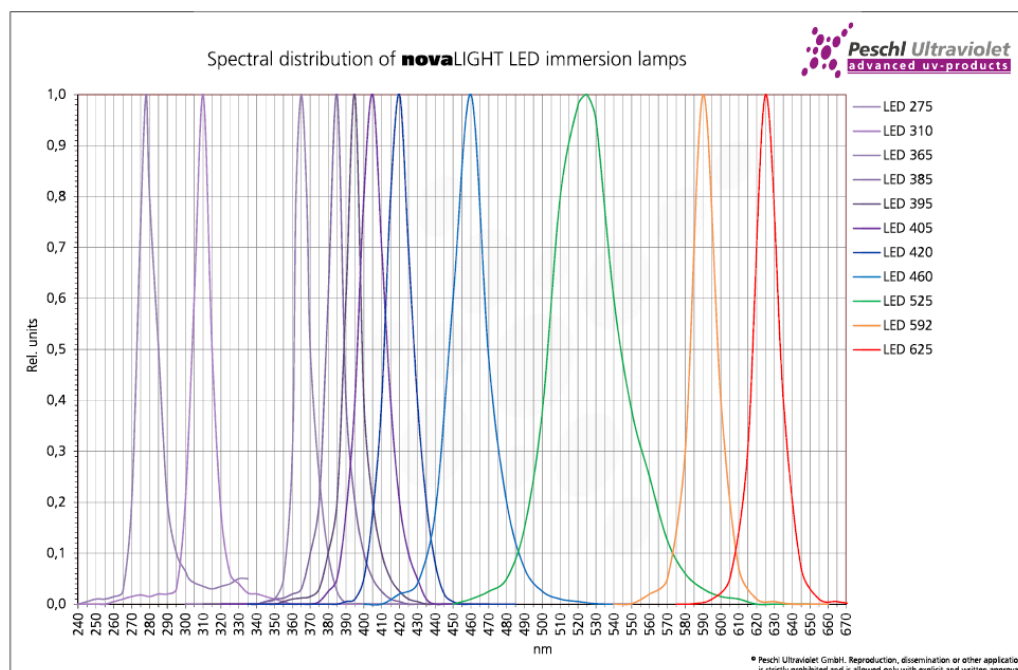


Figure 5.8. Emission spectra of LEDs used in this study (460 nm). Note: intensities are normalized.

Temperature control: Thermal regulation of the reactor was carried out using a Huber CC304 thermostat filled with silicon oil (temperature range $-20\text{ }^{\circ}\text{C}$ to $195\text{ }^{\circ}\text{C}$).

Metering pump: The feed mixture was conveyed through the reactor using a Vapourtec SF-10 peristaltic pump equipped with “blue” peristaltic tubing ($0.02\text{--}10.00\text{ mL/min}$) as metering pump.

Pulsator: Between the metering pump and the reactor, the feed mixture was pulsed using a Creaflow customized ProMinent Beta/4 pump (PTFE/carbon pump head). This had a tunable amplitude ($<5\text{--}100\%$), which was experimentally found to constitute a range of approximately $0.04\text{--}0.44\text{ mL}$ per stroke (see Fig. S14). The frequency could be tuned from $10\text{--}100\%$, corresponding to a range of $0.3\text{--}3\text{ Hz}$.

Pulsation dampener: The pulsation dampener was constituted by a piece of $1/4''$ PFA tubing, filled with air, closed on one side and connected in between the reactor output and the backpressure regulator through a PEEK Y-piece.

Back pressure regulator: A dome-type back pressure regulator (Zaiput Flow Technologies, BPR-10) was installed after the pulsation dampener with a set point of 3 bar.

General connections: Connection between the starting mixture flask and the metering pump was achieved using 1/8" o.d. (~1.6 mm i.d.) PTFE tubing with PEEK fittings. Connection between the metering pump and the pulsator was achieved using 1/8" o.d. (~1.6 mm i.d.) PTFE tubing with PEEK fittings and 1/4" o.d (3.2 mm i.d.) PFA tubing with stainless steel (Swagelok) fittings. Reactor plate input and output, as well as pulsation dampener were connected using 1/4" (3.2 mm i.d.) PFA tubing (Swagelok) with PEEK fittings. Backpressure regulator input and output was achieved using 1/8" o.d. (1.6 mm i.d.) PFA tubing with PEEK fittings. Fittings were lined with PTFE tape, to ensure a tight seal.

5.4.3 Reactor characterization

5.4.3.1 Control reactions examining effect of reaction protocol on concentration/yield

The profile of concentration/yield under two different regimes was examined, in order to gain information on the cause of the unexpected trend. To determine whether this was due to difficulty in reaching steady state, a reaction with a “pre-filled” reactor was attempted, and a reaction simply using a larger volume of stock solution (50 mL rather than 25 mL). The results of these reactions are shown below (Figure 5.9), whereby a similar trend was still observed, leading to the conclusion that this is not the cause of the unexpected behaviour.

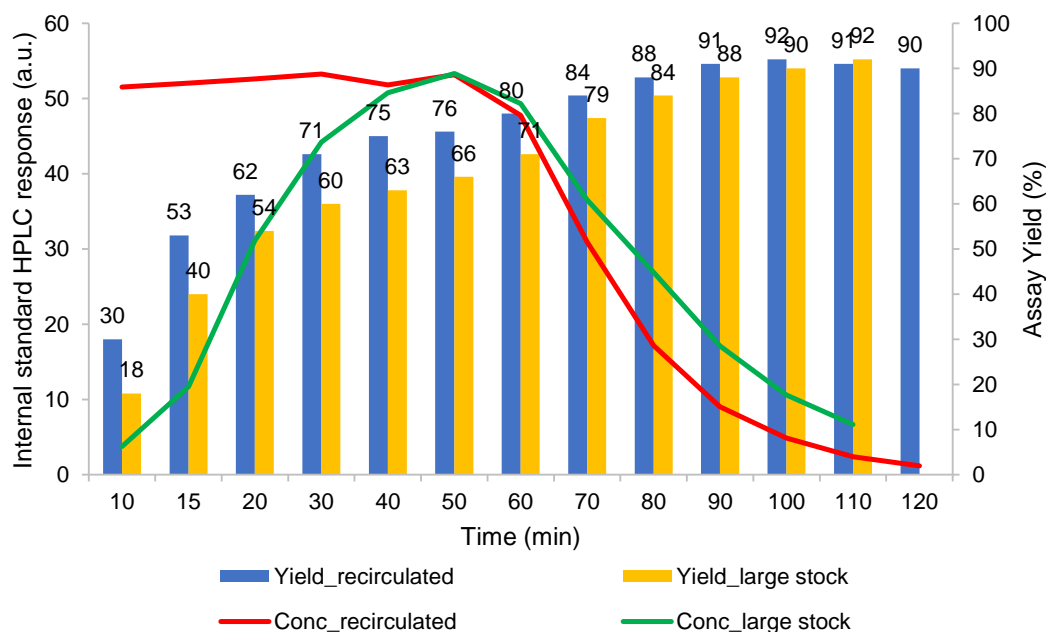


Figure 5.9. Two control experiments: a) Rather than starting with a solvent-filled reactor and swapping the pump input to reaction mixture, a 50 mL solution of reaction mixture was circulated through the reactor, to ensure a constant concentration, prior to turning on the LEDs. b) The standard reaction procedure was used, but with a 50 mL solution of reaction material, rather than 25 mL.

5.4.3.2 Comparison of background reaction between two reactors

In order to determine the cause of the unusual concentration/yield profiles observed (as described in the manuscript), a comparison was carried out, whereby the reaction without carbon nitride photocatalyst (background reaction only) was performed in the HANUTM reactor and Corning Lab Photo Reactor. The resulting trends are shown below (Figure 5.10 and Figure 5.11). The difference in concentration/yield trends implies that this behaviour is due to the characteristics of the reactor.

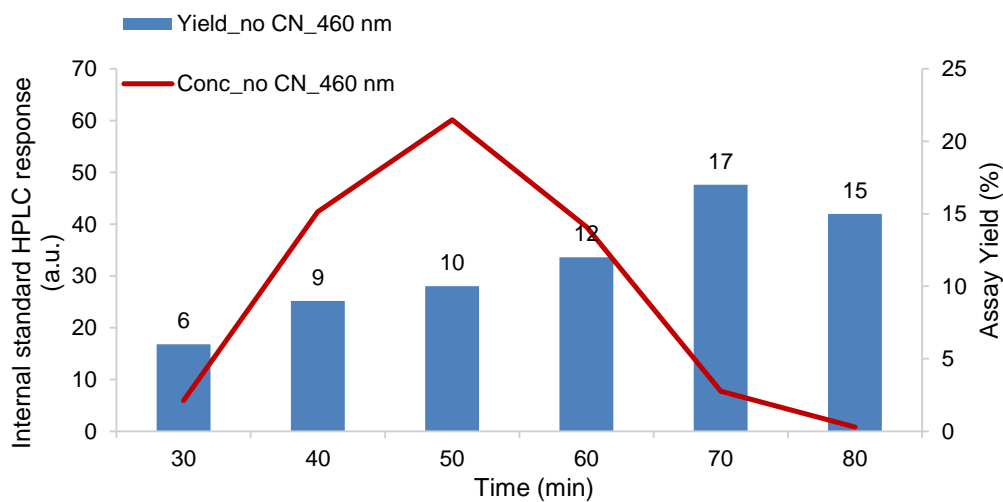


Figure 5.10. Results of the background reaction performed in the HANUTM reactor, without carbon nitride photocatalyst. This demonstrates the trend of increasing yield over time, irrespective of concentration.

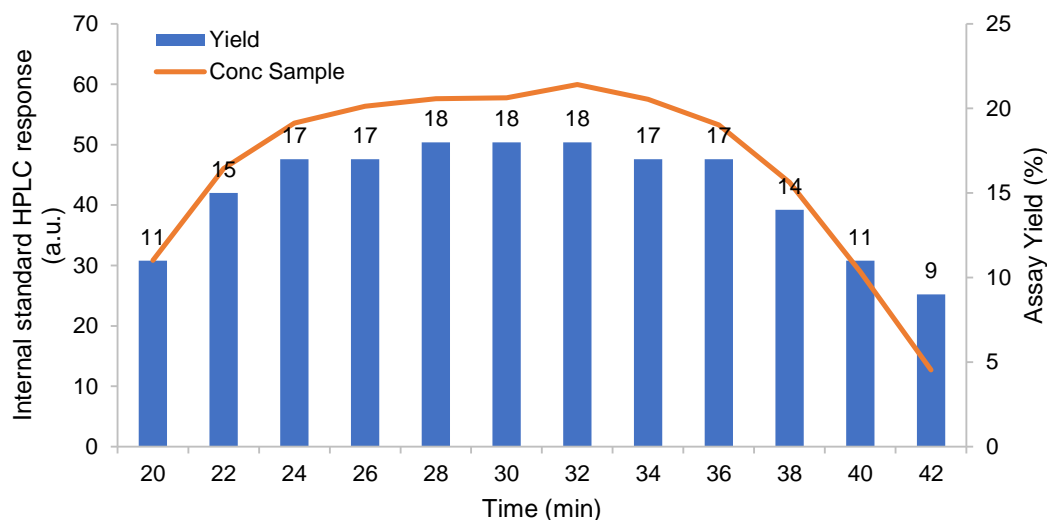


Figure 5.11. Results of the background reaction performed in the Corning Lab Photo reactor using 395 nm lamps, without carbon nitride photocatalyst. This demonstrates the expected trend of increasing yield with increasing concentration.

5.4.3.3 Correlation between pulsation amplitude and displaced volume

An array of experiments was carried out in order to determine the physical correlation between the pulsation amplitude generated by the pulsator and the corresponding displaced volume. For this purpose, a 50 cm length of PFA tubing (1/4" o.d., ~3.2 mm i.d.) was installed after the pulsator and attached to a ruler (see Figure 5.12). The system was filled with toluene, then a solution of methylene blue in water was pumped through to provide a liquid/liquid biphasic mixture inside the aforementioned tubing. In absence of any net flow rate, the pulsator was switched on, allowing the colored slugs to move back and forth inside the tube. The overall motion was recorded using a camera set at high frame per seconds rate (240 FPS) giving the possibility to calculate the resulting displaced volume for the selected pulsation amplitude.

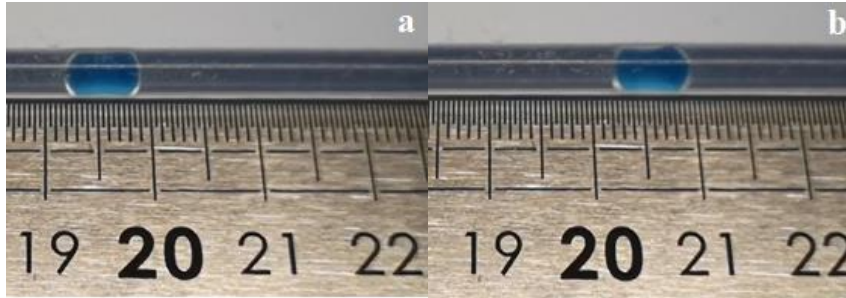


Figure 5.12. Tubing installed after the pulsator, attached to a ruler for the displaced volume determination. a) Initial position of the considered tracer slug after the backward pulsation. b) Final position of the considered tracer slug after the forward pulsation.

A linear relationship was observed between the pulsation amplitude and the displaced volume in absence of any net flow rate (Figure 5.13).

Pulsation Amplitude	Displaced Volume (mL)
<5%	0.036
10%	0.080
20%	0.120
30%	0.161
50%	0.265
70%	0.297
100%	0.442

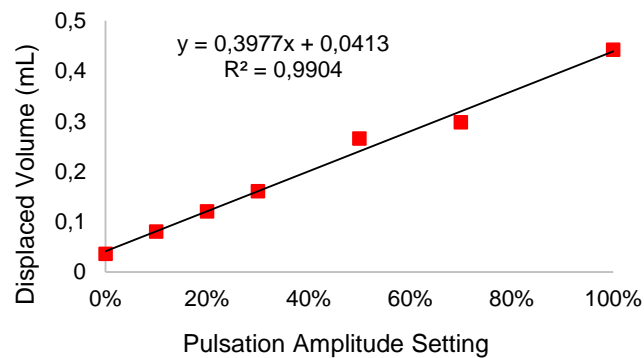
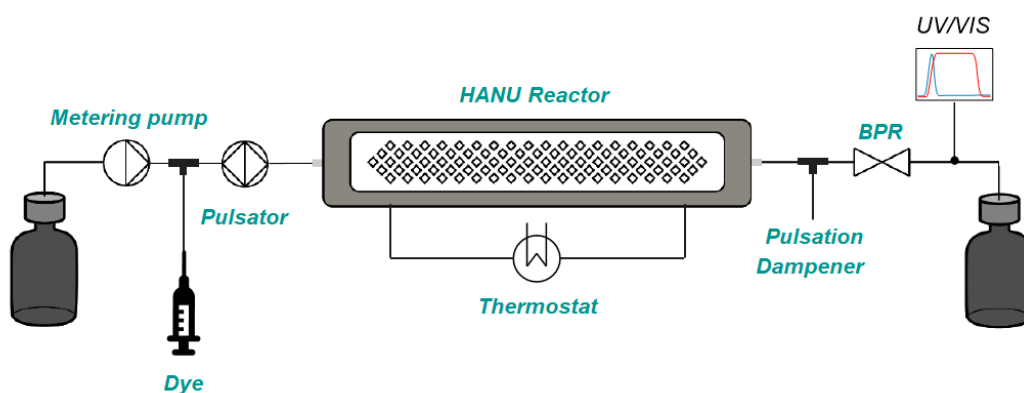


Figure 5.13. Correlation between pulsation amplitude and displaced volume.

5.4.3.4 Residence Time Distribution (RTD) experiments

Residence time distribution (RTD) experiments were performed as shown in Scheme 5.2. Rose Bengal was used as a tracer in DMAc solution (10^{-4} M concentration) and injected via a Y-piece mixer between the metering pump and the pulsator, in a carrier stream of pure DMAc. An in-line UV/Vis flow cell was installed after the back pressure regulator and connected to a spectrometer. Both the reaction setups for the screening experiments (see Figure 5.7) and for the scale-out experiment (see Figure 5.16) have been characterized in terms of RTD.



Scheme 5.2. Flow diagram showing the setup for the RTD experiments.

The RTD profiles for the screening experiments setup are shown in Figure 5.14 and the profiles for the scale-out setup are shown in Figure 5.15

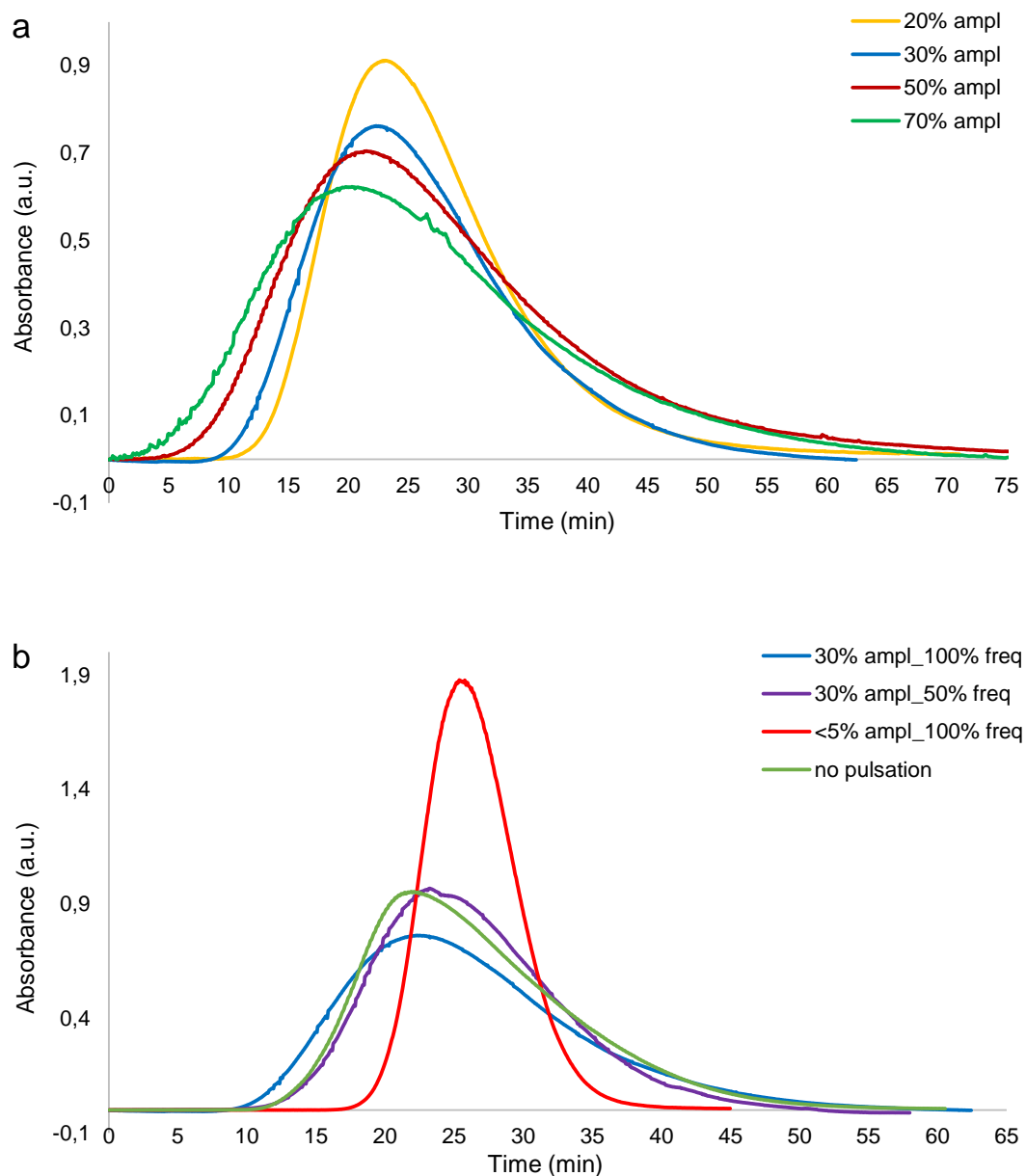


Figure 5.14. RTD profiles at 563 nm in DMAc for the screening experiments setup. Conditions: flow rate = 1 mL/min, backpressure = 3 bar, tracer injected volume = 2 mL, optical path length = 1 cm. a) Experiments performed at 100% pulsation frequency and different pulsation amplitudes. b) Experiments performed at different pulsation frequencies.

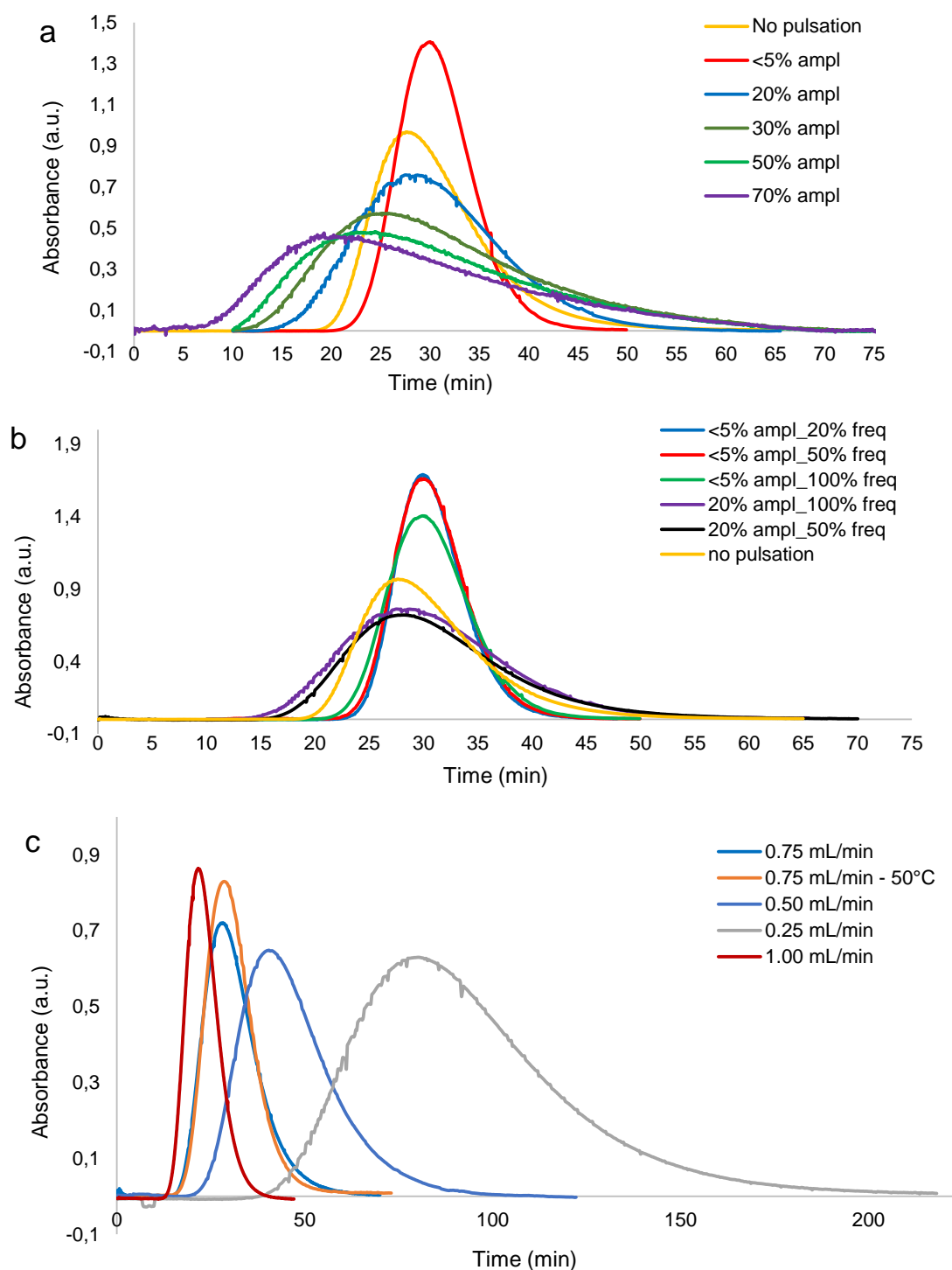


Figure 5.15. RTD profiles at 563 nm in DMAc for the scale-out setup. Conditions: flow rate = 0.75 mL/min, backpressure = 3 bar, tracer injected volume = 1 mL, optical path length = 1 cm. a) Experiments performed at 100% pulsation frequency and different pulsation amplitudes. b) Experiments performed at different pulsation frequencies. c) Experiments performed at different flow rates (at 25°C, unless differently stated).

From each of these RTD profiles, the dimensionless Bodenstein (Bo) number was calculated, consisting of the mean residence time (\bar{t}) multiplied by two, divided by the variance (σ^2):

$$Bo = \frac{2 \cdot \bar{t}}{\sigma^2}$$

The variance can be calculated from a given RTD experiment using the following formula:

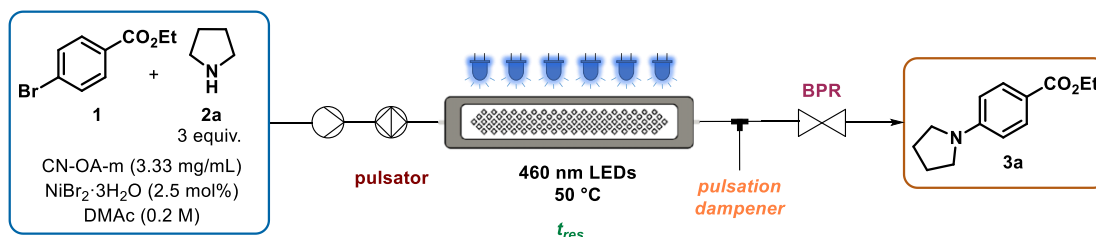
$$\sigma^2 = \frac{\sum t_i^2 \cdot C_i \cdot \Delta t}{\sum C_i \cdot \Delta t} - \bar{t}^2$$

A Bo value greater than 100 indicates that plug flow behavior is exhibited.⁶²

Table 5.4. RTD experiments in the scale-out setup, performed under different pulsation and flow settings, with their corresponding Bodenstein (Bo) numbers, to characterize the extent of axial dispersion in each case. Higher Bo corresponds to a lesser extent of back mixing.

Entry	Flow rate (mL/min)	Pulsation Amplitude (mL/%)	Pulsation Frequency (Hz/%)	Bodenstein number
1	0.75	0 / 0	0/0	48
2	0.75	0.04 / <5	3 / 100	128
3	0.75	0.12 / 20	3 / 100	35
4	0.75	0.16 / 30	3 / 100	16
5	0.75	0.24 / 50	3 / 100	13
6	0.75	0.32 / 70	3 / 100	10
7	0.75	0.04 / <5	1.5 / 50	153
8	0.75	0.04 / <5	0.6 / 20	184
9	0.75	0.12 / 20	1.5 / 50	32
10	0.25	0.12 / 20	1.5 / 50	23
11	0.5	0.12 / 20	1.5 / 50	25
12	1	0.12 / 20	1.5 / 50	76
13 ^a	0.75	0.12 / 20	1.5 / 50	33

5.4.4 General procedure for the model reaction: screening experiments and scale-out



Scheme 5.3. Flow diagram showing general reaction setup for screening experiments.

The LED array, equipped with 460 nm LEDs, was switched on and the reaction plate thermostat was set to 50 °C. A mixture of ethyl 4-bromobenzoate **1** (5 mmol, 1 equiv), pyrrolidine **2a** (15 mmol, 3 equiv), CN-OA-m (3.33 mg/mL with respect to the solvent, 83.2 mg), nickel(II) bromide trihydrate (0.125 mmol, 2.5 mol%), 4-ethylbiphenyl (internal standard, 0.5 mmol, 0.1 equiv) was made up in *N,N*-dimethylacetamide (25 mL total volume in a flask, $[1]_0 = 0.2$ M). Using the back pressure regulator, a pressure of 3 bar was set. The reaction mixture was degassed prior to use by sparging with an argon balloon for 15 minutes, then pumped through the reactor at 0.75 mL/min flow rate, corresponding to 20 min residence time. The pulsator was set to 20% (0.12 mL) pulsation amplitude and 50% (1.5 Hz) pulsation frequency. Samples were collected over the time for analysis by HPLC, after filtration (0.45 μ m syringe filter).

For the scale-out experiment, the setup shown in Figure 5.16 was used. A mixture of ethyl 4-bromobenzoate **1** (75 mmol, 1 equiv), pyrrolidine **2a** (225 mmol, 3 equiv), CN-OA-m (3.33 mg/mL, with respect to the solvent, 832 mg), nickel(II) bromide trihydrate (1.88 mmol, 2.5 mol%), 4-ethylbiphenyl (internal standard, 7.5 mmol, 0.1 equiv) was made up in *N,N*-dimethylacetamide (250 mL total volume in a flask, $[1]_0 = 0.3$ M). Using the back pressure regulator, a pressure of 3 bar was set. The reaction mixture was degassed prior to use by sparging with an argon balloon for 30 minutes, then pumped through the reaction plate at 0.75 mL/min flow rate, corresponding to 20 min residence time, 20% (0.12 mL) pulsation amplitude and 50% (1.5 Hz) pulsation frequency. In order to avoid particle settling

in the tubing, a vibrating motor (Figure 5.17) was installed on the peristaltic pump inlet and a small argon bubble was introduced to the system from the headspace of the starting mixture vessel every 15 minutes. Samples were collected over the time for analysis by HPLC, after filtration (0.45 μm syringe filter). The processed mixture, containing compound **3a**, was collected in the steady state over 270 min (4 hours and 30 min, from minute 50 to minute 320, providing a theoretical yield of 60.75 mmol, see Figure 5.18).

The crude reaction mixture was centrifuged at 6000 rpm for 5 minutes and the liquid phase was carefully separated before being diluted with water and extracted with ethyl acetate. The combined organic phases were washed with water, NaHCO_3 saturated solution and brine, dried over sodium sulfate and concentrated. The crude product was purified by trituration with petroleum ether and filtration to give the corresponding aryl amino compound **3a**.

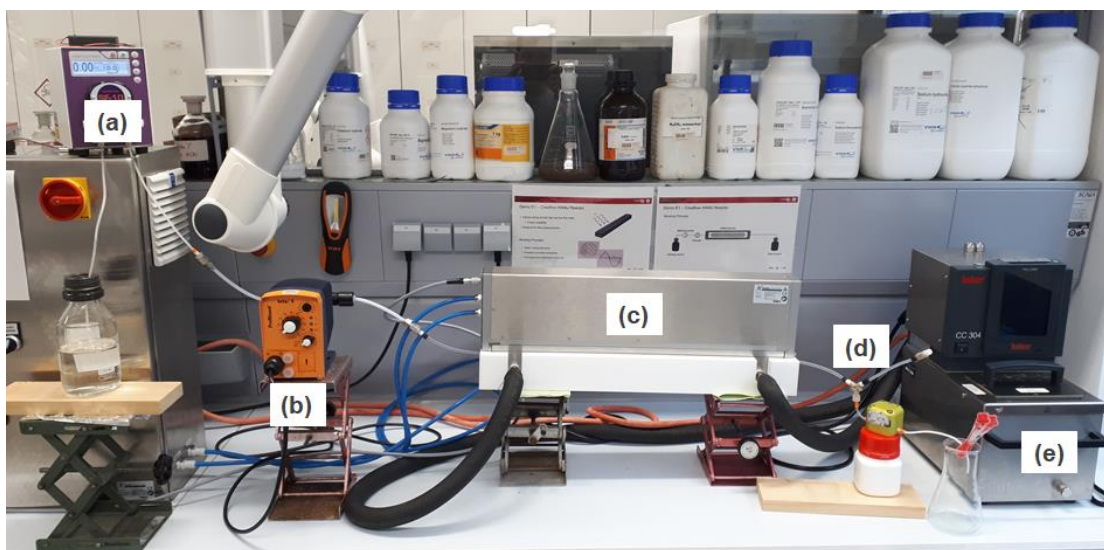


Figure 5.16. Photograph of commercial photoreactor setup for the scale-out experiment: a) metering peristaltic pump (Vapourtec); b) pulsator; c) reactor module housing, within the reaction plate and the LED module on the top; d) backpressure regulator with pulsation dampener; e) temperature control for the reactor (Huber).

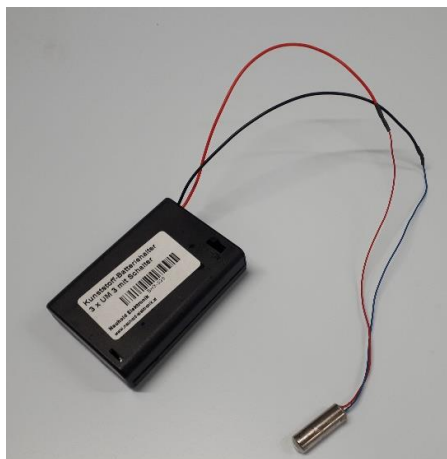


Figure 5.17. Photograph of commercial vibrating motor and the battery power supply installed on the peristaltic pump inlet.⁴⁸

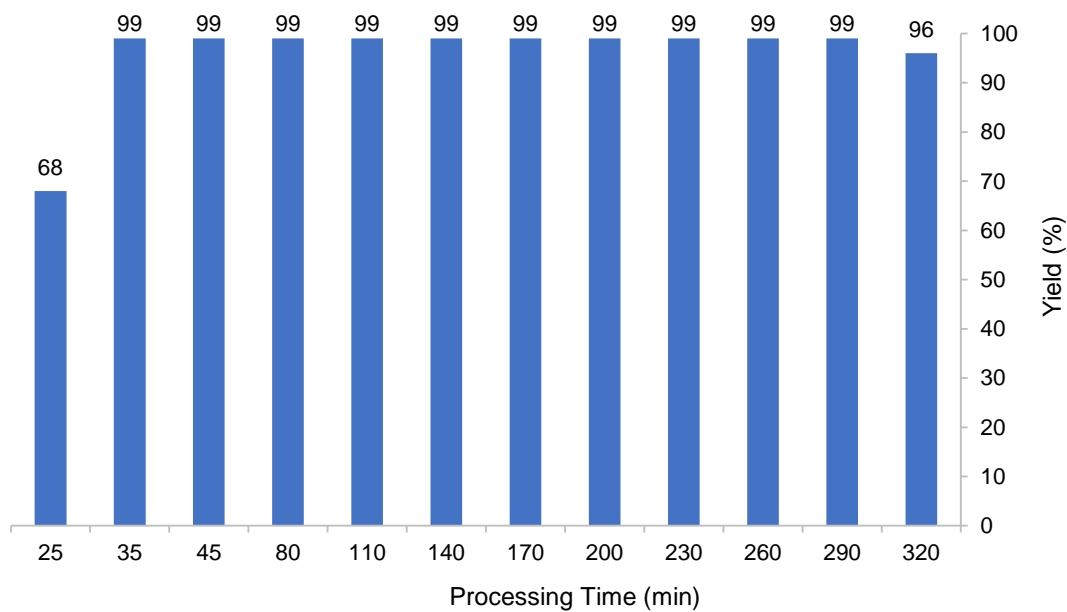
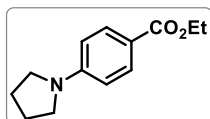


Figure 5.18. HPLC yield profile of the model reaction samples collected over the run time.

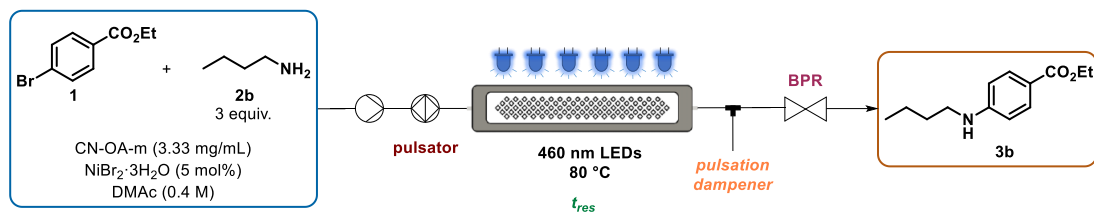


Ethyl 4-(pyrrolidin-1-yl)benzoate (3a). Prepared according to the scale-out procedure C1. The product **3** was obtained as an off-white solid (12.05 g, 90% yield). The characterization of the compound matches the data reported in the literature.²⁷



Figure 5.19. Photograph of the isolated coupling product **3a**.

5.4.5 General procedure for the tetracaine precursor synthesis: Screening experiments and isolation run



Scheme 5.4. Flow diagram showing the reaction setup for the tetracaine intermediate **3b** synthesis.

The LED array, equipped with 460 nm LEDs, was switched on and the reaction plate thermostat was set to 80 °C. A mixture of ethyl 4-bromobenzoate **1** (10 mmol, 1 equiv), butylamine **2b** (30 mmol, 3 equiv), CN-OA-m (3.33 mg/mL with respect to the solvent, 83.2 mg), nickel(II) bromide trihydrate (0.5 mmol, 5 mol%), 4-ethylbiphenyl (internal standard, 1 mmol, 0.1 equiv) was made up in *N,N*-dimethylacetamide (25 mL total volume in a flask, $[1]_0 = 0.4$ M). Using the back pressure regulator, a pressure of 3 bar was set. The reaction mixture was degassed prior to use by sparging with an argon balloon for 15 minutes, then pumped through the reactor at 0.25 mL/min flow rate, corresponding to 60 min residence time. Samples were collected over the time for analysis by HPLC, after filtration (0.45 μ m syringe filter).

For the isolation run experiment, setup shown in Figure 5.16 was used. A mixture of ethyl 4-bromobenzoate **1** (30 mmol, 1 equiv), butylamine **2b** (90 mmol, 3 equiv), CN-OA-m (3.33 mg/mL with respect to the solvent, 250 mg), nickel(II) bromide trihydrate (1.5 mmol, 5 mol%), 4-ethylbiphenyl (internal standard, 3 mmol, 0.1 equiv) was made up in *N,N*-dimethylacetamide (75 mL total volume in a flask, $[1]_0 = 0.4$ M). Using the back pressure regulator, a pressure of 3 bar was set. The reaction mixture was degassed prior to use by sparging with an argon balloon for 30 minutes, then pumped through the reactor at 0.25 mL/min flow rate, corresponding to 60 min residence time. In order to avoid particles settling in the tubing, a vibrating motor (Figure 5.17) was installed on the peristaltic pump inlet and a small argon bubble was let enter to the system from the headspace of the starting mixture vessel every 15 minutes. Samples were collected over the time for analysis by HPLC, after filtration (0.45 μ m syringe filter). The processed mixture, containing compound **3b**, was

collected in the steady state over 80 min (from minute 140 to minute 220, providing a theoretical yield of 8 mmol, see Figure 5.20).

The crude mixture was centrifuged at 6000 rpm for 5 minutes and the liquid phase was carefully separated before being evaporated under reduced pressure. The residue was purified by column chromatography (petroleum ether/ethyl acetate 80:20) to give the corresponding tetracaine precursor **3b**.

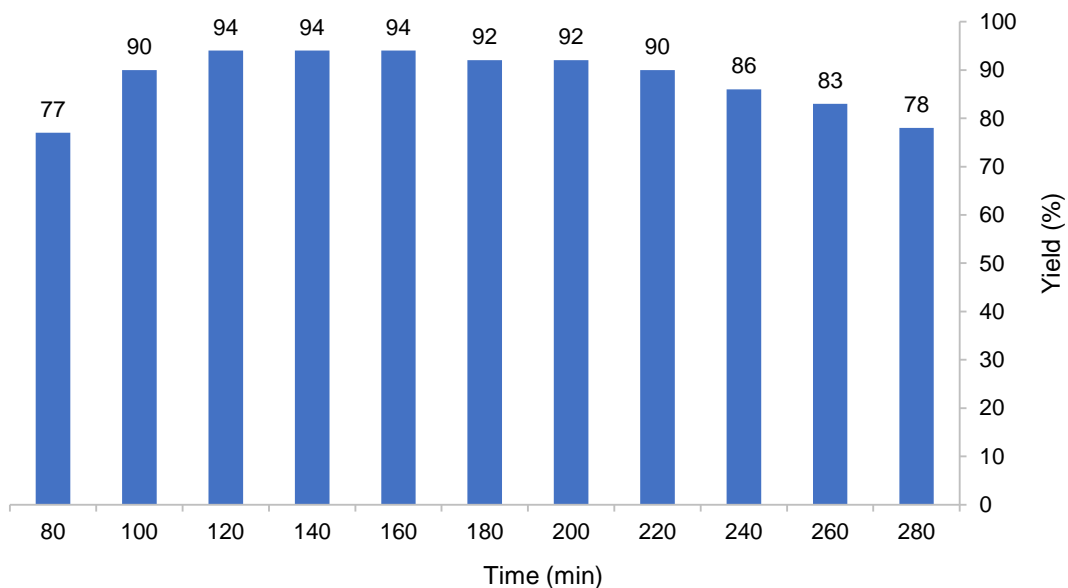
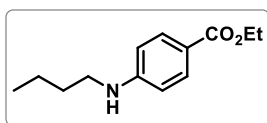


Figure 5.20. HPLC yield profile of the tetracaine precursor samples collected over the run time.



Ethyl 4-(butylamino)benzoate (3b). Prepared according to the isolation run procedure **C2**. The product **3b** was obtained as white solid (1.49 g, 84% yield). The characterization of the compound matches the data reported in the literature.⁶⁹

5.4.6 Optimization of the reaction conditions for the model reaction

A series of optimization experiments were performed using ethyl 4-bromobenzoate (**1**) and pyrrolidine (**2a**) as model reagents in order to explore the reaction parameters. These experiments were carried out following General Procedure 5.4.4. Yields were determined by calibrated HPLC analysis using 4-ethylbiphenyl as the internal standard:

$$[\mathbf{3a}] = \left(\frac{\text{Area}(\mathbf{3a})}{\text{Area}(\text{IS})} - c \right) \times \frac{[\text{IS}]}{k}$$

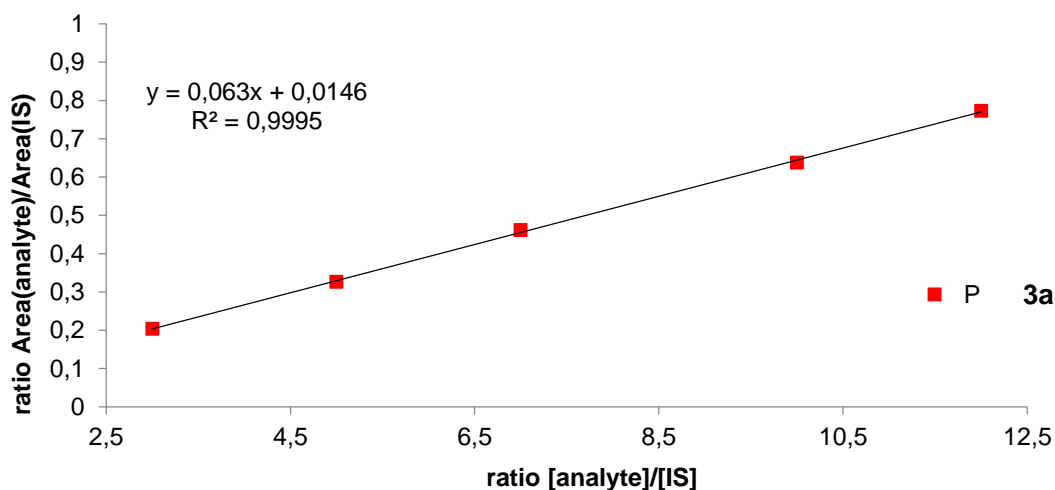
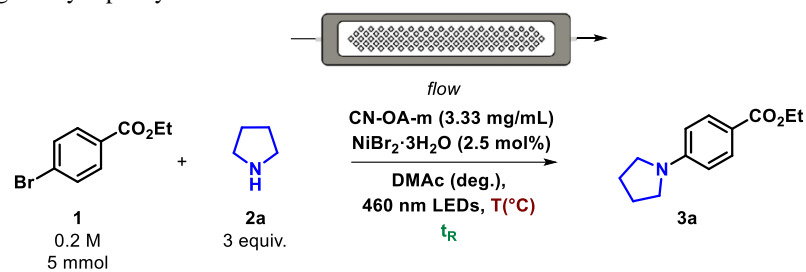


Figure 5.21. HPLC calibration curve for the model reaction.

Table 5.5. Screening of the reaction parameters (residence time, temperature and pulsation amplitude and frequency). Reactions were performed on 5 mmol scale, 25 mL stock solution. ^[a]Yields were determined by HPLC using 4-ethylbiphenyl as the internal standard at the concentration maximum. ^[b]50% LED power.



Entry	Residence Time	Temperature	Pulsation Amplitude	Pulsation Frequency	Yield ^[a]
1	15 min	40°C	70%	100%	66%
2	15 min	50°C	70%	100%	77%
3	15 min	50°C	30%	100%	83%
4	15 min	50°C	20%	100%	86%
5	20 min	50°C	20%	100%	94%
6	20 min	50°C	20%	50%	99%
7	20 min	50°C	20%	50%	89% ^[b]

A series of experiments were performed to optimize the pulsation amplitude in order to find a suitable match between an appropriate carbon nitride dispersion and the minimum longitudinal diffusion (back mixing). For the physical correlation between the numerical values of the pulsation amplitude and the displaced volume see 5.4.3.3.

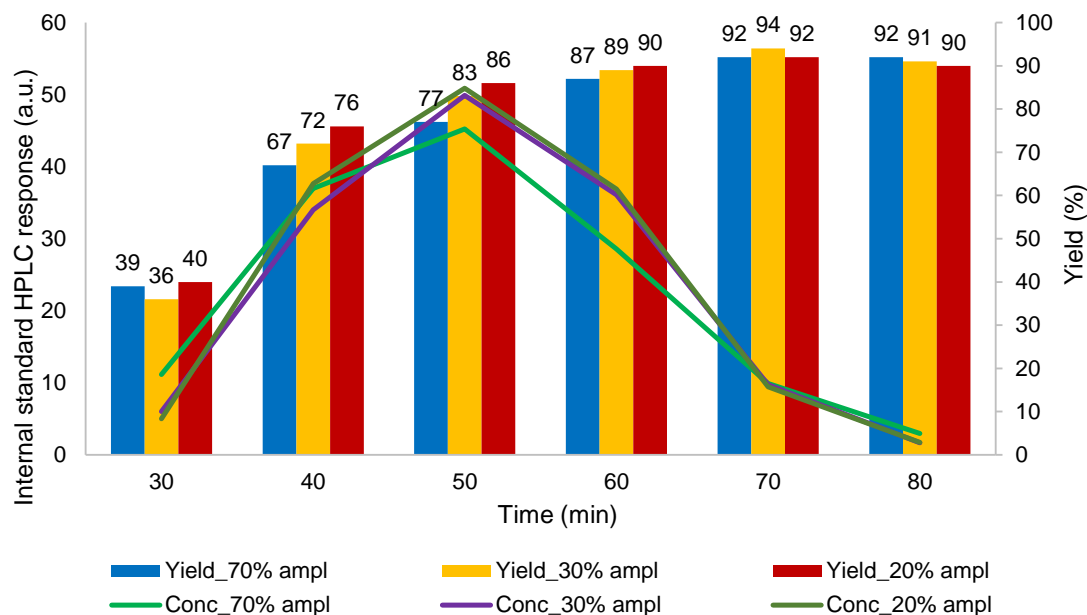


Figure 5.22. Effect of the pulsation amplitude. Reaction conditions: 15 min residence time, 50°C. Yields and concentrations were determined by HPLC using 4-ethylbiphenyl as the internal standard.

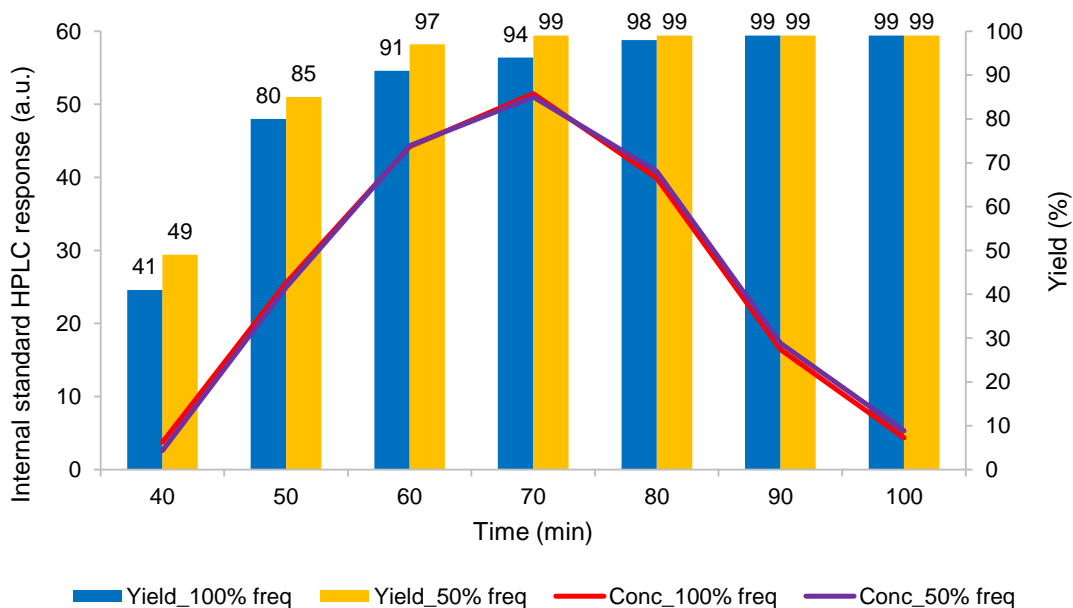


Figure 5.23. Effect of the pulsation frequency. Reaction conditions: 20 min residence time, 50°C. Yields and concentrations were determined by HPLC using 4-ethylbiphenyl as the internal standard.

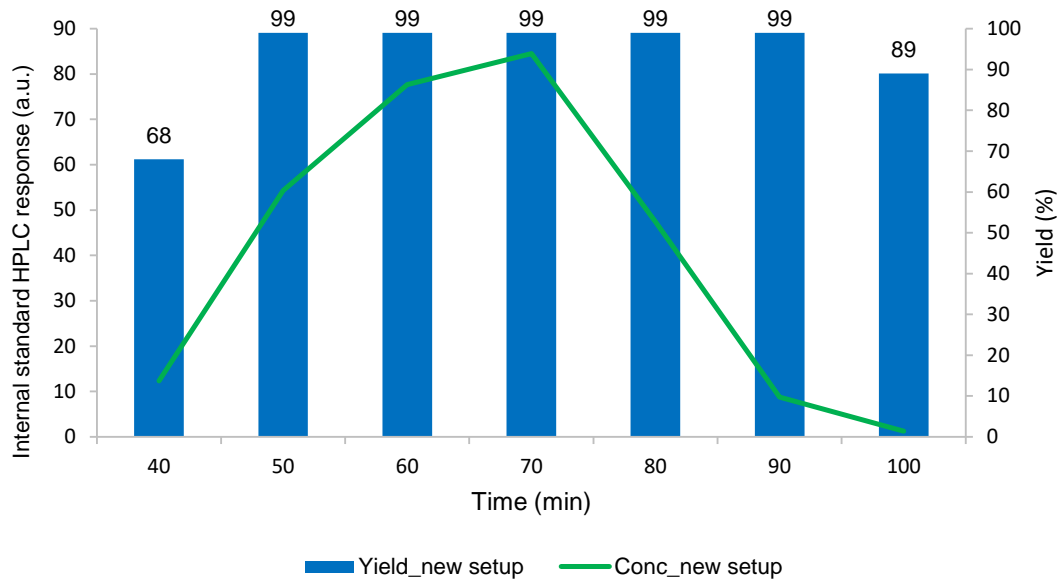


Figure 5.24. Concentration/yield profile of the reaction performed in the new setup at 0.3 M. Reaction conditions: 20 min residence time, 50°C. Yields and concentrations were determined by HPLC using 4-ethylbiphenyl as the internal standard.

5.4.7 Optimization of the reaction conditions for the tetracaine precursor synthesis

A series of optimization studies were performed using ethyl 4-bromobenzoate (**1**) and butylamine (**2b**) as reagents to prepare the tetracaine precursor (**3b**) at 20% pulsation amplitude and 50% pulsation frequency. These experiments were carried out following General Procedure 5.4.5. Yields were determined by calibrated HPLC analysis using 4-ethylbiphenyl as the internal standard.

$$[\mathbf{3b}] = \left(\frac{\text{Area}(\mathbf{3b})}{\text{Area}(\text{IS})} - c \right) \times \frac{[\text{IS}]}{k}$$

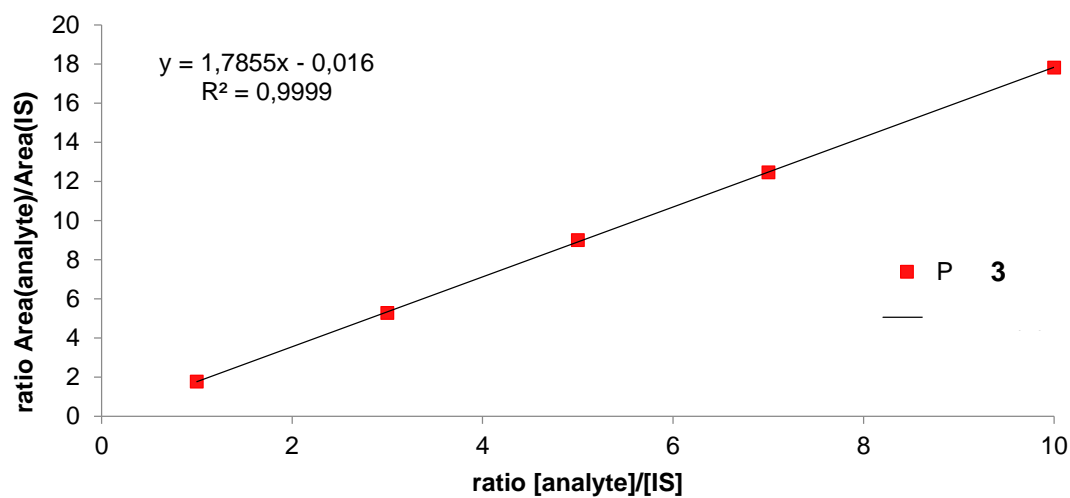
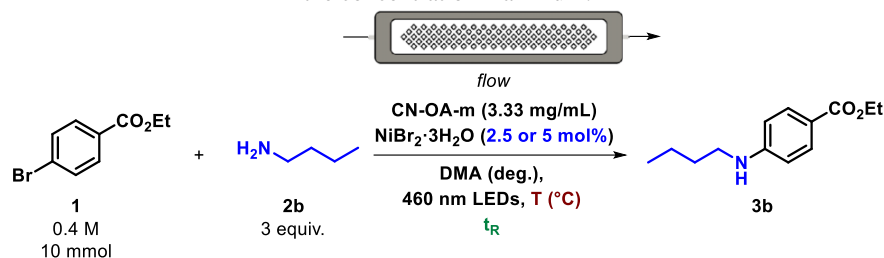


Figure 5.25. HPLC calibration curve for the tetracaine precursor.

Table 5.6. Screening of the reaction parameters (residence time, temperature, concentration, Ni loading) for the tetracaine precursor synthesis. Reactions were performed on 5 to 10 mmol scale, 25 mL stock solution at 20% pulsation amplitude and 50% pulsation frequency. CN-OA-m loading was kept the same for all the experiments carried out. ^[a]Yields were determined by HPLC using 4-ethylbiphenyl as the internal standard at the concentration maximum.



Entry	Residence Time	Temperature	Concentration	NiBr ₂ ·3H ₂ O	Yield ^[a]
1	20 min	60°C	0.2 M	2.5 mol%	24%
2	20 min	60°C	0.3 M	2.5 mol%	30%
3	20 min	60°C	0.4 M	5 mol%	38%
4	60 min	60°C	0.4 M	5 mol%	69%
5	60 min	73°C	0.4 M	5 mol%	85%
6	60 min	80°C	0.4 M	5 mol%	94%

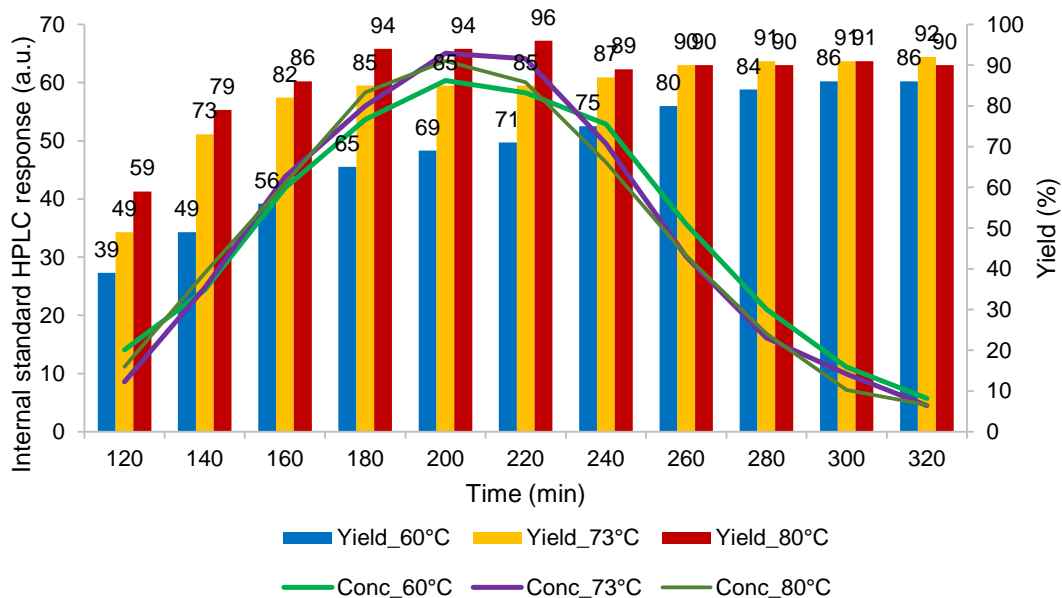


Figure 5.26. Effect of the temperature. Reaction conditions: 60 min residence time, 5 mol% NiBr₂·3H₂O, 0.4 M. Yields and concentrations were determined by HPLC using 4-ethylbiphenyl as the internal standard.

5.4.8 Particle size distribution (PSD) of CN-OA-m

In order to determine the particle size distribution (PSD) of the CN-OA-m, a series of Laser Diffraction (LD) measurements were carried out. Preliminarily, a mixture of CN-OA-m in DMAc (3.33 mg/mL) was pumped through the reaction system (screening experiments setup, Figure 5.7) at 0.75 mL/min, 20% pulsation amplitude and 50% pulsation frequency to simulate a reaction. Therefore, the particles that can pass through the apparatus can be separated from those which in the tubing after the reactor. The latter ones were finally removed by flushing the system at 10 mL/min flow rate and maximum pulsation. The two materials were individually collected, analyzed by LD using the parameters defined in section 5.4.1 and compared with the unprocessed CN-OA-m. The resulting PSD profiles are shown in Figure 5.27.

The D10, D50 and D90 values for these particles were recorded:

D10 = Diameter at which 10% of particles are smaller.

D50 = Median particle diameter.

D90 = Diameter at which 90% of particles are smaller.

The particles passed through the system have shown a PSD centered on $\approx 5 \mu\text{m}$ (D10 = 0.9 μm , D50 = 4.3 μm , D90 = 15 μm , Figure 5.27 b). On the other hand, particles which stuck in the tubing have shown a PSD centered on $\approx 20 \mu\text{m}$ (D10 = 7 μm , D50 = 20 μm , D90 = 40 μm , Figure 5.27 c). Both the distributions are present in the unprocessed CN-OA-m PSD (Figure 5.27 a).

Ball milling of the material was attempted (Retsch MM 400 mill) in efforts to reach a single size distribution, but this failed to show any change from the original PSD (Figure 5.27 a).

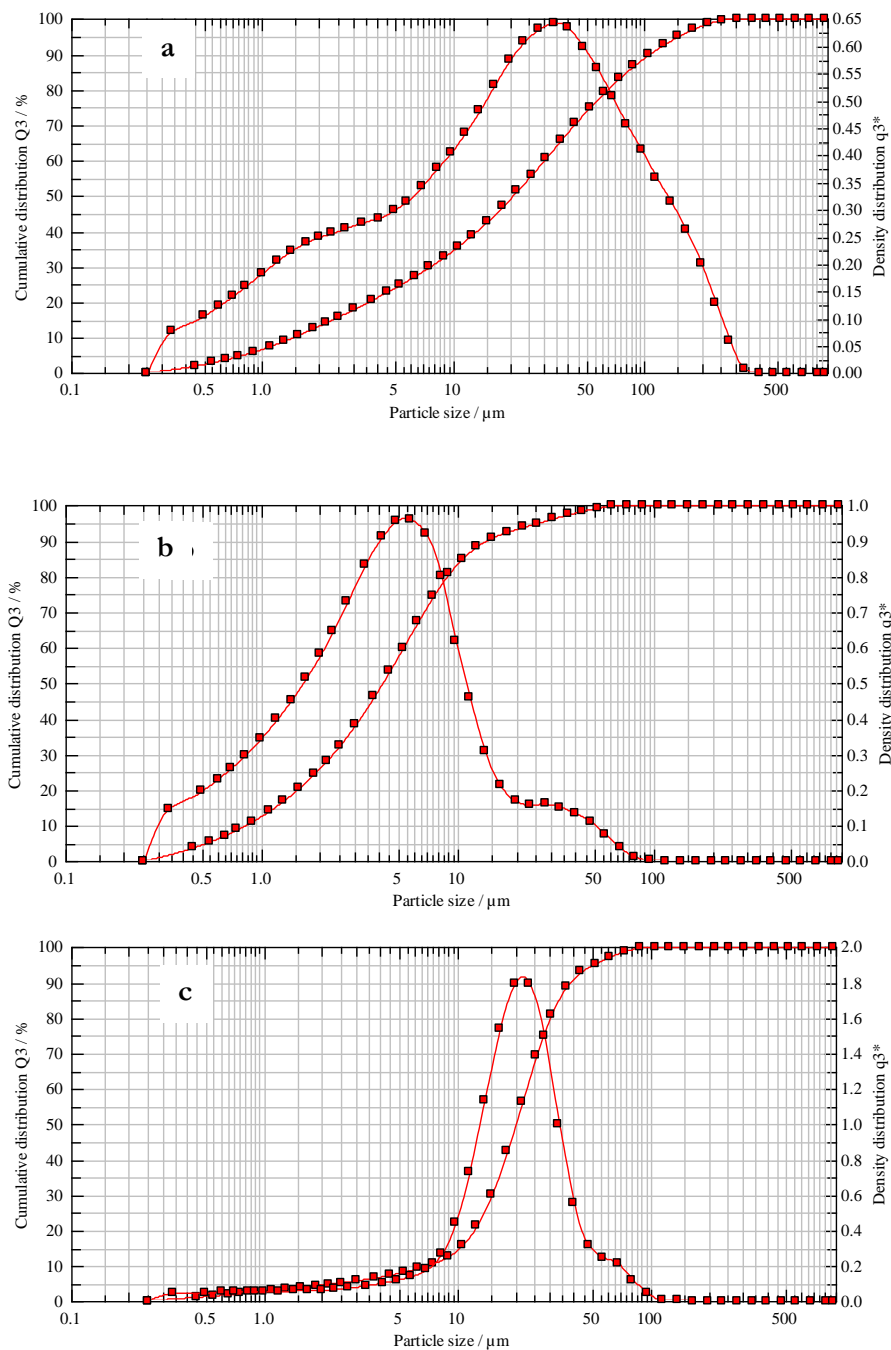


Figure 5.27. PSD profiles obtained from LD analysis. a) unprocessed CN-OA-m; b) particles passed through the reactor system; c) particles which stuck in the tubing after the reactor.

Copies of NMR spectra of isolated compounds

Copies of NMR spectra of isolated compounds are available in the Supporting Information through the website of the Publisher. DOI: <https://doi.org/10.1039/D0RE00036A>

5.5 References

1. Bariwal, J.; Van der Eycken, E., C–N bond forming cross-coupling reactions: an overview. *Chem. Soc. Rev.* **2013**, *42* (24), 9283-9303.
2. Dorel, R.; Grugel, C. P.; Haydl, A. M., The Buchwald–Hartwig Amination After 25 Years. *Angew. Chem. Int. Ed.* **2019**, *58* (48), 17118-17129.
3. Ruiz-Castillo, P.; Buchwald, S. L., Applications of Palladium-Catalyzed C–N Cross-Coupling Reactions. *Chem. Rev.* **2016**, *116* (19), 12564-12649.
4. Butters, M.; Catterick, D.; Craig, A.; Curzons, A.; Dale, D.; Gillmore, A.; Green, S. P.; Marziano, I.; Sherlock, J.-P.; White, W., Critical Assessment of Pharmaceutical Processes A Rationale for Changing the Synthetic Route. *Chem. Rev.* **2006**, *106* (7), 3002-3027.
5. Wolfe, J. P.; Buchwald, S. L., Nickel-Catalyzed Amination of Aryl Chlorides. *J. Am. Chem. Soc.* **1997**, *119* (26), 6054-6058.
6. Li, C.; Kawamata, Y.; Nakamura, H.; Vantourout, J. C.; Liu, Z.; Hou, Q.; Bao, D.; Starr, J. T.; Chen, J.; Yan, M.; Baran, P. S., Electrochemically Enabled, Nickel-Catalyzed Amination. *Angew. Chem. Int. Ed.* **2017**, *56* (42), 13088-13093.
7. Kawamata, Y.; Vantourout, J. C.; Hickey, D. P.; Bai, P.; Chen, L.; Hou, Q.; Qiao, W.; Barman, K.; Edwards, M. A.; Garrido-Castro, A. F.; deGruyter, J. N.; Nakamura, H.; Knouse, K.; Qin, C.; Clay, K. J.; Bao, D.; Li, C.; Starr, J. T.; Garcia-Irizarry, C.; Sach, N.; White, H. S.; Neurock, M.; Minter, S. D.; Baran, P. S., Electrochemically Driven, Ni-Catalyzed Aryl Amination: Scope, Mechanism, and Applications. *J. Am. Chem. Soc.* **2019**, *141* (15), 6392-6402.
8. Corcoran, E. B.; Pirnot, M. T.; Lin, S.; Dreher, S. D.; DiRocco, D. A.; Davies, I. W.; Buchwald, S. L.; MacMillan, D. W. C., Aryl amination using ligand-free Ni(II) salts and photoredox catalysis. *Science* **2016**, *353* (6296), 279-283.
9. Du, Y.; Pearson, R. M.; Lim, C.-H.; Sartor, S. M.; Ryan, M. D.; Yang, H.; Damrauer, N. H.; Miyake, G. M., Strongly Reducing, Visible-Light Organic Photoredox Catalysts as Sustainable Alternatives to Precious Metals. *Chemistry – A European Journal* **2017**, *23* (46), 10962-10968.
10. Lim, C.-H.; Kudisch, M.; Liu, B.; Miyake, G. M., C–N Cross-Coupling via Photoexcitation of Nickel–Amine Complexes. *J. Am. Chem. Soc.* **2018**, *140* (24), 7667-7673.

11. Kudisch, M.; Lim, C.-H.; Thordarson, P.; Miyake, G. M., Energy Transfer to Ni-Amine Complexes in Dual Catalytic, Light-Driven C–N Cross-Coupling Reactions. *J. Am. Chem. Soc.* **2019**, *141* (49), 19479-19486.
12. Caputo, J. A.; Frenette, L. C.; Zhao, N.; Sowers, K. L.; Krauss, T. D.; Weix, D. J., General and Efficient C–C Bond Forming Photoredox Catalysis with Semiconductor Quantum Dots. *J. Am. Chem. Soc.* **2017**, *139* (12), 4250-4253.
13. Liu, Y.-Y.; Liang, D.; Lu, L.-Q.; Xiao, W.-J., Practical heterogeneous photoredox/nickel dual catalysis for C–N and C–O coupling reactions. *Chem. Commun.* **2019**, *55* (33), 4853-4856.
14. Gisbertz, S.; Reischauer, S.; Pieber, B., Overcoming limitations in dual photoredox/nickel-catalysed C–N cross-couplings due to catalyst deactivation. *Nature Catalysis* **2020**, *3* (8), 611-620.
15. Twilton, J.; Le, C.; Zhang, P.; Shaw, M. H.; Evans, R. W.; MacMillan, D. W. C., The merger of transition metal and photocatalysis. *Nature Reviews Chemistry* **2017**, *1*, 0052.
16. Park, B. Y.; Pirnot, M. T.; Buchwald, S. L., Visible Light-Mediated (Hetero)aryl Amination Using Ni(II) Salts and Photoredox Catalysis in Flow: A Synthesis of Tetracaine. *J. Org. Chem.* **2020**, *85* (5), 3234-3244.
17. Qi, Z.-H.; Ma, J., Dual Role of a Photocatalyst: Generation of Ni(0) Catalyst and Promotion of Catalytic C–N Bond Formation. *ACS Catal.* **2018**, *8* (2), 1456-1463.
18. Sun, R.; Qin, Y.; Ruccolo, S.; Schnedermann, C.; Costentin, C.; Nocera, D. G., Elucidation of a Redox-Mediated Reaction Cycle for Nickel-Catalyzed Cross Coupling. *J. Am. Chem. Soc.* **2019**, *141* (1), 89-93.
19. Lavoie, C. M.; Stradiotto, M., Bisphosphines: A Prominent Ancillary Ligand Class for Application in Nickel-Catalyzed C–N Cross-Coupling. *ACS Catal.* **2018**, *8* (8), 7228-7250.
20. Oderinde, M. S.; Jones, N. H.; Juneau, A.; Frenette, M.; Aquila, B.; Tentarelli, S.; Robbins, D. W.; Johannes, J. W., Highly Chemoselective Iridium Photoredox and Nickel Catalysis for the Cross-Coupling of Primary Aryl Amines with Aryl Halides. *Angew. Chem. Int. Ed.* **2016**, *55* (42), 13219-13223.
21. Romero, N. A.; Nicewicz, D. A., Organic Photoredox Catalysis. *Chem. Rev.* **2016**, *116* (17), 10075-10166.

22. Friedmann, D.; Hakki, A.; Kim, H.; Choi, W.; Bahnemann, D., Heterogeneous photocatalytic organic synthesis: state-of-the-art and future perspectives. *Green Chemistry* **2016**, *18* (20), 5391-5411.
23. Riente, P.; Noël, T., Application of metal oxide semiconductors in light-driven organic transformations. *Catal. Sci. Technol.* **2019**, *9* (19), 5186-5232.
24. Gisbertz, S.; Reischauer, S.; Pieber, B., Overcoming limitations in dual photoredox/nickel-catalysed C–N cross-couplings due to catalyst deactivation. *Nat. Catal.* **2020**, *3* (8), 611-620.
25. Wang, Y.; Wang, X.; Antonietti, M., Polymeric Graphitic Carbon Nitride as a Heterogeneous Organocatalyst: From Photochemistry to Multipurpose Catalysis to Sustainable Chemistry. *Angew. Chem. Int. Ed.* **2012**, *51* (1), 68-89.
26. Savateev, A.; Antonietti, M., Heterogeneous Organocatalysis for Photoredox Chemistry. *ACS Catal.* **2018**, *8* (10), 9790-9808.
27. Ghosh, I.; Khamrai, J.; Savateev, A.; Shlapakov, N.; Antonietti, M.; König, B., Organic semiconductor photocatalyst can bifunctionalize arenes and heteroarenes. *Science* **2019**, *365* (6451), 360-366.
28. Markushyna, Y.; Smith, C. A.; Savateev, A., Organic Photocatalysis: Carbon Nitride Semiconductors vs. Molecular Catalysts. *Eur. J. Org. Chem.* **2020**, *2020* (10), 1294-1309.
29. Savateev, A.; Ghosh, I.; König, B.; Antonietti, M., Photoredox Catalytic Organic Transformations using Heterogeneous Carbon Nitrides. *Angew. Chem. Int. Ed.* **2018**, *57* (49), 15936-15947.
30. Dong, Q.; Mohamad Latiff, N.; Mazánek, V.; Rosli, N. F.; Chia, H. L.; Sofer, Z.; Pumera, M., Triazine- and Heptazine-Based Carbon Nitrides: Toxicity. *ACS Applied Nano Materials* **2018**, *1* (9), 4442-4449.
31. Cavedon, C.; Madani, A.; Seeberger, P. H.; Pieber, B., Semiheterogeneous Dual Nickel/Photocatalytic (Thio)etherification Using Carbon Nitrides. *Org. Lett.* **2019**, *21* (13), 5331-5334.
32. Pieber, B.; Malik, J. A.; Cavedon, C.; Gisbertz, S.; Savateev, A.; Cruz, D.; Heil, T.; Zhang, G.; Seeberger, P. H., Semi-heterogeneous Dual Nickel/Photocatalysis using Carbon Nitrides: Esterification of Carboxylic Acids with Aryl Halides. *Angew. Chem. Int. Ed.* **2019**, *58* (28), 9575-9580.

33. Cambié, D.; Bottecchia, C.; Straathof, N. J. W.; Hessel, V.; Noël, T., Applications of Continuous-Flow Photochemistry in Organic Synthesis, Material Science, and Water Treatment. *Chem. Rev.* **2016**, *116* (17), 10276-10341.
34. Plutschack, M. B.; Pieber, B.; Gilmore, K.; Seeberger, P. H., The Hitchhiker's Guide to Flow Chemistry. *Chem. Rev.* **2017**, *117* (18), 11796-11893.
35. Elliott, L. D.; Knowles, J. P.; Koovits, P. J.; Maskill, K. G.; Ralph, M. J.; Lejeune, G.; Edwards, L. J.; Robinson, R. I.; Clemens, I. R.; Cox, B.; Pascoe, D. D.; Koch, G.; Eberle, M.; Berry, M. B.; Booker-Milburn, K. I., Batch versus Flow Photochemistry: A Revealing Comparison of Yield and Productivity. *Chemistry – A European Journal* **2014**, *20* (46), 15226-15232.
36. Knowles, J. P.; Elliott, L. D.; Booker-Milburn, K. I., Flow photochemistry: Old light through new windows. *Beilstein Journal of Organic Chemistry* **2012**, *8*, 2025-2052.
37. Politano, F.; Oksdath-Mansilla, G., Light on the Horizon: Current Research and Future Perspectives in Flow Photochemistry. *Organic Process Research & Development* **2018**, *22* (9), 1045-1062.
38. Noël, T., A personal perspective on the future of flow photochemistry. *Journal of Flow Chemistry JFChem* **2017**, *7* (3-4), 87-93.
39. Hartman, R. L., Managing Solids in Microreactors for the Upstream Continuous Processing of Fine Chemicals. *Organic Process Research & Development* **2012**, *16* (5), 870-887.
40. Wu, K.; Kuhn, S., Strategies for solids handling in microreactors. *Chimica Oggi-chemistry Today* **2014**, *32*, 62-67.
41. Browne, D. L.; Deadman, B. J.; Ashe, R.; Baxendale, I. R.; Ley, S. V., Continuous Flow Processing of Slurries: Evaluation of an Agitated Cell Reactor. *Organic Process Research & Development* **2011**, *15* (3), 693-697.
42. Liguori, L.; Bjørsvik, H.-R., Multijet Oscillating Disc Millireactor: A Novel Approach for Continuous Flow Organic Synthesis. *Organic Process Research & Development* **2011**, *15* (5), 997-1009.
43. Falß, S.; Tomaiuolo, G.; Perazzo, A.; Hodgson, P.; Yaseneva, P.; Zakrzewski, J.; Guido, S.; Lapkin, A.; Woodward, R.; Meadows, R. E., A Continuous Process for Buchwald–Hartwig Amination at Micro-, Lab-, and Mesoscale Using a Novel Reactor Concept. *Organic Process Research & Development* **2016**, *20* (2), 558-567.

44. Filippini, P.; Gioiello, A.; Baxendale, I. R., Controlled Flow Precipitation as a Valuable Tool for Synthesis. *Organic Process Research & Development* **2016**, *20* (2), 371-375.
45. Mo, Y.; Jensen, K. F., A miniature CSTR cascade for continuous flow of reactions containing solids. *React. Chem. Eng.* **2016**, *1* (5), 501-507.
46. Chapman, M. R.; Kwan, M. H. T.; King, G.; Jolley, K. E.; Hussain, M.; Hussain, S.; Salama, I. E.; González Niño, C.; Thompson, L. A.; Bayana, M. E.; Clayton, A. D.; Nguyen, B. N.; Turner, N. J.; Kapur, N.; Blacker, A. J., Simple and Versatile Laboratory Scale CSTR for Multiphasic Continuous-Flow Chemistry and Long Residence Times. *Organic Process Research & Development* **2017**, *21* (9), 1294-1301.
47. Mo, Y.; Lin, H.; Jensen, K. F., High-performance miniature CSTR for biphasic C–C bond-forming reactions. *Chem. Eng. J.* **2018**, *335*, 936-944.
48. Pomberger, A.; Mo, Y.; Nandiwale, K. Y.; Schultz, V. L.; Duvadie, R.; Robinson, R. I.; Altinoglu, E. I.; Jensen, K. F., A Continuous Stirred-Tank Reactor (CSTR) Cascade for Handling Solid-Containing Photochemical Reactions. *Organic Process Research & Development* **2019**, *23* (12), 2699-2706.
49. González Niño, C.; Kapur, N.; King, M.-F.; de Boer, G.; Blacker, A. J.; Bourne, R.; Thompson, H., Computational fluid dynamic enabled design optimisation of miniaturised continuous oscillatory baffled reactors in chemical processing. *International Journal of Computational Fluid Dynamics* **2019**, *33* (6-7), 317-331.
50. Tahir, F.; Krzemieniewska-Nandwani, K.; Mack, J.; Lovett, D.; Siddique, H.; Mabbott, F.; Raval, V.; Houson, I.; Florence, A., Advanced control of a continuous oscillatory flow crystalliser. *Control Engineering Practice* **2017**, *67*, 64-75.
51. McGlone, T.; Briggs, N. E. B.; Clark, C. A.; Brown, C. J.; Sefcik, J.; Florence, A. J., Oscillatory Flow Reactors (OFRs) for Continuous Manufacturing and Crystallization. *Organic Process Research & Development* **2015**, *19* (9), 1186-1202.
52. Okafor, O.; Weilhard, A.; Fernandes, J. A.; Karjalainen, E.; Goodridge, R.; Sans, V., Advanced reactor engineering with 3D printing for the continuous-flow synthesis of silver nanoparticles. *React. Chem. Eng.* **2017**, *2* (2), 129-136.
53. Brown, C. J.; McGlone, T.; Yerdelen, S.; Srirambhatla, V.; Mabbott, F.; Gurung, R.; L. Briuglia, M.; Ahmed, B.; Polyzois, H.; McGinty, J.; Perciballi, F.; Fysikopoulos, D.; MacFhionnghaile, P.; Siddique, H.; Raval, V.; Harrington, T. S.; Vassileiou, A. D.;

- Robertson, M.; Prasad, E.; Johnston, A.; Johnston, B.; Nordon, A.; Srai, J. S.; Halbert, G.; ter Horst, J. H.; Price, C. J.; Rielly, C. D.; Sefcik, J.; Florence, A. J., Enabling precision manufacturing of active pharmaceutical ingredients: workflow for seeded cooling continuous crystallisations. *Molecular Systems Design & Engineering* **2018**, *3* (3), 518-549.
54. Jolliffe, H. G.; Gerogiorgis, D. I., Process modelling, design and techno-economic evaluation for continuous paracetamol crystallisation. *Computers & Chemical Engineering* **2018**, *118*, 224-235.
55. Jiang, M.; Ni, X.-W., Reactive Crystallization of Paracetamol in a Continuous Oscillatory Baffled Reactor. *Organic Process Research & Development* **2019**, *23* (5), 882-890.
56. Cruz, P.; Rocha, F.; Ferreira, A., Effect of operating conditions on batch and continuous paracetamol crystallization in an oscillatory flow mesoreactor. *CrystEngComm* **2016**, *18* (47), 9113-9121.
57. Doyle, B. J.; Gutmann, B.; Bittel, M.; Hubler, T.; Macchi, A.; Roberge, D. M., Handling of Solids and Flow Characterization in a Baffleless Oscillatory Flow Coil Reactor. *Industrial & Engineering Chemistry Research* **2020**, *59* (9), 4007-4019.
58. For more information on the HANU reactor, see: <http://www.creaflow.be/>.
59. Levenspiel, O.; Bischoff, K. B., Backmixing in the Design of Chemical Reactors. *Industrial & Engineering Chemistry* **1959**, *51* (12), 1431-1434.
60. Rosso, C.; Williams, J. D.; Filippini, G.; Prato, M.; Kappe, C. O., Visible-Light-Mediated Iodoperfluoroalkylation of Alkenes in Flow and Its Application to the Synthesis of a Key Fulvestrant Intermediate. *Org. Lett.* **2019**, *21* (13), 5341-5345.
61. Steiner, A.; Williams, J. D.; de Frutos, O.; Rincón, J. A.; Mateos, C.; Kappe, C. O., Continuous photochemical benzylic bromination using in situ generated Br₂: process intensification towards optimal PMI and throughput. *Green Chemistry* **2020**, *22* (2), 448-454.
62. Levenspiel, O., *Chemical Reaction Engineering*. 3rd ed.; John Wiley & Sons: 1999.
63. Pieber, B.; Shalom, M.; Antonietti, M.; Seeberger, P. H.; Gilmore, K., Continuous Heterogeneous Photocatalysis in Serial Micro-Batch Reactors. *Angew. Chem. Int. Ed.* **2018**, *57* (31), 9976-9979.
64. Zhang, G.; Li, G.; Lan, Z.-A.; Lin, L.; Savateev, A.; Heil, T.; Zafeiratos, S.; Wang, X.; Antonietti, M., Optimizing Optical Absorption, Exciton Dissociation, and Charge

Chapter 5

Transfer of a Polymeric Carbon Nitride with Ultrahigh Solar Hydrogen Production Activity. *Angew. Chem. Int. Ed.* **2017**, *56* (43), 13445-13449.

65. Harper, K. C.; Moschetta, E. G.; Bordawekar, S. V.; Wittenberger, S. J., A Laser Driven Flow Chemistry Platform for Scaling Photochemical Reactions with Visible Light. *ACS Cent. Sci.* **2019**, *5* (1), 109-115.

66. Györke, S.; Lukyanenko, V.; Györke, I., Dual effects of tetracaine on spontaneous calcium release in rat ventricular myocytes. *The Journal of Physiology* **1997**, *500* (2), 297-309.

67. World Health Organization Model List of Essential Medicines - 21st List, 2019.

68. Yuan, M.-L.; Xie, J.-H.; Zhou, Q.-L., Boron Lewis Acid Promoted Ruthenium-Catalyzed Hydrogenation of Amides: An Efficient Approach to Secondary Amines. *ChemCatChem* **2016**, *8* (19), 3036-3040.

69. Wahba, A. E.; Hamann, M. T., Reductive N-Alkylation of Nitroarenes: A Green Approach for the N-Alkylation of Natural Products. *J. Org. Chem.* **2012**, *77* (10), 4578-4585.

Chapter 6

Photocatalyst-free, visible-light-mediated nickel catalysis for carbon–heteroatom cross-couplings

Cavedon, C.*; **Gisbertz, S.***; Vogl, S.; Richter, N.; Schrottke, S.; Teutloff, C.; Seeberger, P. H.; Thomas, A.; Pieber, B.

ChemRxiv. Preprint. August 4, 2021.

DOI: <https://doi.org/10.26434/chemrxiv-2021-kt2wr>

**These authors contributed equally.*

Abstract

Metallaphotocatalysis typically requires a photocatalyst to harness the energy of visible-light and transfer it to a transition metal catalyst to trigger chemical reactions. The most prominent example is the merger of photo- and nickel catalysis that unlocked various cross-couplings. The high reactivity of excited photocatalyst can, however, lead to unwanted side reactions limiting this approach. Here we show that a bipyridine ligand that is subtly decorated with two carbazole groups forms a nickel complex that absorbs visible-light and promotes several carbon–heteroatom cross-couplings in absence of an exogenous photocatalysts. The ligand can be polymerized in a simple one-step procedure to afford a porous organic polymer that can be used for heterogeneous nickel catalysis in the same reactions. The material can be easily recovered and reused multiple times maintaining high catalytic activity and selectivity.

Specific contribution

Dr. B. Pieber, C. Cavedon and I conceived the idea behind the project.

N. Richter, C. Cavedon and I verified the feasibility of this approach by screening and optimizing the coupling protocols.

C. Cavedon and I evaluated the scope and limitations of the C–S, C–N and C–O protocols.

S. Vogl synthesized the homogeneous and polymeric ligand and performed material characterizations.

I studied the recycling of the heterogeneous catalytic system.

C. Cavedon and I organized the data and wrote the manuscript.

Dr. B. Pieber, Prof. A. Thomas and Prof. P. H. Seeberger revised and corrected the manuscript.

6.1 Introduction

Strategic carbon–carbon and carbon–heteroatom bond formations are among the most important transformations in the synthesis of fine chemicals.¹⁻² Nickel catalysts are intensively studied as an abundant alternative to palladium catalysts, but reductive elimination is challenging limiting this approach.³⁻⁴ This problem was successfully tackled by combining nickel- and photocatalysis (Figure 6.1, a).⁵⁻⁷ Suitable photocatalysts for dual photo/nickel catalytic carbon–heteroatom cross-couplings range from ruthenium and iridium polypyridyl complexes and organic dyes to heterogeneous semiconductors.⁶ Moreover, nickel complexes and visible-light photocatalysts were combined in bifunctional heterogeneous materials, such as metal-organic frameworks,⁸⁻⁹ organic polymers,¹⁰ or functionalized semiconductors.¹¹⁻¹⁴ Although dual photo/nickel catalytic is attractive, the need of a photocatalyst is a drawback. Common, homogeneous noble-metal based photocatalysts that are mainly applied are expensive, not easily recyclable and unsustainable. Moreover, their high reactivity upon excitation can trigger unwanted side-reactions¹⁵ and deactivation of the nickel catalyst,¹⁶ resulting in low selectivities and severe reproducibility issues.

The first mechanistic hypothesis for dual photo/nickel catalyzed carbon–heteroatom cross-couplings suggested that energy- or electron transfer between the photocatalyst and a thermodynamically stable Ni^{II} intermediate triggers reductive elimination of the desired product.^{6, 17} Recently, this proposal was withdrawn by several studies, which provided evidence that these reactions proceed through Ni^I/Ni^{III} cycles without a Ni^{II} resting state.¹⁸⁻²¹ Doyle and colleagues showed that upon absorption of light, Ni^{II}(dtbbpy) aryl halide complexes (dtbbpy = 4,4'-di-*tert*-butyl-2,2'-bipyridyl) undergo Ni–aryl homolysis to form a catalytically active Ni^I catalyst.²²⁻²³ This observation was expanded to a synthetic protocol for C–O and C–N cross-couplings using UV-light irradiation.²⁴⁻²⁵ More recently, pulse radiolysis together with spectroelectrochemistry indicated that Ni⁰/Ni^{II} comproportionation generates a Ni^I bipyridyl species that rapidly undergoes oxidative addition with iodobenzene.²¹ Moreover, Nocera and coworkers showed that sub-stoichiometric amounts of zinc can be used instead of a photocatalyst and light for C–N and C–O cross-couplings.²⁶ Here, the metal reductant was proposed to generate the active Ni^I catalyst from a Ni^{II} pre-catalyst that engages in a thermally sustained Ni^I/Ni^{III} cycle.

Based on these mechanistic findings, we questioned whether a visible-light-mediated approach to nickel-catalyzed carbon–heteroatom cross-couplings without an exogenous photocatalyst or reductant is feasible. The development of a benchstable Ni^{II} pre-catalyst that can be directly activated by visible-light would overcome the drawbacks associated with the price and reactivity of many photocatalysts without using highly energetic UV-light. We hypothesized that this can be realized via the modification of a bipyridyl ligand with a structural motif that extends the absorption of an *in situ* formed Ni^{II} pre-catalyst to visible-light. We speculated that such a complex might form the key Ni^I species upon irradiation through, for example, homolytic fission of a Ni–halogen bond, or intramolecular charge transfer.

Here we show that this can be indeed achieved by decorating 2-2'-bipyridine with two carbazole units (Figure 6.1, b). This ligand enables visible-light-mediated cross-couplings of several nucleophiles with aryl halides. Moreover, we demonstrate that the ligand can be polymerized to yield a conjugated microporous polymer that serves as a recyclable heterogeneous macroligand for metallaphotocatalytic carbon–heteroatom couplings.

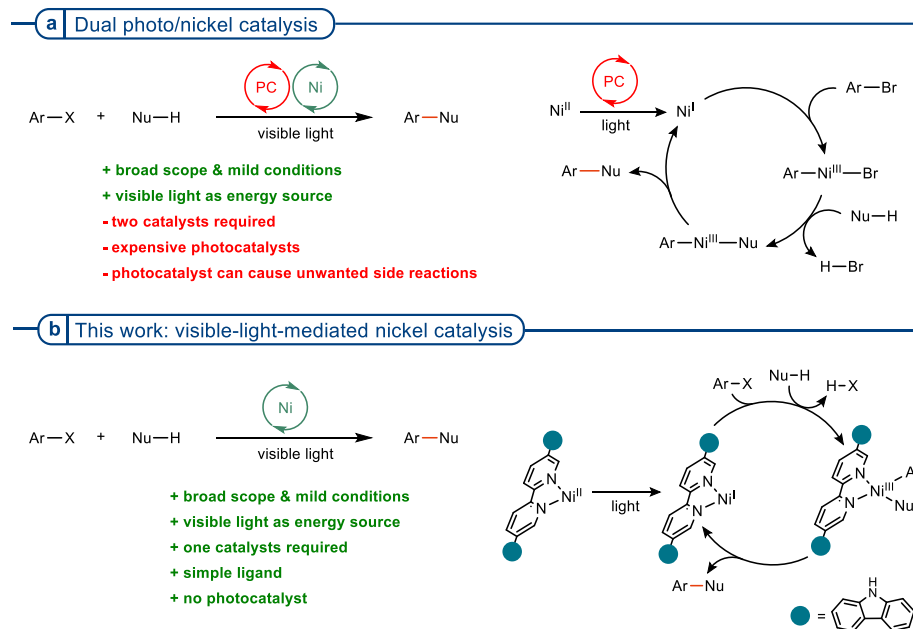


Figure 6.1. Strategies for visible-light mediated nickel catalyzed carbon–heteroatom cross-couplings. a. Dual photo/nickel catalysis requires exogenous photocatalysts. **b.** Visible-light-mediated nickel catalysis through ligand modification (this work).

6.2 Ligand design and evaluation

Ni^{II}(dtbbpy) aryl halide complexes catalyze cross-couplings using UV-light (390 nm LEDs).²²⁻²³ These catalysts are synthesized from Ni(COD)₂ using glove-box- or Schlenk techniques,²²⁻²³ which, together with the constraint to high energy photons, limits their practicability. In dual photo/nickel catalysis, on the contrary, Ni(2,2'-bipyridyl)X₂ (X = Cl, Br) complexes that form *in situ* from cheap, benchstable Ni^{II} salts and the corresponding ligand can be used.⁵⁻⁷ The UV-Vis absorption spectrum of a mixture of NiCl₂·glyme (glyme = 1,2-dimethoxyethane) and dtbbpy in DMAc (*N,N*-dimethylacetamide) shows that the resulting complex only absorbs light below 320 nm (Fig. S5). To shift the absorption towards the visible-light spectrum, we synthesized 5,5'-dicarbazolyl-2,2'-bipyridyl (czbpy) via a copper-catalyzed Ullmann coupling between 5,5'-dibromo-bipyridine and 9*H*-carbazole (Figure 6.2, a).²⁷ The UV-Vis spectrum of czbpy shows a strong absorption band centered at ~350 nm (Figure 6.8). More importantly, dissolving NiCl₂·glyme and czbpy in DMAc resulted in a complex that absorbs visible-light up to 450 nm (see chapter 6.5).

This single, high yielding modification of a commercially available bipyridine derivative resulted in an *in situ* formed nickel catalyst which mitigates the necessity of exogenous photocatalysts (Figure 6.2, b). The ligand was suitable for the coupling of aryl halides with sulfonates, carboxylic acids, and sulfonamides. The coupling of 4-iodobenzotrifluoride and a sodium sulfinate salt (C–S coupling), which was previously reported using combinations of a nickel catalyst with iridium²⁸ or ruthenium²⁹⁻³⁰ polypyridyl complexes as photocatalyst, afforded sulfone **1** in excellent yield after 22 h irradiation with blue light (440 nm, entry 1). No conversion was detected when the reaction was carried out in the dark (entry 2).

Sodium sulfonates and aryl halides can assemble in electron-donor acceptor (EDA) complexes and afford sulfones upon UV light irradiation.³¹ Accordingly, even in absence of NiCl₂·glyme small amounts of **1** were formed (entry 3), due to partial emission in the UV region of the light source. When 2,2'-bipyridine (bpy), 9*H*-carbazole or a combination of bpy and 9*H*-carbazole were used, the desired product was also formed, although with significantly lower selectivity (entry 4-6).

The C–O arylation of 4-iodobenzotrifluoride with *N*-Boc-proline under optimized conditions resulted in 88% of the desired product (**2**). No product formation was observed in the dark, without NiCl₂·glyme, or when 9*H*-carbazole was used as ligand (entry 8-10). While optimized conditions resulted in 88% of the desired product (**2**), only small amounts (<10

%) of **2** were formed using bpy, or bpy together with 9*H*-carbazole (entry 9, 11). This supports our hypothesis that czbpy enables activation of nickel catalysts with wavelengths above 400 nm, which are not accessible to bpy complexes.

Under optimized conditions, the light-mediated, nickel-catalyzed *N*-arylation of sulfonamides afforded **3** in 75% yield (entry 13). Light and the nickel salt were crucial for product formation (entry 13-14). Partial consumption of the starting material in the absence of a nickel salt (entry 15) might be a result of a photocatalytic activation of aryl iodides.¹⁵ Product formation was not detected using bpy as ligand (entry 17), but significant amounts of **3** were obtained in presence of 9*H*-carbazole (entry 16) or a combination of 9*H*-carbazole and bpy (entry 16, 18). Although such reactivity was not observed in the other coupling protocols, this effect might result from formation of photoactive Ni-carbazole complexes. It was recently shown that carbazole acts as a strong σ -donating ligand that reduces the energy difference in MLCT transitions that account for light absorption of nickel complexes.³²⁻³³

Electron paramagnetic resonance (EPR) spectroscopy was carried out to shed some light on the reaction mechanism. Up to two signals were found depending on the solution composition in frozen solution (see SI). The first signal with a linewidth of approx. 20 G was found in all solutions and appeared to be light-independent. We assign this signal to a Cu^{II}-czbpy complex, owing to a residual Cu contamination from the ligand preparation process (~ 1 mg g⁻¹ as measured by ICP-OES analysis). A second, narrow signal occurred upon illumination and rapid freezing to <25 K, when at least Ni-czbpy and an aryl iodide (4-iodobenzotrifluoride) were present. A kinetic analysis of a related protocol using exogenous photocatalysts showed a rate dependence on the aryl halide, which was assigned to a direct photocatalytic activation.¹⁵ Due to its nature (microwave power saturation and linewidth), the light-dependent EPR-signal is of organic origin without involvement of Ni. Therefore we tentatively assign this signal to an elusive paramagnetic species that results from a light-induced reaction between a Ni-czbpy species and the aryl iodide, suggesting that the aryl iodide may play a role in the activation of the pre-catalyst. No signal for the proposed Ni^I intermediate was detected, which can be rationalized instability of such three-coordinate Ni halide complexes, or rapid oxidative addition.²¹

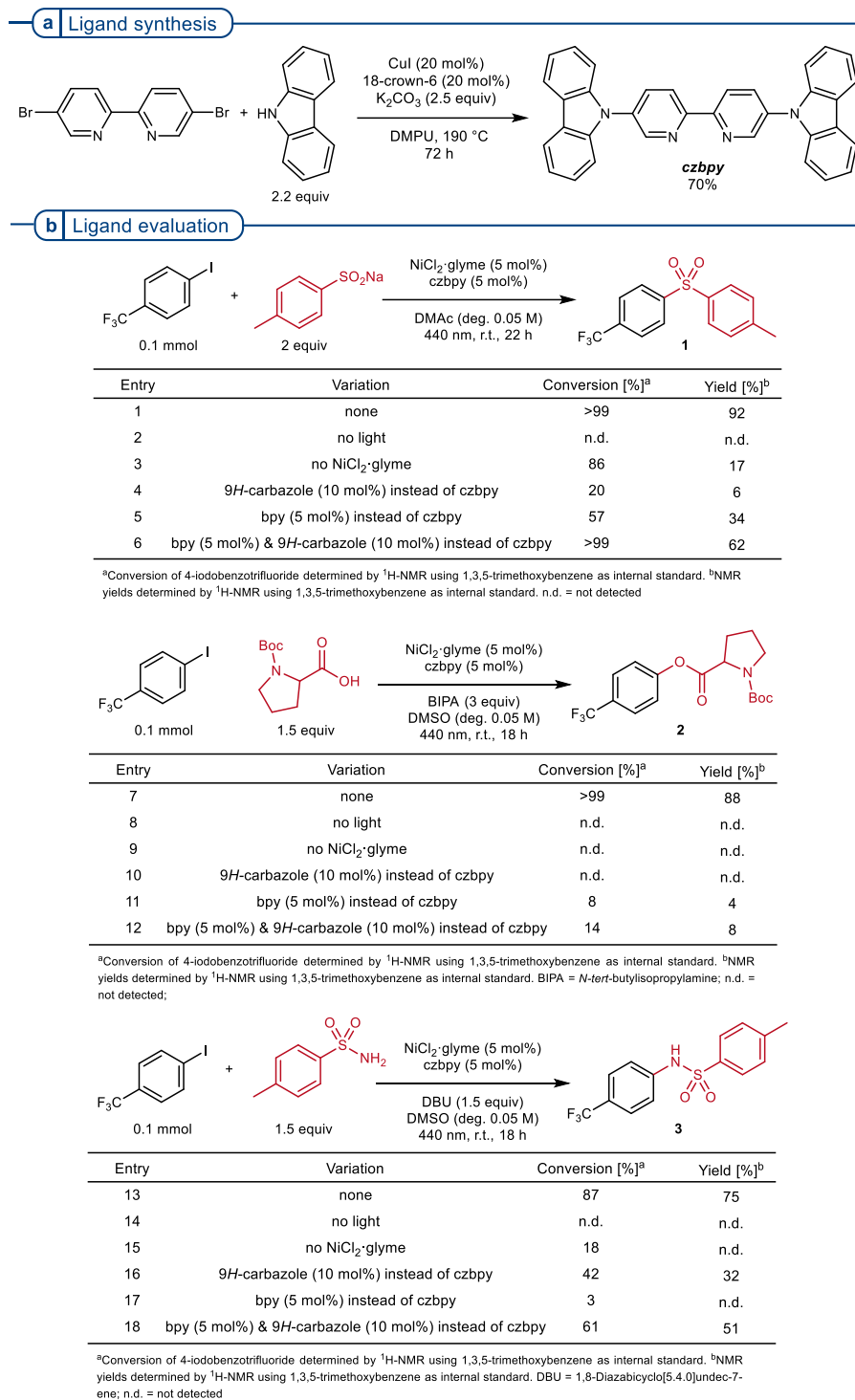


Figure 6.2 | Ligand synthesis, optimized reaction conditions and control experiments. **a**, The ligand for photocatalyst-free, visible-light-mediated nickel catalysis was synthesized via an Ullmann C–N coupling. **b**, Optimized Conditions and control experiments for the coupling of 4-iodobenzotrifluoride with sodium *p*-toluenesulfinate, *N*-Boc-proline and *p*-toluenesulfonamide.

6.3 Scope and limitations

Next, we explored the scope and limitations of photocatalyst-free, visible-light-mediated carbon–heteroatom cross-couplings (Table 6.1). Several aromatic sulfinate salts were successfully coupled with 4-iodobenzotrifluoride (Table 6.1, a, **1**, **4-7**). Optimized reaction conditions did not result in the desired product using sodium methane sulfinate. It is noteworthy that this substrate was earlier reported as a successful coupling partner when NiCl₂·bpy was used in combination with tris(2,2'-bipyridyl)dichlororuthenium(II) hexahydrate as exogenous photocatalyst.²⁹ With regard to the aryl iodide, the reaction affords the corresponding sulfones in presence of electron withdrawing groups such as trifluoromethyl (**1**), nitrile (**8**), ketone (**9-11**), amide (**12**), boron pinacolate ester (**13**), and methyl ester (**14**). Para- (**9**) and ortho- (**11**) substitution showed similar reactivity, whereas meta-substitution (**10**) required a longer reaction time for full conversion. Electron-rich aryl iodides, such as 4-iodotoluene (**15**) and 4-iodoanisole (**16**), were suitable substrates and the presence of an unprotected amine group (**17**) was tolerated. Coupling of 2-iodothiophene (**18**) and 4-iodopyridine (**19**) showed that heteroaryl iodides are suitable substrates.

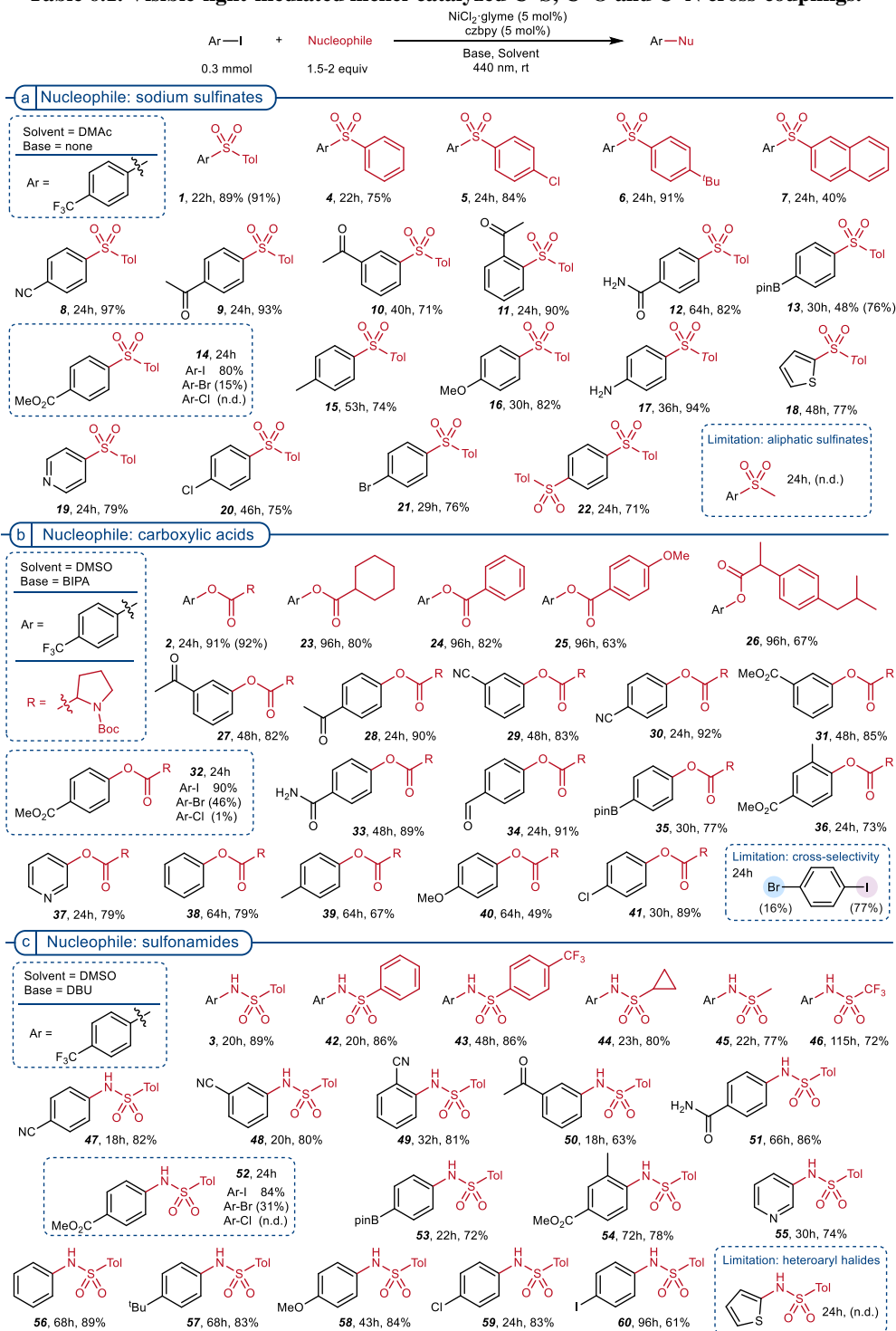
A comparison of different aryl halides showed that an aryl iodide reacts significantly faster than the corresponding bromide (**14**). This is in contrast to dual nickel/photocatalytic protocols, in which iodides and bromides exhibit similar reactivity.^{28, 30} Aryl chlorides undergo nickel/photocatalytic reactions when more electron-donating ligand 4,4'-dimethoxy-bpy is used,²⁸ but czbpy was not suitable for aryl chloride. These observations were applied for selective couplings of aryl iodides that contain a chloride (**20**) or a bromide substituent (**21**). Moreover, diarylated product **22** was synthesized from 1,4-diiodobenzene using 3 equivalents of sodium *p*-toluenesulfinate.

Good to excellent isolated yields were obtained for the C–O arylation of 4-iodobenzotrifluoride with aliphatic and aromatic carboxylic acids (Table 6.1, b, **2**, **23-26**). Further, a range of aryl iodides containing electron-withdrawing groups afforded the corresponding products (**2**, **27-35**). The influence of substituents on reactivity is highlighted by the longer reaction times required for the coupling of meta-substituted (**27**, **29**, **31**) aryl iodides, compared to their para-substituted analogues (**28**, **30**, **32**). The coupling of ortho-substituted aryl iodides was not possible in case of 2-iodoacetophenone, 2-iodobenzonitrile, but **36** was successfully synthesized from methyl 3-methyl-4-iodobenzoate. A heteroaryl iodide was also susceptible to the optimized reaction conditions (**38**). High electron densities

on the aryl iodide decreased their reactivity towards the C–O coupling, as showcased for the series 4-iodobenzene (**38**), 4-iodotoluene (**39**) and 4-iodoanisole (**40**). Similar to the C–S coupling described above, aryl iodides work best in the reaction (**32**, 90% from Ar-I). The reaction is rather slow using the corresponding bromide (46% NMR yield from Ar-Br), and a chloride afforded only traces of the desired product. As a result, 1-chloro-4-iodobenzene (**41**) coupled selectively on the iodo-position, but 1-bromo-4-iodobenzene reacted unselectively. All of these results are in agreement with previous reports on the dual nickel/photocatalytic cross-coupling of carboxylic acids with aryl halides, indicating that the photocatalyst-free strategy follows a similar mechanism.^{11, 15, 26, 34-35}

Aromatic as well as aliphatic sulfonamides (**3**, **42-46**) gave selective C–N cross-couplings with 4-iodobenzotrifluoride (Table 6.1, c), even though long reaction times were necessary in case of electron-withdrawing groups (**43**, **46**). In contrast to the previous C–S and C–O coupling, reactivity is not affected by the substitution pattern of the aryl iodide (**47-49**, **54**) or by the presence of either electron-withdrawing or electron-donating functional groups (**3**, **47-53**, **56-58**). Heteroaryl halides are problematic substrates in dual nickel/photocatalytic sulfonamidation protocols and require a ligand-free approach at elevated temperature.³⁶ Under our optimized conditions 3-iodopyridine gave **55** in good yield, but no product was observed for 2-iodothiophene. Aryl bromides were previously coupled with sulfonamides using combinations of nickel and iridium catalysts.³⁶ Our screening of different halides, showed that bromides are suitable substrates but reactivity of iodides is superior (**52**, 84% from Ar-I, 31% NMR yield from Ar-Br within 24h). Aryl chlorides are not reactive and **59** was obtained with good selectivity from 1-chloro-4-iodobenzene.

Unfortunately this ligand was not suitable for the coupling of aryl halides with amines, thiols or alcohols that were previously reported using dual nickel/photocatalytic methods.⁶ Attempts to form carbon–carbon bonds through coupling of aryl halides with borontrifluorides³⁷ or α -silylamines³⁸ were also unsuccessful or suffered from low selectivity (Table 6.31).

Table 6.1. Visible-light-mediated nickel-catalyzed C–S, C–O and C–N cross-couplings.^a

^aReaction conditions: aryl halide (300 μmol), nucleophile (a, sodium sulfinate, 600 μmol ; b, carboxylic acid, 450 μmol ; c, sulfonamide, 450 μmol), $\text{NiCl}_2 \cdot \text{glyme}$ (15 μmol), czbpy (15 μmol), base (b, *N*-*tert*-butylisopropylamine, 900 μmol ; c, 1,8-diazabicyclo[5.4.0]undec-7-ene, 450 μmol), solvent (a, DMAc, 6 mL; b, DMSO, 3 or 6 mL; c, DMSO, 6 mL), 440 nm LED (2 lamps at full power) at room temperature. Isolated yields are reported. NMR yields are in parentheses and were calculated via $^1\text{H-NMR}$ analysis using 1,3,5-trimethoxybenzene or maleic acid as internal standard. n.d. = not detected. Bpin = boronic acid pinacolate ester.

6.4 Polymerization of czbpy for heterogeneous, visible-light-mediated nickel catalysis

Having shown that czbpy serves as a versatile ligand for visible-light-mediated cross-couplings via homogeneous nickel-catalysis without an exogenous photocatalyst, we aimed to extend this approach to develop a heterogeneous, recyclable catalytic system.³⁹ Defined porous materials are ideal candidates for immobilization of metal catalysts, as they enable optimal access to the catalytic sites. The microporous organic polymer network poly-czbpy was synthesized from czbpy via oxidative polymerization with iron(III) chloride and exhibits a Brunauer-Emmett-Teller surface area (S_{BET}) of $853 \text{ m}^2 \text{ g}^{-1}$ (Figure 6.3, a).⁴⁰ In accordance with the literature,⁴⁰ the chemical structure of poly-czbpy was confirmed by ^{13}C CPMAS NMR spectroscopy (Figure 6.4) showing signals between 130 and 152 ppm, which verify the existence of bipyridine moieties within the structure. Additionally, at 137 ppm a signal corresponding to carbons in vicinity to carbazolyl nitrogen $\text{C}_{\text{Ar-N}}$ was detected. Ni@poly-czbpy was subsequently prepared by refluxing a suspension of poly-czbpy and NiCl_2 in methanol. Investigation of the porosity by nitrogen sorption measurements after the metalation showed a decreased BET surface of $470 \text{ m}^2 \text{ g}^{-1}$ due to the immobilization of the Ni(II) complex. Presence of nickel shifts the absorption of the material up to 650 nm (Figure 6.3, b), while the metal-free ligand framework poly-czbpy absorbs until 550 nm. Characterization of Ni@poly-czbpy by X-ray photoelectron spectroscopy (XPS) confirmed successful immobilization of Ni(II) species on the polymeric material. The N 1s core spectrum (Fig. 3c) contains three signals for nitrogen: i) an intense peak at 400.4 eV corresponding to polymerized carbazole moieties, ii) a signal at 399.7 eV which is assigned to N-Ni coordination of the Ni(II)-complex and iii) a low-intensity peak at 400.2 eV deriving from bipyridine nitrogen species which are not coordinated to nickel. The Ni 2p spectrum (Figure 6.3, d) shows a doublet and its corresponding satellites. Peaks located at 855.6 eV and 873.3 eV are assigned to $2p_{3/2}$ and $2p_{1/2}$ signals for Ni(II) species, respectively. ICP-OES analysis indicated presence of 3.7% w/w of nickel on the material Ni@poly-czbpy, corresponding to an occupation of 40% of bipyridine functionalities. Furthermore, scanning electron microscopy (SEM) images of Ni@poly-czbpy show the morphology of the amorphous polymeric particles analyzed by elemental mapping (Figure 6.5). The images depict a homogeneous distribution of nickel, nitrogen and chlorine within the material.

After confirming that poly-czbpy is suitable to coordinate and immobilize nickel atoms, its use in the previously optimized coupling reactions was studied (Fig. 3e). The desired C–S, C–O and C–N coupling products were obtained by irradiation at 440 nm of mixtures of NiCl₂·glyme (5 mol%) and poly-czbpy (5 mol%), but the selectivity of the reactions was lower than using homogeneous conditions.

Next, we sought to study the recyclability of the heterogeneous catalytic system based on poly-czbpy. Poly-czbpy was recovered after the C–S coupling reaction by centrifugation and was, after washing, reused for the same reaction (Fig. 3f). Initial results confirmed that poly-czbpy can be recycled ten times without significant loss in reactivity (orange bars). The addition of the nickel salt at each reaction cycle was unnecessary in a second set of experiments (green bars) and selectivity of the reaction improved upon washing and reusing the material without addition of fresh nickel salt (1st cycle: 78% yield, 2nd cycle: 90% yield). According to ICP-OES analysis, 40% of the pyridine sites in poly-czbpy coordinate to nickel. Therefore, equimolar amounts of nickel and poly-czbpy lead to an excess of unligated nickel in solution, which presumably has a detrimental effect on the selectivity. This was confirmed during a series of experiments using lower nickel salt/macroligand ratio (2.5 mol% of NiCl₂·glyme, 5 mol% poly-czbpy) that improved selectivity for all transformations (Table 6.23 – 6.25). A final recycling experiment in which 2.5 mol% of NiCl₂·glyme was loaded only for the first reaction (Figure 6.3, f, blue bars) resulted in excellent yields for the C–S coupling reaction without significant loss in activity during ten recycling experiments. The 2p Ni XPS spectra (Figure 6.10) of the recycled catalyst confirm that the Ni(II) species remained intact within the polymer network demonstrating the recyclability of the material. The signals for the doublet were detected at 856.6 eV (2p_{3/2}) and 874.6 eV (2p_{1/2}), respectively. Furthermore, 1s N XPS core-level spectra (Fig. S7) show that by single addition of Ni(II) precursor predominantly the pyridinic nitrogen signal at 399.2 eV was detected due to relatively low amount of Ni(II) coordinated to bipyridine, while by adding Ni(II) after each cycle mainly Ni-N coordination signals at 399.7 eV occur.

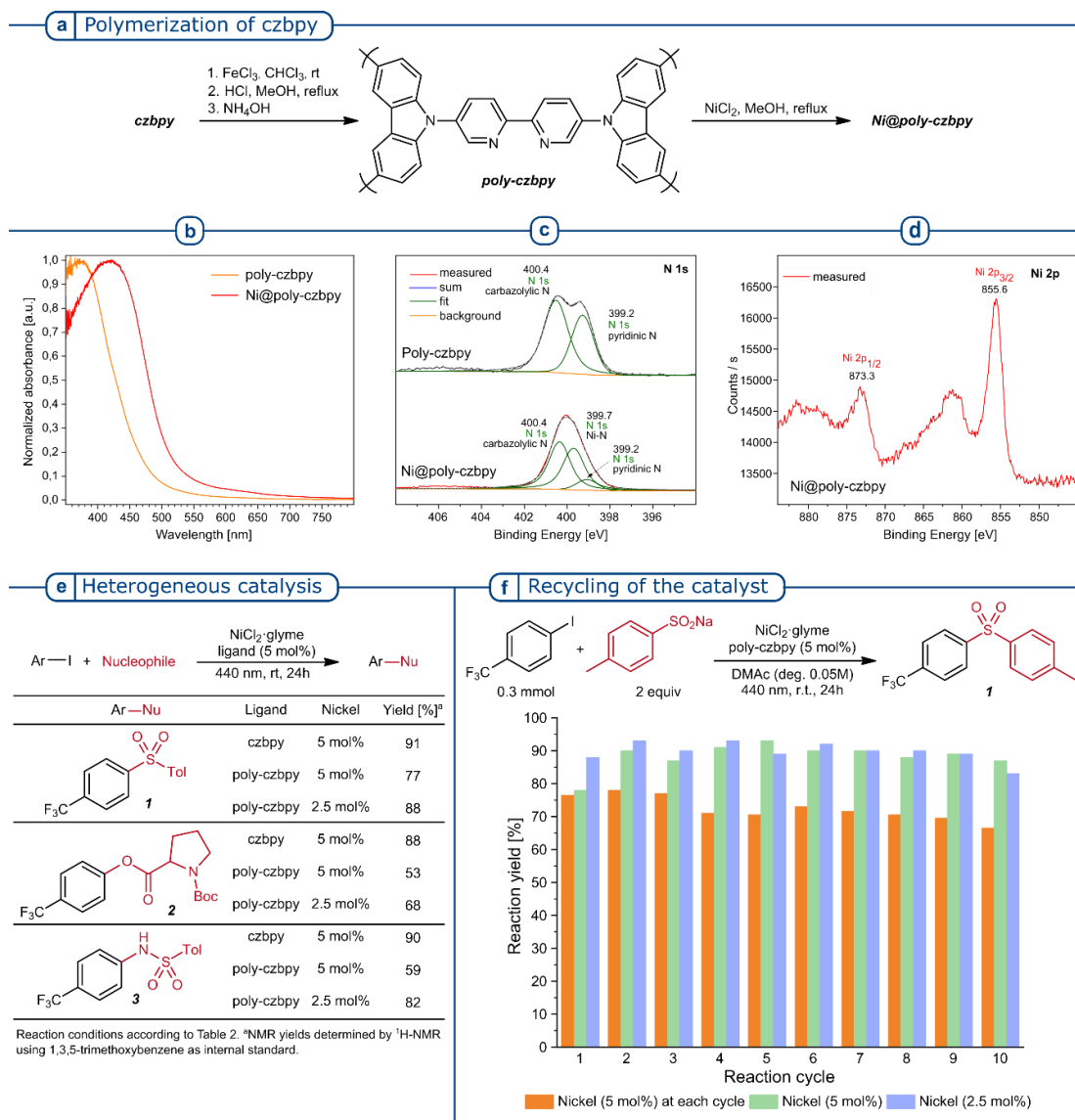


Figure 6.3. Heterogeneous visible-light-mediated nickel catalysis with poly-czbpy.

a, Preparation of the porous organic polymer poly-czbpy and metalation with nickel. **b**, Characterization of poly-czbpy and Ni@poly-czbpy by UV-visible spectroscopy. XPS analysis of Ni@poly-czbpy: N 1s (**c**) and Ni 2p core-level spectra (**d**). **e**, Heterogeneous visible-light-mediated nickel catalysis using poly-czbpy. **f**, Recycling of the catalyst in the C–S coupling reaction. Reaction conditions: 4-iodobenzotrifluoride (300 μmol), sodium *p*-toluenesulfonate (600 μmol), $\text{NiCl}_2\cdot\text{glyme}$ (7.5–15 μmol), poly-czbpy (7.43 mg), DMAc (6 mL), 440 nm LED (2 lamps at full power) at room temperature. Yields were calculated via ¹H-NMR analysis using 1,3,5-trimethoxybenzene as internal standard. Orange: 5 mol% of $\text{NiCl}_2\cdot\text{glyme}$ at each reaction cycle; green: 5 mol% of $\text{NiCl}_2\cdot\text{glyme}$ only for the first cycle; blue: 2.5 mol% of $\text{NiCl}_2\cdot\text{glyme}$ only for the first cycle.

6.5 Conclusion

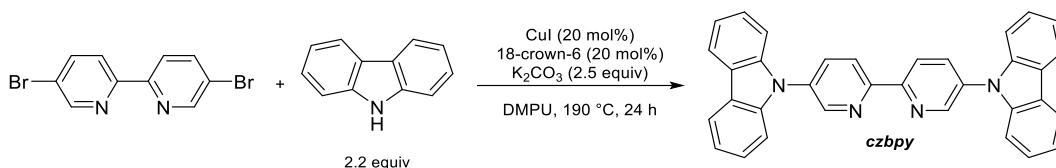
Combining a Ni(II) salt with czbpy results in a homogeneous complex that absorbs up to 450 nm and enables visible-light-mediated carbon–heteroatom cross-couplings without exogenous photocatalysts. Selective C–S, C–O and C–N bond formations were achieved by coupling aryl iodides with sodium sulfinates, carboxylic acids or sulfonamides, respectively. A porous organic polymer that was prepared by oxidative polymerization of czbpy, is suitable for immobilization of nickel and enables heterogeneous, visible-light-mediated nickel catalysis. The heterogeneous material recovered after the reaction can be reused, maintaining a high activity over 10 reaction cycles. EPR experiments indicated an involvement of the aryl iodide for the light-mediated activation of the pre-catalyst. Further investigations to understand the mechanism are currently underway in our laboratory.

6.6 Supporting information

6.6.1 General remarks

All reagents and solvents were purchased from commercial suppliers and used without further purification. Sodium 2-naphthalenesulfinate,⁴¹ sodium 4-*tert*-butylbenzenesulfinate⁴¹ and 1-((trimethylsilyl)methyl)piperidine³⁸ were prepared according to previously reported procedures. LED lamps for photocatalytic experiments were purchased from Kessil Lightning.⁴² ¹H-, ¹³C-, and ¹⁹F spectra were recorded on a Varian 400 spectrometer (400 MHz, Agilent), an AscendTM 400 spectrometer (400 MHz, cryoprobe, Bruker) and a Varian 600 spectrometer (600 MHz, Agilent) at 298 K, and are reported in ppm relative to the residual solvent peaks. Peaks are reported as: s = singlet, d = doublet, t = triplet, q = quartet, m = multiplet or unresolved, with coupling constants in Hz. Analytical thin layer chromatography (TLC) was performed on pre-coated TLC-sheets (ALUGRAM Xtra SIL G/UV₂₅₄ sheets, Macherey-Nagel) and visualized with 254 nm light or staining solutions followed by heating. Purification of final compounds was carried out by flash chromatography using Silica 60 M (0.04-0.063 mm) silica gel (Sigma Aldrich). UV/Vis spectra were recorded using a UV-1900 spectrometer (Shimadzu) for samples in solution and a Cary 5000 UV-Vis-NIR spectrometer (Agilent, USA) for solid samples. High-resolution mass spectral data were obtained using a Waters XEVO G2-XS 4K spectrometer with the XEVO G2-XS QTOF capability kit (ESI) and a Micromass GC-TOF micro (Water Inc.) (EI). X-ray photoelectron spectroscopy (XPS) data were obtained from an ESCA-Lab220i-XL electron spectrometer. The Brunauer-Emmett-Teller specific surface area (S_{BET}) was calculated based on the nitrogen sorption isotherms collected at 77 K using a 3-flex surface characterization analyzer (Micromeritics Instrument Corporation, USA). Nickel contents were measured by inductively coupled plasma-optical emission spectroscopy (ICP-OES 715 ES, Varian, USA) after digesting the polymers in a mixture of nitric acid and sulfuric acid (V:V = 2:1).

6.6.2 Preparation czbpy, poly-czbpy and Ni@poly-czbpy



5,5'-Di(9H-carbazol-9-yl)-2,2'-bipyridine (czbpy) was prepared by adapting a literature procedure.²⁷

In an Argon atmosphere, a mixture of 5,5'-dibromo-2,2'-bipyridine (500 mg, 1.59 mmol), carbazole (586 mg, 3.5 mmol), copper(I) iodide (61 mg, 0.32 mmol), 18-crown-6 (84 mg, 0.32 mmol), potassium carbonate (549 mg, 3.98 mmol) in 1,3-dimethyl-3,4,5,6-tetrahydro-2(1H)-pyrimidinone (DMPU, 1.67 mL) was placed in a pre-heated 100 mL Schlenk flask. The flask was connected to a reflux condenser before the mixture was stirred for 24 h at 190 °C using an oil bath. The yellow reaction solution turned to a black viscous oil after 24 h, at which point was quenched with 2 M HCl (100 mL). The mixture was extracted with dichloromethane (2x125 mL) and washed with NH₃·H₂O (25%, 60 mL) and water (100 mL). The organic layer was dried over magnesium sulfate and the solvent was removed in vacuo. The crude product was purified by column chromatography on amino-functionalized silica gel (gradient 0-50% dichloromethane/cyclohexane). The obtained yellow solid was further purified by recrystallization from cyclohexane/dichloromethane (9:1) to afford the title compound as a light-yellow crystalline solid (540 mg, 1.11 mmol, 70 %).

¹H NMR (400 MHz, CDCl₃) δ 9.03 (d, J = 1.8 Hz, 2H), 8.81 (d, J = 7.7 Hz, 2H), 8.19 (d, J = 7.7 Hz, 4H), 8.15 (dd, J = 8.4, 2.6 Hz, 2H), 7.55 – 7.44 (m, 8H), 7.36 (m, 4H). ¹³C NMR (101 MHz, CDCl₃) δ 153.5, 147.5, 140.6, 135.5, 135.2, 126.6, 124.0, 122.5, 121.0, 120.8, 109.6. HRMS (ESI) m/z calcd for C₃₄H₂₃N₄ [(M+H)⁺] 487.1923, found 487.1918. This data are in full agreement with those reported in literature.⁴³

Preparation of poly-czbpy

The porous organic polymer **poly-czbpy** was prepared by oxidative polymerization of 5,5'-di(9*H*-carbazol-9-yl)-2,2'-bipyridine (czbpy), according to literature.²⁷ Under an Argon atmosphere, 5,5'-di(9*H*-carbazol-9-yl)-2,2'-bipyridine (200 mg, 0.41 mmol) was dissolved in anhydrous chloroform (30 mL) and was added dropwise to an iron(III) chloride (1200 mg, 7.40 mmol, 18 eq) suspension in anhydrous chloroform (30 mL). The reaction mixture was stirred for 24 h at room temperature. Methanol (50 mL) was added to quench the reaction. The yellow solid was filtered off and was refluxed in a mixture of hydrochloric acid solution (6 M, 50 mL) and methanol (50 mL) for 24 h. The process was repeated 3 times before the filtration cake was washed with aqueous ammonia solution (10 wt%), water and methanol. The resulting yellow polymer was purified by Soxhlet extraction from methanol overnight and dried in a vacuum oven at 80 °C. The product was obtained as yellow powder (188 mg, 95%).

¹³C CPMAS NMR (100 MHz, 10 kHz, 25°C): $\delta = 152, 137, 130, 121, 106$ ppm.

S_{ABET} : 853 m² g⁻¹

Preparation of Ni@poly-czbpy

Poly-czbpy (100 mg, 0.21 mmol based on monomer) was dispersed in a methanolic solution of NiCl₂ (42 mL, 5 mM) under inert atmosphere and refluxed for 24 hours while gently stirring. After filtration on a glass frit, the residue was washed with chloroform and dried in an oven at 80 °C to afford Ni@poly-czbpy as a brown solid.

S_{ABET} : 470 m² g⁻¹

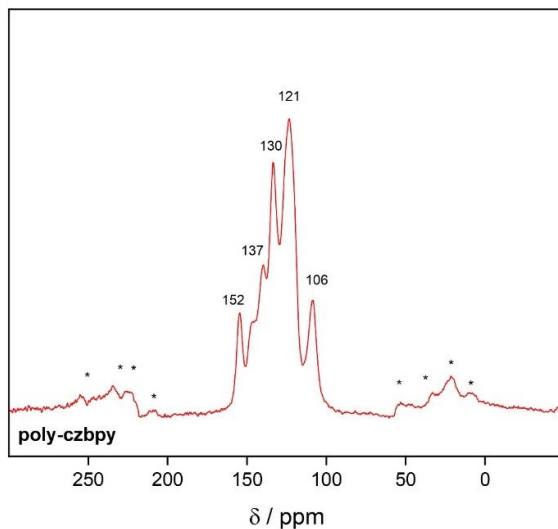


Figure 6.4. ^{13}C CPMAS NMR spectrum of poly-czbp.

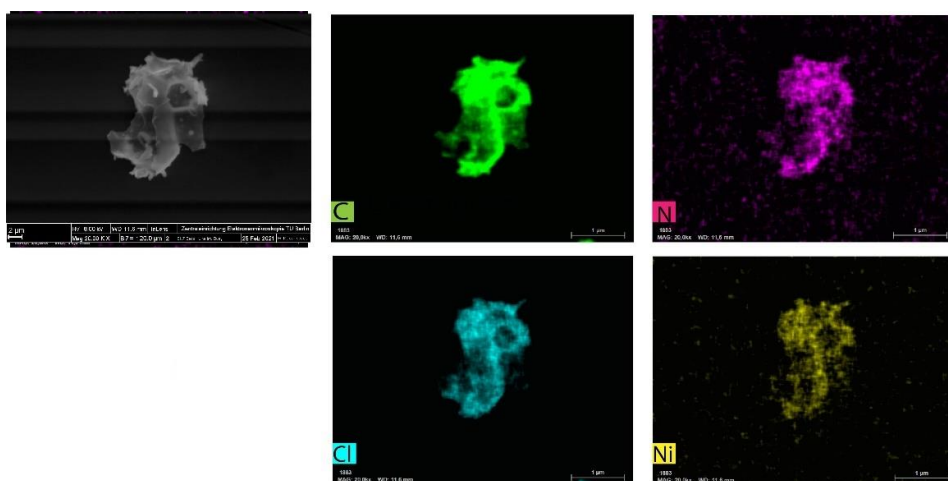


Figure 6.5: Scanning electron microscopy and elemental mapping of Ni@poly-czbp. Elemental mapping of carbon (green), nitrogen (pink), chlorine (blue) and nickel (yellow).

6.6.3 Experimental setup for photochemical experiments

Photochemical experiments involving visible light irradiation were carried out using Kessil PR160L-440 (440nm, blue light) or Kessil PR160L-525 (525 nm, green light) LED lamps with the respective power settings.⁴² One or two lamps were used, depending on the required light intensity to irradiate reaction vessels located on a stirring plate (lamp-vessel distance: 4.5 cm; stirring speed: 800 rpm, Figure 6.5). To avoid heating of the reaction mixture, fans were used for cooling.

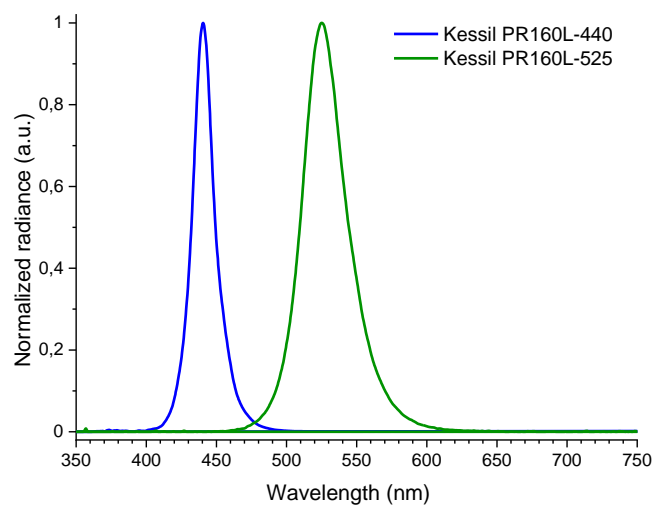


Figure 6.4. Emission spectra of Kessil PR160L-400 (blue) and Kessil PR160L-525 (green) LED lamps.

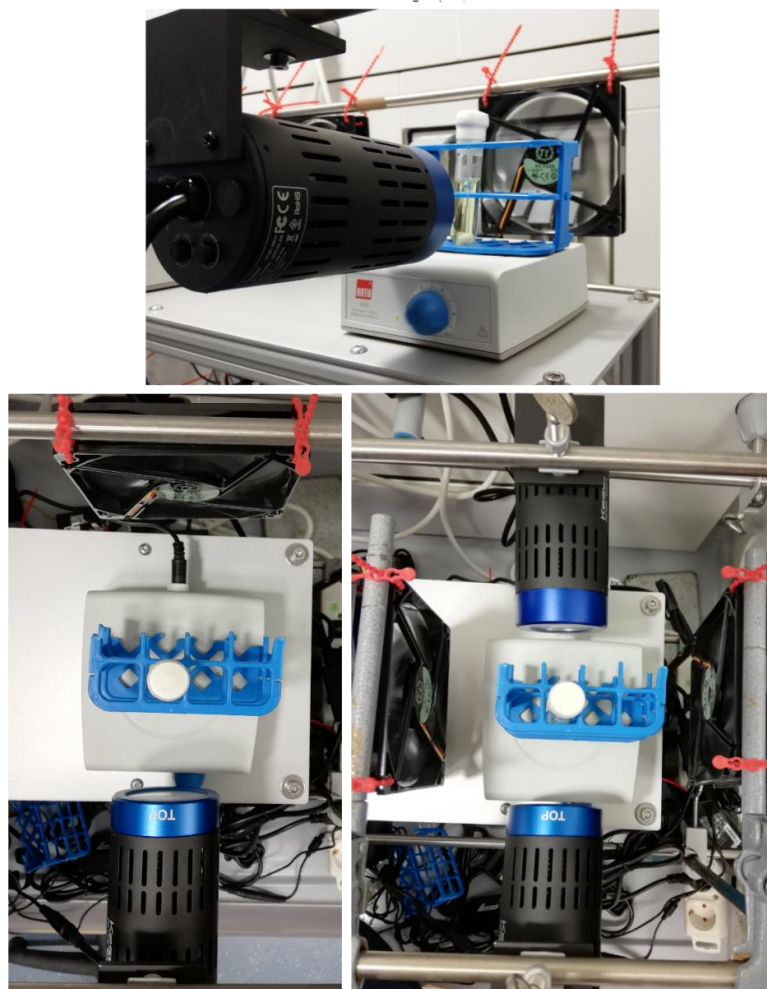


Figure 6.5. Configuration of the experimental setup using one or two LED lamps.

6.6.4 UV-visible spectroscopy measurements

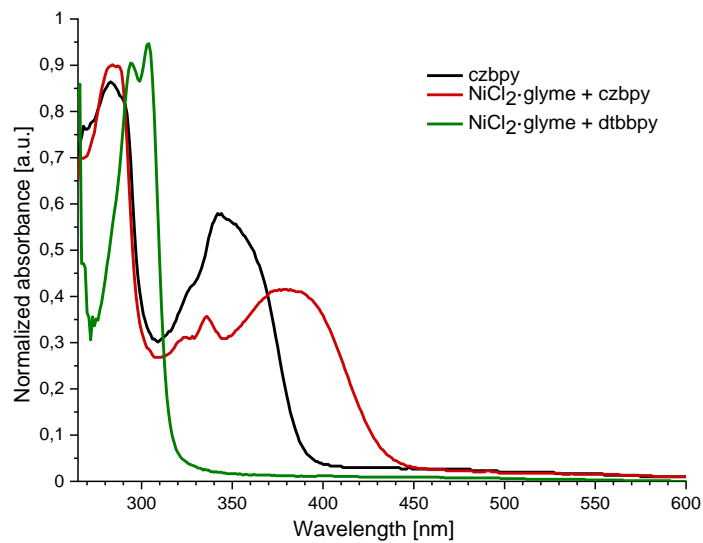


Figure 6.6. UV-visible spectra of 5,5'-di-carbazolyl-2,2'-bipyridyl (czbpy) and mixtures of NiCl₂·glyme and czbpy or 4,4'-di-*tert*-butyl-2,2'-bipyridyne (dtbbpy) in DMAc (10 μM).

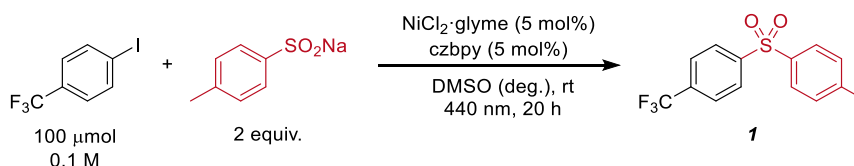
6.6.5 Optimization of the C–S cross-coupling using homogeneous visible-light-mediated nickel catalysis

General procedure for screening experiments

An oven dried vial (19 x 100 mm) equipped with a stir bar was charged with a nickel salt (5–10 μmol), 5,5'-dicarbazyl-2,2'-bipyridyl (czbpy, 5–10 μmol), 4-iodobenzotrifluoride (100–200 μmol) and sodium *p*-toluensulfinate (100–200 μmol). The solvent (anhydrous, 1–2 mL) was added and the vessel was sealed with a septum and Parafilm. The mixture was stirred for 1 minute at high speed, followed by sonication for 5 minutes and degassing by bubbling argon for 10 minutes. The reaction mixture was stirred at 800 rpm and irradiated with 440 nm LED lamps using the reported power settings. After the respective reaction time, 1,3,5-trimethoxybenzene (16.8 mg, 100 μmol , 1 equiv) was added to the reaction vessel, the mixture was shaken and an aliquote (20 μL) was removed, diluted with DMSO-*d*₆ and analyzed by ¹H NMR.

Initial screening experiments

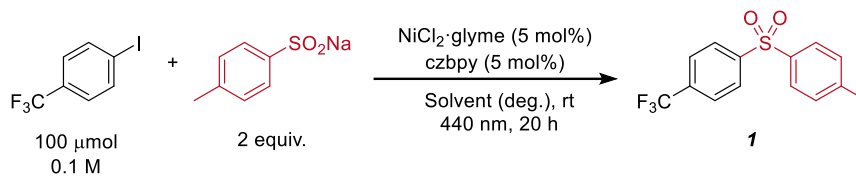
Table 6.2. Screening experiments for the coupling of 4-iodobenzotrifluoride and sodium *p*-toluensulfinate.^a



Entry	Variation	Conversion [%] ^b	1 [%] ^c
1	None	18	18
2	$\text{NiCl}_2 \cdot \text{glyme}$ (10 mol%), czbpy (10 mol%)	41	34
3	525 nm (1 lamp at 50% power)	-	n.d.
4	No irradiation	-	n.d.
5	dtbbpy instead of czbpy	9	6

^aReaction conditions: 4-iodobenzotrifluoride (100 μmol), sodium *p*-toluensulfinate (200 μmol), $\text{NiCl}_2 \cdot \text{glyme}$ (5 μmol), 5,5'-dicarbazolyl-2,2'-bipyridyl (czbpy , 5 μmol), DMSO (anhydrous, 1 mL), 440 nm LED (1 lamp at 50% power). ^bConversion of 4-iodobenzotrifluoride determined by ¹H-NMR using 1,3,5-trimethoxybenzene as internal standard. ^cNMR yields determined by ¹H-NMR using 1,3,5-trimethoxybenzene as internal standard. glyme = 1,2-dimethoxyethane. dtbbpy = 4,4'-di-*tert*-butyl-2,2'-bipyridyl. n.d. = not detected.

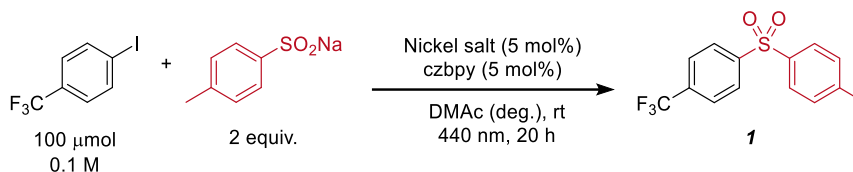
Solvent screening

Table 6.3. Solvent screening for the coupling of 4-iodobenzotrifluoride and sodium *p*-toluenesulfinate.^a

Entry	Solvent	Conversion [%] ^b	1 [%] ^c
1	DMSO	18	18
2	DMF ^d	-	16
3	DMAc	31	27
4	MeCN	-	n.d.
5	Acetone ^e	-	n.d.
6	THF ^e	-	n.d.
7	Dioxane	-	n.d.

^aReaction conditions: 4-iodobenzotrifluoride (100 μmol), sodium *p*-toluenesulfinate (200 μmol), NiCl₂·glyme (5 μmol), 5,5'-dicarbazolyl-2,2'-bipyridyl (czbpy, 5 μmol), Solvent (anhydrous, 1 mL), 440 nm LED (1 lamp at 50% power). ^bConversion of 4-iodobenzotrifluoride determined by ¹H-NMR using 1,3,5-trimethoxybenzene as internal standard. ^cNMR yields determined by ¹H-NMR using 1,3,5-trimethoxybenzene as internal standard. ^dSubstrate and product ratios calculated from ¹⁹F NMR. ^eDegassed by three cycles of freeze-pump-thaw. glyme = 1,2-dimethoxyethane. n.d. = not detected.

Screening of nickel salts

Table 6.4. Screening of nickel salts for the coupling of 4-iodobenzotrifluoride and sodium *p*-toluenesulfinate.^a

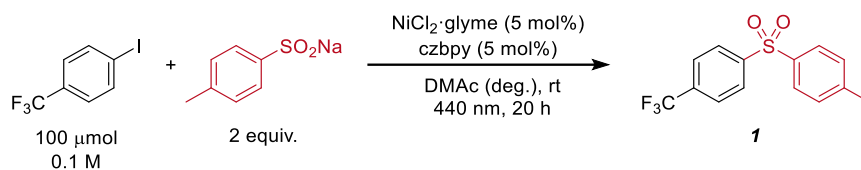
Entry	Nickel salt	Conversion [%] ^b	1 [%] ^c
1	NiCl ₂ ·glyme	31	27
2	NiCl ₂	12	12
3	NiCl ₂ ·6H ₂ O	9	8
4	NiBr ₂ ·glyme	19	19
5	NiBr ₂	4	4
6	NiBr ₂ ·3H ₂ O	22	20
7	NiI ₂	6	6
8	Ni(SO ₄) ₂ ·6H ₂ O	-	n.d.
9	Ni(ClO ₄) ₂ ·6H ₂ O	13	10
10	Ni(NO ₃) ₂ ·6H ₂ O	10	10
11	Ni(OAc) ₂ ·4H ₂ O	12	3
12	Ni(OTf) ₂	-	n.d.
13	Ni(acac) ₂	-	n.d.
14	Ni(COD)(DQ)	12	3

^aReaction conditions: 4-iodobenzotrifluoride (100 μmol), sodium *p*-toluenesulfinate (200 μmol), nickel salt (5 μmol), 5,5'-dicarbazolyl-2,2'-bipyridyl (czbpy, 5 μmol), DMAc (anhydrous, 1 mL), 440 nm LED (1 lamp at 50% power). ^bConversion of 4-iodobenzotrifluoride determined by ¹H-NMR using 1,3,5-trimethoxybenzene as internal standard. ^cNMR yields determined by ¹H-NMR using 1,3,5-trimethoxybenzene as internal standard. n.d. = not detected. glyme = 1,2-dimethoxyethane. acac = acetylacetonate. COD = 1,5-cyclooctadiene. DQ = duroquinone.

After showing that NiCl₂·glyme as nickel source gives best results, different conditions were compared.

NiCl₂·glyme and czbpy were mixed in THF in the reaction flask and gently heated for 10 minutes to preform the nickel complex. After removing THF under vacuum, 4-iodobenzonitrile, sodium *p*-toluensulfinate and DMAc were added and the reaction mixture was irradiated for the corresponding time. This preligation procedure provided lower yield (Table 6.5 entry 2). Further, a ligand-to-nickel ratio of 2:1 didn't improve the yield as well (entry 3).

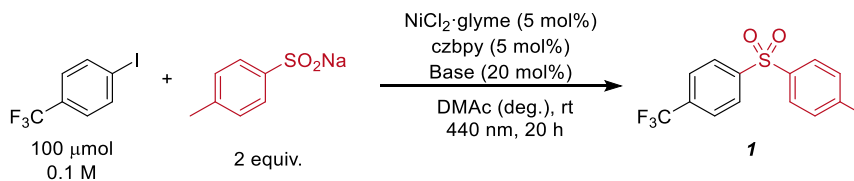
Table 6.5. Screening of different ligation conditions.^a



Entry	Variation	Conversion [%] ^b	1 [%] ^c
1	None	31	27
2	Preligation	21	15
3	czbpy (10 mol%)	30	26

^aReaction conditions: 4-iodobenzotrifluoride (100 μmol), sodium *p*-toluenesulfinate (200 μmol), NiCl₂·glyme (5 μmol), 5,5'-dicarbazolyl-2,2'-bipyridyl (czbpy, 5-10 μmol), DMAc (anhydrous, 1 mL), 440 nm LED (1 lamp at 50% power). ^bConversion of 4-iodobenzotrifluoride determined by ¹H-NMR using 1,3,5-trimethoxybenzene as internal standard. ^cNMR yields determined by ¹H-NMR using 1,3,5-trimethoxybenzene as internal standard. glyme = 1,2-dimethoxyethane.

Base screening

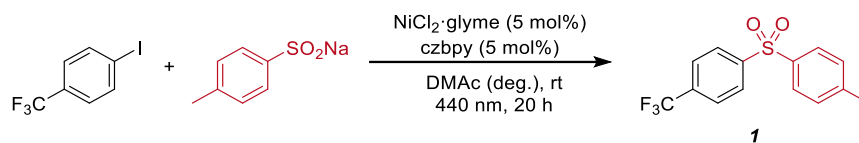
Table 6.6. Base screening for the coupling of 4-iodobenzotrifluoride and sodium *p*-toluenesulfinate.^a

Entry	Base	Conversion [%] ^b	1 [%] ^c
1	None	31	27
2	BIPA	30	22
3	DIPEA	34	30
4	NBu ₃	29	26
5	NEt ₃	27	20
6	Pyridine	32	25
7	2,6-Lutidine	19	19
8	DBU	33	n.d.
9	Quinuclidine	22	15
10	DABCO	36	30
11	Na ₂ HPO ₄	36	31
12	Na ₂ CO ₃	18	18

^aReaction conditions: 4-iodobenzotrifluoride (100 μmol), sodium *p*-toluenesulfinate (200 μmol), NiCl₂·glyme (5 μmol), 5,5'-dicarbazolyl-2,2'-bipyridyl (czbpy, 5 μmol), Base (20 μmol), DMAc (anhydrous, 1 mL), 440 nm LED (1 lamp at 50% power). ^bConversion of 4-iodobenzotrifluoride determined by ¹H-NMR using 1,3,5-trimethoxybenzene as internal standard. ^cNMR yields determined by ¹H-NMR using 1,3,5-trimethoxybenzene as internal standard. glyme = 1,2-dimethoxyethane. BIPA = *N*-*tert*-butylisopropylamine. DIPEA = *N,N*-diisopropylethylamine. DBU = 1,8-diazabicyclo[5.4.0]undec-7-ene. DABCO = 1,4-diazabicyclo[2.2.2]octane. n.d. = not detected.

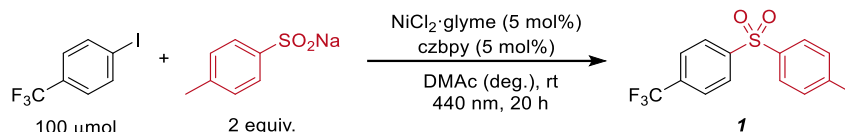
Although the nucleophile is already a salt, the addition of a base was evaluated. Only slightly better yields were obtained using 20 mol% of *N,N*-diisopropylethylamine (DIPEA, Table 6.6, Entry 3), 1,4-diazabicyclo[2.2.2]octane (DABCO, entry 10) and sodium hydrogen phosphate (Na₂HPO₄, entry 11).

Optimization of stoichiometry, light irradiation and concentration

Table 6.7. Optimization of stoichiometry and light irradiation for the coupling of 4-iodobenzotrifluoride and sodium *p*-toluenesulfinate.^a

Entry	Ar-I	Ar-SO ₂ Na	Lamps, power	Conversion [%] ^b	1 [%] ^c
1	100 μmol	200 μmol	1, 50%	31	27
2	100 μmol	200 μmol	1, 100%	36	36
3	100 μmol	200 μmol	2, 100%	92	89
4	100 μmol	150 μmol	1, 100%	47	39
5	100 μmol	120 μmol	1, 100%	40	36
6	100 μmol	120 μmol	2, 100%	73	62
7	100 μmol	110 μmol	1, 100%	42	35
8	150 μmol	100 μmol	1, 100%	26	21

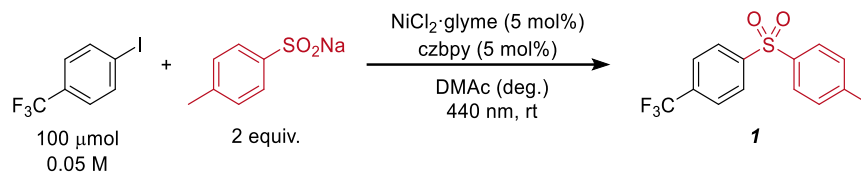
^aReaction conditions: 4-iodobenzotrifluoride (100-150 μmol), sodium *p*-toluenesulfinate (100-200 μmol), NiCl₂·glyme (5 μmol), 5,5'-dicarbazolyl-2,2'-bipyridyl (czbpy, 5 μmol), DMAc (anhydrous, 1 mL), 440 nm LED. ^bConversion of 4-iodobenzotrifluoride determined by ¹H-NMR using 1,3,5-trimethoxybenzene as internal standard. ^cNMR yields determined by ¹H-NMR using 1,3,5-trimethoxybenzene as internal standard. glyme = 1,2-dimethoxyethane.

Table 6.8. Different concentrations for the coupling of 4-iodobenzotrifluoride and sodium *p*-toluenesulfinate.^a

Entry	Concentration	Conversion [%] ^b	1 [%] ^c
1	0.05 M	60	55
2	0.1 M	36	36
3	0.2 M	32	32

^aReaction conditions: 4-iodobenzotrifluoride (100 μmol), sodium *p*-toluenesulfinate (200 μmol), NiCl₂·glyme (5 μmol), 5,5'-dicarbazolyl-2,2'-bipyridyl (czbpy, 5 μmol), DMAc (anhydrous, 0.5-2.0 mL), 440 nm LED (1 lamp at full power). ^bConversion of 4-iodobenzotrifluoride determined by ¹H-NMR using 1,3,5-trimethoxybenzene as internal standard. ^cNMR yields determined by ¹H-NMR using 1,3,5-trimethoxybenzene as internal standard. glyme = 1,2-dimethoxyethane.

Optimized conditions and control experiments

Table 6.9. Optimized conditions and control experiments for the coupling of 4-iodobenzotrifluoride and sodium *p*-toluenesulfinate.^a

Entry	Variation	Time [h]	Conversion [%] ^b	1 [%] ^c
1	None	22	> 99	92
3	NiCl ₂ ·glyme (2.5 mol%) & czbpy (2.5 mol%)	22	82	71
4	Solvent = DMAc/H ₂ O 99:1	22	> 99	90
5	T = 70 °C	7	> 99	88
6	No NiCl ₂ ·glyme	22	86	17
7	no light	22	-	n.d.
8	525 nm	22	-	n.d.
9	4-bromobenzotrifluoride	22	32	27

^aReaction conditions: 4-iodobenzotrifluoride (100 μmol), sodium *p*-toluenesulfinate (200 μmol), NiCl₂·glyme (2.5-5 μmol), 5,5'-dicarbazolyl-2,2'-bipyridyl (czbpy, 2.5-5 μmol), DMAc (anhydrous, 2 mL), 440 or 525 nm LED (2 lamps at full power). ^bConversion of 4-iodobenzotrifluoride determined by ¹H-NMR using 1,3,5-trimethoxybenzene as internal standard. ^cNMR yields determined by ¹H-NMR using 1,3,5-trimethoxybenzene as internal standard. glyme = 1,2-dimethoxyethane. n.d. = not detected.

Table 6.10. Comparison of different ligands for the coupling of 4-iodobenzotrifluoride and sodium *p*-toluenesulfinate.^a

Entry	Ligand system	Time [h]	Conversion [%] ^b	1 [%] ^c
1	czbpy (5 mol%)	22	> 99	92
2	carbazole (10 mol%)	22	20	6
3	bpy (5 mol%)	22	57	34
4	bpy (5 mol%) & carbazole (10 mol%)	22	>99	62
5	poly-czbpy (5 mol%) ^d	24	95	77

^aReaction conditions: 4-iodobenzotrifluoride (100 μmol), sodium *p*-toluenesulfinate (200 μmol), NiCl₂·glyme (5 μmol), ligand, DMAc (anhydrous, 2 mL), 440 nm LED (2 lamps at full power).

^bConversion of 4-iodobenzotrifluoride determined by ¹H-NMR using 1,3,5-trimethoxybenzene as internal standard. ^cNMR yields determined by ¹H-NMR using 1,3,5-trimethoxybenzene as internal standard. ^dThe amount of poly-czbpy was calculated using the molecular weight of the monomer. glyme = 1,2-dimethoxyethane. czbpy = 5,5'-dicarbazolyl-2,2'-bipyridyl. bpy = 2,2'-bipyridyl.

Reactivity of different aryl halides

Table 6.11. Coupling of sodium *p*-toluenesulfinate and methyl 4-halobenzoates.^a

Entry	Aryl halide	Conversion [%] ^b	14 [%] ^c
1	Methyl 4-chlorobenzoate	-	n.d.
2	Methyl 4-bromobenzoate	27	15
3	Methyl 4-iodobenzoate	>99	92

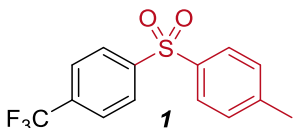
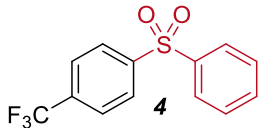
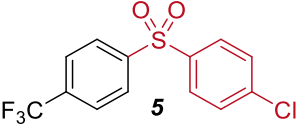
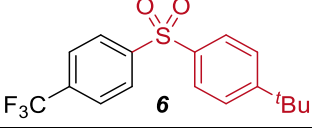
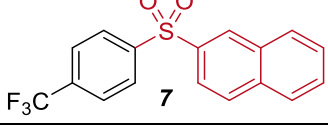
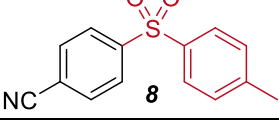
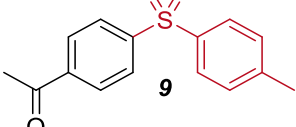
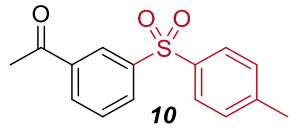
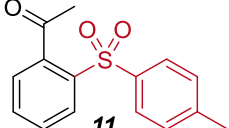
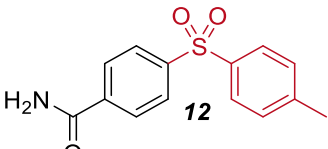
^aReaction conditions: aryl halide (100 μmol), sodium *p*-toluenesulfinate (200 μmol), NiCl₂·glyme (5 μmol), 5,5'-dicarbazolyl-2,2'-bipyridyl (czbpy, 5 μmol), DMAc (anhydrous, 2 mL), 440 nm LED (2 lamps at full power). ^bConversion of aryl halide determined by ¹H-NMR using 1,3,5-trimethoxybenzene as internal standard. ^cNMR yields determined by ¹H-NMR using 1,3,5-trimethoxybenzene as internal standard. glyme = 1,2-dimethoxyethane. n.d. = not detected.

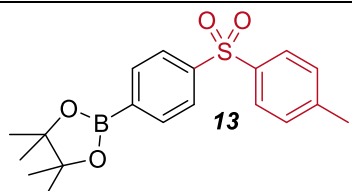
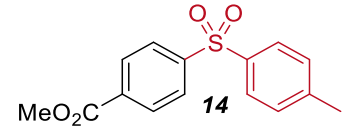
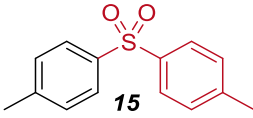
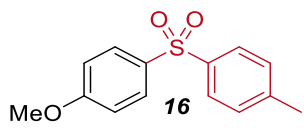
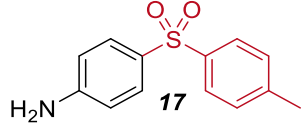
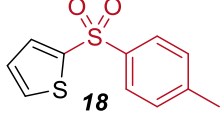
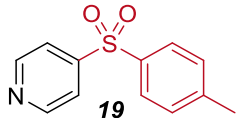
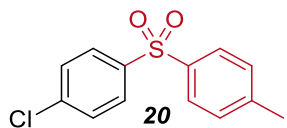
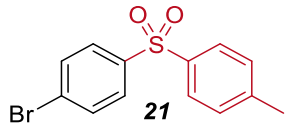
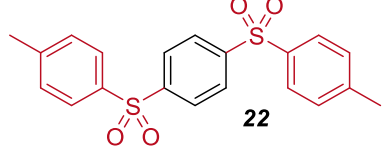
6.6.6 Scope of the C–S cross-coupling using homogeneous visible-light-mediated nickel catalysis

General procedure

An oven dried vial (19 x 100 mm) equipped with a stir bar was charged with NiCl₂·glyme (3.3 mg, 15 μmol, 5 mol%), 5,5'-dicarbazolyl-2,2'-bipyridyl (czbpy, 7.3 mg, 15 μmol, 5 mol%), the aryl iodide (300 μmol) and the sodium sulfinate (600 μmol, 2 equiv). DMAc (anhydrous, 6 mL) was added and the vessel was sealed with a septum and Parafilm. The mixture was stirred for 1 minute at high speed, followed by sonication for 5 minutes and degassing by bubbling argon for 10 minutes. The reaction mixture was stirred at 800 rpm and irradiated with two LED lamps (440 nm) at full power. After the respective reaction time, maleic acid (34.9 mg, 300 μmol, 1 equiv) was added to the reaction vessel, the mixture was shaken and an aliquote (20 μL) was diluted in DMSO-*d*₆ and analyzed by ¹H NMR. The NMR sample and the reaction mixture were combined, diluted with aqueous hydrochloric acid (0.5 M, 60 mL) and extracted with ethyl acetate (3 x 40 mL). The combined organic layers were washed with brine (2 x 40 mL), dried over Na₂SO₄ and concentrated under reduced pressure. The residue was purified by flash chromatography on silica gel using mixtures of hexane/ethyl acetate to obtain the desired product.

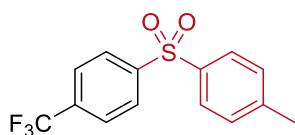
Table 6.12. Scope of the C–S coupling reaction.^a

Product	Reaction time	NMR yield ^b	Isolated yield
 1	22 hours	91%	89%
 4	22 hours	90%	75%
 5	24 hours	85%	84%
 6	24 hours	97%	91%
 7	24 hours	-	40%
 8	24 hours	98%	97%
 9	24 hours	93%	93%
 10	40 hours	77%	71%
 11	24 hours	95%	90%
 12	64 hours	87%	82%

Product	Reaction time	NMR yield ^b	Isolated yield
 13	30 hours	76%	48%
 14	24 hours	86%	80%
 15	53 hours	74%	74%
 16	30 hours	87%	82%
 17	36 hours	97%	94%
 18	48 hours	80%	77%
 19	24 hours	82%	79%
 20	46 hours	80%	75%
 21	29 hours	-	76%
 22	24 hours	82%	71%

^aReaction conditions according to general procedure. ^bNMR yields determined by ¹H-NMR using maleic acid as internal standard

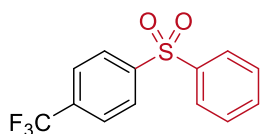
Experimental data



4-Tosylbenzotrifluoride (1) was obtained from 4-iodobenzotrifluoride (81.6 mg, 300 μmol) and sodium *p*-toluenesulfinate (106.9 mg, 600 μmol). Purification by flash chromatography (10% ethyl acetate/hexane) afforded the title compound as a yellowish solid (79.8 mg, 266 μmol , 89%).

Reaction time: 22 hours. NMR yield: 91%.

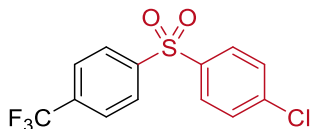
^1H NMR (400 MHz, CDCl_3) δ 8.05 (d, $J = 8.2$ Hz, 2H), 7.84 (d, $J = 8.3$ Hz, 2H), 7.75 (d, $J = 8.3$ Hz, 2H), 7.33 (d, $J = 8.0$ Hz, 2H), 2.41 (s, 3H). ^{13}C NMR (101 MHz, CDCl_3) δ 145.71, 145.08, 137.70, 134.77 (q, $J = 33.1$ Hz), 130.31, 128.17, 128.08, 126.51 (q, $J = 3.7$ Hz), 123.25 (q, $J = 273.1$ Hz), 21.75. ^{19}F NMR (376 MHz, CDCl_3) δ -63.19. These data are in full agreement with those reported in literature.²⁸



1-(Phenylsulfonyl)-4-(trifluoromethyl)benzene (4) was obtained from 4-iodobenzotrifluoride (81.6 mg, 300 μmol) and sodium benzenesulfinate (98.5 mg, 600 μmol). Purification by flash chromatography (gradient 5-15% ethyl acetate/hexane) afforded the title compound as a white solid (64.0 mg, 224 μmol , 75%).

Reaction time: 22 hours. NMR yield: 90%.

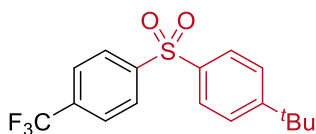
^1H NMR (400 MHz, CDCl_3) δ 8.07 (d, $J = 8.2$ Hz, 2H), 7.96 (d, $J = 7.5$ Hz, 2H), 7.76 (d, $J = 8.3$ Hz, 2H), 7.61 (t, $J = 7.4$ Hz, 1H), 7.53 (t, $J = 7.5$ Hz, 2H). ^{13}C NMR (101 MHz, CDCl_3) δ 145.31, 140.65, 134.93 (q, $J = 33.1$ Hz), 133.92, 129.67, 128.33, 128.01, 126.57 (q, $J = 3.7$ Hz), 123.21 (q, $J = 273.1$ Hz). ^{19}F NMR (376 MHz, CDCl_3) δ -63.21. These data are in full agreement with those reported in literature.³⁰



1-Chloro-4-((4-(trifluoromethyl)phenyl)sulfonyl)benzene (5) was obtained from 4-iodobenzotrifluoride (81.6 mg, 300 μmol) and sodium 4-chlorobenzenesulfinate (119.2 mg, 600 μmol). Purification by flash chromatography (gradient 3-10% ethyl acetate/hexane) afforded the title compound as a white solid (81.0 mg, 253 μmol , 84%).

Reaction time: 24 hours. NMR yield: 85%

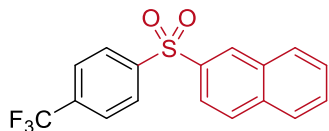
^1H NMR (400 MHz, CDCl_3) δ 8.06 (d, $J = 8.1$ Hz, 2H), 7.89 (d, $J = 8.7$ Hz, 2H), 7.78 (d, $J = 8.3$ Hz, 2H), 7.51 (d, $J = 8.7$ Hz, 2H). ^{13}C NMR (101 MHz, CDCl_3) δ 144.94, 140.80, 139.20, 135.25 (q, $J = 33.1$ Hz), 130.05, 129.49, 128.35, 126.73 (q, $J = 3.6$ Hz), 123.17 (q, $J = 273.2$ Hz). ^{19}F NMR (376 MHz, CDCl_3) δ -63.24. HRMS (EI) m/z calcd for $\text{C}_{13}\text{H}_8\text{ClF}_3\text{O}_2\text{S}$ [(M) $^+$] 319.9886, found: 319.9884.



1-tert-Butyl-4-((4-(trifluoromethyl)phenyl)sulfonyl)benzene (6) was obtained from 4-iodobenzotrifluoride (81.6 mg, 300 μmol) and sodium 4-*tert*-butylbenzenesulfinate (132.2 mg, 600 μmol). Purification by flash chromatography (5% ethyl acetate/hexane) afforded the title compound as a white solid (93.8 mg, 274 μmol , 91%)

Reaction time: 24 hours. NMR yield: 97%

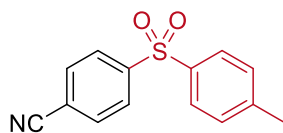
^1H NMR (400 MHz, CDCl_3) δ 8.07 (d, $J = 8.1$ Hz, 2H), 7.87 (d, $J = 8.6$ Hz, 2H), 7.76 (d, $J = 8.3$ Hz, 2H), 7.54 (d, $J = 8.6$ Hz, 2H), 1.31 (s, 9H). ^{19}F NMR (376 MHz, CDCl_3) δ -63.16. ^{13}C NMR (101 MHz, CDCl_3) δ 157.96, 145.66, 137.57, 134.75 (q, $J = 33.0$ Hz), 128.25, 127.90, 126.71, 126.51 (q, $J = 3.7$ Hz), 123.27 (q, $J = 273.0$ Hz), 35.38, 31.10. These data are in full agreement with those reported in literature.⁴⁴



2-((4-(Trifluoromethyl)phenyl)sulfonyl)naphthalene (7) was obtained from 4-iodobenzotrifluoride (81.6 mg, 300 μmol) and sodium 2-naphthalensulfinate (128.5 mg, 600 μmol). Purification by flash chromatography (gradient 5-10% ethyl acetate/hexane) afforded the title compound as a yellowish solid (40.5 mg, 120 μmol , 40%).

Reaction time: 24 hours. NMR yield: not determined due to signal overlap.

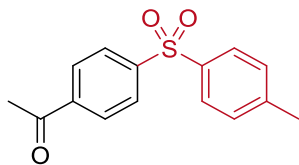
^1H NMR (400 MHz, CDCl_3) δ 8.60 (s, 1H), 8.13 (d, $J = 8.3$ Hz, 2H), 8.00 (d, $J = 7.5$ Hz, 1H), 7.96 (d, $J = 8.7$ Hz, 1H), 7.90 (d, $J = 9.3$ Hz, 1H), 7.85 (dd, $J = 8.7, 2.0$ Hz, 1H), 7.77 (d, $J = 8.5$ Hz, 2H), 7.70 – 7.60 (m, 2H). ^{13}C NMR (101 MHz, CDCl_3) δ 145.40, 137.44, 135.37, 134.97 (q, $J = 33.1$ Hz), 132.36, 130.13, 129.79, 129.69, 129.61, 128.40, 128.14, 128.04, 126.60 (q, $J = 3.7$ Hz), 123.23 (q, $J = 274.1$ Hz), 122.65. ^{19}F NMR (376 MHz, CDCl_3) δ -63.21. HRMS (EI) m/z calcd for $\text{C}_{17}\text{H}_{11}\text{F}_3\text{O}_2\text{S}$ [(M) $^+$] 336.0432, found: 336.0438.



4-Tosylbenzotrile (8) was obtained from 4-iodobenzotrile (68.7 mg, 300 μmol) and sodium *p*-toluenesulfinate (106.9 mg, 600 μmol). Purification by flash chromatography (15% ethyl acetate/hexane) afforded the title compound as a yellowish solid (74.7 mg, 290 μmol , 97%).

Reaction time: 24 hours. NMR yield: 98%

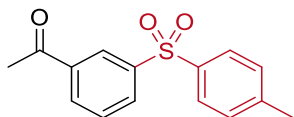
^1H NMR (400 MHz, CDCl_3) δ 8.03 (d, $J = 8.3$ Hz, 2H), 7.82 (d, $J = 8.1$ Hz, 2H), 7.78 (d, $J = 8.3$ Hz, 2H), 7.33 (d, $J = 8.0$ Hz, 2H), 2.41 (s, 3H). ^{13}C NMR (101 MHz, CDCl_3) δ 146.31, 145.36, 137.18, 133.13, 130.38, 128.21, 128.12, 117.31, 116.78, 21.75. These data are in full agreement with those reported in literature.²⁸



4-Tosylacetophenone (9) was obtained from 4-iodoacetophenone (73.8 mg, 300 μmol) and sodium *p*-toluenesulfinate (106.9 mg, 600 μmol). Purification by flash chromatography (gradient 15-25% ethyl acetate/hexane) afforded the title compound as a white solid (76.8 mg, 280 μmol , 93%).

Reaction time: 24 hours. NMR yield: 93%

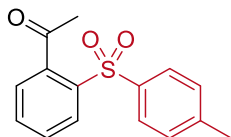
^1H NMR (400 MHz, CDCl_3) δ 8.07 – 7.96 (m, 4H), 7.83 (d, $J = 8.4$ Hz, 2H), 7.31 (d, $J = 8.1$ Hz, 2H), 2.61 (s, 3H), 2.40 (s, 3H). ^{13}C NMR (101 MHz, CDCl_3) δ 196.83, 145.96, 144.90, 140.29, 137.91, 130.24, 129.15, 128.04, 127.95, 27.02, 21.75. These data are in full agreement with those reported in literature.²⁸



3-Tosylacetophenone (10) was obtained from 3-iodoacetophenone (73.8 mg, 300 μmol) and sodium *p*-toluenesulfinate (106.9 mg, 600 μmol). Purification by flash chromatography (gradient 10-30% ethyl acetate/hexane) afforded the title compound as a colorless oil (58.2 mg, 212 μmol , 71%).

Reaction time: 40 hours. NMR yield: 77%

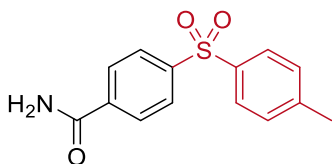
^1H NMR (400 MHz, CDCl_3) δ 8.51 – 8.39 (m, 1H), 8.15 – 8.02 (m, 2H), 7.83 (d, $J = 8.3$ Hz, 2H), 7.60 (t, $J = 7.8$ Hz, 1H), 7.30 (d, $J = 8.1$ Hz, 2H), 2.62 (s, 3H), 2.39 (s, 3H). ^{13}C NMR (101 MHz, CDCl_3) δ 196.30, 144.77, 143.03, 138.02, 137.99, 132.52, 131.64, 130.20, 129.89, 127.91, 127.27, 26.81, 21.69. HRMS (EI) m/z calcd for $\text{C}_{15}\text{H}_{14}\text{O}_3\text{S}$ [M^+] 274.0664, found: 274.0666.



2-Tosylacetophenone (11) was obtained from 2-iodoacetophenone (73.8 mg, 300 μmol) and sodium *p*-toluenesulfinate (106.9 mg, 600 μmol). Purification by flash chromatography (gradient 10-20% ethyl acetate/hexane) afforded the title compound as a colorless oil (73.8 mg, 269 μmol , 90%).

Reaction time: 24 hours. NMR yield: 95%

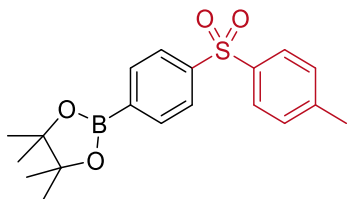
^1H NMR (400 MHz, CDCl_3) δ 8.02 (d, $J = 7.8$ Hz, 1H), 7.81 (d, $J = 8.3$ Hz, 2H), 7.58 (td, $J = 7.5, 1.3$ Hz, 1H), 7.52 (td, $J = 7.7, 1.3$ Hz, 1H), 7.31 – 7.25 (m, 3H, contains residual solvent signal of CDCl_3), 2.67 (s, 3H), 2.37 (s, 3H). ^{13}C NMR (101 MHz, CDCl_3) δ 203.49, 144.53, 142.29, 138.40, 138.38, 133.30, 129.92, 129.88, 129.82, 128.15, 126.01, 32.10, 21.68. HRMS (EI) m/z calcd for $\text{C}_{15}\text{H}_{14}\text{O}_3\text{S}$ [M^+] 274.0664, found: 274.0667.



4-Tosylbenzamide (12) was obtained from 4-iodobenzamide (74.1 mg, 300 μmol) and sodium *p*-toluenesulfinate (106.9 mg, 600 μmol). Purification by flash chromatography (gradient 50-100% ethyl acetate/hexane) afforded the title compound as a white solid (67.4 mg, 245 μmol , 82%).

Reaction time: 64 hours. NMR yield: 87%

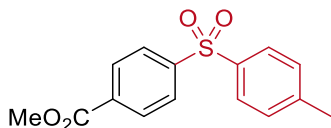
^1H NMR (400 MHz, CDCl_3) δ 8.01 (d, $J = 8.4$ Hz, 2H), 7.90 (d, $J = 8.5$ Hz, 2H), 7.83 (d, $J = 8.3$ Hz, 2H), 7.32 (d, $J = 7.9$ Hz, 2H), 2.41 (s, 3H). ^1H NMR (400 MHz, DMSO-d_6) δ 8.17 (s, 1H), 8.08 – 7.94 (m, 4H), 7.86 (d, $J = 8.2$ Hz, 2H), 7.63 (s, 1H), 7.43 (d, $J = 8.1$ Hz, 2H), 2.36 (s, 3H). ^{13}C NMR (101 MHz, DMSO-d_6) δ 166.53, 144.67, 143.57, 138.76, 137.77, 130.30, 128.71, 127.57, 127.27, 21.06. These data are in full agreement with those reported in literature.³¹



4,4,5,5-tetramethyl-2-(4-tosylphenyl)-1,3,2-dioxaborolane (13) was obtained from 2-(4-iodophenyl)-4,4,5,5-tetramethyl-1,3,2-dioxaborolane (99.0 mg, 300 μmol) and sodium *p*-toluenesulfinate (106.9 mg, 600 μmol). Purification by flash chromatography (gradient 10-40% ethyl acetate/hexane) afforded the title compound as a yellowish solid (51.3 mg, 143 μmol , 48%). The low isolated yield is a result of product decomposition that was also observed during TLC analysis.

Reaction time: 30 hours. NMR yield: 76%

^1H NMR (400 MHz, CDCl_3) δ 7.99 – 7.85 (m, 4H), 7.80 (d, $J = 8.2$ Hz, 2H), 7.27 (d, $J = 8.5$ Hz, 2H, contains residual solvent signal of CDCl_3), 2.37 (s, 3H), 1.32 (s, 12H). ^{13}C NMR (101 MHz, CDCl_3) δ 144.32, 144.15, 138.62, 135.56, 133.11 (br. s), 130.02, 127.82, 126.58, 84.53, 24.95, 21.68. HRMS (EI) m/z calcd for $\text{C}_{19}\text{H}_{23}\text{BO}_4\text{S}$ [(M) $^+$] 358.1410, found: 358.1416.

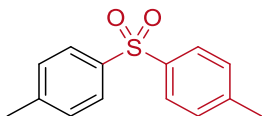


Methyl 4-tosylbenzoate (14) was obtained from methyl 4-iodobenzoate (78.6 mg, 300 μmol) and sodium *p*-toluenesulfinate (106.9 mg, 600 μmol). Purification by flash chromatography (gradient 15-25% ethyl acetate/hexane) afforded the title compound as a white solid (70.1 mg, 241 μmol , 80%)

Reaction time: 24 hours. NMR yield: 86%

^1H NMR (400 MHz, CDCl_3) δ 8.13 (d, $J = 8.6$ Hz, 2H), 7.98 (d, $J = 8.6$ Hz, 2H), 7.83 (d, $J = 8.3$ Hz, 2H), 7.31 (d, $J = 8.1$ Hz, 2H), 3.92 (s, 3H), 2.39 (s, 3H). ^{13}C NMR (101 MHz, CDCl_3) δ 165.63, 145.98, 144.85, 137.91, 134.19, 130.51, 130.21, 128.02, 127.64, 52.78, 21.73.

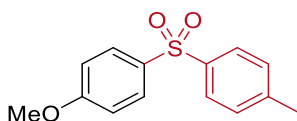
These data are in full agreement with those reported in literature.²⁸



4,4'-Sulfonylbis(methylbenzene) (15) was obtained from 4-iodotoluene (65.4 mg, 300 μmol) and sodium *p*-toluenesulfinate (106.9 mg, 600 μmol). Purification by flash chromatography (gradient 5-10% ethyl acetate/hexane) afforded the title compound as a white solid (54.4 mg, 221 μmol , 74%).

Reaction time: 53 hours. NMR yield: 74%

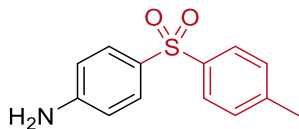
^1H NMR (400 MHz, CDCl_3) δ 7.81 (d, $J = 8.3$ Hz, 4H), 7.28 (d, $J = 7.9$ Hz, 4H, contains residual solvent signal of CDCl_3), 2.38 (s, 6H). ^{13}C NMR (101 MHz, CDCl_3) δ 144.05, 139.16, 129.98, 127.68, 21.68. These data are in full agreement with those reported in literature.⁴⁵



4-Tosylanisole (16) was obtained from 4-iodoanisole (70.2 mg, 300 μmol) and sodium *p*-toluenesulfinate (106.9 mg, 600 μmol). Purification by flash chromatography (gradient 20-40% ethyl acetate/hexane) afforded the title compound as a white solid (64.9 mg, 247 μmol , 82%).

Reaction time: 30 hours. NMR yield: 87%

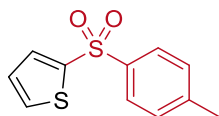
^1H NMR (400 MHz, CDCl_3) δ 7.85 (d, $J = 9.0$ Hz, 2H), 7.79 (d, $J = 8.3$ Hz, 2H), 7.34 – 7.17 (m, 2H, contains residual solvent signal of CDCl_3), 6.94 (d, $J = 8.9$ Hz, 2H), 3.83 (s, 3H), 2.38 (s, 3H). ^{13}C NMR (101 MHz, CDCl_3) δ 163.32, 143.85, 139.51, 133.63, 129.94, 129.81, 127.47, 114.55, 55.75, 21.66. These data are in full agreement with those reported in literature.³¹



4-Tosylaniline (17) was obtained from 4-iodoaniline (65.7 mg, 300 μmol) and sodium *p*-toluenesulfinate (106.9 mg, 600 μmol). Purification by flash chromatography (gradient 0-4% ethyl acetate/dichloromethane) afforded the title compound as a white solid (70.1 mg, 283 μmol , 94%).

Reaction time: 36 hours. NMR yield: 97%

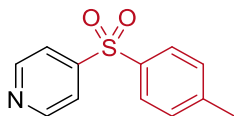
^1H NMR (400 MHz, CDCl_3) δ 7.77 (d, $J = 8.3$ Hz, 2H), 7.69 (d, $J = 8.7$ Hz, 2H), 7.25 (d, $J = 7.9$ Hz, 2H, contains residual solvent signal of CDCl_3), 6.64 (d, $J = 8.7$ Hz, 2H), 4.12 (br. s, 2H), 2.38 (s, 3H). ^{13}C NMR (101 MHz, CDCl_3) δ 150.93, 143.44, 140.16, 130.17, 129.86, 129.84, 127.29, 114.30, 21.65. These data are in full agreement with those reported in literature.²⁸



2-Tosylthiophene (18) was obtained from 4-iodoanisole (63.0 mg, 300 μmol) and sodium *p*-toluenesulfinate (106.9 mg, 600 μmol). Purification by flash chromatography (gradient 5-10% ethyl acetate/hexane) afforded the title compound as a white solid (54.9 mg, 230 μmol , 77 %).

Reaction time: 48 hours. NMR yield: 80%.

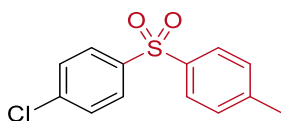
^1H NMR (400 MHz, CDCl_3) δ 7.87 (d, $J = 8.4$ Hz, 2H), 7.67 (dd, $J = 3.8, 1.4$ Hz, 1H), 7.62 (dd, $J = 5.0, 1.4$ Hz, 1H), 7.31 (d, $J = 7.9$ Hz, 2H), 7.06 (dd, $J = 5.0, 3.8$ Hz, 1H), 2.41 (s, 3H). ^{13}C NMR (101 MHz, CDCl_3) δ 144.47, 143.62, 139.25, 133.69, 133.17, 130.08, 127.89, 127.51, 21.73. These data are in full agreement with those reported in literature⁴⁵



4-Tosylpyridine (19) was obtained from 4-iodopyridine (61.5 mg, 300 μmol) and sodium *p*-toluenesulfinate (106.9 mg, 600 μmol). Purification by flash chromatography (gradient 20-50% ethyl acetate/hexane) afforded the title compound as a white solid (55.2 mg, 237 μmol , 79%).

Reaction time: 24 hours. NMR yield: 82%

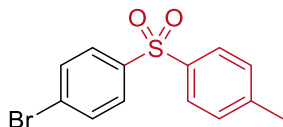
^1H NMR (400 MHz, CDCl_3) δ 8.79 (d, $J = 5.7$ Hz, 2H), 7.83 (d, $J = 8.3$ Hz, 2H), 7.74 (d, $J = 6.0$ Hz, 2H), 7.33 (d, $J = 8.1$ Hz, 2H), 2.41 (s, 3H). ^{13}C NMR (101 MHz, CDCl_3) δ 151.21, 150.23, 145.53, 136.72, 130.37, 128.28, 120.59, 21.77. These data are in full agreement with those reported in literature.⁴⁶



1-Chloro-4-tosylbenzene (20) was obtained from 1-chloro-4-iodobenzene (71.5 mg, 300 μmol) and sodium *p*-toluenesulfinate (106.9 mg, 600 μmol). Purification by flash chromatography (5% ethyl acetate/hexane) afforded the title compound as a yellowish solid (60.0 mg, 225 μmol , 75%).

Reaction time: 46 hours. NMR yield: 80%

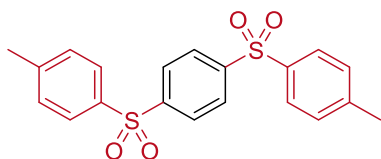
^1H NMR (400 MHz, CDCl_3) δ 7.86 (d, $J = 8.7$ Hz, 2H), 7.81 (d, $J = 8.4$ Hz, 2H), 7.46 (d, $J = 8.6$ Hz, 2H), 7.30 (d, $J = 8.1$ Hz, 2H), 2.40 (s, 3H). ^{13}C NMR (101 MHz, CDCl_3) δ 144.64, 140.66, 139.80, 138.36, 130.18, 129.68, 129.11, 127.84, 21.73. These data are in full agreement with those reported in literature.⁴⁵



1-Bromo-4-tosylbenzene (21) was obtained from 1-bromo-4-iodobenzene (84.9 mg, 300 μmol) and sodium *p*-toluensulfinate (106.9 mg, 600 μmol). Purification by flash chromatography (gradient 5-20% ethyl acetate/hexane) afforded the title compound as a yellowish solid (70.9 mg, 228 μmol , 76%).

Reaction time: 29 hours. NMR yield: not calculated due to signal overlap.

^1H NMR (400 MHz, CDCl_3) δ 7.85 – 7.67 (m, 4H), 7.61 (d, $J = 8.6$ Hz, 2H), 7.30 (d, $J = 8.2$ Hz, 2H), 2.39 (s, 3H). ^{13}C NMR (101 MHz, CDCl_3) δ 144.65, 141.11, 138.20, 132.62, 130.16, 129.13, 128.30, 127.79, 21.71. These data are in full agreement with those reported in literature.⁴⁷



1,4-Ditosylbenzene (22) was obtained from 1,4-diiodobenzene (99.0 mg, 300 μmol) and sodium *p*-toluensulfinate (160.4 mg, 900 μmol). Purification by flash chromatography (gradient 20-100% ethyl acetate/hexane) afforded the title compound as a yellowish solid (81.9 mg, 212 μmol , 71%).

Reaction time: 24 hours. NMR yield: 82%

^1H NMR (400 MHz, CDCl_3) δ 8.01 (s, 4H), 7.80 (d, $J = 8.3$ Hz, 4H), 7.31 (d, $J = 8.1$ Hz, 4H), 2.40 (s, 6H). ^{13}C NMR (101 MHz, CDCl_3) δ 146.40, 145.27, 137.35, 130.35, 128.51, 128.16, 21.78. These data are in full agreement with those reported in literature.⁴⁵

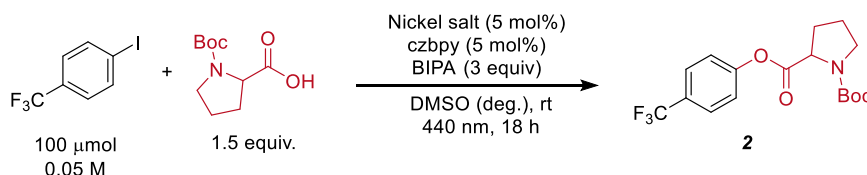
6.6.7 Optimization of the C–O cross-coupling using homogeneous visible-light-mediated nickel catalysis

General procedure for screening experiments

An oven dried vial (19 x 100 mm) equipped with a stir bar was charged with a nickel salt (5 μmol), 5,5'-dicarbazolyl-2,2'-bipyridyl (czbpy, 2.4 mg, 5 μmol), 4-iodobenzotrifluoride (27.2 mg, 100 μmol) and *N*-(*tert*-butoxycarbonyl)proline (32.3 mg, 150 μmol). DMSO (anhydrous, 2 mL) and *N*-*tert*-butylisopropylamine (BIPA, 34.6 mg, 300 μmol) were added and the vessel was sealed with a septum and Parafilm. The mixture was stirred for 1 minute at high speed, followed by sonication for 5 minutes and degassing by bubbling argon for 10 minutes. The reaction mixture was stirred at 800 rpm and irradiated with 440 nm LED lamps using the respective power settings. After the respective reaction time, 1,3,5-trimethoxybenzene (16.8 mg, 100 μmol , 1 equiv) was added to the reaction vessel, the mixture was shaken and an aliquote (300 μL) was removed, diluted with DMSO-*d*₆ and analyzed by ¹H NMR.

Screening of nickel salts

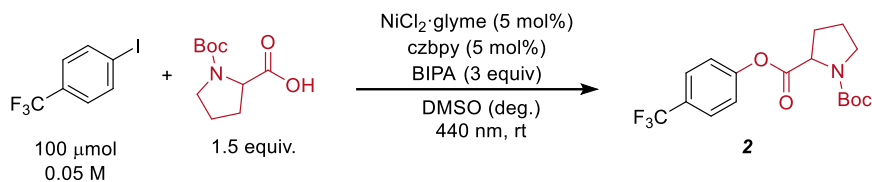
Table 6.13. Screening of nickel salts for the coupling of 4-iodobenzotrifluoride and *N*-Boc-proline.^a



Entry	Nickel salt	Conversion [%] ^b	2 [%] ^c
1	NiCl ₂ ·glyme	>99	88
2	NiBr ₂ ·glyme	46	39
3	NiBr ₂ ·3H ₂ O	>99	90

^aReaction conditions: 4-iodobenzotrifluoride (100 μmol), (*tert*-butoxycarbonyl)proline (*N*-Boc-proline, 150 μmol), *N*-*tert*-butylisopropylamine (BIPA, 150 μmol), nickel salt (5 μmol), 5,5'-dicarbazolyl-2,2'-bipyridyl (czbpy, 5 μmol), DMSO (anhydrous, 2 mL), 440 nm LED (1 lamp at full power). ^bConversion of 4-iodobenzotrifluoride determined by ¹H-NMR using 1,3,5-trimethoxybenzene as internal standard. ^cNMR yields determined by ¹H-NMR using 1,3,5-trimethoxybenzene as internal standard. glyme = 1,2-dimethoxyethane.

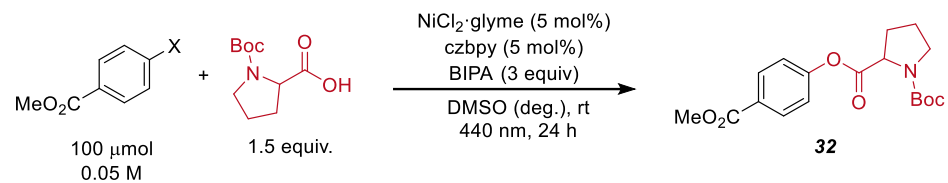
Optimized conditions and control experiments

Table 6.14. Optimized conditions and control experiments for the coupling of 4-iodobenzotrifluoride and *N*-Boc-proline.^a

Entry	Variation	Time [h]	Conversion [%] ^b	2 [%] ^c
1	None	18	>99	88
2	carbazole (10 mol%) instead of <i>czbpy</i>	18	0	n.d.
3	<i>bpy</i> (5 mol%) instead of <i>czbpy</i>	18	8	4
4	<i>bpy</i> (5 mol%) & carbazole (10 mol%) instead of <i>czbpy</i>	18	14	8
5	No $\text{NiCl}_2 \cdot \text{glyme}$	18	0	n.d.
6	No <i>czbpy</i>	18	0	n.d.
7	No BIPA	18	5	5
8	No light	18	0	n.d.
9	poly- <i>czbpy</i> (5 mol%) ^d	24	75	53

^aReaction conditions: 4-iodobenzotrifluoride (100 μ mol), (*tert*-butoxycarbonyl)proline (*N*-Boc-proline, 150 μ mol), *N-tert*-butylisopropylamine (BIPA, 150 μ mol), $\text{NiCl}_2 \cdot \text{glyme}$ (5 μ mol), 5,5'-dicarbazolyl-2,2'-bipyridyl (*czbpy*, 5 μ mol), DMSO (anhydrous, 2 mL), 440 nm LED (1 lamp at full power). ^bConversion of 4-iodobenzotrifluoride determined by ¹H-NMR using 1,3,5-trimethoxybenzene as internal standard. ^cNMR yields determined by ¹H-NMR using 1,3,5-trimethoxybenzene as internal standard. ^dThe amount of poly-*czbpy* was calculated using the molecular weight of the monomer. *glyme* = 1,2-dimethoxyethane. *bpy* = 2,2'-bipyridyl.

Reactivity of different aryl halides

Table 6.15. Coupling of *N*-Boc-proline and methyl 4-halobenzoates.^a

Entry	Aryl halide	Conversion [%] ^b	32 [%] ^c
1	Methyl 4-chlorobenzoate	5	1
2	Methyl 4-bromobenzoate	78	46
3	Methyl 4-iodobenzoate	>99	84

^aReaction conditions: aryl halide (100 μmol), (*tert*-butoxycarbonyl)proline (*N*-Boc-proline, 150 μmol), *N-tert*-butylisopropylamine (BIPA, 150 μmol) NiCl₂·glyme (5 μmol), 5,5'-dicarbazoyl-2,2'-bipyridyl (czbpy, 5 μmol), DMSO (anhydrous, 2 mL), 440 nm LED (2 lamps at full power). ^bConversion of 4-iodobenzotrifluoride determined by ¹H-NMR using 1,3,5-trimethoxybenzene as internal standard. ^cNMR yields determined by ¹H-NMR using 1,3,5-trimethoxybenzene as internal standard. glyme = 1,2-dimethoxyethane.

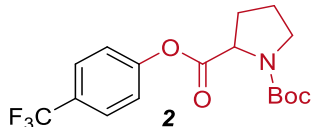
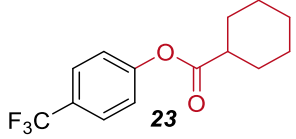
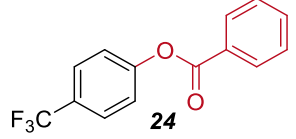
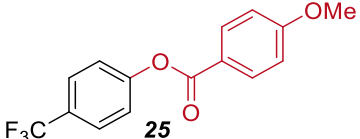
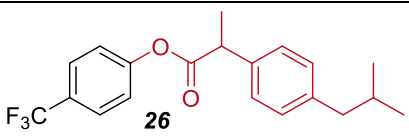
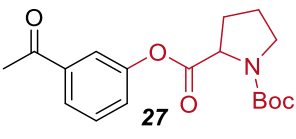
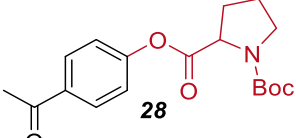
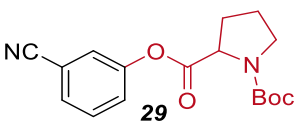
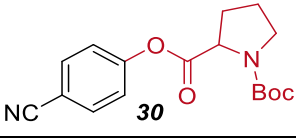
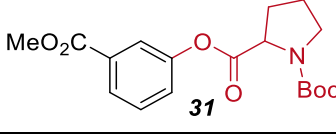
6.6.8 Scope of the C–O cross-coupling using homogeneous visible-light-mediated nickel catalysis

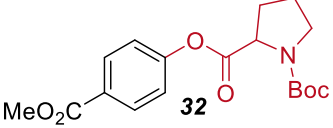
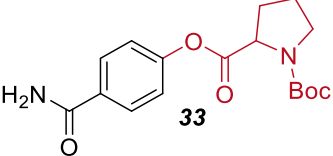
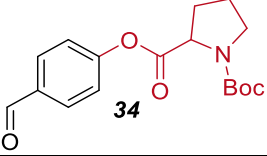
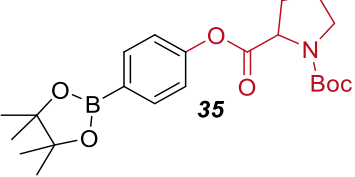
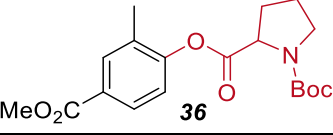
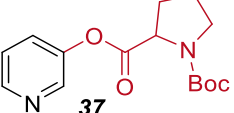
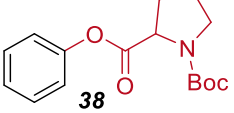
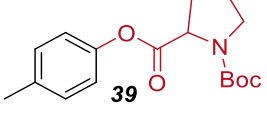
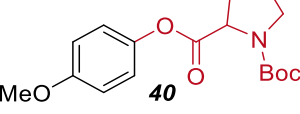
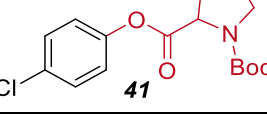
General procedure

An oven dried vial (19 x 100 mm) equipped with a stir bar was charged with NiCl₂·glyme (3.3 mg, 15 μmol, 5 mol%), 5,5'-dicarbazolyl-2,2'-bipyridyl (czbpy, 7.3 mg, 15 μmol, 5 mol%), the aryl iodide (300 μmol) and the carboxylic (450 μmol, 1.5 equiv). DMSO (anhydrous, 3 mL) was added, followed by *N*-tert-butylisopropylamine (BIPA, 103.8 mg, 0.9 mmol, 3.0 equiv), before sealing the vessel with a septum and Parafilm. The mixture was sonicated for 5 minutes and degassed by bubbling argon for 10 minutes. The reaction mixture was stirred at 800 rpm and irradiated with two LED lamps (440 nm) at full power. After the respective reaction time, maleic acid (34.9 mg, 300 μmol, 1.0 equiv) was added to the reaction vessel, the mixture was stirred and an aliquote (~200 μL) was removed, diluted with DMSO-*d*₆ and analyzed by ¹H NMR. The NMR sample was combined with the reaction mixture, diluted with H₂O (40 mL) and extracted with dichloromethane (3 x 40 mL). The combined organic phases were washed with brine (50 mL), dried over Na₂SO₄ and concentrated. The residue was purified by flash chromatography on silica gel using mixtures of hexane/ethyl acetate to obtain the desired product.

In case of **23**, **24**, **25** and **26**, the reaction was slow using the above reported conditions. Less concentrated conditions (300 μmol of the aryl iodide in 6 mL of DMSO) resulted in faster reactions for these substrates.

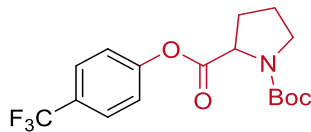
Table 6.16. Scope of the C–O coupling reaction.^a

Product	Reaction time	NMR yield ^b	Isolated yield
 2	24 hours	92%	91%
 23	96 hours	85%	80%
 24	96 hours	87%	82%
 25	96 hours	full conversion	63%
 26	96 hours	70%	67%
 27	48 hours	86%	82%
 28	24 hours	92%	90%
 29	48 hours	88%	83%
 30	24 hours	94%	92%
 31	48 hours	87%	85%

Product	Reaction time	NMR yield ^b	Isolated yield
 32	24 hours	91%	90%
 33	48 hours	94%	89%
 34	24 hours	96%	91%
 35	30 hours	96%	77%
 36	24 hours	74%	73%
 37	24 hours	85%	79%
 38	64 hours	81% yield	79%
 39	64 hours	73%	67%
 40	64 hours	65%	49%
 41	30 hours	93%	89%

^aReaction conditions according to general procedure. ^bNMR yields determined by ¹H-NMR using maleic acid as internal standard

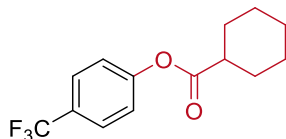
Experimental data



1-(*tert*-Butyl) 2-(4-(trifluoromethyl)phenyl) pyrrolidine-1,2-dicarboxylate (2) was obtained from 4-iodobenzotrifluoride (81.6 mg, 300 μ mol) and (*tert*-butoxycarbonyl)proline (96.9 mg, 450 μ mol). Purification by flash chromatography (gradient 0-5% ethyl acetate/hexane) afforded the title compound as a colorless oil (98.5 mg, 274 μ mol, 91%).

Reaction time: 24 hours. NMR yield: 92%

^1H NMR (400 MHz, CDCl_3) rotameric mixture δ 7.67 (m, 2H), 7.30 – 7.22 (m, 2H, contains residual solvent signal of CDCl_3), 4.51 (dd, $J = 8.5, 4.4$ Hz, 0.4H), 4.44 (dd, $J = 8.7, 4.4$ Hz, 0.6H), 3.71 – 3.42 (m, 2H), 2.44 – 2.27 (m, 1H), 2.24 – 2.12 (m, 1H), 2.12 – 1.93 (m, 2H), 1.52 – 1.45 (m, 9H). ^{13}C NMR (101 MHz, CDCl_3) rotameric mixture, resonances for minor rotamer are enclosed in parenthesis δ (171.27) 171.16, (154.50) 153.63, (153.31) 153.07, 128.16 (d, $J = 32.6$ Hz) (127.99 (d, $J = 32.8$ Hz)), 126.91 (q, $J = 3.7$ Hz) (126.74 (q, $J = 3.8$ Hz)), (123.83 (d, $J = 271.9$ Hz)) 123.74 (d, $J = 272.1$ Hz). (122.03) 121.66, 80.37 (80.18), 59.16 (59.08), (46.66) 46.47, 31.04 (29.99), 28.41, (24.58) 23.74. ^{19}F NMR (564 MHz, CDCl_3) rotameric mixture δ -62.22, -62.28. These data are in full agreement with those previously published in the literature.³⁴

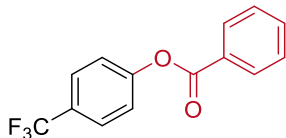


4-(Trifluoromethyl)phenyl cyclohexanecarboxylate (23) was obtained from 4-iodobenzotrifluoride (81.6 mg, 300 μ mol) and cyclohexanecarboxylic acid (57.7 mg, 450 μ mol), using 6 mL of DMSO as solvent. Purification by flash chromatography (gradient 0-3% ethyl acetate/hexane) afforded the title compound as a white solid (65.3 mg, 240 μ mol, 80%).

Reaction time: 96 hours. NMR yield: 85%

^1H NMR (400 MHz, CDCl_3) δ 7.64 (d, $J = 8.4$ Hz, 2H), 7.19 (d, $J = 8.4$ Hz, 2H), 2.58 (tt, $J = 11.2, 3.7$ Hz, 1H), 2.13 – 2.02 (m, 2H), 1.87 – 1.78 (m, 2H), 1.75 – 1.66 (m, 1H), 1.66 – 1.53 (m, 2H), 1.46 – 1.22 (m, 3H). ^{13}C NMR (101 MHz, CDCl_3) δ 174.02, 153.45, 127.89

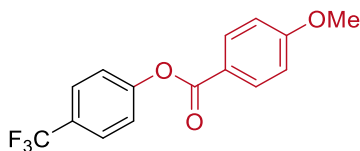
(q, $J = 32.8$ Hz), 126.73 (q, $J = 3.8$ Hz), 123.92 (q, $J = 272.1$ Hz), 122.09, 43.17, 28.89, 25.66, 25.31. ^{19}F NMR (564 MHz, CDCl_3) δ -62.21. These data are in full agreement with those reported in literature.⁴⁸



4-(Trifluoromethyl)phenyl benzoate (24) was obtained from 4-iodobenzotrifluoride (81.6 mg, 300 μmol) and benzoic acid (55.0 mg, 450 μmol), using 6 mL of DMSO as solvent. Purification by flash chromatography (gradient 0-3% ethyl acetate/hexane) afforded the title compound as a white solid (65.4 mg, 246 μmol , 82%).

Reaction time: 96 hours. NMR yield: 87%

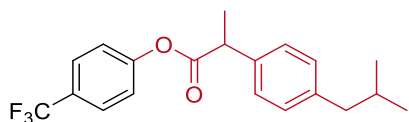
^1H NMR (400 MHz, CDCl_3) δ 8.22 (d, $J = 7.0$ Hz, 2H), 7.72 (d, $J = 8.5$ Hz, 2H), 7.68 (t, $J = 7.5$ Hz, 1H), 7.54 (t, $J = 7.8$ Hz, 2H), 7.37 (d, $J = 8.5$ Hz, 2H). ^{13}C NMR (101 MHz, CDCl_3) δ 164.69, 153.51 (d, $J = 1.5$ Hz), 134.01, 130.29, 128.98, 128.73, 128.19 (q, $J = 33.0$ Hz), 126.89 (q, $J = 3.7$ Hz), 123.95 (q, $J = 271.9$ Hz), 122.31. ^{19}F NMR (564 MHz, CDCl_3) δ -62.16. These data are in full agreement with those reported in literature.²⁶



4-(Trifluoromethyl)phenyl 4-methoxybenzoate (25) was obtained from 4-iodobenzotrifluoride (81.6 mg, 300 μmol) and 4-methoxybenzoic acid (68.5 mg, 450 μmol), using 6 mL of DMSO as solvent. Purification by flash chromatography (gradient 0-3% ethyl acetate/hexane) afforded the title compound as a white solid (56.2 mg, 190 μmol , 63%).

Reaction time: 96 hours. NMR analysis: full conversion of aryl iodide.

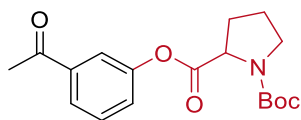
^1H NMR (400 MHz, CDCl_3) δ 8.16 (d, $J = 9.0$ Hz, 2H), 7.70 (d, $J = 8.4$ Hz, 2H), 7.34 (d, $J = 8.4$ Hz, 2H), 7.00 (d, $J = 9.0$ Hz, 2H), 3.91 (s, 3H). ^{13}C NMR (101 MHz, CDCl_3) δ 164.40, 164.20, 153.62, 132.45, 127.83, 126.82 (q, $J = 3.8$ Hz), 125.30, 122.35, 121.19, 113.99, 55.59. ^{19}F NMR (564 MHz, CDCl_3) δ -62.16. These data are in full agreement with those reported in literature.⁴⁹



4-(Trifluoromethyl)phenyl 2-(4-isobutylphenyl)propanoate (26) was obtained from 4-iodobenzotrifluoride (81.6 mg, 300 μmol) and ibuprofen (92.8 mg, 450 μmol), using 6 mL of DMSO as solvent. Purification by flash chromatography (gradient 0-3% ethyl acetate/hexane) afforded the title compound as a colorless oil (72.9 mg, 200 μmol , 67%).

Reaction time: 96 hours. NMR yield: 70%

^1H NMR (400 MHz, CDCl_3) δ 7.60 (d, $J = 8.3$ Hz, 1H), 7.29 (d, $J = 8.1$ Hz, 2H), 7.15 (d, $J = 8.3$ Hz, 2H), 7.12 (d, $J = 8.2$ Hz, 1H), 3.95 (q, $J = 7.1$ Hz, 1H), 2.47 (d, $J = 7.2$ Hz, 2H), 1.87 (m, 1H), 1.61 (d, $J = 7.1$ Hz, 3H), 0.91 (d, $J = 6.6$ Hz, 6H). ^{13}C NMR (101 MHz, CDCl_3) δ 172.75, 153.41 (d, $J = 1.5$ Hz), 141.09, 136.86, 129.65, 128.02 (q, $J = 32.8$ Hz), 127.22, 126.71 (q, $J = 3.7$ Hz), 123.90 (d, $J = 271.9$ Hz), 121.97, 45.29, 45.08, 30.24, 22.41, 18.45. ^{19}F NMR (564 MHz, CDCl_3) δ -62.19. HRMS (EI) m/z calcd for $\text{C}_{20}\text{H}_{21}\text{F}_3\text{O}_2$ [(M) $^+$] 350.1491, found: 350.1491

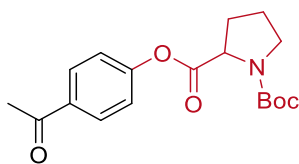


2-(3-Acetylphenyl) 1-(*tert*-butyl) pyrrolidine-1,2-dicarboxylate (27) was obtained from 3-iodoacetophenone (78.8 mg, 300 μmol) and (*tert*-butoxycarbonyl)proline (96.9 mg, 450 μmol). Purification by flash chromatography (gradient 0-10% ethyl acetate/hexane) afforded the title compound as a colorless oil (82.4 mg, 247 μmol , 82%).

Reaction time: 48 hours. NMR yield: 86%

^1H NMR (400 MHz CDCl_3) rotameric mixture δ 7.84 – 7.76 (t, $J = 7.4$ Hz, 1H), 7.68 – 7.63 (m, 1H), 7.51 – 7.42 (m, 1H), 7.36 – 7.26 (m, 1H), 4.51 (dd, $J = 8.6, 4.4$ Hz, 0.4H), 4.45 (dd, $J = 8.7, 4.3$ Hz, 0.6H), 3.66 – 3.39 (m, 2H), 2.60 – 2.54 (m, 3H), 2.46 – 2.27 (m, 1H), 2.24 – 2.09 (m, 1H), 2.08 – 1.88 (m, 2H), 1.48 – 1.44 (m, 9H). ^{13}C NMR (101 MHz, CDCl_3) rotameric mixture, resonances for minor rotamer are enclosed in parenthesis δ (197.11) 196.86, (171.56) 171.53, (154.50) 153.67, (150.99) 150.82, 138.57 (138.43), 129.80 (129.64), (126.48) 126.01, 125.99 (125.76), (121.34) 120.93, 80.34 (80.11), 59.13 (59.07),

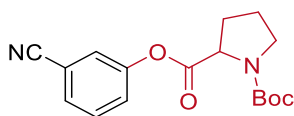
(46.66) 46.47, 31.05 (30.00), 28.43, (26.72) 26.72, (24.58) 23.75. These data are in full agreement with those previously published in the literature.³⁴



2-(4-Acetylphenyl) 1-(tert-butyl) pyrrolidine-1,2-dicarboxylate (28) was obtained from 4-iodoacetophenone (78.8 mg, 300 μmol) and (*tert*-butoxycarbonyl)proline (96.9 mg, 450 μmol). Purification by flash chromatography (gradient 0-10% ethyl acetate/hexane) afforded the title compound as a colorless oil (89.8 mg, 269 μmol , 90%).

Reaction time: 24 hours. NMR yield: 92%

¹H NMR (400 MHz, CDCl₃) rotameric mixture δ 8.02 – 7.94 (m, 2H), 7.23 – 7.15 (m, 2H), 4.50 (dd, J = 8.6, 4.4 Hz, 0.4H), 4.44 (dd, J = 8.7, 4.4 Hz, 0.6H), 3.67 – 3.42 (m, 2H), 2.60 – 2.55 (m, 3H), 2.45 – 2.27 (m, 1H), 2.23 – 2.11 (m, 1H), 2.08 – 1.89 (m, 2H), 1.49 – 1.40 (m, 9H). ¹³C NMR (101 MHz, CDCl₃) rotameric mixture, resonances for minor rotamer are enclosed in parenthesis δ (196.96) 196.79, (171.21) 171.15, 154.53 (154.48), 154.24 (153.63), 134.81 (134.70), 130.05 (129.92), (121.70) 121.34, 80.34 (80.15), 59.18 (59.10), (46.66) 46.47, 31.04 (29.99), 28.41, 26.65, (24.58) 23.76. These data are in full agreement with those previously published in the literature.³⁵

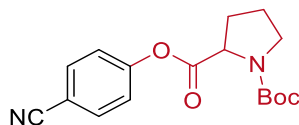


1-(tert-Butyl) 2-(3-cyanophenyl) pyrrolidine-1,2-dicarboxylate (29) was obtained from 3-iodobenzonitrile (68.7 mg, 300 μmol) and (*tert*-butoxycarbonyl)proline (96.9 mg, 450 μmol). Purification by flash chromatography (gradient 0-10% ethyl acetate/hexane) afforded the title compound as a colorless oil (78.6 mg, 248 μmol , 82%).

Reaction time: 48 hours. NMR yield: 88%

¹H NMR (400 MHz, CDCl₃) rotameric mixture δ 7.58 – 7.32 (m, 4H), 4.52 – 4.42 (m, 1H), 3.67 – 3.39 (m, 2H), 2.48 – 2.27 (m, 1H), 2.22 – 1.87 (m, 3H), 1.54 – 1.37 (m, 9H). ¹³C NMR (101 MHz, CDCl₃) rotameric mixture, resonances for minor rotamer are enclosed in parenthesis δ (171.22) 171.09, (154.50) 153.55, (150.91) 150.69, 130.55 (130.38), 129.69 (129.59), (126.61) 126.15, (125.29) 124.92, (117.86) 117.75, (113.59) 113.38, 80.42

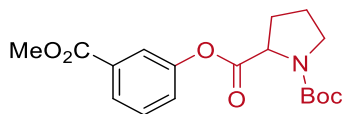
(80.27), (59.07) 59.03, (46.66) 46.46, 31.04 (29.97), 28.43 (28.41), 24.63 (23.74). These data are in full agreement with those previously published in the literature.³⁴



1-(*tert*-Butyl) 2-(4-cyanophenyl) pyrrolidine-1,2-dicarboxylate (30) was obtained from 4-iodobenzonitrile (68.7 mg, 300 μ mol) and (*tert*-butoxycarbonyl)proline (96.9 mg, 450 μ mol). Purification by flash chromatography (gradient 0-10% ethyl acetate/hexane) afforded the title compound as a colorless oil (87.6 mg, 277 μ mol, 92%).

Reaction time: 24 hours. NMR yield: 94%

¹H NMR (400 MHz, CDCl₃) rotameric mixture, δ 7.74 – 7.65 (m, 2H), 7.29 – 7.22 (m, 2H, contains residual solvent signal of CDCl₃), 4.49 (dd, J = 8.6, 4.6 Hz, 0.5H), 4.44 (dd, J = 8.7, 4.4 Hz, 0.5H), 3.65 – 3.38 (m, 2H), 2.48 – 2.30 (m, 1H), 2.20 – 1.88 (m, 3H), 1.51 – 1.44 (m, 9H). ¹³C NMR (101 MHz, CDCl₃) rotameric mixture, resonances for minor rotamer are enclosed in parenthesis δ (171.01) 170.88, (154.50) 154.11, 153.82 (153.54), 133.81 (133.66), (122.71) 122.31, (118.33) 118.15, (109.91) 109.71, 80.43 (80.28), 59.14 (59.07), (46.66) 46.47, (31.03) 29.96, 28.41, (24.63) 23.76. These data are in full agreement with those previously published in the literature.³⁴

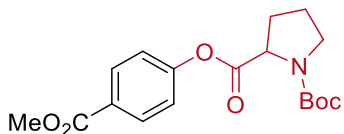


1-(*tert*-Butyl) 2-(3-(methoxycarbonyl)phenyl) pyrrolidine-1,2-dicarboxylate (31) was obtained from methyl 3-iodobenzoate (78.6 mg, 300 μ mol) and (*tert*-butoxycarbonyl)proline (96.9 mg, 450 μ mol). Purification by flash chromatography (gradient 0-10% ethyl acetate/hexane) afforded the title compound as a colorless oil (89.2 mg, 255 μ mol, 85%).

Reaction time: 48 hours. NMR yield: 87%

¹H NMR (400 MHz, CDCl₃) rotameric mixture δ 7.94 – 7.87 (m, 1H), 7.77 – 7.73 (m, 1H), 7.49 – 7.40 (m, 1H), 7.36 – 7.27 (m, 1H), 4.52 (dd, J = 8.6, 4.3 Hz, 0.4H), 4.45 (dd, J = 8.7, 4.3 Hz, 0.6H), 3.92 – 3.88 (m, 3H), 3.67 – 3.39 (m, 2H), 2.46 – 2.27 (m, 1H), 2.23 – 2.11 (m, 1H), 2.11 – 1.89 (m, 2H), 1.51 – 1.41 (m, 9H). ¹³C NMR (101 MHz, CDCl₃) rotameric mixture, resonances for minor rotamer are enclosed in parenthesis δ 171.47, (166.19) 166.05,

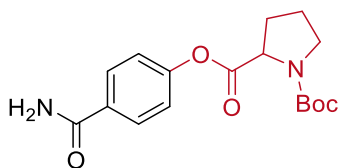
(154.48) 153.70, (150.71) 150.53, 131.76 (131.59), 129.56 (129.41), 127.12 (127.04), (126.34) 125.81, (122.67) 122.48, 80.37 (80.09), 59.15 (59.05), 52.37 (52.28), (46.64) 46.48, 31.05 (30.00), 28.42, (24.55) 23.74. These data are in full agreement with those previously published in the literature.³⁴



1-(*tert*-Butyl) 2-(4-(methoxycarbonyl)phenyl) pyrrolidine-1,2-dicarboxylate (32) was obtained from methyl 4-iodobenzoate (78.6 mg, 300 μ mol) and (*tert*-butoxycarbonyl)proline (96.9 mg, 450 μ mol). Purification by flash chromatography (gradient 0-10% ethyl acetate/hexane) afforded the title compound as a colorless oil (94.5 mg, 270 μ mol, 90%).

Reaction time: 24 hours. NMR yield: 91%

¹H NMR (400 MHz, CDCl₃) rotameric mixture, δ 8.10 – 8.01 (m, 2H), 7.20 – 7.13 (m, 2H), 4.52 (dd, J = 8.6, 4.3 Hz, 0.4H), 4.46 (dd, J = 8.7, 4.3 Hz, 0.6H), 3.93 – 3.85 (m, 3H), 3.67 – 3.41 (m, 2H), 2.45 – 2.26 (m, 1H), 2.21 – 2.09 (m, 1H), 2.08 – 1.88 (m, 2H), 1.50 – 1.38 (m, 9H). ¹³C NMR (101 MHz, CDCl₃) rotameric mixture, resonances for minor rotamer are enclosed in parenthesis δ (171.17) 171.12, (166.34) 166.20, (154.47) 154.19, 153.64, 131.25 (131.11), 127.83 (127.67), (121.52) 121.16, 80.34 (80.13), 59.19 (59.10), 52.24 (52.18), (46.65) 46.46, 31.02 (29.97), 28.41, (24.55) 23.73. These data are in full agreement with those previously published in the literature.³⁴

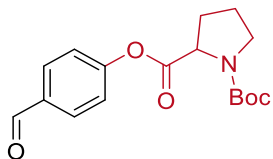


1-(*tert*-Butyl) 2-(4-carbamoylphenyl) pyrrolidine-1,2-dicarboxylate (33) was obtained from 4-iodobenzamide (74.1 mg, 300 μ mol) and (*tert*-butoxycarbonyl)proline (96.9 mg, 450 μ mol). Purification by flash chromatography (50% ethyl acetate/hexane) afforded the title compound as a colorless oil (90.2 mg, 270 μ mol, 89%).

Reaction time: 48 hours. NMR yield: 94%

¹H NMR (400 MHz, CDCl₃) rotameric mixture δ 7.89 – 7.76 (m, 2H), 7.12 (d, J = 8.7 Hz, 2H), 6.74 – 6.22 (m, 2H), 4.52 (dd, J = 8.6, 4.4 Hz, 0.4H), 4.45 (dd, J = 8.7, 4.4 Hz, 0.6H), 3.66 – 3.38 (m, 2H), 2.43 – 2.25 (m, 1H), 2.21 – 2.09 (m, 1H), 2.06 – 1.84 (m, 2H), 1.51 –

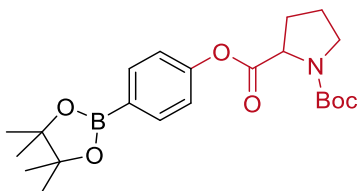
1.35 (m, 9H). ^{13}C NMR (101 MHz, CDCl_3) rotameric mixture, resonances for minor rotamer are enclosed in parenthesis δ (171.42) 171.33, (168.93) 168.79, 154.55 (153.72), (153.42) 153.23, 131.25 (131.11), 129.11 (128.98), (121.58) 121.26, 80.39 (80.22), 59.17 (59.10), (46.69) 46.47, 30.99 (29.98), 28.40, (24.54) 23.72. HRMS (ESI) m/z calcd for for $\text{C}_{17}\text{H}_{24}\text{N}_2\text{NaO}_5$ [(M+Na) $^+$] 357.1421, found: 357.1397.



1-(*tert*-Butyl) 2-(4-formylphenyl) pyrrolidine-1,2-dicarboxylate (34) was obtained from 4-iodobenzaldehyde (69.6 mg, 300 μmol) and (*tert*-butoxycarbonyl)proline (96.9 mg, 450 μmol). Purification by flash chromatography (gradient 0-10% ethyl acetate/hexane) afforded the title compound as a colorless oil (87.2 mg, 273 μmol , 91%).

Reaction time: 24 hours. NMR yield: 96%

^1H NMR (400 MHz, CDCl_3) rotameric mixture δ 9.98 (s, 0.6H), 9.97 (s, 0.4H), 7.95 – 7.86 (m, 2H), 7.32 – 7.24 (m, 2H, contains residual solvent signal of CDCl_3), 4.51 (dd, $J = 8.5$, 4.4 Hz, 0.4H), 4.45 (dd, $J = 8.7$, 4.4 Hz, 0.6H), 3.66 – 3.40 (m, 2H), 2.46 – 2.29 (m, 1H), 2.22 – 2.10 (m, 1H), 2.11 – 1.90 (m, 2H), 1.51 – 1.41 (m, 9H). ^{13}C NMR (101 MHz, CDCl_3) rotameric mixture, resonances for minor rotamer are enclosed in parenthesis δ (190.989) 190.81, (171.10) 171.02, (155.55) 155.24, (154.49) 153.60, 134.09 (134.00), 131.30 (131.19), (122.31) 121.93, 80.38 (80.20), 59.20 (59.11), (46.66) 46.47, 31.04 (29.99), 28.42, (24.59) 23.75. These data are in full agreement with those previously published in the literature.³⁴

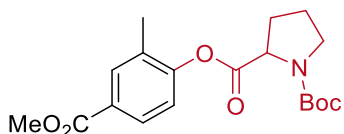


1-(*tert*-Butyl) 2-(4-(4,4,5,5-tetramethyl-1,3,2-dioxaborolan-2-yl)phenyl) pyrrolidine-1,2-dicarboxylate (35) was obtained from 4-iodophenylboronic acid pinacol ester (99.0 mg, 300 μmol) and (*tert*-butoxycarbonyl)proline (96.9 mg, 450 μmol). Purification by flash chromatography (gradient 0-10% ethyl acetate/hexane) afforded the title compound as a white solid (96.1 mg, 230 μmol , 77%).

In order to avoid hydrolysis of the boronic acid ester, no washing with a NaOH solution can be carried out and mixed fractions have to be discarded or further purified by a second column chromatography step.

Reaction time: 30 hours. NMR yield: 96%

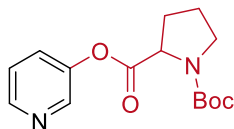
^1H NMR (400 MHz, CDCl_3) rotameric mixture δ 7.87 – 7.77 (m, 2H), 7.14 – 7.05 (m, 2H), 4.51 (dd, $J = 8.6, 4.2$ Hz, 0.4H), 4.43 (dd, $J = 8.7, 4.3$ Hz, 0.6H), 3.67 – 3.38 (m, 2H), 2.44 – 2.26 (m, 1H), 2.25 – 2.14 (m, 1H), 2.10 – 1.86 (m, 2H), 1.49 – 1.41 (m, 9H), 1.33 (s, 12H). ^{13}C NMR (101 MHz, CDCl_3) rotameric mixture, resonances for minor rotamer are enclosed in parenthesis δ 171.35, (154.46) 153.75, (153.34) 153.10, 136.24 (136.13), 126.65 (br s), (120.85) 120.50, 83.94 (83.87), 80.26 (79.99), 59.23 (59.11), (46.64) 46.46, 31.03 (30.00), (28.43) 28.40, 24.86, (24.51) 23.73. These data are in full agreement with those previously published in the literature.³⁴



1-(*tert*-Butyl) 2-(4-(methoxycarbonyl)-2-methylphenyl) pyrrolidine-1,2-dicarboxylate (36) was obtained from methyl 4-iodo-3-methylbenzoate (77.8 mg, 300 μmol) and (*tert*-butoxycarbonyl)proline (96.9 mg, 450 μmol). Purification by flash chromatography (gradient 0-10% ethyl acetate/hexane) afforded the title compound as a colorless oil (79.3 mg, 218 μmol , 73%).

Reaction time: 24 hours. NMR yield: 74%

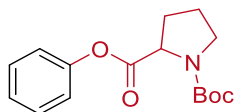
^1H NMR (400 MHz, CDCl_3) rotameric mixture δ 7.96 – 7.83 (m, 2H), 7.12 – 7.05 (m, 1H), 4.57 – 4.48 (m, 1H), 3.89 – 3.85 (m, 3H), 3.65 – 3.40 (m, 2H), 2.45 – 2.28 (m, 1H), 2.27 – 2.11 (m, 4H), 2.10 – 1.89 (m, 2H), 1.50 – 1.41 (m, 9H). ^{13}C NMR (101 MHz, CDCl_3) rotameric mixture, resonances for minor rotamer are enclosed in parenthesis δ (170.95) 170.71, (166.52) 166.39, (154.42) 153.71, 153.02 (152.77), 132.76 (132.63), (130.69) 130.23, 128.64 (128.53), 127.91 (127.80), (122.00) 121.56, 80.37 (80.06), 59.06 (59.01), 52.18 (52.12), (46.62) 46.43, 31.16 (30.11), 28.42, (24.56) 23.62, 16.25 (16.18). These data are in full agreement with those previously published in the literature.³⁴



1-(*tert*-Butyl) 2-(pyridin-3-yl) pyrrolidine-1,2-dicarboxylate (37) was obtained from 3-iodopyridine (77.8 mg, 300 μmol) and (*tert*-butoxycarbonyl)proline (96.9 mg, 450 μmol). Purification by flash chromatography (gradient 15-33% ethyl acetate/hexane) afforded the title compound as a colorless oil (68.9 mg, 236 μmol , 79%).

Reaction time: 24 hours. NMR yield: 85%

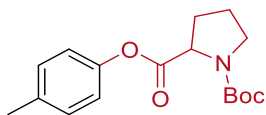
^1H NMR (400 MHz, CDCl_3) rotameric mixture δ 8.50 – 8.37 (m, 2H), 7.55 – 7.44 (m, 1H), 7.37 – 7.28 (m, 1H), 4.50 (dd, $J = 8.5, 4.5$ Hz, 0.4H), 4.45 (dd, $J = 8.7, 4.4$ Hz, 0.6H), 3.64 – 3.39 (m, 2H), 2.44 – 2.27 (m, 1H), 2.11 – 2.09 (m, 1H), 2.06 – 1.87 (m, 2H), 1.48 – 1.38 (m, 9H). ^{13}C NMR (101 MHz, CDCl_3) rotameric mixture, resonances for minor rotamer are enclosed in parenthesis δ (171.26) 171.24, (154.47) 153.57, (147.55) 147.29, 147.02 (146.72), (143.06) 142.96, (129.46) 128.86, 124.04 (123.96), 80.39 (80.21), 59.06 (59.02), (46.64) 46.45, 31.06 (30.00), 28.40, (24.59) 23.74. HRMS (ESI) m/z calcd for $\text{C}_{15}\text{H}_{20}\text{N}_2\text{NaO}_4$ [(M+H) $^+$] 293.1495, found: 293.1465.



1-(*tert*-Butyl) pyrrolidine-1,2-dicarboxylate (38) was obtained from iodobenzene (61.2 mg, 300 μmol) and (*tert*-butoxycarbonyl)proline (96.9 mg, 450 μmol). Purification by flash chromatography (gradient 0-8% ethyl acetate/hexane) afforded the title compound as a colorless oil (69.0 mg, 237 μmol , 79%).

Reaction time: 64 hours. NMR yield: 81%

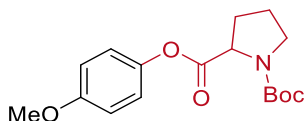
^1H NMR (400 MHz CDCl_3) rotameric mixture δ 7.42 – 7.31 (m, 2H), 7.26 – 7.17 (m, 1H), 7.14 – 7.05 (m, 2H), 4.51 (dd, $J = 8.6, 4.4$ Hz, 0.4H), 4.45 (dd, $J = 8.7, 4.3$ Hz, 0.6H), 3.67 – 3.39 (m, 2H), 2.44 – 2.26 (m, 2H), 2.22 – 2.11 (m, 1H), 2.11 – 1.87 (m, 2H), 1.52 – 1.40 (m, 9H). ^{13}C NMR (101 MHz, CDCl_3) rotameric mixture, resonances for minor rotamer are enclosed in parenthesis δ 171.63, (154.46) 153.76, (150.80) 150.59, 129.51 (129.36), 125.95 (125.79), (121.48) 121.15, 80.21 (79.96), 59.19 (59.09), (46.64) 46.46, 31.07 (30.03), 28.44, (24.50) 23.71. These data are in full agreement with those previously published in the literature.⁵⁰



1-(*tert*-Butyl) 2-(4-tolyl) pyrrolidine-1,2-dicarboxylate (39) was obtained from 4-iodotoluene (65.4 mg, 300 μ mol) and (*tert*-butoxycarbonyl)proline (96.9 mg, 450 μ mol). Purification by flash chromatography (gradient 0-10% ethyl acetate/hexane) afforded the title compound as a colorless oil (61.5 mg, 201 μ mol, 67%).

Reaction time: 64 hours. NMR yield: 73%

^1H NMR (400 MHz, CDCl_3) rotameric mixture δ 7.20 – 7.11 (m, 2H), 7.00 – 6.93 (m, 2H), 4.51 (dd, $J = 8.6, 4.4$ Hz, 0.4H), 4.43 (dd, $J = 8.7, 4.4$ Hz, 0.6H), 3.68 – 3.39 (m, 2H), 2.41 – 2.26 (m, 4H), 2.22 – 2.10 (m, 1H), 2.09 – 1.87 (m, 2H), 1.51 – 1.43 (m, 9H). ^{13}C NMR (101 MHz, CDCl_3) rotameric mixture, resonances for minor rotamer are enclosed in parenthesis δ 171.80, (154.48) 153.79, (148.55) 148.35, 135.59 (135.38), 130.00 (129.85), (121.14) 120.82, 80.17 (79.92), 59.19 (59.07), (46.63) 46.45, 31.07 (30.03), (28.58) 28.44, (24.49) 23.71, 20.88. HRMS (ESI) m/z calcd for $\text{C}_{17}\text{H}_{23}\text{NNaO}_4$ [(M+Na) $^+$] 328.1519, found: 328.1493.



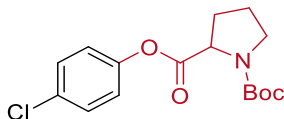
1-(*tert*-Butyl) 2-(4-methoxyphenyl) pyrrolidine-1,2-dicarboxylate (40) was obtained from 4-iodoanisole (70.2 mg, 300 μ mol) and (*tert*-butoxycarbonyl)proline (96.9 mg, 450 μ mol). Purification by flash chromatography (gradient 0-10% ethyl acetate/hexane) afforded the title compound as a colorless oil (47.1 mg, 147 μ mol, 49%).

Reaction time: 64 hours. NMR yield: 65%

^1H NMR (400 MHz, CDCl_3) rotameric mixture δ 7.05 – 6.95 (m, 2H), 6.91 – 6.82 (m, 2H), 4.49 (dd, $J = 8.6, 4.4$ Hz, 0.4H), 4.42 (dd, $J = 8.7, 4.4$ Hz, 0.6H), 3.80 – 3.76 (m, 3H), 3.65 – 3.39 (m, 2H), 2.42 – 2.24 (m, 1H), 2.21 – 2.09 (m, 1H), 2.08 – 1.89 (m, 2H), 1.48 – 1.44 (m, 9H). ^{13}C NMR (101 MHz, CDCl_3) rotameric mixture, resonances for minor rotamer are enclosed in parenthesis δ 171.97, 157.29 (157.22), (154.45) 153.78, (144.28) 144.06, (122.22) 121.90, 114.50 (114.37), (80.17) 79.93, 59.15 (59.04), 55.60, (46.63) 46.45, 31.07

Chapter 6

(30.03), 28.44, (24.50) 23.71. HRMS (ESI) m/z calcd for $C_{17}H_{23}NNaO_5 [(M+Na)^+]$ 344.1468, found : 344.1443.



1-(*tert*-Butyl) 2-(4-chlorophenyl) pyrrolidine-1,2-dicarboxylate (41) was obtained from 1-chloro-4-iodobenzene (71.6 mg, 300 μ mol) and (*tert*-butoxycarbonyl)proline (96.9 mg, 450 μ mol). Purification by flash chromatography (gradient 0-5% ethyl acetate/hexane) afforded the title compound as a colorless oil (86.9 mg, 267 μ mol, 89%).

Reaction time: 30 hours. NMR yield: 93%

1H NMR (400 MHz $CDCl_3$) rotameric mixture δ 7.37 – 7.29 (m, 2H), 7.08 – 7.00 (m, 2H), 4.49 (dd, $J = 8.6, 4.3$ Hz, 0.4H), 4.42 (dd, $J = 8.7, 4.4$ Hz, 0.6H), 3.64 – 3.39 (m, 2H), 2.43 – 2.26 (m, 1H), 2.20 – 1.87 (m, 3H), 1.49 – 1.42 (m, 9H). ^{13}C NMR (101 MHz, $CDCl_3$) rotameric mixture, resonances for minor rotamer are enclosed in parenthesis δ (171.48) 171.41, (154.47) 153.67, (149.27) 149.05, 131.31 (131.15), 129.57 (129.41), (122.88) 122.51, 80.28 (80.09), 59.14 (59.04), (46.64) 46.45, 31.04 (29.99), 28.42, (24.55) 23.73. These data are in full agreement with those previously published in the literature.³⁴

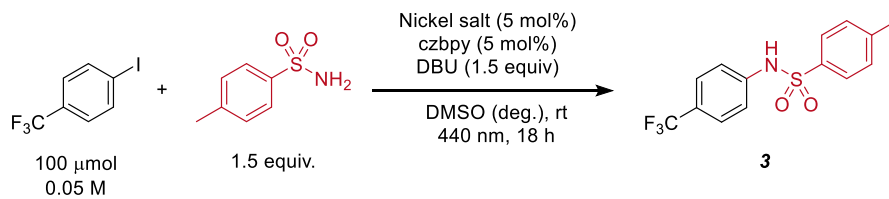
6.6.9 Optimization of the C–N cross-coupling using homogeneous visible-light-mediated nickel catalysis

General procedure for screening experiments

An oven dried vial (19 x 100 mm) equipped with a stir bar was charged with a nickel salt (5 μmol), 5,5'-dicarbazyl-2,2'-bipyridyl (czbpy, 5 μmol), 4-iodobenzotrifluoride (100 μmol) and the *p*-toluensulfonamide (150 μmol). The solvent (anhydrous, 2 mL) was added, followed by the base (150 μmol), before sealing the vessel with a septum and Parafilm. The mixture was stirred for 1 minute at high speed, followed by sonication for 5 minutes and degassing by bubbling argon for 10 minutes. The reaction mixture was stirred at 800 rpm and irradiated with one LED lamp (440 nm) using full power. After the respective reaction time, 1,3,5-trimethoxybenzene (16.8 mg, 100 μmol , 1 equiv) was added to the reaction vessel, the mixture was shaken and an aliquote (20 μL) was removed, diluted with DMSO- d_6 and analyzed by ^1H NMR.

Screening of nickel salts

Table 6.17. Screening of nickel salts for the coupling of 4-iodobenzotrifluoride and *p*-toluensulfonamide.^a

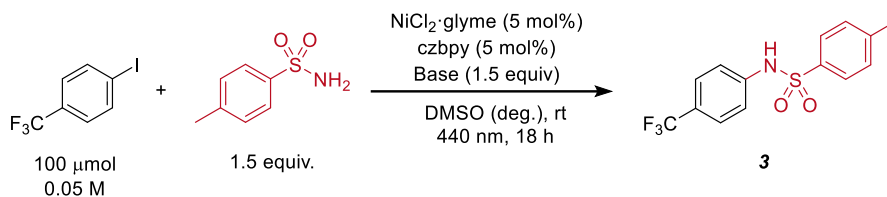


Entry	Nickel salt	Conversion [%] ^b	3 [%] ^c
1	NiCl ₂ ·glyme	98	80
2	NiBr ₂ ·glyme	69	55
3	NiBr ₂ ·3H ₂ O	63	46

^aReaction conditions: 4-iodobenzotrifluoride (100 μmol), *p*-toluensulfonamide (150 μmol), 1,8-diazabicyclo[5.4.0]undec-7-ene (DBU, 150 μmol), nickel salt (5 μmol), 5,5'-dicarbazyl-2,2'-bipyridyl (czbpy, 5 μmol), DMSO (anhydrous, 2 mL), 440 nm LED (2 lamps at full power).

^bConversion of 4-iodobenzotrifluoride determined by ^1H -NMR using 1,3,5-trimethoxybenzene as internal standard. ^cNMR yields determined by ^1H -NMR using 1,3,5-trimethoxybenzene as internal standard. glyme = 1,2-dimethoxyethane.

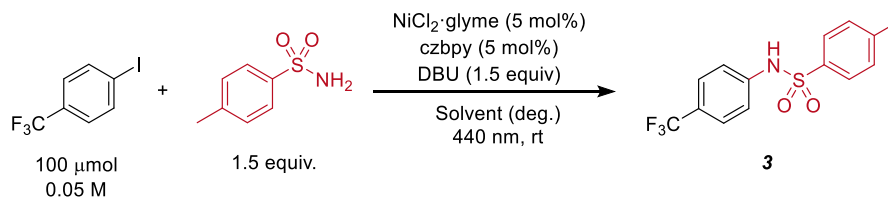
Base screening

Table 6.18. Base screening for the coupling of 4-iodobenzotrifluoride and *p*-toluenesulfonamide.^a

Entry	Base	Conversion [%] ^b	3 [%] ^c
1	1,8-Diazabicyclo[5.4.0]undec-7-ene (DBU)	98	80
2	7-Methyl-1,5,7-triazabicyclo[4.4.0]dec-5-en (MTBD)	98	74
3	1,1,3,3-Tetramethylguanidine (TMG)	65	61
4	2- <i>tert</i> -Butyl-1,1,3,3-tetramethylguanidine (BTMG)	18	18

^aReaction conditions: 4-iodobenzotrifluoride (100 μmol), *p*-toluenesulfonamide (150 μmol), base (150 μmol), NiCl₂·glyme (5 μmol), 5,5'-dicarbazyl-2,2'-bipyridyl (czbpy, 5 μmol), DMSO (anhydrous, 2 mL), 440 nm LED (2 lamps at full power). ^bConversion of 4-iodobenzotrifluoride determined by ¹H-NMR using 1,3,5-trimethoxybenzene as internal standard. ^cNMR yields determined by ¹H-NMR using 1,3,5-trimethoxybenzene as internal standard. glyme = 1,2-dimethoxyethane.

Solvent screening

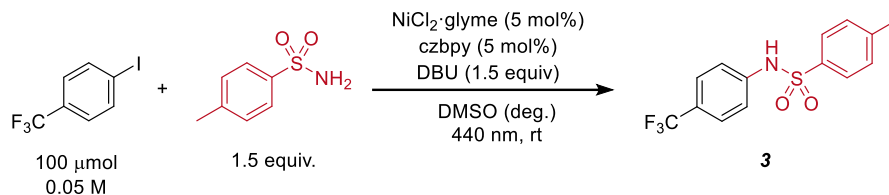
Table 6.19. Solvent screening for the coupling of 4-iodobenzotrifluoride and *p*-toluenesulfonamide.^a

Entry	Solvent	Time [h]	Conversion [%] ^b	3 [%] ^c
1	DMSO	18	98	80
2	MeCN	18	43	40
3	DMAc	18	62	39

^aReaction conditions: 4-iodobenzotrifluoride (100 μmol), *p*-toluenesulfonamide (150 μmol), 1,8-diazabicyclo[5.4.0]undec-7-ene (DBU, 150 μmol), NiCl₂·glyme (5 μmol), 5,5'-dicarbazyl-2,2'-bipyridyl (czbpy, 5 μmol), solvent (anhydrous, 2 mL), 440 nm LED (2 lamps at full power).

^bConversion of 4-iodobenzotrifluoride determined by ¹H-NMR using 1,3,5-trimethoxybenzene as internal standard. ^cNMR yields determined by ¹H-NMR using 1,3,5-trimethoxybenzene as internal standard. glyme = 1,2-dimethoxyethane.

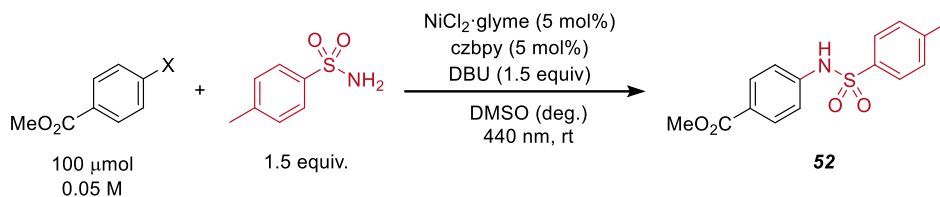
Optimized conditions and control experiments

Table 6.20. Optimized conditions and control experiments for the coupling of 4-iodobenzotrifluoride and *p*-toluenesulfonamide.^a

Entry	Variation	Time [h]	Conversion [%] ^b	3 [%] ^c
1	None	18	87	75
2	carbazole (10 mol%) instead of <i>czbpy</i>	18	42	32
3	<i>bpy</i> (5 mol%) instead of <i>czbpy</i>	18	3	n.d.
4	<i>bpy</i> (5 mol%) & carbazole (10 mol%) instead of <i>czbpy</i>	18	61	51
5	No $\text{NiCl}_2 \cdot \text{glyme}$	18	18	n.d.
6	No <i>czbpy</i>	18	-	n.d.
7	No DBU	18	5	5
8	No light	18	-	n.d.
9	poly- <i>czbpy</i> (5 mol%) ^d	24	98	59

^aReaction conditions: 4-iodobenzotrifluoride (100 μmol), *p*-toluenesulfonamide (150 μmol), 1,8-diazabicyclo[5.4.0]undec-7-ene (DBU, 150 μmol), $\text{NiCl}_2 \cdot \text{glyme}$ (5 μmol), 5,5'-dicarbazyl-2,2'-bipyridyl (*czbpy*, 5 μmol), DMSO (anhydrous, 2 mL), 440 nm LED (2 lamps at full power). ^bConversion of 4-iodobenzotrifluoride determined by ¹H-NMR using 1,3,5-trimethoxybenzene as internal standard. ^cNMR yields determined by ¹H-NMR using 1,3,5-trimethoxybenzene as internal standard. ^dThe amount of poly-*czbpy* was calculated using the molecular weight of the monomer. glyme = 1,2-dimethoxyethane. *bpy* = 2,2'-bipyridyl. n.d. = not detected.

Reactivity of different aryl halides

Table 6.21. Coupling of *p*-toluenesulfonamide and methyl 4-halobenzoates.^a

Entry	Aryl halide	Time [h]	Conversion [%] ^b	52 [%] ^c
1	Methyl 4-chlorobenzoate	24	-	n.d.
2	Methyl 4-bromobenzoate	24	57	31
3	Methyl 4-iodobenzoate	24	>99	82

^aReaction conditions: aryl halide (100 μmol), *p*-toluenesulfonamide (150 μmol), 1,8-diazabicyclo[5.4.0]undec-7-ene (DBU, 150 μmol), $\text{NiCl}_2 \cdot \text{glyme}$ (5 μmol), 5,5'-dicarbazyl-2,2'-bipyridyl (*czbpy*, 5 μmol), DMSO (anhydrous, 2 mL), 440 nm LED (2 lamps at full power). ^bConversion of aryl halide determined by ¹H-NMR using 1,3,5-trimethoxybenzene as internal standard. ^cNMR yields determined by ¹H-NMR using 1,3,5-trimethoxybenzene as internal standard. *glyme* = 1,2-dimethoxyethane. n.d. = not detected.

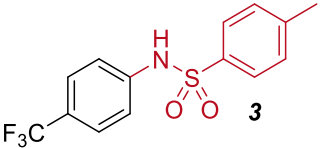
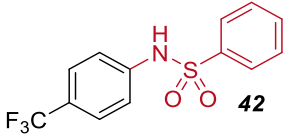
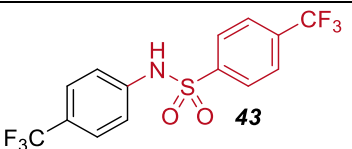
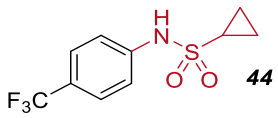
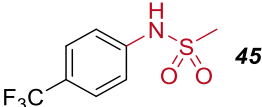
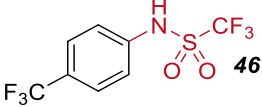
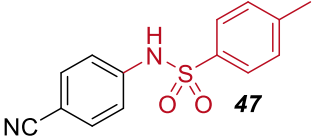
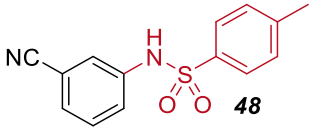
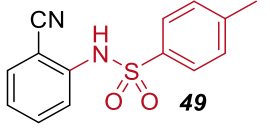
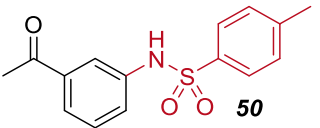
6.6.10 Scope of the C–N cross-coupling using homogeneous visible-light-mediated nickel catalysis

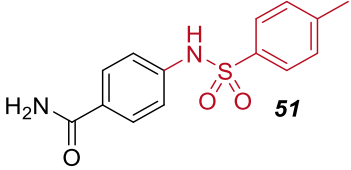
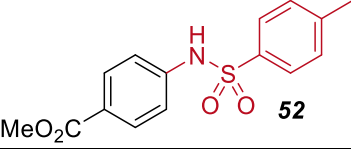
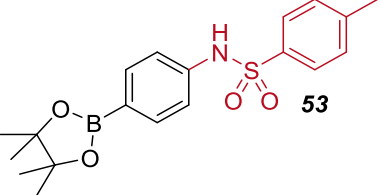
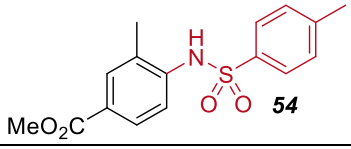
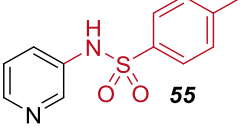
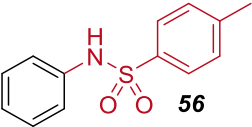
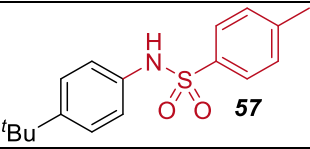
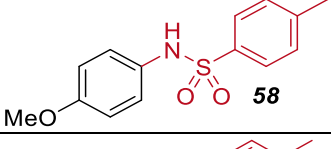
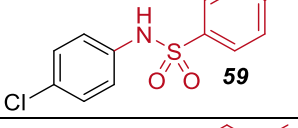
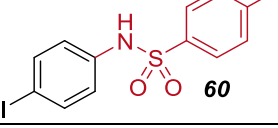
General procedure

An oven dried vial (19 x 100 mm) equipped with a stir bar was charged with NiCl₂·glyme (3.3 mg, 15 μmol, 5 mol%), 5,5-dicarbazolyl-2,2'-bipyridyl (czbpy, 7.3 mg, 15 μmol, 5 mol%), the aryl iodide (300 μmol) and the sulfonamide (450 μmol, 1.5 equiv). DMSO (anhydrous, 6 mL) was added, followed by 1,8-diazabicyclo[5.4.0]undec-7-ene (DBU, 68.5 mg, 450 μmol, 1.5 equiv), before sealing the vessel with a septum and Parafilm. The mixture was stirred for 1 minute at high speed, followed by sonication for 5 minutes and degassing by bubbling argon for 10 minutes. The reaction mixture was stirred at 800 rpm and irradiated with two LED lamps (440 nm) at full power. After the respective reaction time, maleic acid (34.8 mg, 300 μmol, 1.0 equiv) was added to the reaction vessel, the mixture was stirred and an aliquote (20 μL) was removed, diluted with DMSO-*d*₆ and analyzed by ¹H NMR. The NMR sample and the reaction mixture were combined and diluted with water (60 mL). The aqueous phase was extracted with ethyl acetate (3 x 40 mL). The combined organic layers were washed with brine (2 x 40 mL), dried over Na₂SO₄ and concentrated. The residue was purified by flash chromatography on silica gel using mixtures of hexane/ethyl acetate to obtain the desired product.

In some cases, we were not able to determine NMR yields reliably. In these cases, only consumption of the starting material (conversion) and isolated yields were determined.

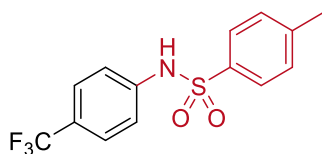
Table 6.22. Scope of the C–O coupling reaction.^a

Product	Reaction time	NMR yield ^b	Isolated yield
 3	20 hours	full conversion	89%
 42	20 hours	full conversion	86%
 43	48 hours	full conversion	86%
 44	23 hours	83% yield	80%
 45	22 hours	78% yield	77%
 46	115 hours	74% yield	72%
 47	18 hours	full conversion	82%
 48	20 hours	full conversion	80%
 49	32 hours	82% yield	81%
 50	18 hours	89% yield	63%

Product	Reaction time	NMR yield ^b	Isolated yield
	66 hours	89% yield	86%
	24 hours	95% yield	84%
	22 hours	full conversion	72%
	72 hours	full conversion	78%
	30 hours	76% yield	74%
	68 hours	full conversion	89%
	68 hours	-	83%
	43 hours	95% conversion	84%
	24 hours	86% yield	83%
	96 hours	65% yield	61%

^aReaction conditions according to general procedure. ^bNMR yields determined by ¹H-NMR using maleic acid as internal standard

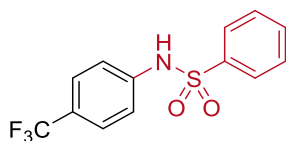
Experimental data



4-Methyl-*N*-(4-(trifluoromethyl)phenyl)benzenesulfonamide (3) was obtained from 4-iodobenzotrifluoride (81.6 mg, 300 μmol) and *p*-toluenesulfonamide (77.0 mg, 450 μmol). Purification by flash chromatography (gradient 5-20% ethyl acetate/hexane) afforded the title compound as a yellowish solid (84.2 mg, 267 μmol , 89%).

Reaction time: 20 hours. NMR analysis: full conversion of aryl iodide.

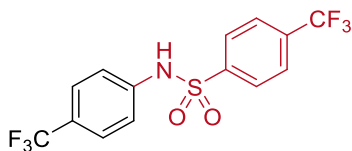
^1H NMR (400 MHz, CDCl_3) δ 7.74 (d, $J = 8.4$ Hz, 2H), 7.48 (d, $J = 8.5$ Hz, 2H), 7.42 (br. s, 1H), 7.27 (d, $J = 7.8$ Hz, 2H, contains residual solvent signal of CDCl_3), 7.19 (d, $J = 8.3$ Hz, 2H), 2.39 (s, 3H). ^{13}C NMR (101 MHz, CDCl_3) δ 144.71, 140.04, 135.77, 130.10, 127.39, 126.78 (q, $J = 3.8$ Hz), 126.78 (q, $J = 32.9$ Hz), 124.01 (d, $J = 270.9$ Hz), 119.75, 21.72. ^{19}F NMR (376 MHz, CDCl_3) δ -62.24. These data are in full agreement with those reported in literature.⁵¹



***N*-(4-(Trifluoromethyl)phenyl)benzenesulfonamide (42)** was obtained from 4-iodobenzotrifluoride (81.6 mg, 300 μmol) and benzenesulfonamide (70.7 mg, 450 μmol). Purification by flash chromatography (gradient 10-20% ethyl acetate/hexane) afforded the title compound as a white solid (77.6 mg, 258 μmol , 86%).

Reaction time: 20 hours. NMR analysis: full conversion of aryl iodide.

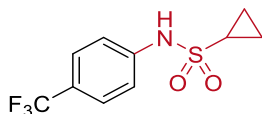
^1H NMR (400 MHz, CDCl_3) δ 7.92 – 7.86 (m, 2H), 7.82 (br. s, 1H), 7.58 (t, $J = 7.5$ Hz, 1H), 7.51 – 7.44 (m, 4H), 7.22 (d, $J = 8.2$ Hz, 2H). ^{13}C NMR (101 MHz, CDCl_3) δ 139.82, 138.57, 133.60, 129.39, 127.21, 126.89 (d, $J = 32.8$ Hz), 126.68 (q, $J = 3.7$ Hz), 123.89 (q, $J = 271.7$ Hz), 119.78. ^{19}F NMR (564 MHz, CDCl_3) δ -62.26. These data are in full agreement with those reported in literature.⁵²



4-(Trifluoromethyl)-N-(4-(trifluoromethyl)phenyl)benzenesulfonamide (43) was obtained from 4-iodobenzotrifluoride (81.6 mg, 300 μmol) and 4-(trifluoromethyl)benzenesulfonamide (101.3 mg, 450 μmol). Purification by flash chromatography (10% ethyl acetate/hexane) afforded the title compound as a white solid (95.2 mg, 258 μmol , 86%).

Reaction time: 48 hours. NMR analysis: full conversion of aryl iodide.

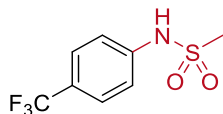
^1H NMR (400 MHz, CDCl_3) δ 7.99 (d, $J = 8.2$ Hz, 2H), 7.75 (d, $J = 8.3$ Hz, 2H), 7.61 (s, 1H), 7.52 (d, $J = 8.4$ Hz, 2H), 7.22 (d, $J = 8.4$ Hz, 2H). ^{13}C NMR (101 MHz, CDCl_3) δ 142.11, 139.09, 135.25 (q, $J = 33.3$ Hz), 127.74, 127.53 (q, $J = 32.8$ Hz), 126.91 (q, $J = 3.8$ Hz), 126.60 (q, $J = 3.7$ Hz), 123.73 (q, $J = 271.8$ Hz), 122.97 (q, $J = 273.2$ Hz), 120.20. ^{19}F NMR (564 MHz, CDCl_3) δ -62.40, -63.29. HRMS (EI) m/z calcd for $\text{C}_{14}\text{H}_9\text{F}_6\text{NO}_2\text{S}$ [(M) $^+$] 369.0258, found: 369.0256.



N-(4-(Trifluoromethyl)phenyl)cyclopropanesulfonamide (44) was obtained from 4-iodobenzotrifluoride (81.6 mg, 300 μmol) and cyclopropanesulfonamide (54.5 mg, 450 μmol). Purification by flash chromatography (gradient 10-20% ethyl acetate/hexane) afforded the title compound as a white solid (63.7 mg, 240 μmol , 80%).

Reaction time: 23 hours. NMR yield: 83%.

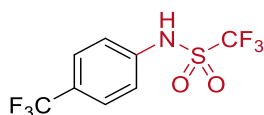
^1H NMR (400 MHz, CDCl_3) δ 7.59 (d, $J = 8.5$ Hz, 2H), 7.35 (d, $J = 8.5$ Hz, 2H), 7.16 (s, 1H), 2.60 – 2.51 (m, 1H), 1.27 – 1.21 (m, 2H), 1.05 – 0.98 (m, 2H). ^{13}C NMR (101 MHz, CDCl_3) δ 140.26, 126.87 (q, $J = 32.9$ Hz), 126.82 (q, $J = 3.8$ Hz), 123.94 (q, $J = 271.3$ Hz), 119.95, 30.41, 5.84. ^{19}F NMR (564 MHz, CDCl_3) δ -62.22. HRMS (EI) m/z calcd for $\text{C}_{10}\text{H}_{10}\text{F}_3\text{NO}_2\text{S}$ [(M) $^+$] 265.0384, found: 265.0390.



N-(4-(Trifluoromethyl)phenyl)methanesulfonamide (45) was obtained from 4-iodobenzotrifluoride (81.6 mg, 300 μmol) and methanesulfonamide (42.8 mg, 450 μmol). Purification by flash chromatography (gradient 10-20% ethyl acetate/hexane) afforded the title compound as a white solid (55.6 mg, 232 μmol , 77%).

Reaction time: 22 hours. NMR yield: 78%.

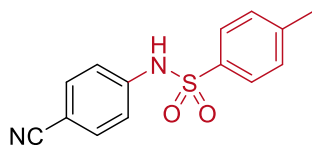
^1H NMR (400 MHz, CDCl_3) δ 7.65 – 7.57 (m, 2H), 7.39 (s, 1H), 7.36 – 7.29 (m, 2H), 3.10 (s, 3H). ^{13}C NMR (101 MHz, CDCl_3) δ 140.07, 127.04 (q, $J = 3.7$ Hz), 126.93 (q, $J = 32.9$ Hz), 123.89 (q, $J = 271.5$ Hz), 119.13, 39.88. ^{19}F NMR (564 MHz, CDCl_3) δ -62.27. These data are in full agreement with those reported in literature.⁵²



1,1,1-Trifluoro-N-(4-(trifluoromethyl)phenyl)methanesulfonamide (46) was obtained from 4-iodobenzotrifluoride (81.6 mg, 300 μmol) and trifluoromethanesulfonamide (42.8 mg, 450 μmol). Purification by flash chromatography (gradient 5-20% ethyl acetate/hexane) afforded the title compound as a white solid (63.2 mg, 216 μmol , 72%).

Reaction time: 115 hours. NMR yield: 74%.

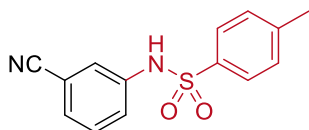
^1H NMR (400 MHz, CDCl_3) δ 7.66 (d, $J = 8.4$ Hz, 2H), 7.39 (d, $J = 8.4$ Hz, 2H), 7.29 (s, 1H). ^{13}C NMR (101 MHz, CDCl_3) δ 137.12, 129.32 (q, $J = 33.2$ Hz), 127.04 (q, $J = 3.7$ Hz), 123.5 (q, $J = 271.5$ Hz), 122.21, 119.6 (q, $J = 322.7$ Hz). ^{19}F NMR (377 MHz, CDCl_3) δ -62.65, -75.49. These data are in full agreement with those reported in literature.⁵³



N-(4-Cyanophenyl)-4-methylbenzenesulfonamide (47) was obtained from 4-iodobenzonitrile (68.7 mg, 300 μmol) and *p*-toluenesulfonamide (77.0 mg, 450 μmol). Purification by flash chromatography (gradient 1-3% ethyl acetate/dichloromethane) afforded the title compound as a white solid (67.3 mg, 247 μmol , 82%).

Reaction time: 18 hours. NMR analysis: full conversion of aryl iodide.

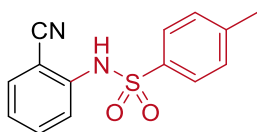
^1H NMR (400 MHz, CDCl_3) δ 7.72 (d, $J = 8.4$ Hz, 2H), 7.53 (d, $J = 8.7$ Hz, 2H), 7.28 (d, $J = 7.9$ Hz, 2H, contains residual solvent signal of CDCl_3), 7.15 (d, $J = 8.7$ Hz, 2H), 2.40 (s, 3H). ^{13}C NMR (101 MHz, CDCl_3) δ 145.00, 141.08, 135.64, 133.74, 130.19, 127.38, 119.44, 118.58, 107.87, 21.76. These data are in full agreement with those reported in literature.⁵⁴



***N*-(3-Cyanophenyl)-4-methylbenzenesulfonamide (48)** was obtained from 3-iodobenzonitrile (68.7 mg, 300 μmol) and *p*-toluenesulfonamide (77.0 mg, 450 μmol). Purification by flash chromatography (gradient 10-20% ethyl acetate/hexane) afforded the title compound as a white solid (65.3 mg, 240 μmol , 80%).

Reaction time: 20 hours. NMR yield: 80%.

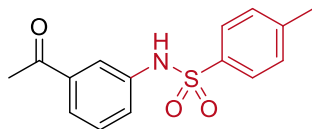
^1H NMR (400 MHz, CDCl_3) δ 7.72 (d, $J = 8.4$ Hz, 2H), 7.66 (s, 1H), 7.40 – 7.38 (n, 1H), 7.37 – 7.34 (m, 3H), 7.27 (d, $J = 8.0$ Hz, 2H), 2.39 (s, 3H). ^{13}C NMR (101 MHz, CDCl_3) δ 144.75, 137.79, 135.38, 130.35, 130.06, 128.47, 127.23, 124.98, 123.47, 118.13, 113.33, 21.63. These data are in full agreement with those reported in literature.⁵⁵



***N*-(2-Cyanophenyl)-4-methylbenzenesulfonamide (49)** was obtained from 2-iodobenzonitrile (68.7 mg, 300 μmol) and *p*-toluenesulfonamide (77.0 mg, 450 μmol). Purification by flash chromatography (gradient 10-15% ethyl acetate/hexane) afforded the title compound as a colorless oil (66.2 mg, 243 μmol , 81%).

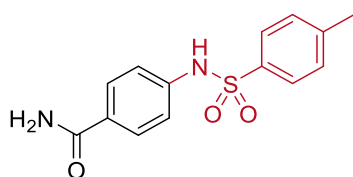
Reaction time: 32 hours. NMR yield: 82%.

^1H NMR (400 MHz, CDCl_3) δ 7.75 – 7.67 (m, 3H), 7.58 – 7.52 (m, 1H), 7.47 (dd, $J = 7.8$ Hz, 1.6 Hz, 1H), 7.28 – 7.23 (m, 2H, contains residual solvent signal of CDCl_3), 7.17 (td, $J = 7.6$ Hz, 1.1 Hz, 1H), 7.13 (br. s, 1H), 2.39 (s, 3H). ^{13}C NMR (101 MHz, CDCl_3) δ 144.78, 139.35, 135.43, 134.22, 132.80, 129.97, 127.39, 125.18, 121.72, 115.74, 104.26, 21.64. These data are in full agreement with those reported in literature.⁵⁶



N-(3-Acetylphenyl)-4-methylbenzenesulfonamide (50) was obtained from 3-iodoacetophenone (73.8 mg, 300 μmol) and *p*-toluenesulfonamide (77.0 mg, 450 μmol). Purification by flash chromatography (1st gradient 10-20% ethyl acetate/hexane; 2nd 15% ethyl acetate/hexane) afforded the title compound as a white solid (54.7 mg, 189 μmol , 63%). Reaction time: 18 hours. NMR yield: 89%.

¹H NMR (400 MHz, CDCl₃) δ 7.75 – 7.70 (m, 3H), 7.67 (t, J = 2.0 Hz, 1H), 7.46 – 7.36 (m, 2H), 7.32 – 7.23 (m, 2H, contains residual solvent signal of CDCl₃), 2.59 (s, 3H), 2.41 (s, 3H). ¹³C NMR (101 MHz, CDCl₃) δ 197.65, 144.36, 138.20, 137.40, 135.93, 129.93, 129.81, 127.40, 125.73, 125.16, 120.82, 26.82, 21.69. These data are in full agreement with those reported in literature.⁵⁴

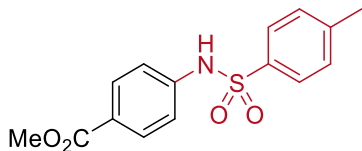


4-((4-Methylphenyl)sulfonamido)benzamide (51) was obtained from 4-iodobenzamide (74.1 mg, 300 μmol) and *p*-toluenesulfonamide (77.0 mg, 450 μmol). Purification by flash chromatography (gradient 80-100% ethyl acetate/hexane) afforded the title compound as a white solid (75.0 mg, 258 μmol , 86%).

Reaction time: 66 hours. NMR yield: 89%.

¹H NMR (400 MHz, DMSO) δ 10.59 (s, 1H), 7.82 (s, 1H), 7.72 (d, J = 8.7 Hz, 2H), 7.69 (d, J = 8.3 Hz, 2H), 7.35 (d, J = 8.1 Hz, 2H), 7.25 (s, 1H), 7.13 (d, J = 8.7 Hz, 2H), 2.32 (s, 3H). ¹³C NMR (101 MHz, DMSO-d₆) δ 167.23, 143.57, 140.58, 136.47, 129.83, 129.33, 128.76, 126.76, 118.16, 20.98.

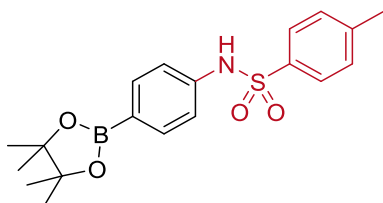
These data are in full agreement with those reported in literature.⁵⁷



Methyl 4-((4-methylphenyl)sulfonamido)benzoate (52) was obtained from methyl 4-iodobenzoate (78.6 mg, 300 μmol) and *p*-toluensulfonamide (77.0 mg, 450 μmol). Purification by flash chromatography (gradient 15-30% ethyl acetate/hexane) afforded the title compound as a white solid (76.5 mg, 251 μmol , 84%).

Reaction time: 24 hours. NMR yield: 95%.

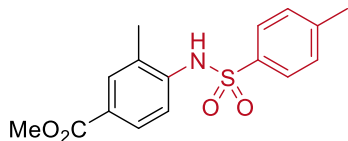
^1H NMR (400 MHz, DMSO- d_6) δ 10.80 (br. s, 1H), 7.81 (d, J = 8.8 Hz, 2H), 7.70 (d, J = 8.3 Hz, 2H), 7.36 (d, J = 8.2 Hz, 2H), 7.20 (d, J = 8.8 Hz, 2H), 3.77 (s, 3H), 2.33 (s, 3H). ^{13}C NMR (101 MHz, DMSO- d_6) δ 165.66, 143.71, 142.52, 136.36, 130.63, 129.87, 126.74, 124.25, 118.08, 51.95, 20.97. These data are in full agreement with those reported in literature.⁵⁴



4-Methyl-N-(4-(4,4,5,5-tetramethyl-1,3,2-dioxaborolan-2-yl)phenyl)benzenesulfonamide (53) was obtained from 2-(4-iodophenyl)-4,4,5,5-tetramethyl-1,3,2-dioxaborolane (99.0 mg, 300 μmol) and *p*-toluensulfonamide (77.0 mg, 450 μmol). Purification by flash chromatography (gradient 15-25% ethyl acetate/hexane) afforded the title compound as a white solid (80.1 mg, 215 μmol , 72%).

Reaction time: 22 hours. NMR analysis: full conversion of aryl iodide.

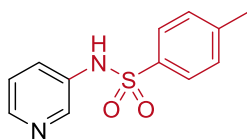
^1H NMR (400 MHz, CDCl_3) δ 7.71 – 7.64 (m, 4H), 7.21 (d, J = 8.6 Hz, 2H), 7.06 (d, J = 8.5 Hz, 2H), 6.74 (s, 1H), 2.36 (s, 3H), 1.31 (s, 12H). ^{13}C NMR (101 MHz, CDCl_3) δ 144.16, 139.36, 136.14, 136.05, 129.84, 127.40, 119.57, 83.98, 24.98, 21.68. The signal corresponding to the $\text{C}(\text{sp}^2)\text{-B}$ carbon was detected at 124.92 ppm in a HMBC experiment. These data are in full agreement with those reported in literature.⁵⁸



Methyl 3-methyl-4-((4-methylphenyl)sulfonamido)benzoate (54) was obtained from methyl 4-iodo-3-methylbenzoate (77.8 mg, 300 μmol) and *p*-toluenesulfonamide (77.0 mg, 450 μmol). Purification by flash chromatography (gradient 10-15% ethyl acetate/hexane) afforded the title compound as a white solid (74.9 mg, 235 μmol , 78%).

Reaction time: 72 hours. NMR analysis: full conversion of aryl iodide.

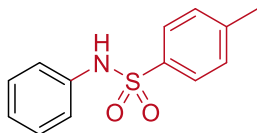
^1H NMR (400 MHz, CDCl_3) δ 7.81 – 7.77 (m, 1H), 7.77 – 7.74 (m, 1H), 7.68 (d, $J = 8.4$ Hz, 2H), 7.47 (d, $J = 8.5$ Hz, 1H), 7.22 (d, $J = 7.9$ Hz, 2H), 7.05 (s, 1H), 3.86 (s, 3H), 2.37 (s, 3H), 2.09 (s, 3H). ^{13}C NMR (101 MHz, CDCl_3) δ 166.61, 144.33, 139.17, 136.28, 132.16, 129.84, 128.80, 128.58, 127.16, 126.55, 120.96, 52.12, 21.59, 17.58. HRMS (EI) m/z calcd for $\text{C}_{16}\text{H}_{17}\text{NO}_4\text{S}$ [(M) $^+$] 319.0878, found: 319.0877.



4-Methyl-N-(pyridin-3-yl)benzenesulfonamide (55) was obtained from 3-iodopyridine (61.5 mg, 300 μmol) and *p*-toluenesulfonamide (77.0 mg, 450 μmol). Purification by flash chromatography (gradient 15-50% ethyl acetate/hexane) afforded the title compound as a white solid (55.6 mg, 224 μmol , 74%).

Reaction time: 30 hours. NMR analysis: full conversion of aryl iodide; 76% NMR yield.

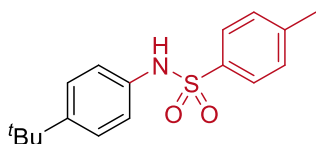
^1H NMR (400 MHz, DMSO-d_6) δ 10.50 (br. s, 1H), 8.27 (d, $J = 2.7$ Hz, 1H), 8.24 (dd, $J = 4.7, 1.5$ Hz, 1H), 7.65 (d, $J = 8.1$ Hz, 2H), 7.49 (ddd, $J = 8.3, 2.7, 1.5$ Hz, 1H), 7.35 (d, $J = 8.1$ Hz, 2H), 7.27 (dd, $J = 8.1, 4.7$ Hz, 1H), 2.32 (s, 3H). ^{13}C NMR (101 MHz, DMSO-d_6) δ 145.69, 144.10, 142.12, 136.63, 134.93, 130.32, 127.68, 127.18, 124.44, 21.43. These data are in full agreement with those reported in literature.⁵⁹



4-Methyl-N-phenylbenzenesulfonamide (56) was obtained from iodobenzene (61.2 mg, 300 μmol) and *p*-toluenesulfonamide (77.0 mg, 450 μmol). Purification by flash chromatography (gradient 10-20% ethyl acetate/hexane) afforded the title compound as a white solid (66.4 mg, 268 μmol , 89%).

Reaction time: 68 hours. NMR analysis: full conversion of aryl iodide.

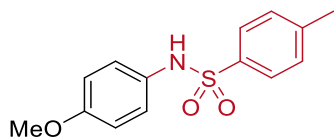
^1H NMR (400 MHz, CDCl_3) δ 7.68 (d, $J = 8.3$ Hz, 2H), 7.26 – 7.19 (m, 3H, contains residual solvent signal of CDCl_3), 7.12 – 7.06 (m, 4H), 2.37 (s, 3H). ^{13}C NMR (101 MHz, CDCl_3) δ 144.01, 136.67, 136.12, 129.78, 129.42, 127.40, 125.38, 121.60, 21.67. These data are in full agreement with those reported in literature.⁵⁴



N-(4-(*tert*-Butyl)phenyl)-4-methylbenzenesulfonamide (57) was obtained from 1-iodo-4-*tert*-butylbenzene (78.0 mg, 300 μmol) and *p*-toluenesulfonamide (77.0 mg, 450 μmol). Purification by flash chromatography (gradient 10-20% ethyl acetate/hexane) afforded the title compound as a white solid (75.7 mg, 249 μmol , 83%).

Reaction time: 68 hours. NMR yield: not calculated due to signal overlap.

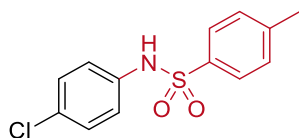
^1H NMR (400 MHz, CDCl_3) δ 7.67 (d, $J = 8.4$ Hz, 2H), 7.26 – 7.20 (m, 4H), 6.98 (d, $J = 8.6$ Hz, 2H), 6.73 (s, 1H), 2.38 (s, 3H), 1.25 (s, 9H). ^{13}C NMR (101 MHz, CDCl_3) δ 148.57, 143.85, 136.47, 133.81, 129.74, 127.39, 126.30, 121.72, 34.49, 31.41, 21.70. These data are in full agreement with those reported in literature.³⁶



***N*-(4-Methoxyphenyl)-4-methylbenzenesulfonamide (58)** was obtained from 4-iodoanisole (70.2 mg, 300 μ mol) and *p*-toluenesulfonamide (77.0 mg, 450 μ mol). Purification by flash chromatography (gradient 10-25% ethyl acetate/hexane) afforded the title compound as a white solid (69.6 mg, 251 μ mol, 84%).

Reaction time: 43 hours. NMR analysis: 95% conversion of aryl iodide.

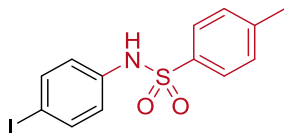
^1H NMR (400 MHz, CDCl_3) δ 7.59 (d, J = 8.3 Hz, 2H), 7.21 (d, J = 7.8 Hz, 2H), 6.98 (d, J = 8.9 Hz, 2H), 6.75 (d, J = 9.0 Hz, 2H), 6.62 (br. s, 1H), 3.75 (s, 3H), 2.38 (s, 3H). ^{13}C NMR (101 MHz, CDCl_3) δ 158.05, 143.80, 136.09, 129.68, 129.01, 127.45, 125.55, 114.52, 55.53, 21.68. These data are in full agreement with those reported in literature.⁵⁴



***N*-(4-Chlorophenyl)-4-methylbenzenesulfonamide (59)** was obtained from 1-chloro-4-iodobenzene (71.6 mg, 300 μ mol) and *p*-toluenesulfonamide (77.0 mg, 450 μ mol). Purification by flash chromatography (gradient 10-15% ethyl acetate/hexane) afforded the title compound as a colorless oil (70.3 mg, 250 μ mol, 83%).

Reaction time: 24 hours. NMR yield: 86%.

^1H NMR (400 MHz, CDCl_3) δ 7.68 (d, J = 8.4 Hz, 2H), 7.44 (s, 1H), 7.23 (d, J = 8.4 Hz, 2H), 7.20 – 7.14 (m, 2H), 7.07 – 7.01 (m, 2H), 2.37 (s, 3H). ^{13}C NMR (101 MHz, CDCl_3) δ 144.25, 135.57, 135.20, 130.78, 129.83, 129.41, 127.30, 122.78, 21.59. These data are in full agreement with those reported in literature.⁶⁰



***N*-(4-Iodophenyl)-4-methylbenzenesulfonamide (60)** was obtained from 1,4-diiodobenzene (99.0 mg, 300 μmol) and *p*-toluenesulfonamide (77.0 mg, 450 μmol). Purification by flash chromatography (gradient 10-20% ethyl acetate/hexane) afforded the title compound as a white solid (68.3 mg, 183 μmol , 61%).

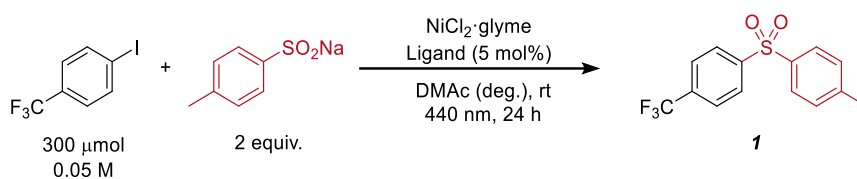
Reaction time: 96 hours. NMR analysis: 85% conversion of aryl iodide; 65% NMR yield.

^1H NMR (400 MHz, CDCl_3) δ 7.66 (d, $J = 8.4$ Hz, 2H), 7.52 (d, $J = 8.7$ Hz, 2H), 7.24 (d, $J = 8.0$ Hz, 2H), 7.00 (s, 1H), 6.84 (d, $J = 8.7$ Hz, 2H), 2.39 (s, 3H). ^{13}C NMR (101 MHz, CDCl_3) δ 144.38, 138.44, 136.53, 135.79, 129.95, 127.38, 123.21, 89.30, 21.71. These data are in full agreement with those reported in literature.⁶⁰

6.6.11 Heterogeneous visible-light-mediated nickel catalysis and recycling studies

Screening experiments

Table 6.23. Comparison of czbpy and poly-czbpy for the coupling of 4-iodobenzotrifluoride and sodium *p*-toluensulfinate.^a



Entry	Ligand	NiCl ₂ ·glyme	Conversion [%] ^b	1 [%] ^c
1	czbpy	2.5 mol%	97	84
2	czbpy	5 mol%	97	91
3	poly-czbpy	2.5 mol%	96	88
4	poly-czbpy	5 mol%	97	77

^aReaction conditions: 4-iodobenzotrifluoride (300 μmol), sodium *p*-toluensulfinate (600 μmol), NiCl₂·glyme (7.5-15 μmol), ligand (7.4 mg, 15 μmol), DMAc (anhydrous, 6 mL), 440 nm LED (2 lamps at full power). ^bConversion of 4-iodobenzotrifluoride determined by ¹H-NMR using 1,3,5-trimethoxybenzene as internal standard. ^cNMR yields determined by ¹H-NMR using 1,3,5-trimethoxybenzene as internal standard. glyme = 1,2-dimethoxyethane. czbpy = 5,5'-dicarbazolyl-2,2'-bipyridyl.

Table 6.24. Comparison of czbpy and poly-czbpy for the coupling of 4-iodobenzotrifluoride and *N*-Boc-proline.^a

Entry	Ligand	NiCl ₂ ·glyme	Conversion [%] ^b	2 [%] ^c	Ar-H [%] ^c	Ar-Cl [%] ^c
1	czbpy	2.5 mol%	98	76	14	3
2	czbpy	5 mol%	>99	88	9	n.d.
3	poly-czbpy	2.5 mol%	97	68	7	n.d.
4	poly-czbpy	5 mol%	75	53	18	n.d.

^aReaction conditions: 4-iodobenzotrifluoride (300 μmol), *N*-Boc-proline (450 μmol), *N*-tert-butylisopropylamine (BIPA, 450 μmol), NiCl₂·glyme (7.5-15 μmol), ligand (7.4 mg, 15 μmol), DMSO (anhydrous, 6 mL), 440 nm LED (2 lamps at full power). ^bConversion of 4-iodobenzotrifluoride determined by ¹H-NMR using 1,3,5-trimethoxybenzene as internal standard. ^cNMR yields determined by ¹H-NMR using 1,3,5-trimethoxybenzene as internal standard. glyme = 1,2-dimethoxyethane. czbpy = 5,5'-dicarbazolyl-2,2'-bipyridyl.

Table 6.25. Comparison of czbpy and poly-czbpy for the coupling of 4-iodobenzotrifluoride and *N*-Boc-proline.^a

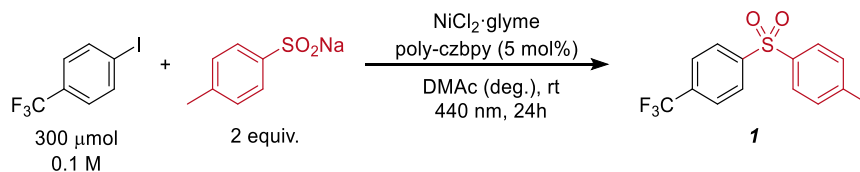
Entry	Ligand	NiCl ₂ ·glyme	Conversion [%] ^b	3 [%] ^c
1	czbpy	2.5 mol%	>99	91
2	czbpy	5 mol%	99	90
3	poly-czbpy	2.5 mol%	>99	82
4	poly-czbpy	5 mol%	99	59

^aReaction conditions: 4-iodobenzotrifluoride (300 μmol), *p*-toluene sulfonamide (450 μmol), 1,8-diazabicyclo[5.4.0]undec-7-ene (DBU, 450 μmol), NiCl₂·glyme (7.5-15 μmol), Ligand (7.4 mg, 15 μmol), DMSO (anhydrous, 6 mL), 440 nm LED (2 lamps at full power). ^bConversion of 4-iodobenzotrifluoride determined by ¹H-NMR using 1,3,5-trimethoxybenzene as internal standard. ^cNMR yields determined by ¹H-NMR using 1,3,5-trimethoxybenzene as internal standard. glyme = 1,2-dimethoxyethane. czbpy = 5,5'-dicarbazolyl-2,2'-bipyridyl.

General procedure for recycling experiments

An oven dried vial (13 x 80 mm) equipped with a stir bar was charged with poly-czbpy (7.3 mg, 5 mol% calculated using monomer's molecular weight), sodium *p*-toluenesulfinate (106.9 mg, 600 μ mol, 2 equiv) and NiCl₂·glyme (7.5-15 μ mol). Subsequently, 4-iodobenzotrifluoride (81.6 mg, 300 μ mol) and DMAc (anhydrous, 6 mL) were added and the vial was sealed with a septum and Parafilm. The reaction mixture was sonicated for 5 minutes, followed by stirring to obtain a fine dispersion of the solids, before degassing by bubbling nitrogen for 10 min. The mixture was stirred at 800 rpm and irradiated with two LED lamps (440 nm) at full power. After 24 hours, 1,3,5-trimethoxybenzene (50.5 mg, 300 μ mol, 1 equiv) was added and the mixture was stirred for 5 min. The reaction mixture was centrifuged at 3500 rpm for 15 min. The liquid phase was carefully separated and analyzed by ¹H-NMR. Poly-czbpy was washed two times with DMAc (anhydrous, 6 mL, followed by centrifugation at 3500 rpm for 15 min and separation of the liquid phase), lyophilized (overnight) and reused in the next reaction.

Reusability of the polymer poly-czbpy was tested with and without addition of NiCl₂·glyme in each cycle (Table 5.31).

Table 6.26. Reusability of the polymer poly-czbpy.^a

Nickel loading	5 mol% at each cycle	2.5 mol% at each cycle	5 mol% only at cycle 1	2.5 mol% only at cycle 1
Reaction Cycle	1 [%] ^b	1 [%] ^b	1 [%] ^b	1 [%] ^b
1	77	86	78	88
2	78	80	90	93
3	77	84	87	90
4	71	83	91	93
5	71	85	93	89
6	73	83	90	92
7	72	86	90	90
8	71	87	88	90
9	70	80	89	89
10	67	83	87	83

^aReaction conditions: 4-iodobenzotrifluoride (300 μmol), sodium *p*-toluenesulfonate (600 μmol), $\text{NiCl}_2\cdot\text{glyme}$ (7.5–15 μmol), poly-czbpy (7.3 mg, 15 μmol calculated using monomer's molecular weight), DMAc (anhydrous, 6 mL), 440 nm LED (2 lamps at full power). ^bNMR yields determined by ¹H-NMR using 1,3,5-trimethoxybenzene as internal standard. glyme = 1,2-dimethoxyethane.

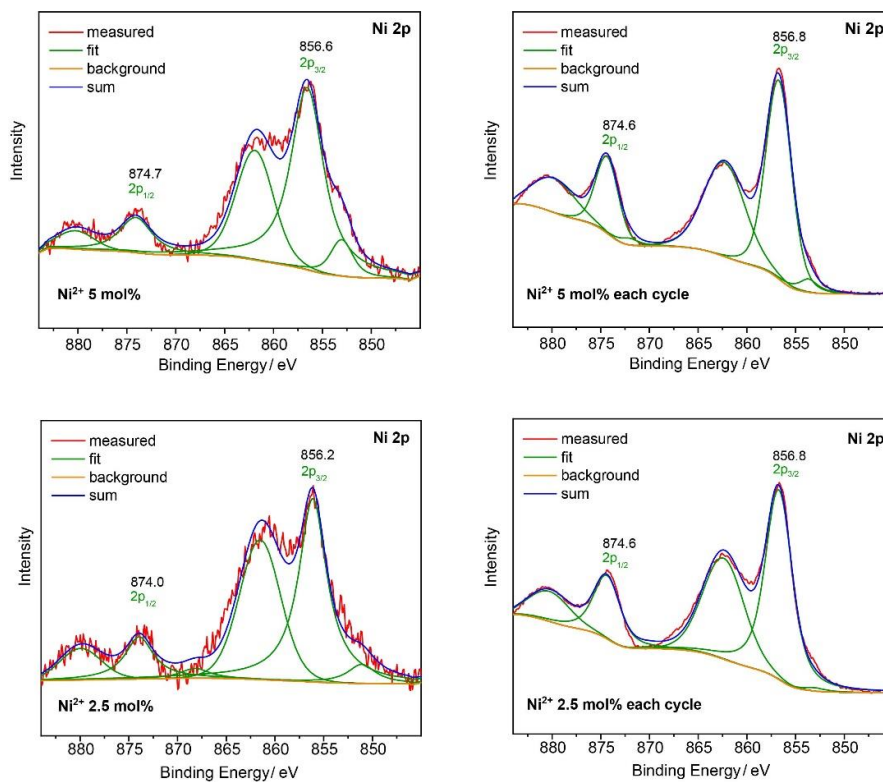


Figure 6.10. Ni 2p XPS spectra of recycled Ni@poly-czbp after 10 cycles applying 5 and 2.5 mol%, respectively.

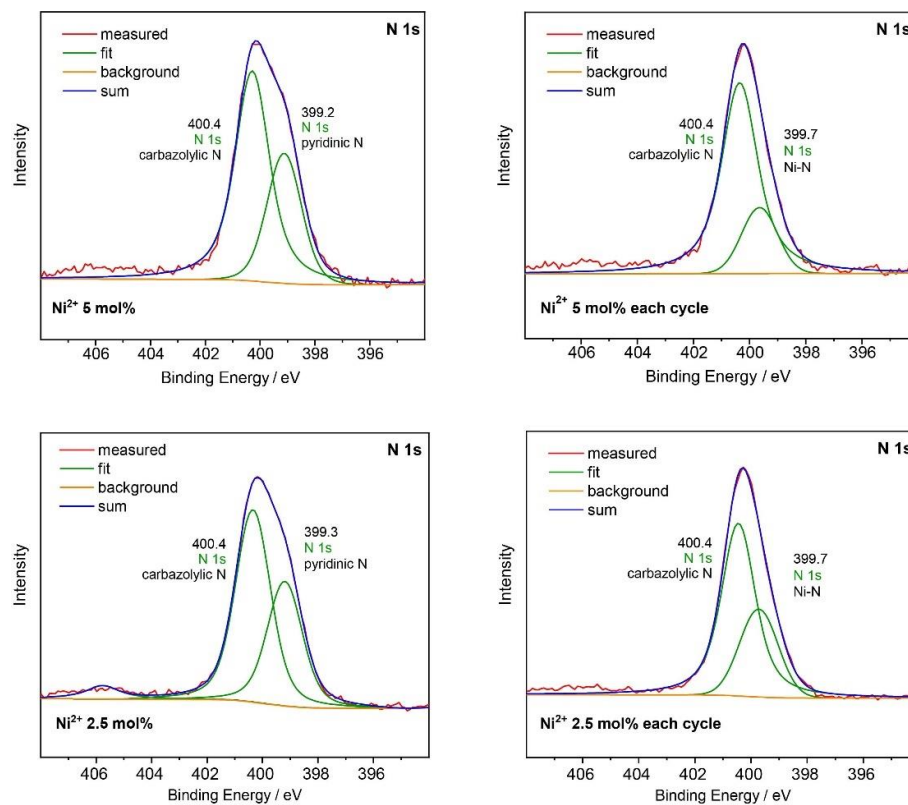
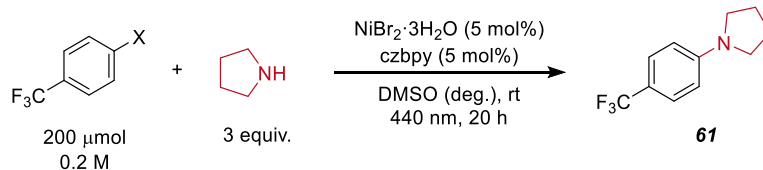


Figure 6.11. N 1s XPS spectra of recycled Ni@poly-czby after 10 cycles applying 5 and 2.5 mol%, respectively.

6.6.12 Unsuccessful coupling reactions using homogeneous visible-light-mediated nickel catalysis

Table 6.27. Screenings for the coupling of 4-halobenzotrifluorides and pyrrolidine.^{a, 16, 61}

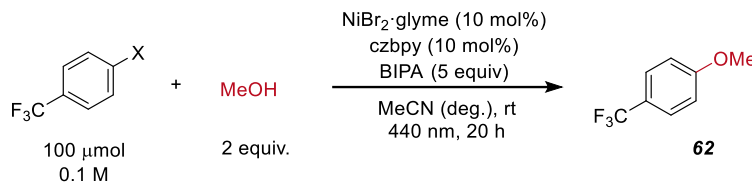


Entry	Aryl halide	Conversion [%] ^b	61 [%] ^c
1	Bromide	2	n.d.
2	Iodide	5	n.d.

^aReaction conditions: 4-iodobenzotrifluoride (200 μmol), pyrrolidine (600 μmol), $\text{NiBr}_2 \cdot 3\text{H}_2\text{O}$ (10 μmol), 5,5'-dicarbazoyl-2,2'-bipyridyl (czbpy, 10 μmol), DMSO (anhydrous, 1 mL), 440 nm LED (1 lamp at 50% power).

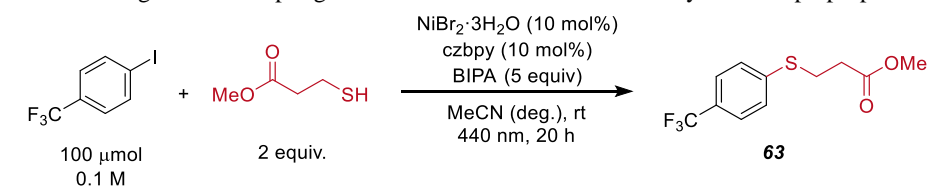
^bConversion of aryl halide determined by ¹H-NMR using 1,3,5-trimethoxybenzene as internal standard. ^cNMR yields determined by ¹H-NMR using 1,3,5-trimethoxybenzene as internal standard. n.d. = not detected.

Table 6.28. Screenings for the coupling of 4-halobenzotrifluorides and methanol.^{a, 62-63}



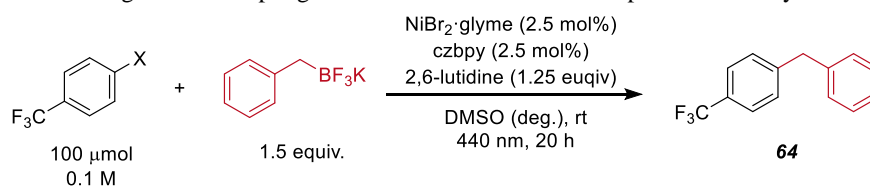
Entry	Aryl halide	Conversion [%] ^b	62 [%] ^c
1	Bromide	1	n.d.
2	Iodide	<1	n.d.

^aReaction conditions: aryl halide (100 μmol), methanol (100 μmol), $\text{NiBr}_2 \cdot \text{glyme}$ (10 μmol), 5,5'-dicarbazoyl-2,2'-bipyridyl (czbpy, 10 μmol), *N,N*-*tert*-butylisopropylamine (BIPA, 500 μmol), MeCN (anhydrous, 1 mL), 440 nm LED (1 lamp at 50% power). ^bConversion of aryl halide determined by ¹H-NMR using 1,3,5-trimethoxybenzene as internal standard. ^cNMR yields determined by ¹H-NMR using 1,3,5-trimethoxybenzene as internal standard. glyme = 1,2-dimethoxyethane. n.d. = not detected.

Table 6.29. Screenings for the coupling of 4-iodobenzotrifluoride and methyl 3-mercaptopropanoate.^{a, 63}

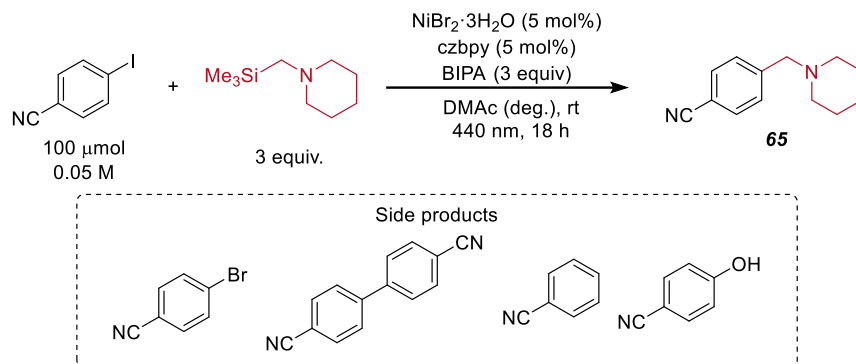
Entry	Conversion [%] ^b	63 [%] ^c
1	3	n.d.

^aReaction conditions: 4-iodobenzotrifluoride (100 μmol), methyl 3-mercaptopropanoate (200 μmol), NiBr₂·glyme (10 μmol), 5,5'-dicarbazoyl-2,2'-bipyridyl (czbpy, 10 μmol), *N,N*-*tert*-butylisopropylamine (BIPA, 500 μmol), MeCN (anhydrous, 1 mL), 440 nm LED (1 lamp at 50% power). ^bConversion of 4-iodobenzotrifluoride determined by ¹H-NMR using 1,3,5-trimethoxybenzene as internal standard. ^cNMR yields determined by ¹H-NMR using 1,3,5-trimethoxybenzene as internal standard. n.d. = not detected.

Table 6.30. Screenings for the coupling of 4-halobenzotrifluorides and potassium benzyltrifluoroborate.^{a, 64}

Entry	Aryl halide	Conversion [%] ^b	64 [%] ^c
1	Bromide	2	n.d.
2	Iodide	-	n.d.

^aReaction conditions: aryl halide (100 μmol), potassium benzyltrifluoroborate (150 μmol), NiBr₂·glyme (2.5 μmol), 5,5'-dicarbazoyl-2,2'-bipyridyl (czbpy, 2.5 μmol), 2,6-lutidine (125 μmol), DMSO (anhydrous, 1 mL), 440 nm LED (1 lamp at 50% power). ^bConversion of aryl halide determined by ¹H-NMR using 1,3,5-trimethoxybenzene as internal standard. ^cNMR yields determined by ¹H-NMR using 1,3,5-trimethoxybenzene as internal standard. glyme = 1,2-dimethoxyethane. n.d. = not detected.

Table 6.31. Screenings for the coupling of 4-iodobenzonitrile and 1-((trimethylsilyl)methyl)piperidine.^{a, 38}

Entry	Variation	Conversion [%] ^b	65 [%] ^c	Ar-Br [%] ^c	Ar-Ar [%] ^c	Ar-H [%] ^c	Ar-OH [%] ^c
1	None	>99	38	n.d.	25	10	n.d.
2	$\text{NiCl}_2 \cdot \text{glyme}$	>99	29	n.d.	23	20	n.d.
3	$\text{NiBr}_2 \cdot \text{glyme}$	88	28	8	22	11	1
4	No $\text{NiBr}_2 \cdot 3\text{H}_2\text{O}$	>99	n.d.	n.d.	n.d.	70	n.d.
5	Solvent = DMSO	53	n.d.	9	0	20	0
6	Solvent = DMF	>99	27	n.d.o.	10	n.d.o.	4
7	Aryl iodide = 4-iodoanisole	>99	32	n.d.	33	n.d.	n.d.
11	No czbpy	>99	7	n.d.	n.d.	25	n.d.
12	No light	-	n.d.	n.d.	n.d.	n.d.	n.d.

^aReaction conditions: 4-iodobenzonitrile (100 μmol), 1-((trimethylsilyl)methyl)piperidine (300 μmol), $\text{NiBr}_2 \cdot 3\text{H}_2\text{O}$ (5 μmol), 5,5'-dicarbazolyl-2,2'-bipyridyl (czbpy, 5 μmol), *N,N*-*tert*-butylisopropylamine (BIPA, 300 μmol), DMAc (anhydrous, 2 mL), 440 nm LED (1 lamp at full power). ^bConversion of 4-iodobenzonitrile determined by ¹H-NMR using 1,3,5-trimethoxybenzene as internal standard. ^cDetermined by ¹H-NMR using 1,3,5-trimethoxybenzene as internal standard. Glyme = 1,2-dimethoxyethane. n.d. = not detected. n.d.o. = not detected due to overlap with solvent's signals.

6.6.13 EPR Experiments

Sample Preparation

As a basis for EPR experiments and to investigate the influence of the involved reaction components, several samples were prepared in DMAc:

- A) czbpy
- B) czbpy + NiCl₂*glyme
- C) czbpy + NiCl₂*glyme + 4-iodobenzotriflouride
- D) czbpy + NiCl₂*glyme + sodium *p*-toluensulfinate
- E) czbpy + NiCl₂*glyme + 4-iodobenzotriflouride + sodium *p*-toluensulfinate
- F) czbpy + 4-iodobenzotriflouride

EPR samples were prepared in a glovebox (M. Braun, Germany) to minimize water infiltration (O₂<0.1ppm, H₂O<0.1ppm), using a concentration of 1.5 mM for all individual components. Samples were transferred into 3.9mm quartz tubes, sealed and immediately frozen in liquid N₂.

EPR Measurements

Continuous wave EPR measurements were performed on a home-built X-band spectrometer employing the following devices from Bruker (Karlsruhe, Germany): microwave bridge (ER 041 MR), microwave controller (ER 048 R), magnet power supply (ER 081 S), field controller (B-H-15), and a Super-HQ cavity resonator. Detection was carried out with a Lock-In Amplifier (SR 810 DSP) by Stanford Research Systems. Temperature stabilisation was accomplished by using a ESR910 He-cryostat and a temperature controller from Oxford instruments (Abingdon, UK).

Capturing the light-sensitive narrow EPR signal was achieved by illuminating the sample at room temperature with a Kessil PR160L-440 LED for several minutes, followed by quick insertion of the sample in the cold probehead (T ≈ 10K).

Table 6.32. Overview over the occurrence of the observed broad and narrow cw EPR signals dependent on the sample composition and illumination state.

Composition	dark		illuminated	
	Broad peak	Narrow peak	Broad peak	Narrow peak
czbpy	x		x	
czbpy + NiCl ₂ *glyme	x		x	
czbpy + NiCl ₂ *glyme + sodium <i>p</i> -toluenesulfinate	x		x	
czbpy + NiCl ₂ *glyme + 4-iodobenzotrifluoride	x		x	x
czbpy + NiCl ₂ *glyme + 4-iodobenzotrifluoride + sodium <i>p</i> -toluenesulfinate	x		x	x
czbpy + 4-iodobenzotrifluoride	x		x	

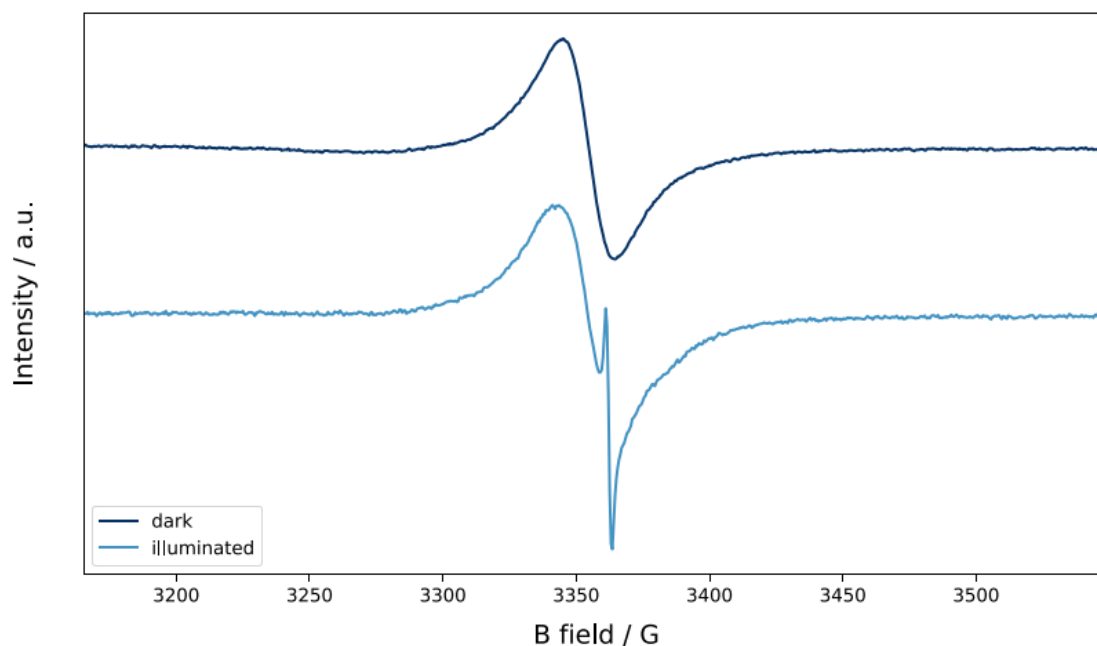


Figure 6.12. X band cw EPR spectra of czbpy + NiCl₂·glyme + 4-iodobenzotrifluoride after rapid freezing in dark conditions (dark blue) as well as after blue light illumination (light blue)

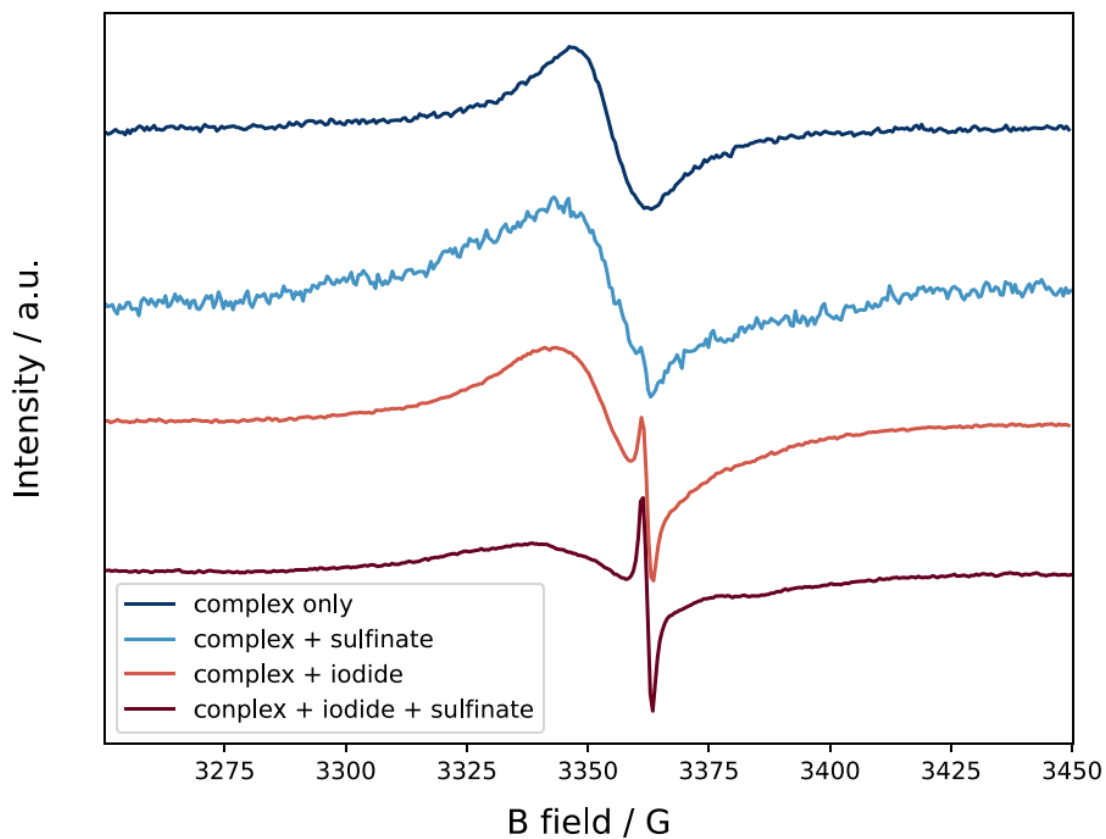


Figure 6.13. X band cw EPR spectra of czbpy + NiCl₂·glyme mixed with various combinations of sodium *p*-toluensulfinate and 4-iodobenzotrifluoride, all measured after illumination with blue light and rapid freezing.

Chapter 6

Copies of NMR spectra of isolated compounds

Copies of NMR spectra of isolated compounds are available in the Supporting Information through the website of the Publisher. DOI: <https://doi.org/10.26434/chemrxiv-2021-kt2wr>

6.7 References

1. Biffis, A.; Centomo, P.; Del Zotto, A.; Zecca, M., Pd Metal Catalysts for Cross-Couplings and Related Reactions in the 21st Century: A Critical Review. *Chem. Rev.* **2018**, *118* (4), 2249-2295.
2. Ruiz-Castillo, P.; Buchwald, S. L., Applications of Palladium-Catalyzed C-N Cross-Coupling Reactions. *Chem. Rev.* **2016**, *116* (19), 12564-12649.
3. Tasker, S. Z.; Standley, E. A.; Jamison, T. F., Recent advances in homogeneous nickel catalysis. *Nature* **2014**, *509* (7500), 299-309.
4. Ananikov, V. P., Nickel: The "Spirited Horse" of Transition Metal Catalysis. *ACS Catal.* **2015**, *5* (3), 1964-1971.
5. Twilton, J.; Le, C.; Zhang, P.; Shaw, M. H.; Evans, R. W.; MacMillan, D. W. C., The merger of transition metal and photocatalysis. *Nat. Rev. Chem.* **2017**, *1* (7), 0052.
6. Zhu, C.; Yue, H.; Jia, J.; Rueping, M., Nickel-Catalyzed C-Heteroatom Cross-Coupling Reactions under Mild Conditions via Facilitated Reductive Elimination. *Angew. Chem. Int. Ed.* **2021**, *60*, 17810.
7. Cavedon, C.; Seeberger, P. H.; Pieber, B., Photochemical Strategies for Carbon-Heteroatom Bond Formation. *Eur. J. Org. Chem.* **2019**, *2020* (10), 1379-1392.
8. Lan, G.; Quan, Y.; Wang, M.; Nash, G. T.; You, E.; Song, Y.; Veroneau, S. S.; Jiang, X.; Lin, W., Metal-Organic Layers as Multifunctional Two-Dimensional Nanomaterials for Enhanced Photoredox Catalysis. *J. Am. Chem. Soc.* **2019**, *141* (40), 15767-15772.
9. Zhu, Y. Y.; Lan, G.; Fan, Y.; Veroneau, S. S.; Song, Y.; Micheroni, D.; Lin, W., Merging Photoredox and Organometallic Catalysts in a Metal-Organic Framework Significantly Boosts Photocatalytic Activities. *Angew. Chem. Int. Ed.* **2018**, *57* (43), 14090-14094.
10. Pan, Y.; Zhang, N.; Liu, C. H.; Fan, S. L.; Guo, S.; Zhang, Z. M.; Zhu, Y. Y., Boosting Photocatalytic Activities for Organic Transformations through Merging Photocatalyst and Transition-Metal Catalyst in Flexible Polymers. *ACS Catal.* **2020**, *10* (20), 11758-11767.
11. Reischauer, S.; Strauss, V.; Pieber, B., Modular, Self-Assembling Metallaphotocatalyst for Cross-Couplings Using the Full Visible-Light Spectrum. *ACS Catal.* **2020**, *10* (22), 13269-13274.

12. Vijeta, A.; Casadevall, C.; Roy, S.; Reisner, E., Visible-Light Promoted C–O Bond Formation with an Integrated Carbon Nitride-Nickel Heterogeneous Photocatalyst. *Angew. Chem. Int. Ed.* **2021**, *60* (15), 8494-8499.
13. Zhao, X.; Deng, C. Y.; Meng, D.; Ji, H. W.; Chen, C. C.; Song, W. J.; Zhao, J. C., Nickel-Coordinated Carbon Nitride as a Metallaphotoredox Platform for the Cross-Coupling of Aryl Halides with Alcohols. *ACS Catal.* **2020**, *10* (24), 15178-15185.
14. Reischauer, S.; Pieber, B., Recyclable, Bifunctional Metallaphotocatalysts for C–S Cross-Coupling Reactions. *ChemPhotoChem* **2021**, *5*, 716.
15. Malik, J. A.; Madani, A.; Pieber, B.; Seeberger, P. H., Evidence for Photocatalyst Involvement in Oxidative Additions of Nickel-Catalyzed Carboxylate O-Arylations. *J. Am. Chem. Soc.* **2020**, *142* (25), 11042-11049.
16. Gisbertz, S.; Reischauer, S.; Pieber, B., Overcoming limitations in dual photoredox/nickel-catalysed C–N cross-couplings due to catalyst deactivation. *Nat. Catal.* **2020**, *3* (8), 611-620.
17. Qi, Z. H.; Ma, J., Dual Role of a Photocatalyst: Generation of Ni(0) Catalyst and Promotion of Catalytic C–N Bond Formation. *ACS Catal.* **2018**, *8* (2), 1456-1463.
18. Qin, Y.; Sun, R.; Gianoulis, N. P.; Nocera, D. G., Photoredox Nickel-Catalyzed C–S Cross-Coupling: Mechanism, Kinetics, and Generalization. *J. Am. Chem. Soc.* **2021**, *143* (4), 2005-2015.
19. Till, N. A.; Tian, L.; Dong, Z.; Scholes, G. D.; MacMillan, D. W. C., Mechanistic Analysis of Metallaphotoredox C–N Coupling: Photocatalysis Initiates and Perpetuates Ni(I)/Ni(III) Coupling Activity. *J. Am. Chem. Soc.* **2020**, *142* (37), 15830-15841.
20. Sun, R.; Qin, Y.; Ruccolo, S.; Schnedermann, C.; Costentin, C.; Daniel, G. N., Elucidation of a Redox-Mediated Reaction Cycle for Nickel-Catalyzed Cross Coupling. *J. Am. Chem. Soc.* **2019**, *141* (1), 89-93.
21. Till, N. A.; Oh, S.; MacMillan, D. W. C.; Bird, M. J., The Application of Pulse Radiolysis to the Study of Ni(I) Intermediates in Ni-Catalyzed Cross-Coupling Reactions. *J. Am. Chem. Soc.* **2021**, *143* (25), 9332-9337.
22. Ting, S. I.; Garakyaraghi, S.; Taliaferro, C. M.; Shields, B. J.; Scholes, G. D.; Castellano, F. N.; Doyle, A. G., (3)d-d Excited States of Ni(II) Complexes Relevant to Photoredox Catalysis: Spectroscopic Identification and Mechanistic Implications. *J. Am. Chem. Soc.* **2020**, *142* (12), 5800-5810.

23. Shields, B. J.; Kudisch, B.; Scholes, G. D.; Doyle, A. G., Long-Lived Charge-Transfer States of Nickel(II) Aryl Halide Complexes Facilitate Bimolecular Photoinduced Electron Transfer. *J. Am. Chem. Soc.* **2018**, *140* (8), 3035-3039.
24. Li, G.; Yang, L.; Liu, J. J.; Zhang, W.; Cao, R.; Wang, C.; Zhang, Z.; Xiao, J.; Xue, D., Light-Promoted C–N Coupling of Aryl Halides with Nitroarenes. *Angew. Chem. Int. Ed.* **2021**, *60* (10), 5230-5234.
25. Yang, L.; Lu, H. H.; Lai, C. H.; Li, G.; Zhang, W.; Cao, R.; Liu, F.; Wang, C.; Xiao, J.; Xue, D., Light-Promoted Nickel Catalysis: Etherification of Aryl Electrophiles with Alcohols Catalyzed by a Ni(II) -Aryl Complex. *Angew. Chem. Int. Ed.* **2020**, *59* (31), 12714-12719.
26. Sun, R.; Qin, Y.; Nocera, D. G., General Paradigm in Photoredox Nickel-Catalyzed Cross-Coupling Allows for Light-Free Access to Reactivity. *Angew. Chem. Int. Ed.* **2020**, *59* (24), 9527-9533.
27. Liang, H.-P.; Acharjya, A.; Anito, D. A.; Vogl, S.; Wang, T.-X.; Thomas, A.; Han, B.-H., Rhenium-Metalated Polypyridine-Based Porous Polycarbazoles for Visible-Light CO₂ Photoreduction. *ACS Catalysis* **2019**, *9* (5), 3959-3968.
28. Yue, H.; Zhu, C.; Rueping, M., Cross-Coupling of Sodium Sulfinates with Aryl, Heteroaryl, and Vinyl Halides by Nickel/Photoredox Dual Catalysis. *Angew. Chem. Int. Ed.* **2018**, *57* (5), 1371-1375.
29. Liu, N. W.; Hofman, K.; Herbert, A.; Manolikakes, G., Visible-Light Photoredox/Nickel Dual Catalysis for the Cross-Coupling of Sulfinic Acid Salts with Aryl Iodides. *Org. Lett.* **2018**, *20* (3), 760-763.
30. Cabrera-Afonso, M. J.; Lu, Z.-P.; Kelly, C. B.; Lang, S. B.; Dykstra, R.; Gutierrez, O.; Molander, G. A., Engaging sulfinate salts via Ni/photoredox dual catalysis enables facile Csp²–SO₂R coupling. *Chem. Sci.* **2018**, *9* (12), 3186-3191.
31. Chen, L.; Liang, J.; Chen, Z.-y.; Chen, J.; Yan, M.; Zhang, X.-j., A Convenient Synthesis of Sulfones via Light Promoted Coupling of Sodium Sulfinates and Aryl Halides. *Advanced Synthesis & Catalysis* **2019**, *361* (5), 956-960.
32. Wong, Y. S.; Tang, M. C.; Ng, M.; Yam, V. W., Toward the Design of Phosphorescent Emitters of Cyclometalated Earth-Abundant Nickel(II) and Their Supramolecular Study. *J. Am. Chem. Soc.* **2020**, *142* (16), 7638-7646.

Chapter 6

33. Alrefai, R.; Hörner, G.; Schubert, H.; Berkefeld, A., Broadly versus Barely Variable Complex Chromophores of Planar Nickel(II) from κ^3 -N,N',C and κ^3 -N,N',O Donor Platforms. *Organometallics* **2021**, *40* (8), 1163-1177.
34. Pieber, B.; Malik, J. A.; Cavedon, C.; Gisbertz, S.; Savateev, A.; Cruz, D.; Heil, T.; Zhang, G.; Seeberger, P. H., Semi-heterogeneous Dual Nickel/Photocatalysis using Carbon Nitrides: Esterification of Carboxylic Acids with Aryl Halides. *Angew. Chem. Int. Ed.* **2019**, *58* (28), 9575-9580.
35. Welin, E. R.; Le, C.; Arias-Rotondo, D. M.; McCusker, J. K.; MacMillan, D. W. C., Photosensitized, energy transfer-mediated organometallic catalysis through electronically excited nickel(II). *Science* **2017**, *355* (6323), 380-385.
36. Kim, T.; McCarver, S. J.; Lee, C.; MacMillan, D. W. C., Sulfonamidation of Aryl and Heteroaryl Halides through Photosensitized Nickel Catalysis. *Angew. Chem. Int. Ed.* **2018**, *57* (13), 3488-3492.
37. Tellis, J. C.; Primer, D. N.; Molander, G. A., Dual catalysis. Single-electron transmetalation in organoboron cross-coupling by photoredox/nickel dual catalysis. *Science* **2014**, *345* (6195), 433-6.
38. Remeur, C.; Kelly, C. B.; Patel, N. R.; Molander, G. A., Aminomethylation of Aryl Halides Using α -Silylamines Enabled by Ni/Photoredox Dual Catalysis. *ACS Catal.* **2017**, *7* (9), 6065-6069.
39. Gisbertz, S.; Pieber, B., Heterogeneous Photocatalysis in Organic Synthesis. *ChemPhotoChem* **2020**, *4* (7), 456-475.
40. Liang, H. P.; Acharjya, A.; Anito, D. A.; Vogl, S.; Wang, T. X.; Thomas, A.; Han, B. H., Rhenium-Metalated Polypyridine-Based Porous Polycarbazoles for Visible-Light CO₂ Photoreduction. *ACS Catal.* **2019**, *9* (5), 3959-3968.
41. Kim, W.; Kim, H. Y.; Oh, K., Electrochemical Radical–Radical Cross-Coupling Approach between Sodium Sulfinates and 2H-Indazoles to 3-Sulfonylated 2H-Indazoles. *Org. Lett.* **2020**, *22* (16), 6319-6323.
42. *Kessil Photoredox products overview* <https://www.kessil.com/photoreaction/PR160L.php>. **2019**.
43. Li, H.-Y.; Wu, J.; Zhou, X.-H.; Kang, L.-C.; Li, D.-P.; Sui, Y.; Zhou, Y.-H.; Zheng, Y.-X.; Zuo, J.-L.; You, X.-Z., Synthesis, structural characterization and photoluminescence

properties of rhenium(I) complexes based on bipyridine derivatives with carbazole moieties. *Dalton Tran.* 2009, pp 10563-10569.

44. Yang, X.; Shi, L.; Fu, H., Copper-Mediated Cascade Synthesis of Diaryl Sulfones via the Sandmeyer Reaction. *Synlett* **2014**, 25 (06), 847-852.

45. Phanindrudu, M.; Jaya, P.; Likhar, P. R.; Tiwari, D. K., Nano copper catalyzed synthesis of symmetrical/unsymmetrical sulfones from aryl/alkyl halides and p-toluenesulfonylmethylisocyanide: TosMIC as a tosyl source. *Tetrahedron* **2020**, 76 (25), 131263.

46. Nguyen, V. D.; Nguyen, V. T.; Haug, G. C.; Dang, H. T.; Arman, H. D.; Ermler, W. C.; Larionov, O. V., Rapid and Chemodivergent Synthesis of N-Heterocyclic Sulfones and Sulfides: Mechanistic and Computational Details of the Persulfate-Initiated Catalysis. *ACS Catal.* **2019**, 9 (5), 4015-4024.

47. Cacchi, S.; Fabrizi, G.; Goggiamani, A.; Parisi, L. M., Unsymmetrical Diaryl Sulfones through Palladium-Catalyzed Coupling of Aryl Iodides and Arenesulfinates. *Org. Lett.* **2002**, 4 (26), 4719-4721.

48. Lu, J.; Pattengale, B.; Liu, Q.; Yang, S.; Shi, W.; Li, S.; Huang, J.; Zhang, J., Donor-Acceptor Fluorophores for Energy-Transfer-Mediated Photocatalysis. *J. Am. Chem. Soc.* **2018**, 140 (42), 13719-13725.

49. Meng, J.-J.; Gao, M.; Wei, Y.-P.; Zhang, W.-Q., N-Heterocyclic Carbene-Catalyzed Aerobic Oxidative Direct Esterification of Aldehydes with Organoboronic Acids. *Chemistry – An Asian Journal* **2012**, 7 (5), 872-875.

50. Ackerman, L. K. G.; Martinez Alvarado, J. I.; Doyle, A. G., Direct C–C Bond Formation from Alkanes Using Ni-Photoredox Catalysis. *J. Am. Chem. Soc.* **2018**, 140 (43), 14059-14063.

51. Ye, F.; Berger, F.; Jia, H.; Ford, J.; Wortman, A.; Börgel, J.; Genicot, C.; Ritter, T., Aryl Sulfonium Salts for Site-Selective Late-Stage Trifluoromethylation. *Angew. Chem. Int. Ed.* **2019**, 58 (41), 14615-14619.

52. Meyer, D.; Jangra, H.; Walther, F.; Zipse, H.; Renaud, P., A third generation of radical fluorinating agents based on N-fluoro-N-arylsulfonamides. *Nat. Commun.* **2018**, 9 (1), 4888.

53. Thiam, A.; Iojoiu, C.; Leprêtre, J. C.; Sanchez, J. Y., Lithium salts based on a series of new aniliny-perfluorosulfonamide salts and their polymer electrolytes. *J. Power Sources* **2017**, *364*, 138-147.
54. Zhang, W.; Xie, J.; Rao, B.; Luo, M., Iron-Catalyzed N-Arylsulfonamide Formation through Directly Using Nitroarenes as Nitrogen Sources. *J. Org. Chem.* **2015**, *80* (7), 3504-3511.
55. Zhao, F.; Li, B.; Huang, H.; Deng, G.-J., Palladium-catalyzed N-arylsulfonamide formation from arylsulfonyl hydrazides and nitroarenes. *RSC Advances* **2016**, *6* (16), 13010-13013.
56. Michaelidou, S. S.; Koutentis, P. A., Detosylation of 3-amino-1-tosylindole-2-carbonitriles using DBU and thiophenol. *Tetrahedron* **2010**, *66* (16), 3016-3023.
57. Zhang, K.; Zhang, Y.; Liu, Q.; He, D.; Tian, J.; Zhou, H., Metal-Free One-Pot Synthesis of Sulfonamides from Nitroarenes and Arylsulfonyl Chlorides in Water. *ChemistrySelect* **2019**, *4* (25), 7413-7415.
58. Nitelet, A.; Thevenet, D.; Schiavi, B.; Hardouin, C.; Fournier, J.; Tamion, R.; Pannecoucke, X.; Jubault, P.; Poisson, T., Copper-Photocatalyzed Borylation of Organic Halides under Batch and Continuous-Flow Conditions. *Chem. Eur. J.* **2019**, *25* (13), 3262-3266.
59. Bordi, S.; Starr, J. T., Hydropyridylation of Olefins by Intramolecular Minisci Reaction. *Org. Lett.* **2017**, *19* (9), 2290-2293.
60. Fu, Y.; Li, Q.-Z.; Xu, Q.-S.; Hügél, H.; Li, M.-P.; Du, Z., NaI-Catalyzed Oxidative Amination of Aromatic Sodium Sulfinates: Synergetic Effect of Ethylene Dibromide and Air as Oxidants. *Eur. J. Org. Chem.* **2018**, *2018* (48), 6966-6970.
61. Corcoran, E. B.; Pirnot, M. T.; Lin, S.; Dreher, S. D.; DiRocco, D. A.; Davies, I. W.; Buchwald, S. L.; MacMillan, D. W. C., Aryl amination using ligand-free Ni(II) salts and photoredox catalysis. *Science* **2016**, *353* (6296), 279-283.
62. Terrett, J. A.; Cuthbertson, J. D.; Shurtleff, V. W.; MacMillan, D. W. C., Switching on elusive organometallic mechanisms with photoredox catalysis. *Nature* **2015**, *524*, 330-334.
63. Cavedon, C.; Madani, A.; Seeberger, P. H.; Pieber, B., Semiheterogeneous Dual Nickel/Photocatalytic (Thio)etherification Using Carbon Nitrides. *Org. Lett.* **2019**, *21* (13), 5331-5334.

64. Tellis, J. C.; Primer, D. N.; Molander, G. A., Single-electron transmetalation in organoboron cross-coupling by photoredox/nickel dual catalysis. *Science* **2014**, *345* (6195), 433-436.

Chapter 7

Discussion & Outlook

7.1 Discussion of the individual works in a common context

Cross-coupling reactions are essential tools for the synthesis of complex organic motifs, including, pharmaceuticals¹ and agrochemicals². To date, the majority of cross-coupling reactions proceed via palladium catalysis and many developments have enabled efficient couplings across a wide variety of substrate classes.³ Nevertheless, the increasing price and the shortage of rare noble metals has led to a scientific pursuit for more sustainable and abundant alternatives. Based on having similar electronic properties to palladium, nickel has shown promise as a capable candidate.⁴ In several cases nickel complexes have presented suitable reactivity⁵, yet for carbon-heteroatom cross-couplings high temperatures and tailored ancillary ligands⁶ are still required to induce the reductive elimination step of the thermodynamically stable key Ni^{II} intermediate.⁷⁻⁸ An alternative way to destabilized the Ni^{II} intermediate is by oxidation to a Ni^{III} species using stoichiometric oxidants. Currently, the growing societal interest in sustainability and green chemistry⁹ has evolved new methods for such oxidations using visible light photocatalysis. By merging nickel catalysis with visible light photocatalysis (metallaphotocatalysis), many efficient and synthetically attractive methods of various carbon-carbon and carbon-heteroatom bond formations have been showcased.¹⁰ However, these methodologies rely on iridium and ruthenium polypyridyl complexes and/or synthetic organic dyes which are expensive and unrecyclable.

The main motivation for this thesis was the development of viable protocols which omit unsustainable photocatalysts for metallaphotocatalyzed carbon-heteroatom bond formations. To reach this goal, different key aspects were defined, and milestones were achieved during the thesis (Figure 7.1). The main focus of the work was the replacement of the typically applied iridium or ruthenium complexes for dual nickel/photocatalyzed cross-couplings. Such a replacement should be easily recyclable. In an ideal case a fully recyclable catalyst system, where also the nickel catalyst can be reused, would be developed. Initially, a heterogeneous semiconductor material would be synthesized and tested as surrogate of the noble metal photocatalyst complexes. Afterwards a tailor-made ligand design and synthesis

of a microporous organic polymer version of the designed ligand should enable a fully recyclable (photo)catalyst material for visible light-mediated nickel catalyzed carbon-heteroatom cross-couplings without the need of an exogenous photocatalyst.

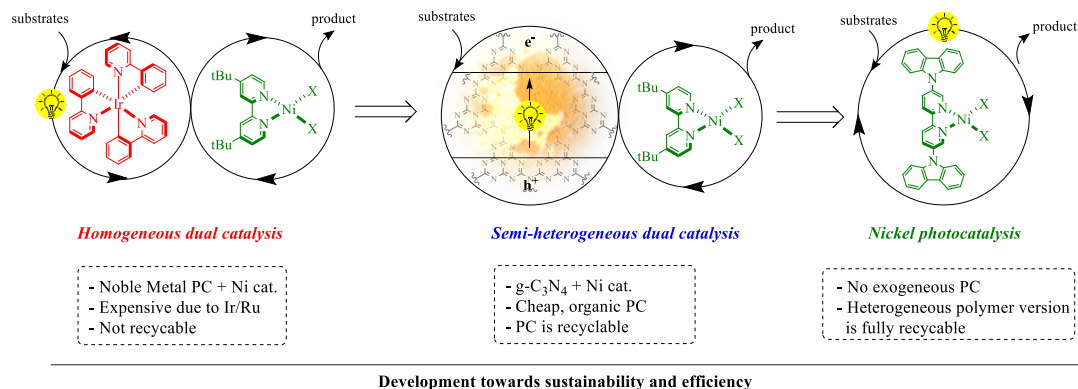


Figure 7.1. Development of dual nickel/photocatalytic cross-couplings using more sustainable and cost-efficient methods.

In stark contrast to conventional catalysis, where homogeneous catalysts are not able to be simply substituted by a heterogeneous material, semiconductors have already proven to be promising alternatives to homogeneous photocatalysts for artificial photosynthesis, waste water treatment, as well as organic synthesis due to their high stability and recyclability. These concepts can be found in Chapter 2, which was published as a review in *ChemPhotoChem*, and gives an overview about “Heterogeneous photocatalysis in organic synthesis”. In summation, upon light illumination a charge separation in the semiconductor is induced that generates an excited electron and an electron hole, which can participate in single electron transfer events. These electron-hole pairs can trigger the same reactions as the excited states of homogeneous photocatalysts. Semiconductors tunability makes them appealing substitutes for rare noble metal complexes in photocatalysis. Such materials that include microporous materials, such as conjugated organic polymers, covalent organic frameworks, and metal organic frameworks and can be tuned and designed on a molecular level.

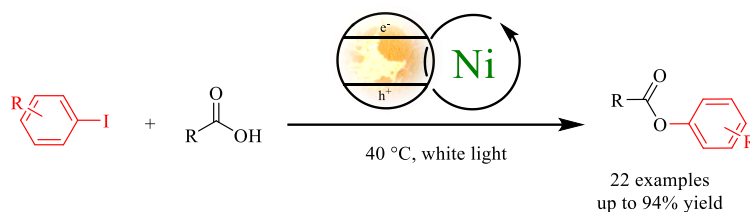
As a result of the acquired overview in Chapter 2, I focused on carbon nitrides, a class of organic semiconductors of rare metal complexes. The optical and electronic properties of carbon nitrides, can be tuned to fit the requirements of a specific reaction by manipulating the precursors and synthetic conditions of the polymerization. I used these organic

semiconductors for dual nickel/photocatalytic cross-couplings in a semi-heterogeneous procedure (Chapter 3-5). In this way, not only a recyclable photocatalyst for C–N and C–O bond formations was introduced, but for dual nickel/photocatalytic aryl amination, the scope was expanded by overcoming limitations for the coupling of electron-rich and electron-neutral aryl halides. The achievement was possible due to enhanced visible light absorption of the applied carbon nitride material and the associated avoidance of catalyst deactivation through nickel-black formation. Additionally, a special flow set-up using an oscillatory pump and a microstructured plug flow photoreactor enabled semi-heterogeneous C–N cross-couplings on a multi-gram scale with short reaction times.

In the final chapter (Chapter 6) I describe the development of a ligand (czbpy), which combines a chelating bipyridyne unit and a chromophoric, redox active carbazole moiety that results in a nickel complex that catalyzes different carbon–heteroatom couplings in the presence of visible-light without an additional photocatalyst. By this means a completely new paradigm for visible-light mediated nickel catalyzed cross-couplings was established. Subsequently, a conjugated organic polymer of czbpy was synthesized and in this way a fully recyclable catalyst system for cross-coupling reactions obtained.

7.2 Semi-heterogeneous dual nickel/photocatalytic carbon-heteroatom cross-couplings using graphitic carbon nitrides

The first milestone towards my ultimate goal, the development of truly sustainable carbon-heteroatom cross-couplings, was the application of a heterogeneous organic semiconductor as the photocatalyst in nickel catalyzed cross-couplings (Chapter 3). It was shown that in combination with a simple nickel complex, graphitic carbon nitrides, a class of metal-free, polymeric semiconductors that can be prepared from inexpensive and abundant bulk chemicals, can induce selective C–O cross-couplings of aryl halides and carboxylic acids (Scheme 7.1). The study with the title “Semi-Heterogeneous Dual Nickel/Photocatalysis using Carbon Nitrides: Esterification of Carboxylic Acids with Aryl Halides” was published in *Angewandte Chemie International Edition*.

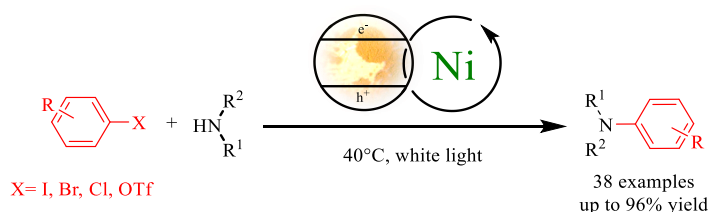


Scheme 7.1. Semi-heterogeneous dual nickel/ photocatalytic C–O couplings of aryl iodides and carboxylic acids using a carbon nitride as photocatalyst.

Among the tested carbon nitrides, the material CN-OA-m, which was prepared by calcination of urea and oxamide at 500 °C, followed by anaerobic polymerization at 550 °C using molten potassium salts as a structural template gave the best results.¹¹ CN-OA-m absorbs visible-light up to 700 nm. The heterogeneous, organic photocatalyst in combination with a Ni^{II} salt and a bipyridyl ligand was applicable for a broad range of substrates in the cross-coupling of aryl iodides with carboxylic acids under white light irradiation. Limitations were identified for electron-rich aryl halides. In contrast to homogeneous protocol that uses Ir(ppy)₃ as photocatalysts¹², long reactions are necessary for aryl bromides. Kinetic analysis suggested that the photocatalyst facilitates oxidative addition to nickel by formation of aryl radicals.¹³ Due to the higher reduction potential of Ir^{III*}/Ir^{IV}, –1.73 V, this is faster for aryl iodides and bromides in comparison to the analogous excited state of the used graphitic carbon nitride which have a lower potential (up to –1.65 V vs SCE) and minimized capacity for electron transfer. Nevertheless, the carbon nitride material shows

superior properties in comparison to the homogeneous iridium photocatalyst, as it can promote the C–O arylation using green light and can be easily recycled multiple times without significant loss in efficiency.

By employing the same carbon nitride material for the coupling of aryl halides with amines, I could significantly expand the scope for dual nickel/photocatalytic C–N cross-couplings (Chapter 4/ Scheme 7.2). Previous reports on dual photoredox/nickel catalyzed C–N cross-couplings suffer from low yields for electron-rich aryl halides. I could identify that the formation of catalytically inactive nickel-black is responsible for this limitation and causes severe reproducibility issues. These results were published with the title “Overcoming Limitations in Dual Photoredox/Nickel catalyzed C–N Cross-Couplings due to Catalyst Deactivation” in *Nature Catalysis*.



Scheme 7.2. Semi-heterogeneous dual nickel/ photocatalytic C–N couplings of aryl halides and amines using a carbon nitride as photocatalyst.

During this study, I demonstrated that catalyst deactivation can be avoided by using the already introduced carbon nitride photocatalyst CN-OA-m. The catalyst deactivation *via* the formation of nickel black arises from the accumulation of low valent Ni^0 species during the slow oxidative addition of electron rich aryl halides. To countermeasure this undesired effect, the relative rate of oxidative addition (OA) must be equal or higher than the rate of reductive elimination (RE) (Figure 7.3). The carbon nitride material CN-OA-m absorbs weakly upon green light irradiation, and this ends up in a reduced rate of reductive elimination compared to blue light irradiation. As a result of the broad absorption of the heterogeneous photocatalyst a wavelength dependent control of the rate of reductive elimination was achieved and consequently nickel black formation was prevented during the coupling of cyclic, secondary amines with electron-neutral and electron-rich aryl bromides. Additionally, the recycling issues of the carbon nitride were overcome by switching from white light to green light to avoid catalyst deactivation due to nickel black formation. In this

way the heterogeneous photocatalyst could be recycled by simple centrifugation over five cycles without drop in efficiency.

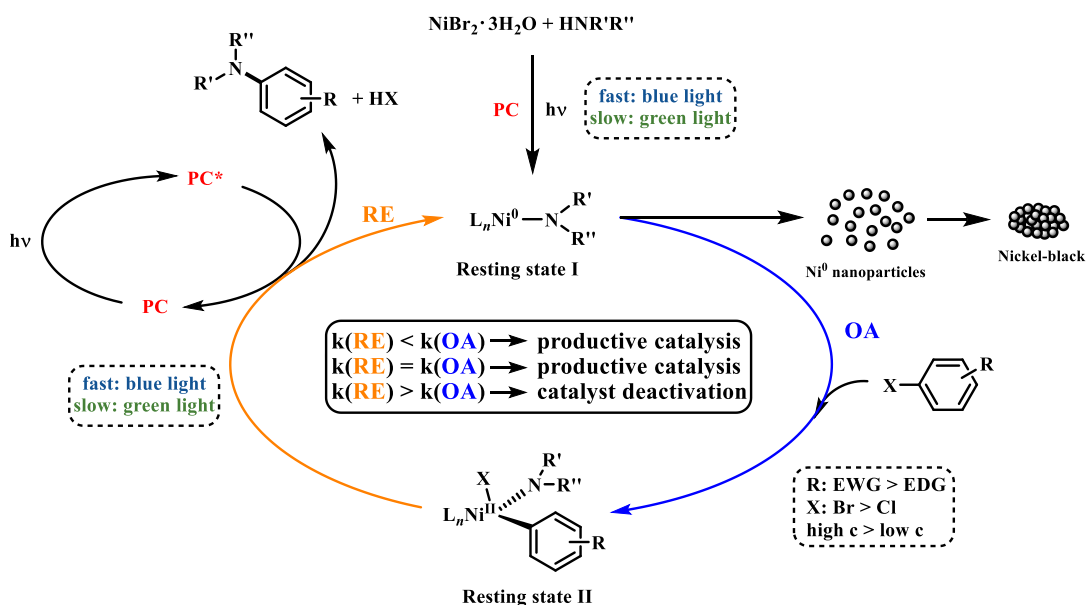


Figure 7.2. Catalyst deactivation due to photo-generated Ni^0 agglomerates (Nickel black).

In an alternative approach, the rate of oxidative addition could be increased by using a high substrate concentration. In this way even blue light irradiation could be used for the efficient and reproducible coupling of electron-rich aryl bromides and electron-poor aryl chlorides with secondary amines. For less nucleophilic, primary amines, it turned out that the coupling with electron-rich aryl halides is accomplishable by stabilizing low valent nickel intermediates with MTBD as an additive. These protocols enable reproducible, selective C–N cross-couplings of electron-poor as well as electron-rich aryl bromides and can be also applied for electron-poor aryl chlorides, which were previously challenging substrates for dual photoredox/nickel catalyzed C–N cross-coupling.

Next, the problems regarding scalability were tackled by developing a suitable continuous flow protocol. The difficulties associated with handling solids in flow were overcome by combining an oscillatory pump with a microstructured plug flow photoreactor (Chapter 5). In the presented work “An oscillatory plug flow photoreactor facilitates semi-heterogeneous dual nickel/carbon nitride photocatalytic C–N couplings“ published in *Reaction Chemistry & Engineering*, a stable suspension of the photocatalyst can be maintained and in this way

clogging of the reactor channels was avoided. Careful tuning of the oscillator properties enabled an optimized residence time distribution (RTD) and a stable catalyst suspension was preserved. In this manner the illumination efficiency of the reaction solution was improved and consequently short residence times (20 min) were attained. Throughout a stable 4.5 hour scale-out demonstration, a model compound could be prepared on a multigram scale (Figure 7.3).

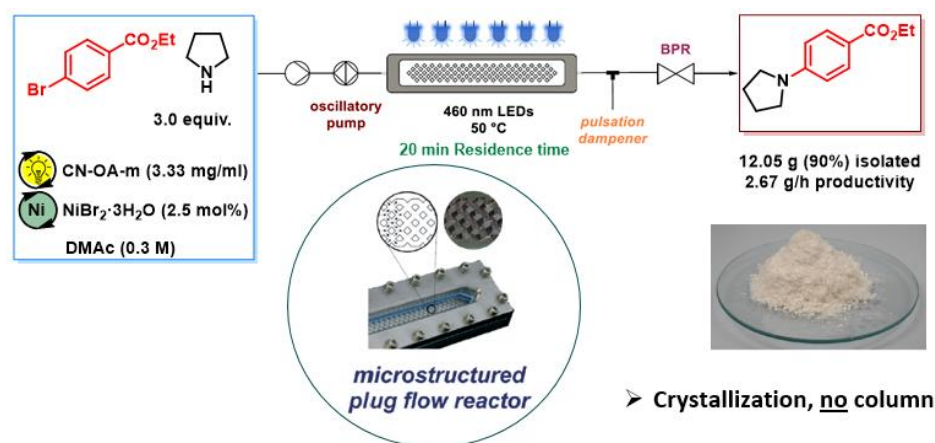


Figure 7.3. An oscillatory plug flow photoreactor facilitates semi-heterogeneous dual nickel/carbon nitride photocatalytic C–N couplings.

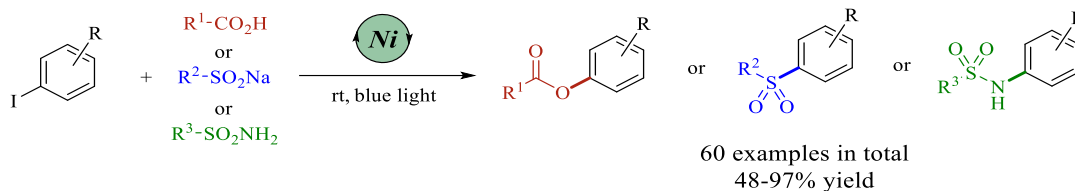
Using these conditions, the recyclability of the photocatalyst was also demonstrated over 10 cycles with no loss of activity. Moreover, the technology was suitable to apply the semi-heterogeneous protocol for the gram-scale synthesis of an intermediate of the active pharmaceutical ingredient tetracaine.

7.3 Photocatalyst-free, visible-light-mediated nickel catalysis for carbon-heteroatom cross-couplings

Chapter 6, consists of the work “Photocatalyst-free, visible-light-mediated nickel catalysis for carbon–heteroatom cross-couplings”, which is available as a preprint on *ChemRxiv* and was submitted for publication to a peer-reviewed journal. This study constitutes a paradigm shift in metallaphotocatalytic cross-couplings by omitting the necessity of an exogenous photocatalyst.

The currently accepted mechanistic proposal for dual nickel/photocatalytic carbon–heteroatom cross-couplings suggests that the role of the excited photocatalyst is an initial reduction of a Ni^{II}-precatalyst, or re-activation of deactivated Ni^{II} species after off-cycle reactions¹⁴, to a catalytically active Ni^I-complex. After the initial activation, the reactions likely proceed through thermally sustained Ni^I-Ni^{III} cycles.¹⁵⁻¹⁶ This mechanistic proposal was further supported by the results of photocatalyst-free C–O and C–N couplings of aryl halides using substoichiometric amounts of zinc for the initial reduction of the inactive Ni^{II} complex to start the self-sustaining Ni^I/Ni^{III} cycle.¹⁷ Simultaneously, it was shown that the catalytically active Ni^I complexes were also formed by photoexcitation and disproportionation of Ni^{II} complexes under UV light irradiation.¹⁸ This concept was subsequently employed in photocatalyst-free C–N and C–O cross-coupling reactions.¹⁹⁻²² Despite that progress, the demand of UV light irradiation for excitation of these nickel catalysts can cause side reactions resulting in low selectivity.

Together with my colleagues, I showed that the requirement of an exogenous photocatalyst to harness the energy of visible light for the reduction of the Ni^{II} pre-catalyst to the active Ni^I species can be overcome by a functionalized bipyridyl ligand that forms a visible-light responsive nickel complex. Therefore, the ligand 5,5'-dicarbazolyl-2,2'-bipyridyl²³ (czbpy), which contains bipyridyne as chelating unit and two carbazole units that extend the absorption of the resulting nickel complex up to 450 nm, was synthesized. The nickel complex can promote cross-coupling of aryl iodides with carboxylic acids, sodium sulfonates, and sulfonamides under blue light irradiation without an additional photocatalyst (Scheme 7.3).



Scheme 7.3. Photocatalyst-free, visible-light-mediated nickel catalysis for C–O, C–S and C–N couplings.

With the aid of Fe^{III} chloride, the czbpy ligand can be polymerized affording a porous organic polymer (poly-czbpy). The formed heterogeneous ligand framework incorporates nickel by coordination to the nitrogen atoms of bipyridine units, which was validated by XPS analysis. The macrocomplex absorbs visible light up to 600 nm and is also able to catalyze the light-mediated cross-couplings of aryl iodides with carboxylic acid, sodium sulfonates and sulfonamides. Interestingly, lower nickel-to-polymer ratios proved to be beneficial due to the optimal immobilization of nickel into the ligand framework. ICP-OES analysis proved that approximately 40% of the bipyridine sites in the polymer structure are accessible for the coordination of nickel. Therefore, lowering the nickel salt/macroligand ratio led to less unligated nickel in solution, and thus less side reactions. In this way increased selectivity of the C–N, C–O and C–S coupling was obtained. The heterogeneous porous polymer with incorporated nickel can be recycled by simple centrifugation over at least 10 cycles without significant loss in efficiency for the C–S coupling (Figure 7.4).

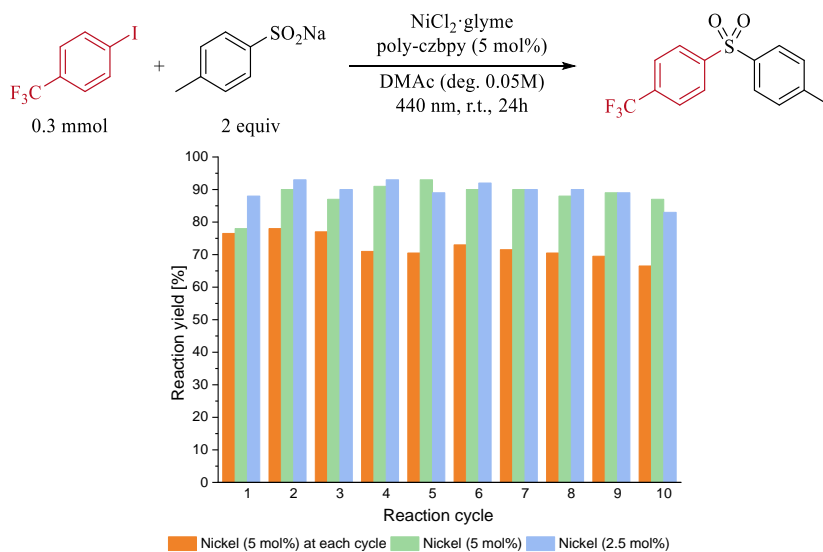


Figure 7.4. Recycling of the heterogeneous catalyst for the C–S coupling using different nickel loadings.

Chapter 7

Due to ability of this catalytic system to use visible light to promote reaction without the requirement of an exogeneous photocatalyst, an adaptable catalytic instrument for nickel catalyzed carbon-heteroatom cross-coupling reaction was created. The possibility to form a heterogeneous version of the ligand, and thereby immobilize and recycle the nickel catalyst increases the attractiveness considerably.

8.4 Outlook

In metallaphotocatalysis, a dedicated photocatalyst is commonly responsible for harvesting energy from light and activating the nickel catalyst towards carbon–heteroatom cross-couplings. Most protocols in dual nickel/photoredox protocols still rely on a dedicated, homogeneous noble metal based photocatalyst. I showed in the first action that these noble metal complexes can be replaced by sustainable and recyclable heterogeneous carbon nitride photocatalysts. Subsequently, I showed a completely new approach, in which tailored ligand design enables the utilization of visible-light for the direct excitation of the nickel catalyst. Thereby the effectiveness and sustainability of light-mediated nickel catalyzed cross-couplings was further increased. Polymerization of the ligand and immobilization of nickel into the ligand framework offers the opportunity of a fully recyclable catalyst system.

Based on these achievements, the next logical step is the synthesis of new ligands by rational ligand design, to study structure-activity relationships, tailor the absorbance of the formed nickel catalysts, and thereby broaden the scope and applicability of this approach. Systematic modifications of both, the carbazole substituents as well as the molecular core in terms of substitution pattern, can be employed to alter the redox potentials and absorption properties of the catalysts. Tuned redox potentials could enable the application of this catalytic platform for various carbon-carbon bond formations. This extension of the scope would be very appealing for many fields like medicinal chemistry and material science, as C–C cross-coupling methods are commonly used synthetic tools. Additionally, the possibility to couple nucleophiles with generally inexpensive aryl bromides or aryl chlorides, as well as pseudohalides would make the reaction more cost-efficient and versatile while increasing the interest of a broader scientific community. Furthermore, the feasibility of synthetic useful scale should be demonstrated. The proper strategy will be by development of a suitable continuous flow protocol. If the heterogeneous macroligand is employed, the combination of an oscillatory pump with a microstructured plug flow photoreactor, which was previously an excellent system for the handling of the heterogeneous carbon nitride photocatalyst, represents a good solution.

8.5 References

1. Brown, D. G.; Boström, J., Analysis of Past and Present Synthetic Methodologies on Medicinal Chemistry: Where Have All the New Reactions Gone? *J. Med. Chem.* **2016**, *59* (10), 4443-4458.
2. Devendar, P.; Qu, R.-Y.; Kang, W.-M.; He, B.; Yang, G.-F., Palladium-Catalyzed Cross-Coupling Reactions: A Powerful Tool for the Synthesis of Agrochemicals. *J. Agric. Food. Chem.* **2018**, *66* (34), 8914-8934.
3. Johansson Seechurn, C. C. C.; Kitching, M. O.; Colacot, T. J.; Snieckus, V., Palladium-Catalyzed Cross-Coupling: A Historical Contextual Perspective to the 2010 Nobel Prize. *Angew. Chem. Int. Ed.* **2012**, *51* (21), 5062-5085.
4. Ananikov, V. P., Nickel: The “Spirited Horse” of Transition Metal Catalysis. *ACS Catalysis* **2015**, *5* (3), 1964-1971.
5. Frisch, A. C.; Beller, M., Catalysts for Cross-Coupling Reactions with Non-activated Alkyl Halides. *Angew. Chem. Int. Ed.* **2005**, *44* (5), 674-688.
6. Lavoie, C. M.; Stradiotto, M., Bisphosphines: A Prominent Ancillary Ligand Class for Application in Nickel-Catalyzed C–N Cross-Coupling. *ACS Catal.* **2018**, *8* (8), 7228-7250.
7. Matsunaga, P. T.; Hillhouse, G. L.; Rheingold, A. L., Oxygen-atom transfer from nitrous oxide to a nickel metallacycle. Synthesis, structure, and reactions of [cyclic] (2,2'-bipyridine)Ni(OCH₂CH₂CH₂CH₂). *J. Am. Chem. Soc.* **1993**, *115* (5), 2075-2077.
8. Han, R.; Hillhouse, G. L., Carbon–Oxygen Reductive-Elimination from Nickel(II) Oxametallacycles and Factors That Control Formation of Ether, Aldehyde, Alcohol, or Ester Products. *J. Am. Chem. Soc.* **1997**, *119* (34), 8135-8136.
9. Anastas, P.; Eghbali, N., Green Chemistry: Principles and Practice. *Chem. Soc. Rev.* **2010**, *39* (1), 301-312.
10. Twilton, J.; Le, C.; Zhang, P.; Shaw, M. H.; Evans, R. W.; MacMillan, D. W. C., The merger of transition metal and photocatalysis. *Nat. Rev. Chem.* **2017**, *1*, 0052.
11. Zhang, G.; Li, G.; Lan, Z.-A.; Lin, L.; Savateev, A.; Heil, T.; Zafeiratos, S.; Wang, X.; Antonietti, M., Optimizing Optical Absorption, Exciton Dissociation, and Charge Transfer of a Polymeric Carbon Nitride with Ultrahigh Solar Hydrogen Production Activity. *Angew. Chem. Int. Ed.* **2017**, *56* (43), 13445-13449.

12. Welin, E. R.; Le, C.; Arias-Rotondo, D. M.; McCusker, J. K.; MacMillan, D. W. C., Photosensitized, energy transfer-mediated organometallic catalysis through electronically excited nickel(II). *Science* **2017**, *355* (6323), 380-385.
13. Malik, J. A.; Madani, A.; Pieber, B.; Seeberger, P. H., Evidence for Photocatalyst Involvement in Oxidative Additions of Nickel-Catalyzed Carboxylate O-Arylations. *J. Am. Chem. Soc.* **2020**, *142* (25), 11042-11049.
14. Till, N. A.; Tian, L.; Dong, Z.; Scholes, G. D.; MacMillan, D. W. C., Mechanistic Analysis of Metallaphotoredox C–N Coupling: Photocatalysis Initiates and Perpetuates Ni(I)/Ni(III) Coupling Activity. *J. Am. Chem. Soc.* **2020**, *142* (37), 15830-15841.
15. Qin, Y.; Sun, R.; Gianoulis, N. P.; Nocera, D. G., Photoredox Nickel-Catalyzed C–S Cross-Coupling: Mechanism, Kinetics, and Generalization. *J. Am. Chem. Soc.* **2021**, *143* (4), 2005-2015.
16. Sun, R.; Qin, Y.; Rucolo, S.; Schnedermann, C.; Costentin, C.; Daniel, G. N., Elucidation of a Redox-Mediated Reaction Cycle for Nickel-Catalyzed Cross Coupling. *J. Am. Chem. Soc.* **2019**, *141* (1), 89-93.
17. Sun, R.; Qin, Y.; Nocera, D. G., General Paradigm in Photoredox Nickel-Catalyzed Cross-Coupling Allows for Light-Free Access to Reactivity. *Angew. Chem. Int. Ed.* **2020**, *59* (24), 9527-9533.
18. Shields, B. J.; Kudisch, B.; Scholes, G. D.; Doyle, A. G., Long-Lived Charge-Transfer States of Nickel(II) Aryl Halide Complexes Facilitate Bimolecular Photoinduced Electron Transfer. *J. Am. Chem. Soc.* **2018**, *140* (8), 3035-3039.
19. Yang, L.; Lu, H.-H.; Lai, C.-H.; Li, G.; Zhang, W.; Cao, R.; Liu, F.; Wang, C.; Xiao, J.; Xue, D., Light-Promoted Nickel Catalysis: Etherification of Aryl Electrophiles with Alcohols Catalyzed by a NiII-Aryl Complex. *Angew. Chem. Int. Ed.* **2020**, *59* (31), 12714-12719.
20. Li, G.; Yang, L.; Liu, J.-J.; Zhang, W.; Cao, R.; Wang, C.; Zhang, Z.; Xiao, J.; Xue, D., Light-Promoted C–N Coupling of Aryl Halides with Nitroarenes. *Angew. Chem. Int. Ed.* **2021**, *60* (10), 5230-5234.
21. Lim, C.-H.; Kudisch, M.; Liu, B.; Miyake, G. M., C–N Cross-Coupling via Photoexcitation of Nickel–Amine Complexes. *J. Am. Chem. Soc.* **2018**, *140* (24), 7667-7673.

Chapter 7

22. Xue, D.; Song, G.; Yang, L.; Li, J.-S.; Tang, W.-J.; Zhang, W.; Cao, R.; Wang, C.; Xiao, J., Chiral Arylated Amines via C-N Coupling of Chiral Amines with Aryl Bromides Promoted by Light. *Angew. Chem. Int. Ed.* **2021**, *60*, 21536.
23. Liang, H.-P.; Acharjya, A.; Anito, D. A.; Vogl, S.; Wang, T.-X.; Thomas, A.; Han, B.-H., Rhenium-Metalated Polypyridine-Based Porous Polycarbazoles for Visible-Light CO₂ Photoreduction. *ACS Catal.* **2019**, *9* (5), 3959-3968.

Abbreviations List

ξ	Photon efficiency
Φ	Quantum yield
$^1\text{O}_2$	Singlet oxygen
$^3\text{MLCT}$	Triplet excited state resulting from a metal-to-ligand charge transfer transition
4-CzIPN	1,2,3,5-Tetrakis(carbazol-9-yl)-4,6-dicyanobenzene
A	Electron acceptor
acac	Acetylacetonate
API	Active pharmaceutical ingredient
ARS	Alizarin red s (3,4-Dihydroxy-9,10-dioxo-9,10-dihydroanthracene-2-sulfonic acid)
ATRA	Atom transfer radical addition
BET	Brunauer-Emmett-Teller (surface area)
BINAP	2,2'-Bis(diphenylphosphino)-1,1'-binaphthyl
BIPA	<i>N-tert</i> -Butylisopropylamine
Bo	Bodenstein number
Boc-Pro-OH	<i>N</i> -(<i>tert</i> -Butoxycarbonyl)proline
BODIPY	Boron dipyrromethenes
Bpin	Boronic acid pinacolate ester
bpy	2,2'-Bipyridine
bpz	2,2'-Bipyrazine
Brettphos	2-(Dicyclohexylphosphino)3,6-dimethoxy-2',4',6'-triisopropyl-1,1'-biphenyl
BTMG	2- <i>tert</i> -Butyl-1,1,3,3-tetramethylguanidine
Bz	Benzoyl

CB	Conduction band
cbz	Benzyloxycarbonyl
CDC	Cross-dehydrogenative coupling
CMB-CN	Carbon nitride material from cyanuric acid, melamine and barbituric acid
CMP	Conjugated microporous polymer
CN	Carbon nitride
CN-OA-m	Carbon nitride based on urea and oxamide, synthesized in molten salt
COD	1,5-Cyclooctadiene
COF	Covalent organic framework
ConPET	Consecutive photoinduced electron transfer
CTF	Covalent triazine network
CV	Cyclic voltammetry
CyPF- <i>t</i> -Bu	(R)-1-[(SP)-2-(Dicyclohexylphosphino)ferrocenyl]ethyldi-tert-butylphosphine
czbpy	5,5'-Dicarbazolyl-2,2'-bipyridyl
D	Electron donor
d	Doublet
DABCO	1,4-Diazabicyclo[2.2. 2]octane
Davephos	2-Dicyclohexylphosphino-2'-(<i>N,N</i> -dimethylamino)biphenyl
DBU	1,8-Diazabicyclo[5.4.0]undec-7-ene
DCE	Dichloroethane
DCM	Dichloromethane
dF(CF ₃)ppy	2-(2,4-Difluorophenyl)-5-(trifluoromethyl)pyridine
diglyme	Diethylene glycol dimethyl ether
DHIMQ	6,7-dihydroxy-2-methylisoquinolinium

DHIPQ	1,3-disubstituted-5,6-dihydropyrrolo[2,1-a]isoquinoline
DIPEA	<i>N,N</i> -diisopropylethylamine
DMA or DMAc	<i>N,N</i> -Dimethylacetamide
DMAP	<i>N,N</i> -Dimethylaminopyridine
dme	Dimethyl ether
DMF	<i>N,N</i> -Dimethylformamide
dmg	Dimethylglyoxime
DMPU	<i>N,N'</i> -Dimethylpropyleneurea
DMSO	Dimethylsulfoxide
donor*	Excited state participating in energy transfers
dppf	1,1'-Bis(diphenylphosphino)ferrocene
DSP	Dye-sensitized photocatalyst
DSSC	Dye-sensitized solar cell
dtbbpy	4,4'-Di-tert-butyl-2,2'-bipyridine
EDA	Electron-donor acceptor (complex)
EdX	Energy-dispersive X-ray
EI	Electronic ionization
EnT	Energy transfer
EPR	Electron paramagnetic resonance spectroscopy
ESI	Electrospray ionization
ET	Electron transfer
EY	Eosin Y
EY*	Excited state of Eosin Y
EY ^{ox}	Eosin Y after oxidative quenching
FDA	Formaldehyde dimethyl acetal
FEP	Fluorinated ethylene-propylene

Fmoc	9-Fluorenylmethoxycarbonyl
FTIR	Fourier-transform infrared spectroscopy
g-CN	Graphitic carbon nitride
glyme	1,2-Dimethoxyethane
HAADF	High-angle annular dark-field
HAT	Hydrogen atom transfer
HOMO	Highest occupied molecular orbital
HPLC	High-performance liquid chromatography
HR-MS	High resolution mass spectrometry
ICP-OES	Inductively coupled plasma - optical emission spectroscopy
ISC	Intersystem crossing
Josiphos	(2R)-1-[(1R)-1-(Dicyclohexylphosphino)ethyl]-2-(diphenylphosphino)ferrocene
K-PHI	Potassium poly(heptazine imide)
LD	Laser diffraction
LED	Light emitting diode
LUMO	Lowest unoccupied molecular orbital
m	Multiplet
MeCN	Acetonitrile
MeOH	Methanol
MLCT	Metal-to-ligand charge transfer
MOF	Metal organic framework
mpg-CN	mesoporous graphitic carbon nitride
MTBD	7-Methyl-1,5,7-triazabicyclo[4.4.0]dec-5-en
n.d.	Not detected
n.d.o.	Not determined due to overlapping peaks

NCS	<i>N</i> -Chlorosuccinimide
NHC	<i>N</i> -Heterocyclic carbenes
NIR	near-infrared
NIS	<i>N</i> -Iodosuccinimide
NMR	Nuclear magnetic resonance spectroscopy
NP	Nanoparticle
Nu-H	Nucleophile in its protonated form
OA	Oxidative Addition
OMs	Methanesulfonate
OTf	Trifluoromethanesulfonate
OTs	<i>para</i> -Toluensulfonate
PC	Photocatalyst
PC*	Excited state of the photocatalyst
PC ^{·+}	Photocatalyst after oxidative quenching
PC ^{·-}	Photocatalyst after reductive quenching
PET	Photoinduced electron transfer
PFA	Perfluoroalkoxy polymer
Phos-Texas Red	5-(3-Aminoallyl)-2'-deoxyuridine 5'-triphosphate triethyl ammonium salt
ppy	2-Phenylpyridine
PRC	Photoredox catalysis
PSD	Particle size distribution
PTFE	Polytetrafluoroethylene
p-TSA	<i>para</i> -Toluensulfonic acid
q	Quartet
QD	Quantum dot

quinuclidine	1-Azabicyclo[2.2.2]octane
RE	Reductive Elimination
Rhodamine B	9-(2-Carboxyphenyl)-3,6-bis(diethylamino)xanthyliumchlorid
Rh-6G	Rhodamine 6G
RTD	Residence time distribution
s	Singlet
S ₀	Singlet state
S ₁	Singlet excited state
SCE	Saturated calomel electrode
SED	Sacrificial electron donor
SEM	Scanning electron microscopy
sens	Sensitizer
SET	Single electron transfer
S _N Ar	Nucleophilic aromatic substitutions
SMBR	Serial micro-batch reactors
STEM	Scanning transmission electron microscopy
t	Triplet
T ₁	Triplet excited state
TA	Transient absorption
TBAI	Tetrabutylammonium iodide
TBD	1,5,7-Triazabicyclodec-5-ene.
TEM	Transmission electron microscopy
TEMPO	2,2,6,6-Tetramethylpiperidine-1-oxyl
TEOA	Triethanolamine
TFE	Trifluoroethane
THF	Tetrahydrofurane

TLC	Thin layer chromatography
TMEDA	<i>N,N,N',N'</i> -tetramethylethylenediamine
TMG	1,1,3,3-Tetramethylguanidine
TMSCN	Trimethylsilyl cyanide
Tol	Toluene
Ts	<i>para</i> -Toluensulfonyl
UV	Ultraviolet
Vis	Visible
VB	Valence band
XPS	X-ray photoelectron spectroscopy
XRD	X-ray powder diffraction